frontiers | Research Topics

Drylands under the influence of climate change and human activities

Edited by
Zhiming Han, Mou Leong Tan, Jing Zhao,
Xiaoping Wang and Song Feng

Published in
Frontiers in Environmental Science

ISSN 1664-8714
ISBN 978-2-8325-7281-8
DOI 10.3389/978-2-8325-7281-8

Generative AI statement
Any alternative text (Alt text) provided alongside figures in the articles in this ebook has been generated by Frontiers with the support of artificial intelligence and reasonable efforts have been made to ensure accuracy, including review by the authors wherever possible. If you identify any issues, please contact us.

About Frontiers

Frontiers is more than just an open access publisher of scholarly articles: it is a pioneering approach to the world of academia, radically improving the way scholarly research is managed. The grand vision of Frontiers is a world where all people have an equal opportunity to seek, share and generate knowledge. Frontiers provides immediate and permanent online open access to all its publications, but this alone is not enough to realize our grand goals.

Frontiers journal series

The Frontiers journal series is a multi-tier and interdisciplinary set of open-access, online journals, promising a paradigm shift from the current review, selection and dissemination processes in academic publishing. All Frontiers journals are driven by researchers for researchers; therefore, they constitute a service to the scholarly community. At the same time, the *Frontiers journal series* operates on a revolutionary invention, the tiered publishing system, initially addressing specific communities of scholars, and gradually climbing up to broader public understanding, thus serving the interests of the lay society, too.

Dedication to quality

Each Frontiers article is a landmark of the highest quality, thanks to genuinely collaborative interactions between authors and review editors, who include some of the world's best academicians. Research must be certified by peers before entering a stream of knowledge that may eventually reach the public - and shape society; therefore, Frontiers only applies the most rigorous and unbiased reviews. Frontiers revolutionizes research publishing by freely delivering the most outstanding research, evaluated with no bias from both the academic and social point of view. By applying the most advanced information technologies, Frontiers is catapulting scholarly publishing into a new generation.

What are Frontiers Research Topics?

Frontiers Research Topics are very popular trademarks of the *Frontiers journals series*: they are collections of at least ten articles, all centered on a particular subject. With their unique mix of varied contributions from Original Research to Review Articles, Frontiers Research Topics unify the most influential researchers, the latest key findings and historical advances in a hot research area.

Find out more on how to host your own Frontiers Research Topic or contribute to one as an author by contacting the Frontiers editorial office: frontiersin.org/about/contact

Drylands under the influence of climate change and human activities

Topic editors

Zhiming Han — Northwest A&F University, China
Mou Leong Tan — Universiti Sains Malaysia, Malaysia
Jing Zhao — Xi'an University of Technology, China
Xiaoping Wang — Northwest A&F University, China
Song Feng — University of Arkansas, United States

Citation

Han, Z., Tan, M. L., Zhao, J., Wang, X., Feng, S., eds. (2025). *Drylands under the influence of climate change and human activities*. Lausanne: Frontiers Media SA. doi: 10.3389/978-2-8325-7281-8

Table of contents

frontiers | Frontiers in Environmental Science

TYPE Original Research
PUBLISHED 21 March 2024
DOI 10.3389/fenvs.2024.1385604

OPEN ACCESS

EDITED BY
Xiaoping Wang,
Northwest A&F University, China

REVIEWED BY
Wang Juan,
Soil and Water Conservation Monitoring Center of Pearl River Basin, Pearl River, China
Zhenyu Zhang,
Nanjing University, China

*CORRESPONDENCE
Zhilei Zhen,
zhencheng@sxau.edu.cn

RECEIVED 14 February 2024
ACCEPTED 11 March 2024
PUBLISHED 21 March 2024

CITATION
Wang J, Lv Z, Cao Y, Wang S and Zhen Z (2024), Spatial-temporal evolution and influencing factors of ecological resilience in urban agglomerations: a case study of Shanxi section of the Yellow River Basin.
Front. Environ. Sci. 12:1385604.
doi: 10.3389/fenvs.2024.1385604

Spatial-temporal evolution and influencing factors of ecological resilience in urban agglomerations: a case study of Shanxi section of the Yellow River Basin

Jinfang Wang[1], Zhihong Lv[2], Ye Cao[1], Shifeng Wang[3] and Zhilei Zhen[1]*

[1]College of Urban and Rural Construction, Shanxi Agricultural University, Taigu, Shanxi, China, [2]School of Arts Communication, Jinzhong College of Information, Taigu, Shanxi, China, [3]Shanxi Yituo Land Engineering Consulting Co., Ltd., Taiyuan, Shanxi, China

Scientific assessment of the development status and factors influencing the urban ecological resilience of the Yellow River Basin (YRB) is highly significant for promoting its development. This study constructed an evaluation index system for urban ecological resilience considering the four dimensions of pressure, state, response, and innovation. The spatiotemporal ecological resilience of the urban agglomeration (UA) in the Shanxi section of the YRB from 2012 to 2021 was studied using kernel density estimation, Dagum Gini coefficient, and standard deviation ellipse, and the influencing factors of urban ecological resilience were analyzed using a geographic detector. This research revealed that (1) the ecological resilience of cities in the Shanxi section of the YRB experienced a fluctuation process of rise—fall—rise. The urban ecological resilience generally reflected a gradient decreasing spatial pattern of Central Shanxi UA > South Shanxi UA > North Shanxi UA, and gradually changed from the dual core of "Taiyuan—Jincheng City" to the single core of Taiyuan City. (2) The migration trajectory of urban ecological resilience center of gravity fluctuated in the direction of "northwest-southeast," and moved 12.63 km to the southeast overall. (3) The water supply per ten thousand Yuan GDP, occupied area of construction land per ten thousand Yuan GDP, green coverage rate in built-up areas, ratio of research and experimental development funds (R&D) to GDP, proportion of science and technology expenditure in local fiscal expenditure, and patent licensing quantity index have a high influence on urban ecological toughness at all stages. This influence was further strengthened by the interaction between factors. This study provides an important scientific basis for shaping high-quality development advantages in the YRB and creating a resilient and livable environment.

KEYWORDS

Yellow River Basin, urban ecological resilience, spatiotemporal evolution, high quality development, influencing factors

1 Introduction

With continuously advancing urbanization and industrialization, the excessive use of resources, environmental pollution, climate change, and other problems have a serious impact on the ecosystem (Li and Wang, 2023b), which weakens the ecological carrying capacity, increases the ecological risk, threatens the regional and even entire ecological security, and finally leads to a decrease in ecological resilience. The Yellow River Basin (YRB) is the birthplace of Chinese civilization and is an important economic zone and ecological barrier in China. It plays an important role in maintaining ecological security and promoting economic growth (Huang et al., 2023). In September 2019, China formally established a strategy for ecological protection and high-quality development of the YRB. The "Outline of the Plan for Ecological Protection and High-quality Development of the YRB" was issued in October 2021, which provides an important basis and action guide for the ecological environment protection of the YRB for the present and future.

Urban agglomeration (UA) is an important factor in YRB development. The key to realizing the development of ecological resilience in YRB lies in the effective improvement of urban ecological resilience in the UA (Wang et al., 2024). Shanxi Province is rich in mineral resources and is an important national energy base. Because of its special natural conditions and layout of economic and industrial structures, Shanxi Province has one of the most fragile ecological environments and weakest foundations in the YRB. The Shanxi section of the YRB is located in the arid and semi-arid regions of northern China, with an uneven distribution of resources, lack of water resources, and sensitive and fragile ecosystem. Cities in this region are relatively less resilient to disasters and their risks. Therefore, scientifically evaluating the spatiotemporal evolutionary characteristics and influencing factors of urban ecological resilience in the Shanxi section of the YRB is highly significant to determine the current status of urban ecological resilience in the region and explore ways to improve the adaptability and resilience of urban ecosystems to cope with increasingly serious environmental pressures and natural disasters.

In urbanized areas, the fragmentation of natural habitats, homogenization of species composition, destruction of hydrological systems, and changes in energy flow and nutrient cycling reduce cross-scale ecological resilience (Alberti and Marzluff, 2004). The "urban ecology" category includes human wellbeing, urban livability, ecosystem services, complex adaptive systems, and urban resilience, which emphasize the sustainable development of cities (Wu, 2014). Improving the resilience of urban ecosystems and building resilient cities to resist eco-environmental risks have become research hotspots. The connotations and research strategies for urban ecological resilience are constantly being updated. From the perspective of evolution theory, urban ecological resilience is an inherent property of urban ecosystems that undergoes non-deterministic dynamic evolution with time and emphasizes the learning ability and innovation of the system (Hosseini et al., 2016). Under the increasingly complex situation of system development and change, "evolutionary resilience" is more suitable for the current study of urban ecological resilience, which is helpful in realizing the leap from stable equilibrium to dynamic development (Boschma, 2015). Urban ecological resilience is based on "social-ecological" aspect, which enables urban ecosystems to adjust its structure and change its path to achieve transformation and development (Hosseini et al., 2016), reflecting the ability of urban ecosystem to resist pressure, respond and recover when it is affected by pressure and disturbance (Meerow et al., 2016). China's ecological environment resilience showed a increasing trend in fluctuations by the longitudinal and horizontal pull-out grading method (Li et al., 2023). Zhou et al. (2022) used the entropy and the linear weighting methods and the obstacle degree model to calculate the ecological resilience level and study its influence factors of UAs in Chengdu-Chongqing Economic Circle, suggesting an upward trend of ecological resilience level and disasters was the main influencing factors. When constructing an urban ecological resilience evaluation system, Yang et al. (2022) used the entropy weight method to evaluate the resilience level of cities in the Chengdu-Chongqing Economic Circle and used the Fuzzy Set Qualitative Comparative Analysis method to analyze the influencing factors, suggesting a relatively low urban resilience level and financial and innovation were the key driving factors. Lately, Liao and Zhang (2023) constructed an urban ecological resilience evaluation model based on resistance, adaptability, and resilience, and evaluated the spatiotemporal change pattern of urban ecological resilience in Guangzhou from 2000 to 2020, which suggested that the areas with low ecological resilience expanded to the northeast and southeast, while the areas with high ecological resilience decreased obviously. To sum up, the analysis showed that evaluation system and evaluation indicators remains in the exploration and improvement stages. At present, an evaluation system for urban ecological resilience research has not yet been developed for the YRB.

In this study, we considered the UA in the Shanxi section of the YRB as the research object, constructed an urban ecological resilience evaluation system from the four dimensions of "pressure-state-response-innovation", and revealed its spatiotemporal evolution characteristics based on urban socioeconomic data from 2012 to 2021. The Dagum-Gini coefficient was used to analyze spatial differences and their causes, and a standard deviation ellipse was used to analyze the spatial location and development trends of urban ecological resilience. Finally, geographical detectors were used to analyze the driving factors affecting urban ecological resilience. This research will help understand the evolutionary trends of urban ecological resilience in the Shanxi section of the YRB, clarify the development gaps between different UAs, and provide empirical support for shaping the high-quality development advantages of the YRB and creating a resilient and livable environment.

2 Data and methods

2.1 Study area

The Shanxi section is located in the middle reaches of the YRB. The Yellow River enters from Laoniuwan, Pianguan County, Xinzhou City, and exits from Nianpangou, Yuanqu County, Yuncheng City, with a total length of 965 km, nearly 1/5 of the

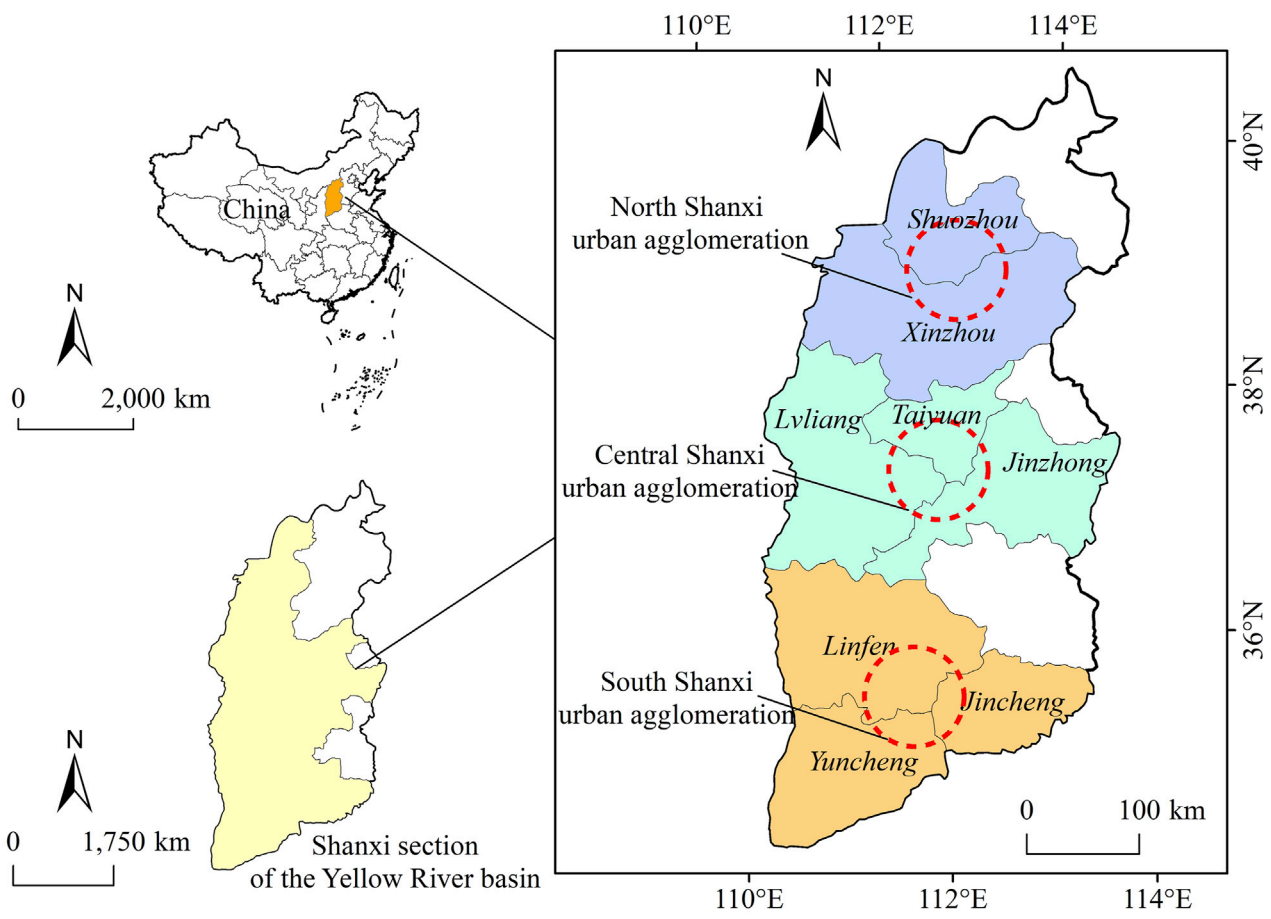

FIGURE 1
Urban agglomeration (UA) in Shanxi section of the YRB.

total length of the Yellow River. The Shanxi section of the YRB is located in Huangtu plateau, with various topographical features, with mountains and hills accounting for greater than 80%, and plains and basins in mountain valleys for approximately 20%. Shanxi Province has a temperate continental monsoon climate with four distinct seasons. The average annual temperature is 4.2°C–14.2°C and the annual precipitation is 350–625 mm. Based on the administrative unit of Shanxi section of the YRB and considering the integrity of the research region, the study area was defined as Shuozhou City, Xinzhou City, Lvliang City, Taiyuan City, Jinzhong City, Linfen City, Jincheng City and Yuncheng City. The study area was divided into North Shanxi UA (Shuozhou, Xinzhou), Central Shanxi UA (Lvliang, Taiyuan, Jinzhong), and South Shanxi UA (Linfen, Jincheng, Yuncheng) (Figure 1).

2.2 Data sources

The data used in this study were obtained from the Statistical Yearbook of Shanxi Province from 2012 to 2021 (https://tjj.shanxi.gov.cn/tjsj/), Statistical Yearbook of Urban Construction of China (https://www.mohurd.gov.cn/gongkai/fdzdgknr/sjfb/tjxx/jstjnj/index.html), Bulletin of Water Resources of Shanxi Province (https://slt.shanxi.gov.cn/), Bulletin of Environmental Status of Shanxi Province (https://sthjt.shanxi.gov.cn/zwgk/hjgb/hjzkgb/index.shtml), Statistical Bulletin of the National Economic and Social Development of Prefecture-Level Cities, and Final Accounts Report of the Government. The normalized vegetation Index (NDVI) was obtained from the Resource and Environmental Science and Data Center of the Chinese Academy of Sciences (http://www.resdc.cn/). Missing data were supplemented using linear interpolation. The initial data can be found in Supplementary Table S1.

2.3 Methods

2.3.1 Comprehensive evaluation model of urban ecological resilience

2.3.1.1 Entropy method

The entropy method (Wang et al., 2018; Chen et al., 2021) was used to assign the weight of the urban ecological resilience index of the UA in the Shanxi section of the YRB. First, the original data were normalized to ensure comparability (Chen et al., 2022). The formula is as follows:

$$\text{Positive index: } X'_{ij} = \left(X_{ij} - X_{min}\right) \Big/ \left(X_{max} - X_{min}\right) \quad (1)$$

$$\text{Negative index: } X'_{ij} = \left(X_{max} - X_{ij}\right) \Big/ \left(X_{max} - X_{min}\right) \quad (2)$$

TABLE 1 Index system of urban ecological resilience.

Target layer	First-level index	Secondary index	Unit	Attribute	Weight (%)
Urban ecological resilience	Pressure dimension	Water supply per ten-thousand Yuan GDP (X_{01})	m^3/ten-thousand yuan	-	2.20
		Comprehensive power consumption per ten-thousand Yuan GDP (X_{02})	kw·h/ten-thousand yuan	-	2.65
		Occupied area of construction land per ten-thousand Yuan GDP (X_{03})	km^2/yuan	-	0.46
		Industrial sulfur dioxide emissions per ten-thousand Yuan GDP (X_{04})	t/ten-thousand yuan	-	1.66
	State dimension	Total water resources per unit area (X_{05})	m^3/km^2	+	8.79
		Normalized vegetation index (X_{06})		+	1.93
		Green coverage rate in built-up area (X_{07})	%	+	1.18
		Excellent air days (X_{08})	day	+	2.13
	Response dimension	Centralized treatment rate of sewage treatment plant (X_{09})	%	+	0.64
		Harmless treatment rate of municipal solid waste (X_{10})	%	+	2.51
		Comprehensive utilization rate of general industrial solid waste (X_{11})	%	+	5.80
		Ratio of expenditure on energy conservation and environmental protection to local fiscal expenditure (X_{12})	%	+	12.58
	Innovation dimension	Ratio of research and experimental development funds (R&D) to GDP (X_{13})	%	+	16.24
		The proportion of science and technology expenditure in local fiscal expenditure (X_{14})	%	+	13.90
		Patent licensing quantity index (X_{15})	Number	+	27.32

Here, X_{ij} is the original value of the index j in year i, X_{max} and X_{min} are the maximum and minimum values of the same index, respectively, and $X_{ij}^{'}$ is the normalized value.

Second, the specific gravity (P_{ij}) of index j in the ith year is calculated as follows:

$$P_{ij} = X_{ij}^{'} \Big/ \sum_{i=1}^{n} X_{ij}^{'} \tag{3}$$

Third, the information entropy (e_j) and utility value (d_j) of index j are calculated as follows:

$$e_j = -k \sum_{i=1}^{n} P_{ij} \ln P_{ij} \tag{4}$$

$$d_j = 1 - e_j \tag{5}$$

$$k = 1 / \ln(n) \tag{6}$$

Finally, the weight (W_j) of each index was obtained and the value of urban ecological resilience (Y) was calculated as follows:

$$W_j = d_j \Big/ \sum_{j=1}^{n} d_j \tag{7}$$

$$Y = \sum X_{ij}^{'} W_j \tag{8}$$

2.3.1.2 Evaluation model

Based on existing documents (Li and Wang, 2023b; Huang et al., 2023), this study constructed an index system of urban ecological resilience from the four dimensions of "pressure-state-response-innovation" (Table 1). Among the dimensions, pressure indicates the disturbance and impact of human production and living activities on the urban ecosystem (Zhou et al., 2022); state refers to the recovery state of the urban ecosystem in the face of pressure in terms of ecological environment and biological resources (Zhou et al., 2022); response is the ability to adjust the function and structure of the ecosystem upon disturbance (Li and Wang, 2023b); and innovation is the ability of the ecosystem to achieve ecological resilience evolution and development through learning and innovation (Wang et al., 2024).

2.3.2 Kernel density estimation

Kernel density estimation describes the distribution characteristics of random variables using continuous density curves (Zambom and Ronaldo, 2013) and is a nonparametric estimation method for studying spatially unbalanced distributions. The formula is as follows:

$$f(x) = \frac{1}{nh} \sum_{h}^{n} k\left(\frac{X_i - x}{h}\right) \tag{9}$$

Here, $f(x)$ is the kernel density function, X_i is the ecological resilience of city i, x is the average ecological resilience of each city, n is the number of cities, h is the bandwidth, and $k\left(\frac{X_i - x}{h}\right)$ is the Gaussian function.

2.3.3 Dagum Gini coefficient

The Dagum-Gini coefficient can measure several sub-regions decomposed from the study area and calculate overall, intra-

regional, and inter-regional differences (Zhang et al., 2022). The formula is as follows:

$$G = \frac{\sum_{j=1}^{k}\sum_{h=1}^{k}\sum_{i=1}^{n_j}\sum_{r=1}^{n_h}\left|x_{ji} - x_{hr}\right|}{2n^2\bar{x}} \tag{10}$$

Here, n represents the number of cities in the Shanxi section, $\bar{x}$ represents the average development level of urban ecological resilience in the Shanxi section, and k represents the number of divided study areas (three in this study). n_j and n_h represent the number of cities in j and h, respectively; x_{ji} and x_{hr} represent the development level of urban ecological resilience in j and h, respectively.

The Dagum–Gini coefficient can be divided into three parts: intra-regional difference G_w, inter-regional difference G_{nb}, and hypervariable density G_t. The formula is as follows:

$$G = G_w + G_{nb} + G_t \tag{11}$$

$$G_w = \sum_{j=1}^{k} G_{jj}P_jS_j \tag{12}$$

$$G_{jj} = \frac{\sum_{i=1}^{n_j}\sum_{r=1}^{n_h}\left|x_{ji} - x_{jr}\right|}{2\bar{x}n_j^2} \tag{13}$$

$$G_{nb} = \sum_{j=2}^{k}\sum_{h=1}^{j-1} G_{jh}\left(P_jS_h + P_hS_j\right)D_{jh} \tag{14}$$

$$G_{jh} = \frac{\sum_{i=1}^{n_j}\sum_{r=1}^{n_h}\left|x_{ji} - x_{hr}\right|}{n_jn_h\left(\bar{x}_j + \bar{x}_h\right)} \tag{15}$$

$$G_t = \sum_{j=2}^{k}\sum_{h=1}^{j-1} G_{jh}\left(P_jS_h + P_hS_j\right)\left(1 - D_{jh}\right) \tag{16}$$

$$D_{jh} = \frac{d_{jh} - P_{jh}}{d_{jh} + P_{jh}} \tag{17}$$

$$d_{jh} = \int_0^{\infty} dF_j(x)\int_0^{x}(x - y)dF_h(y) \tag{18}$$

$$P_{jh} = \int_0^{\infty} dF_h(x)\int_0^{x}(x - y)dF_j(y) \tag{19}$$

Here, G_{jj} is the Gini coefficient in partition j, G_{jh} is the Gini coefficient between the areas between j and h, D_{jh} is the influence degree of relative contribution rate between j and h divisions, d_{jh} is the difference in contribution rate between regions, P_{jh} is the difference in the contribution rate of the remaining terms of the cross-influence between j and h subregions.

2.3.4 Standard deviation ellipse

Using the standard deviation ellipse model, the main spatial layout and dynamic development trend of UA urban ecological resilience in the Shanxi section of the YRB were analyzed for the study period (Yuill, 1971; Song et al., 2017). The formula is as follows:

$$\bar{X} = \frac{\sum_{i=1}^{n}W_iX_i}{\sum_{i=1}^{n}W_i};\ \bar{Y} = \frac{\sum_{i=1}^{n}W_iY_i}{\sum_{i=1}^{n}W_i} \tag{20}$$

$$S = \pi\sigma_X\sigma_Y \tag{21}$$

Here, n is the number of cities, $(\bar{X}, \bar{Y})$ is the center of gravity coordinates of urban ecological resilience, (X_i, Y_i) is the geographical coordinates of city i, W_i is the development level of ecological resilience of each city, σ_X and σ_Y are the standard deviations of X and Y axis, respectively; S is the center of gravity migration distance.

TABLE 2 Interaction types of two independent variables on dependent variables.

Criterion	Interaction
$q\ (x_1 \cap x_2) < min\ (q\ (x_1), q\ (x_2))$	Nonlinear weakening
$min\ (q(x_1), q\ (x_2)) < q\ (x_1 \cap x_2) < max\ (q\ (x_1), q\ (x_2))$	One-factor nonlinear weakening
$max\ (q\ (x_1), q\ (x_2)) < q\ (x_1 \cap x_2)$	Two-factor enhancement
$q\ (x_1 \cap x_2) > q\ (x_1) + q\ (x_2)$	Independent
$q\ (x_1 \cap x_2) = q\ (x_1) + q\ (x_2)$	Nonlinear enhancement

2.3.5 Geographic detector

A geographic detector is a first-order statistical method for detecting spatial differentiation and indicating the driving force behind it (Wang and Xu, 2017). The formula is as follows:

$$q = 1 - \frac{\sum_{h=1}^{L}N_h\sigma_h^2}{N\sigma^2} = 1 - \frac{SSW}{SST} \tag{22}$$

Here, h is the stratification of variable Y or factor X, N_h and N are the number of units of layer h and the entire region, respectively; σ_h^2 and σ^2 are the variance of layer h and Y value of the entire region, respectively; SSW and SST are the sum of variance in the layer and the total variance of the entire region, respectively; q is the influence of the influence factor on urban ecological resilience, with a value from 0 to 1. The higher the q value, the more clear the influence.

Interaction detection identifies the interaction effects of different influencing factors and evaluates the effect of increasing or weakening the dependent variable when these factors work together (Wang et al., 2010). First, the q values of the two factors are calculated, recorded as $q(x_1)$ and $q(x_2)$, respectively, and then the superimposed q values of the two factors are calculated as $q(x_1 \cap x_2)$. By comparing the relationships among $q(x_1)$, $q(x_2)$, and $q(x_1 \cap x_2)$, five interaction types were obtained (Table 2).

3 Results and analysis

3.1 Temporal evolution characteristics of urban ecological resilience in shanxi section of the YRB

During the period 2012–2021, the average level of ecological resilience in UAs of the Shanxi section of YRB was relatively low, and had experienced a fluctuation trend of "rise—fall—rise," with an overall upward trend (Figure 2). The average urban ecological resilience increased from 0.192 in 2012 to 0.233 in 2013, fell to a minimum of 0.188 in 2015, and then slowly rose to 0.319 by 2021, with a average of 0.213 from 2012 to 2021. The urban ecological resilience of the Central Shanxi UA was always higher than the average level of the study area, with an annual average of 0.269 and an average annual growth rate of 8.15%. The urban ecological resilience of South Shanxi UA was slightly lower than average, with an annual average of 0.194 and an average annual growth rate of 4.92%. The development in the North Shanxi UA was relatively

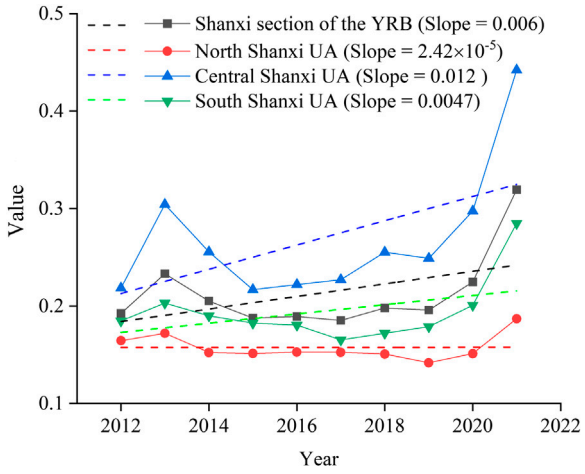

FIGURE 2
Trend of urban ecological resilience of UAs in Shanxi Section of the YRB.

backward, with an annual average of 0.158 and an average annual growth rate of 1.44%.

The kernel density estimate (Figure 3) revealed that the Shanxi section of the YRB had an overall right shift in 2012 and 2021. The kernel density curves in Central Shanxi UA and South Shanxi UA gradually shifted to the right to different degrees, indicating improvements in the level of urban ecological resilience and some achievements in the ecological protection of the YRB. The curve of North Shanxi UA had a small movement to the right, and with no noticeable improvement in urban ecological resilience.

In terms of the curve distribution pattern (Figure 3), the main peak of the kernel density curve in the Shanxi section of the YRB decreased, and the width gradually increased after fluctuation, indicating a gradually increasing absolute difference in urban ecological resilience in the study area. The width and height of the main peak of the North Shanxi UA decreased slightly, with no large change overall, indicating that the absolute difference in urban ecological resilience in the region was stable, with a decreasing trend. The height of the main peak of the Central Shanxi UA first increased and then decreased, and the width fluctuated and then decreased slightly, indicating that the absolute difference in urban ecological resilience in the region tended to decrease. The main peak of the South Shanxi UA exhibited a downward trend and the width increased slightly, indicating a gradual expansion in the absolute difference in urban ecological resilience.

From the perspective of the curve distribution ductility (Figure 3), the left trailing distribution of the Shanxi section of the YRB remained unchanged, the right trailing gradually elongated, and the extension of the curve expanded. High values of urban ecological resilience have appeared and gradually increased in this region. The curve of the North Shanxi UA was basically unchanged on the left trailing and slightly elongated on the right trailing, with little change overall, indicating that the curve of the North Shanxi UA had a certain extension convergence, with more synchronous urban development in the region. The curves of the Central Shanxi UA and South Shanxi UA shortened annually, while the right trailing gradually lengthened, indicating that the extension of these regional distribution curves was expanding.

In terms of polarization characteristics, the kernel density curves of the Shanxi section of the YRB and the three urban agglomerations were all single peaks, indicating that the level of urban ecological resilience was in a single equilibrium, with no noticeable polarization.

3.2 Spatial evolution characteristics of urban ecological resilience in shanxi section of the YRB

3.2.1 Spatial distribution characteristics

As suggested by Fan (2023) and the actual situation of urban ecological resilience in the Shanxi section of the YRB, the UAs was divided into five levels by the deviation ratio around the average of 0.213: low, medium-low, medium, medium-high, and high (Table 3). The urban ecological resilience of the Shanxi section of the YRB generally exhibited a gradient of decreasing spatial pattern in the order Central Shanxi UA > South Shanxi UA > North Shanxi UA (Figure 4). In Central Shanxi UA, the ecological resilience of Taiyuan City was high, rising from 0.299 in 2012 to 0.485 in 2021. The level of ecological resilience in Jinzhong City improved significantly from 0.184 in 2012 to 0.545 in 2021. The level of ecological resilience in Lvliang City increased slowly from 0.172 in 2012 to 0.296 in 2021. In the South Shanxi UA, the ecological resilience of Jincheng City was high, ranging from 0.240 in 2012 to 0.408 in 2021, Yuncheng City from 0.151 in 2012 to 0.211 in 2021, and Linfen City from 0.164 in 2012 to 0.235 in 2021. The two cities in Northern Shanxi UA were below the medium level, and the level of resilience was low.

From 2012 to 2021, the urban ecological resilience gradually changed from Taiyuan—Jincheng City spatial dual-core leadership to Taiyuan City as a single core. The ecological resilience of Taiyuan, the capital of the Shanxi Province, was significantly higher than that of the other cities, resulting in a decrease in ecological resilience from the core to the peripheral cities. Economic and industrial development in North Shanxi has been restricted by resources for a long time. The ecological environment base is weak, and the improvement of urban ecological resilience is slow. In future developments, special attention should be paid to the ecological protection and governance of other cities.

From the changes in the urban ecological resilience grade in the Shanxi section of the YRB (Figure 5), a city with a medium-high level of ecological resilience in 2012 was optimized to a high level by 2021. Of the four cities that were at medium-low level in 2012, two developed to a high-level, one developed to a medium-high level, one remained at a medium-low level. Of the two cities that were at low-level in 2012, one developed to a medium-level, one developed to a medium-low level. One high-level cities in 2012 remained unchanged by 2021. The ecological resilience level of each city showed a trend of continuous optimization, generally floating at two adjacent levels, which indicates that although Shanxi Province attached great importance to the protection of the ecological environment and the industrial structure has gradually adjusted in the past 10 years, the urban eco-environmental problems have not been fully alleviated.

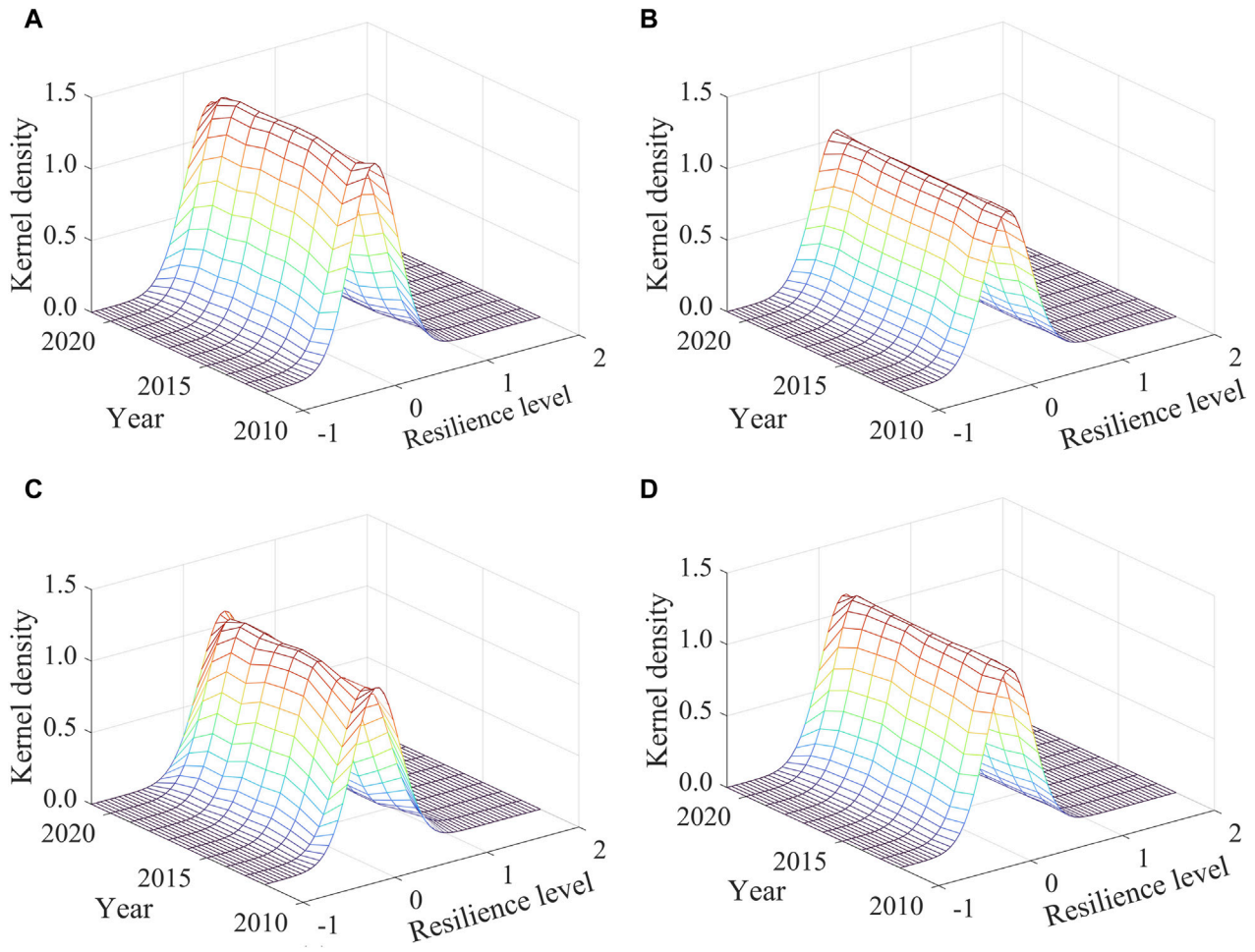

FIGURE 3
Kernel density estimation of urban ecological resilience of UA in Shanxi Section of the YRB. **(A)** Shanxi section of the YRB. **(B)** North Shanxi UA. **(C)** Central Shanxi UA. **(D)** South Shanxi UA.

TABLE 3 Classification of urban ecological resilience.

Level	Deviation ratio	Interaction
Low	−25% and below	(0,0.1598]
Medium-Low	(−25%,−10%]	(0.1599–0.1918]
Medium	(−10%,10%]	(0.1919–0.2344]
Medium-High	(10%,25%]	(0.2345–0.2663]
High	25% and above	(0.2664–0.5452]

3.2.2 Characteristics of spatial differences

The Gini coefficient of ecological resilience in the UAs of the Shanxi section of the YRB remained relatively low with a fluctuating upward trend (Figure 6). It decreased during 2013–2016 and 2018–2019, indicating a narrowing gap in urban ecological resilience and improved spatial balance during these periods. The increase in the Gini coefficient during 2012–2013, 2016–2018, and 2019–2021 indicated an expanding gap in urban ecological resilience, with evident spatial disequilibrium during these periods. The Gini coefficient in 2021 was the highest over the past decade, indicating that efforts should be made to narrow the differences between cities in the Shanxi section of the YRB.

The average Gini coefficient of the UAs was in the order: Central Shanxi (0.142) > South Shanxi (0.099) > North Shanxi (0.036) (Figure 6). The Central Shanxi UA had the highest Gini coefficient, indicating that the difference in ecosystem adaptability and resilience was owing to economic growth between cities within the UA. The ecological resilience of the North Shanxi UA was affected by geographical factors and the economic industrial structure. The regional differences were small and far lower than the average level in the Shanxi section of the YRB. Central Shanxi UA exhibited a fluctuating change with a decreasing trend. The regional difference in South Shanxi UA first decreased and then suddenly increased from 2020 to 2021, surpassing the Central Shanxi UA. The North Shanxi UA exhibited a fluctuating decreasing trend, the difference in ecological resilience between the two cities in the region gradually decreased, and development was gradually balanced.

The order of the average Gini coefficients among the three UAs in the Shanxi section of the YRB was: North and Central Shanxi

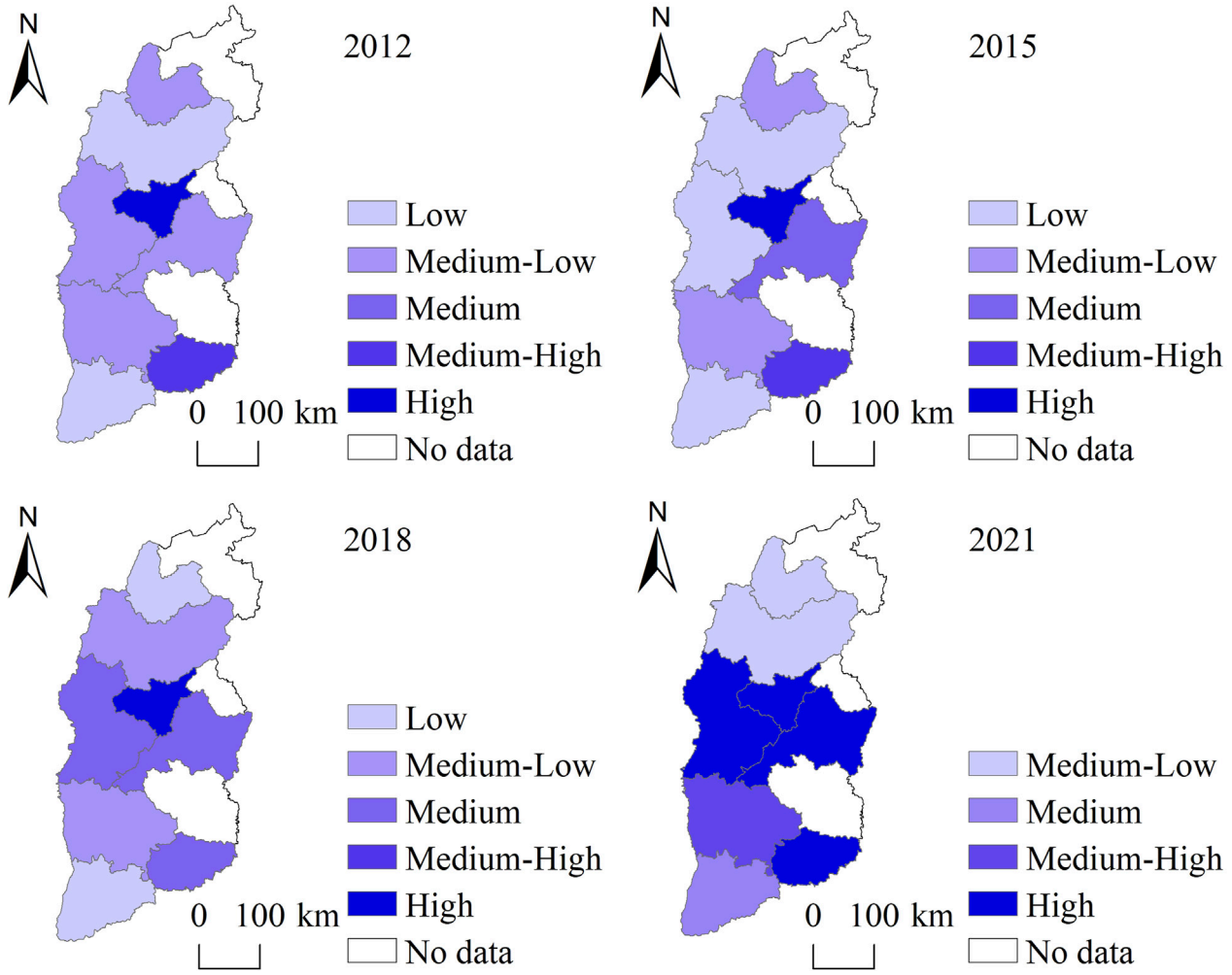

FIGURE 4
Spatial distribution of urban ecological resilience of UA in Shanxi Section of the YRB.

(0.252) > Central and South Shanxi (0.191) > North and South Shanxi (0.118). The gap in natural conditions, economic and social development, and ecological level between the North, Central, and South Shanxi UAs led to the greatest difference in ecological resilience between the North and Central Shanxi UAs and the smallest difference between the North and South Shanxi UAs. Evolutionally, although differences in the urban ecological resilience among the three UAs displayed several fluctuations in 2013, 2016, and 2018, overall they exhibited an upward trend, and the differences among the UAs gradually increased (Figure 7). The urban ecological resilience of Central Shanxi UA has grown rapidly in the past 10 years, and the difference between this and the other two UAs has gradually increased. The natural environment foundation of North Shanxi UA is weak, the infrastructure is not perfect, social and economic development is relatively lagging, and the improvement in urban ecological resilience is relatively slow.

The contribution rate of differences among UAs (65.82%) > differences within UAs (24.59%) > transariation (9.59%) (Figure 7). The development of differences within the UAs in the Shanxi section of the YRB was relatively stable, and exhibited a narrowing trend. The difference in change was mainly caused by the difference among the UAs, and this difference exhibited a rising trend. Combined with the above results, we should pay attention to the development of urban ecological resilience in North Shanxi UA and narrow the differences among the regions of North, Central, and South Shanxi UAs.

3.3 Characteristics of center of gravity transfer

From 2012 to 2021, the ecological resilience of UAs in the Shanxi section of the YRB demonstrated a north-south distribution and moved slightly to the southeast (Figure 8). The azimuth decreased from 4.02° in 2012° to 3.73° in 2015, then increased to 4.38° in 2018, and finally decreased to 3.11° in 2021, indicating a counterclockwise shift in urban ecological resilience (Table 4). The centers of urban ecological resilience in 2012, 2015, 2018, and 2021 were located in Lvliang Wenshui County (112.159591°E, 37.325122°N), Jinzhong Pingyao County (112.177048°E, 37.295967°N), Lvliang Wenshui County (112.158105°E, 37.344768°N), and Jinzhong Pingyao County (112.234174°E, 37.227414°N), respectively. The trajectory

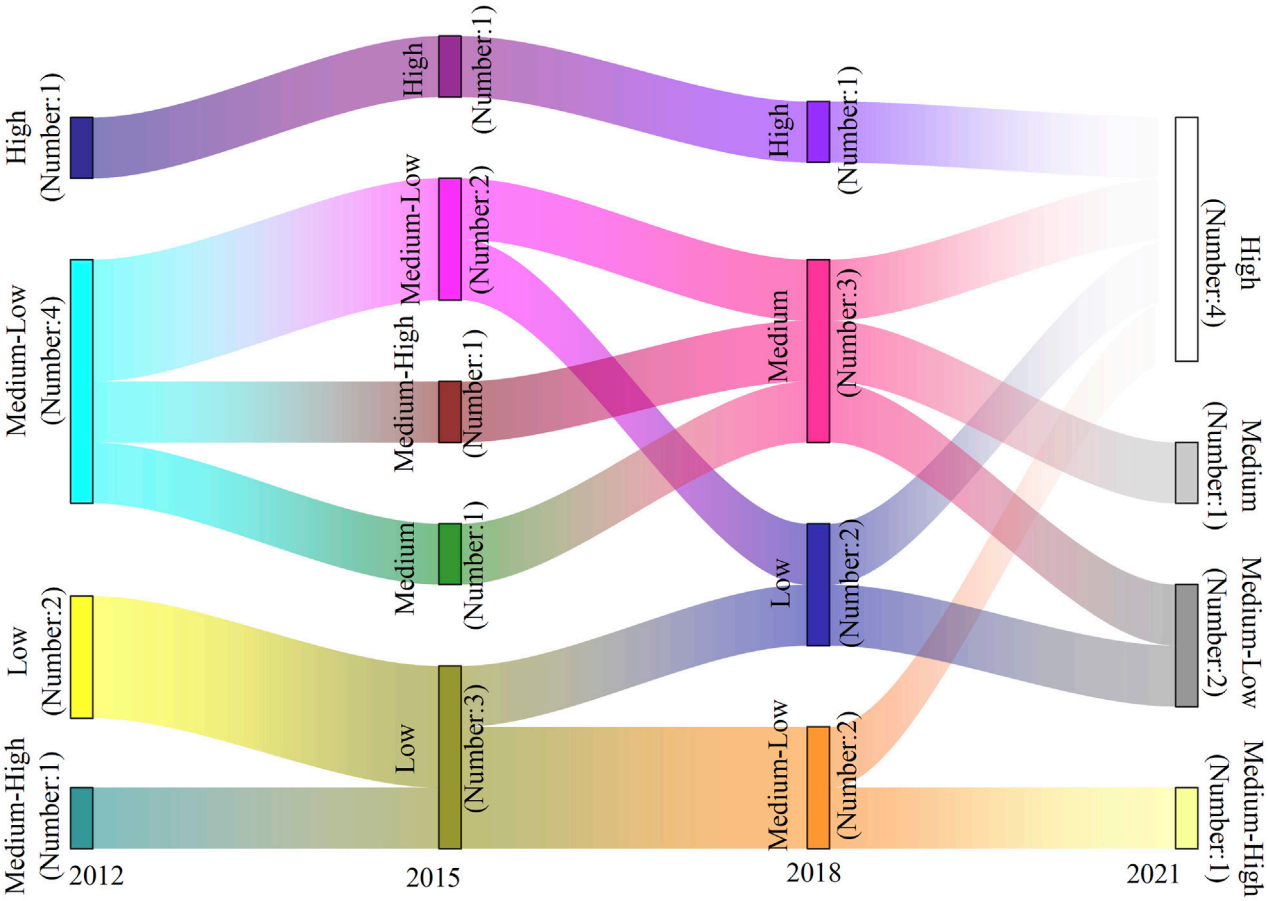

FIGURE 5
Change of ecological resilience grade of the UA in Shanxi Section of the YRB.

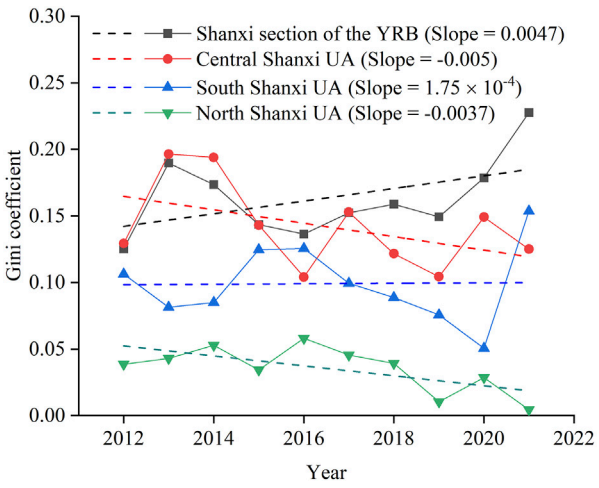

FIGURE 6
Difference of urban ecological resilience of the UA in Shanxi Section of the YRB.

of the center of gravity fluctuated in the northwest-southeast direction and moved 3.61 km from 2012 to 2015, 5.88 km from 2015 to 2018, 14.76 km from 2018 to 2021, and 12.63 km to the southeast overall. The standard deviation elliptical long axis continuously shortened from 452.53 km in 2012 to 406.45 km in 2021, the short axis increased from 152.91 km in 2012 to 160.39 km in 2021, and the oblateness decreased from 0.662 in 2012 to 0.605 in 2021. This indicates a clear agglomeration effect on the urban ecological resilience of the YRB along the long axis and an expansion trend along the short axis. From 2012 to 2021, the elliptical coverage area decreased from 54,346.16 km^2 to 51,200.56 km^2, with a total reduction of 3,145.6 km^2, which further indicates a gradual enhancement in the single core agglomeration model of the urban ecological resilience in Shanxi section of the YRB and a strengthening of the radiation effect of Central Shanxi UA on other cities.

3.4 Influencing factors of urban ecological resilience in Shanxi section of the YRB

We considered the value of urban ecological resilience in the Shanxi section of the YRB as the dependent variable and the 15 influencing factors in Table 1 as independent variables. First, the data for each factor were converted into grade data using the natural breakpoint method. Then, the explanatory power q of each factor was calculated by introducing a geographical detector, that is,

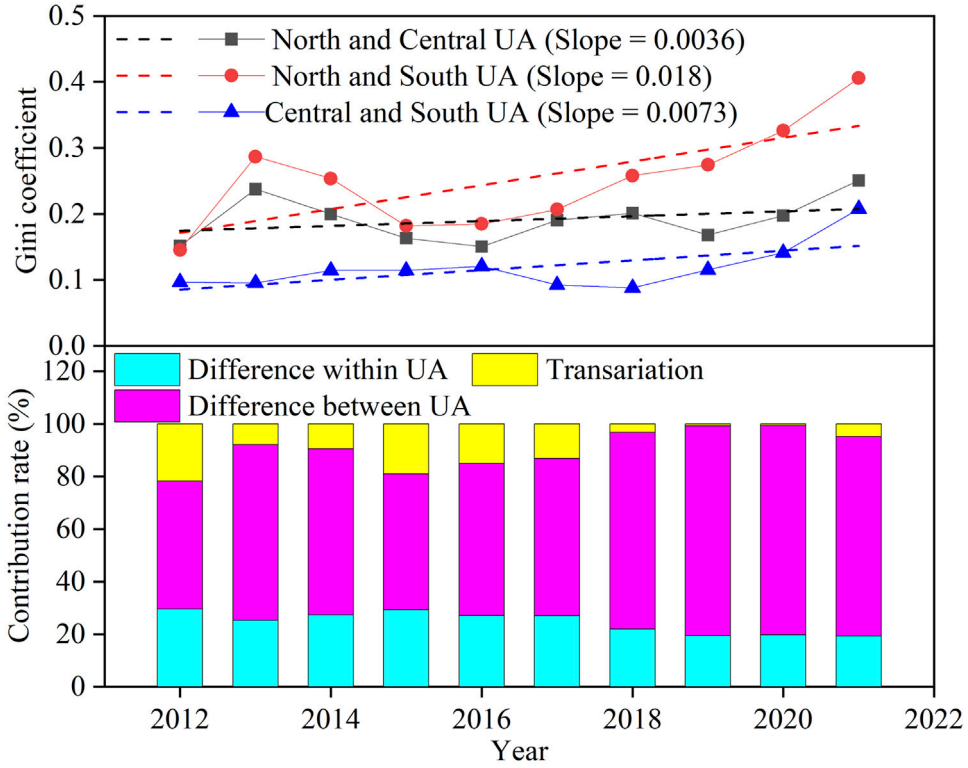

FIGURE 7
Difference and contribution rate of urban ecological resilience of UAs in Shanxi Section of the YRB.

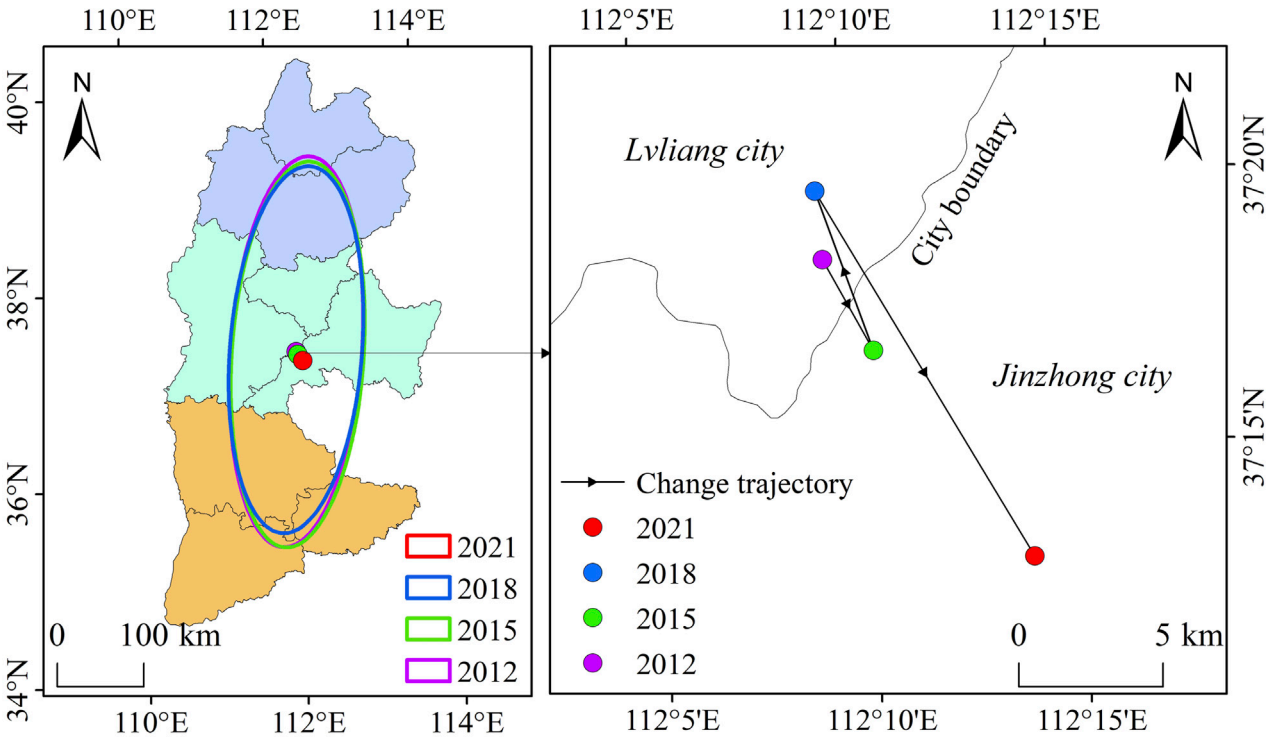

FIGURE 8
Standard deviation ellipse and center of gravity trajectory of urban ecological resilience in Shanxi section of the YRB.

TABLE 4 Standard deviation ellipse parameters of urban ecological resilience of UA.

Year	Center of gravity coordinates	Long axis (km)	Short axis (km)	Area (km^2)	Oblateness	Azimuth angle
2012	112.159591°E, 37.325122°N	452.526	152.910	54,346.161	0.662	4.016
2015	112.177048°E, 37.295967°N	446.540	152.638	53,531.803	0.658	3.727
2018	112.158105°E, 37.344768°N	424.909	152.934	51,037.457	0.640	4.383
2021	112.234174°E, 37.227414°N	406.445	160.392	51,200.562	0.605	3.108

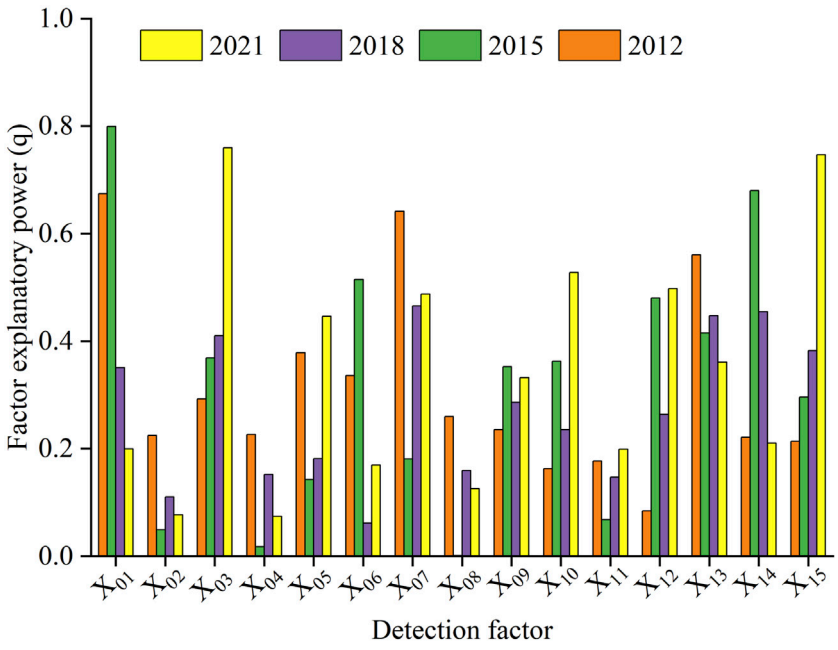

FIGURE 9
Explanatory power of different detection factors.

the influence of each factor on urban ecological toughness. The results indicated the top five influencing factors were $X_{01} > X_{07} > X_{13} > X_{05} > X_{06}$ in 2012; $X_{01} > X_{14} > X_{06} > X_{12} > X_{13}$ in 2015; $X_{07} > X_{14} > X_{13} > X_{03} > X_{15}$ in 2018; and $X_{03} > X_{15} > X_{10} > X_{12} > X_{07}$ in 2021 (Figure 9). Although the degree of influence of each factor on urban ecological resilience was different during different periods, the water supply per ten-thousand Yuan GDP, occupied area of construction land per ten-thousand Yuan GDP, green coverage rate in built-up areas, ratio of research and experimental development funds (R&D) to GDP, proportion of science and technology expenditure in local fiscal expenditure, and patent licensing quantity index were higher at each stage, which had a higher influence on urban ecological resilience.

The results of the factor interaction detection revealed that most types of factor interactions were nonlinear enhancements (Figure 10). The q values of the interactions among the 15 factors in 2012, 2015, 2018, and 2021 increase significantly, indicating that the degree of interaction among the factors is significantly greater than a single factor. In 2012, X_{01}, X_{07}, and X_{13} had the most significant interactions with other factors; in 2015, X_{01}, X_{06}, and X_{14} had the most significant interactions with other factors; in 2018, X_{03} and X_{07} had the most significant interactions with other factors; and in 2021, X_{03} and X_{15} had the most significant interactions with other factors. The evolution of the interaction between two factors from 2012 to 2021 further shows that these factors are the leading factors affecting urban ecological resilience, and their influence tended to increase annually.

4 Discussion

Due to the development of urbanization and industrialization, the urban ecological environment is under great pressure. Resource-based cities have a long history and resource advantages, and have been the driving force of rapid economic development (Mohamed et al., 2021; Al-Housani et al., 2023). However, overdevelopment and serious environmental degradation are inevitable side effects of the development of resource-based cities (Taelman et al., 2018). As a province with large coal resources, Shanxi's economic and industrial structure is relatively simple, the problem of ecological environmental debt is prominent, and ecological protection remains arduous.

Urban ecological resilience provides a set of new methods and tools for exploring the nonlinear relationship between urban

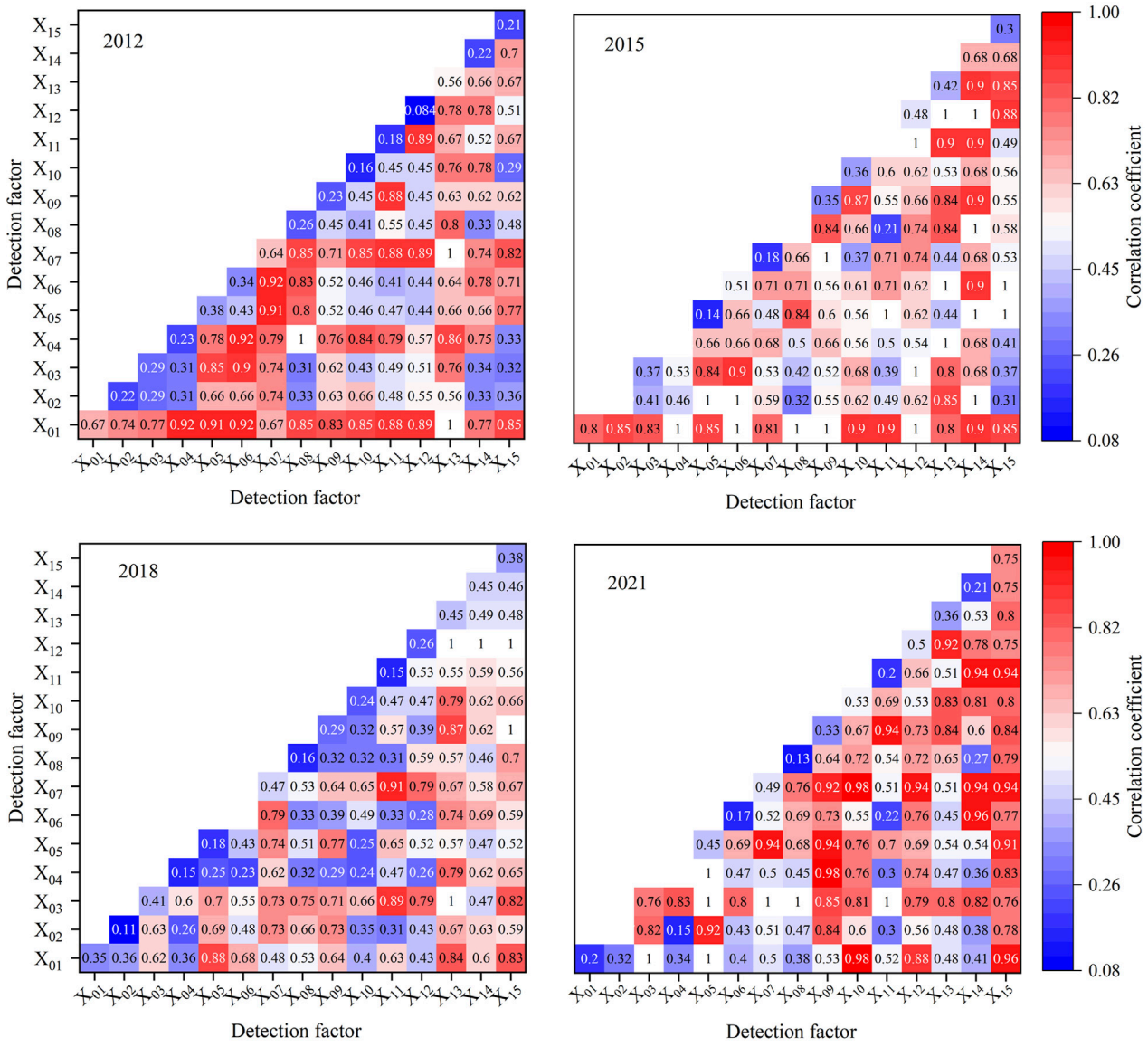

FIGURE 10
Results of interactive detection of urban ecological resilience factors.

ecosystems (Bottero et al., 2020; Zhao et al., 2021). Based on the theory of landscape ecology, the research paradigm of ecological network "identifying ecological source-building resistance surface-extracting ecological corridor" is established to explore how to enhance the resilience of ecosystem from the ecological point of view (Qiao et al., 2023; Wang et al., 2023). However, these studies often ignore the importance that ecological resilience is affected by human social activities. At present, The index system for evaluating urban ecological resilience still has limitations, and it is necessary to consider the impact of social activities on the ecosystem more comprehensively (Scheffer et al., 2015; Jia et al., 2023). When constructing the index system, we drew lessons from previous research results and highlighted the importance of ecosystem innovation ability. The weight assignment result of the entropy method further illustrates the important position of innovation development in the evaluation system. The analysis of the spatiotemporal evolution of urban ecological resilience reveals that the overall level of urban ecological resilience in the study area is low, which is consistent with existing research results of urban ecological resilience in the YRB (Li et al., 2023a; Wang et al., 2024). The results of this study reveal that the level of urban ecological resilience in the Shanxi Section of the YRB has an overall growth trend; however, the growth process of each UA fluctuates is slow, and the growth rate varies greatly. Since the 18th Communist Party of China National Congress made the strategic decision to "vigorously promote the construction of an ecological civilization," the traditional development model of the YRB has improved, and the average level of ecological resilience of UAs in the Shanxi section of YRB improved during the study period. However, the process of improvement is difficult and must be repeated. In 2012, the

level of urbanization gradually improved, the social and economic levels developed, and the natural growth rate of the population increased, exceeding the carrying capacity of ecological resources, which further affected the development of urban ecological resilience. Since 2015, with the vigorous promotion of supply-side reforms, Shanxi has begun to explore the transformation of its resource-based economy. The Soil and Water Conservation Plan of Shanxi Province (2016–2030) was declared in 2017, and the ecological restoration of "two mountains, seven rivers, and one watershed" was launched in 2018, guaranteeing the improvement of urban ecological resilience.

Taiyuan, the provincial capital city, has a leading advantage in terms of ecological resilience. The integrated development of Taiyuan, Xinzhou, and Jinzhong City is strengthening the coordinated development of surrounding cities. However, regional development in the North Shanxi UA lags behind, and is insufficient and unbalanced, which is the main reason for the difference in urban ecological resilience with other UAs. The results of the center-of-gravity migration also indicate that the development power of the North Shanxi UA is insufficient, and the center of gravity has moved to the southeast. According to the Outline of the National Plan for the Protection of Ecologically Fragile Areas (https://www.mee.gov.cn/), the two cities in Northern Shanxi belong to ecologically fragile areas and are most affected by human activities because of their special natural geographical conditions and concentrated mineral resources. The regional development of North Shanxi urgently needs to strengthen its ties with other regions and form a mutual aid link for overall development to enhance the urban ecological resilience of Shanxi Province.

Tong et al. (2023) suggested that both natural and human factors affected the spatial distribution of ecological resilience of the northernslope of Tianshan Mountain. Shi et al. (2022) suggested that socio-economic development was the main influencing factors of urban ecological resilience. In the present study, X_{01} and X_{03} in the pressure dimension had relatively high explanatory power, indicating the pressure of urban ecological resilience in the Shanxi Section of the YRB, mainly from urban water consumption intensity and land development intensity. In the state dimension, X_{07} reflected the level of urban greening, with higher influence level, indicating that increasing the green coverage area in built-up areas can effectively improve the quality of the urban ecological environment. In the response dimension, X_{09}, X_{10}, and X_{12} had the same intensity of forces, indicating that environmental governance, improvement in human settlements, and level of investment in environmental protection play important roles in the improvement of urban ecological resilience. The three factors X_{13}, X_{14}, and X_{15} in the innovation dimension had strong explanatory power, which demonstrates the importance of urban ecosystems in adapting to external disturbances and obtaining ecological resilience through learning and innovation functions. Considering the factors that restrict the development of urban ecological resilience, there are a few suggestions for the development of the Shanxi Section of the YRB.

(1) Scientific and technological innovations play a positive role in promoting urban ecological resilience. To improve urban ecological resilience, we should focus on the advantages of scientific and technological innovation, increase the introduction and training of researchers, and attach importance to investing scientific and technological funds and research and experimental development funds in the North Shanxi UA. Moreover, we should improve the output of scientific research in Central Shanxi and enhance the transformation capacity of urban ecosystems.
(2) The pressure of urban ecological resilience should be transformed and industrial transformation and upgradation encouraged, a green industrial system should be built, and the urban development model for high energy consumption changed. Strengthen common links among UAs, benign interactions among cities have to be encouraged, and a multidimensional cooperation mechanism established.
(3) Continue increasing efforts to promote ecological restoration and management of the YRB. The level of water resource management should be improved and water quality significantly improved, forest coverage and green coverage in built-up areas increased, urban green spaces expanded, the comprehensive utilization rate of general industrial solid waste strengthened, harmless treatment rate of domestic waste improved, centralized treatment rate of sewage treatment plants, and other urban pollution control efforts implemented.

It is necessary to acknowledge the limitations of this work. Considering the data availability, this study selected prefecture-level cities in the Shanxi Section of the YRB as the research objects. The sample size was relatively small, and the research scale was not detailed enough. Counties can be added for further detailed exploration to reflect the developmental status of urban ecological resilience more accurately. In addition, the related research on urban ecological resilience is still under exploration, with relatively limited references, The evaluation system is also still being improved, which needs to be further refined.

5 Conclusion

By constructing an evaluation index system for urban ecological toughness, this study explores the spatiotemporal evolution characteristics and dynamic development trends of urban ecological resilience in the Shanxi section of the YRB and discusses the influencing factors.

(1) From 2012 to 2021, the average level of urban ecological resilience in the Shanxi Section of the YRB was relatively low. The urban ecological resilience gradually transformed from the dual core of Taiyuan—Jincheng City to Taiyuan City as a single core, exhibiting a decreasing trend from the core to the peripheral cities.
(2) The spatial differences in the ecological resilience of the UAs in the Shanxi Section of the YRB are mainly caused by interregional differences, and this difference has an increasing trend. The largest regional differences were

observed between Central Shanxi UA and North Shanxi UA, and those between North Shanxi UA and South Shanxi UA are minimal. During the study period, the standard deviation ellipse of urban ecological resilience in the UA in the Shanxi section of the YRB displayed a counterclockwise shifting trend; the oblateness decreased by 0.057, and the ellipse coverage area decreased by 3,145.6 km^2. The center of gravity migration trajectory fluctuated in the "northwest-southeast" direction, and overall moved 12.63 km to the southeast.

(3) The water supply per ten-thousand Yuan GDP, occupied area of construction land per ten-thousand Yuan GDP, green coverage rate in built-up area, ratio of research and experimental development funds (R&D) to GDP, proportion of science and technology expenditure in local fiscal expenditure, and patent licensing quantity index have relatively high factor explanatory power at each stage. Most factor interaction types are nonlinear enhancements and the degree of influence of the interaction between factors is greater than a single factor.

Data availability statement

The raw data supporting the conclusion of this article will be made available by the authors, without undue reservation.

Author contributions

JW: Methodology, Writing–original draft. ZL: Methodology, Writing–review and editing. YC: Conceptualization, Writing–review and editing. ZZ: Conceptualization, Writing–review and editing. SW: Writing–review and editing.

Funding

The author(s) declare that financial support was received for the research, authorship, and/or publication of this article. This research was funded by the Planning Subject of Philosophy and Social Sciences in Shanxi Province (No.2023YY069) and the Research Project of Philosophy and Social Sciences at Shanxi Universities (No. 2023W048).

Conflict of interest

Author ZL was employed by Shanxi Yituo Land Engineering Consulting Co., Ltd.

The remaining authors declare that the research was conducted in the absence of any commercial or financial relationships that could be construed as a potential conflict of interest.

Publisher's note

All claims expressed in this article are solely those of the authors and do not necessarily represent those of their affiliated organizations, or those of the publisher, the editors and the reviewers. Any product that may be evaluated in this article, or claim that may be made by its manufacturer, is not guaranteed or endorsed by the publisher.

Supplementary material

The Supplementary Material for this article can be found online at: https://www.frontiersin.org/articles/10.3389/fenvs.2024.1385604/full#supplementary-material

References

Alberti, M., and Marzluff, J. M. (2004). Ecological resilience in urban ecosystems: linking urban patterns to human and ecological functions. *Urban Ecosyst.* 7, 241–265. doi:10.1023/B:UECO.0000044038.90173.c6

Al-Housani, M. I., Koç, M., and Al-Sada, M. S. (2023). Investigations on entrepreneurship needs, challenges, and models for countries in transition to sustainable development from resource-based economy—Qatar as a case. *Sustainability* 15, 7537. doi:10.3390/su15097537

Boschma, R. (2015). Towards an evolutionary perspective on regional resilience. *Reg. Stud.* 49, 733–751. doi:10.1080/00343404.2014.959481

Bottero, M., Datola, G., and De Angelis, E. (2020). A system dynamics model and analytic network process: an integrated approach to investigate urban resilience. *Land* 9, 242. doi:10.3390/land9080242

Chen, H., Xu, J., Zhang, K., Guo, S., Lv, X., Mu, X., et al. (2022). New insights into the DPSIR model: revealing the dynamic feedback mechanism and efficiency of ecological civilization construction in China. *J. Clean. Prod.* 348, 131377. doi:10.1016/j.jclepro.2022.131377

Chen, Y., Su, X., and Zhou, Q. (2021). Study on the spatiotemporal evolution and influencing factors of urban resilience in the Yellow River Basin. *Int. J. Environ. Res. Public Health.* 18(19), 10231. doi:10.3390/ijerph181910231

Fan, Z. Y. (2023). *Research on evolution of spatial-temporal patterns and influencing factors of urban resilience in China's loess plateau*. Lanzhou: Lanzhou University. doi:10.27204/d.cnki.glzhu.2023.000579

Hosseini, S., Barker, K., and Ramirez-Marquez, J. E. (2016). A review of definitions and measures of system resilience. *Reliab. Eng. Syst. Saf.* 145, 47–61. doi:10.1016/j.ress.2015.08.006

Huang, J., Zhong, P. S., Zhang, J. Z., and Zhang, L. (2023). Spatial-temporal differentiation and driving factors of ecological resilience in the Yellow River Basin, China. *Ecol. Indic.* 154, 110763. doi:10.1016/j.ecolind.2023.110763

Jia, H., Luo, P., Yang, H., Luo, C., Li, H., Cheng, Y., et al. (2023). Constructing an indices system for evaluating the ecological integrity of forests in western Sichuan, China based on structural equation modeling. *Ecol. Indic.* 146, 109745. doi:10.1016/j.ecolind.2022.109745

Li, D., Yang, W., and Huang, R. (2023a). The multidimensional differences and driving forces of ecological environment resilience in China. *Environ. Impact Asses.* 98, 106954. doi:10.1016/j.eiar.2022.106954

Li, G. Z., and Wang, L. Q. (2023b). Study of regional variations and convergence in ecological resilience of Chinese cities. *Ecol. Indic.* 154, 110667. doi:10.1016/j.ecolind.2023.110667

Liao, Z., and Zhang, L. (2023). Spatio-temporal analysis and simulation of urban ecological resilience in Guangzhou City based on the FLUS model. *Sci. Rep.* 13, 7400. doi:10.1038/s41598-023-33342-5

Meerow, S., Newell, J. P., and Stults, M. (2016). Defining urban resilience: a review. *Landsc. Urban Plan.* 147, 38–49. doi:10.1016/j.landurbplan.2015.11.011

Mohamed, B. H., Ari, I., Al-Sada, M. b.S., and Koç, M. (2021). Strategizing human development for a country in transition from a resource-based to a knowledge-based economy. *Sustainability* 13, 13750. doi:10.3390/su132413750

Qiao, Q., Zhen, Z., Liu, L., and Luo, P. (2023). The construction of ecological security pattern under rapid urbanization in the Loess Plateau: a case study of Taiyuan City. *Remote Sens.* 15 (6), 1523. doi:10.3390/rs15061523

Scheffer, M., Carpenter, S. R., Dakos, V., and van Nes, E. H. (2015). Generic indicators of ecological resilience: inferring the chance of a critical transition. *Annu. Rev. Ecol. Evol. Syst.* 46, 145–167. doi:10.1146/annurev-ecolsys-112414-054242

Shi, C., Zhu, X., Wu, H., and Li, Z. (2022). Assessment of urban ecological resilience and its influencing factors: a case study of the beijing-tianjin-hebei urban agglomeration of China. *Land* 11, 921. doi:10.3390/land11060921

Song, Y., Gui, Z., Wu, H., and Wei, Y. (2017). A web-based framework for visualizing industrial spatiotemporal distribution using standard deviational ellipse and shifting routes of gravity centers. *Int. Arch. Photogramm. Remote Sens. Spat. Inf. Sci. XLII–2/W7*, 129–135. doi:10.5194/isprs-archives-XLII-2-W7-129-2017

Taelman, S. E., Tonini, D., Wandl, A., and Dewulf, J. (2018). A holistic sustainability framework for waste management in European cities: concept development. *Sustainability* 10, 2184. doi:10.3390/su10072184

Tong, Y., Lei, J., Zhang, S., Zhang, X., Rong, T., Fan, L., et al. (2023). Analysis of the spatial and temporal variability and factors influencing the ecological resilience in the urban agglomeration on the northern slope of tianshan mountain. *Sustainability* 15, 4828. doi:10.3390/su15064828

Wang, J. F., Li, X. H., Christakos, G., Liao, Y. L., Zhang, T., Gu, X., et al. (2010). Geographical detectors-based health risk assessment and its application in the neural tube defects study of the Heshun Region, China. *Int. J. Geogr. Inf. Sci.* 24, 107–127. doi:10.1080/13658810802443457

Wang, J. F., and Xu, C. D. (2017). Geodetector: principle and prospective. *Acta Geogr. Sin.* 72, 116–134. doi:10.11821/dlxb201701010

Wang, M. X., Zhao, H. H., Cui, J. X., Fan, D., Lv, B., Wang, G., et al. (2018). Evaluating green development level of nine cities within the Pearl River Delta, China. *J. Clean. Prod.* 174, 315–323. doi:10.1016/j.jclepro.2017.10.328

Wang, S. M., Ning, W. P., Niu, J. L., and An, K. (2024). Spatiotemporal differentiation and convergence of urban ecological resilience in the Yellow River Basin: an empirical analysis based on 61 cities in seven major urban agglomerations. *Arid. Land Geogr.* 47, 93–103. doi:10.12118/j.issn.1000-6060.2023.323

Wang, Y., Cai, Y., Xie, Y., Chen, L., and Zhang, P. (2023). An integrated approach for evaluating dynamics of urban eco-resilience in urban agglomerations of China. *Ecol. Indic.* 146, 109859. doi:10.1016/j.ecolind.2023.109859

Wu, J. G. (2014). Urban ecology and sustainability: the state-of-the-science and future directions. *Landsc. Urban Plan.* 125, 209–221. doi:10.1016/j.landurbplan.2014.01.018

Yang, M., Jiao, M., and Zhang, J. (2022). Research on urban resilience and influencing factors of Chengdu-Chongqing economic Circle. *Sustainability* 14, 10585. doi:10.3390/su141710585

Yuill, R. S. (1971). The standard deviational ellipse; an updated tool for spatial description. *Geogr. Ann. B* 53, 28–39. doi:10.1080/04353684.1971.11879353

Zambom, A. Z., and Ronaldo, D. (2013). A review of kernel density estimation with applications to econometrics. *Int. Econ. Rev.* 5, 20–42. doi:10.48550/arXiv.1212.2812

Zhang, L., Ma, X., Ock, Y. S., and Qing, L. (2022). Research on regional differences and influencing factors of Chinese industrial green technology innovation efficiency based on dagum Gini coefficient decomposition. *Land* 11, 122. doi:10.3390/land11010122

Zhao, R., Fang, C., Liu, H., and Liu, X. (2021). Evaluating urban ecosystem resilience using the DPSIR framework and the ENA model: a case study of 35 cities in China. *Sustain. Cities Soc.* 72, 102997. doi:10.1016/j.scs.2021.102997

Zhou, Y., Chen, Y., Li, Z., and Jiang, W. (2022). Ecological resilience assessment of an emerging urban agglomeration: a case study of Chengdu-Chongqing economic circle, China. *Pol. J. Environ. Stud.* 31, 2381–2395. doi:10.15244/pjoes/144098

frontiers | Frontiers in Environmental Science

TYPE Original Research
PUBLISHED 02 April 2024
DOI 10.3389/fenvs.2024.1349228

OPEN ACCESS

EDITED BY
Zhiming Han,
Northwest A&F University, China

REVIEWED BY
Yong Wang,
China Institute of Water Resources and Hydropower Research, China
Panxing He,
Henan Normal University, China
Jing Zhao,
Xi'an University of Technology, China

*CORRESPONDENCE
Jiamin Li,
l17513250032@icloud.com
Pingping Luo,
lpp@chd.edu.cn

RECEIVED 04 December 2023
ACCEPTED 15 January 2024
PUBLISHED 02 April 2024

CITATION
Zhu Y, Li J, Xi X, Zhang J, Ma P, Liang L and Luo P (2024), Spatial and temporal characteristics of drought in the Mu Us Sandy Land based on the Standardized Precipitation Index.
Front. Environ. Sci. 12:1349228.
doi: 10.3389/fenvs.2024.1349228

Spatial and temporal characteristics of drought in the Mu Us Sandy Land based on the Standardized Precipitation Index

Yonghua Zhu[1,2,3], Jiamin Li[2]*, Xiaokang Xi[4], Jie Zhang[2], Pengfei Ma[5], Li'e Liang[2] and Pingping Luo[1,3]*

[1]School of Water and Environment, Chang'an University, Xi'an, China, [2]College of Civil Engineering and Architecture, Yan'an University, Yan'an, China, [3]Key Laboratory of Subsurface Hydrology and Ecological Effects in Arid Region, Ministry of Education, Chang'an University, Xi'an, China, [4]Shaanxi Provincial Hydrology and Water Resources Survey Center, Xi'an, Shaanxi, China, [5]Tongliao Hydrotechnics Service Center, Tongliao, Inner Mongolia, China

The environment of the Mu Us Sandy Land, northern Shaanxi, is fragile, so the temporal and spatial evolution of drought can provide a reference for ecological construction and agricultural production. Based on the daily precipitation data of five meteorological stations from 1967 to 2020, the spatial and temporal evolution characteristics of drought in the Mu Us Sandy Land of northern Shaanxi were analyzed using the methods Standardized Precipitation Index (SPI) and run-length theory. The results show that 1) the smaller the time scale, the higher the sensitivity of the SPI to primary precipitation. 2) The annual, summer, autumn, and winter SPI showed an upward and a wetting trend, and the fastest wetting speed is observed in summer, while spring showed an increasing trend of drought. 3) In the past 54 years, the duration, degree, and intensity of drought events at SPI-3 and SPI-12 scales in the Mu Us Sandy Land of northern Shaanxi showed an insignificant decreasing trend, but the decreasing rate at the SPI-12 scale was faster than that at the SPI-3 scale. The serious periods of drought are November 2018 to May 2019 and April 1999 to July 2021. 4) The duration of drought events at two timescales in each region showed a decreasing trend. The longest durations of drought were in Yulin and Jingbian; Shenmu and Dingbian are the regions with the fastest reduction rate of drought degree at the two scales. Hengshan shows rapid reduction of drought intensity at the two scales and also the region with large average drought intensity. These results are helpful in understanding and describing drought events for drought risk management under the condition of global warming.

KEYWORDS

sandy, drought events, Standardized Precipitation Index, spatio-temporal characteristic, global warming

1 Introduction

Drought is a natural disaster caused by insufficient precipitation for a long period of time, with the characteristics of wide influence range, high occurrence frequency, and long duration, making it one of the main climate disasters (Zhang et al., 2021; Cao et al., 2022). In typical arid areas in Northwest China, drought leads to dry land, which directly affects the growth and development of xerophytes (Kang et al., 2020), and it easily causes continuous

desertification of land and becomes the source of sandstorms (Yang et al., 2021). Therefore, research on drought in Northwest China has attracted much attention (Luo et al., 2021a; Li et al., 2022; Wang et al., 2022).

Droughts represent an extended imbalance between water supply and demand with devastating and extended impacts often requiring long periods to reverse the recorded damages (Soulsby et al., 2021; Zhu et al., 2022). Therefore, continuous drought monitoring must be carried out to provide decisive policy support for medium- and long-term planning of mitigation measures. Initially, hydrological and meteorological elements (e.g., soil moisture, stream flow, temperature, and precipitation) were adopted as the main input for the generation of indices for quantitative modeling of drought severity in the early last century (Munger, 1916; Kincer, 1992). Subsequently, more than hundreds of indices used for drought studies were identified under space and time at different scales (Niemeyer, 2008). At present, there are two kinds of indicators in the analysis and research of drought. One indicator reflects the physical process of drought through drought mechanisms, represented by the Palmer Drought Severity Index (PDSI) considering multiple factors (Zhu et al., 2021). The other is to study the statistical distribution of precipitation using meteorological methods to reflect the characteristics of drought, represented by the Standardized Precipitation Evapotranspiration Index (Camarero et al., 2021) (SPEI) and the Standardized Precipitation Index (Xu et al., 2021) (SPI). The potential evapotranspiration is often used in the calculation of the SPEI, while it is often greater than the actual evapotranspiration, resulting in deviations in the calculation results (Ortiz-Gómez. et al., 2022), whereas the SPI index has the advantages of simple calculation, strong adaptability, and sensitive response to drought changes (Hayes et al., 1999), and hence is the drought index recommended by the World Meteorological Organization. Many studies (Yang et al., 2017; Tja et al., 2020) showed that SPI, as a drought reconstruction index, is suitable for Northwest China, and its multi-timescale application characteristics can serve in water resource assessment and drought monitoring at different timescales.

As a key area for the construction of an ecological security barrier in China, the Mu Us Sandy Land belongs to semi-arid climate, located in a climate sensitive area characterized by fragile ecological environment and frequent drought disasters. It is an agricultural–pastoral ecotone. At present, many research studies on the Mu Us Sandy Land mostly focus on the multi-timescale climate change characteristics, such as the multi-timescale change characteristics and change trend of main climate factors (Ding et al., 2021; Wei et al., 2021), and the change characteristics of precipitation and extreme temperature (Zhou et al., 2020).

Our overarching purpose is to assess regional drought across the Mu Us Sandy Land, northwest China, using the SPI. The specific objectives of this study are to (1) analyze the temporal distinctions of the SPI with 1-, 3-, and 12-month timescales of the Mu Us Sandy Land and (2) reveal the characteristics of drought intensity, drought duration, and drought frequency of the SPI at different timescales. The findings from this study are helpful in understanding and describing drought events for drought risk management under the condition of global warming.

2 Materials and methods

2.1 Study area

As a transitional area from the Ordos Plateau to the Loess Plateau in northern Shaanxi, the Mu Us Sandy Land is a staggered area of agriculture, forestry, and animal husbandry, belonging to a typical ecologically fragile area located north of the first line of the Great Wall in Yulin City, Shaanxi, with an area of 16,300 km^2, including Dingbian (DB), Jingbian (JB), Hengshan (HS), Yulin (YL), and Shenmu (SM) and other counties of Yulin City (Figure 1). The land regulation and development of this region has made an important contribution to the dynamic balance of the total cultivated land in Shaanxi Province. The sandy land is inclined from northwest to southeast, with an altitude of 1,000–1,500 m, mainly composed of sand dunes and meadows. This study area belongs to the semi-arid climate zone of the middle temperate zone, with a gradual decrease in annual average precipitation from 400 to 450 mm in the southeast to approximately 250 mm in the northwest region, the annual average temperature is 6°C–9°C, and the annual average evaporation is 2,100–2,600 mm. Sandy land has less precipitation but its occurrence is more, resulting in abundant surface water and groundwater resources. There are several main rivers, such as Kuye River, Tuwei River, and Wuding River.

2.2 Data

The daily precipitation data of DB, JB, HS, YL, and SM meteorological stations, from 1967 to 2020, in the Mu Us Sandy Land in Northern Shaanxi was used in this paper, which comes from the China surface climate data daily dataset (V3.0) in the China meteorological data sharing service network (the missing rate is less than or equal to 10%), with good consistency, reliability, and representativeness (http://data.CMA.CN).

2.3 Method

Taking the Mu Us Sandy Land in northern Shaanxi as the study area, the drought characteristic indexes of each station are obtained using the SPI and run-length theory in 1 month (SPI-1), 3 months (SPI-3), and 12 months (SPI-12). The regional annual and seasonal SPI values were obtained by arithmetic average (spring: March, April and May; summer: June, July and August; autumn: September, October and November; and winter: December, January and February). Based on linear regression, Daniel's test, ArcGIS, and other methods, the time-varying trend and spatial distribution characteristics of the standardized precipitation index, drought duration, drought degree, and drought intensity of each scale were identified. The SPI-3 and SPI-12 scale indexes that can significantly identify hydrological drought are selected to study the variation characteristics of duration, drought degree, and intensity of hydrological drought in the Mu Us Sandy Land in northern Shaanxi in the past 54 years.

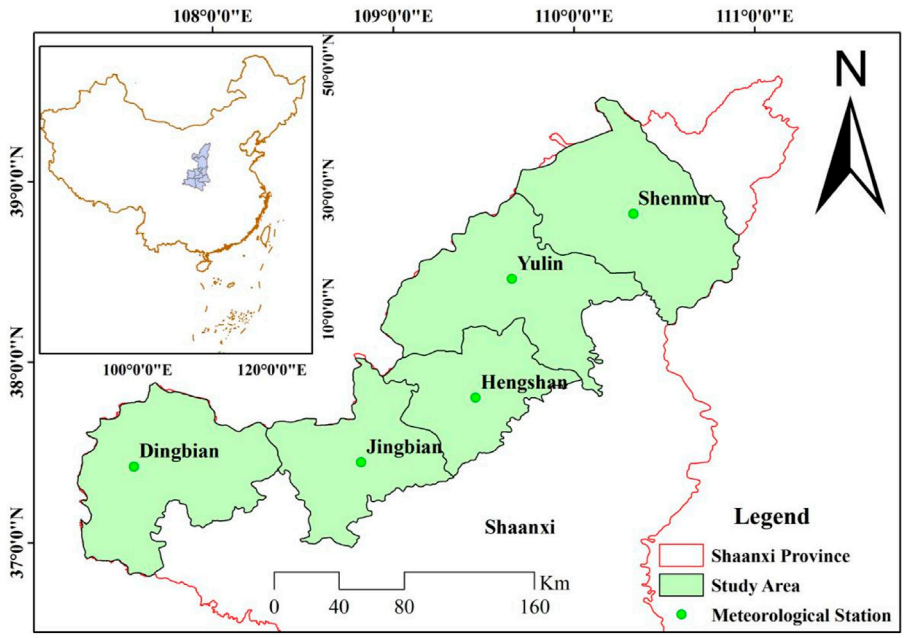

FIGURE 1
Administrative scope and distribution of study areas in the Mu Us Sandy Land.

TABLE 1 Standardized Precipitation Index drought grading.

Drought grade	SPI
Extreme drought	SPI≤−2.0
Heavy drought	−2<SPI≤−1.5
Moderate drought	−1.5<SPI≤−1.0
Mild drought	−1<SPI≤−0.5
Normal	SPI>−0.5

2.3.1 Standardized Precipitation Index

Because the precipitation distribution is a partial distribution, not a normal distribution, and the precipitation changes greatly in different space–timescales, it is difficult to compare the precipitation on different space–time scales. Therefore, in the precipitation analysis, the gamma distribution probability is used to describe the change of precipitation, which is normalized first, and finally, the SPI value is obtained from the standardized precipitation cumulative frequency distribution. The specific calculation formula is found in relevant literature, and the classification of meteorological drought grade in our manuscript (Table 1) is formulated by the National Climate Center.

2.3.2 Run-length theory

In this paper, the three characteristic indexes of drought duration, drought degree, and drought intensity are used to represent the drought characteristics of a drought event, which can be obtained by run-length theory (Xiao et al., 2012). According to the run-length theory, the series of the same symbols that meet certain conditions is called a "run," and the number of occurrences of the same symbol in a run is called the length of the run. Long-lasting SPI <0 events will lead to drought-related problems, so 0 is taken as the cut-off level of the run. When SPI ≤ 0, it is defined as a drought event, and drought duration D is the run length. During drought event, the absolute value of the cumulative SPI value is drought degree, and the ratio of drought degree to drought duration is drought intensity (I), which can be obtained from drought classification, where $0 \leq I < 1$ is mild drought, $1 \leq I < 1.5$ is moderate drought, $1.5 \leq I < 2$ is heavy drought, and $I \geq 2$ is extreme drought.

2.3.3 Linear regression

The change trend and its significance level are judged by the slope of the regression equation between the Standardized Precipitation Index, drought duration, drought degree, drought intensity, and time series. When the slope is > 0, the research object has an upward trend, and when the slope is < 0, it has a downward trend. In addition, Daniel's test is used to judge whether the change trend of the research object is significant, and the significance level is judged according to the statistics. When $p \leq 0.05$, the research object has a significant upward or downward trend in the time series, and when $p > 0.05$, the research object has no significant change trend.

3 Results

3.1 SPI sensitivity analysis

It can be seen from the analysis in Figure 2 that there is a fluctuation in the SPI value, but there are significant differences in the sensitivity of different timescales. The smaller the timescale is,

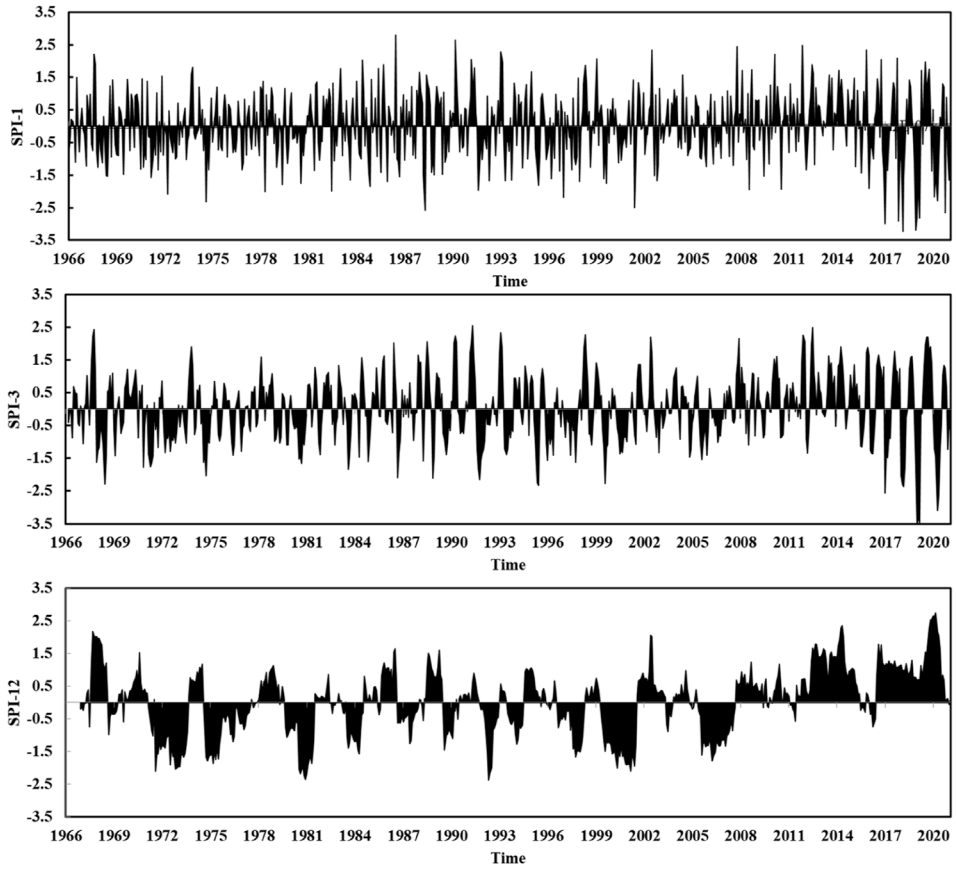

FIGURE 2
Variation of the SPI at different time scales in the Mu Us Sandy Land in northern Shaanxi over 54 years.

the more obvious the fluctuation is and the higher the sensitivity is. It even shows the phenomenon of a dry–wet sharp turn. Furthermore, The larger the time scale is, the more gentle the fluctuation tends to be and the lower the sensitivity is. SPI-1 is closely related to monthly precipitation, and its value fluctuates greatly, reflecting the influence of monthly precipitation on drought. SPI-3 has hysteresis and has no significant response to monthly precipitation. Only precipitation in a long period of time will lead to its fluctuation, reflecting the drought caused by seasonal precipitation shortage. The SPI-12 value is relatively concentrated with a relatively slow change trend, which can reflect the change trend of annual timescale drought in the study area, especially around 1971–1973, 1975–1976, 1980–1981, 1999–2001, and 2005–2006. Following the integrated analysis, the SPI values of different timescales show an increasing trend. From 1967 to 2020, the frequency of drought, extreme drought, heavy drought, moderate drought, and mild drought in SPI-1 was 37.8 times/10a, 2.7 times/10a, 4.9 times/10a, 11.1 times/10a, and 11.9 times/10a, respectively; that of SPI-3 was 37.4 times/10a, 3.1 times/10a, 3.1 times/10a, 12.9 times/10a, and 18.2 times/10a; SPI-12 was 34.7 times/10a, 2.2 times/10a, 8.5 times/10a, 11.6 times/10a, and 12.4 times/10a, respectively. These results demonstrated the extension of the timescale. The frequency of drought, extreme drought, and severe drought is not significantly different, while the frequency of moderate drought and mild drought is significantly different. The occurrence time of different drought grades identified by SPI-1, SPI-3, and SPI-12 is obviously different, and it shows the contrast between drought and flood in some specific years. For example, in 2017–2020, SPI-1 and SPI-3 identified moderate and above drought grades, while SPI-12 has almost no drought in this time period, which indicates that there is an obvious scale effect and time heterogeneity in regional annual precipitation distribution and drought grades.

3.2 Drought variation characteristics

Based on the SPI-12 value, the annual drought characteristics in the study area were analyzed (Figure 3A). The annual SPI showed an extremely significant upward trend (Daniel's test $p < 0.01$), with the variation rate being 0.206/10a, the drought year being 16a, and the drought occurrence frequency being 29%. The SPI value was −1.64 in 2000, indicating severe drought, and there was moderate to mild drought in other years. From the interdecadal variation characteristics of drought shown in Figure 3B, the SPIs of 1970s, 1980s, 1990s, and 2000s were negative, and there were five times, four times, three times, and four times of drought years, respectively, which was the arid period. The 1970s was the most arid period, 2010s was the most humid period, while there was no drought event during the period.

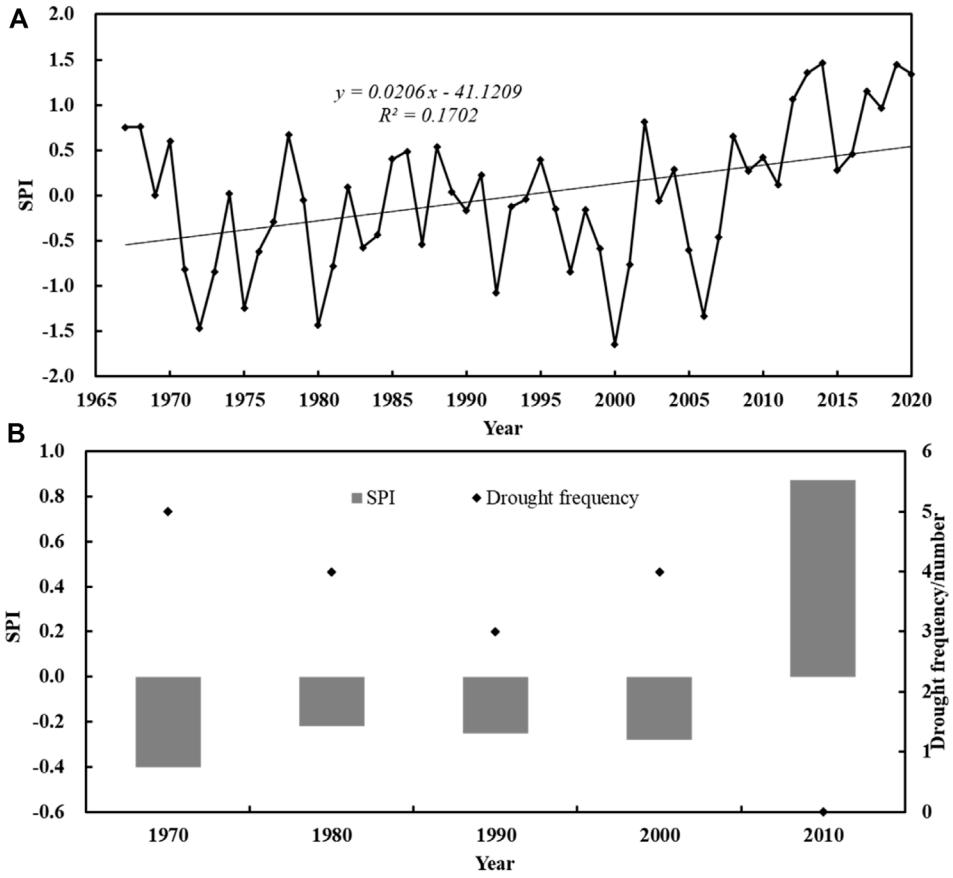

FIGURE 3
Annual SPI variation and interdecadal drought frequency in the Mu Us Sandy Land in northern Shaanxi.

As shown in Figure 4, spring SPI in the study area showed a downward trend from 1967 to 2020, with the rate of 0.076/10a. Summer, autumn, and winter SPI showed an upward trend, with the rate of 0.171/10a, 0.145/10a, and 0.006/10a, respectively. Daniel's test showed that the SPI in summer showed a significant upward trend ($p < 0.05$) and that the values in other seasons did not pass the significance test, indicating that there was a wetting trend during summer, autumn, and winter, and the wetting rate was the fastest in summer, while there was an increasing trend of drought in spring. The seasonal droughts in the Mu Us Sandy Land, northern Shaanxi, from 1967 to 2020 are shown in Table 2. Drought occurred in spring for 14 years, and the frequency of drought was 26%. The SPI values in spring of 2020 and 1971 were −2.39 and −1.58, respectively, which indicate extreme drought and severe drought. During the summer, the drought season lasted for 17 years, with the frequency of drought occurrence of 31%, which was moderate to mild drought; the autumn drought spanned 19 years, with a drought frequency of 36%, including the autumn of 1991, with an SPI value −1.84, indicating severe drought; winter drought lasted for 9 years, with a drought frequency of 17%, including the winter of 2018, with an SPI value −2.86, indicating extreme drought. In addition, seasonal drought occurred frequently during the study period, with varying degrees of seasonal drought occurring in 36 of 54 years. The above analysis showed that seasonal drought occurs frequently in the study area, and the highest frequency of drought occurs in summer and autumn, characterized by mainly mild drought; this is followed by spring, when moderate drought occurs mostly; and the lowest frequency of drought occurs in winter, with mostly moderate and mild drought.

3.3 Temporal variation characteristics of drought events

3.3.1 Variation characteristics of drought event duration

In SPI-3 and 12-month scale, the beginning time of a drought event was determined with the name of the event. SPI-3 and SPI-12 were selected for analyzing the variation characteristics of drought event duration (Figures 5A, B). From the time series, the duration of drought events at the SPI-3 scale showed an insignificant decreasing trend (Daniel's test $p > 0.05$), with a change tendency rate of −0.074/10a. The result of the 5-year moving average showed that the duration of drought events at the SPI-3 scale was relatively stable before the 1970s and 2007–2015 and showed an upward trend since 2015. The other periods showed a sharp fluctuation of increase and decrease. During 1965–2020, a total of 96 drought events occurred in the Mu Us Sandy Land, northern Shaanxi, with an average of 3.40 months. The longest drought events occurred in February 1980 and April 2000, lasting 12 months, followed by drought

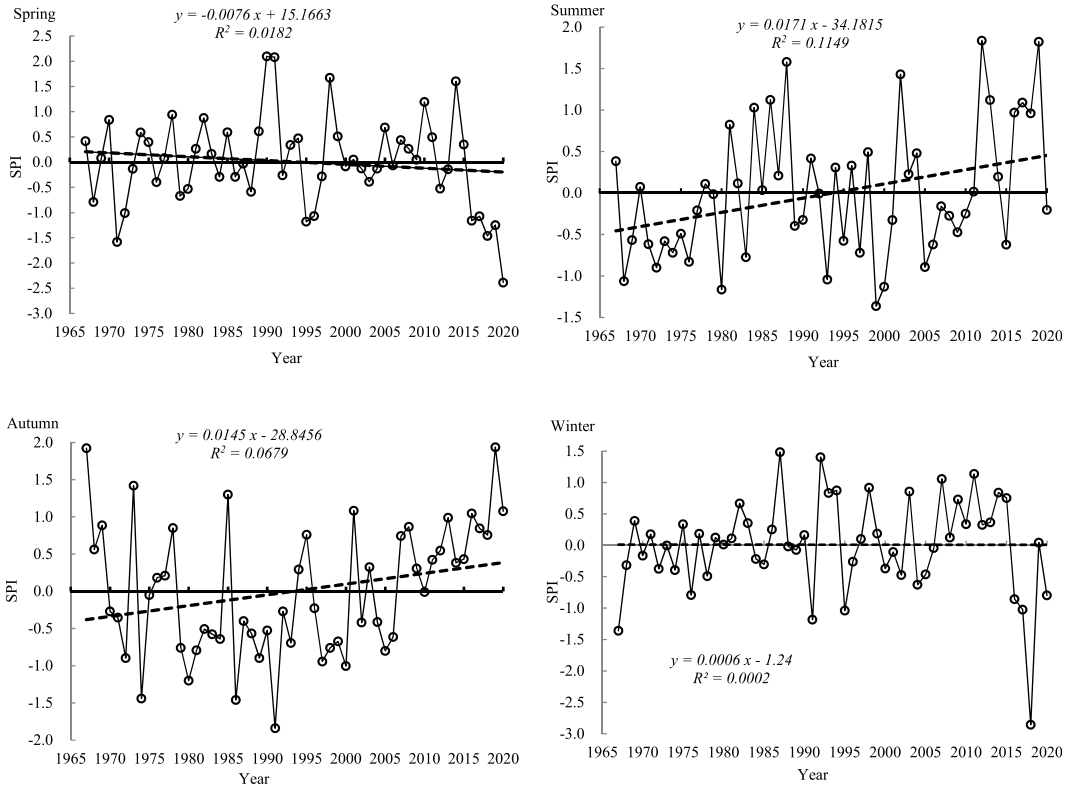

FIGURE 4
SPI changes in four seasons in the Mu Us Sandy Land in northern Shaanxi.

TABLE 2 Statistics on the frequency of seasonal drought in the Mu Us Sandy Land in northern Shaanxi from 1967 to 2020 (%).

Season	Extreme drought	Heavy drought	Moderate drought	Mild drought	Sum
Spring	1.85	1.85	12.96	9.26	25.93
Summer	0.00	0.00	9.26	22.22	31.48
Autumn	0.00	1.82	7.27	27.27	36.36
Winter	1.85	0.00	7.41	7.41	16.67
Year	0.00	1.85	9.26	18.52	29.63

events in February 1972 and January 1997, lasting 11 months. From the perspective of interdecadal changes, the dispersion degree of drought event duration is also gradually flat. The duration of drought events in 1970s, 1980s, 1990s, and 2000s is 3.76 months, 3.20 months, 3.82 months, and 3.25 months, respectively. The shortest duration of drought in 2010s is 3.00 months, and the minimum number of drought events is 17.

The duration of drought events in the SPI-12 scale had a decreasing trend similar to that in SPI-3 (Daniel's test $p > 0.05$), but the decrease was faster, and the change tendency rate was −0.282/10a. The 5-year moving average showed that the duration of drought events at the SPI-12 scale increased first and then decreased from 1970s to the early 1980s and was relatively stable from 1980s to 2000s and then showed a downward trend. Compared with SPI-3, SPI-12 drought events occurred 32 times, but the duration increased significantly, with an average of 9.34 months between 1 and 36 months. The drought event in August 1974 lasted the longest, for 36 months, followed by the drought events in April 1999 and June 2005, which lasted for 28 months.

3.3.2 Variation characteristics of the drought degree during drought events

According to Figures 5C, D, the drought degree of drought events at the SPI-3 and SPI-12 scales in the study area did not show an insignificant downward trend (Daniel's test $p > 0.05$). The drought degree of the SPI-3 scale drought events was 0.06–12.60, with the average value of 2.68. The most serious drought event occurred in October 2018, with a drought degree of 12.60, followed by drought events in August 1991 and December 1967, with drought degrees of 10.29 and 10.17, respectively. The drought degree of the SPI-12 scale drought events fluctuated between 0 and 40.79, with an average drought degree of 8.13. The most serious drought event

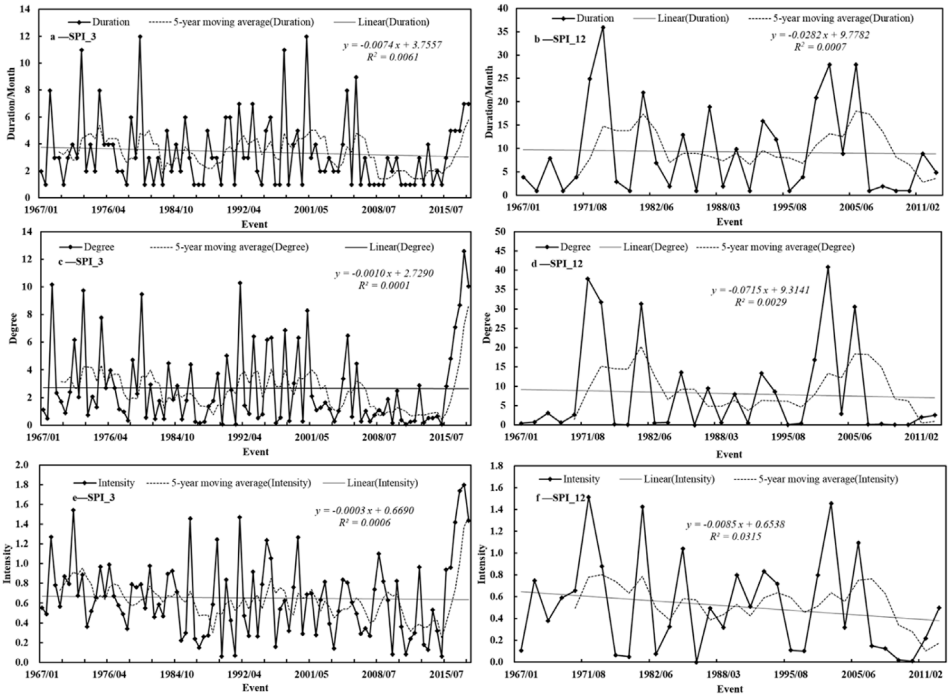

FIGURE 5
Variation of the duration, degree, and intensity of the SPI-3/12 drought event.

occurred in April 1999, with a drought degree of 40.79, followed by drought events in August 1971 and August 1974, with drought degrees of 37.84 and 31.71, respectively. The result of the 5-year moving average showed that the drought degree and drought duration of drought events at different scales had a similar change trend as a whole, basically showing the characteristics that the longer the drought duration was, the more serious the drought degree was. According to SPI-3 and SPI-12, the drought events lasting from November 2018 to May 2019 and April 1999 to July 2021 were the most severe periods of drought in the Maowusu sandy land of northern Shaanxi in the past 54 years at different scales.

3.3.3 Variation characteristics of drought intensity in drought events

According to Figures 5E, F, the drought intensity of drought events at SPI-3 and SPI-12 scales showed an insignificant decreasing trend (Daniel's test $p > 0.05$), with the change tendency rates of −0.003/10a and −0.085/10a, respectively. At the SPI-3 scale, there were three severe drought events (2018/11, 2018/01, and 1971/03), 10 moderate drought events, and 83 mild drought events. The strongest drought event occurred in April 2018, with a value of 1.8, which was a severe drought event. At the SPI-12 scale, there were one severe drought event, four moderate drought events, and 27 mild drought events. The strongest drought event occurred in August 1971, with a value of 1.5, which was a severe drought event. From the 5-year moving average, drought intensity has a similar trend with drought duration and drought degree, but it is different from the two in specific time. Both of the scales of drought events were dominated by mild drought, but the intensity variation trends were slightly different. The intensity of drought events at the SPI-3 scale decreases slower than that at the SPI-12 scale, and the average and fluctuation range of drought intensity are larger, indicating that the intensity of agricultural drought in the study area is larger than the hydrological drought intensity.

3.4 Spatial variation characteristics of drought events

3.4.1 Spatial characteristics of drought event duration

There are differences in the variation characteristics of drought event duration in different regions of the Mu Us Sandy Land, northern Shaanxi, at the same timescale (Figures 6A, D). At the SPI-3 scale, the duration of drought events in the whole region shows a decreasing trend, with the change tendency rates of DB, JB, HS, YL, and SM from west to east being −0.213/10a, −0.133/10a, −0.043/10a, −0.076/10a, and −0.270/10a, respectively. According to Daniel's test, the duration of drought events in SM and DB shows a significant decreasing trend ($p < 0.05$). SM decreases the fastest, followed by DB, JB, and HS. The duration of drought events in the YL area showed an insignificant decreasing trend ($p > 0.05$), and the decrease was slow; in the past 54 years, the largest number of 109 drought events occurred in the DB area, but the average duration was only 2.95 months. The lowest number of drought events occurred in JB, which is 91 times, but the average duration was the longest, 3.81 months.

The duration of drought events in the whole region showed an insignificant decreasing trend ($p > 0.05$) at the SPI-12 scale. DB and

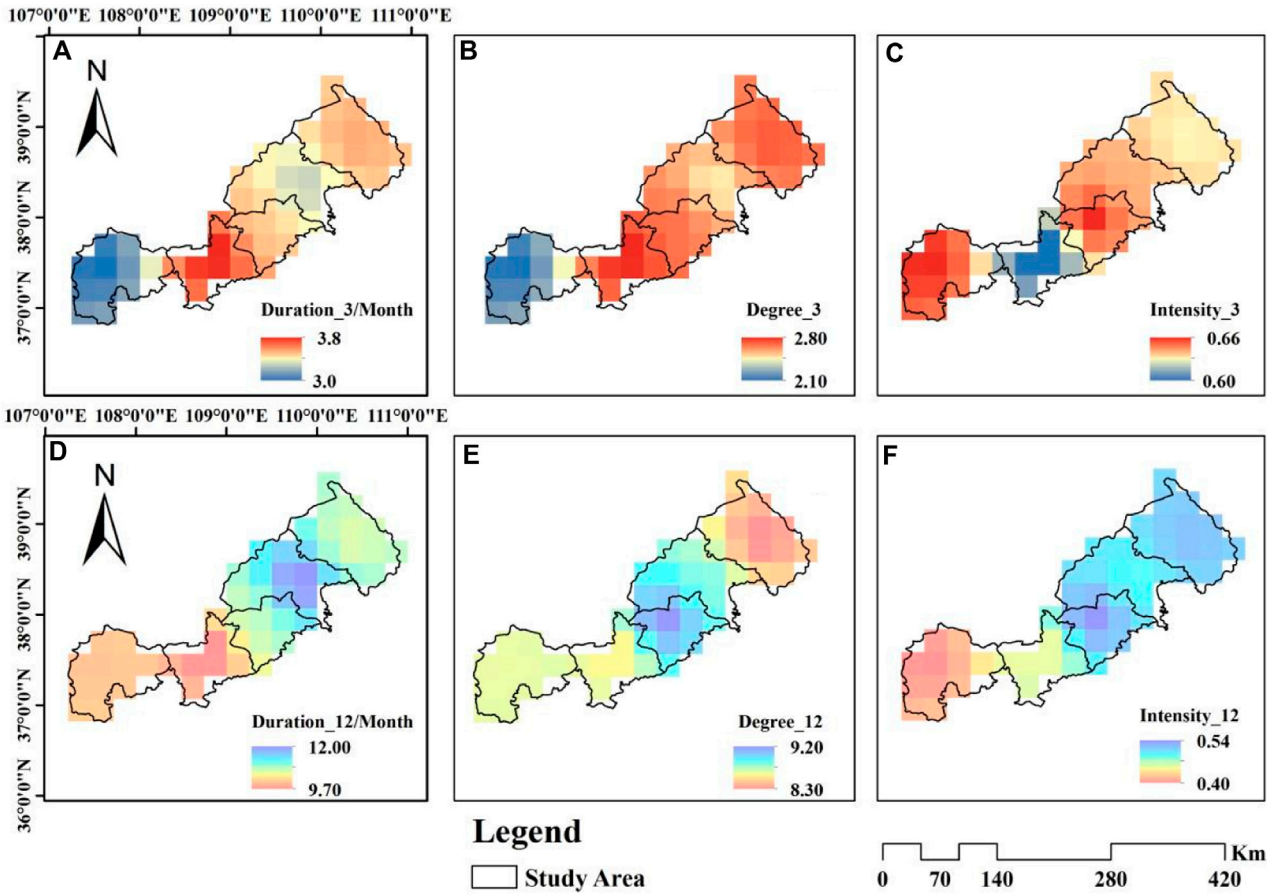

FIGURE 6
Drought characteristics of SPI-3 and SPI-12 drought events of the Mu Us Sandy Land.

YL had the fastest decreasing speed, with trend rates of −3.350/10a and −3.542/10a, respectively. In terms of the average duration of drought events in each region, the duration of drought events in JB was the shortest, 9.58 months, and that in YL was the longest, 12.21 months. These results show that the duration of drought events at two timescales in the Mu Us Sandy Land, northern Shaanxi, shows a decreasing trend. The duration of hydrological drought in the Shenmu region decreases the fastest, while the duration of hydrological drought in DB and YL undergoes the fastest decrease. JB is the region with the longest duration of hydrological drought, and YL is the region with a longer duration of hydrological drought.

3.4.2 Spatial characteristics of the drought degree of drought events

As shown in Figures 6B, E, the drought degree of drought events in all regions has shown a decreasing trend at the SPI-3 scale, while that in SM and DB has shown a significant decreasing trend ($p < 0.05$), with the change tendency rates being −0.297/10a and −0.148/10a, respectively. The maximum average drought degree is 2.78 in JB, and the minimum is 2.12 in DB. The drought degree in all regions, except Jingbian, showed an insignificant decreasing trend ($p > 0.05$) at the SPI-12 scale. the drought degree in Dingbian had the fastest decrease, followed by Yulin, with the change tendency rates of −4.175/10a and −2.668/10a, respectively. The maximum average drought degree was 9.16 in HS, and the minimum was 8.31 in SM. In summary, drought degree in SM and DB decreases fastest at SPI-3 and SPI-12 scales, respectively, indicating that the water deficit in this region has been alleviated, while the spatial distribution of the average drought degree of drought events shows different spatial distribution patterns. At the same time, the agricultural water deficit and hydrological water deficit are large in JB and HS, respectively.

3.4.3 Spatial characteristics of the drought intensity of drought events

As shown in Figures 6C, F, the drought intensity of SPI-3 and SPI-12 drought events has similar distribution characteristics with the drought degree. The drought intensity of each region shows a decreasing trend at the SPI-3 scale, of which JB, HS, and YL show a significant decreasing trend ($p < 0.05$). From the average drought intensity of drought events in the past 54 years at the two scales, the maximum values at the SPI-3 and SPI-12 scales are in HS, and the minimum values at SPI-3 and SPI-12 scales are in JB and DB, respectively. In summary, in HS, the drought intensity of drought events at two scales decreases rapidly, with large average drought intensity, indicating that serious hydrological drought events and hydrological drought events occur frequently.

4 Discussion

As a parameter, the SPI describes the status of water in an ecosystem more immediately than meteorological indexes (Luo et al., 2021b; Duan et al., 2021) (e.g., precipitation and evaporation). Estimating the climatic warming and humidification and drought at regional or global scales using an algorithm based on the SPI has become critical to cope with possible climate change. In this study, based on the sensitivity analysis shown in Figure 2, SPI reveals that the drought change trend affected by the accumulated precipitation in the early stage of different timescales (short term, medium term, and long term), with obvious function for short-term drought, seasonal drought, and annual scale drought, and can reflect the hydrological drought. The purpose is to determine whether the SPI can be used as a climate change evaluation index for sandy land, northern Shaanxi, Yellow River Basin. The precipitation data in our manuscript for 1965–2020 are considered most desirable as long records provide more reliable statistics for the SPI, given that it is a statistical approach. Many studies found that the SPI, which has more advantages in reflecting the drought trend and climate change because it does not consider potential evaporation, underlying surface, crops, and other relevant factors, has gained importance in recent years as a potential drought indicator permitting comparisons across different precipitation zones (Kalisa et al., 2020; Mga et al., 2021).

Based on the SPI, this study provides a strong indication that changes in climate altered the hydrothermal condition in the Mu Us Sandy Land, northern Shaanxi, Yellow River Basin. The findings show that the inter-annual, summer, autumn, and winter droughts in the study area showed a wetting trend, while the spring drought showed an increasing trend. Moreover, the directions of changes in the hydrothermal condition by climate change (i.e., precipitation) in this study are in line with hydrological studies in tropical regions, as proposed by Tian et al. (2015) and Xu et al. (2017). It is well known that the climatic warm–wet situation may cause not only an increase in the precipitation which significantly increases recharge for both soil water and groundwater but also promotes vegetation growth in the semi-arid area. The reliable water supply from soil and underground affects crop production in the growing season (Wu et al., 2021). However, in the present study, we find that regional drought characteristics are unevenly distributed, especially in spring, which shows an increasing trend. The spatial–temporal heterogeneity of precipitation, which is controlled by multiple scales and complex physical mechanisms, may probably be the main reason for the significant impacts on increasing of spring drought. In Northwestern China, air temperature in spring increases with the surface temperature affected by solar radiation. It is difficult to form precipitation conditions because of dry surface and air conditions. Moreover, precipitation in China mainly comes from the water vapor transported by the southeast monsoon of the Pacific Ocean and the southwest monsoon of the Indian Ocean. Under the action of the Hawaiian low-pressure system and the Asian high-pressure system, the southeast wind is mainly blowing, while the south is closer to the landing point of the summer wind. As the summer wind moves northward, the moisture content becomes less and less, and the rainfall in the north also decreases.

Several studies (Zhang et al., 2019; Jiang et al., 2020; Mu et al., 2020; Huang et al., 2021) have investigated the correlation between climate and drought in semiarid regions, and the results are similar to ours.

There are some potential socio-economic impacts of an appropriate drought (Asish et al., 2022; Espinosa-Tasón et al., 2022), such as agricultural losses and economic losses. As an agricultural–pastoral ecotone, the Mu Us Sandy Land has a semi-arid climate, located in a climate sensitive area characterized by a fragile ecological environment and frequent drought disasters. Spring precipitation and soil moisture play an important limiting role in crop growth in the region. The results of this article show an increase in spring drought, which could lead to reduced water availability for irrigation, resulting in crop failures and livestock losses. This can have a direct impact on farmers' livelihoods and food security and also affect food prices and availability in the markets. It is important to note that the impacts of drought can vary depending on factors such as the severity and duration of the drought, the socioeconomic conditions of the affected regions, and the availability of coping mechanisms and adaptive strategies. Effective drought management and preparedness measures, such as water conservation practices, early warning systems, and drought-resistant crop varieties, can help mitigate these impacts.

5 Conclusion

(1) The smaller the timescale of the SPI, the higher its sensitivity to a single precipitation, and *vice versa*. SPI-1, SPI-3, and SPI-12 have identification functions for short-term drought, seasonal drought, and annual scale drought, respectively, and can reflect the hydrological drought situation in the Mu Us Sandy Land in northern Shaanxi.

(2) There are differences in the frequency and level of drought identified by the SPI at different scales in different spaces and times.

(3) In the past 54 years, the SPI values of the Mu Us Sandy Land in northern Shaanxi have shown a decreasing trend only in spring, while drought has an increasing trend. The duration, degree, and intensity of drought events at the SPI-3 and SPI-12 scales have not significantly decreased, but the duration, degree, and intensity of drought events at the SPI-12 scale have decreased faster than those at the SPI-3 scale.

Data availability statement

The original contributions presented in the study are included in the article/Supplementary Material; further inquiries can be directed to the corresponding authors.

Author contributions

YZ: writing–original draft. JL: writing–review and editing. XX: writing–review and editing. JZ: writing–review and editing. PM: writing–review and editing. LL: writing–review and editing. PL: writing–review and editing.

Funding

The author(s) declare that financial support was received for the research, authorship, and/or publication of this article. This research was funded by Shaanxi Provincial Department of Science and Technology Project (2023JCYB449); Yan'an Science and Technology Bureau Announcement System Project (2023LJBZ002); Yan'an University College Student Innovation and Entrepreneurship Training Program Project (D2022106 and D2023142).

Acknowledgments

The authors would like to thank the editors and the reviewers for their crucial comments, which improved the quality of this paper.

Conflict of interest

The authors declare that the research was conducted in the absence of any commercial or financial relationships that could be construed as a potential conflict of interest.

Publisher's note

All claims expressed in this article are solely those of the authors and do not necessarily represent those of their affiliated organizations, or those of the publisher, the editors, and the reviewers. Any product that may be evaluated in this article, or claim that may be made by its manufacturer, is not guaranteed or endorsed by the publisher.

References

Asish, S., Subodh, C. P., Chowdhuri, I., Roy, P., Chakrabortty, R., and Shit, M. (2022). Vulnerability assessment of drought in India: insights from meteorological, hydrological, agricultural and socio-economic perspectives. *Gondwana Res.* 123, 68–88. doi:10.1016/J.GR.2022.11.006

Camarero, J. J., Gazol, A., Linares, J. C., Fajardo, A., Colangelo, M., Valeriano, C., et al. (2021). Differences in temperature sensitivity and drought recovery between natural stands and plantations of conifers are species-specific. *Sci. Total Environ.* 796, 148930. doi:10.1016/j.scitotenv.2021.148930

Cao, Z., Wang, S., Luo, P., Xie, D., and Zhu, W. (2022). Watershed ecohydrological processes in a changing environment: opportunities and challenges. *Water* 14, 1502. doi:10.3390/w14091502

Ding, Z., Lu, R., Wang, L., Yu, L., Liu, X., Liu, Y., et al. (2021). Early-mid holocene climatic changes inferred from colors of eolian deposits in the mu us desert. *Geoderma* 401, 115172. doi:10.1016/j.geoderma.2021.115172

Duan, W., Maskey, S., Chaffe, P., Luo, P., He, B., Wu, Y., et al. (2021). Recent advancement in remote sensing technology for hydrology analysis and water resources management. *Remote Sens.* 13 (6), 1097. doi:10.3390/rs13061097

Espinosa-Tasón, J., Berbel, J., Gutiérrez-Martín, C., and Musolino, D. A. (2022). Socioeconomic impact of 2005–2008 drought in Andalusian agriculture. *Sci. Total Environ.* 826, 154148. doi:10.1016/j.scitotenv.2022.154148

Hayes, M. J., Svoboda, M. D., Wilhite, D. A., and Vanyarkho, O. V. (1999). Monitoring the 1996 drought using the standardized precipitation index. *Bull. Am. Meteorological Soc.* 80 (3), 429–438. doi:10.1175/1520-0477(1999)080<0429:mtduts>2.0.co;2

Huang, W. J., Duan, W. L., and Chen, Y. (2021). Rapidly declining surface and terrestrial water resources in Central Asia driven by socio-economic and climatic changes. *Sci. Total Environ.* 784, 147193. doi:10.1016/j.scitotenv.2021.147193

Jiang, D. B., Hu, Z., Tian, X., and Lang, X. (2020). Differences between cmip6 and cmip5 models in simulating climate over China and the east Asian monsoon. *Adv. Atmos. Sci.* 37 (10), 1102–1118. doi:10.1007/s00376-020-2034-y

Kalisa, W., Zhang, J., Igbawua, T., Ujoh, F., Ebohon, O. J., Namugize, J. N., et al. (2020). Spatio-temporal analysis of drought and return periods over the east African region using standardized precipitation index from 1920 to 2016. *Agric. Water Manag.* 237, 106195. doi:10.1016/j.agwat.2020.106195

Kang, J. J., Zhao, W. Z., Zhou, H., and Wang, Z. (2020). The features of main osmolytes, silicon and their coupling effects in improving drought resistance of the typical xerophytes in the desert areas of northwest China. *Land Degrad. Dev.* 31 (17), 2720–2733. doi:10.1002/ldr.3631

Kincer, J. B. (1992). The seasonal distribution of precipitation and its frequency and intensity in the United States. *Res. Prog. Rep. - West. Soc. Weed Sci. (USA)* 3 (3), 109–127.

Li, Q., Chen, L., and Xu, Y. (2022). Drought risk and water resources assessment in the beijing-tianjin-hebei region, China. *Sci. Total Environ.* 832, 154915. doi:10.1016/j.scitotenv.2022.154915

Luo, P. P., Mu, Y., Wang, S. T., Zhu, W., Mishra, B. K., Huo, A. D., et al. (2021b). Exploring sustainable solutions for the water environment in Chinese and Southeast Asian cities. *AMBIO* 3, 13280. doi:10.1007/s13280-021-01654-3

Luo, P. P., Mu, Y., Wang, S. T., Zhu, W., Mishra, B. K., Huo, A., et al. (2021a). Exploring sustainable solutions for the water environment in Chinese and Southeast Asian cities. *AMBIO* 51, 1199–1218. doi:10.1007/s13280-021-01654-3

Mga, B., Wya, B., Twc, D., Zheng, N., and Wu, L. (2021). Assessing the use of standardized groundwater index for quantifying groundwater drought over the conterminous us. *J. Hydrology* 598, 126227. doi:10.1016/j.jhydrol.2021.126227

Mu, D., Luo, P. P., Lyu, J., Zhou, M., Huo, A., Duan, W., et al. (2020). Impact of temporal rainfall patterns on flash floods in Hue City, Vietnam. *J. Flood Risk Manag.* 14 (3), e12668. doi:10.1111/jfr3.12668

Munger, T. T. (1916). Graphic method of representing and comparing drought intensities. *Mon. Weather Rev.* 44, 642–643. doi:10.1175/1520-0493(1916)44<642:gmorac>2.0.co;2

Niemeyer, S. (2008). New drought indices. *Options Mditerranennes Sri A Sminaires Mditerranens* 80, 267–274.

Ortiz-Gómez., R., Flowers-Cano, R. S., and Medina-García., G. (2022). Sensitivity of the RDI and SPEI drought indices to different models for estimating evapotranspiration potential in semiarid regions. *Water Resour. Manag.* 36 (7), 2471–2492. doi:10.1007/s11269-022-03154-9

Soulsby, C., Scheliga, B., Neill, A., Comte, J., and Tetzlaff, D. (2021). A longer-term perspective on soil moisture, groundwater and stream flow response to the 2018 drought in an experimental catchment in the scottish highlands. *Hydrol. Process.* 35 (6), 14206. doi:10.1002/hyp.14206

Tian, H., Lan, Y. C., Wen, J., Jin, H. J., Wang, C. H., Wang, X., et al. (2015). Evidence for a recent warming and wetting in the source area of the Yellow River (SAYR) and its hydrological impacts. *J. Geogr. Sci.* 06, 643–668. doi:10.1007/s11442-015-1194-7

Tja, B., Yi, L., Sr, C., Li, F., Hu, Q., Feng, H., et al. (2020). Performance and relationship of four different agricultural drought indices for drought monitoring in China's mainland using remote sensing data. *Sci. Total Environ.* 759 (10), 143530. doi:10.1016/j.scitotenv.2020.143530

Wang, S., Cao, Z., Luo, P., and Zhu, W. (2022). Spatio-temporal variations and climatological trends in precipitation indices in shaanxi province, China. *Atmosphere* 13 (5), 744. doi:10.3390/atmos13050744

Wei, X., Wang, N., Luo, P., Yang, J., Zhang, J., and Lin, K. (2021). Spatiotemporal assessment of land marketization and its driving forces for sustainable urban–rural development in shaanxi province in China. *Sustainability* 13 (14), 7755–7820. doi:10.3390/su13147755

Wu, R., Liu, Y., and Xing, X. (2021). Evaluation of evapotranspiration deficit index for agricultural drought monitoring in north China. *J. Hydrology* 596 (2), 126057. doi:10.1016/j.jhydrol.2021.126057

Xiao, M., Zhang, Q., and Chen, X. (2012). Study on drought characteristics of the Pearl River basin based on multivariate probability analysis. *Acta Geogr. Sin.* 67 (1), 83–92. (In Chinese).

Xu, K., Wu, C., Zhang, C., and Hu, B. X. (2021). Uncertainty assessment of drought characteristics projections in humid subtropical basins in China based on multiple cmip5 models and different index definitions. *J. Hydrology* 600 (10), 126502. doi:10.1016/j.jhydrol.2021.126502

Xu, M., Kang, S., Wu, H., and Yuan, X. (2017). Detection of spatio-temporal variability of air temperature and precipitation based on long-term meteorological station observations over Tianshan mountains, central Asia. *Atmos. Res.* 203 (5), 141–163. doi:10.1016/j.atmosres.2017.12.007

Yang, P., Xia, J., Zhang, Y., and Wang, L. (2017). Drought assessment in northwest China during 1960-2013 using the standardized precipitation index. *Clim. Res.* 72 (1), 73–82. doi:10.3354/cr01451

Yang, P., Xia, J., Zhang, Y., Zhan, C., Cai, W., Zhang, S., et al. (2021). Quantitative study on characteristics of hydrological drought in arid area of northwest China under changing environment. *J. Hydrology* 597 (25), 126343. doi:10.1016/j.jhydrol.2021.126343

Zhang, Q., Shi, R., Singh, V. P., Xu, C. Y., Yu, H., Fan, K., et al. (2021). Droughts across China: drought factors, prediction and impacts. *Sci. Total Environ.* 803 (4), 150018. doi:10.1016/j.scitotenv.2021.150018

Zhang, Y., Huang, C. C., Tan, Z., Chen, Y., Qiu, H., Huang, C., et al. (2019). Prehistoric and historic overbank floods in the luoyang basin along the luohe river, middle yellow river basin, China. *Quat. Int.* 521, 118–128. doi:10.1016/j.quaint.2019.06.023

Zhou, C., Chen, D., Wang, K., Dai, A., and Qi, D. (2020). Conditional attribution of the 2018 summer extreme heat over northeast China: roles of urbanization, global warming, and warming-induced circulation changes. *Bull. Am. Meteorological Soc.* 101 (1), S71–S76. doi:10.1175/bams-d-19-0197.1

Zhu, L., Cooper, D. J., Han, S., Yang, J., Zhang, Y., Li, Z., et al. (2021). Influence of the atlantic multidecadal oscillation on drought in northern daxing'an mountains, northeast China. *Catena* 198, 105017. doi:10.1016/j.catena.2020.105017

Zhu, W., Wang, S., Luo, P., Zha, X., Cao, Z., Lyu, J., et al. (2022). A quantitative analysis of the influence of temperature change on the extreme precipitation. *Atmosphere* 13, 612. doi:10.3390/atmos13040612

frontiers | Frontiers in Environmental Science

TYPE Original Research
PUBLISHED 05 April 2024
DOI 10.3389/fenvs.2024.1380421

OPEN ACCESS

EDITED BY
Zhiming Han,
Northwest A&F University, China

REVIEWED BY
Xiaoyu Meng,
Henan University, China
Chenfeng Wang,
Chinese Academy of Sciences (CAS), China

*CORRESPONDENCE
Jiale Cai,
caijiale191@126.com
Zhongju Meng,
mengzhongju@126.com

RECEIVED 05 February 2024
ACCEPTED 19 March 2024
PUBLISHED 05 April 2024

CITATION
Cai J, Meng Z, Meng R, Li H, Chen X, Ren X, Guo L and Hao M (2024), Exploring a path of vegetation restoration best suited for a photovoltaic plant in the Hobq desert. *Front. Environ. Sci.* 12:1380421. doi: 10.3389/fenvs.2024.1380421

Exploring a path of vegetation restoration best suited for a photovoltaic plant in the Hobq desert

Jiale Cai[1]*, Zhongju Meng[1]*, Ruibing Meng[1], Haonian Li[1], Xiaoyan Chen[2], Xiaomeng Ren[3], Lijun Guo[4] and Meijun Hao[4]

[1]College of Desert Control Science and Engineering, Inner Mongolia Agricultural University, Hohhot, China, [2]Inner Mongolia Autonomous Region Academy of Social Science, Hohhot, China, [3]Inner Mongolia Institute of Meteorological Sciences, Hohhot, China, [4]Hangjin Banner Forestry and Grassland Business Development Center, Inner Mongolia, China

To investigate the soil improvement effects of different vegetation restoration measures during the operation and maintenance of photovoltaic power plants in the Hobq Desert. This study determined the soil grain size composition and soil nutrient content of 0–5 cm under four vegetation restoration measures and within the mechanical sand barriers by laser diffraction techniques and chemical experiments. The results showed that: (1) Soil particle size composition in the study area is predominantly sandy, with 1.02%, 6.63%, 5.34% and 2.61% less sand in *Leymus chinensis* (YC), *Glycyrrhiza uralensis* (GC), *Artemisia ordosica Krasch* (YH) and *Hedysarum scoparium* (HB), respectively, compared to mechanical sand barriers (CK). Soil particle distributions of YC, GC, and HB showed better sorting and more concentrated patterns, and all four vegetation restoration measures had higher fractal dimensions than CK. (2) AN (Alkali-hydrolyzable Nitrogen) content performance: The content of YC, GC, and HB was significantly higher than that of YH and CK, AP (Available Phosphorus) content did not differ significantly between measures, AK (Available Potassium) content was higher than that of CK in all measures, with YC content being the highest and SOM content being the highest for GC. (3) Soil total nutrient is unstable across vegetation restoration measures. Overall, the performance showed that the three vegetation restoration measures, YC, GC, and HB, were more evident in the soil total nutrient content improvement. Each particle size characteristic parameter and soil nutrient response vegetation restoration measures ameliorate sandy soil in PV power plants during operation and maintenance. YC and GC have the most apparent effect on soil amelioration.

KEYWORDS

photovoltaic vegetation restoration Hobq desert, solor, photovoltaic, rehabilitation of vegetation, particle size characteristics, soil nutrients

Introduction

With global fossil energy consumption increasing and greenhouse gas (CO_2) emissions rising every year A global warming worsens, the transition from traditional energy to new energy has become inevitable (Sinke, 2019). Faced with market demand, photovoltaics, a cleaner form of energy that is expected to occupy a significant place in energy development over the next decade, has made impressive progress in terms of scale of deployment, cost reductions, and performance improvements after several generations of updates, PV power

generation technology is becoming more and more mature (El Chaar and El Zein, 2011; Lupangu and Bansal, 2017).

As one of the eight significant deserts in China, the Hobq Desert, with its vast area, low vegetation cover, and frequent and strong wind and sand activities, is the primary source of wind and sand sources in Beijing and Tianjin (Du et al., 2014; Ren et al., 2022). Therefore, it is necessary to adopt effective desert control and sand fixation methods in the Hobq Desert region according to local conditions. The construction of photovoltaic power plant in the desert not only effectively use the land but also can achieve the purpose of desert control, two birds with one stone. Yuan et al. (2022) found through their research that the erection of photovoltaic panels is conducive to transforming and consuming the power source of sandstorms and wind-sand flow in desert areas, reducing the occurrence of sandstorms. Photovoltaic development in desert areas changes the environment in which vegetation grows and increases surface roughness, providing new ideas for combating desertification. Chang et al. (2020) found that constructing photovoltaic panels in the desert can effectively reduce the role of high winds in the sand flow, prevent wind, and fix sand. Its effect is three times the effect of mechanical sand barriers. Photovoltaic panels of the rain effect can promote the growth of vegetation in the desert. Yue et al. (2021) found that the shaded portion of PV panels helped to reduce soil temperature and increase soil moisture. Wang et al. (2021) found that the erosion intensity without any restoration measures under the PV panels is significantly higher than with restoration measures and outside the PV plant. However, most scholars have found through research that the construction of photovoltaic power plants in desertified areas will accelerate the development of desertification if corresponding restoration measures are not constructed (Yue et al., 2021). Tang et al. (2021) found that large-scale photovoltaic power plants will accelerate the process of surface erosion in the power plant after the completion of the surface erosion process caused by the geomorphological changes seriously affect the production, operation, and maintenance of solar energy.

It is urgent to carry out vegetation ecological restoration and reconstruction measures in response to the destruction of the ecological environment in the sandy area during the construction of photovoltaic power plant projects and the prevention and control of sand damage in photovoltaic power plants. Previous studies have concluded that the construction of photovoltaic power plants is prone to erosion of the lower part of the panels. However, in desert areas where evaporation is more significant than rainfall, the rain-collecting effect of photovoltaic panels is precious. The reasonable tilt angle of the photovoltaic panels behind the panels can form a wind-blocking effect, which is more conducive to constructing measures to restore the vegetation in desert areas (Chang et al., 2020; Yue et al., 2021). Revegetation measures reduce the intensity of wind and sand activity, increase soil erosion resistance, and improve soil fertility (Huang, 2020). Soil properties directly influence the processes of vegetation growth, development and succession, and conversely, the processes of vegetation growth, development, and succession closely influence the physical and chemical properties of soils (Hong et al., 2006). Plant roots are intertwined in a network that improves soil structure and consolidates the soil; the biological crust makes the soil more stable and enhances the soil's resistance to erosion (Zhang et al., 2006).

Therefore, adopting vegetation measures during the operation and maintenance of desert photovoltaic power plants is very effective, and the planting of vegetation in desertified areas is beneficial to desertification control efforts and can also bring local side income. Liu X. et al. (2020) found that the ecosystem service function provided by composite system land is 24 times higher than that of naturally restored land (Rodriguez-Pastor et al., 2023). Planting plants under photovoltaic panels during the hot season helps to reduce the module temperature and thus increases the power generation rate.

The above studies as well as the previous studies are mostly on the impact of PV panels on the environment and the impact of the environment on PV panels, etc., while there are relatively few studies on vegetation restoration measures and traditional sand fixation measures during the operation and maintenance period of desert PV power plants. Based on this study, this study takes several vegetation restoration measures such as planting *Leymus chinensis* (from now on referred to as YC), *Glycyrrhiza uralensis* (from now on referred to as GC), *Artemisia ordosica Krasch* (from now on referred to as YH), *Hedysarum scoparium* (from now on referred to as HB) under the PV panels in Yili 200 MP PV plant in Hobq Desert, and setting up local commonly used mechanical sand barriers (from now on referred to as CK) as a control group, YC, GC, YH, and HB are widely distributed in the Hobq Desert, and all are locally dominant species that play a significant role in fixing local mobile sands, and analyses different restoration techniques in terms of their physicochemical properties (Soil particle size characteristics, and soil nutrients), and combines them with the different vegetation's growth habit, economic value, adaptability, and survival rate. The purpose of this study is to analyze different aspects and perspectives of different vegetation restoration techniques, such as growth habit, economic value, adaptability, and survival rate, in order to explore the most suitable path of vegetation restoration measures in the Hobq Desert PV power station and also to provide a theoretical basis for the restoration of other photovoltaic power stations, and contribute to the construction of the ecological environment.

Methods

Study area and patch characteristics

The study area is located in Yili Photovoltaic Ecological Park (40°26′7″N, 108°50′8″E), Duguitara Town, Hangjin Banner, Ordos City, Inner Mongolia Autonomous Region, with an altitude of 1103 m. It is in the northwestern part of Ordos City, spanning the Ordos Plateau and the Hetao Plain, and is situated in the transition zone of temperate arid steppe and desert steppe, and has the typical temperate continental climate, with the average annual temperature of 5°C–8°C; arid and little rain, spring drought every year, the average rainfall is 245mm, 60% of rainfall is concentrated in July - September, the average evaporation is 2720mm; the average annual wind speed is 3.0 m/s, generally seen in the spring, the maximum wind speed reaches 28.7 m/s, and accompanied by sandstorms, and the wind direction is dominated by the north-west wind. The study area was mostly flowing sandy land before restoration measures were taken; very rarely were *Phragmites australis, Ammopiptanthus mongolicus,*

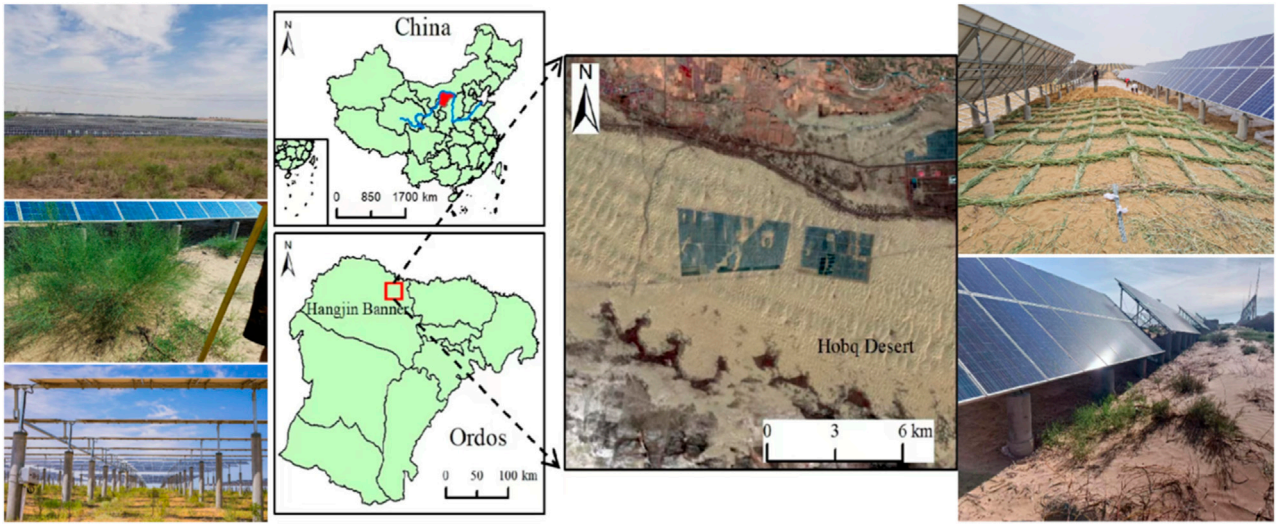

FIGURE 1
Overview map of the study area.

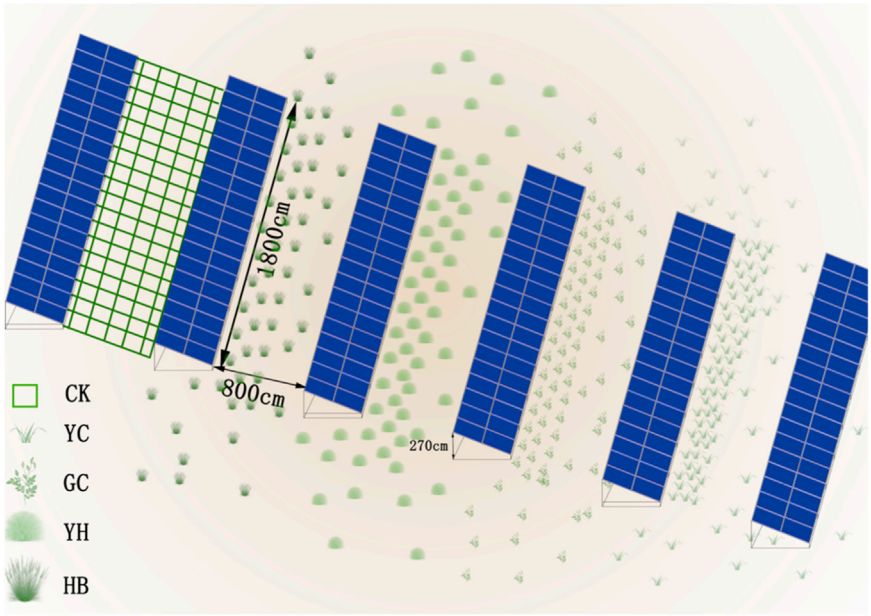

FIGURE 2
Schematic diagram of restoration measures within a photovoltaic power plant.

Agriophyllum squarrosum, and T*amarix chinensis* Lour An overview map of the study area is shown in Figure 1 below.

The angle of the photovoltaic panels to the ground is 36°, and a single set of photovoltaic panels consists of two rows and 18 columns of 1950 mm × 990 mm. The specification of the whole photovoltaic panel is 4 m × 18 m, and the height of the back edge of the panel from the ground is 2700 mm. The height of the front edge of the panel from the ground is 300 mm. The panels face south and run east-west, and the spacing between two neighbouring PV panels is 8 m. A schematic diagram of the PV plant is shown in Figure 2.

Research methodology

Experimental design and sample collection

Sample collection was carried out in June 2022. YC, GC, YH, HB, and CK, which are typical restoration measures in the sample area, were selected as the collection sites for the experimental samples, and five 1 m × 1 m sample squares were randomly selected from each sample area. Five points were selected from each sample square according to the five-point method. The soil sampling was carried out in the 0–5 cm soil layer after removing the

dead debris and humus from the ground surface. Five samples obtained from each sample square were mixed equally, and the quadratic method selected enough soil samples. After removing surface litter and humus, soil samples were taken from the 0–5 cm soil layer; the five samples obtained from each sample square were mixed equally, and then enough soil samples were selected by the quadratic method and sealed in self-sealing bags and then put into ice boxes to be brought back to the laboratory. The soil inside the plastic bags was placed in a cool and dry place to be naturally air-dried and then sieved after drying. After removing the impurities, it was divided into two parts: characterizing the soil particle size and determining the soil nutrient content.

Measurement methods

Determination of soil mechanical composition: An Analysette 22 Micro-Tec Plus model laser particle sizer determined soil particle size composition. The classification was based on the grain size composition of the US-made soil: clayey (<2 μm), chalky (2–50 μm), very fine (50–100 μm), alumina (100–250 μm), medium (250–500 μm), coarse (500–1,000 μm), very coarse (1,000–2000 μm), and gravelly (>2000 μm). Screening outputs particle diameters corresponding to cumulative volume fractions of soil particles of 5 percent, 10 percent, 16 percent, 25 percent, 50 percent, 75 percent, 84 percent, 90 percent, and 95 percent for later calculations.

$$\Phi = -\log_2 D \tag{1}$$

Using the Udden-Wenworth grain size criterion, a logarithmic transformation was performed according to Kumdein's algorithm, which converted the previously output particle diameters corresponding to the cumulative volume fraction of each soil particle into Φ-values (Blair and McPherson, 1999), respectively, to facilitate subsequent calculations, the conversion equation is: where D is the diameter of soil particles.

The soil particle size parameters such as mean particle size (d_0), standard deviation (σ_0), skewness (SK) and kurtosis (Kg) were calculated based on the graphical method of Folk and Ward (1957). Determination of the volume content of different soil particle sizes using a laser particle sizer and characterization of the soil fractal model using the particle size volume distribution to calculate the fractal dimension (Armstrong, 1986; Ahmadi et al., 2011); the formula is:

$$d_0 = \frac{1}{3}(\Phi_{16} + \Phi_{50} + \Phi_{84}) \tag{2}$$

$$\sigma_0 = \frac{(\Phi_{84} - \Phi_{16})}{4} + \frac{(\Phi_{95} - \Phi_5)}{6.6} \tag{3}$$

$$\mathrm{SK} = \frac{\Phi_{16} + \Phi_{84} - 2\Phi_{50}}{2(\Phi_{84} - \Phi_{16})} + \frac{\Phi_5 + \Phi_{95} - 2\Phi_{50}}{2(\Phi_{95} - \Phi_5)} \tag{4}$$

$$\mathrm{K_g} = \frac{\Phi_{95} - \Phi_5}{2.44(\Phi_{75} - \Phi_{25})} \tag{5}$$

$$\frac{V(r < R_i)}{V_t} = \left(\frac{R_i}{R_{\max}}\right)^{3-D} \tag{6}$$

Where: D is the fractal dimension; Ri denotes the measured soil particle size; Rmax is the diameter of the largest particle; V (r < Ri) is expressed as the volume percentage of soil grain size smaller than the measured grain size (Ri); Vt is expressed as the total volume percentage of the volume of each grain size of the soil.

Soil organic matter (SOM) content was determined using the potassium dichromate volumetric method with external heating (Nelson and Sommers, 1983); Quick-acting potassium (AK) by NH4OAc leaching-flame photometric method (Zheng and Zheng, 2022); Quick-acting phosphorus (AP) was determined by leaching with 0.5 mol-L-1NaHCO3, followed by spectrophotometric determination of the test solution (Munhoz et al., 2011); Alkaline nitrogen (AN) is determined by the alkaline diffusion method (Chen et al., 2016); Total Nitrogen (TN) was determined using the semi-micro Kjeldahl method (Kirk, 1950); Total phosphorus (TP) was determined by NaOH melting-molybdenum antimony colorimetric method (Bremner and Mulvaney, 1983); Total potassium (TK) was determined by NaOH melting and flame photometric method (Gao et al., 2018).

Processing and analysing data

Excel 2021 and Origin 2023 software were used to collate and analyze the data, as well as graphical work. SPSS 25 software was used to perform one-way ANOVA and principal component analysis on the data.

Results

Mechanical composition of soil particles under different vegetation restoration measures in a photovoltaic power plant

As can be seen from Table 1, the soil grain size composition of the five restoration measures in this study, YC, GC, YH, HB and CK, all showed a predominance of sand grains, were all above 90%, with CK having a significantly higher sand content than the other four restoration measures ($p < 0.05$); The content of sticky meal grains increased by 1.02%, 6.63%, 5.34% and 2.61% for the four restoration measures compared to CK, respectively; further analysis of the sand particles reveals that the YC wonderful sand is significantly lower than the other three restoration measures ($p < 0.05$), the acceptable sand content of YH was significantly lower than the other measures ($p < 0.05$), and the performance of the medium sand content did not differ significantly among the restoration measures ($p > 0.05$), the overall content of coarse and very coarse sand also showed higher ($p < 0.05$) for the YH restoration measure than for the other restoration measures. The sticky grain content of each restoration measure did not exceed 1%, except for GC, and showed a non-significant difference in sticky grain content under each restoration measure.

Soil particle size parameters of different vegetation restoration measures in photovoltaic power plants

From Table 2, it can be seen that the mean particle size of all five restoration modes showed significant differences ($p < 0.05$), the YH recovery mode has the smallest average grain size, the HB recovery mode has the largest average grain size, and the HB recovery mode

TABLE 1 Soil particle size content under different restoration measures.

Rehabilitation measures	Agglomerate	Granule	Grit				
			Extremely fine sand	Fine sand	Alumina	Coarse sand	Very coarse sand
YC	0.51 ± 0.05b	1.70 ± 0.11b	0.63 ± 0.04bc	69.62 ± 0.81c	26.53 ± 0.95b	0.17 ± 0.12a	0.83 ± 0.40a
GC	1.08 ± 0.06a	6.74 ± 0.12a	3.74 ± 0.14a	59.43 ± 2.41c	26.27 ± 1.40a	1.03 ± 0.28bc	1.70 ± 0.32b
YH	0.76 ± 0.03bc	5.77 ± 0.31a	6.07 ± 0.27a	47.75 ± 0.38d	17.78 ± 1.02b	14.1 ± 1.17a	7.77 ± 1.16a
HB	0.89 ± 0.10a	2.91 ± 0.21a	3.02 ± 0.32a	71.93 ± 0.61c	20.03 ± 0.84 ab	0.42 ± 0.36 ab	0.77 ± 0.08c
CK	0.26 ± 0.05a	0.93 ± 0.03c	0.38 ± 0.01d	64.46 ± 0.76a	31.51 ± 0.57c	0.53 ± 0.11a	1.85 ± 0.32a

Note: Peers with different lowercase letters in the table indicate significant differences between the restoration measures($p < 0.05$).

TABLE 2 Soil particle size parameters for different restoration models.

Soil particle size parameters	Average particle size	Standard deviation	Skewness	Peak state	Fractal dimension
YC	2.17 ± 0.01c	0.47 ± 0.01d	0.11 ± 0.00c	1.01 ± 0.01b	2.05 ± 0.02c
GC	2.26 ± 1.31b	0.84 ± 0.02b	0.35 ± 0.01a	1.71 ± 0.01a	2.24 ± 0.01a
YH	1.78 ± 0.28e	1.47 ± 0.00a	−0.17 ± 0.00e	0.98 ± 0.26b	2.25 ± 0.01a
HB	2.32 ± 1.17a	0.59 ± 0.03c	0.18 ± 0.00b	1.16 ± 0.05b	2.16 ± 0.03b
CK	1.58 ± 0.52d	1.87 ± 0.01e	0.06 ± 0.00d	1.00 ± 0.01b	1.95 ± 0.05d

has the largest average grain size; According to the Folk Ward diagrammatic classification criteria, they belonged to chalk, fine sand, medium sand and coarse sand, respectively, and differed significantly ($p < 0.05$) from each other; The standard deviations were significantly different from each other ($p < 0.05$), with better sorting for YC and moderate sorting for GC and HB, YH and CK were poorly sorted; Significant differences ($p < 0.05$) were found between restoration measures for bias; Only YH was negatively biased for the five recovery measures, indicating that the grain size of YH was moving towards finer grains; In terms of peak state performance, GC was significantly higher than the other four measures ($p < 0.05$), and the difference between the other four was not significant ($p > 0.05$); The fractal dimension of CK was significantly lower ($p < 0.05$) than the other four vegetation restoration measures, indicating that the content of fine-grained material within CK was significantly lower than the other four restoration measures.

Scatter plots were produced with the soil particle size parameters of the four vegetation restoration measures and CK, respectively, which allowed direct observation of the distribution of soil particle size parameters in the five sample plots. From Figure 3., it can be seen that there are apparent boundaries between the two restoration measures of GC and YH and the restoration measures of YC and HB, which can be clearly distinguished by the scatter plots of each granularity parameter, and the difference between the two restoration measures of YC and HB is not significant, and the performance site is evident on d_0-Kg and d_0-D, and the rest of the plots can be clearly identified. From the scatter plot of particle size parameters, it can be seen that CK recovery measures have the most extensive distribution range of each particle size parameter, YC has the most concentrated distribution range, followed by GC, and YH and HB are worse.

Soil particle frequency distribution curves for different vegetation restoration measures in photovoltaic power plants

Soil particle frequency distribution curves are often used to analyze the size distribution of particles, not only to obtain the skewness, kurtosis, and other information qualitatively but also to determine the deposition dynamics of the particles and the source of the material from the peak properties of the curve. Particle distribution curves were made with the mean surface soil particle size of the four vegetation restoration measures and the control group (CK), respectively. It can be seen that there are differences between the samples, among which there are apparent differences between the YH restoration measure and the other samples, with the YH restoration measure showing a bimodal state and the remaining four samples showing an unimodal state. Soil particle size was concentrated near 200–300 μm in the single peak state, and the first part of the double peak state was concentrated near 200–300 μm. It appeared in the second peak

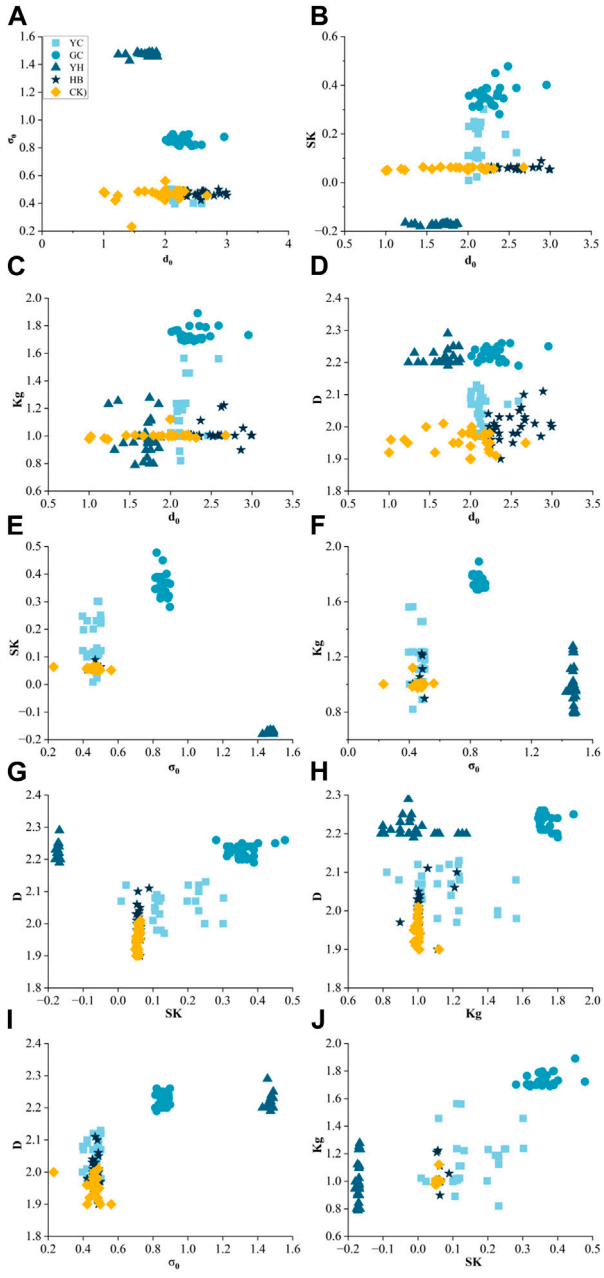

FIGURE 3
Scatter plot of particle size parameters. d_0-σ_0 **(A)**, d_0-SK **(B)**, d_0-Kg **(C)**, d_0-D **(D)**, σ_0-SK **(E)**, σ_0-Kg **(F)**, σ_0-D **(G)**, SK-Kg **(H)**, SK-D **(I)**, Kg-D **(J)**.

state near 1,000 μm, and before 100 μm, several restoration measures, YC, GC, HB, and CK, were slightly lower than YH restoration measures. It can be found that the content of clayey silt and wonderful sand of YH is higher than that of other measures, and the content of coarse sand and very coarse sand of other measures is significantly lower than that of YH, which is also more resistant to wind erosion, it can also be seen that YH is less concentrated in particle size than the other three measures. The cumulative frequency distribution curve can reflect the distribution of soil particles; generally, the steeper the curve, the more uniform the distribution of particles; at the same time, it can characterise the proportion of soil particles. As can be seen from Figure 4, the soil particle uniformity of YC, GC, and HB in the sample plot was higher than that of YH, and the curve suddenly became steeper at 100 μm and smoother at 500 μm, indicating that the soil particle size characteristics were concentrated in the range of 100–500 μm. Moreover, near 400 μm, the YH restoration measure became flat and less steep than the remaining four measures, indicating that YH is less sortable and homogeneous than the other four vegetation restoration measures. The cumulative frequency curve of soil particles also showed that coarse and very coarse sand content was significantly higher in YH than in CK, YC, GC and HB.

Soil available nutrient content under different vegetation restoration measures in photovoltaic power stations

Figure 5 shows that the content of available nutrients between the PV array panels of all four vegetation restoration measures has been improved to different degrees compared with the traditional sand fixation measures. Specifically, the AK content of the four vegetation restoration measures as a whole was significantly higher than that of CK, and the AK content of YC was the highest, and the AK content of YC was the highest; several other restoration measures had significantly lower AK levels than YC. In terms of AP content performance, only the HB restoration measure was comparable to the other three restoration measures and CK; there were individual groups of CK that had higher AP content than the HB recovery measure, and YC and GC were stable in AP content and did not differ significantly from each other; The content of AN was shown to be significantly higher than that of CK for all four vegetation restoration measures, with YC, GC, and HB showing the most significant. Figure 3 shows that the combined quick nutrient content YH of the four vegetation restoration measures was not significantly different from each other. However, each of them was not high, while the other three restoration measures all showed significant differences among the three available nutrient contents.

Soil total nutrient and organic matter content under different restoration measures in a photovoltaic power plant

From Figure 6, it can be found that the SOM content of GC > HB > YC>CK > YH, only the SOM content of YH was reduced by 34.51% compared with that of CK. The remaining three types of vegetation restoration measures were enhanced by 45.49%, 365.49%, and 148.63%, respectively, compared with that of CK. There were apparent differences between the vegetation restoration measures and CK, most evident in GC. TN content of GC and HB was significantly higher than that of the other two vegetation restoration measures and CK, the minimum content of YC and YH was even lower than that of CK, the median was also lower than that of CK, and the spacing between the upper edge and the lower edge was lower than that of CK, the unique values of the four vegetation restoration measures and CK were within

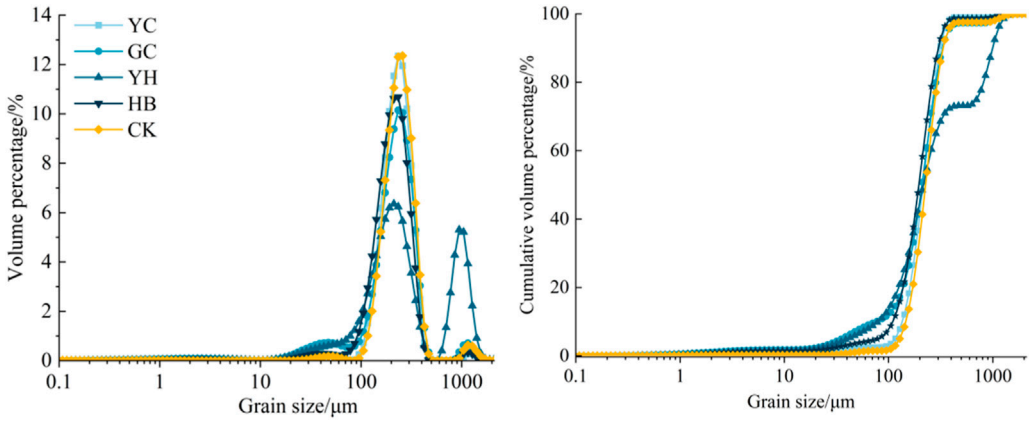

FIGURE 4
Scatter plot of particle size parameters.

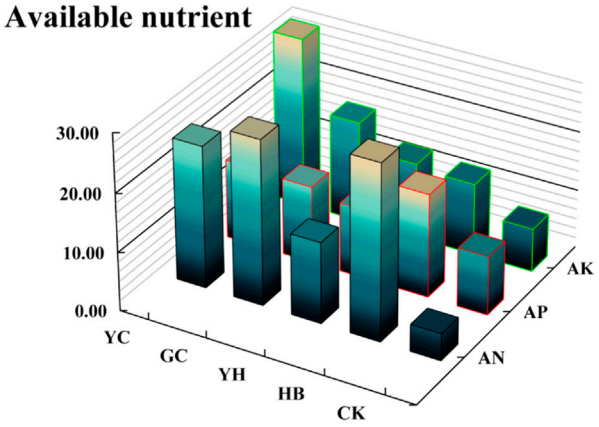

FIGURE 5
Soil available nutrient content of different restoration measures.

the confidence interval, the figure showed the TN content of soil of the four vegetation restoration measures, and the TN content of soil of the three restoration measures increased by 45.49%, 365.49% and 148.63% respectively compared with CK. The soil TN content of the four vegetation restoration measures was stable, as shown in the figure TP content was higher than that of CK in YC and HB, as shown in the box plot, in which the content of YC was higher than CK's; although HB's content was higher than CK's, the difference was not noticeable. The soil TP content of GC and YH was significantly lower than that of CK, and the confidence interval of GC and YH was more significant than that of CK, which indicated that the distribution of the TP content of GC and YH was not as concentrated as that of CK. TK content was not as concentrated as that of CK. The TK contents of YC and CK were significantly higher than those of the other three vegetation restoration measures, with the lowest content in YH, and the total potash contents of GC and HB were in the range of 35–43 g/kg. The TK contents of GC, YH, and HB were 55.09%, 112.17%, and 74.42% less than those of CK.

Discussion

Effects of different restoration measures on soil particle size characteristics between photovoltaic panels

The PV power stations in the study area are subjected to severe wind erosion during operation and maintenance, and the desert area is windy and sandy, with frequent and intense wind and sand activities; during the wind and sand movement, the surface fine-grained material is lost, which leads to an increase in the content of coarse-grained material in the mechanical composition of the soil material, and the surface is coarsened significantly. Pan et al. (2020) found that vegetation can effectively improve the fine-grained tendency of soil and can increase the roughness of the ground surface. Similarly, in this study, the content of sticky and powdery particles in the mechanical sand barriers of the control group differed significantly from the remaining four vegetation restoration measures, and the content of the mechanical sand barriers was significantly lower than that of the four vegetation restoration measures. The higher the content of fine-grained matter, the more microporosity of the soil, the higher the complexity of the soil, and the greater the fractal dimension of the soil, indicating a decrease in the degree of sanding of the soil. Some scholars (Liu Y. et al., 2020) found that the content of fine-grained matter in soil particle size parameters under vegetation with high vegetation cover and lush foliage was significantly higher than that under vegetation with low vegetation cover and depression. Qi et al. (2018) found that the value of soil fractal dimension was significantly positively correlated with the content of clay and powder particles and significantly negatively correlated with the content of sand particles, indicating that the less clay and powder particles or the higher the proportion of sand particles in the soil, the higher the roughness and inhomogeneity of the soil particle composition. The results of this study found similar patterns to the above results, we found that the content of sticky and powdery particles in GC and YH was significantly higher than that of the other two restoration measures and CK. The fractal dimension was also higher than that of the other two vegetation restoration measures because the

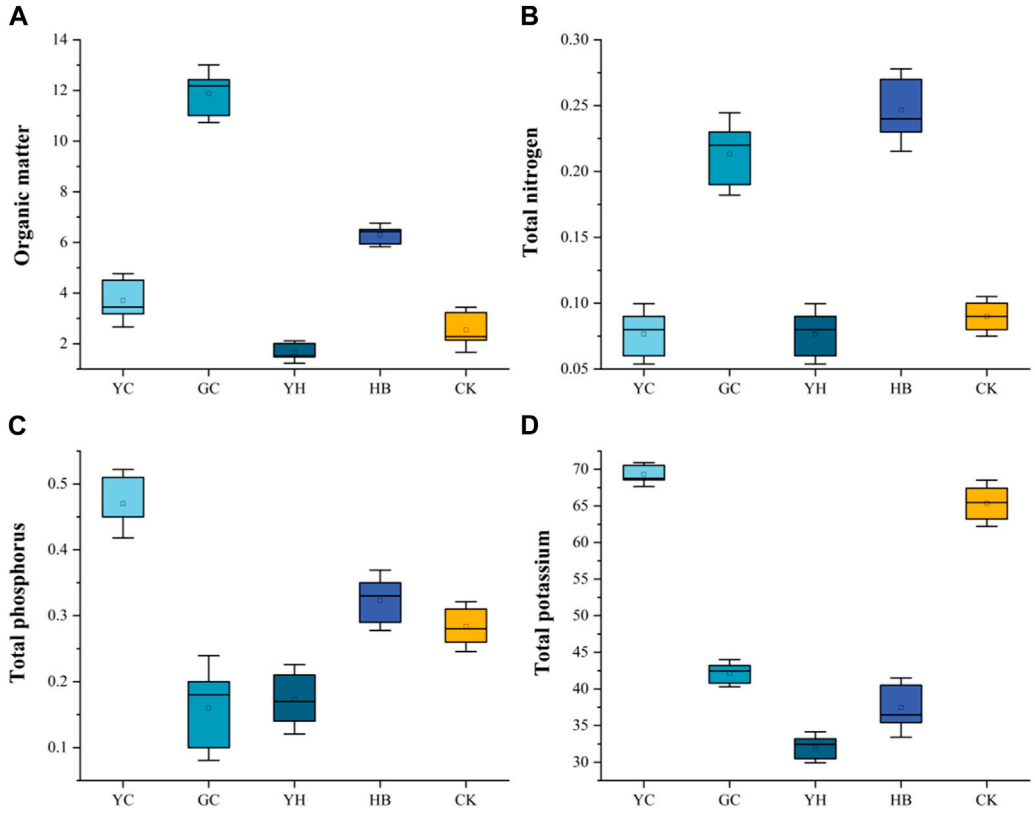

FIGURE 6
Organic matter **(A)**, Total nitrogen **(B)**, Total phosphorus **(C)**, Total potassium **(D)**.

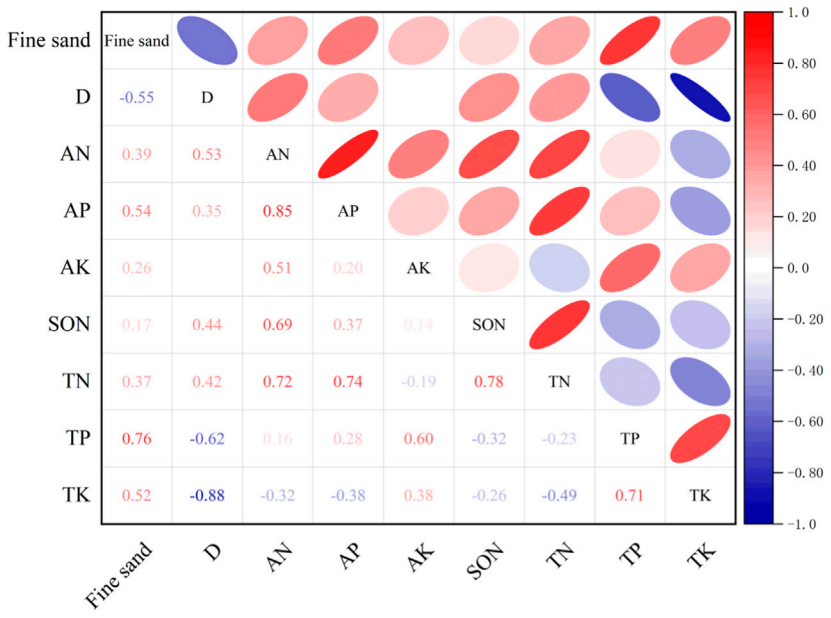

FIGURE 7
Heat map of soil physical and chemical properties.

vegetation cover of GC and YH was higher than that of the other two vegetation restoration measures, and the branching and foliage of Chengdu were also higher. From the above findings, it was found that GC and YH were the most obviously fine-grained in terms of particle size characteristics and particle size parameter performance, and the trend of fine-graining was also more apparent.

Effect of different restoration measures on soil nutrients between PV panels

Different vegetation restoration measures mainly influenced the differences in soil nutrients between locations between photovoltaic panels. This study showed that with the restoration of soil vegetation, the degree of change of soil fast-acting soil nutrients was higher than that of full-acting nutrients, especially AN and AK, which indicated that soil fast-acting nutrients were more sensitive than full-acting nutrients to the changes in the restoration of the plant community, which was in line with the results of the previous study. As the number of years of vegetation restoration increased, more plant litter was returned to the soil due to vegetation restoration, which increased the organic matter content of the soil. Figure 3, 4 show that the quick-acting nutrient content of each vegetation restoration measure was higher than that of CK except for a few locations. However, each vegetation restoration measure's full-acting nutrient and organic matter content was lower than CK's. Huang et al. (2020) found that the content of soil nutrients increased significantly with the increase of restoration time. However, Weltzin and Coughenour (1990) found higher concentrations of nitrogen and organic carbon in shallow soils near tree trunks, suggesting a negative effect of nutrient inputs from tree trunks and shading on soil nutrient loss. It showed that vegetation can sometimes hurt the soil and that most of the surface soil nutrients under vegetation come from deadfall; therefore, it can be explained that the nutrient content of some of the vegetation restoration measures in this study was lower than that of CK, which may be due to the short years of vegetation restoration in this study or the loss of soil nutrients due to the shading effect of vegetation., Some scholars (Wu et al., 2020) found that vegetation degradation leads to a significant decrease in soil nutrients, and conversely, an increase in vegetation richness leads to an increase in soil nutrients. Combining the present study with the above studies, it can be seen that the adoption of vegetation restoration measures in PV power plants can effectively improve the soil nutrient content and play a positive role in the improvement of soil quality in PV power plants.

An investigation of the combined value of four vegetation measures within a photovoltaic power plant in the hobq desert

In this study, four types of local sandy vegetation were selected as restoration measures, aiming to find a green and long-lasting vegetation restoration measure during the operation and maintenance of PV power stations in the Hobq Desert. In order to prevent and control secondary sand damage during the operation of the PV plant, if it can be done to increase local income, it is just like the icing on the cake, and it can be done on the basis of green management to restore the vegetation and increase income. *Leymus chinensis* is rich in diversity and ecological adaptations, widely distributed in the inland areas of China, and is not only able to provide genetic material for forage improvement but also a potential contributor of genes for resistance to harsh environments (Wu et al., 2020). *Glycyrrhiza uralensis* it is an excellent medicinal herb, and in addition to its medicinal uses, *Glycyrrhiza uralensis* is a drought-tolerant and deep-rooted plant that is important for windbreaks, sand fixation, and soil formation in semi-arid ecosystems (Weltzin and Coughenour, 1990). Artemisia ordosica Krasch is a dry, deciduous, multi-stemmed shrub (Sha et al., 2014), and is a typical sandy half-shrub of the Maowusu Sand. It has dry, linear-lobed leaves that form scrubby sand mounds of about 0.5–1 m. Its primary roots reach up to 3 m below the surface, and it is endemic to Ordos in northern China, where it is absolutely dominant (Liu et al., 2007). Although its sand-fixing capacity is strong, and it was once fly-seeded over large areas in northwestern China, the pollen of Artemisia oleifera causes allergic rhinitis in residents (Li et al., 2021). *Hedysarum scoparium* has the characteristics of sand burial, wind erosion resistance, and strong sprouting capsule force, which is widely used for windbreak and sand fixation, and it is one of the excellent pioneer tree species in creating windbreak and sand fixation forests in desert areas (Kobayashi et al., 1995). It is a perennial shrub, which is the main tree species for windbreak and water retention. It is resistant to wind erosion and sand burial, and after sand burial, it can rapidly sprout adventitious roots with substantial windbreak and sand fixation. its horizontal root system is well developed, so it is suitable for flowing sand areas (Xiao et al., 2020). Although the *Hedysarum scoparium* is suitable for flowing sand if planted in the photovoltaic power station, with the growth of the recovery years, the plant height and crown width of the flower stick will increase, which will be involved in the later stage will be shading photovoltaic panels and the later flat stubble maintenance and so on.

In this study area, the four vegetation restoration measures and the control group (mechanical sand barriers) were planted individually, and no mixed planting was used. From this study, combined with the correlation of hot map (Figure 7), it was found that most of the soil physicochemical properties in this study area showed a positive correlation, with a positive correlation accounting for 72.2% of the total, which indicated that the soil physicochemical properties were in a certain degree in mutual constraints; A few showed negative correlations and only AN and TN stood out in terms of very positive correlations. The results of this study showed that none of the restoration measures were outstanding in terms of physical and chemical properties but only in one or more of the indicators. Based on the above studies, we can infer that planting vegetation under the inter-slabs of photovoltaic panels with a mixed vegetation planting method will be superior to planting a single species (Li, 2022). Rodríguez-Loinaz et al. (2008) found that soil physicochemical properties showed a positive correlation with biodiversity through her research, and the species richness of herbaceous plants showed a significant positive correlation with the functional diversity of soil. Some scholars (Chandra et al., 2016) the results of the study showed that in oak marriages located in the temperate zone, the soil carbon, nitrogen, and phosphorus contents were relatively high, as well as the microbial activity.

Conclusion

(1) The following conclusions were reached by analyzing the soil particle size characteristics and soil nutrients within the four vegetation restoration measures and the control group (grass square sand barriers) during the operation and maintenance of the Hobq Desert PV plant:
(2) The soil particle size distribution in the study area was concentrated, with sand grains dominating. The percentage of sand grains of the four vegetation restoration measures was reduced compared with CK by 1.02%, 6.63%, 5.34%, and 2.61%, respectively. YC, GC, and HB were better sorted, and their distribution was more concentrated; the fractal dimension of the four vegetation restoration measures was higher than that of CK.
(3) The AP content of each vegetation restoration measure was slightly higher than that of HB, and the difference in content between several other restoration measures was not apparent; the AN content of YC, GC, and HB was significantly higher than that of YH and CK; and the AK content of the four vegetation restoration measures was higher than that of CK, of which YC had the highest content. Regarding the performance of SOM content, the content of GC was the highest, the content of YC and HB was also higher than that of CK, and only YH was lower than that of CK.

In terms of allosteric nutrient performance, the TN content of GC and HB was higher than that of CK, and the remaining two restoration measures were more minor than or close to CK; the TN content was significantly higher only for YC than that of CK, and the remaining three restoration measures were lower than CK, with some individual contents close to CK. The content of TP was higher only for goatgrass than that of CK, and the remaining three measures were significantly lower than that of CK. Combined with the soil particle size composition, particle size parameters, and soil nutrient content, the development of fine-grained soil and the accumulation of soil nutrients indicate that YC and GC are more suitable for the PV plant in the study area. Vegetation restoration measures in the study area have begun to have an effect, and the unique habitat characteristics formed by the PV power plant, which are different from the local environmental background, are essential for the development of local production.

Data availability statement

The original contributions presented in the study are included in the article/Supplementary material, further inquiries can be directed to the corresponding authors.

Author contributions

JC: Conceptualization, Data curation, Formal Analysis, Methodology, Writing–original draft, Writing–review and editing. ZM: Conceptualization, Methodology, Supervision, Writing–review and editing, Writing–original draft. RM: Data curation, Investigation, Methodology, Writing–review and editing. HL: Conceptualization, Supervision, Validation, Writing–review and editing. XC: Conceptualization, Formal Analysis, Resources, Writing–review and editing. XR: Conceptualization, Formal Analysis, Investigation, Resources, Validation, Writing–review and editing. LG: Project administration, Funding acquisition, Writing–review and editing. MH: Supervision, Investigation, Writing–review and editing.

Funding

The author(s) declare that financial support was received for the research, authorship, and/or publication of this article. This research was funded by Desert Ecosystem Conservation and Restoration Innovation Team (BR22-13-03) Research on integrated technology for sand control in photovoltaic power plants (2022EEDSKJZDZX020-4). Commercialization of Scientific and Technological Achievements in Inner Mongolia Autonomous Region (2020CG0066).

Conflict of interest

The authors declare that the research was conducted in the absence of any commercial or financial relationships that could be construed as a potential conflict of interest.

Publisher's note

All claims expressed in this article are solely those of the authors and do not necessarily represent those of their affiliated organizations, or those of the publisher, the editors and the reviewers. Any product that may be evaluated in this article, or claim that may be made by its manufacturer, is not guaranteed or endorsed by the publisher.

References

Ahmadi, A., Neyshabouri, M. R., Rouhipour, H., and Asadi, H. (2011). Fractal dimension of soil aggregates as an index of soil erodibility. *J. Hydrology* 400 (3-4), 305–311. doi:10.1016/j.jhydrol.2011.01.045

Armstrong, A. C. (1986). On the fractal dimensions of some transient soil properties. *J. soil Sci.* 37 (4), 641–652. doi:10.1111/j.1365-2389.1986.tb00393.x

Blair, T. C., and McPherson, J. G. (1999). Grain-size and textural classification of coarse sedimentary particles. *J. Sediment. Res.* 69 (1), 6–19. doi:10.1306/d426894b-2b26-11d7-8648000102c1865d

Bremner, J. M., and Mulvaney, C. S. (1983). Nitrogen—total. *Methods of soil analysis: part 2 chemical and microbiological properties* 9, 595–624.

Chandra, L. R., Gupta, S., Pande, V., and Singh, N. (2016). Impact of forest vegetation on soil characteristics: a correlation between soil biological and physico-chemical properties. *3 Biotech.* 6 (2), article188. doi:10.1007/s13205-016-0510-y

Chang, Z., Liu, S., Fu, J., Wang, Q., Wang, F., Sun, T., et al. (2020). Effect of desert photovoltaic on sand prevention and control—taking Gansu Gulang Zhenfa

photovoltaic DC field as an example. *IOP Conf. Ser. Earth Environ. Sci.* 601 (1), 012032. doi:10.1088/1755-1315/601/1/012032

Chen, B., Yang, H., Song, W., Liu, C., Xu, J., Zhao, W., et al. (2016). Effect of N fertilization rate on soil alkali-hydrolyzable N, subtending leaf N concentration, fiber yield, and quality of cotton. *Crop J.* 4 (4), 323–330. doi:10.1016/j.cj.2016.03.006

Du, H., Xue, X., and Wang, T. (2014). Estimation of saltation emission in the kubuqi desert, north China. *Sci. Total Environ.* 479, 77–92. doi:10.1016/j.scitotenv.2014.01.095

El Chaar, L., and El Zein, N. (2011). Review of photovoltaic technologies. *Renew. Sustain. energy Rev.* 15 (5), 2165–2175. doi:10.1016/j.rser.2011.01.004

Folk, R. L., and Ward, W. C. (1957). Brazos river bar: a study in the significance of grain size parameters. *J. Sediment. Petrology* 27 (1), 3–26. doi:10.1306/74d70646-2b21-11d7-8648000102c1865d

Gao, T., Gao, M., Peng, J., and Li, N. (2018). Effects of different amount of biochar on nitrogen, phosphorus and potassium nutrients in soil. *IOP Conf. Ser. Mater. Sci. Eng.* 394 (2), 022043. doi:10.1088/1757-899x/394/2/022043

Hong, C., Tao, X., and Chun, T. (2006). Overview of mechanism of plant roots improving soil reinforcement and slope stabilization. *Bull. Soil Water Conservation* 26 (1), 97–102.

Huang, B. (2020). *Analysis of soil physical and chemical properties undertypical plant communities in the southeast margin of the MuUs Sandy land*. Xi'an: Xi'an University of Science and Technology.

Huang, C., Zeng, Y., Wang, L., and Wang, S. (2020). Responses of soil nutrients to vegetation restoration in China. *Reg. Environ. Change* 20, 82–12. doi:10.1007/s10113-020-01679-6

Kirk, P. L. (1950). Kjeldahl method for total nitrogen. *Anal. Chem.* 22 (2), 354–358. doi:10.1021/ac60038a038

Kobayashi, T., Liao, R. T., and Li, S. Q. (1995). Ecophysiological behavior of Artemisia ordosica on the process of sand dune fixation. *Ecol. Res.* 10, 339–349. doi:10.1007/bf02347860

Li, Q. (2022). Stumping for rejuvenation of hedysarum scoparium plantationin minqin desert area. *Shaanxi For. Sci. Technol.* 50 (06), 12–16.

Li, X., Yu, M. H., Ding, G. D., He, Y., Liu, W., and Wang, C. Y. (2021). Soil biocrusts reduce seed germination and contribute to the decline in Artemisia ordosica Krasch. shrub populations in the Mu Us Sandy Land of North China. *Glob. Ecol. Conservation* 26, e01467. doi:10.1016/j.gecco.2021.e01467

Liu, J., Wu, L., Wei, S., Xiao, X., Su, C., Jiang, P., et al. (2007). Effects of arbuscular mycorrhizal fungi on the growth, nutrient uptake and glycyrrhizin production of licorice (Glycyrrhiza uralensis Fisch). *Plant Growth Regul.* 52, 29–39. doi:10.1007/s10725-007-9174-2

Liu, X., Xie, Y., Zhou, D., Li, X., Ding, J., Wu, X., et al. (2020a). Soil grain-size characteristics of nitraria tangutorum nebkhas with different degrees of vegetation coverage in a desert-oasis ecotone. *Pol. J. Environ. Stud.* 29 (5), 3703–3714. doi:10.15244/pjoes/115866

Liu, Y., Zhang, R. Q., Ma, X. R., and Wu, G. L. (2020b). Combined ecological and economic benefits of the solar photovoltaic industry in arid sandy ecosystems. *J. Clean. Prod.* 262, 121376. doi:10.1016/j.jclepro.2020.121376

Lupangu, C., and Bansal, R. C. (2017). A review of technical issues on the development of solar photovoltaic systems. *Renew. Sustain. Energy Rev.* 73, 950–965. doi:10.1016/j.rser.2017.02.003

Munhoz, R. O., and Bertonde Camargo, R. S. O. A. (2011). Phosphorus sorption and redistribution on soil solid phase in a Brazilian haplorthox amended with biosolids. *Appl. Environ. Soil Sci.* 2011, 283061–283067. doi:10.1155/2011/283061

Nelson, D. W., and Sommers, L. E. (1983). Total carbon, organic carbon, and organic matter. *Methods of soil analysis: Part 2 chemical and microbiological properties* 9, 539–579.

Pan, X., Wang, Z., and Gao, Y. (2020). Effects of compound sand barrier for habitat restoration on sediment grain-size distribution in ulan buh desert. *Sci. Rep.* 10 (1), 2566. doi:10.1038/s41598-020-59538-7

Qi, F., Zhang, R., Liu, X., Niu, Y., Zhang, H., Li, H., et al. (2018). Soil particle size distribution characteristics of different land-use types in the Funiu mountainous region. *Soil Tillage Res.* 184, 45–51. doi:10.1016/j.still.2018.06.011

Ren, M., Chen, W., and Wang, H. (2022). Ecological policies dominated the ecological restoration over the core regions of kubuqi desert in recent decades. *Remote Sens.* 14 (20), 5243. doi:10.3390/rs14205243

Rodríguez-Loinaz, G., Onaindia, M., Amezaga, I., Mijangos, I., and Garbisu, C. (2008). Relationship between vegetation diversity and soil functional diversity in native mixed-oak forests. *Soil Biol. Biochem.* 40 (1), 49–60. doi:10.1016/j.soilbio.2007.04.015

Rodriguez-Pastor, D. A., Ildefonso-Sanchez, A. F., Soltero, V. M., Peralta, M., and Chacartegui, R. (2023). A new predictive model for the design and evaluation of bifacial photovoltaic plants under the influence of vegetation soils. *J. Clean. Prod.* 385, 135701. doi:10.1016/j.jclepro.2022.135701

Sha, L. N., Fan, X., Zhang, H. Q., Kang, H., Wang, Y., Wang, X., et al. (2014). Phylogenetic relationships in Leymus (Triticeae; Poaceae): evidence from chloroplast trnH-psbA and mitochondrial coxII intron sequences. *J. Syst. Evol.* 52 (6), 722–734. doi:10.1111/jse.12097

Sinke, W. C. (2019). Development of photovoltaic technologies for global impact. *Renew. Energy* 138, 911–914. doi:10.1016/j.renene.2019.02.030

Tang, G., Meng, Z., Gao, Y., and Dang, X. (2021). Impact of utility-scale solar photovoltaic array on the aeolian sediment transport in Hobq Desert, China. *J. Arid Land* 13, 274–289. doi:10.1007/s40333-021-0096-y

Wang, C., Hill, R. L., Bu, C., Li, B., Yuan, F., Yang, Y., et al. (2021). Evaluation of wind erosion control practices at a photovoltaic power station within a sandy area of northwest, China. *Land Degrad. Dev.* 32 (4), 1854–1872. doi:10.1002/ldr.3839

Weltzin, J. F., and Coughenour, M. B. (1990). Savanna tree influence on understory vegetation and soil nutrients in northwestern Kenya. *J. Veg. Sci.* 1 (3), 325–334. doi:10.2307/3235707

Wu, J., Wang, H., Li, G., Ma, W., and Gong, Y. (2020). Vegetation degradation impacts soil nutrients and enzyme activities in wet meadow on the Qinghai-Tibet Plateau. *Sci. Rep.* 10 (1), 21271. doi:10.1038/s41598-020-78182-9

Xiao, B., Wang, J. H., Zhou, C. Y., Chen, J. M., Zhang, N., Zhao, N., et al. (2020). Ethno-medicinal study of Artemisia ordosica Krasch.(traditional Chinese/Mongolian medicine) extracts for the treatment of allergic rhinitis and nasosinusitis. *J. Ethnopharmacol.* 248, 112262. doi:10.1016/j.jep.2019.112262

Yuan, B., Wu, W., Yue, S., Zou, P., Yang, R., and Zhou, X. (2022). Multi-scale impact of large-scale photovoltaic power station construction on wind field in the desert area. *Int. Conf. Sustain. Technol. Manag.* 12299, 35–40. doi:10.1117/12.2646619

Yue, S., Guo, M., Zou, P., Wu, W., and Zhou, X. (2021). Effects of photovoltaic panels on soil temperature and moisture in desert areas. *Environ. Sci. Pollut. Res.* 28, 17506–17518. doi:10.1007/s11356-020-11742-8

Zhang, Y. M., Wang, H. L., Wang, X. Q., Yang, W., and Zhang, D. (2006). The microstructure of microbiotic crust and its influence on wind erosion for a sandy soil surface in the Gurbantunggut Desert of Northwestern China. *Geoderma* 132 (3-4), 441–449. doi:10.1016/j.geoderma.2005.06.008

Zheng, J. M., and Zheng, Y. S. (2022). Exploring the species and phylogenetic diversity, phylogenrtic structure df mixed communities along the costal grandient. A case study in a subtropical island, China. *Appl. Ecol. Environ. Res.* 20 (4), 3129–3141. doi:10.15666/aeer/2004_31293141

frontiers | Frontiers in Environmental Science

TYPE Original Research
PUBLISHED 09 April 2024
DOI 10.3389/fenvs.2024.1389587

OPEN ACCESS

EDITED BY
Zhiming Han,
Northwest A&F University, China

REVIEWED BY
Peng Sun,
Anhui Normal University, China
Ning Ma,
Chinese Academy of Sciences (CAS), China
Zhaoqiang Zhou,
Northeast Agricultural University, China

*CORRESPONDENCE
Limin Duan,
duanlimin820116@163.com

RECEIVED 21 February 2024
ACCEPTED 20 March 2024
PUBLISHED 09 April 2024

CITATION
Tu L and Duan L (2024), Spatial downscaling analysis of GPM IMERG precipitation dataset based on multiscale geographically weighted regression model: a case study of the Inner Mongolia Reach of the Yellow River basin. *Front. Environ. Sci.* 12:1389587. doi: 10.3389/fenvs.2024.1389587

Spatial downscaling analysis of GPM IMERG precipitation dataset based on multiscale geographically weighted regression model: a case study of the Inner Mongolia Reach of the Yellow River basin

Lihui Tu[1,2,3] and Limin Duan[1,2,3]*

[1]Water Conservancy and Civil Engineering College, Inner Mongolia Agricultural University, Hohhot, China, [2]Inner Mongolia Key Laboratory of Protection and Utilization of Water Resources, Hohhot, China, [3]Collaborative Innovation Center for Integrated Management of Water Resources and Water Environment in the Inner Mongolia Reaches of the Yellow River, Hohhot, China

The Inner Mongolia Reach of the Yellow River Basin is characterized by a relative scarcity of meteorological stations. While satellite precipitation products can complement observations from meteorological stations, their limited spatial resolution restricts their efficacy in regional studies. This study utilizes the GPM IMERG precipitation dataset, considering various factors that influence the spatial distribution of precipitation, such as the Normalized Difference Vegetation Index (NDVI), elevation, slope, aspect, and topographical relief, to construct a multiscale geographically weighted regression (MGWR) model. A spatial downscaling method for the GPM IMERG precipitation dataset is proposed, and its reliability is validated through an accuracy assessment. Moreover, the scale differences in the impact of different factors on the spatial pattern of precipitation in the Inner Mongolia Reach of the Yellow River Basin are scrutinized. The results indicate that: 1) The downscaled GPM IMERG precipitation data (1 km × 1 km) exhibit enhanced accuracy compared to the pre-downscaled data (approximately 11 km × 11 km). The correlation coefficient, Bias, and RMSE of the annual precipitation data after downscaling of GPM IMERG are 0.865, 6.05%, and 68.50 mm/year, respectively. For the monthly downscaled precipitation data, the correlation coefficient, Bias, and RMSE are 0.895, 6.09%, and 16.25 mm/month, respectively. The downscaled GPM IMERG precipitation dataset exhibit high accuracy on both annual and monthly temporal scales. 2) Different factors demonstrate localized effects on precipitation in both dry and wet years. Elevation is the dominant factor influencing the spatial heterogeneity of annual precipitation. The findings from this study can provide technical support for hydrological modeling, drought monitoring, and water resource management in data-scarce areas of the Inner Mongolia Reach of the Yellow River Basin.

KEYWORDS

precipitation, GPM IMERG, MGWR, downscaling, scale difference

1 Introduction

Precipitation is a crucial component of the global water cycle and a key driver of surface hydrological processes (Zhang et al., 2014). Obtaining high temporal and spatial resolution raster precipitation data is of great importance in fields such as ecology, hydrology, and meteorology (Ma et al., 2021; Xue et al., 2022; Li et al., 2023). Conventional approaches to precipitation data collection rely on spatial interpolation of data from rain gauge measurements. However, the accuracy of interpolation is limited by the coverage and representativeness of the rain gauge stations, making it difficult to obtain precise regional precipitation spatial distribution information, especially in arid and semi-arid areas with complex terrain and sparsely distributed stations (Fang et al., 2013; Wang et al., 2022).

Satellite remote sensing-based precipitation estimation offers comprehensive coverage, continuous time series, and convenient data acquisition, making it an effective approach for regional or global-scale precipitation measurements (Kidd and Levizzani, 2011; Tang et al., 2020). Using satellite remote sensing technology, applications like the Tropical Rainfall Measuring Mission Multi-satellite Precipitation Analysis (TMPA) (Huffman et al., 2007), Integrated Multi-satellite Retrievals for Global Precipitation Measurement (GPM IMERG) (Nan et al., 2021), Global Satellite Mapping of Precipitation (GSMaP) (Kubota et al., 2007), Multi-Source Weighted-Ensemble Precipitation (MSWEP) (Beck et al., 2017), Climate Prediction Center Morphing technique (CMORPH) (Joyce et al., 2004), and Precipitation Estimation from Remotely Sensed Information using Artificial Neural Networks-Climate Data Record (PERSIANN-CDR) (Ashouri et al., 2015) have been developed. However, the spatial resolution of the precipitation dataset is coarse (approximately 11km–28 km) (Joyce et al., 2004; Huffman et al., 2007; Kubota et al., 2007; Ashouri et al., 2015; Beck et al., 2017; Nan et al., 2021), limiting its ability to accurately depict precipitation distribution patterns at the scale of small watersheds (Yu et al., 2020). Spatial downscaling methods can be used to effectively overcome this limitation (Kofidou et al., 2023).

Downscaling methods include dynamic and statistical downscaling. Dynamic downscaling involves scale reduction by simulating atmospheric physical processes using models (Sylla et al., 2009; Hu et al., 2018). Although this method possesses a clear physical basis, its applicability is limited due to high computational costs and extensive data requirements. Statistical downscaling relies on empirical statistical relationships between the target variable and explanatory variables to achieve downscaling (Kofidou et al., 2023). It is characterized by relatively lower computational demands, flexibility in application, and ease of operation. It is, therefore, widely used in downscaling studies of satellite remote sensing precipitation products. Immerzeel et al. through the analysis of the correlation between TRMM precipitation and annual scale NDVI, established a regional precipitation downscaling model based on an exponential regression (ER) model, obtaining TRMM precipitation dataset for the Iberian Peninsula in Spain with a spatial resolution of 1 km (Immerzeel et al., 2009). Building upon the research by Immerzeel et al., Jia et al. considered that the spatial distribution of precipitation is influenced by more than a single variable. They included topographic factors within the scope of their variables and established a Multiple Linear Regression (MLR) model between TRMM, NDVI, and topographic factors, enhancing the TRMM precipitation dataset for the Qaidam Basin in China from a 0.25° resolution to 1 km (Jia et al., 2011). Jing et al. demonstrated that using the random forest (RF) model for precipitation downscaling achieves higher simulation accuracy than both the exponential regression and the linear regression models (Jing et al., 2016). However, these models assume that the relationships between precipitation and environmental variables are homogeneous in space and do not account for the spatial non-stationarity between precipitation and variable factors, because their relationship should vary with changes in spatial location (Brunsdon et al., 1998). The Geographically Weighted Regression (GWR) model can account for the spatial non-stationarity between precipitation and explanatory variables in downscaling studies of precipitation (Xu et al., 2015). However, the GWR model assumes that all variable factors have the same optimal bandwidth, neglecting scale differences in the effects of different influencing factors on precipitation (Arshad et al., 2021). Thus, Fotheringham et al. proposed the Multi-Scale Geographically Weighted Regression (MGWR) model, based on the GWR model, which considers different spatial bandwidths for various influencing factors (Fotheringham et al., 2017). This model better reveals scale differences in the mechanisms of various factors affecting precipitation. Noor et al. applied the MGWR model and the RF model to downscale the TRMM precipitation dataset (Noor et al., 2023), while Arshad et al. used the MGWR model and the GWR model for downscaling the TRMM precipitation dataset over the Indus River Basin (Abdollahipour et al., 2021). The results showed that the simulation accuracy of the MGWR model was superior to the other two models. Therefore, the MGWR model can be widely used in precipitation downscaling studies.

Currently, downscaling studies based on the MGWR model are relatively scarce and primarily focused on the TRMM precipitation dataset. The TRMM mission ceased operation on 8 April 2015, and its successor, the Global Precipitation Measurement (GPM) mission, has ushered in a new era of satellite precipitation measurement (Tang et al., 2016). The GPM Core Observatory (GPMCO) is equipped with a dual-frequency radar (Ku and Ka bands), capable of detecting lower minimum echo intensities and employing a high-sensitivity mode for staggered sampling (Hou et al., 2014). Additionally, the microwave radiometer at the GPMCO has four high-frequency channels, providing more accurate data for light precipitation intensity and solid precipitation (Hou et al., 2014).

Currently, there are relatively many studies on downscaling of GPM IMERG precipitation datasets in humid areas (Ma et al., 2018; Min et al., 2020; Yan et al., 2021a), but relatively few in arid and semi-arid areas. The Inner Mongolia Reach of the Yellow River Basin is located in an arid and semi-arid area, where the terrain is diverse and complex, and precipitation exhibits distinct regional and seasonal variations (Wang et al., 2023). In this study, we focused on the Inner Mongolia Reach of the Yellow River Basin. We selected the GPM IMERG precipitation dataset and used NDVI, elevation, slope, aspect, and topographical relief as explanatory variables to construct a Multi-Scale Geographically Weighted Regression (MGWR) model. This model was used to generate precipitation data at a resolution of

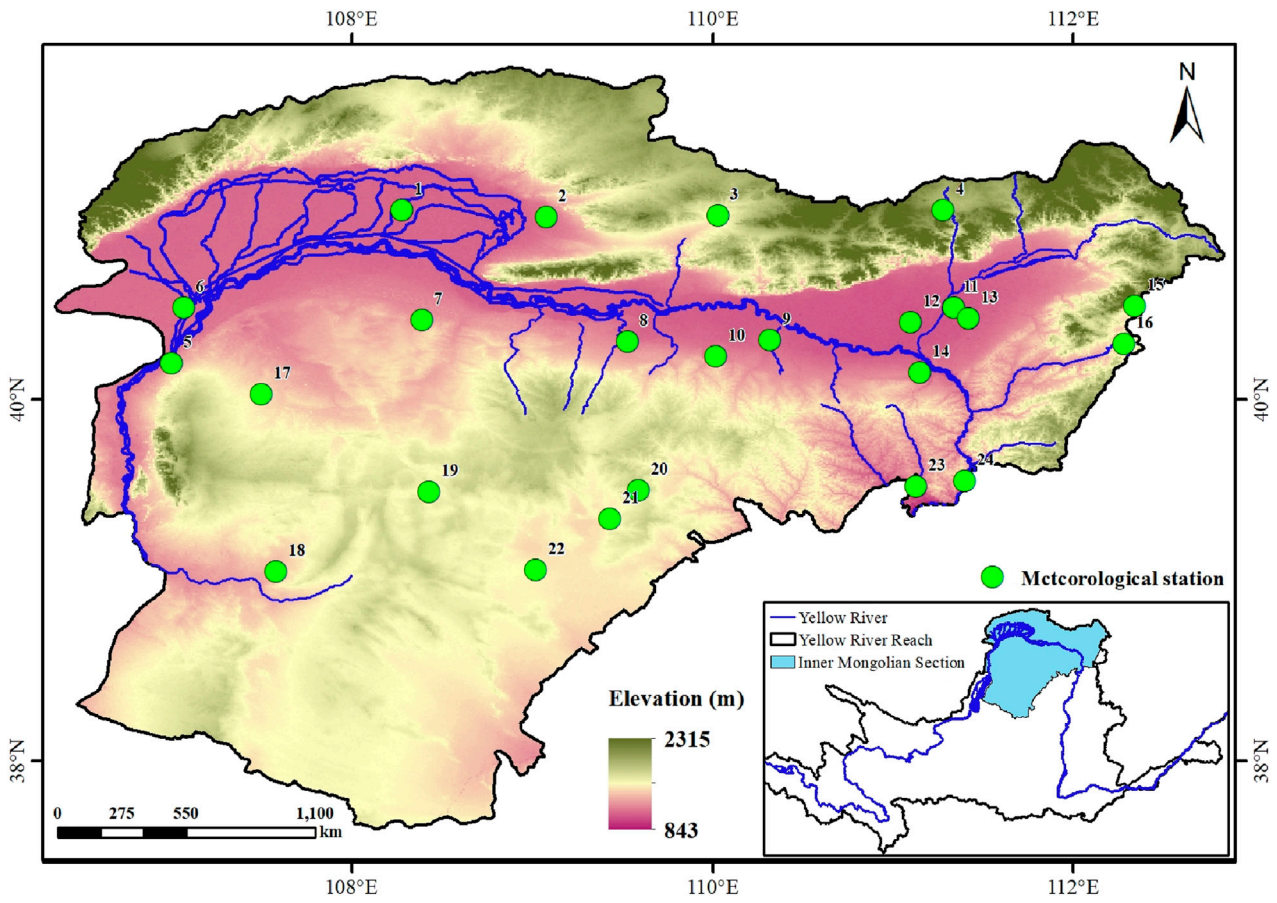

FIGURE 1
Location of the Inner Mongolia Reach of the Yellow River Basin and the meteorological stations in the study area.

1 km at both monthly and annual scales for the years 2001–2019. The resulting dataset offers essential support for meteorological and hydrological research within the basin.

2 Materials and methods

2.1 Study area

The Inner Mongolia Reach of the Yellow River Basin is situated in the upper reaches of the Yellow River (37°37′–41°50′N, 106°28′–112°50′E), covering a total area of approximately 149,029 km^2. This accounts for about 18.63% of the total area of the Yellow River Basin, with elevations ranging from 843 to 2,315 m (Figure 1). The study area is located in an arid and semi-arid region, characterized by drought and scarce rainfall, strong evaporation, large diurnal temperature variations, and is typical of a mid-temperate continental climate (Wang et al., 2023). It has an annual average precipitation of 305 mm and an average annual temperature of 6.5°C (Zhang et al., 2023). Annual average Precipitation gradually decreases from east to west (Table 1). In the basin, grasslands account for 74.20%, cultivated land for 18.95%, and forests for 6.85% (Zhang et al., 2023).

2.2 Data preparation

2.2.1 GPM IMERG

IMERG is a new generation of multi-satellite combined precipitation data introduced through the GPM program. It offer three types of products (Early, Late, and Final) based on different data inversion algorithms. The IMERG Final product is considered more accurate owing to its incorporation of rain gauge data from the Global Precipitation Climatology Centre (GPCC) (Wang et al., 2017). The IMERG V06 integrates information from available GPM and TMPA sensors. This integration involves mutual calibration, merging, interpolation, and fusion to generate consistent precipitation estimates from June 2000 to the present (Yu et al., 2022). For this study, we selected IMERG V06 (IMERG_Final) daily data for the period 2001–2019, which we obtained from the official NASA website (https://www.nasa.gov/). This dataset has a spatial resolution of 0.1 ° × 0.1 ° (approximately 11 km × 11 km), and annual and monthly precipitation data were derived from the daily dataset.

2.2.2 Environment variables

Shuttle Radar Topography Mission (SRTM) data, accessible at http://www.gscloud.cn, were utilized to derive a Digital Elevation

TABLE 1 Basic information of meteorological stations in the study area.

Number	Name	Latitude (E°)	longitude (N°)	Elevation(m)	Annual mean precipitation (mm)
1	Wuyuan	41.05	108.28	1023.3	177.9
2	Dayutai	41.01	109.08	1078.7	241.4
3	Guyang	41.02	110.03	1360.4	308.1
4	Wuchuan	41.05	111.28	1637.3	354.4
5	Dengkou	40.20	107.00	1055.3	143.9
6	Haggin Rear	40.51	107.07	1024.0	137.4
7	Urad Front	40.44	108.39	1020.4	219.8
8	Baotou	40.32	109.53	1004.7	301.0
9	Tumd Right	40.33	110.32	998.6	381.1
10	Dalad	40.24	110.02	1011.0	326.2
11	Hohhot	40.51	111.34	1153.5	418.2
12	Tumed Left	40.43	111.10	1042.7	402.3
13	Suburb of Hohhot	40.45	111.42	1045.4	405.4
14	Togtoh	40.15	111.15	1015.9	372.3
15	Zhuozi	40.52	112.34	1451.7	390.0
16	Liangcheng	40.31	112.28	1268.9	410.9
17	Ikwusu	40.03	107.50	1180.3	189.1
18	Etuoke	39.05	107.58	1381.4	284.4
19	haggin	39.49	108.43	1414.0	304.5
20	Dongsheng	39.50	109.59	1461.9	393.2
21	Ejin Horo	39.34	109.43	1367.0	375.7
22	Wushenzhao	39.06	109.02	1312.2	437.7
23	Jungar	39.52	111.13	1221.4	426.3
24	Qingshuihe	39.55	111.40	1208.0	437.4

Note: The annual mean precipitation is the annual mean precipitation during 2001–2019.

Model (DEM) with a spatial resolution of 90 m × 90 m. Within ArcGIS 10.7, topographic factors such as elevation, slope, aspect, and topographical relief were extracted from the DEM data. NDVI data, sourced from the Moderate Resolution Imaging Spectroradiometer (MODIS) on the Terra satellite, were obtained from NASA at https://ladsweb.modaps.eosdis.nasa.gov/. MOD13A3 monthly composite NDVI data, with a spatial resolution of 1 km × 1 km, were used. The MOD13A3 data underwent preprocessing using the MODIS Reprojection Tool (MRT) software, and annual NDVI data were derived was generated using a maximum value composite method. To maintain consistency with the GPM IMERG precipitation dataset and MGWR downscaling, NDVI, elevation, slope, aspect, and topographical relief data were resampled to two spatial scales, 0.1° and 1 km, in ArcGIS 10.7. This resampling was performed using the cubic convolution method because it offers good smoothing performance, detail preservation, and edge sharpening. Cubic convolution yields more satisfactory results compared to the Nearest Neighbor and Bilinear Interpolation methods (Molinaro et al., 2005).

2.2.3 Rain gauge data

Meteorological station precipitation data from 2001 to 2019 were acquired from the China Meteorological Data Network (http://data.cma.cn) to validate the accuracy of both the original GPM IMERG precipitation data and the downscaled precipitation data. A total of 24 meteorological stations were chosen, with observed precipitation data having an accuracy of 0.1 mm. Daily data from these stations were aggregated into monthly and annual precipitation values. Basic information about these stations is available in Table 1.

2.3 Methods

2.3.1 Multiscale geographically weighted regression (MGWR)

The Multiscale Geographically Weighted Regression (MGWR) model is a regional regression model, that is widely used to study dynamic relationships between target and explanatory variables

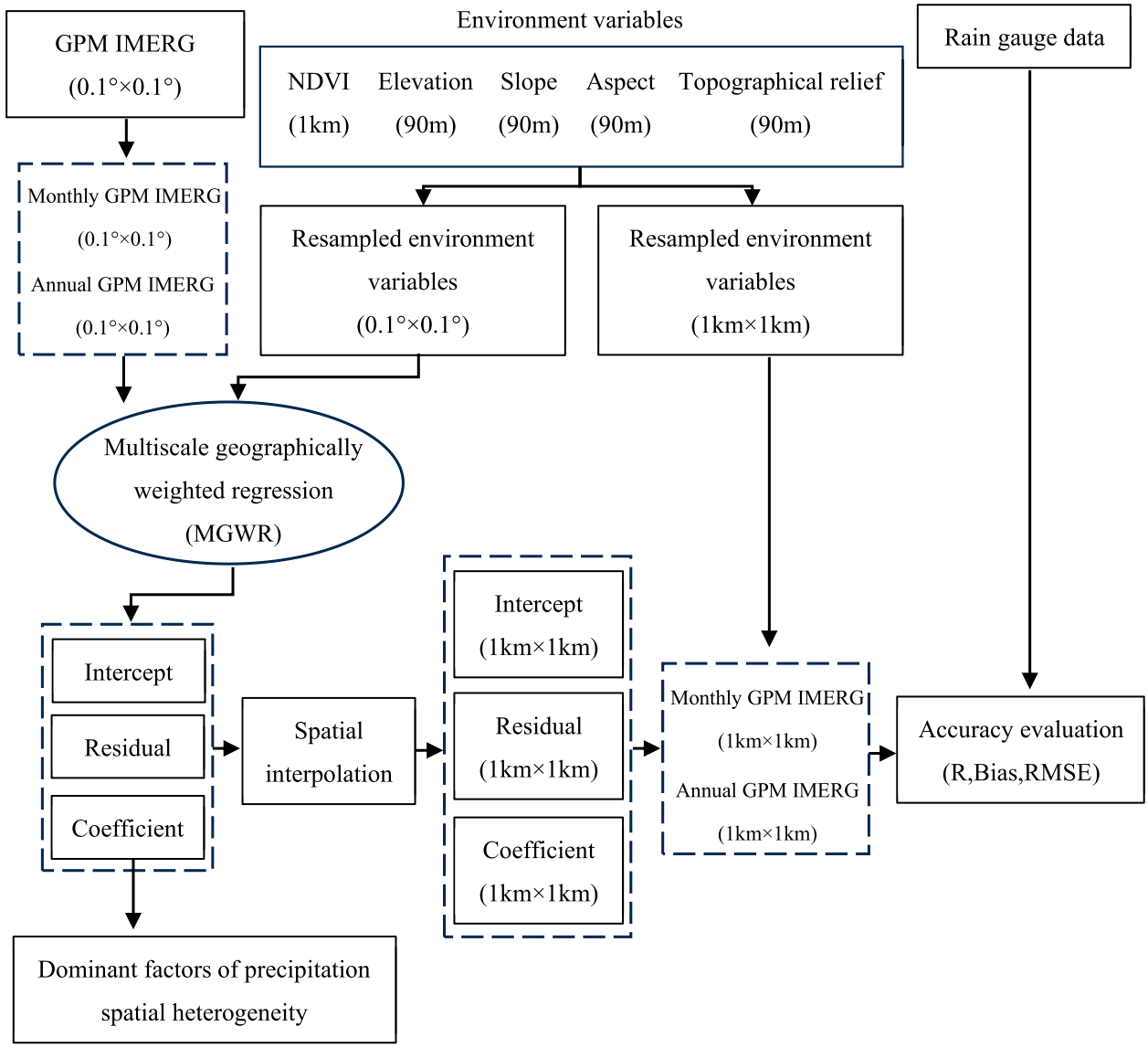

FIGURE 2
Flowchart of GPM IMERG downscaling process.

(Fotheringham et al., 2017). It allows each explanatory variable to vary at different spatial scales, facilitating the capture of spatial non-stationarity relationships among them. The MGWR model is expressed as follows:

$$Y_i = \beta_0(\mu_i, \nu_i) + \sum_{i=1}^{n} \beta_{bwj}(\mu_i, \nu_i) X_{ij} + \varepsilon_i \quad (1)$$

where Y_i represents the target variable; $\beta_0(\mu_i, \nu_i)$ is the intercept; n is the number of observation points; $\beta_{bwj}(\mu_i, \nu_i)$ is the regression coefficient for the *jth* variable at location *i*, with *bwj* being the bandwidth used for calibrating the *jth* variable; X_{ij} is the *jth* explanatory variable; and ε_i is the error term. The regression coefficient is calculated as follows (Noor et al., 2023):

$$\beta(\mu_i, \nu_i) = \left(X^T W(\mu_i, \nu_i) X\right)^{-1} \left(X^T W(\mu_i, \nu_i) Y\right) \quad (2)$$

where $\beta(\mu_i, \nu_i)$ denotes the regression coefficient to be estimated at the location (μ_i, ν_i); X and Y represent the vectors of the explanatory and target variables, respectively; and $W(\mu_i, \nu_i)$ is the weight matrix.

Based on previous studies, the adaptive bi-square was chosen to solve the weight matrix, with the AICc (corrected Akaike information criterion) as the bandwidth selection criterion, and the golden section search method was used to determine the bandwidth (Chao et al., 2018; Arshad et al., 2021). All processes were conducted using MGWR 2.2 software. The formula for the adaptive bi-square is as follows:

$$w_{ij} = \begin{cases} \left(1 - \frac{d_{ij}^2}{\theta_{i(k)}}\right)^2, d_{ij} < \theta_{i(k)} \\ 0, d_{ij} > \theta_{i(k)} \end{cases} \quad (3)$$

where w_{ij} represents the weight of the jth observation point for estimating the coefficient at location i; d_{ij} represents the Euclidean distance between the jth and ith points; and $\theta_{i(k)}$ represents the size of the adaptive bandwidth for the kth nearest neighbor distance, determined by the AICc.

2.3.2 Precipitation downscaling process based on MGWR

Previous research indicates that NDVI, elevation, slope, aspect, and topographical relief are important factors influencing precipitation (Wang et al., 2022; Bai et al., 2023). Considering the spatial non-stationarity between precipitation and factors such as vegetation and topography, and the considerable scale differences in the spatial impact of NDVI, elevation, slope, aspect, and ruggedness on precipitation, this study used the MGWR model to downscale the GPM IMERG precipitation dataset at both monthly and annual scales. The specific steps were as follows (Figure 2):

(1) Data preparation: Environmental variables with spatial resolutions of 0.1° and 1 km, as well as the original GPM IMERG precipitation data at a resolution of 0.1°, were prepared. The GPM IMERG data spanned the period from January 2001 to December 2019, and was summarized at both monthly and annual scales. Environmental variables included NDVI, elevation, slope, aspect, and topographical relief, with NDVI aligned with the temporal scale of the GPM IMERG precipitation data.

(2) MGWR model establishment: Duan et al. have found that the lag time of vegetation response to precipitation in the study area is approximately 10 days (Duan et al., 2019). Therefore, at a monthly scale, the current month's NDVI data was selected as the explanatory variable for the monthly precipitation scale model. At monthly and annual time scales, the GPM IMERG data with a resolution of 0.1° were used as the target variable, and NDVI, elevation, slope, aspect, and topographical relief of the same resolution and time scale were used as explanatory variables. The MGWR model was constructed at monthly and annual scales to obtain the regression coefficients $\beta(\mu_i, \nu_i)$, intercept term $\beta_0(\mu_i, \nu_i)$, and residuals ε_i for each explanatory variable at these scales. MGWR 2.2 software was used to establish the MGWR model.

(3) Parameter interpolation: Using the Kriging method, intercepts, slopes, and regression residuals from step (2) were interpolated. This yielded high-resolution (1 km) raster data of regression coefficients, intercept terms, and residuals at monthly and annual scales.

(4) Downscaling completion: Based on Eq. 1, monthly and annual precipitation values at a 1 km resolution were obtained after downscaling using the MGWR model.

2.3.3 Simulation accuracy assessment

Using the MGWR downscaling approach outlined in Section 2.3.2, downscaled GPM IMERG data for the years 2001–2019 were generated. The accuracy of the downscaled results (1 km) and the original GPM IMERG precipitation data (0.1°) at annual and monthly scales was validated using observed data from 24 meteorological stations in the study area. Three indicators—correlation coefficient (R), Bias, and root mean square error (RMSE)—were employed for the validation (Wang et al., 2022), with the following formulas:

$$R = \frac{\sum_i^n (M_i - \bar{M})(P_i - \bar{P})}{\sqrt{\sum_i^n (M_i - \bar{M})^2 (P_i - \bar{P})^2}} \tag{4}$$

$$Bias = \frac{\sum_i^n P_i}{\sum_i^n M_i} - 1 \tag{5}$$

$$RMSE = \sqrt{\frac{\sum_i^n (P_i - M_i)^2}{n}} \tag{6}$$

Where M_i (mm) and $\bar{M}$ (mm) represent the measured precipitation amount and its average value corresponding to the meteorological station, respectively; P_i and $\bar{P}$ (mm) represent the original or downscaled GPM IMERG precipitation raster value and its average value corresponding to the meteorological station, respectively; n is the number of meteorological stations.

3 Results

3.1 Accuracy of downscaled GPM IMERG precipitation

Observed precipitation from 24 meteorological stations in the study area for the period 2001–2019 were used to validate the GPM IMERG precipitation data that were downscaled using the MGWR method. Figures 3, 4 represent the validation results of annual and monthly downscaled and original precipitation, respectively.

The accuracy of annual precipitation from 2001 to 2019 is shown in Figure 3 The accuracies of the downscaled precipitation are better than that of the original precipitation. The annual trends of three accuracy indicators for the original GPM IMERG and the downscaled precipitation data were consistent (Figure 3). Overall, on an annual scale, the downscaled data maintained a certain level of accuracy while providing an improved reflection of the distribution of precipitation in the study area. The correlation coefficient of the downscaled annual precipitation varied from 0.648 to 0.937, with an average of 0.843, indicating good correlation between the annual downscaled precipitation and the measured data from the meteorological stations. The Bias varied from −0.219 to 0.177, with an average of 0.059. Except for the year 2013, the Bias was less than 0.2, and Bias values were mostly positive, suggesting that the simulated annual precipitation was generally overestimated compared to the measured data from the meteorological stations. The RMSE ranged from 45.53 mm to 99.88 mm, with an average of 66.33 mm.

As shown in Figure 4, at a monthly scale, the trends of the three accuracy indicators for both the original GPM IMERG and the downscaled precipitation remained consistent. Overall, the accuracy of the downscaled precipitation was greater than that of the original precipitation from February to November. However, from December to the following January, the accuracy of the downscaled precipitation was lower than that of the original GPM IMERG. The correlation coefficient for the downscaled precipitation ranged from 0.552 to 0.932, with an average of

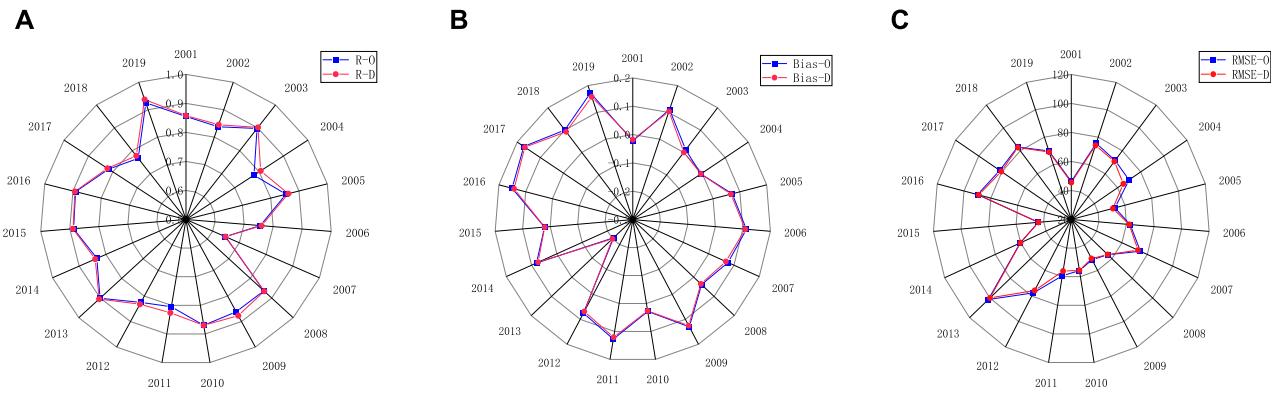

FIGURE 3
Correlation coefficient (R) **(A)**, Bias **(B)**, and root mean squared error (RMSE) **(C)** of the observed and downscaled annual precipitation from 2001 to 2019. D represents the downscaled precipitation and O denotes the original GPM IMERG precipitation, similarly hereinafter.

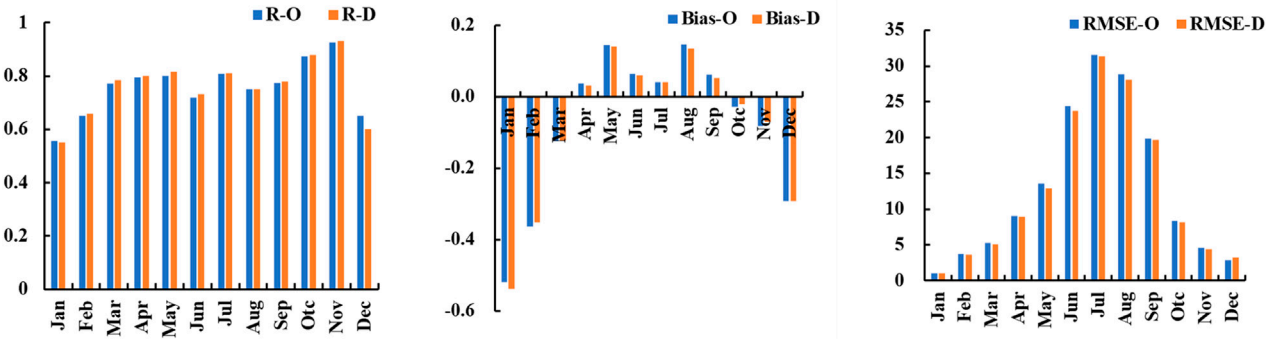

FIGURE 4
Correlation coefficient (R), Bias, and root mean squared error (RMSE) values between measured precipitation and monthly precipitation from 2001 to 2019 before and after Downscaling.

0.758. Precipitation estimation accuracy in spring and autumn was higher than that in summer and winter. This was attributed to higher amount of precipitation in summer and the predominance of snowfall in winter. The Bias was positive from April to October, peaking in August (0.134), and negative from November to March, reaching its lowest value in January (−0.538). This suggested that increased vegetation growth and precipitation contribute to an overestimation of monthly downscaled precipitation results. The RMSE exhibited a unimodal variation pattern correlated with the amount of monthly precipitation, ranging from 1.075 mm to 31.333 mm, with an average of 12.528 mm.

3.2 Downscaling results of GPM IMERG precipitation datasets

Figures 5, 6 present a comparison of the spatial distribution of annual and monthly average precipitation in the study area from 2001 to 2019, before and after downscaling. Downscaling using the MGWR model considerably improved the spatial resolution of the annual and monthly average GPM IMERG images compared to the original GPM IMERG images. While the spatial distribution remained consistent before and after downscaling, the representation of precipitation distribution became more refined post-downscaling. The multi-year average precipitation demonstrated a decreasing trend from the southeast to the northwest of the study area. Multi-year average precipitation ranged from 145.4 to 475.4 mm before downscaling and from 138.8 to 481.3 mm after downscaling. Compared to the original GPM IMERG data, the range of the downscaling simulation results increased. While enhancing the spatial resolution, the precipitation information became more comprehensive. The maximum monthly average precipitation occurred in July, and the minimum in January. The spatial distribution trends of monthly average precipitation and annual average precipitation are consistent.

3.3 Analysis of variable effect scale based on the MGWR model

To investigate scale differences in the impact of terrain and vegetation factors on the spatial distribution of precipitation at an

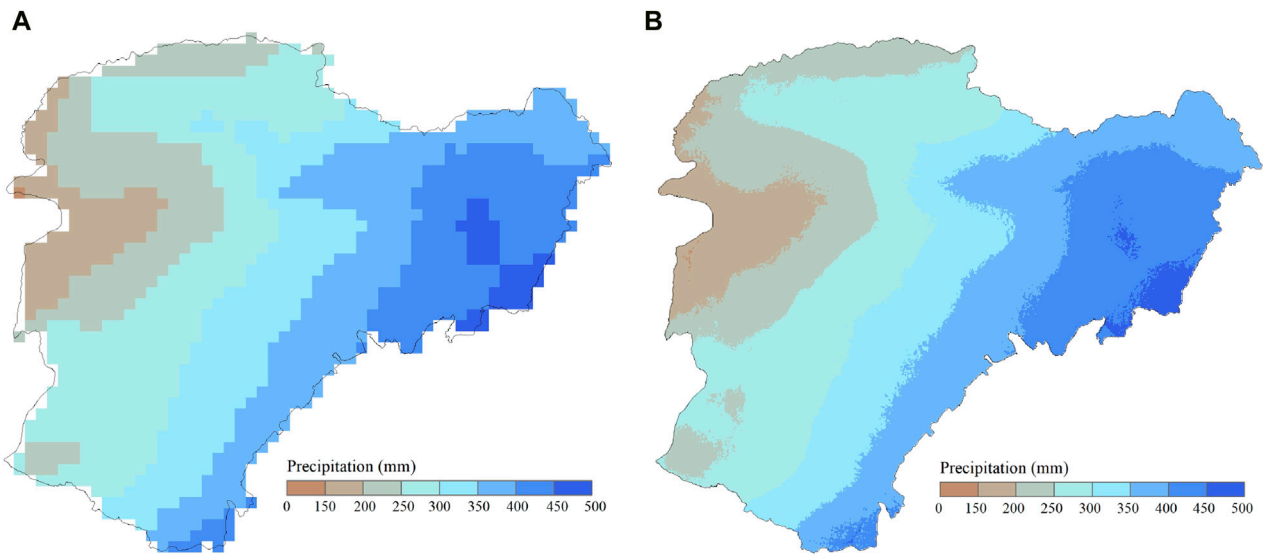

FIGURE 5
Spatial distributions of the **(A)** original and **(B)** downscaled mean annual precipitation from 2001 to 2019.

annual scale, this study selected the years 2005 and 2016 as typical dry and wet years, respectively. The bandwidths in the MGWR model were used to understand the range of influence of terrain and vegetation factors in each typical year. Smaller bandwidths indicated that the variable had a more localized influence on precipitation, designating it as a local influencing factor, whereas larger bandwidths suggested that the variable had a regional influence, designating it as a regional influencing factor (Fotheringham et al., 2017). Table 2 presents the bandwidth sizes of each variable obtained from the MGWR model, revealing relatively small differences in the scale of impact of variables in the dry year and comparatively larger differences in the wet year. However, variables in each typical year demonstrated localized impacts. Overall, precipitation in the Inner Mongolia Reach of the Yellow River Basin exhibited considerable spatial variation across different terrain and vegetation cover intervals.

Regression coefficients indicate the extent of the impact of vegetation and terrain factors on the spatial distribution of precipitation. The trend of the regression coefficients (RC) of variables in each typical year was generally consistent (Figure 7). In dry and wet years, The areas in which NDVI had a positive effect on the spatial variation in annual precipitation accounted for 59.73% and 61.88% of the total area in the dry and wet years, respectively. The positive effect of NDVI on annual precipitation was greater in wet years than in dry years. This was because the presence of ample soil moisture in wet years allowed plants to absorb more water from the soil and release it into the atmosphere through their leaves, increasing the atmospheric moisture content and promoting precipitation (Vicente-Serrano et al., 2013). In dry years, areas where topographical relief, aspect, and slope had a positive effect on the spatial variation in annual precipitation accounted for 68.05%, 50.40%, and 53.96% of the total area, respectively. In wet years, these areas where topographical relief, aspect, and slope positively influenced the spatial variation in annual precipitation accounted for 68.93%, 55.77%, and 69.53% of the total area, respectively. Elevation primarily exerted a negative effect on the spatial variation of annual precipitation, affecting 86.38% and 84.43% of the total area in dry and wet years, respectively. As elevation, topographical relief, and slope increased, their impact on annual precipitation gradually diminished due to the weakening distribution of spatial precipitation influenced by terrain on the transport and vertical movement of atmospheric moisture (Sokol and Bliznák, 2009).

Utilizing the absolute values of standardized regression coefficients to identify the primary factors influencing spatial precipitation differences, Figure 8 illustrates that, irrespective of dry or wet years, elevation emerges as the predominant factor in shaping precipitation variations in the Inner Mongolia Reach of the Yellow River Basin, encompassing approximately 50% of the basin area.

4 Discussion

The downscaled simulation data, generated through the MGWR model, were consistent with the GPM IMERG data in terms of spatial distribution of precipitation and exhibited improved spatial resolution and more detailed precipitation information. This is in agreement with the findings of Arshad et al., who employed the MGWR model for downscaling TRMM data in the Indus Basin (Arshad et al., 2021). However, at the monthly scale, the accuracy of some of the downscaled precipitation data was lower than that of the GPM IMERG data. Arshad et al. used the Geographically Weighted Regression Disaggregation Approach (GDA) to implement corrections based on meteorological station data for downscaled data with lower accuracy than the original data, and the accuracy of the resulting downscaled data was superior to that of the original data (Arshad et al., 2021). In the Inner Mongolia Reach of the Yellow River Basin, the scarcity of meteorological station data and difficulty in obtaining this data have precluded the possibility of interpolation

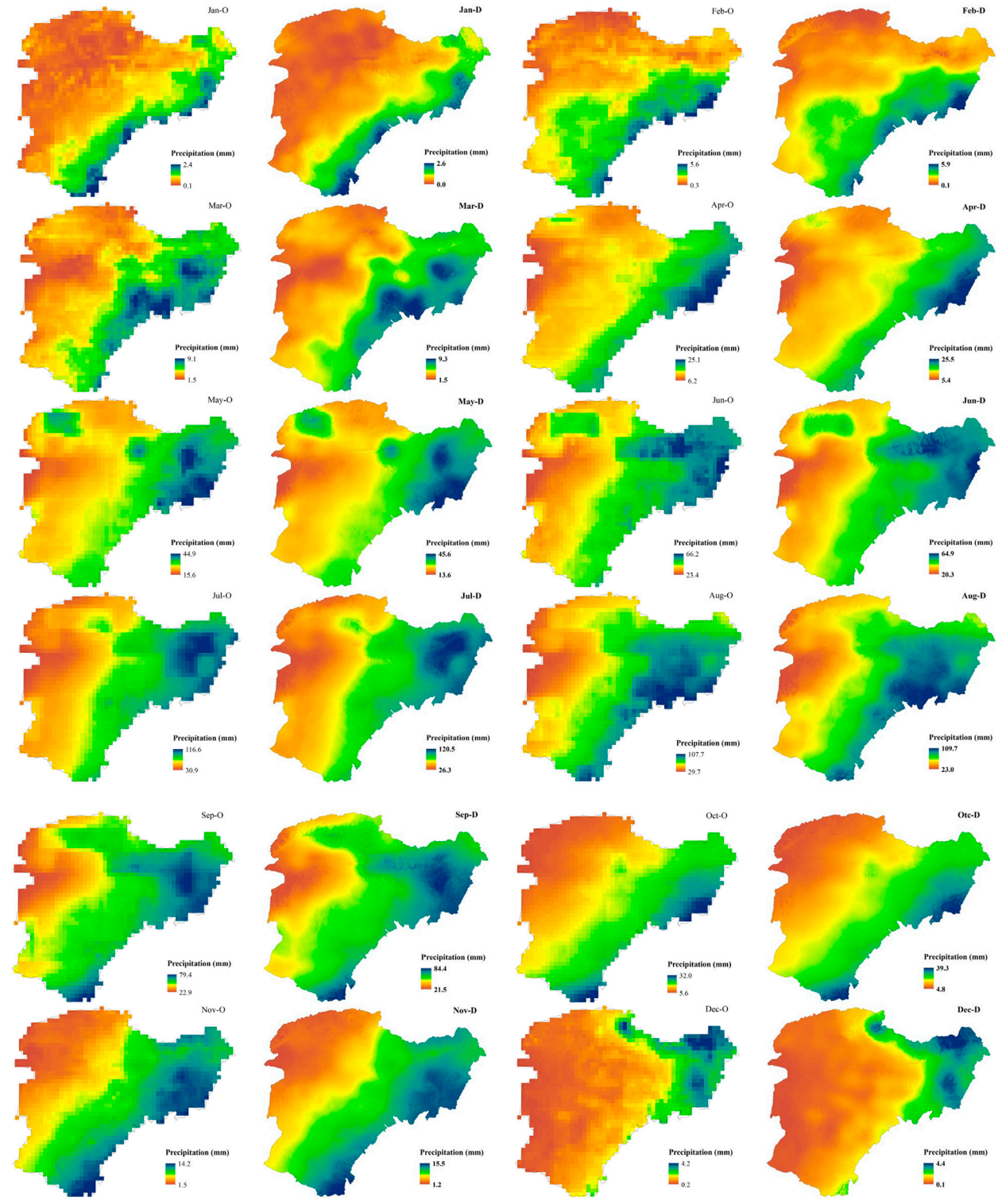

FIGURE 6
Spatial distributions of the **(O)** original and **(D)** downscaled mean monthly precipitation from 2001 to 2019.

corrections based on meteorological station data for downscaled simulation data. This highlights the fact that the accuracy of downscaled data obtained only through linear downscaling may not consistently be superior to that of the original data. Therefore, the development of new downscaling algorithms is imperative to obtain more accurate and reliable precipitation datasets at high spatial resolution.

The selection of appropriate explanatory variables plays a crucial role in the precipitation downscaling process and the performance of the MGWR model. In this study, five explanatory variables were

TABLE 2 Differences in factor bandwidths in MGWR.

Variable	Total bandwidth	MGWR				
		NDVI	Topographical relief	Aspect	Slope	Elevation
Dry year (2005)	1490	43	47	47	70	43
Wet year (2016)		44	70	99	154	43

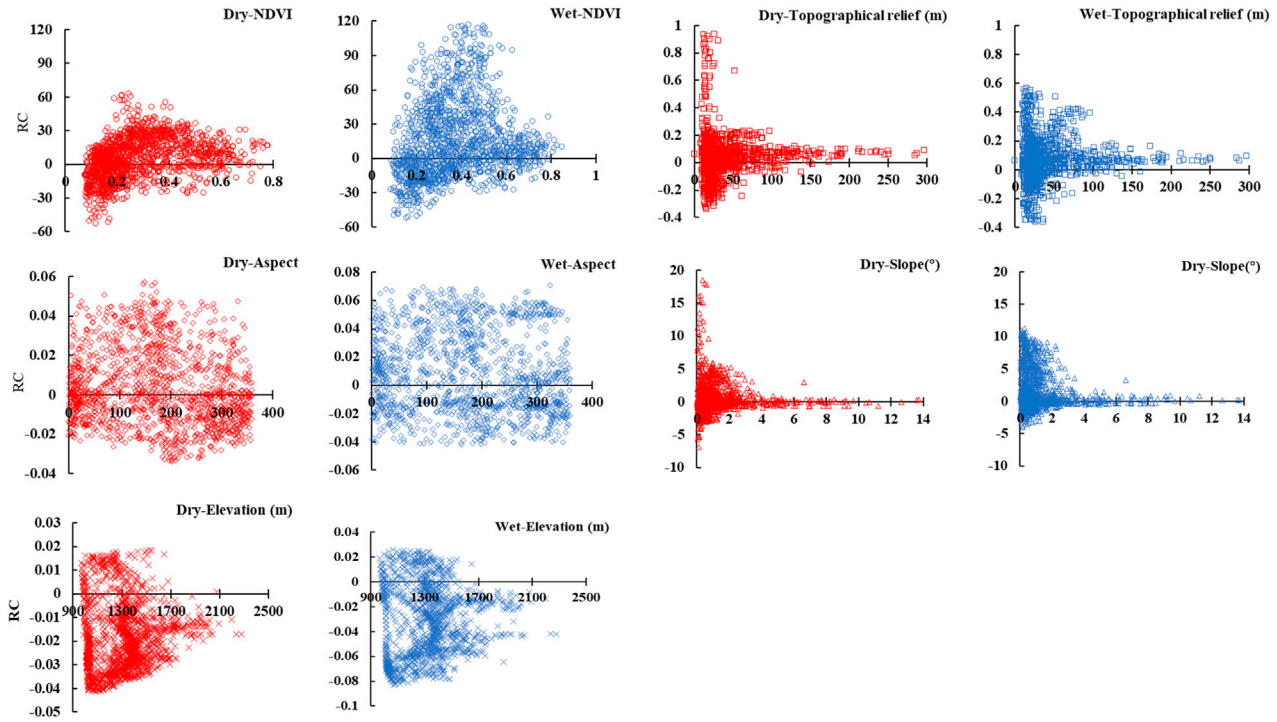

FIGURE 7
Variation patterns of regression coefficients of each variable with respect to the variables in typical years.

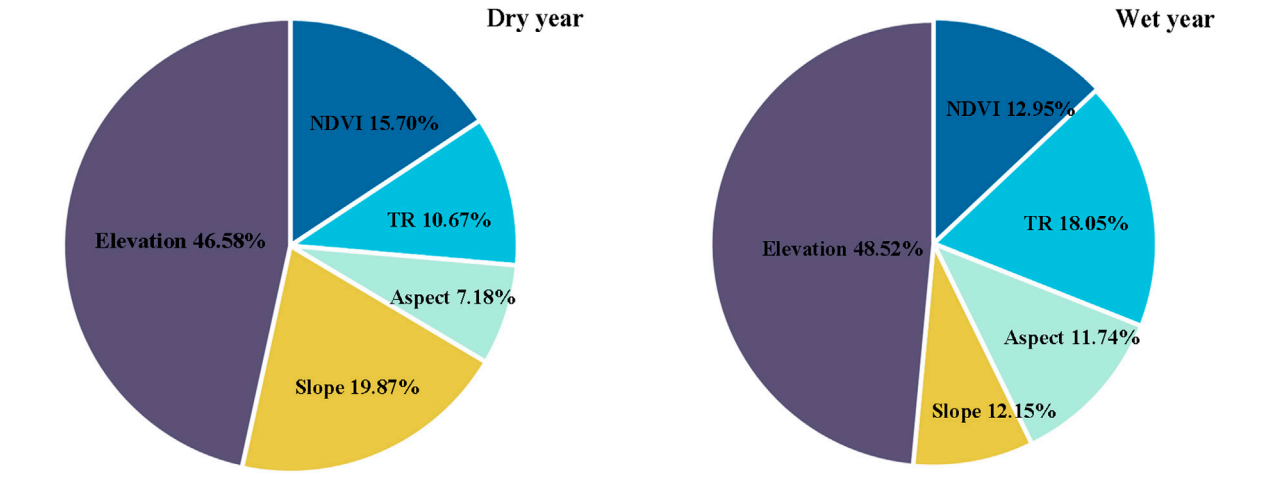

FIGURE 8
Proportion of Variable Impacts on Precipitation in the MGWR Model. TR represents topographical relief.

chosen for precipitation downscaling: NDVI, elevation, slope, aspect, and topographical relief. These variables were selected based on their regional importance and overall influence on the spatial variation in precipitation (Lu et al., 2020). The five chosen explanatory variables are commonly employed in precipitation downscaling studies across various global basins (Chen et al., 2014; Zhang et al., 2017; Zhang et al., 2018). It is noteworthy that additional environmental variables, such as surface characteristics (soil moisture and evapotranspiration) (Chen et al., 2019; Yan et al., 2021b) and meteorological factors (temperature, humidity, radiation, atmospheric circulation, and cloud cover) (Arshad et al., 2021) can impact the spatial distribution of precipitation. Future studies should consider incorporating these environmental variables to further assess the downscaling performance of precipitation.

5 Conclusion

Analysis of the spatial distribution of data before and after downscaling indicated that the detailed features were better represented post-downscaling. Following downscaling, the GPM IMERG precipitation dataset exhibited a relative increase in correlation coefficient, Bias, and RMSE when compared to the values calculated from the measured precipitation data. Overall, the accuracy of the data after downscaling was somewhat enhanced and the data reflected the actual precipitation information and distribution patterns across various time scales in the study area with greater accuracy.

The MGWR model adopted different bandwidths for different variables, thereby demonstrating the varying scale of influence of different factors. The findings of this study indicate that the patterns of spatial variation in both dry and wet years in the Inner Mongolia Reach of the Yellow River Basin are determined by multiple spatial scale processes of several variable factors. The impact of NDVI, elevation, aspect, slope, and topographical relief displayed a localized effect on precipitation in both wet and dry years. The MGWR regression results highlighted elevation as the primary factor influencing the spatial differentiation of precipitation in both wet and dry years.

In summary, for the GPM IMERG precipitation dataset, the application of the MGWR model enhances the spatial resolution of precipitation data, revealing more detailed features. It also ensures the consistency of data accuracy and spatial distribution. This can provide a relatively reliable high-resolution precipitation dataset for drought monitoring, hydrological modeling, and water resource management in the Inner Mongolia Reach of the Yellow River Basin.

Data availability statement

The data presented in this study are available on request from the corresponding author.

Author contributions

LT: Conceptualization, Data curation, Formal Analysis, Investigation, Methodology, Software, Visualization, Writing–original draft. LD: Conceptualization, Data curation, Funding acquisition, Project administration, Resources, Supervision, Writing–review and editing.

Funding

The author(s) declare that financial support was received for the research, authorship, and/or publication of this article. This work was supported by the National Natural Science Foundation of China (U23A2001 and 51939006), the National Natural Science Foundation of China (the Yellow River Water Science Research Joint Fund U2243234), the National Key Research and Development Plan Project of China (2022YFC3204401 and 2021YFC3201200), the Major Science and Technology Projects of Inner Mongolia Autonomous Region (2020ZD0009 and 2022EEDSKJXM005), the Inner Mongolia Autonomous Region Science and Technology Leading Talent Team (2022LJRC0007), the Natural Science Foundation of Inner Mongolia Autonomous Region of China (2020JQ06) and the Inner Mongolia Agricultural University Basic Research Business Expenses Project (BR221012 and BR221204).

Conflict of interest

The authors declare that the research was conducted in the absence of any commercial or financial relationships that could be construed as a potential conflict of interest.

Publisher's note

References

Abdollahipour, A., Ahmadi, H., and Aminnejad, B. (2021). Evaluating the reconstruction method of satellite-based monthly precipitation over Golestan province, Northern Iran. *Acta geophys.* 69 (6), 2305–2323. doi:10.1007/s11600-021-00623-4

Arshad, A., Zhang, W. C., Zhang, Z. J., Wang, S. H., Zhang, B., Cheema, M. J. M., et al. (2021). Reconstructing high-resolution gridded precipitation data using an improved downscaling approach over the high altitude mountain regions of Upper Indus Basin (UIB). *Sci. Total Environ.* 784, 147140. doi:10.1016/j.scitotenv.2021.147140

Ashouri, H., Hsu, K. L., Sorooshian, S., Braithwaite, D. K., Knapp, K. R., Cecil, L. D., et al. (2015). PERSIANN-CDR daily precipitation climate data record from multisatellite observations for hydrological and climate studies. *Bull. Am. Meteorol. Soc.* 96 (1), 69–83. doi:10.1175/bams-d-13-00068.1

Bai, X. Y., Fan, Z. M., and Yue, T. X. (2023). Dynamic pattern-effect relationships between precipitation and vegetation in the semi-arid and semi-humid area of China. *CATENA* 232, 107425. doi:10.1016/j.catena.2023.107425

Beck, H. E., van Dijk, A. I. J. M., Levizzani, V., Schellekens, J., Miralles, D. G., Martens, B., et al. (2017). MSWEP: 3-hourly 0.25° global gridded precipitation (1979–2015) by merging gauge, satellite, and reanalysis data. *Hydrol. Earth Syst. Sci.* 21, 589–615. doi:10.5194/hess-21-589-2017

Brunsdon, C., Fotheringham, S., and Charlton, M. (1998). Geographically weighted regression. *J. R. Stat. Soc. Ser. D. Stat.* 47, 431–443. doi:10.1111/1467-9884.00145

Chao, L. J., Zhang, K., Li, Z. J., Zhu, Y. L., Wang, J. F., and Yu, Z. B. (2018). Geographically weighted regression based methods for merging satellite and gauge precipitation. *J. Hydrol.* 558, 275–289. doi:10.1016/j.jhydrol.2018.01.042

Chen, F. R., Liu, Y., Liu, Q., and Li, X. (2014). Spatial downscaling of TRMM 3B43 precipitation considering spatial heterogeneity. *Int. J. Remote Sens.* 35, 3074–3093. doi:10.1080/01431161.2014.902550

Chen, S. D., Zhang, L. P., She, D. X., and Chen, J. (2019). Spatial downscaling of tropical rainfall measuring mission (TRMM) annual and monthly precipitation data over the middle and lower reaches of the yangtze River Basin, China. *China. Water* 11, 568. doi:10.3390/w11030568

Duan, L. M., Fan, K. K., Li, W., and Liu, T. X. (2019). Spatial downscaling algorithm of TRMM precipitation based on multiple high-resolution satellite data for Inner Mongolia, China. *Theor. Appl. Climatol.* 135, 45–59. doi:10.1007/s00704-017-2347-7

Fang, J., Du, J., Xu, W., Shi, P. J., Li, M., and Ming, X. D. (2013). Spatial downscaling of TRMM precipitation data based on the orographical effect and meteorological conditions in a mountainous area. *Adv. Water Resour.* 61, 42–50. doi:10.1016/j.advwatres.2013.08.011

Fotheringham, A. S., Yang, W. B., and Kang, W. (2017). Multiscale geographically weighted regression (MGWR). *Ann. Am. Assoc. Geogr.* 107, 1247–1265. doi:10.1080/24694452.2017.1352480

Hou, A. Y., Kakar, R. K., Neeck, S., Azarbarzin, A. A., Kummerow, C. D., Kojima, M., et al. (2014). The global precipitation measurement mission. *Bull. Am. Meteorol. Soc.* 95, 701–722. doi:10.1175/bams-d-13-00164.1

Hu, X. M., Xue, M., McPherson, R. A., Martin, E., Rosendahl, D. H., and Qiao, L. (2018). Precipitation dynamical downscaling over the great plains. *J. Adv. Model. Earth Syst.* 10, 421–447. doi:10.1002/2017ms001154

Huffman, G. J., Bolvin, D. T., Nelkin, E. J., Wolff, D. B., Adler, R. F., Gu, G. J., et al. (2007). The TRMM multisatellite precipitation analysis (TMPA): quasi-global, multiyear, combined-sensor precipitation estimates at fine scales. *J. Hydrometeorol.* 8, 38–55. doi:10.1175/jhm560.1

Immerzeel, W. W., Rutten, M. M., and Droogers, P. (2009). Spatial downscaling of TRMM precipitation using vegetative response on the Iberian Peninsula. *Remote Sens. Environ.* 113 (2), 362–370. doi:10.1016/j.rse.2008.10.004

Jia, S. F., Zhu, W. B., Lu, A. F., and Yan, T. T. (2011). A statistical spatial downscaling algorithm of TRMM precipitation based on NDVI and DEM in the Qaidam Basin of China. *Remote Sens. Environ.* 115 (12), 3069–3079. doi:10.1016/j.rse.2011.06.009

Jing, W. L., Yang, Y. P., Yue, X. F., and Zhao, X. D. (2016). A comparison of different regression algorithms for downscaling monthly satellite-based precipitation over North China. *Remote Sens.* 8 (10), 835. doi:10.3390/rs8100835

Joyce, R. J., Janowiak, J. E., Arkin, P. A., and Xie, P. P. (2004). CMORPH: a method that produces global precipitation estimates from passive microwave and infrared data at high spatial and temporal resolution. *J. Hydrometeorol.* 5, 487–503. doi:10.1175/1525-7541(2004)005<0487:camtpg>2.0.co;2

Kidd, C., and Levizzani, V. (2011). Status of satellite precipitation retrievals. *Hydrol. Earth Syst. Sci.* 15, 1109–1116. doi:10.5194/hess-15-1109-2011

Kofidou, M., Stathopoulos, S., and Gemitzi, A. (2023). Review on spatial downscaling of satellite derived precipitation estimates. *Environ. Earth Sci.* 82, 424. doi:10.1007/s12665-023-11115-7

Kubota, T., Shige, S., Hashizurne, H., Aonashi, K., Takahashi, N., Seto, S., et al. (2007). Global precipitation map using satellite-borne microwave radiometers by the GSMaP project: production and validation. *IEEE Trans. Geosci. Remote Sens.* 45, 2259–2275. doi:10.1109/tgrs.2007.895337

Li, X. Y., Wang, Y. T., Xue, B. L., A, Y. L., Zhang, X. J., and Wang, G. Q. (2023). Attribution of runoff and hydrological drought changes in an ecologically vulnerable basin in semi-arid regions of China. *Hydrol. Process.* 37 (10), e15003. doi:10.1002/hyp.15003

Lu, X. Y., Tang, G. Q., Wang, X. Q., Liu, Y., Wei, M., and Zhang, Y. X. (2020). The development of a two-step merging and downscaling method for satellite precipitation products. *Remote Sens.* 12 (3), 398. doi:10.3390/rs12030398

Ma, N., Szilagyi, J., and Zhang, Y. Q. (2021). Calibration-free complementary relationship estimates terrestrial evapotranspiration globally. *Water Resour. Res.* 57 (9), e2021WR029691. doi:10.1029/2021wr029691

Ma, Z. Q., Tan, X., Yang, Y., Chen, X., Kan, G. Y., Ji, X., et al. (2018). The first comparisons of IMERG and the downscaled results based on IMERG in hydrological utility over the ganjiang River Basin. *Water* 10 (10), 1392. doi:10.3390/w10101392

Min, X. X., Ma, Z. Q., Xu, J. T., He, K., Wang, Z. G., Huang, Q. L., et al. (2020). Spatially downscaling IMERG at daily scale using machine learning approaches over zhejiang, southeastern China. *Front. Earth Sci.* 8, 146. doi:10.3389/feart.2020.00146

Molinaro, A. M., Simon, R., and Pfeiffer, R. M. (2005). Prediction error estimation: a comparison of resampling methods. *Bioinformatics* 21, 3301–3307. doi:10.1093/bioinformatics/bti499

Nan, L. J., Yang, M. X., Wang, H., Xiang, Z. L., and Hao, S. K. (2021). Comprehensive evaluation of global precipitation measurement mission (GPM) IMERG precipitation products over mainland China. *Water* 13, 3381. doi:10.3390/w13233381

Noor, R., Arshad, A., Shafeeque, M., Liu, J. P., Baig, A., Ali, S., et al. (2023). Combining APHRODITE rain gauges-based precipitation with downscaled-TRMM data to translate high-resolution precipitation estimates in the indus basin. *Remote Sens.* 15 (2), 318. doi:10.3390/rs15020318

Sokol, Z., and Bliznák, V. (2009). Areal distribution and precipitation-altitude relationship of heavy short-term precipitation in the Czech Republic in the warm part of the year. *Atmos. Res.* 94 (4), 652–662. doi:10.1016/j.atmosres.2009.03.001

Sylla, M. B., Gaye, A. T., Pal, J. S., Jenkins, G. S., and Bi, X. Q. (2009). High-resolution simulations of West African climate using regional climate model (RegCM3) with different lateral boundary conditions. *Theor. Appl. Climatol.* 98 (3-4), 293–314. doi:10.1007/s00704-009-0110-4

Tang, G. Q., Ma, Y. Z., Long, D., Zhong, L. Z., and Hong, Y. (2016). Evaluation of GPM Day-1 IMERG and TMPA Version-7 legacy products over Mainland China at multiple spatiotemporal scales. *J. Hydrol.* 533, 152–167. doi:10.1016/j.jhydrol.2015.12.008

Tang, Y. F., Wu, J., Bai, L., and Wang, B. (2020). Reliability of gridded precipitation products in the Yellow River Basin, China. *Remote Sens.* 12, 374. doi:10.3390/rs12030374

Vicente-Serrano, S. M., Gouveia, C., Camarero, J. J., Begueria, S., Trigo, R., Lopez-Moreno, J. I., et al. (2013). Response of vegetation to drought time-scales across global land biomes. *Proc. Natl. Acad. Sci. U. S. A.* 110 (1), 52–57. doi:10.1073/pnas.1207068110

Wang, H., Zang, F., Zhao, C. Y., and Liu, C. L. (2022). A GWR downscaling method to reconstruct high-resolution precipitation dataset based on GSMaP-Gauge data: a case study in the Qilian Mountains, Northwest China. *Sci. Total Environ.* 810, 152066. doi:10.1016/j.scitotenv.2021.152066

Wang, Y. X., Duan, L. M., Tong, X., Liu, T. X., Li, D. F., and Li, W. (2023). Non-stationary modeling of wet-season precipitation over the Inner Mongolia section of the Yellow River basin. *Theor. Appl. Climatol.* 151, 389–405. doi:10.1007/s00704-022-04279-y

Wang, Z. L., Zhong, R. D., Lai, C. G., and Chen, J. C. (2017). Evaluation of the GPM IMERG satellite-based precipitation products and the hydrological utility. *Atmos. Res.* 196, 151–163. doi:10.1016/j.atmosres.2017.06.020

Xu, S. G., Wu, C. Y., Wang, L., Gonsamo, A., Shen, Y., and Niu, Z. (2015). A new satellite-based monthly precipitation downscaling algorithm with non-stationary relationship between precipitation and land surface characteristics. *Remote Sens. Environ.* 162, 119–140. doi:10.1016/j.rse.2015.02.024

Xue, B. L., A, Y. L., Wang, G. Q., Helman, D., Sun, G., Tao, S. L., et al. (2022). Divergent hydrological responses to forest expansion in dry and wet basins of China: implications for future afforestation planning. *Water Resour. Res.* 58 (5), e2021WR031856. doi:10.1029/2021wr031856

Yan, X., Chen, H., Tian, B. R., Sheng, S., Wang, J. X., and Kim, J. S. (2021a). A downscaling-merging scheme for improving daily spatial precipitation estimates based on random forest and cokriging. *Remote Sens.* 13 (11), 2040. doi:10.3390/rs13112040

Yan, X., Chen, H., Tian, B. R., Sheng, S., Wang, J. X., and Kim, J. S. (2021b). A downscaling-merging scheme for improving daily spatial precipitation estimates based on random forest and cokriging. *Remote Sens.* 13 (11), 2040. doi:10.3390/rs13112040

Yu, C., Hu, D. Y., Liu, M. Q., Wang, S. S., and Di, Y. F. (2020). Spatio-temporal accuracy evaluation of three high-resolution satellite precipitation products in China area. *Atmos. Res.* 241, 104952. doi:10.1016/j.atmosres.2020.104952

Yu, L. F., Leng, G. Y., and Python, A. (2022). A comprehensive validation for GPM IMERG precipitation products to detect extremes and drought over mainland China. *Weather Clim. Extrem.* 36, 100458. doi:10.1016/j.wace.2022.100458

Zhang, H. R., Zhang, J. N., Lv, Z. Z., Yao, L. J., Zhang, N., and Zhang, Q. (2023). Spatio-temporal assessment of landscape ecological risk and associated drivers: a case study of the Yellow River Basin in Inner Mongolia. *Land* 12, 1114. doi:10.3390/land12061114

Zhang, Q., Peng, J. T., Singh, V. P., Li, J. F., and Chen, Y. Q. D. (2014). Spatio-temporal variations of precipitation in arid and semiarid regions of China: the Yellow River basin as a case study. *Glob. Planet. Change.* 114, 38–49. doi:10.1016/j.gloplacha.2014.01.005

Zhang, Q., Shi, P. J., Singh, V. P., Fan, K. K., and Huang, J. J. (2017). Spatial downscaling of TRMM-based precipitation data using vegetative response in Xinjiang, China. *Int. J. Climatol.* 37, 3895–3909. doi:10.1002/joc.4964

Zhang, T., Li, B. L., Yuan, Y. C., Gao, X. Z., Sun, Q. L., Xu, L. L., et al. (2018). Spatial downscaling of TRMM precipitation data considering the impacts of macro-geographical factors and local elevation in the Three-River Headwaters Region. *Remote Sens. Environ.* 215, 109–127. doi:10.1016/j.rse.2018.06.004

frontiers | Frontiers in Environmental Science

TYPE Original Research
PUBLISHED 10 May 2024
DOI 10.3389/fenvs.2024.1403490

OPEN ACCESS

EDITED BY
Zhiming Han,
Northwest A&F University, China

REVIEWED BY
Xiaoliang Ma,
Lanzhou University, China
Shuang Song,
Shenyang Agricultural University, China

*CORRESPONDENCE
Yingjie Wu,
wuyingjie1230@163.com

RECEIVED 19 March 2024
ACCEPTED 26 April 2024
PUBLISHED 10 May 2024

CITATION
Li W, Guan J, Wang W, Wu Y, Zhao Y, Zhang W, Wang S and Chen Z (2024), Analysis of extreme precipitation variation characteristics in mountain grasslands of arid and semi-arid regions in China.
Front. Environ. Sci. 12:1403490.
doi: 10.3389/fenvs.2024.1403490

Analysis of extreme precipitation variation characteristics in mountain grasslands of arid and semi-arid regions in China

Wei Li[1,2], Jing Guan[3], Wenjun Wang[1,2], Yingjie Wu[1,2]*, Yawen Zhao[4], Weijie Zhang[1,2], Sinan Wang[1,2] and Zexun Chen[1,2]

[1]Yinshanbeilu National Field Research Station of Desert Steppe Eco-hydrological System, China Institute of Water Resources and Hydropower Research, Beijing, China, [2]Institute of Water Resource for Pastoral Area Ministry of Water Resources of the People's Republic of China, Hohhot, China, [3]Yellow River Engineering Consulting Co., Ltd, Zhengzhou, China, [4]Shaanxi Normal University, Xi'an, China

Introduction: With global warming, the disaster losses caused by extreme precipitation events are increasing. The poor natural conditions and climate change make the arid and semi-arid mountainous grassland area a sensitive region of climate change. The study on the spatio-temporal variation characteristics of extreme precipitation events in this region is helpful to improve the ability of climate prediction and disaster prevention and reduction in grassland.

Methods: Based on the daily precipitation data of four meteorological monitoring stations in the Yinshanbeilu from 1970 to 2020, the trend analysis, M-K test and wavelet analysis were used to select seven typical extreme precipitation indicators to analyze the temporal and spatial characteristics of extreme precipitation.

Results and Discussion: The results showed that the precipitation in the Yinshanbeilu increased in the past 51a, and the number of heavy rain days increased significantly. The significance test of CDD and CWD showed that the number of continuous dry days and continuous wet days decreased abruptly. The spatial analysis showed that the high value areas of R95p, R95d and PRCRTOT were all located in Siziwang Banner, and it could be concluded that the extreme precipitation risk was the highest in Siziwang Banner, while the low value areas of SDII, Rx1day, R95p and PRCRTOT were all located in Sonid Right Banner, which could be inferred that the Sonid Right Banner was relatively dry. The first main cycle of the seven indexes of extreme precipitation almost runs through the whole time series, and the starting point of the minimum main cycle changes inconsistent. In addition to the number of consecutive dry days, the other indices have a good correlation with annual precipitation, flood season and monthly precipitation from June to September, and July is the peak period of extreme precipitation events.

KEYWORDS

extreme precipitation, arid and semi-arid regions, Yinshanbeilu, wavelet analysis, M-K test

1 Introduction

Precipitation is an important source of water resources (Wang et al., 2023). Extreme precipitation occurs when the precipitation intensity exceeds a given threshold or percentile (Li et al., 2024). Extreme precipitation events are projected to occur more frequently under climate change (Cardoso Pereira et al., 2020; Tradowsky et al., 2023). This increase in extreme precipitation may lead to serious natural disasters such as urban waterlogging and flash floods, especially in arid areas (Abd-Elaty et al., 2023). The increase in the frequency of extreme precipitation poses a huge threat to the safety of life and property on a global and regional scale. (Zia et al., 2023). Therefore, by studying extreme precipitation events, we can better understand the supply and demand of water resources and formulate effective water resources management strategies. it is of great significance in regional flood prevention and disaster reduction (Mashao et al., 2023).

In recent years, researchers have used trend, abrupt change, and period algorithms to analyze extreme precipitation events in various regions. Research and explore the spatiotemporal changes of extreme precipitation index, summarize its changing rules, and improve local capabilities to cope with extreme precipitation (Zhao et al., 2024). For example, Chaubey et al. (2022) found that the frequency of heavy precipitation in mid-latitude areas has generally increased in the past 50–100 years Yang et al. (2024) analyzed the spatiotemporal characteristics of precipitation use efficiency (PUE) from 2001 to 2021 and studied climate driving factors. The climate driving force analysis showed that the regional contribution of precipitation was 19.57%. Wu et al. (2021) Based on weather station data in the middle and lower reaches of the Yangtze River from 1970 to 2018, the spatial and temporal distribution of 11 extreme precipitation indices was analyzed, and it was found that most of the mutations in extreme precipitation indices occurred in the 1980s and 1990s. In the globe, there is an increasing trend in the probability of extreme precipitation events, with a significant rise in the total amount of extreme precipitation. Moreover, tropical regions experience the highest frequency of extreme precipitation events (Alexander et al., 2006; Asadieh et al., 2014). Additionally, regions exhibiting a significant increase in extreme precipitation volume, intensity, and frequency outnumber those showing a decreasing trend (Donat et al., 2013). On an intercontinental scale, previous studies indicate extreme variability in precipitation levels, albeit lacking spatial consistency. Extreme precipitation in North America is on the rise (Peterson et al., 2008), while in Central and Western Africa, it is declining (Aguilar et al., 2009). Corresponding to global trends, China is witnessing an upward trend in the frequency and intensity of extreme precipitation events. From the 1960s to the 1980s, precipitation totals in China showed an upward trend, but have been declining since the 1980s (Peng et al., 2020). Regional studies, including those of the Yangtze River Basin and Northeast China, demonstrate the most pronounced positive trends (Wang et al., 2011).

The Yinshanbeilu in Inner Mongolia is not only the transition zone from Yinshan Mountain to the Mongolian Plateau, but also the transition area from a semi-arid to arid climate (WANG et al., 2005). The region serves as an extremely important functional area for windbreak, sand fixation, and biodiversity protection. Its ecosystem is fragile and highly sensitive to changes in precipitation. In recent years, extreme precipitation events have occurred frequently in this region, which are accompanied by flood events and have brought great challenges to the ecological security of the region. In this study, we applied precipitation data (1970–2020) from four regional rainfall stations in the grassland area at the Yinshanbeilu, i.e., Urad Middle Banner, Siziwang Banner, Damao Banner, and Sonid Right Banner. The investigation applied trend analysis, Kriging interpolation, M-K abrupt change analysis, wavelet transform, and correlation analyses to assess the spatiotemporal transformation characteristics, abrupt change characteristics, and periodic characteristics of the seven extreme precipitation indices in the study area. The results of this study may be applied to support the description of universally applicable rules, improve our ability to tackle extreme precipitation, and provide a reference for human and ecological protection, disaster early warning, and climate change.

2 Study area

Yinshanbeilu grassland area of Yinshan Mountain (107°25′E −114°26′E, 41°18′N −43°76′N) is located in the north-central region of Inner Mongolia (Figure 1). It is the transition zone between Yinshan Mountain and the Mongolian Plateau. It has a mid-temperate semi-arid continental monsoon climate, with large temperature differences between winter and summer and between day and night. Meteorological data from four weather stations in the statistical study area from 1970 to 2020 were obtained the multi-year average precipitation is 284 mm, mainly concentrated from July to September, and the multi-year average evaporation is 2,305 mm. The annual average temperature is 2.5°C, the annual average sunshine hours are 3,100 h, and the frost-free period is 83 d. The annual average wind speed is 4.5 $m{\cdot}s^{-1}$, with northerly and northwesterly winds prevailing in winter and spring. The annual number of windy days is 63, and the number of sandstorm days is 20–25 (Yang et al., 2024).

3 Data and methods

3.1 Data

Complete daily precipitation data for a total of 51 years (1970–2020) were used in this study. The data were retrieved from four national weather stations (https://data.cma.cn/) located in Urad Middle Banner, Siziwang Banner, Damao Banner, and Sonid Right Banner in Inner Mongolia (Figure 1).

The World Meteorological Organization (WMO) Expert Team on Climate Change Detection Monitoring and Indices (ETCCDMI) recommended 27 core indices (https://community.wmo.int/en/climate-change-detection-and-indices) to define the extreme precipitation index (Booth et al., 2012; Indices, 2019). Table 1 describes the seven extreme precipitation indices selected to quantitatively analyze the extreme precipitation characteristics in the study area. To calculate the heavy precipitation threshold and extremely heavy precipitation threshold, we first arranged the daily precipitation data (Daily precipitation ≥1 mm) from 1970 to 2020 in ascending order $(x_1, x_2, x_3, \ldots, x_n)$ and then calculated the probability of a certain value $\geq x_m$. The calculation formula was as follows (Bonsal et al., 2001): $P = m - 0.31n + 0.38$, where n is the number of precipitation data points.

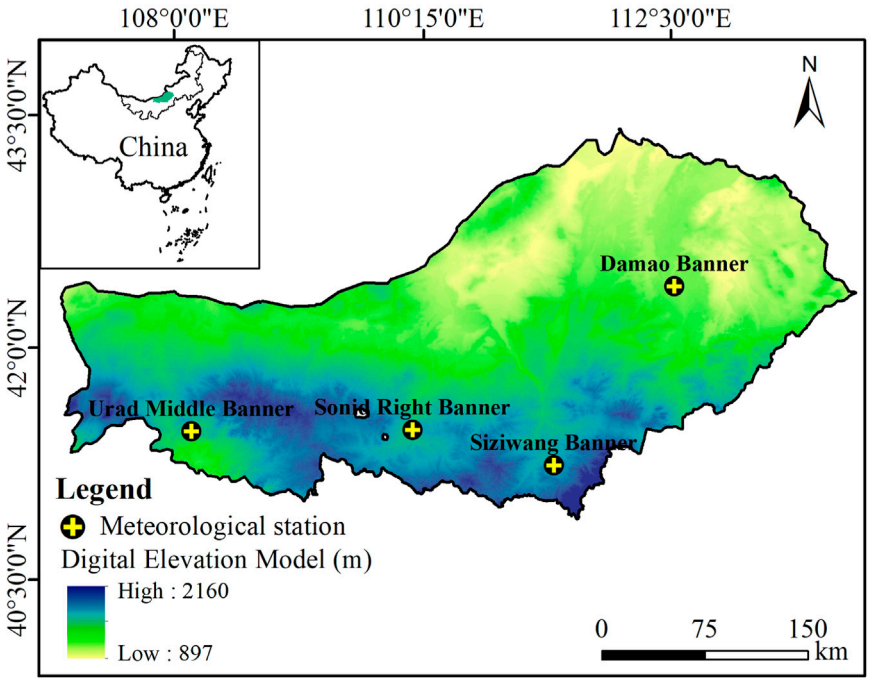

FIGURE 1
Study area location and site distribution map.

TABLE 1 Description of the seven extreme precipitation indices applied in this study.

Name	Abbreviation	Definition	Unit
Total annual precipitation	PRCPTOT	Sum of daily precipitation in the year ≥1 mm	mm
Precipitation intensity	SDII	Ratio of total annual precipitation to number of precipitation days	mm·d^{-1}
Extreme precipitation	R95p	Annual daily precipitation > sum of 95th percentile precipitation	mm
Extreme precipitation days	R95d	Annual daily precipitation >95th percentile number of precipitation days	d
Maximum daily precipitation	Rx1day	Maximum daily precipitation per year (or month)	mm
Consecutive dry days	CDD	The number of consecutive days with daily precipitation <1 mm	d
Consecutive wet days	CWD	The number of consecutive days with daily precipitation ≥1 mm	d

3.2 Research methods

We applied the linear trend analysis method with a 10a moving average to analyze the time series of each extreme precipitation index year by year from 1970 to 2020. Mann–Kendall (M-K) abrupt change analysis and sliding T-test were applied to analyze the abrupt change characteristics of each extreme precipitation index time series (Li et al., 2020). The wavelet analysis method was used to study the periodicity of each extreme precipitation index (Rathinasamy et al., 2019). Correlation analysis was conducted using Origin software and correlation heat maps were produced using Kriging in the spatial analysis module of ArcGIS 10.7.

3.2.1 M-K test

The M-K test was used to analyze the abrupt change characteristics of each extreme precipitation index (Sa'adi et al., 2019). The M-K test is a widely used non-parametric test method in time series trend analysis. The null hypothesis H_0 is a time series $(x_1, \cdots, x_n)$, which is n independent samples with the same distribution of random variables, and there is no certain upward or downward trend. The M-K test calculated UF and UB for each time series and its reverse series. A sequence of one rank is constructed for a long sequence of n samples as follows: for calculation methods, see Eqs 1 and 2

$$S_k = \sum_{i=1}^{k} m_i \frac{n!}{r!(n-r)!} \quad (1)$$

$$UF_K = \frac{|S_k - E(S_k)|}{\sqrt{\mathrm{var}(S_k)}}, k = 1, 2, \cdots, n \quad (2)$$

where S_k is the cumulative number of cases in which x_i exceeded x_j $(1 < j < i)$. When $k = 1$, $UF_1 = 0$, where $E(S_k)$ is the mean value of S_k. We calculated UB_K using the same process in reverse time series and make $UB_K = -UF_K$ $(k = n, k = n - 1 \ldots, 1)$. When $k = 1$, $UB_1 = 0$. For a significance level of $\alpha = 0.05$, the critical value $U_{0.05} = \pm 1.96$.

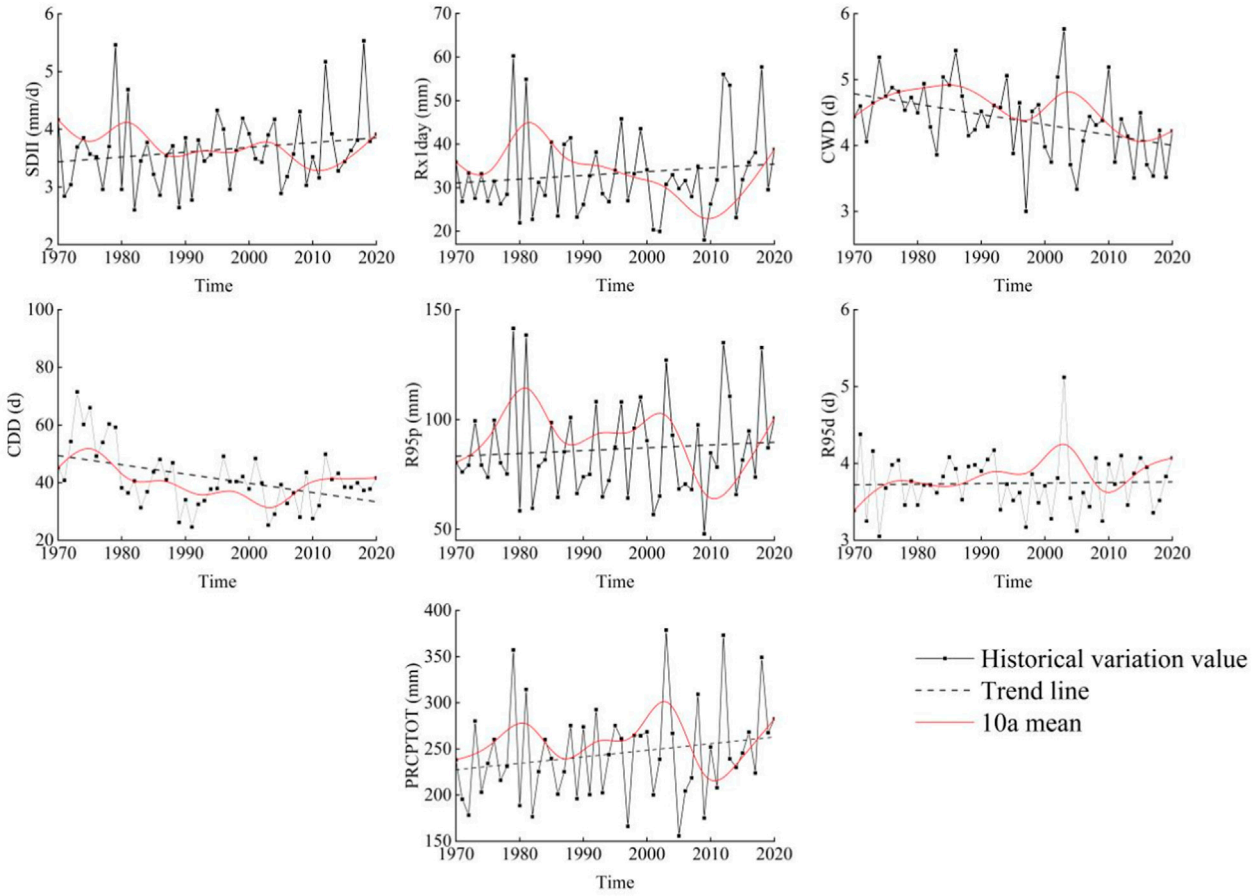

FIGURE 2
Interannual changes in extreme precipitation indices in the grassland area at Yinshanbeilu during 1970–2020.

A value of UF > 0 indicates that the variable is increasing, while UF < 0 indicates that the variable is decreasing. A UF line and UB line exceeding the critical straight line indicates that this upward or downward trend is statistically significant. If the curves of UF and UB intersect, and the intersection is positioned between the two critical lines, then the moment corresponding to the intersection indicates the time when the abrupt change begins, described in this study as the abrupt change year.

3.2.2 Wavelet analysis

The wavelet analysis method was selected to study the periodicity of each extreme precipitation index (Beecham and Chowdhury, 2010). Each extreme precipitation index is represented by a cluster of wavelet function systems to reveal the multiple changing trends and periods present in the time series. The following equation was used to calculate the wavelet coefficient: See Eq. 3 for calculation method

$$W_f(a,b) = \frac{1}{\sqrt{a}} \int_{-\infty}^{\infty} f(t) \Psi^* \left(\frac{t-b}{a} \right) dt \quad (3)$$

where $W_f(a,b)$ is the wavelet coefficient, a is the scale factor, which determines the wavelet width; b is the translation factor, which reflects the parameter of the wavelet position movement; and Ψ^* is the complex total function.

The real-part coefficients of the wavelet were obtained from wavelet analysis using MATLAB software, and Origin drawing software was used to draw the real-part contour map of the wavelet coefficients. The isoline diagram of the real part of the wavelet coefficient can be used to reflect the periodic changes of the time series at different time scales and its distribution.

4 Results

4.1 Extreme precipitation index changes

The interannual variation diagram and statistical table of the extreme precipitation indices in various regions at the Yinshanbeilu during 1970–2020 are shown in Figure 2 and Table 2, respectively. The 10a moving average curve indicates that there was a general increasing trend in precipitation intensity (SDII) in the study area, with a non-significant change rate of 0.08 mm·d^{-1}·(10a)$^{-1}$ (Figure 2). There was a rapid decrease in SDII in the early 1980s, with the minimum value (i.e., 2.6 mm·d^{-1}) occurring in 1982. The SDII was relatively stable until the early 1990s, and it showed a V-shaped fluctuation change from 1990 to 2010. The maximum 1-day precipitation (RX1day) demonstrated a fluctuating upward trend, with a change rate of 0.87 mm·(10a)$^{-1}$. The 10a moving average

TABLE 2 Statistics of extreme precipitation indices in the grassland area at Yinshanbeilu during 1970–2020.

	SDII (mm·d^{-1})	Rx1day (mm)	CWD (d[a])	CDD (d[a])	R95p (mm)	R95d (d)	PRCPTOT (mm)
Max	5.35	60.2	5.77	100.84	141.52	5.12	378.77
Min	2.6	17.96	3	24.56	47.91	3.05	155.82
Rate of change (10 a)$^{-1}$	0.08	0.87	−0.15	−3.2	1.27	0	7.1

[a]$p < 0.05$ indicates significant level.

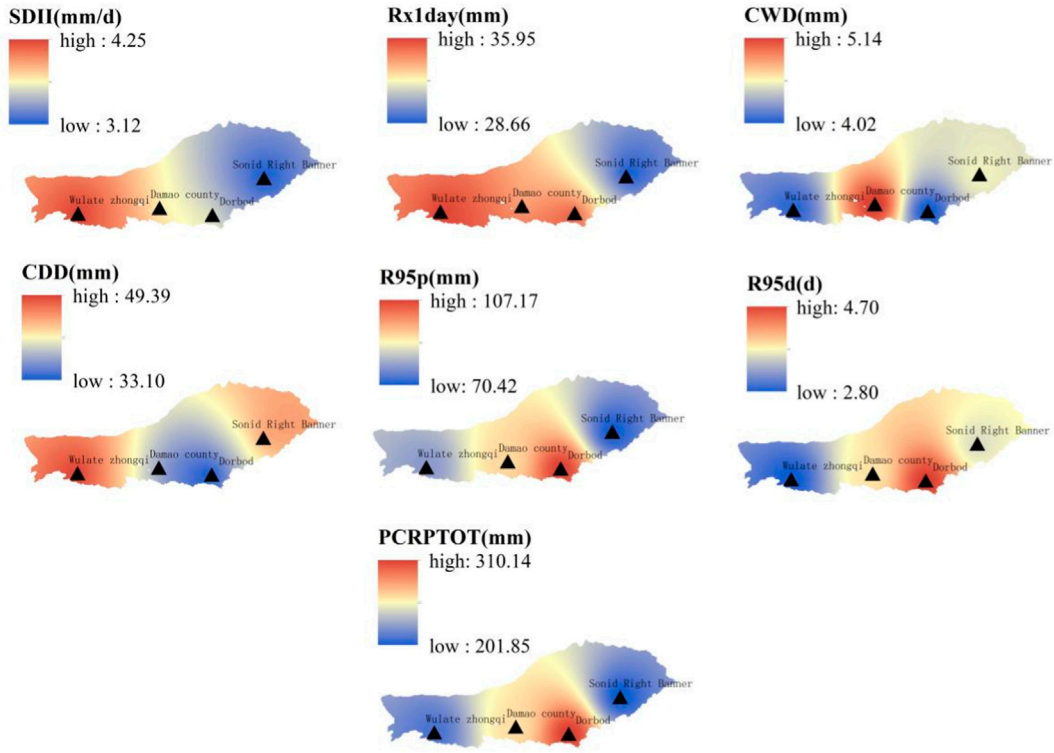

FIGURE 3
Spatial distribution of extreme precipitation index at Yinshanbeilu during 1970–2020.

RX1day continued to decline from the 1980s to the 2010s, reaching a minimum value of 17.96 mm in 2009, followed by a rapid increasing trend.

During the study period, both the number of consecutive wet days (CWD) and the number of consecutive dry days (CDD) showed a decreasing trend, which reached the 0.05 significance level. The CDD decreased at a rapid rate, with an average decrease of 3.2 d every 10 years. The maximum CWD (5.77 d) occurred in 2003, and the minimum (3 d) occurred in 1997. The maximum CDD (100.84 d) occurred in 2001 and the minimum of 24.56 d occurred in 1991. Extreme precipitation (R95p) increased slowly at a rate of 1.27 mm·(10a)$^{-1}$, where the maximum (141.52 mm) and minimum (47.91 mm) values occurred in 1979 and 2009, respectively. The change rate of extreme precipitation days (R95d) in the past 50 years was 0, with a maximum value of 5.12 d in 2003 and a minimum value of 3.05 d in 1974. The annual total precipitation (PRCPTOT) showed an upward trend from 1961 to 2010, with a change rate of 7.1 mm·(10a)$^{-1}$. Its maximum (378.77 mm) and minimum (152.82 mm) values occurred in 2003 and 2005, respectively.

Overall, although SDII, RX1day, R95p, and PRCPTOT changed at different rates, they all showed an increasing trend. This indicates that, under the general trend of global warming during the study period, precipitation generally showed an increasing trend at the Yinshanbeilu in the northern arid area. The number of heavy rain days increased significantly and the overall climate gradually became humid. This is consistent with a previous report on the changing trends of extreme precipitation events in the arid areas in the northwestern China during 1960–2010 (Wang et al., 2023).

4.2 Spatial distribution

The average extreme precipitation indices of the four stations in the grassland area at Yinshanbeilu were calculated from 1970 to 2020. The Kriging interpolation method in ArcGIS software was used for spatial interpolation. The spatial distribution characteristics of each extreme precipitation index were obtained, as shown in Figure 3.

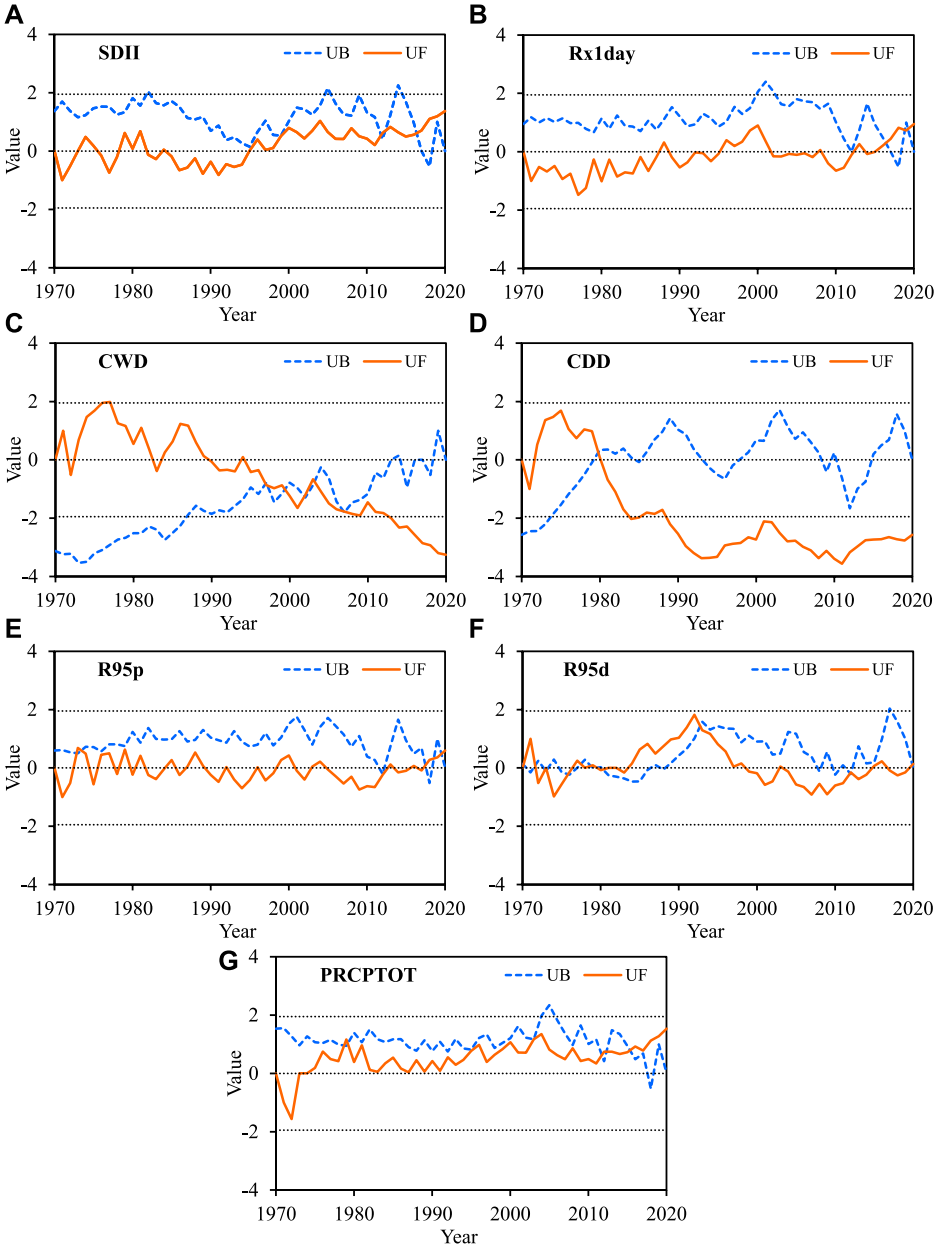

FIGURE 4
M-K mutation trend of extreme precipitation index in the grassland area at Yinshanbeilu from 1970 to 2020 (UF (Upward Fluctuation) and UB (Downward Fluctuation) curve distributions represent the changes in upward and downward trends in time series data).

The extreme precipitation indices SDII and Rx1day in the study area showed a gradually decreasing trend from southwest to northeast. The maximum CWD and CDD values were observed in Damao Banner (5.14 d) and Urad Middle Banner (49.39 d), respectively. The minimum CWD and CDD values were both observed in Siziwang Banner, at 4.02 d and 33.10 d, respectively. The maximum R95p, R95d, and PRCRTOT values were observed in Siziwang Banner, with values of 107.17 mm, 4.07 d and 310.14 mm, respectively. The minimum R95p (70.42 mm) and PRCRTOT (201.85 mm) values were observed in Sonid Right Banner. The low value area of R95d (2.80 d) occurred in the Urad Middle Banner.

Combined with the spatial distribution map, the highest values of R95p, R95d, and PRCRTOT all occurred in Siziwang Banner. This indicates that Siziwang Banner has the highest risk of extreme precipitation. The minimum SDII, Rx1day, R95p, and PRCRTOT values all occurred in Sonid Right Banner, indicating that Sonid Right Banner has a low precipitation level and is relatively dry. The extreme precipitation indices show significant spatial differences across the study area, with the risk of extreme precipitation significantly greater in the southeast than in the northwest.

4.3 Abrupt change analysis

Using the M-K test method, we conducted an abrupt change analysis for extreme precipitation indices in the grassland area at

TABLE 3 Cyclical variation characteristics of extreme precipitation indices in the grassland area at Yinshanbeilu during 1970–2020.

Index	First main period (Year)	Second main period (Year)	Third main period (Year)	Fourth main period (Year)
SDII (mm·d^{-1})	55	30	43	7
Rx1day (mm)	55	8	29	–
CWD (d*)	55	35	13	6
CDD (d*)	56	19	30	10
R95p (mm)	56	30	44	6
R95d (d)	55	–	–	–
PRCPTOT (mm)	55	31	44	7

Yinshanbeilu during 1970–2020 (Figure 4), with a significance level of 0.05. The UF curves of CWD and CDD (Figure 4) exceed the critical line and UF < 0. Other indices only exceed the critical line for a few years and UF > 0, indicating a clear downward trend in the regional precipitation intensity and the number of continuous precipitation days. The other indices show a non-significant upward trend.

The UB and UF curves of each extreme precipitation index have intersection points and are within the confidence interval (Figure 4), indicating that the precipitation index has experienced multiple abrupt changes over the study period. The abrupt change points of CDD, R95d, and PRCPTOT were all in the 20th century. Comparative analysis combined with the sliding T-test showed that the abrupt change point of SDII appeared in 2012, and that of R95d appeared in 1994, indicating that the precipitation intensity and the number of extreme precipitation days in the grassland area at Yinshanbeilu suddenly increased. Both passed the significance test, but there was no clear abrupt change. The abrupt changes in CDD and CWD occurred in 1993 and 1979, respectively. They reached significant levels and the abrupt changes were evident, indicating that the number of consecutive dry and consecutive wet days suddenly decreased. The remaining two extreme precipitation indices showed no significant abrupt change points.

4.4 Wavelet analysis

With the help of the Wavelet Analyzer tool in MATLAB 2018a and origin-assisted mapping, the contour maps of the real part of the wavelet coefficient of the 51-year extreme precipitation index in the Yinshanbeilu are generated. From cold to warm colors, it represents the increase in the fingertip precipitation index. The periods of wavelet analysis of each index are shown in Table 3. The cyclical characteristics of the extreme precipitation index series are analyzed (Figure 5). The SDII, CWD, CDD, R95p, and PRCPTOT indices contain four periods: Rx1day has three periods, and R95d has one period. The first main period of the seven indices was 55–56 a, which shows clear cyclical changes of abundance and drought. The average length of the four SDII periods were 25 a, 18 a, 24 a, and 5 a. In the entire time series, the first and second main periods were relatively regular and prominent, the third main period was not prominent, and the fourth main period began after 1985 (Figure 5A). The three average periods of Rx1day were 31 a, 5 a, and 17 a, with clear changes in the first and third periods. The average periods of CWD were 33 a, 23 a, 8 a and 4 a. The third and fourth main periods showed evident patterns after 2013 and 1978, respectively. The average periods of CDD were 30 a, 12 a, 24 a, and 6 a. Except for the first main period, the changes in other periods were not evident. The average periods of R95p were 35 a, 19 a, 23 a, and 4 a, and the average periods of PRCPTOT were 36 a, 20 a, 23 a, and 4 a. The period changes of these two indicators were basically the same. The period of R95p changed significantly throughout the time series. The fourth main period of PRCPTOT changed significantly after 1998. The R95d index contained only one main period, corresponding to an average period of 32 d, and the change was significant. In general, the average period corresponding to the first main period of the seven indices of extreme precipitation had two main variation ranges: 25 a and 30–36 a, and this period continued through almost the entire time series. The average period corresponding to the minimum main period was 4–6 a. In addition, we found that the starting point of each index changes inconsistently and was regional.

4.5 Correlation between extreme precipitation indices and multi-scale precipitation

Figure 6 shows a correlation heat map based on correlation analysis and calculation of each extreme precipitation index and the total precipitation at each scale. Overall, except for CDD, good correlations were observed between the extreme precipitation indices and the annual precipitation, flood season, and monthly precipitation from June to September. There was a strong positive correlation between PRCPTOT and the total precipitation in the flood season, indicating that the precipitation in the flood season had a significant indicative effect on the annual precipitation. This indicates that the precipitation in the flood season has a decisive role in the intensity of annual precipitation, and extreme precipitation between June and September in the flood season. The total annual precipitation showed a strong positive correlation with SDII and R95p, and a positive correlation with Rx1day and R95d, indicating a significant impact of these indices on annual precipitation. By comparing the correlation between various extreme precipitation indices and precipitation in the flood and the

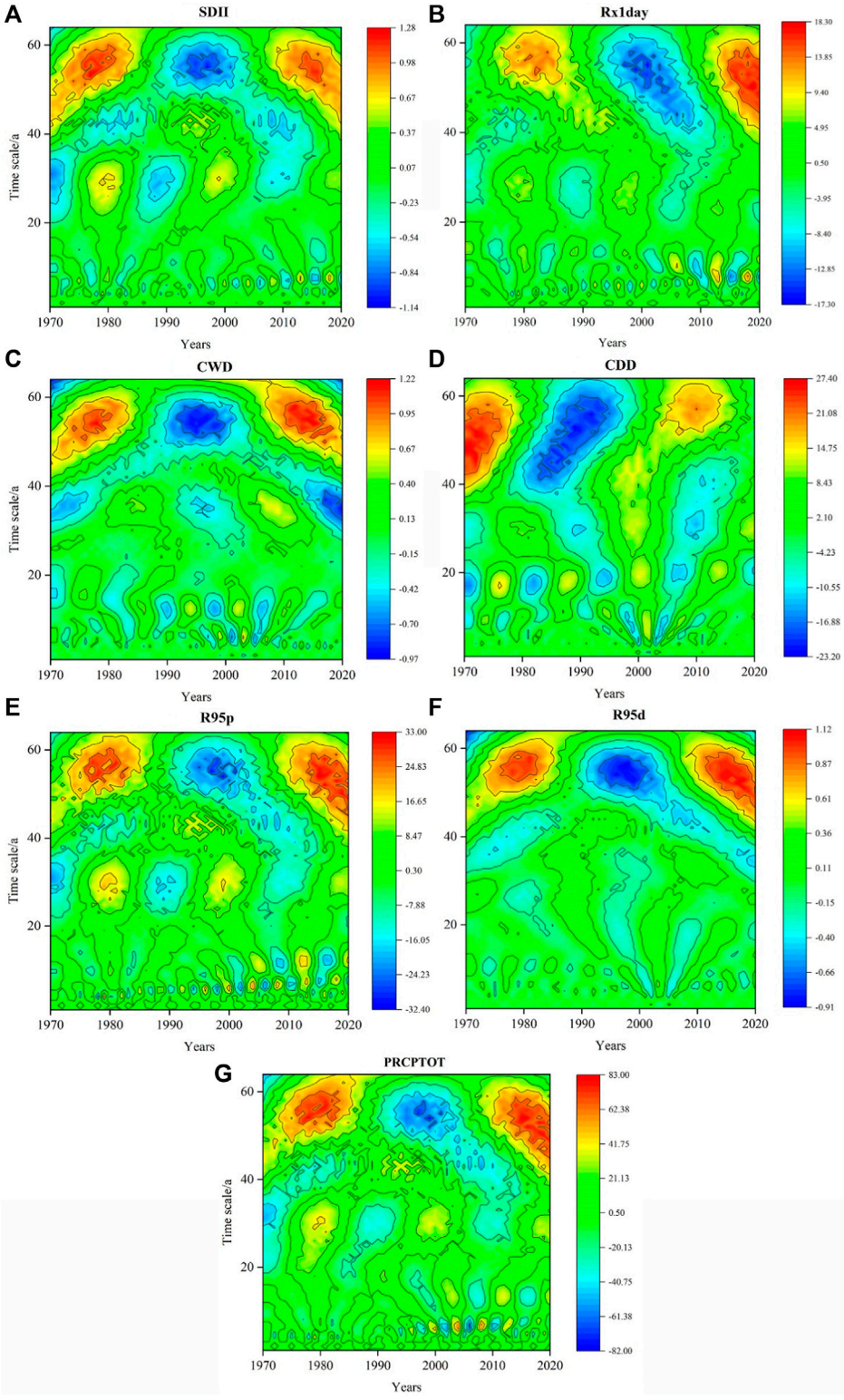

FIGURE 5
Contour map of the real part of the wavelet coefficient of extreme precipitation index in the grassland area at Yinshanbeilu.

non-flood seasons, we observed strong correlations between the extreme precipitation indices and flood season precipitation. Further correlation analyses on precipitation from June to September during the flood season revealed that the correlations with extreme precipitation indices in July during the entire flood season were stronger than in other months. This indicates that July is the main month associated with high occurrence of extreme precipitation events in the study area.

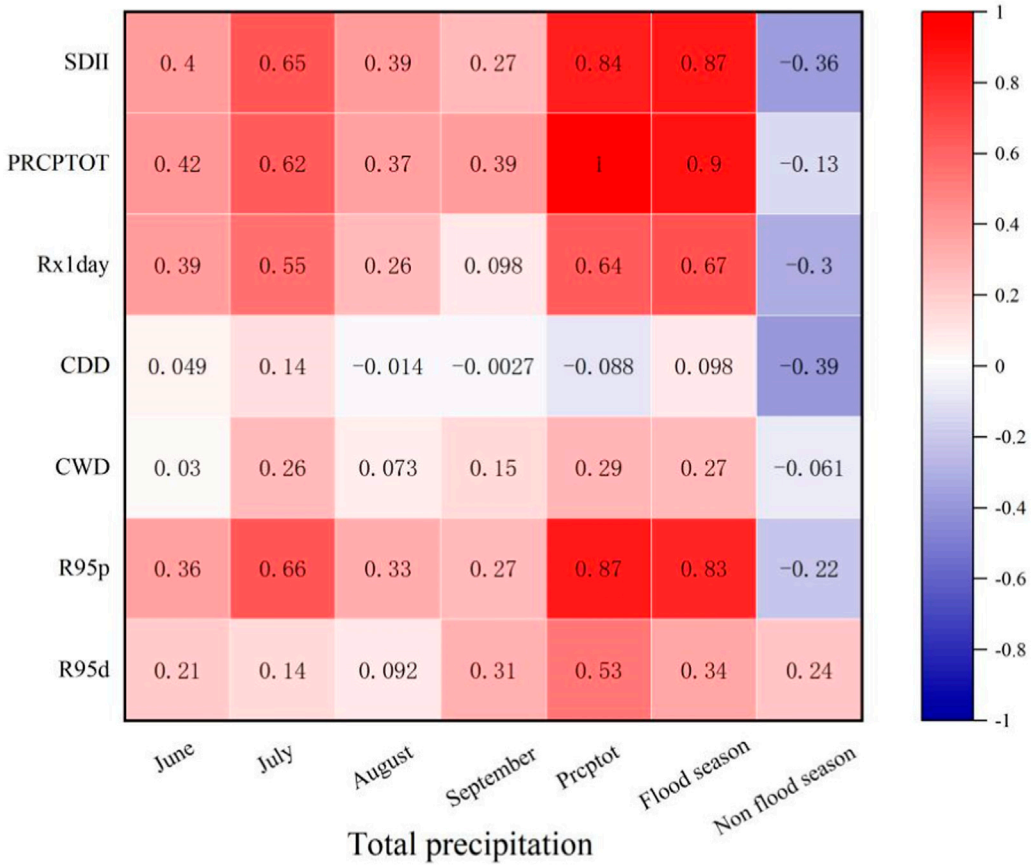

FIGURE 6
Correlation between extreme precipitation indices and multi-scale precipitation in the grassland area at Yinshanbeilu during 1970–2020.

5 Discussion

In this study, we found that the R95p index in the desert grassland area at Yinshanbeilu in Inner Mongolia increased slowly at a rate of 1.27 mm·(10a)$^{-1}$ from 1970 to 2020, whereas the change rate of R95d in the past 50 years was 0. Although SDII, RX1day, R95p, and PRCPTOT demonstrated changes at different rates, they all showed an increasing trend, which was opposite to the extreme precipitation indices changes in the northern semi-arid area during 1961–2010 (Xu et al., 2021). The characteristics of regional precipitation changes may be influenced by the unique cyclical nature of each atmospheric circulation (Li et al., 2015). Li et al. (2015) found that the change in precipitation in Inner Mongolia has a strong relationship with the Northern boundary of WASMR, which moved southward because of the enhanced westerlies, and that the regional precipitation cycles may be influenced by their own periods of NAO and PDO. This might be due to the local characteristics of extreme precipitation, which can present major differences in spatial distribution within a region. Since our study was limited by the number of sites, the spatial distribution characteristics described are somewhat different from those in large-area studies (Gvoždíková et al., 2019). Our findings reflect the situation that the global warming trend is still intensifying, causing the acceleration in water cycle process. It also indicates that extreme precipitation in the grassland basin might continue to increase in the future.

Precipitation is directly affected by the atmospheric circulation and the water vapor supply in the source area (Gimeno et al., 2020; Peng et al., 2020). Through abrupt change test analysis, we found that CWD and CDD suddenly declined in 1979 and 1993, respectively. Both reached significant levels, and were strongly correlated to the precipitation in July during the flood season. The extreme precipitation conditions in this study are divided into two categories: drought conditions and heavy rainfall conditions, which can be characterized by CDD and R95P, and these two extreme indicators have good correlation with other indicators. Regimes belonging to the same category (Huang et al., 2005). In addition, the extreme index has a good correlation with the ENSO index, among which SDII and R95P are more sensitive to ENSO. The Lagrangian HYSPLIT backward air mass trajectory model was used to analyze the movement trajectory of atmospheric water vapor in the study area during the flood season (July) of the abrupt change year (1979; Figure 7), and explore the impact of water vapor on abrupt changes in CDD and CWD (Yang et al., 2020). During the flood season in 1979, the precipitation mainly came from local evaporative water vapor in the inland northwest and westerly air masses, which were mainly continental. By 1993, the water vapor in the flood season mainly came from Arctic Ocean water vapor. Regardless of whether the climate became dry or wet, local evaporation in the northwest of the study area in 1979 was a kind of “dry transport”,

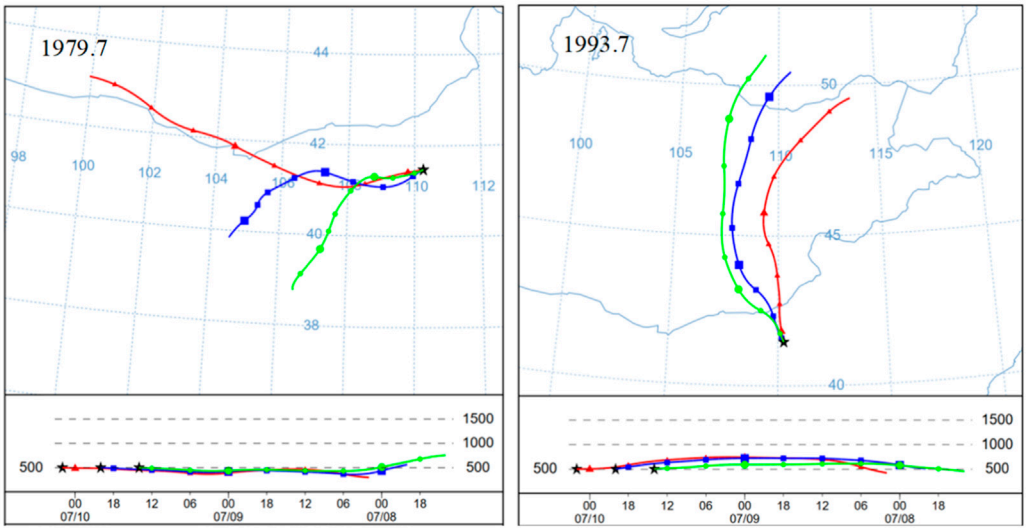

FIGURE 7
HYSPLIT model output source of precipitation and water vapor in the study area during the flood season in the abrupt change year.

which was the cause of water vapor leading to drought, and the number of consecutive wet days decreased. In 1993, the water vapor in the study area mostly came from the northern ocean circulation. This oceanic water vapor brought heavy precipitation, with a high number of precipitation days, thus reducing CDD. It was also accompanied by the influence of local water vapor circulation (Jacox et al., 2020).

6 Conclusion

In this paper, the temporal evolution and spatial distribution characteristics of extreme precipitation index in the Yinshanbeilu during 1970–2020 are analyzed. The main conclusions are as follows: From 1970 to 2020, the extreme precipitation index CDD and CWD in the grassland area of the Yinshanbeilu both passed the significance test and showed a decreasing trend. The changing trend of the extreme precipitation index indicates that the precipitation in Yinshanbeilu has an overall increasing trend in the past 50 years, and the number of heavy rain days has increased significantly. The mutation point of SDII appeared in 2012, and R95d appeared in 1994. Both of them passed the significance test, and the mutation was not obvious. The mutation points of CDD and CWD appeared in 1993 and 1979, respectively, indicating that the number of consecutive dry days and consecutive wet days decreased. The spatial distribution analysis showed that Siziwang Banner had the greatest risk of extreme precipitation, while Sonid Right Banner had less precipitation. The average cycle corresponding to the first main cycle of the 7 indicators of extreme precipitation mainly has two variation ranges, namely, 25a and 30–36A, and the change of this cycle is significant. Except for the number of consecutive dry days, the other indices have good correlation with annual precipitation, flood season and monthly precipitation from June to September. July is the high occurrence period of extreme precipitation events. The research results can provide scientific theoretical basis for the prevention of meteorological disasters in arid and semi-arid areas.

Data availability statement

The data analyzed in this study is subject to the following licenses/restrictions: Data will be disclosed upon request by contacting the author. Requests to access these datasets should be directed to liweixl0012@163.com.

Author contributions

WL: Conceptualization, Methodology, Project administration, Writing–original draft, Writing–review and editing. JG: Conceptualization, Methodology, Supervision, Writing–review and editing. WW: Data curation, Methodology, Supervision, Writing–review and editing. YW: Investigation, Methodology, Software, Supervision, Writing–review and editing. YZ: Formal Analysis, Supervision, Validation, Writing–review and editing. WZ: Investigation, Methodology, Project administration, Software, Writing–review and editing. SW: Project administration, Resources, Supervision, Visualization, Writing–review and editing. ZC: Data curation, Methodology, Software, Supervision, Writing–review and editing.

Funding

The author(s) declare that financial support was received for the research, authorship, and/or publication of this article. This work was financially supported by the Yinshanbeilu Grassland Eco-hydrology Observation and Research Station (Grant YS2022001); the Fundamental Research Fund of the China Institute of Water Resources and Hydropower Research (Grant MK 2023J07, MK 2022J06); the Science and technology plan key project of Inner Mongolia Autonomous Region of China (2021GG0072; 2021GG0020; 2021GG0050; 2020ZD0020).

Conflict of interest

Author JG was employed by Yellow River Engineering Consulting Co., Ltd.

The remaining authors declare that the research was conducted in the absence of any commercial or financial relationships that could be construed as a potential conflict of interest.

Publisher's note

References

Abd-Elaty, I., Kuriqi, A., Pugliese, L., Zelenakova, M., and El Shinawi, A. (2023). Mitigation of urban waterlogging from flash floods hazards in vulnerable watersheds. *J. Hydrology Regional Stud.* 47, 101429. doi:10.1016/j.ejrh.2023.101429

Beecham, S., and Chowdhury, R. (2010). Temporal characteristics and variability of point rainfall: a statistical and wavelet analysis. *Int. J. Climatol. A J. R. Meteorological Soc.* 30, 458–473. doi:10.1002/joc.1901

Bonsal, B., Zhang, X., Vincent, L., and Hogg, W. (2001). Characteristics of daily and extreme temperatures over Canada. *J. Clim.* 14, 1959–1976. doi:10.1175/1520-0442(2001)014<1959:codaet>2.0.co;2

Booth, E. L., Byrne, J. M., and Johnson, D. L. (2012). Climatic changes in western North America, 1950–2005. *Int. J. Climatol.* 32, 2283–2300. doi:10.1002/joc.3401

Cardoso Pereira, S., Marta-Almeida, M., Carvalho, A. C., and Rocha, A. (2020). Extreme precipitation events under climate change in the Iberian Peninsula. *Int. J. Climatol.* 40, 1255–1278. doi:10.1002/joc.6269

Chaubey, P. K., Mall, R., Jaiswal, R., and Payra, S. (2022). Spatio-temporal changes in extreme rainfall events over different Indian river basins. *Earth Space Sci.* 9, e2021EA001930. doi:10.1029/2021ea001930

Gimeno, L., Vázquez, M., Eiras-Barca, J., Sorí, R., Stojanovic, M., Algarra, I., et al. (2020). Recent progress on the sources of continental precipitation as revealed by moisture transport analysis. *Earth-Science Rev.* 201, 103070. doi:10.1016/j.earscirev.2019.103070

Gvoždíková, B., Müller, M., and Kašpar, M. (2019). Spatial patterns and time distribution of central European extreme precipitation events between 1961 and 2013. *Int. J. Climatol.* 39 (7), 3282–3297. doi:10.1002/joc.6019

Huang, M., Peng, G., Leslie, L. M., Shao, X., and Sha, W. (2005). Seasonal and regional temperature changes in China over the 50 year period 1951–2000. *Meteorology Atmos. Phys.* 89, 105–115. doi:10.1007/s00703-005-0124-0

Indices, E. P. (2019). Analysis of the extreme rainfall events over upper catchment of sabarmati River Basin in western India using. *Adv. Water Resour. Eng. Manag. Sel. Proc. TRACE* 39, 2018.

Jacox, M. G., Alexander, M. A., Siedlecki, S., Chen, K., Kwon, Y.-O., Brodie, S., et al. (2020). Seasonal-to-interannual prediction of North American coastal marine ecosystems: forecast methods, mechanisms of predictability, and priority developments. *Prog. Oceanogr.* 183, 102307. doi:10.1016/j.pocean.2020.102307

Li, S., Chen, Y., Wei, W., Fang, G., and Duan, W. (2024). The increase in extreme precipitation and its proportion over global land. *J. Hydrology* 628, 130456. doi:10.1016/j.jhydrol.2023.130456

Li, W. B., Li, C. Y., Liu, Z. J., et al. (2015). Distribution of precipitation and its effect factors analysis in the central and western regions of Inner Mongolia during the last 60 years. *J. Inn. Mong. Agric. Univ.(Nat. Sci. Ed.)* 36, 84–94.

Li, X. H., Chen, Z. F., and Wang, L. (2020). Analysis of the spatiotemporal variation characteristics of main extreme climate indices in Sichuan Province of China from 1968 to 2017. *Appl. Ecol. Environ. Res.* 18 (2), 3211–3242. doi:10.15666/aeer/1802_32113242

Mashao, F. M., Mothapo, M. C., Munyai, R. B., Letsoalo, J. M., Mbokodo, I. L., Muofhe, T. P., et al. (2023). Extreme rainfall and flood risk prediction over the East Coast of South Africa. *Water* 15, 50. doi:10.3390/w15010050

Peng, D., Zhou, T., and Zhang, L. (2020). Moisture sources associated with precipitation during dry and wet seasons over Central Asia. *J. Clim.* 33, 10755–10771. doi:10.1175/jcli-d-20-0029.1

Rathinasamy, M., Agarwal, A., Sivakumar, B., Marwan, N., and Kurths, J. (2019). Wavelet analysis of precipitation extremes over India and teleconnections to climate indices. *Stoch. Environ. Res. Risk Assess.* 33, 2053–2069. doi:10.1007/s00477-019-01738-3

Sa'adi, Z., Shahid, S., Ismail, T., Chung, E.-S., and Wang, X.-J. (2019). Trends analysis of rainfall and rainfall extremes in Sarawak, Malaysia using modified Mann–Kendall test. *Meteorology Atmos. Phys.* 131, 263–277. doi:10.1007/s00703-017-0564-3

Tradowsky, J. S., Philip, S. Y., Kreienkamp, F., Kew, S. F., Lorenz, P., Arrighi, J., et al. (2023). Attribution of the heavy rainfall events leading to severe flooding in Western Europe during July 2021. *Clim. Change* 176, 90. doi:10.1007/s10584-023-03502-7

Wang, J., Zhuo, L., Han, D., Liu, Y., and Rico-Ramirez, M. A. (2023). Hydrological model adaptability to rainfall inputs of varied quality. *Water Resour. Res.* 59, e2022WR032484. doi:10.1029/2022wr032484

Wang, Q. S., Teng, J. W., Wang, G. J., and Xu, Y. (2005). The region gravity and magnetic anomaly fields and the deep structure in Yinshan mountains of Inner Mongolia. *Chin. J. Geophys.* 48, 348–355. doi:10.1002/cjg2.660

Wu, S., Hu, Z., Wang, Z., Cao, S., Yang, Y., Qu, X., et al. (2021). Spatiotemporal variations in extreme precipitation on the middle and lower reaches of the Yangtze River Basin (1970–2018). *Quat. Int.* 592, 80–96. doi:10.1016/j.quaint.2021.04.010

Xu, L., Zheng, C., and Ma, Y. (2021). Variations in precipitation extremes in the arid and semi-arid regions of China. *Int. J. Climatol.* 41, 1542–1554. doi:10.1002/joc.6884

Yang, H., Xu, G., Mao, H., and Wang, Y. (2020). Spatiotemporal variation in precipitation and water vapor transport over Central Asia in winter and summer under global warming. *Front. Earth Sci.* 8, 297. doi:10.3389/feart.2020.00297

Yang, Y., Liu, H., Tao, W., and Shan, Y. (2024). Spatiotemporal variation characteristics and driving force analysis of precipitation use efficiency at the north foot of Yinshan Mountain. *Water* 16, 99. doi:10.3390/w16010099

Zhao, Y., Zhu, D., Wu, Z., and Cao, Z. (2024). Extreme rainfall erosivity: research advances and future perspectives. *Sci. Total Environ.* 917, 170425. doi:10.1016/j.scitotenv.2024.170425

Zia, A., Rana, I. A., Arshad, H. S. H., Khalid, Z., and Nawaz, A. (2023). Monsoon flood risks in urban areas of Pakistan: a way forward for risk reduction and adaptation planning. *J. Environ. Manag.* 336, 117652. doi:10.1016/j.jenvman.2023.117652

frontiers | Frontiers in Environmental Science

TYPE Original Research
PUBLISHED 15 May 2024
DOI 10.3389/fenvs.2024.1406546

OPEN ACCESS

EDITED BY
Zhiming Han,
Northwest A&F University, China

REVIEWED BY
Baoli Fan,
Northwest Normal University, China
Ping Wang,
Beijing Forestry University, China

*CORRESPONDENCE
Benli Liu,
liubenli@lzb.ac.cn

RECEIVED 25 March 2024
ACCEPTED 30 April 2024
PUBLISHED 15 May 2024

CITATION
Wang Y, Liu B, Xing Y, Peng H, Wu H and Zhong J (2024), Ecological construction status of photovoltaic power plants in China's deserts. *Front. Environ. Sci.* 12:1406546. doi: 10.3389/fenvs.2024.1406546

Ecological construction status of photovoltaic power plants in China's deserts

Yimeng Wang[1,2], Benli Liu[1,3]*, Yu Xing[1,2], Huaiwu Peng[4], Hui Wu[4] and Jianping Zhong[4]

[1]Key Laboratory of Ecological Safety and Sustainable Development in Arid Lands Research Station of Gobi Desert Ecology and Environment in Dunhuang of Gansu Province, Northwest Institute of Eco-environment and Resources, Chinese Academy of Sciences, Lanzhou, China, [2]University of Chinese Academy of Sciences, Beijing, China, [3]Academy of Plateau Science and Sustainability, Qinghai Normal University, Xining, China, [4]Northwest Engineering Corporation Limited, Xian, China

Solar photovoltaic (PV) is one of the most environmental-friendly and promising resources for achieving carbon peak and neutrality targets. Despite their ecological fragility, China's vast desert regions have become the most promising areas for PV plant development due to their extensive land area and relatively low utilization value. Artificial ecological measures in the PV plants can reduce the environmental damage caused by the construction activity and promote the ecological condition of fragile desert ecosystems, therefore yield both ecological and economic benefits. However, the understanding of the current status and ecological benefits of this approach in existing desert PV plants is limited. Here we surveyed 40 PV plants in northern China's deserts to identify the ecological construction modes and their influencing factors. We quantified the ecosystem service value (ESV) provided by these PV plants using remote sensing data and estimated the potential for ESV enhancement. Our results show that PV plant construction in desert regions can significantly improve the ecosystem, even with natural restoration measures (M1) alone, resulting in a 74% increase in average fractional vegetation cover (FVC) during the growing season, although the maximum average FVC of only about 10%. The integrated mode M4, which combined artificial vegetation planting M2 and sand control measures M3, further enhance the average growing season FVC to 14.53%. Currently, 22.5% of plants lack ecological measures, 40% employ only a single measure, but 92% of new plants since 2017 have adopted at least one ecological construction mode. The main influencing factors include surface type, policy support, water resources, ecological construction costs, and scientific management guidance. If artificial ecological construction were incorporated, a significant ESV could be achieved in these PV plants, reaching $8.9 million (a 7.7-fold increase) if assuming a targeted 50% vegetation coverage. This study provides evidence for evaluating the ecological benefit and planning of large-scale PV farms in deserts.

KEYWORDS

photovoltaic plants, desert ecosystem, ecological construction, ecosystem services value, economic benefits

1 Introduction

Due to factors such as the growing global energy demand, the non-renewable energy crisis, and climate change, etc., there is an international consensus to promote the utilization of renewable energy and develop a low-carbon society (Riahi et al., 2012; Hertwich et al., 2015). As one of the most important renewable resources, solar energy possesses the qualities of clean environmental protection-friendly and inexhaustibility (Mekhilef et al., 2011; Hernandez et al., 2015). Currently, photovoltaic (PV) power generation is the predominant method of solar energy utilization (Yan et al., 2007). In the past 5 years, the global PV installed capacity had nearly tripled, increasing from 402.5 GW in 2017 to 1185 GW in 2022 (IEA Photovoltaic Power Systems Programme, 2018; IEA Photovoltaic Power Systems Programme, 2023). China added 106 GW of new installations in the year of 2022 alone, accounting for 44% of the world's new installed capacity, with a total installed capacity of 414.5 GW, solidifying its position as the largest contribution to the PV market for eighth consecutive year (IEA Photovoltaic Power Systems Programme, 2023).

China has a vast area of deserts (including gravel deserts, sandy deserts, desert steppes, and alpine deserts), mainly distributed in northern and northwest parts of the country, and the Qinghai-Tibet Plateau, which accounts for 27.2% of China's total land area (National Forestry and Grassland Administration, 2015). More than 60% of China's PV resources and development capabilities are concentrated in the deserts (Xinhua News Agency, 2021), together with the flat terrain, low population density, and limited land expenditure costs, which making the deserts ideal for the growth of large-scale PV farms (Xiao et al., 2011; Wu et al., 2014; Tanner et al., 2020). Besides, the construction of PV farms in deserts can improve the utilization rate of degraded land and enable the spatial coexistence of PV with other industries, such as farming and livestock raising (Yan et al., 2007; Marco et al., 2014). The National Development and Reform Commission and the Energy Bureau issued a notice titled *"Planning and Layout Scheme for Large-scale Wind and Solar Power Bases with a Focus on Desert"* in 2022, which plans the construction of large-scale wind and PV farms focusing on desert in northwest China, with a total capacity of 455 GW by 2030 (People's Daily Overseas Edition, 2023), of which 284 GW are in Kubuqi, Ulanbh, Tengger and Badain Jaran deserts (China Securries Journal, 2022). By the end of 2022, the cumulative grid-connected capacity of PV plants in the desert regions such as Gansu, Qinghai, Xinjiang, Ningxia, Inner Mongolia, Shaanxi, and Tibet has reached 96.19 GW, accounting for 24.54% in China's total cumulative grid-connected capacity and still holding great development potential (National Energy Administration, 2023).

The land surface and the overall ecological environment are fragile in deserts, which can be easily affected or aggravated by irresponsible human activities (Wu et al., 2014; Borrelli et al., 2020). As the quantity and scale of PV installations continue to grow, so does the scrutiny regarding their impact on the local ecological environment. Some studies indicate that the construction of large-scale PV farms will disturb the land surface, destroy surface vegetation and soil crusts, and cause severe wind erosion, posing a significant threat to the normal operation of PV plants and the local ecological environment (Grodsky and Hernandez, 2020; Scarrow, 2020). However, the construction of PV plants in deserts can usually facilitate plant growth. After installation, the PV arrays can increase surface roughness, reduce the surface wind speed, and decrease wind-driven sand and dust (Wu et al., 2014; Chang et al., 2016). Simultaneously, a large area of PV panels can effectively reduce direct solar radiation and surface water evaporation, thereby promoting vegetation growth and aiding in the restoration of damaged ecosystems (Wu et al., 2014; Liu et al., 2020; Xia et al., 2022b). Nevertheless, these positive factors are hard to yield significant effects if relying solely on natural process, and artificial vegetation is often required to accelerate the ecosystem improvement process (Marrou et al., 2013; Li Y. et al., 2018; Liu et al., 2020). In desert, a composite system of PV plus agriculture and animal husbandry is possible to construct by manually installing sand fences and sand barriers, tying grass grids to the surface, and sowing and breeding in PV farm (Semeraro et al., 2022). Current research mainly focuses on the use of remote sensing data to study the changes in vegetation cover before and after the construction of PV power plants (Marrou et al., 2013; Li Y. et al., 2018; Xia et al., 2022a; Xia et al., 2022b; Semeraro et al., 2022), or in-depth studies of the ecological impacts and values of PV power plants on a small scale (Li Y. et al., 2018; Luo et al., 2023). However, no regional-scale field research on the ecological construction condition of PV power plants in desert areas has been conducted so far, and there is a lack of comprehensive understanding and assessment of their existing status.

In light of the fact that many large-scale PV farms have already been constructed in the vast China's deserts, it is of great importance to understand the existing wind-sand prevention measures and ecological construction status of desert PV plants, as well as the environmental improvement and ecological service value (ESV) enhancement benefits that brought by ecological construction activities, which are essential for preventing and eliminating any negative impact of power plants construction on the environment and guiding ecological construction activities. This paper aims to: 1) assess the ecological environment status of PV plants in China's deserts through field survey and investigate the wind-sand control measures, ecological construction, and vegetation growth conditions and 2) estimate the ESV and potential ecological service function that can be brought by the ecological construction measures in the large-scale PV plants in deserts.

2 Material and methods

2.1 Study area

The study area is located in the Badain Jaran Desert, Tengger Desert and surrounding areas in northwest China (98°79′E–105°95′E, 37°05′N-42°20′N), which includes the western portion of Inner Mongolia Autonomous Region, northern Gansu and western Ningxia provinces (Figure 1A). With an area of 52,162 km^2, the Badain Jaran Desert is the second largest desert in China (Zhu et al., 2010). The Tengger Desert is the fourth largest desert in China with an area of 42,700 km^2 (Wu et al., 1980). This region has abundant solar energy resources and is home to the greatest concentration of grid-connected solar power farms in China (Xia et al., 2022a). The sunshine duration is between 2661 and 3406 h,

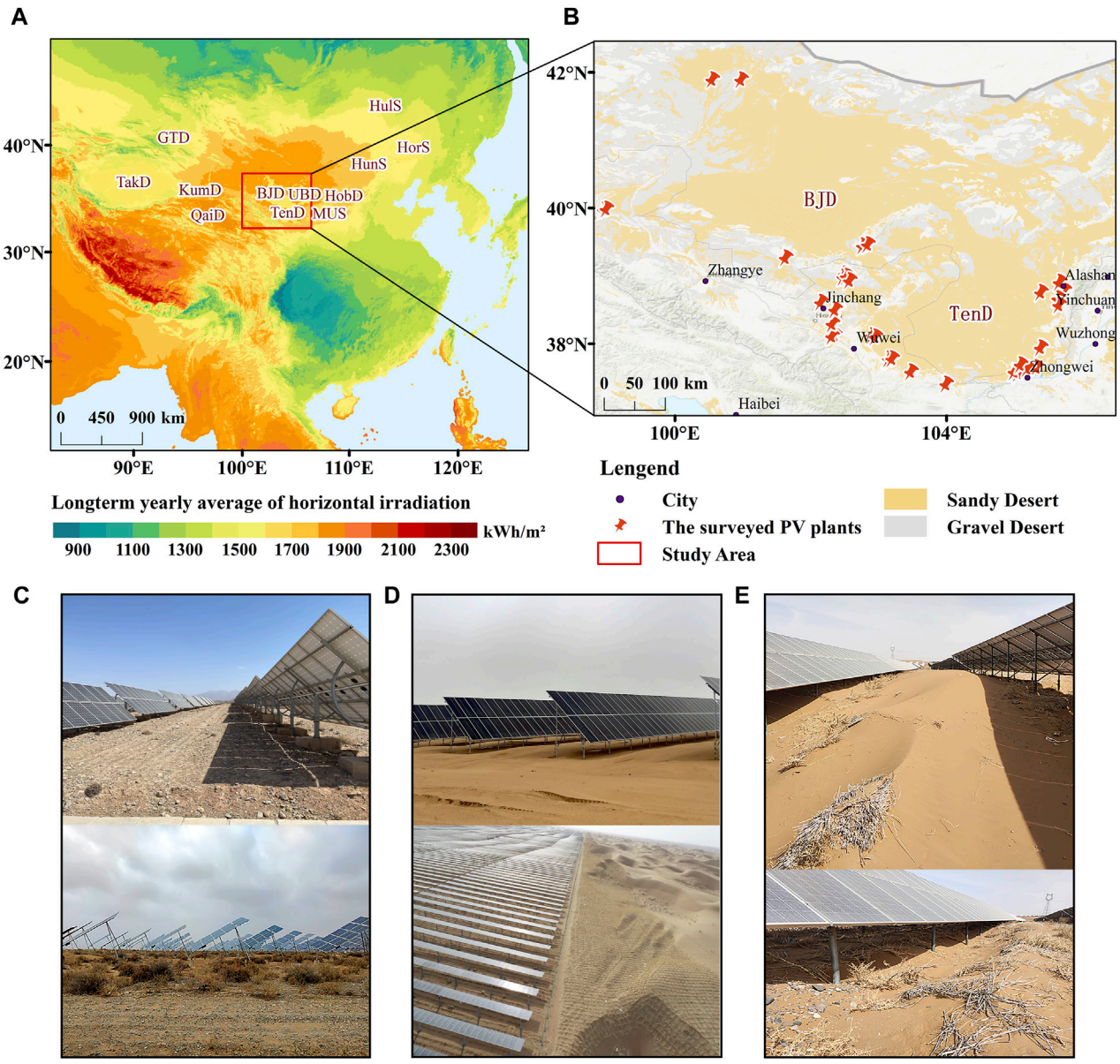

FIGURE 1
Map of the distribution of solar horizontal irradiance and large deserts in China [Data from The World Bank (Solar Energy Industries Association SEIA, 2022)]. Location of the Badain Jaran Desert and Tengger Desert **(A)**, locations of the surveyed PV plants **(B)**, gravel surface **(C)**, sandy surface in PV plants **(D)** and PV plants subject to sand accumulation and wind erosion problems **(E)**.

and the average annual solar radiation reaches 1550–1819 kWh/(m^2·a) (Figure 1A), which is higher than the lower limit of 1400 kWh/(m^2·a) for the economic development feasibility of solar projects (Guo and Wang, 2014). The altitude of this region is between 800 and 1500 m, with an area of about 33.69 × 10^4 km^2. This region has a temperate continental arid climate with scarce water resources, high evaporation (about 1000 mm), an average annual temperature of 7.2°C, and average annual precipitation of 50–150 mm which concentrates in the plant growing season (from May to September). The natural landscape here is dominated by dunes, gravel desert, and desert grasslands. The natural vegetation is relatively sparse, mostly shrubs and semi-shrubs including *Artemisia desertorum, Agriophyllum squarrosum, Allium mongolicum, Haloxylon ammodendron, Tamarix ramosissima, Halogeton arachnoideus, Peganum harmala, Neotrinia splendens, Calligonum mongolicum, Ephedra przewalskii*, etc (Sun, 2018).

The used data in this paper come from a field investigation of 40 PV plants and remote sensing data in the study area. We used face-to-face questionnaire interviews with the operators of each plant. Figure 1B displays all the surveyed sites, including 23 gravel desert PV plants (Figure 1C) and 17 sandy desert ones (Figure 1D). The survey contents include basic information about PV plants, wind-sand disaster situations, wind-breaking and sand-fixing measures and their implementation areas, the types and growth conditions of natural vegetation, ecological construction measures and artificial planting vegetation types, the cleaning and maintenance cycle of PV panels, and so on (View the Supplementary Table A1 for the details of

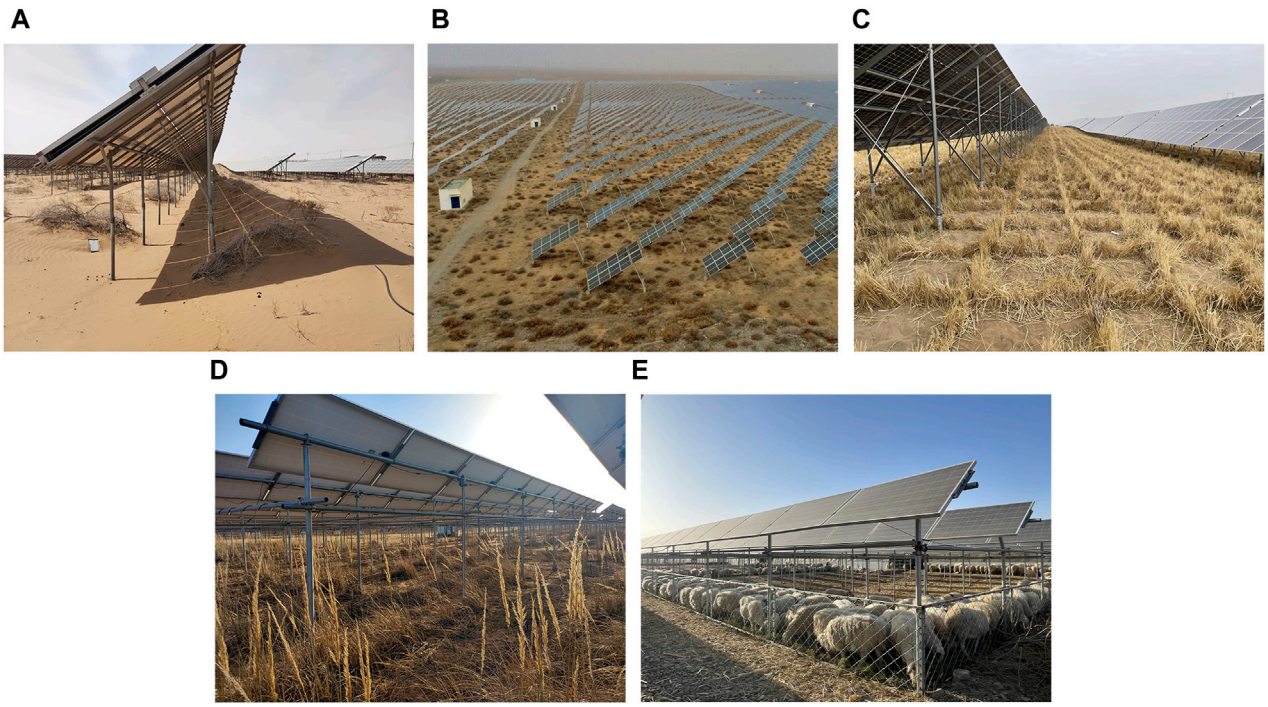

FIGURE 2
Different ecological construction modes status in PV plants. PV plants adopting modes of M1 (No measures) **(A)**, M2 (Artificial planting) **(B)**, M3 (Sand-prevention measures) **(C)**, M4 (Sand-prevention measures + Artificial planting) **(D)**, and M5 (Sand-prevention measures + Artificial planting) **(E)**.

questionnaire's contents). According to the survey, the wind and sand control and ecological construction of PV plants in desert can be classified into five modes: no measures (M1), artificial planting (M2), sand-prevention measures (M3), sand-prevention measures + artificial planting (M4), and sand-prevention measures + farming or animal husbandry (M5). The five modes are categorized for discussion according to the land surface type and policy impact. Additional information of each plant is provided in the Supplementary Table A2.

2.2 Ecological construction modes of PV plants

2.2.1 No measures (M1)

This mode (Figure 2A) refers to the natural restoration of ecosystems in PV plants without human intervention. This is because PV panels and their supports can reduce soil evaporation, block wind and sand, and decrease surface wind speed, thereby facilitating plant growth (Lu, 2013). In this mode, natural vegetation growth relies on precipitation and water from PV panel cleaning at no additional cost. However, this mode has the problems of relatively long vegetation restoration period and limited application areas (only in regions with relatively high rainfall and stable ground surface) (Cui et al., 2017).

2.2.2 Artificial planting (M2)

This mode involves artificial planting of native shrubs or herbs, such as *Haloxylon ammodendron, Hippophae rhamnoides,* inside and around the perimeter of the PV plants. Additionally, low drought-tolerant windbreak and sand-fixing plants like *Agriophyllum squarrosum, Medicago sativa*, and *Calligonum mongolicum*, etc., can be planted beneath the PV equipment to serve as barrier against wind and blown sand (Cui et al., 2017; Mai and Bai, 2023) (Figure 2B). This mode is frequently visited in the PV plants at gravel desert. The gravel desert is flat, and the surface is predominantly covered with gravel of varying sizes. The strong winds allow the blown sand to travel through the PV equipment area rapidly. In these plants, accumulation, erosion, and other wind-related hazards are not severe, and sand control and fixing measures are not indispensable.

2.2.3 Sand-prevention measures (M3)

The M3 mode refers to the implementation of wind and sand control measures, including artificial sand fences, sand barriers with straw, high density polyethylene (HDPE) or clay, gravel coverage, and the establishment of grass grids that beneath, between, and around PV equipment to prevent wind and sand disasters (Lu, 2013; Cui et al., 2017; Shen et al., 2021; Mai and Bai, 2023). Artificial sand-prevention measures can increase the roughness of surface, reduce the wind speed, weaken the mobility of sand, and create more favorable conditions for the growth of natural plants, together with the improving of local climatic conditions by PV systems, so that it can also contribute to promoting plant growth (Cui et al., 2017; Shen et al., 2021; Yue et al., 2021; Mai and Bai, 2023). The lifespan of straw barrier is typically around 3 years. They offer effective sand control with relatively low costs, making them the preferred sand control method for PV plants (Figure 2C). Gravel coverage is also a common measure that mimics gravel desert surfaces, protects sand-fixing plants from wind erosion and burial while improving soil moisture conditions, which are beneficial for plant survival and growth. Nevertheless, due to the higher cost involved, gravel coverage is employed only selectively in

the plants, typically applied to maintenance roads, the first several rows of PV panels at the boundary of the plants, and the vicinity of equipment foundations in order to effectively reduce surface wind erosion and dust generation from maintenance vehicles.

2.2.4 Sand-prevention measures + artificial planting (M4)

This mode combines the M2 and M3 modes and can effectively prevent the severe wind erosion disasters as well as improve vegetation survival rates in desert PV plants. The application of this integrated mode can accelerate the formation of organic crust on desert surfaces and gradually establish a stable green protective system, thereby promoting a virtuous cycle of the ecological environment in PV plants (Cui et al., 2017) (Figure 2D).

2.2.5 Sand-prevention measures + farming or animal husbandry (M5)

This integrated ecological construction mode combines sand-prevention and artificial planting measures with agricultural or livestock industries by means such as "power generation on the board, planting between the boards, and raising sheep under the boards (Xiao et al., 2021) (Figure 2E)." This mode can create more job opportunities, provide convenience for local farmers and herders, and generate economic, social, and ecological benefits (Xiao et al., 2021; Jing et al., 2022). In this mode, the PV modules must be raised from about 50 cm to more than 150 cm above the ground, while grass grids and drip irrigation pipelines are installed beneath the PV panels to cultivate forage grass and cash crops (Zhao and Zhong, 2022). This mode requires cooperation with neighboring herders to enable livestock access to the PV equipment area for foraging or to regularly harvest the grass under the panels for feeding livestock in the breeding area. This approach not only addresses the issue of excessive grass height in the PV equipment area, which leads to shading and reduced conversion efficiency of the modules, but also reduces the risk of fire in the PV plants (Hernandez et al., 2014; Vaverková et al., 2022).

2.3 Estimation of ecosystem service value

Costanza et al. (1997) proposed the ESV evaluation method and assessed the value of ecosystem services on a global scale. The method has been widely used for assessing the value of world ecosystem services and natural capital. Xie et al. (2001) further divided China's grasslands into 18 ecosystem types and corrected the unit service function values using a biomass index, and the results has been referred and adopted by a group of following studies. Wang and Qin (2007) further improved this method from a remote sensing perspective, incorporating vegetation coverage data to better suit the specific context of China's ecosystems. In the present study, the predominant land type found in the investigated PV plants belong to temperate desert ecosystem. We calculates the ESV per unit area of temperate desert in 2022 using the values proposed by Xie et al. (2001) for the year 2000 as the baseline data.

As economic indicators fluctuate over time, the ESV needs to be adjusted to the 2022 level. This adjustment is performed by Eqs 1, 2 as follows Costanza et al. (2014):

$$\mathrm{ESV}(2022) = \mathrm{ICR} \times \mathrm{ESV}(2000) + \mathrm{ESV}(2000) \tag{1}$$

$$\mathrm{ICR} = \frac{\mathrm{CPI}(2022) - \mathrm{CPI}(2000)}{\mathrm{CPI}(2000)} \times 100\% \tag{2}$$

in which ESV (2022) and ESV (2000) represent the ESV per unit area of temperate desert grassland ecosystems in 2022 and 2000 ($ yr^{-1} ha^{-1}). ICR is the inflation conversion rate, while CPI (2022) and CPI (2000) are the US consumer price index in 2022 and 2000. The ESV (2000) per unit area of temperate desert was 67.9 $ yr^{-1} ha^{-1} (Xie et al., 2001). The CPI (2000) and CPI (2022) are derived from U.S. Bureau of Labor Statistics data (U.S. Bureau of Labor Statistics, 2023). The U.S. CPI was used to calculate the inflation conversion rate to ensure comparability across different time periods, as the original ESV data from Xie et al. (2001) was estimated in U.S. dollars as well as the majority of following studies (Costanza et al., 2014; Liu et al., 2020).

The ESV of the PV plants area, which fluctuates over time and is proportional to the temperate desert ecosystem's type, area, and quality, was estimated by adapting the method proposed by Costanza et al. (1997) of multiplying each biome's land area by its unit value. Inspired by Liu et al. (2020), who used biomass proportion as an ecological parameter, we modified the biomass parameter with the more readily available vegetation coverage data to calculate the existing ESV and estimated the potential for its increase in the PV plants area. The calculation formulas Eqs (3, 4) are as follows:

$$ESV_i(N) = \mathrm{ESV}(2022) \times S_i \tag{3}$$

$$ESV_i(P) = \frac{FVC_P}{FVC_i(N)} \times \mathrm{ESV}(2022) \times S_i \tag{4}$$

where $ESV_i(N)$ ($ yr^{-1}) represents the existing ESV of the ith PV plant. $ESV_i(P)$ ($ yr^{-1}) indicates the value of ecosystem services that can be improved when ith PV plant takes ecological construction and reaches the threshold of vegetation coverage improvement. S_i is the area (ha) of ith PV plant, and $FVC_i(N)$ is the existing growing season vegetation coverage of the ith PV plant. FVC_p is the threshold of vegetation coverage. $i = 1, 2, 3... 40$, which represents the 40 investigated PV plants.

Existing total value of ecological services ($\mathrm{ESV_N}$) and total value of ecological services improvement potential ($\mathrm{ESV_P}$) of the 40 investigated PV plants are calculated by summing up the corresponding value of every plant as Eqs 5, 6:

$$\mathrm{ESV_N} = \sum_{i=1}^{n} ESV_i(N) \tag{5}$$

$$\mathrm{ESV_P} = \sum_{i=1}^{n} ESV_i(P) \tag{6}$$

In addition, we calculated the 95% confidence intervals for the mean fractional vegetation cover ($FVC_i(N)$) at each surveyed PV power plant to quantify the margin of error in the derived potential ecological service values.

2.4 Other data sources

Normalized difference vegetation index data are acquired by the National Tibetan Plateau Scientific Data Center from the Aqua/Terra-MODIS satellite sensor MOD13Q1 product and land use data with a

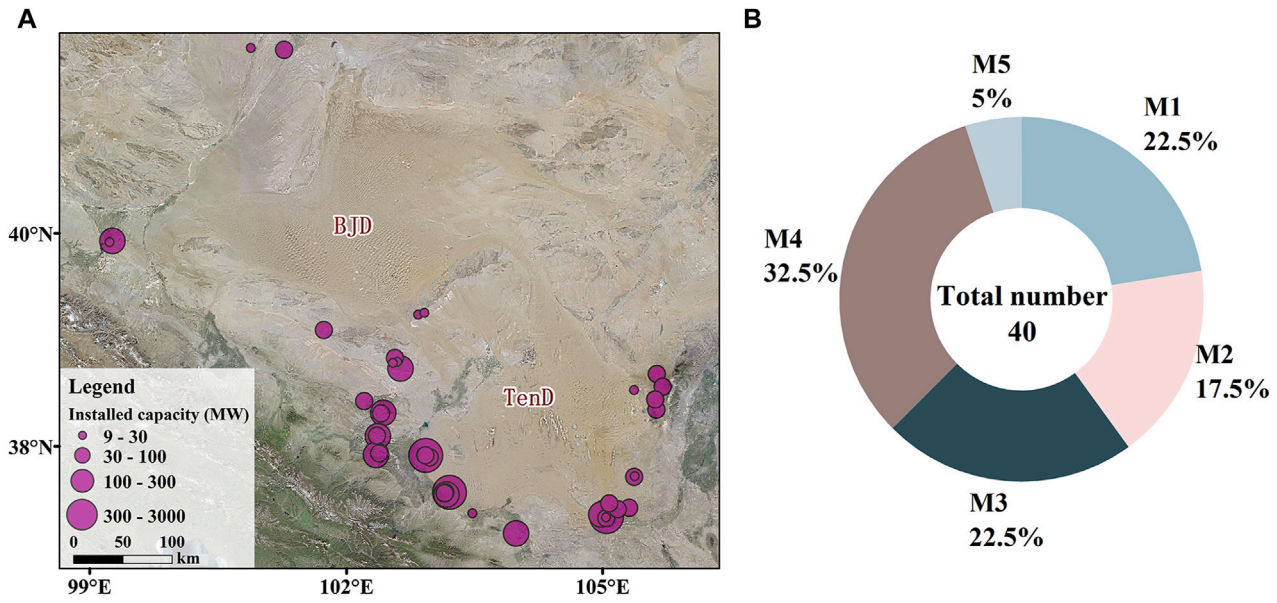

FIGURE 3
Spatial distribution map of installed capacity of PV plants (Satellite data from 2022 The ArcGIS Satellite) **(A)**, pie chart of the proportions of five ecological construction modes in PV plants **(B)**.

250 m spatial resolution (Gao et al., 2023a). The FVC data at growing season are based on the vegetation index data set and calculated using the normalized difference vegetation index pixel dichotomy model, also with a 250 m spatial resolution (Gao et al., 2023b). The potential vegetation coverage used as the threshold value in Eq. 4 is set to 50%, because this value in a desert is sufficient to achieve sufficient windbreak and sand fixation benefits (Zhao, 2016).

3 Results

3.1 The current status of ecological construction in desert PV plants

3.1.1 Statistics of surveyed PV plants

We summarized the conditions of the surveyed PV plants based on five ecological construction modes as classified in Section 2.2. The total area of the plants is 112.85 km^2, and the total installed capacity is 7029.97 MW. The large-scale PV plants (≥30 MW) are mainly distributed in the southeast and southwest parts of the Tengger Desert and the western part of the Badain Jaran Desert, while the middle and small scale plants (<30 MW) are mostly distributed in the desert margins and external areas (Figure 3A).

3.1.2 Statistics of ecological construction modes of the PV plants

The proportion of PV plants adopting each of the five ecological construction modes is shown in Figure 3B. It can be seen that the number of PV plants adopting the M4 is the largest of thirteen, followed by M1 and M3 with nine each. There are seven PV plants taking M2, accounting for 17.5%. The plants adopt the combination of sand-prevention measures and farming or animal husbandry (M5) have the least number of only two.

Although a large number of PV plants take the M4 mode, there are still 22.5% of PV plants that have not taken any measures, 40% of PV plants without sand-prevention measures, and 45% of PV plants that have not taken any artificial vegetation measures. In PV plants that adopt M1, there are serious wind and sand hazards (inter-panel sand accumulation and under-panel scouring), and sparse natural vegetation (Figure 1E). In the PV plants with M3, the wind-sand disaster is substantially controlled, the surface beneath and surrounding the PV panels is usually free of sand, and the vegetation density in the areas with sand control measures is significantly higher than the areas without measures. The M4 and M5 plants have the best treatment effects. There is no obvious sand damage in these plants, the vegetation is rich in variety and grows vigorously, and the average cleaning cycle of PV panels is reduced by 3–5 times per year on average.

3.1.3 Differences in ecological construction mode of PV plants over desert surface types

Figure 4A shows that the PV plants with M1 and M2 are primarily distributed on gravel desert, the ones with M3 and M4 mainly on sandy desert, and the number of PV plants with M5 is equally distributed on two kinds of deserts. From the perspective of the area (Figure 4B), installed capacity (Figure 4C), and power generation (Figure 4D) of the investigated PV plants, the proportion of plants adopting M4 is the largest in the sandy desert, which is 83.88%, 89.93% and 90.88%, respectively. The proportion of plants adopting M2 in the gravel desert is the largest, which is 56.40%, 54.54% and 57.74%, respectively. The PV plants in the sandy desert have a higher proportion of taking ecological construction than that of the gravel desert. This is due to the fact that wind and sand disasters on gravel desert are less severe, allowing for simpler measures, while sandy desert requires more ecological measures.

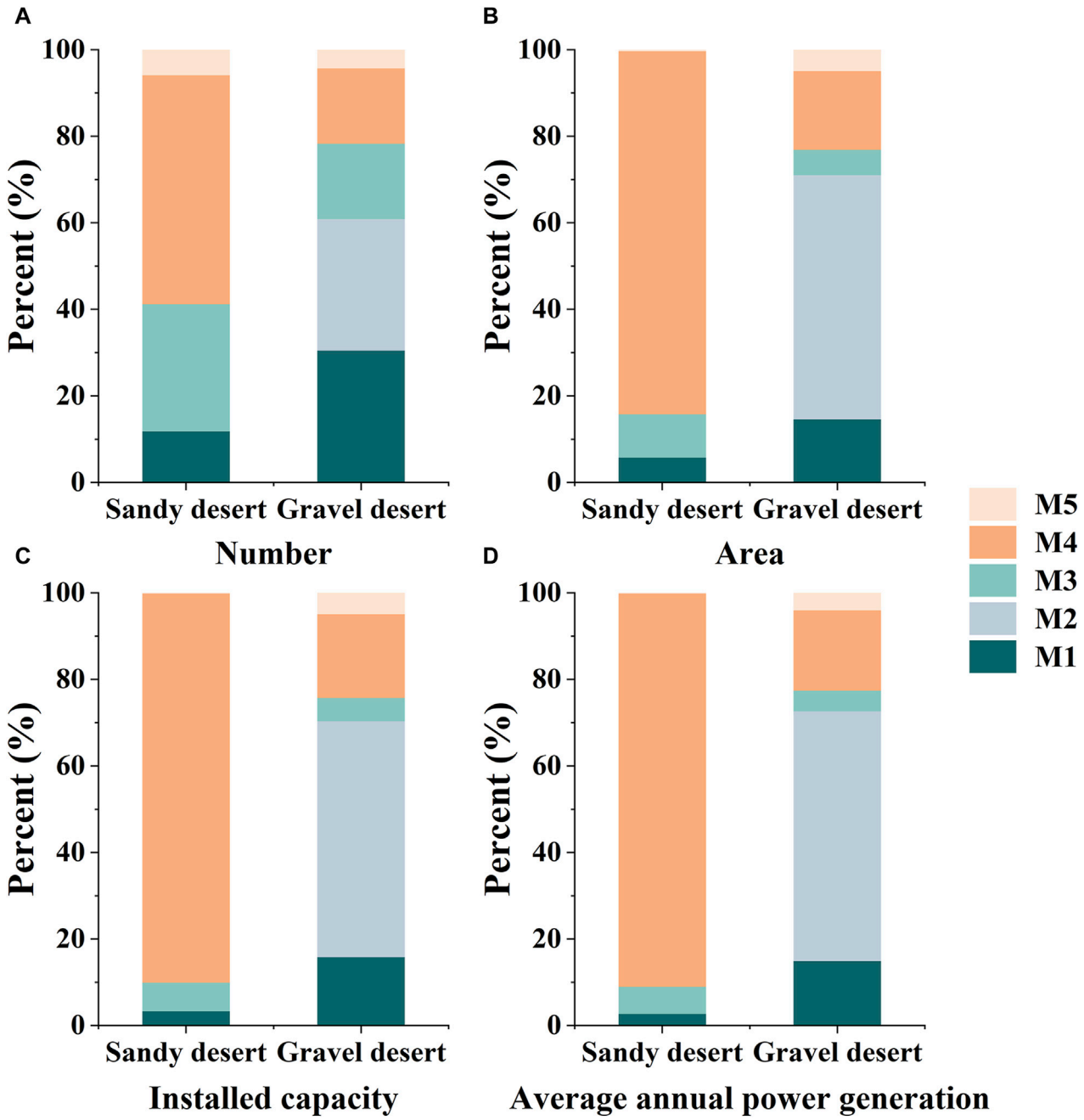

FIGURE 4
The ratios of number **(A)**, area **(B)**, installed capacity **(C)**, and annual average power generation **(D)** of the investigated PV plants with five modes over sandy deserts and gravel deserts.

3.1.4 Changes in ecological construction mode of PV plants over time

The distribution of the number and scale of PV plants over time is shown in Figure 5A. All the surveyed PV plants were constructed between 2011 and 2022. Since 2011, both the construction number and total installed capacity of PV plants declined until 2017, when the construction number rebounded with an average installed capacity of 556 MW per plant. Compared to the situation before 2017, the average installed capacity of PV plants has increased by 7.9 times, indicating a recent emphasis on the development of large-scale PV farms in desert regions.

Figures 5B–E displays the change of each ecological construction mode adopted by PV plants over time. For the PV plants that built before 2017, the number of M1 is the largest, accounting for 29.6%. Among the PV plants built after 2017, M4 has the largest proportion (50%). From the perspective of the plant number, the proportion of M1 and M2 in the newly built PV plants after 2017 has both decreased by 21.3% and 1.9%, respectively, while the proportion of M3 and M4 has increased by 2.8% and 24.1%, respectively (Figure 5B). From the perspective of construction area (Figure 5C), installed capacity (Figure 5D), and annual average

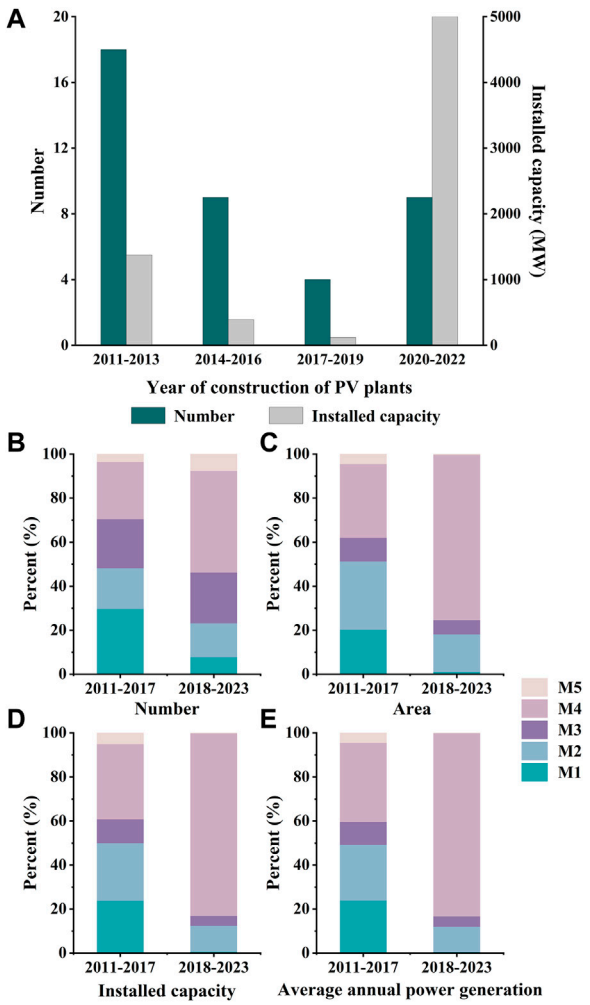

FIGURE 5
Distribution of the number and installed capacity of investigated PV plants by construction time **(A)**, percentage of number **(B)**, area **(C)**, installed capacity **(D)**, and average annual power generation **(E)** of the five ecological construction modes before and after 2017.

power generation (Figure 5E) of PV plants, the proportion of plants adopting M4 after 2017 increased to 75.1%, 83.0% and 83.3% from 41.7%, 49.0% and 47.3% before 2017, respectively. We observed a significant change in the ecological construction mode adopted by PV plants around 2017, and we will discuss the reasons in the following sections.

3.2 Analysis of ESV changes in PV plants investigated under different modes

The statistical analysis of the growing season vegetation coverage in the surveyed PV power plants under different ecological construction modes (Table 1) reveals a significant enhancement in vegetation. As the ESV is linearly related to the FVC, the improvement in ESV can be represented by the changes of FVC. In the M1 mode plants that rely solely on the natural restoration of vegetation after the construction, the average FVC at growing season increase from initially 5.92%–10.31% by 2022, resulting in an increase of 74% of the ESV. The M2 mode plants experienced a 5.73% increase in FVC, with the ESV being enhanced by 102%. The M3 mode and M5 mode had relatively lower ESV enhancements of 16% and 12%, despite their higher initial FVC. It is worth noting that the M5 mode plants that incorporate grazing activities within the site still exhibited overall increasing trend in vegetation coverage, despite being significantly influenced by human activities. However, due to the limited sample size of only two PV power plants in the M5 mode, further validation of this result is required. The M4 mode achieved the highest average growing season FVC among the five modes, reaching 14.53%, with the ESV being enhanced by 58%.

These findings demonstrate that PV plants can facilitate vegetation restoration and enhance ecological service functions, with a 74% increase in the average growing season FVC of the nine PV plants adopting the M1 mode. However, ecological improvement activities, such as sand control measures and artificial vegetation planting, can significantly increase the upper limit of FVC in desert regions from 10.31% (M1) to 14.53% (M4). The M4 mode is the most effective in improving FVC and ESV, followed by the M2 mode. Notably, the M5 mode not only facilitates ecological restoration but also provides additional economic benefits to local residents, suggesting considerable development potential for a sustainable future that balances environmental conservation with socio-economic growth.

3.3 Estimation of ESV potential of PV plants

The PV plants that carry out ecological construction can produce significant biomass increase, promote rapid vegetation growth, and have a high ESV (Liu et al., 2020; Xia et al., 2022b). From 2011 to 2022, the average FVC in the vegetation growing seasons of the surveyed PV plants (under all ecological construction modes) increased from 8.5% to 10.5%, with an average annual increase of 0.2%. While this growth rate is limited, the maximum fractional growing season vegetation coverage increased from 33.6% to 57.9% during the same period (Figure 6), with the highest value observed in a PV plant adopting the M4 mode, indicating the substantial potential for ecological restoration in PV plants. However, to fully realize this potential, it is essential for all PV plants to adopt comprehensive sand control measures and artificial ecological construction. With these measures, the FVC can be increased to about 50% in the future, which is the threshold required to fix the sandy surface in the desert and significantly reduce wind and sand problems (Zhao, 2016). It provides additional ecological and environmental benefits by enhancing carbon fixation, which in turn reduces the negative impact of PV plants construction. It also has a positive impact on the planning, policy and management, and sustainability of large-scale PV systems.

Using the ESV assessment model, the total ESV provided by the surveyed PV plants at the current stage and after implementing ecological construction were calculated (Table 2). The results show that the investigated PV plants can provide an average of approximately $1.2 million of ESV per year, and if artificial ecological construction is effectively implemented and given sufficient growing time, the ESV provided by the plants could be increased by 7.7 (7.1–8.3, confidence interval, and the same below) times to approximately $8.9 (8.2–9.5) million per year.

TABLE 1 Growing season vegetation coverage and ESV change rate in the surveyed PV power plants under different ecological construction modes.

Modes	Number of plants	Initial FVC (Avg.) (%)	Existing FVC (Avg.) (%)	Change rate of FVC and ESV (%)
M1	9	5.92	10.31	74
M2	5	5.61	11.35	102
M3	7	10.30	11.95	16
M4	9	9.22	14.53	58
M5	2	12.56	14.03	12

Note: Initial FVC (Avg.) represents the FVC, in the year of PV, plant construction and grid connection. Existing FVC (Avg.) denotes the 2022 FVC., The plants that were newly built in 2022 were not selected in the calculation.

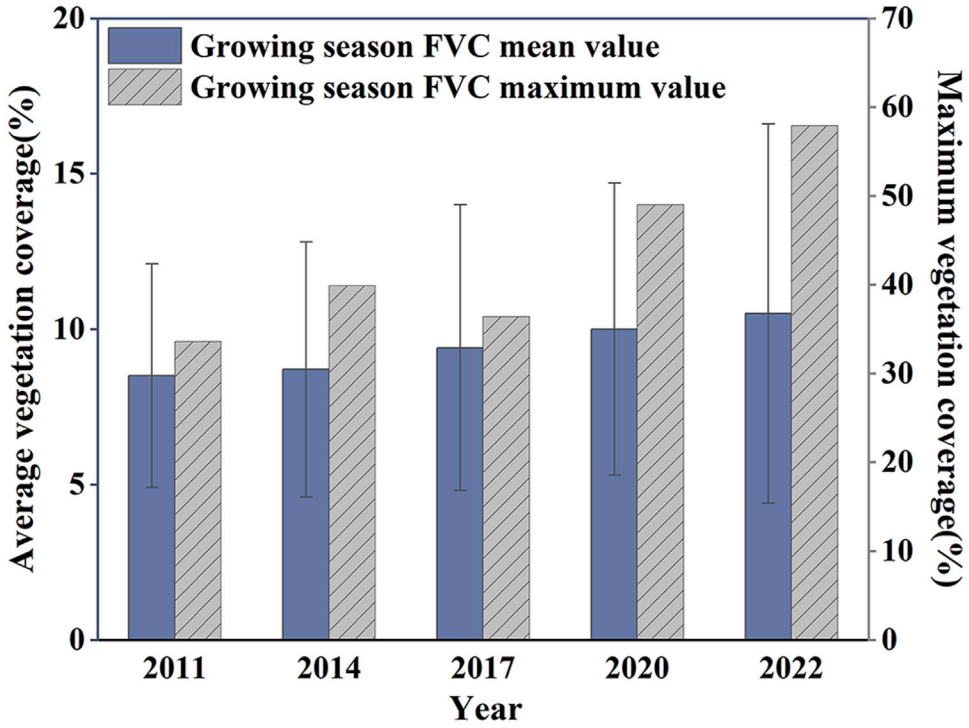

FIGURE 6
Average and maximum growing season FVC changes in the surveyed PV plants.

4 Discussion

4.1 Ecological construction contributes to enhancing ESV in desert

Desert has become the hot development zone of large-scale wind and PV farms. According to *China's Renewable Energy Development Plan*, the total installed capacity of wind and solar power farms in desert will reach 200 GW in 2025 and 455 GW in 2030 (National Development and Reform Commission and National Energy Administration, 2021). The rapid development of renewable energy in desert faces great challenges, as wind and sand activities, as well as the expansion of desertification land, pose serious threats to the safety and sustainable development of PV plants. Previous studies have indicated that the construction activities of PV plants, especially the leveling of ground, can disrupt the original soil environment, leading to a significant decline in vegetation coverage and very fragile surface soil (Wu et al., 2014; Hernandez et al., 2015).

However, in most deserts, the degradation of vegetation caused by the construction of PV plants is small. This is partially due to the fact that these regions may have very little vegetation prior to the installation of the plants, but more importantly that the vegetation removed during the construction process can be recovered after the completion of the PV plants (Wu et al., 2014; Uldrijan et al., 2021; Xia et al., 2022b). Furthermore, the installation of PV plants can alter the local microclimate, regulate the thermal balance in desert, reduce the amount of wind-blown sand, and contribute to the improvement of growth conditions for plants in arid regions (Chang et al., 2016). Previous studies utilizing remote sensing imagery, field monitoring, and surveys have found that the construction of PV plants has resulted in significant vegetation changes, with most PV plants showing positive vegetation growth, while a few PV plants resulted in vegetation degradation (Chang et al., 2018; Liu et al., 2020;

TABLE 2 The existing ecosystem service value (ESV_N) and the potential for enhancing ecosystem service value (ESV_P) of the surveyed PV plants.

i	PV plants name	Latitude	Longitude	Area (ha)	Ecological construction modes	Initial FVC (construction year)	FVC_i in 2022	ESV_i (N) (10^4 $ yr^{-1})	ESV_i (P) (10^4 $ yr^{-1})	Confidence interval
1	Shengyang	105°01′16″	37°35′20″	100	M3	8.35 (2013)	10.78	1.02	4.34	[4.13, 4.55]
2	CHN Zhongwei	105°04′62″	37°53′80″	152.67	M3	9.33 (2013)	9.62	1.56	7.50	[7.21, 7.79]
3	Hengjiweiye	105°20′13″	37°51′51″	200	M4	11.58 (2015)	11.59	2.04	7.80	[7.16, 8.44]
4	CHNE Tengger	105°20′	37°51′	1866.67	M4	9.02 (2022)	9.02	19.06	103.12	[101.70, 104.50]
5	Tianyun	105°31′35″	37°63′33″	273.77	M1	10.07 (2015)	18.5	2.80	6.71	[5.92, 7.49]
6	Meiliyun	105°17′71″	37°63′07″	93.33	M4	31.07 (2019)	26.88	0.95	1.32	[1.14, 1.50]
7	CECEP Tengger	105°07′53″	37°67′41″	66.67	M3	8.60 (2015)	9.68	0.68	3.22	[3.07, 3.38]
8	CECEP Alashan	105°38′07″	37°93′02″	201.33	M4	13.84 (2011)	18.58	2.06	5.28	[4.40, 6.17]
9	Shenghao	105°38′36″	38°74′76″	24	M4	9.93 (2018)	13.43	0.25	0.82	[0.72, 0.91]
10	Jinxinghalun	105°72′32″	38°77′13″	133.33	M3	17.04 (2016)	15.76	1.36	3.87	[3.74, 3.99]
11	CHNE Alashan Left Banner	105°63′14″	38°65′10″	106.67	M1	9.09 (2011)	17.09	1.09	2.66	[2.51, 2.81]
12	CHNE Xinyang	105°64′39″	38°55′62″	106.67	M4	6.50 (2015)	18.54	1.09	2.39	[2.13, 2.64]
13	Shenghui	105°65′72″	38°88′94″	226.67	M5	15.19 (2013)	14.63	2.31	7.13	[6.53, 7.72]
14	Saihan Taolai	100°53′71″	41°87′47″	68.20	M1	2.74 (2017)	7.7	0.70	4.35	[3.47, 5.24]
15	LJRE Subo Naoer	100°96′00″	41°87′56″	143.33	M4	0.67 (2014)	1	1.46	159.54	[138.74, 180.35]
16	CHNE Jinta	98°93′95″	39°95′75″	64	M1	2.56 (2011)	7.37	0.65	7.52	[0.72, 14.30]
17	GEPIC Huineng	98°93′69″	39°95′47″	50	M3	0.28 (2011)	2.07	0.51	13.02	[9.46, 16.39]
18	Power China Jinta	98°97′36″	39°96′89″	566.67	M2	3.82 (2022)	3.82	5.79	74.82	[69.11, 80.58]
19	Wuling Power	101°60′27″	39°25′08″	180.8	M4	4.05 (2020)	3.18	1.85	29.78	[27.35, 32.12]
20	Zhenfa	102°75′28″	39°42′72″	24	M5	6.38 (2016)	5.35	0.25	2.21	[2.21, 2.21]
21	Zhongdian Kexin	102°82′74″	39°44′43″	24	M3	7.23 (2015)	5.25	0.25	2.21	[2.02, 2.39]
22	CHNE Minqin	102°48′89″	39°01′17″	133.33	M1	5.26 (2013)	4.83	1.36	13.53	[13.03, 14.02]
23	CHNE-GSNE Minqin	102°46′46″	38°96′38″	13.33	M1	4.16 (2013)	5.16	0.14	1.26	[1.17, 1.35]
24	CHNE-GSNE Huineng	102°51′81″	38°97′65″	29.2	M1	5.31 (2013)	5.33	0.30	2.65	[2.61, 2.68]
25	Tianhe Yineng	102°55′98″	38°91′42″	276.67	M1	4.41 (2013)	5.98	2.83	22.69	[21.58, 23.79]

(Continued on following page)

10.3389/fenvs.2024.1406546

TABLE 2 (*Continued*) The existing ecosystem service value (ESV_N) and the potential for enhancing ecosystem service value (ESV_P) of the surveyed PV plants.

i	PV plants name	Latitude	Longitude	Area (ha)	Ecological construction modes	Initial FVC (construction year)	FVC_i in 2022	ESV_i (N) (10^4 \$ yr^{-1})	ESV_i (P) (10^4 \$ yr^{-1})	Confidence interval
26	CHN Jiuduntan	102°50′58″	38°03′25″	1175.93	M4	3.26 (2022)	3.26	12.01	180.12	[176.69, 183.84]
27	CEEC jiuduntan	102°88′71″	38°09′79″	86.07	M3	3.26 (2022)	3.26	0.88	13.18	[12.93, 13.46]
28	CHN Wuwei	102°93′62″	38°08′05″	286.13	M4	3.73 (2022)	3.73	2.92	38.72	[36.71, 40.59]
29	Power China Wuwei	102°33′62″	38°10′97″	86.07	M1	9.66 (2013)	20.81	0.88	1.76	[1.58, 1.93]
30	CECEP Wuwei	102°29′94″	38°09′35″	533.33	M2	6.82 (2011)	23.78	5.45	10.89	[10.41, 11.37]
31	Zhengtai Yongchang	102°31′36″	38°27′18″	474	M4	5.25 (2013)	15.72	4.84	13.17	[12.74, 13.58]
32	Sanxia Dazhaitan	102°30′25″	38°27′61″	113.33	M4	4.26 (2013)	14.77	1.16	3.38	[3.24, 3.52]
33	Zhenxin	102°13′38″	38°59′68″	467	M2	3.86 (2013)	6.92	4.77	32.81	[31.82, 33.78]
34	JinChuan Dongdatan	102°36′85″	38°49′15″	522.67	M2	7.19 (2022)	7.19	5.34	34.37	[31.65, 37.13]
35	CHN Shuangwan	102°34′32″	38°48′56″	225.67	M2	5.07 (2013)	10.42	2.30	10.21	[8.30, 12.11]
36	CNNL Huanghuatan	103°15′17″	37°74′13″	268.63	M3	10.42 (2022)	10.42	2.74	12.15	[9.88, 14.42]
37	CNNL Zhenye Lvzhou	103°13′79″	37°76′38″	386.67	M4	8.26 (2014)	20.51	3.95	7.90	[7.74, 8.05]
38	CEEC Wuwei	103°16′62″	38°05′79″	1219.27	M4	22.38 (2022)	22.38	12.45	25.90	[24.06, 27.72]
39	Gulang Poverty Alleviation	103°46′14″	38°57′05″	62	M3	25.96 (2018)	31.08	0.63	0.72	[0.61, 0.83]
40	SPIC Baiyin	103°98′05″	37°38′91″	253.33	M2	5.88 (2013)	10.26	2.59	12.11	[11.08, 13.12]
Total		-	-	11285.39	-		10.5 (Avg.)	115.24	887.11	[821.28, 952.78]

10.3389/fenvs.2024.1406546

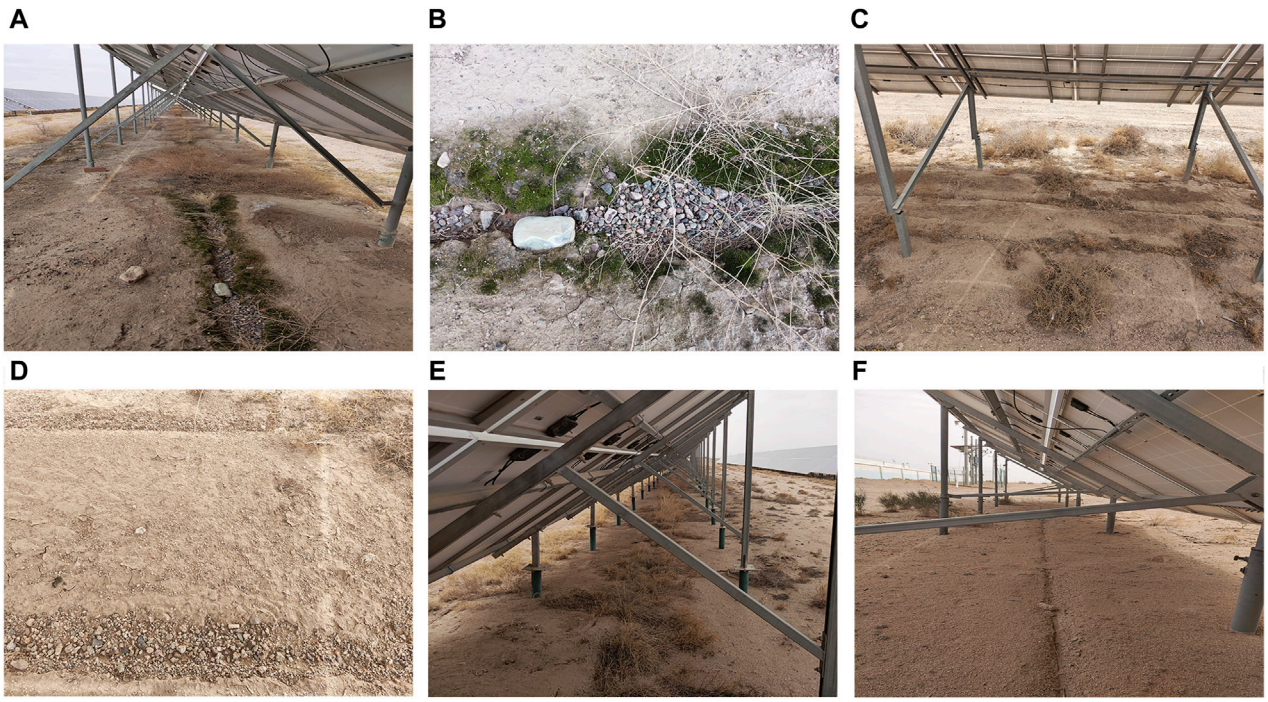

FIGURE 7
Cleaning water and rainwater flow down through the gaps between PV panels, forming drip lines **(A,B)**, hydraulic erosion lines **(C,D)**, moss and biological crusts **(E,F)** around the drip lines.

Uldrijan et al., 2021; Xia et al., 2022b; Luo et al., 2023). The 74% increase of FVC in the surveyed plants with M1 mode proves this ecological enhancement ability of PV system. Moreover, the less surface-disturbing construction methods such as the using of screw pile are increasingly used in the new plants. The Sanxia Dazhaitan (No. 32 in Table 2) plant, as an example of coexistence between PV panels and *Hippophae rhamnoides* in the Tengger Desert near Jinchang, Gansu Province, provides additional evidence of the function of PV panels in improving the overall environment against erosion.

In addition, numerous biological soil crusts were found around the drip lines beneath the PV plants (Figures 7E, F). The presence of these biological crusts enhances the stability of desert soil, reduces soil erosion, and fosters the recovery of desert ecosystems (Li X. et al., 2018; Choi et al., 2020; Luo et al., 2023). This occurrence is attributed to the periodic cleaning operations required to remove dust particles from the PV panel surfaces. According to the survey results, the PV panels are typically cleaned 7–8 times per year. During the cleaning process, the PV panels intercept a portion of the cleaning water that drops from the edges and gaps of the panels and forms drip lines beneath. As substantial cleaning water falling to the ground, the soil moisture content increases, thereby providing the growth of vegetation underneath the panels (Figures 7D, E). It is important to note that although the PV plants are situated in the desert where water evaporates quickly, the regular cleaning operations ensure a consistent supply of water to the ground surfaced, which significantly helps the vegetation growth and biological crust development.

Unfortunately, the intensity of these positive effects is inherently limited, and the resulting change processes can be very slow. Implementing wind-break and sand-fixation measures, as well as artificial planting (M4) in PV plants, can effectively prevent and control wind and sand disasters, protect soil from erosion, enhance vegetation coverage, and provide higher ESV. This approach enables the simultaneous development of ecology and economy, achieving a synergy effect between environmental and economic benefits. All of these suggest that vegetation construction in desert PV plants has a promising future.

4.2 Restrictions of ecological construction in current PV plants

The rapid development of PV industry necessitates a heightened focus on its ecological functions (Semeraro et al., 2022). However, 22.5% of the surveyed PV plants still did not take any sand prevention or vegetation construction measures, and 45% of them did not take artificial vegetation construction measures. In addition to the differences of surface landforms, the implementation of ecological construction measures for PV plants is also affected by resource shortages and economic costs.

The scarcity of resources in desert is primarily due to the prevalent aridity and water scarcity. It is estimated that the northwest China's deserts will require an additional 20 billion cubic meters of water per year from 2010 to 2030, and the water scarcity crisis will exacerbate due to climate change and human activity (Wu et al., 2014). Water is mainly sourced from water tankers and groundwater wells for daily consumption and panel cleaning in the PV plants, while some PV plants located near towns could access tap water. However, a substantial portion of the water used for PV plants cleaning is lost via surface runoff, which can even

contribute to hydraulic erosion beneath the panel (Figures 7A–D). The limited water resources are not fully utilized.

The issue of economic cost primarily arises from the significant human labor and financial resources required for the ecological construction of PV plants, which may take several years to yield returns (Jing et al., 2022). The increase in the construction and operational costs of the PV plants may dampen the desire of owners to carried out ecological construction practices (Li et al., 2020). Although the ecological construction of the plants can generate substantial ESV, these potential values cannot be directly transferred to the plant owners and operators (Semeraro et al., 2022). Therefore, additional policy support to encourage investment in ecological construction initiatives is required if we want to obtain the high potential ESV (Li et al., 2020). Ecological construction measures and their economic costs vary largely under different ecological modes (see 2.2.3), So that the accurate assessment of their economic costs and benefits requires further study, as well as reasonable financial policies (regulation, subsidies or taxes).

4.3 Unsatisfactory effects of current ecological construction measures in PV plants

The effectiveness of existing sand-prevention and artificial planting measures in the PV plants may not meet expectations (Mai and Bai, 2023). According to the survey, only 36.4% of the PV plants with artificial planting would reseed grass in the later stages, while the remaining plants have not implemented any maintenance measures, thereby failing to guarantee the survival rate of plants after ecological construction. Moreover, only 23% of the plants have a vegetation maintenance regulation, and would irrigate periodically. As a result, the anticipated ecological and economic benefits may not be achieved.

Our study also revealed that many PV plants lack scientific sand control and ecological construction guidelines during the construction phase. In terms of sand control, the surveyed plants only implemented limited traditional methods such as straw barrier and surface compaction with gravel, while many updated techniques such as new materials sand barriers, environmental-friendly chemical sand stabilization materials, and bio crust were not utilized. Also, no effective standards were developed for the implementation area of the sand control measures. Some plants covered the whole equipment area with sand control measures but without specific targeting, resulting in the waste of funds. Others only built barriers at places with severe sand damage without considering the source or transportation path of sands, leading to an incomplete protection system with low control effectiveness. In terms of ecological construction, most surveyed PV plants adopt the approach of artificial vegetation establishment by sowing mixed grass species. However, due to the absence of sufficient irrigation, the lack of a mature irrigation system, and the inadequacy of plant species selection, issues arise such as low plant survival rates and excessive plant growth obstructing the PV panels.

It is evident that the current implementation of ecological construction measures may only address the dichotomous question of "presence or absence" of such measures, while the actual ecological outcomes have not received adequate attention. The future challenges include developing tailored and scientifically sound ecological construction plans, conducting reasonable evaluations on the ecological construction effects to quantify the generated economic and ecological benefits, and correcting underperforming projects (Shen et al., 2021).

4.4 Strong policies can stimulate the ecological construction of PV plants

Energy policy plays a crucial role in driving the rapid development of PV plants in China (Li et al., 2020). Since 2017, the Chinese government has demonstrated a heightened focus on modes such as "solar energy + sand control" and "solar energy + ecological restoration," accompanied by the implementation of a series of policies designed to foster the development of desert ecological PV plants. For instance, in 2017, the Ministry of Land and Resources issued a notification indicating that no administrative fees would be imposed on PV + projects that change land use types, thereby reducing land utilization costs (Ministry of Land and Resources, 2017). In 2019, "PV +" projects received priority in renewable subsidy payments, providing support for off-grid projects that aimed at poverty alleviation (Shen et al., 2021). In 2020, the Inner Mongolia energy regulatory agency prioritized the development of integrated solar energy projects incorporating desertification control measures, terminating subsidies for standalone solar PV plants that fail to contribute to ecological restoration efforts (IMAR Development and Reform Commission, 2020). Additionally, some regional authorities have declared more favorable policies for the innovative application of solar PV projects installed on barren land and deserts (Ministry of Natural Resources et al., 2023).

In line with the implementation of these boosting government policies, the construction quantity and scale of PV plants reached a turning point at 2017, initially declining but subsequently recovering. The ecological construction modes adopted by PV plants have undergone a significant transformation since the same time point. Among the 13 newly built PV plants after 2017, 12 (92%) adopted M2 to M5 modes, with 7 (54%) employing M4 and M5 modes. The proportion of PV plants employing the M4 mode has risen substantially in terms of construction area, installed capacity, and annual average power generation. This shift in ecological construction modes has led to an increase in the FVC and corresponding ESV values for the region, with PV plants adopting M2 to M5 measures experiencing an approximately 7.2% improvement of net ESV from the completion of PV plants to 2022. We therefore recommend the government to encourage and guide PV plants in adopting scientific ecological construction measures, thereby promoting the ecological construction and sustainable development of PV plants in desert regions.

5 Conclusion

This research presents a comprehensive study based on field survey and remote sensing investigations of 40 PV plants in the Badain Jaran Desert and Tengger Desert, two of the hot solar energy exploration areas in China. We examine the existing ecological construction mode and key influencing factors of PV plants, and estimate the current and potential ecosystem service value (ESV) within the investigated plant areas.

We found that PV plants without ecological construction (M1 mode) boost vegetation cover by 74%, highlighting their capacity to enhance desert ecosystems. However, the highest FVC only reaches approximately 10%. By implementing sand control and vegetation planting measures, the average growing season FVC can be elevated to 14.53%, with a peak of 57.9%. Currently, 22.5% of PV plants lack ecological construction measures, 40% lack sand control, and 45% do not employ vegetation, agricultural, or pastoral measures. Nevertheless, over 92% of PV plants constructed after 2017 have adopted at least one ecological construction mode (M2 to M5). The key factors influencing the choice of ecological construction mode are land surface types, policy support, water scarcity, and ecological construction costs. The surveyed plant areas' annual ecological service value could surge from $1.2 million to $8.9 (8.2–9.5) million, representing a 7.7-fold (7.1–8.3) increase. This substantial ESV deserves further attention and policy guidance.

It is noteworthy that large-scale PV farms face several challenges regarding ecological improvement. These include the lack of scientific sand control management and ecological construction guidelines, inadequate evaluation of the ecological service value (ESV) of implemented ecological construction measures, and the failure to achieve the desired ecological, economic, and social benefits. In the future, it is crucial to establish sand control and ecological construction guidelines tailored to PV plants in desert areas, considering various factors like land surface types, sand disaster status, water availability, and vegetation conditions. Additionally, evaluations must be conducted on the economic costs of various ecological construction modes, along with on-site assessments of the ecological service value of large-scale PV plants.

Data availability statement

The original contributions presented in the study are included in the article/Supplementary Material, further inquiries can be directed to the corresponding author.

Author contributions

YW: Data curation, Formal Analysis, Investigation, Visualization, Writing–original draft. BL: Conceptualization, Funding acquisition, Methodology, Resources, Supervision, Writing–review and editing. YX: Data curation, Investigation, Writing–review and editing. HP: Funding acquisition, Project administration, Supervision, Writing–review and editing. HW: Project administration, Supervision, Writing–review and editing. JZ: Project administration, Supervision, Writing–review and editing.

Funding

The author(s) declare that financial support was received for the research, authorship, and/or publication of this article. This research was funded by the National Key R&D Program of China (grant number 2022YFB4202102), the National Natural Science Foundation of China (grant number 42071014), and the Excellent Member of Youth Innovation Promotion Association CAS (grant number Y202085).

Conflict of interest

Authors HP, HW, and JZ were employed by Northwest Engineering Corporation Limited.

The remaining authors declare that the research was conducted in the absence of any commercial or financial relationships that could be construed as a potential conflict of interest.

Publisher's note

Supplementary material

The Supplementary Material for this article can be found online at: https://www.frontiersin.org/articles/10.3389/fenvs.2024.1406546/full#supplementary-material

References

Borrelli, P., Robinson, D. A., Panagos, P., Lugato, E., Yang, J. E., Alewell, C., et al. (2020). Land use and climate change impacts on global soil erosion by water (2015-2070). *Proc. Natl. Acad. Sci.* 117 (36), 21994–22001. doi:10.1073/pnas.2001403117

Chang, Z. F., Liu, S. Z., Zhu, S. J., Han, F. G., Zhong, S. N., and Duan, X. F. (2016). Ecological functions of PV power plants in the Desert and gobi. *J. Resour. Ecol.* 7 (2), 130–136. doi:10.5814/j.issn.1674-764x.2016.02.008

Chang, Z. F., Wang, Q., and Liu, S. Z. (2018). Sand fixation effect of photovoltaic field of gobi desert - take Gansu hexi corridor as an example (in Chinese with English abstract). *Soil Water Conservation China.* 08, 18–22. doi:10.14123/j.cnki.swcc.2018.0172

China Securries Journal (2022). The 14th Five-Year Plan" installed capacity of about 200 million kilowatts, the second batch of scenery base planning landing. Available at: https://www.cs.com.cn/cj2020/202202/t20220228_6245405.html (Accessed May 31, 2023).

Choi, C. S., Cagle, A. E., Macknick, J., Bloom, D. E., Caplan, J. S., and Ravi, S. (2020). Effects of revegetation on soil physical and chemical properties in solar photovoltaic infrastructure. *Front. Environ. Sci.* 8, 140. doi:10.3389/fenvs.2020.00140

Costanza, R., d'Arge, R., de Groot, R., Farber, S., Grasso, M., Hannon, B., et al. (1997). The value of the world's ecosystem services and natural capital. *Nature* 387 (6630), 253–260. doi:10.1038/387253a0

Costanza, R., de Groot, R., Sutton, P., van der Ploeg, S., Anderson, S. J., Kubiszewski, I., et al. (2014). Changes in the global value of ecosystem services. *Glob. Environ. Change-Human Policy Dimensions* 26, 152–158. doi:10.1016/j.gloenvcha.2014.04.002

Cui, Y. Q., Feng, Q., Sun, J. H., and Xiao, J. H. (2017). A review of revegetation patterns of photovoltaic plant in northwest China. *Bull. Soil Water Conservation* 37 (3), 200–203. doi:10.1016/j.seta.2023.103120

Gao, J. X., Zhang, H. W., Zhang, W. G., Chen, X. H., Shen, W. M., Xiao, T., et al. (2023a) "Data from: China regional 250m normalized difference vegetation index data set (2000-2022)," in *National Tibetan plateau date center third Pole environment data center*. doi:10.11888/Terre.tpdc.300328

Gao, J. X., Zhang, H. W., Zhang, W. G., Chen, X. H., Shen, W. M., Xiao, T., et al. (2023b) "Data from: China regional 250m fractional vegetation cover data set (2000-

2022)," in *National Tibetan plateau date center third Pole environment data center*. doi:10.11888/Terre.tpdc.300330

Grodsky, S. M., and Hernandez, R. R. (2020). Reduced ecosystem services of desert plants from ground-mounted solar energy development. *Nat. Sustain.* 3 (12), 1036–1043. doi:10.1038/s41893-020-0574-x

Guo, J. B., and Wang, Y. (2014) *Key technology of photovoltaic power plants design*. Beijing: China Electric Power Press.

Hernandez, R. R., Easter, S. B., Murphy-Mariscal, M. L., Maestre, F. T., Tavassoli, M., Allen, E. B., et al. (2014). Environmental impacts of utility-scale solar energy. *Renew. Sustain. Energy Rev.* 29, 766–779. doi:10.1016/j.rser.2013.08.041

Hernandez, R. R., Hoffacker, M. K., Murphy-Mariscal, M. L., Wu, G. C., and Allen, M. F. (2015). Solar energy development impacts on land cover change and protected areas. *Proc. Natl. Acad. Sci. U. S. A.* 112 (44), 13579–13584. doi:10.1073/pnas.1517656112

Hertwich, E. G., Gibon, T., Bouman, E. A., Arvesen, A., Suh, S., Heath, G. A., et al. (2015). Integrated life-cycle assessment of electricity-supply scenarios confirms global environmental benefit of low-carbon technologies. *Proc. Natl. Acad. Sci.* 112 (20), 6277–6282. doi:10.1073/pnas.1312753111

IEA Photovoltaic Power Systems Programme (2018). Snapshot of global PV markets 2018. Available at: https://iea-pvps.org/wp-content/uploads/2020/01/IEA-PVPS_-_A_Snapshot_of_Global_PV_-_1992-2017.pdf (Accessed May 25, 2023).

IEA Photovoltaic Power Systems Programme (2023). Snapshot of global PV markets 2023. Available at: https://iea-pvps.org/snapshot-reports/snapshot-2023/ (Accessed May 25, 2023).

IMAR Development and Reform Commission (2020). Inner Mongolia electricity sector Reform plan. Available at: https://www.ndrc.gov.cn/fzggw/jgsj/tgs/sjdt/201610/W020190906633217378679.pdf (Accessed May 31, 2023).

Jing, R., He, Y., He, J. J., Liu, Y., and Yang, S. B. (2022). Global sensitivity based prioritizing the parametric uncertainties in economic analysis when co-locating photovoltaic with agriculture and aquaculture in China. *Renew. Energy* 194, 1048–1059. doi:10.1016/j.renene.2022.05.163

Li, B., Wang, Y., Xia, G. C., and Jiang, G. (2020). Comparative efficacy of treatments for patients with knee osteoarthritis: a network meta-analysis. *Qinghai Sci. Technol.* 25 (05), 27–33. doi:10.1186/s40001-020-00426-1

Li, X., Tan, H., Hui, R., Zhao, Y., Huang, L., Jia, R., et al. (2018a). Researches in biological soil crust of China: a review. *Chin. Sci. Bull.* 63 (23), 2320–2334. doi:10.1360/N972018-00390

Li, Y., Kalnay, E., Motesharrei, S., Rivas, J., Kucharski, F., Kirk-Davidoff, D., et al. (2018b). Climate model shows large-scale wind and solar farms in the Sahara increase rain and vegetation. *Science* 361 (6406), 1019–1022. doi:10.1126/science.aar5629

Liu, Y., Zhang, R. Q., Ma, X. R., and Wu, G. L. (2020). Combined ecological and economic benefits of the solar photovoltaic industry in arid sandy ecosystems. *J. Clean. Prod.* 262, 121376. doi:10.1016/j.jclepro.2020.121376

Lu, X. (2013) *The environmental effect analysis of PV power plant construction in desert gobbi —take dongdongtan million kilowatt solar power demonstration base, jiuquan city as an example*. LanZhou University. [dissertation/master's thesis], [LanZhou (GanSu)].

Luo, L. H., Zhuang, Y. L., Liu, H., Zhao, W. Z., Chen, J. Z., Du, W. T., et al. (2023). Environmental impacts of photovoltaic power plants in northwest China. *Sustain. Energy Technol. Assessments* 56, 103120. doi:10.1016/j.seta.2023.103120

Mai, F. J., and Bai, R. L. (2023). Discussion on PV desertification control Scheme (in Chinese with English abstract). *Sol. Energy* 01, 30–34. doi:10.19911/j.1003-0417.tyn20211202.06

Marco, De, Irene, S., Teodoro, P., Rita, M., Aretano, R., and Zurlini, G. (2014). The contribution of Utility-Scale Solar Energy to the global climate regulation and its effects on local ecosystem services. *Glob. Ecol. Conservation* 2, 324–337. doi:10.1016/j.gecco.2014.10.010

Marrou, H., Dufour, L., and Wery, J. (2013). How does a shelter of solar panels influence water flows in a soil-crop system? *Eur. J. Agron.* 50, 38–51. doi:10.1016/j.eja.2013.05.004

Mekhilef, S., Saidur, R., and Safari, A. (2011). A review on solar energy use in industries. *Renew. Sustain. Energy Rev.* 15 (4), 1777–1790. doi:10.1016/j.rser.2010.12.018

Ministry of Land and Resources (2017). Opinions on supporting PV poverty alleviation and regulating land use for PV power generation industry. Available at: www.nea.gov.cn/2017-10/10/c_136669687.htm (Accessed july 25, 2020).

Ministry of Natural Resources, PRC., National Forestry and Grassland Administration., and Administration (2023). Notice on supporting the development of photovoltaic power generation industry and regulating land use management related work. Available at: https://www.gov.cn/zhengce/zhengceku/2023-04/03/content_5749824.htm (Accessed May 20, 2023).

National Development and Reform Commission, and National Energy Administration (2021). China's 14th five-year plan for renewable energy development. Available at: https://www.ndrc.gov.cn/xwdt/tzgg/202206/P020220602315650388122.pdf (Accessed July 14, 2023).

National Energy Administration (2023). Construction and operation status of photovoltaic power generation in 2022. Available at: http://www.nea.gov.cn/2023-02/17/c_1310698128.htm (Accessed June 11, 2023).

National Forestry and Grassland Administration (2015). State bulletin of desertification and desertification in China. Available at: https://www.forestry.gov.cn/main/65/20151229/835177.html (Accessed May 31, 2023).

People's Daily Overseas Edition (2023). Three ministries jointly issue document to encourage the construction of large-scale photovoltaic power plants in desert. Available at: https://www.gov.cn/zhengce/2023-04/06/content_5750194.htm (Accessed june 11, 2023).

Riahi, K., Dentener, F., Gielen, D., Grubler, A., Jewell, J., Klimont, Z., et al. (2012). "Energy pathways for sustainable development," in *Global energy assessment: toward a sustainable future* (Cambridge: Cambridge University Press), 1205–1306.

Scarrow, R. (2020). Solar plants versus desert plants. *Nat. Plants* 6 (8), 908. doi:10.1038/s41477-020-00753-5

Semeraro, T., Scarano, A., Santino, A., Emmanuel, R., and Lenucci, M. (2022). An innovative approach to combine solar photovoltaic gardens with agricultural production and ecosystem services. *Ecosyst. Serv.* 56, 101450. doi:10.1016/j.ecoser.2022.101450

Shen, W., He, J. J., and Yao, S. H. (2021). Green industrial policy in the post grid parity era: governing integrated Solar + projects in China. *Energy Policy* 150, 112129. doi:10.1016/j.enpol.2020.112129

Solar Energy Industries Association (SEIA) (2022) Data from: global solar atlas 2.0-solar resource data-global horizontal irradiation. Available at: https://solargis.com/maps-and-gis-data/download/world.

Sun, J. (2018) *Biodiversity of the plant community and ecosystem assessments at different scales in alxa deserts*. LanZhou University. [dissertation/doctoral's thesis], [LanZhou (GanSu)].

Tanner, K. E., Moore-O'leary, K. A., Parker, I. M., Pavlik, B. M., and Hernandez, R. R. (2020). Simulated solar panels create altered microhabitats in desert landforms. *Ecosphere* 11 (4). doi:10.1002/ecs2.3089

Uldrijan, D., Kováčiková, M., Jakimiuk, A., Vaverková, M. D., and Winkler, J. (2021). Ecological effects of preferential vegetation composition developed on sites with photovoltaic power plants. *Ecol. Eng.* 168, 106274. doi:10.1016/j.ecoleng.2021.106274

U.S. Bureau of Labor Statistics (2023). Consumer price index summary. Available at: https://www.bls.gov/news.release/ (Accessed May 20, 2023).

Vaverková, M. D., Winkler, J., Uldrijan, D., Ogrodnik, P., Vespalcová, T., Aleksiejuk-Gawron, J., et al. (2022). Fire hazard associated with different types of photovoltaic power plants: effect of vegetation management. *Renew. Sustain. Energy Rev.* 162, 112491. doi:10.1016/j.rser.2022.112491

Wang, R. J., and Qin, Z. H. (2007). Valuation of Chinese grassland ecosystem services using MODIS data (in Chinese with English abstract). *Chin. J. Grassl.* 29 (1), 50–54. doi:10.3969/j.issn.1673-5021.2007.01.009

Wu, Z. D., Wu, Z., Liu, S., and Di, X. M. (1980) *Introduction to deserts in China (Revised version)*. Beijing: Science Press.

Wu, Z. Y., Hou, A. P., Chang, C., Huang, X., Shi, D. Q., and Wang, Z. F. (2014). Environmental impacts of large-scale CSP plants in northwestern China. *Environ. Science-Processes Impacts* 16 (10), 2432–2441. doi:10.1039/c4em00235k

Xia, Z. L., Li, Y. J., Chen, R. S., Sengupta, D., Guo, X. N., Xiong, B., et al. (2022a). Mapping the rapid development of photovoltaic power stations in northwestern China using remote sensing. *Energy Rep.* 8, 4117–4127. doi:10.1016/j.egyr.2022.03.039

Xia, Z. L., Li, Y. J., Zhang, W., Chen, R. S., Guo, S. C., Zhang, P., et al. (2022b). Solar photovoltaic program helps turn deserts green in China: evidence from satellite monitoring. *J. Environ. Manag.* 324, 116338. doi:10.1016/j.jenvman.2022.116338

Xiao, J. H., Si, J. H., Liu, C., Li, X. J., Xi, H. Y., Yu, T. F., et al. (2021). Concept,connotation and development model of Desert Energy Ecosphere (in Chinese with English abstract). *J. Desert Res.* 05, 11–20. doi:10.7522/j.issn.1000-694X.2021.00038

Xiao, J. H., Yao, Z. Y., and Sun, J. H. (2011). Review on optimal site selection for grid-connected solar photovoltaic plants (in Chinese with English abstract). *J. Desert Res.* 06, 1598–1605.

Xie, G. D., Zhang, Y. L., Lu, C. X., Zheng, D., and Cheng, S. K. (2001). Study on valuation of rangeland ecosystem services of China (in Chinese with English abstract). *J. Nat. Resour.* 01, 47–53. doi:10.3321/j.issn:1000-3037.2001.01.009

Xinhua News Agency (2021). Large-scale wind and photovoltaic power projects in China's desert commence in an orderly manner. Available at: https://www.gov.cn/xinwen/2021-10/30/content_5647888.htm (Accessed May 31, 2023).

Yan, L. G., Xia, X. C., Zhou, F. Q., and Zhao, Z. X. (2007). A development study for Chinese large scale renewable energy source base and technology (in Chinese with English abstract). *Adv. Technol. Electr. Eng. Energy* 26 (1), 13. doi:10.3969/j.issn.1003-3076.2007.01.002

Yue, S. J., Guo, M. J., Zou, P. H., Wu, W., and Zhou, X. D. (2021). Effects of photovoltaic panels on soil temperature and moisture in desert areas. *Environ. Sci. Pollut. Res.* 28 (14), 17506–17518. doi:10.1007/s11356-020-11742-8

Zhao, H. L. (2016) *Desertification control science*. Beijing: Modern Education Press.

Zhao, Y., and Zhong, Y. J. (2022). Analysis of optimal design of photovoltaic power generation system (in Chinese with English abstract). *Energy Conserv.* 04, 16–18. doi:10.3969/j.issn.1004-7948.2022.04.005

Zhu, J. F., Wang, N. A., Chen, H. B., Dong, C. Y., and Zhang, H. A. (2010). Study on the boundary and the area of Badain Jaran Desert based on remote sensing imagery (in Chinese with English abstract). *Prog. Geogr.* 09, 1087–1094. doi:10.11820/dlkxjz.2010.09.010

frontiers | Frontiers in Environmental Science

TYPE Original Research
PUBLISHED 27 May 2024
DOI 10.3389/fenvs.2024.1424578

OPEN ACCESS

EDITED BY
Jing Zhao,
Xi'an University of Technology, China

REVIEWED BY
Panxing He,
Henan Normal University, China
Xiaoyu Meng,
Henan University, China
Xiaojing Qin,
Henan Polytechnic University, China

*CORRESPONDENCE
Yuxin Li,
20200043@immu.edu.cn
Fang Yang,
yang.fang@craes.org.cn

RECEIVED 28 April 2024
ACCEPTED 13 May 2024
PUBLISHED 27 May 2024

CITATION
Fu C, Hao H, Li T, Li Y and Yang F (2024), Lag effects of vegetation of temperature stress on and its ecological risk assessment.
Front. Environ. Sci. 12:1424578.
doi: 10.3389/fenvs.2024.1424578

Lag effects of vegetation of temperature stress on and its ecological risk assessment

Chenxing Fu[1], Hongke Hao[1], Te Li[1], Yuxin Li[2]* and Fang Yang[3]*

[1]Yangling Vocational and Technical College, Yangling, China, [2]College of Basic Medical Science, Inner Mongolia Medical University, Inner Mongolia Key Lab of Molecular Biology, Hohhot, China, [3]State Key Laboratory of Environmental Criteria and Risk Assessment, Chinese Research Academy of Environmental Sciences, Beijing, China

Extreme high and low temperatures both exert impacts on terrestrial ecosystems. However, current research still lacks a precise assessment of the risk of vegetation loss under simultaneous consideration of different temperature stresses and lag effects. To this end, we propose a methodology for assessing the risk of vegetation loss under temperature stress that incorporates lag effects, based on weekly normalized difference vegetation index and temperature data. Quantified risk probabilities of different terrestrial ecosystems to warming and cooling stresses in Heilongjiang Province, China. The results of the study revealed a strong association between vegetation and temperature change during the growing season, reaching the most sensitive state around 9 weeks and 23 weeks lag, respectively, with high spatial consistency. The study identifies the eastern and western edges of the study area as high-risk zones for vegetation loss, while the risk is comparatively lower in the northwestern and central regions. The probability of risk increased by about 0.5% for every 1°C of warming in average temperatures and by about 0.7% for every 1°C of cooling. This indicates that cooling has a greater impact on vegetation than warming. Farmland ecosystems had a higher change in risk to temperature stress and forest ecosystems had the least. This study provides new perspectives for understanding the specific impacts of temperature extremes on different ecosystems and provides a scientific basis for developing adaptive management measures.

KEYWORDS

temperature stress, lag time, vegetation loss, risk assessment, heilongjiang province

1 Introduction

Amidst global change, climate warming has provoked global concern, especially regarding its potential impacts on terrestrial ecosystems. Warmer temperatures may lead to impaired plant physiology and dysfunctional ecological balance, which may have far-reaching impacts on biodiversity (Khan et al., 2013), soil and water conservation (Jia et al., 2022), and the global carbon cycle (Hoover et al., 2022). On the other hand, vegetation serves as an indicator of global climate change, not only maintaining the Earth's biodiversity but also regulating atmospheric carbon dioxide levels. It is a key component in sustaining the Earth's life systems (National Research Council, Division of Behavioral, Policy Division, Board on Environmental Change, Committee on the Human Dimensions of Global Change, and Committee on Global Change Research, 1999; Rani et al., 2020). Therefore, assessing and understanding the response of vegetation to climate change under the backdrop of global warming, particularly the potential risk of vegetation loss, is crucial for predicting and mitigating the impacts of climate change.

The response of vegetation to environmental changes often exhibits a temporal lag, and this lag effect may lead to an underestimation of vegetation's response to extreme climatic events. In many instances, vegetation may require an extended period to manifest physiological and ecological responses to environmental changes (Becklin et al., 2016; Gillison, 2019). For example, extreme high temperatures may affect plant photosynthesis immediately, but changes in plant growth and community structure may not be apparent until several subsequent seasons or even years later (De Boeck et al., 2011). Additionally, rising temperatures may further affect vegetation status by altering soil moisture evaporation and plant transpiration processes, which can also exhibit delayed effects. Conversely, extreme low temperatures can significantly affect multiple physiological processes in vegetation (Reyer et al., 2013). Low temperatures decrease the activity of enzymes within plants, thereby slowing metabolic rates and leading to reduced growth rates (Bhattacharya, 2022). Particularly under conditions of extreme low temperatures, the structure of plant cells may be directly damaged, leading to cell death. However, current research focuses more on high temperature conditions and ignores the effects of low temperatures on vegetation. Therefore, this study addresses both warming and cooling conditions and their impacts on vegetation, aiming to comprehensively assess and quantify the lag effects of different temperatures on vegetation and the probability of associated risks.

Indeed, in areas with scarce precipitation and higher latitudes, temperature is a key factor influencing vegetation growth (Fu et al., 2014; Zhao et al., 2018). Wang et al., 2021 research found that compared to vegetation in humid regions, vegetation in semi-arid areas responds more quickly to precipitation changes. Deciduous broadleaf forests exhibit a response lag of approximately 1 month to temperature changes, and as this lag time increases, the correlation coefficient also rises (Lu et al., 2020). These studies provide valuable references for understanding vegetation dynamics and their response to temperature changes, but they predominantly focus on the monthly scale interactions between vegetation and temperature variations. In fact, different types of vegetation exhibit variations in the lag time of their response to temperature changes, which may manifest on decadal, weekly, or even daily scales. It remains difficult to characterize the lagged effect of vegetation on temperature change on finer time scales.

Based on this, this study selected Heilongjiang province (HLJ), which has the highest latitude in China. Not only does it experience significant annual temperature variations, but its rich diversity of ecosystems also provides favorable conditions for studying responses to temperature changes. Particularly, as HLJ serves as China's largest commodity grain base (ZHOU and CHENG, 2015), assessing the risk of vegetation loss due to temperature changes is especially urgent and critical. To this end, we develop a risk assessment model for vegetation loss that takes into account temperature lag effects. Using high-resolution climate and vegetation data, we have developed a framework that comprehensively evaluates the risk of vegetation loss under conditions of both warming and cooling stress. The research methodology and results are expected to provide a more accurate tool for relevant sectors such as agriculture and risk management to help them better understand and manage potential risks to vegetation under temperature change. This will in turn help to develop effective ecological conservation and climate adaptation strategies.

2 Materials and methods

2.1 Study region

The HLJ is located in the northeast of China, is China's northernmost and highest latitude province, with a total area of 473,105 km^2 (Figure 1). The HLJ belongs to the cold temperate and temperate continental monsoon climate. It is characterized by low temperatures and dryness in spring, hot and rainy summers, prone to flooding and early frost in autumn, and cold and lengthy winters with a short frost-free period. The regional climatic differences across the province are significant. The annual average temperature in HLJ ranges from −4–5°C, with average precipitation exceeding 500 mm. The climate transitions from temperate in the south to cold temperate in the north, and exhibits distinct monsoonal characteristics. The province hosts a diverse array of vegetation types, with forests and agricultural ecosystems constituting a significant proportion (Liu and Li, 2024). In addition, the HLJ is located in one of the world's three largest black land areas, with the largest arable land area in the country (Pan et al., 2018). Studying the effects of temperature change on vegetation is key to securing food production.

2.2 Data

The daily maximum temperature data are sourced from the Climate Prediction Center Global Unified Temperature dataset, with a spatial resolution of 0.5° on a daily scale (https://psl.noaa.gov/data/gridded/data.cpc.globaltemp.html). The gridded daily Normalized Difference Vegetation Index (NDVI) is derived from the National Oceanic and Atmospheric Administration) Climate Data Record of Advanced Very High Resolution Radiometer NDVI Version 5 (https://www.ncei.noaa.gov). The data features a spatial resolution of 0.05°. To better align with the temperature data, we have interpolated the NDVI data to a resolution of 0.25°. In addition, considering the climatic period of vegetation growth within the year, only data from the growing season (NDVI from the 15th to 39th week of the year) were selected for this study. Ecosystem delineation data from Resource and Environmental Science Data Platform's 2020 1 km resolution (https://www.resdc.cn/DOI/DOI.aspx?DOIID=131).

2.3 Methodology

To comprehensively assess the impacts of both warming and cooling on vegetation, the Spearman correlation between temperature and NDVI was calculated at various lag times. Additionally, the optimal lag times for both periods were determined by identifying the maximum and minimum correlation coefficients. Further, a copula function was employed to jointly model the temperature and NDVI variables at their optimal lag times for both periods. A copula function is a flexible

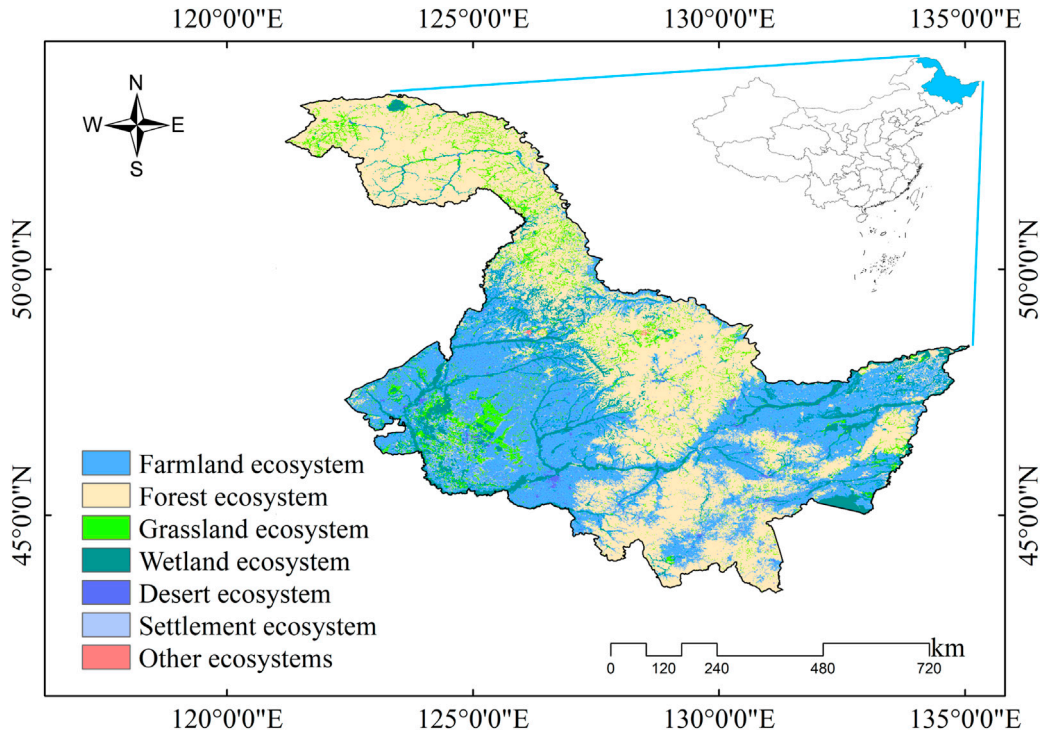

FIGURE 1
Location of the study area and ecosystem delineation.

method for representing multivariate joint distributions, unconstrained by the marginal distributions of random variables or the types of their joint distribution functions. This avoids assumptions about linearity or underlying probability distributions (Sklar, 1959; Nelsen, 2006). For any two random variables and, the corresponding joint distribution is expressed as follows

$$F(x, y) = C(u, v) \tag{1}$$

where C represents the cumulative copula distribution function; u and v represent the marginal distribution functions of the random variables x and y, respectively.

Further, the kernel functions are employed to fit the marginal distributions, as described in Eq. 2. Given the properties of different types of copula functions and the fact that this study is mainly concerned with the risk scenarios of warming and cooling on vegetation loss. We used Clayton (Eq. 3) and Gaussian copula functions (Eq. 4) to fit the joint probability distribution, respectively.

$$f_h(x) = \frac{1}{nh}\sum_{i=1}^{n} K\left(\frac{x - x_i}{h}\right) \tag{2}$$

where x_1, x_2, … x_n are random samples from an unknown distribution, n is the sample size, K is the kernel smoothing function, and h represents the bandwidth (Han et al., 2023a).

$$C_\theta(u, v) = max\left(\left[u^{-\theta} + v^{-\theta} - 1\right]^{-\frac{1}{\theta}}, 0\right), \theta \in (0, +\infty) \tag{3}$$

$$\int_{-\infty}^{\phi^{-1}(u)} \int_{-\infty}^{\phi^{-1}(v)} \frac{1}{2\pi\sqrt{1-\theta^2}} \exp\left\{-\frac{s^2 - 2\theta st + t^2}{2(1-\theta^2)}\right\} dsdt, \theta \in (-1, 1) \tag{4}$$

where θ is the Copula parameters, and θ value gained by the maximum likelihood estimate method in this study.

Based on the joint distribution of the two copula functions constructed, the Bayesian conditional probability approach can then be used to assess the conditional probability of the risk of vegetation loss under temperature stress. In this study, scenarios combining temperature and vegetation are configured using percentile-based measures. Given the extensive and patterned nature of the scenario outcomes, we focus here on the vegetation loss scenarios at the 40th and 10th percentiles during cooling at the 40th, 30th, 20th, and 10th percentiles. For better comparison, the warming corresponds to the 60th, 70th, 80th, and 90th percentile scenarios, respectively. In this case, the conditional probabilities P of temperature and vegetation can be calculated separately for the combined cooling (Eq. 5) and warming (Eq. 6) scenarios.

$$P(Y \le y \mid X \le x) = \frac{C(F_X(x), F_Y(y))}{F_X(x)} = \frac{C(u, v)}{u} \tag{5}$$

$$P(Y \le y \mid X > x) = \frac{F_Y(y) - C(F_X(x), F_Y(y))}{1 - F_X(x)} = \frac{v - C(u, v)}{1 - u} \tag{6}$$

3 Results and discussion

3.1 Lag effect of NDVI on temperature

In general, vegetation growth is subject to a combination of climate change and environmental factors. Especially for vegetation at higher latitudes, the effect of temperature is relatively more

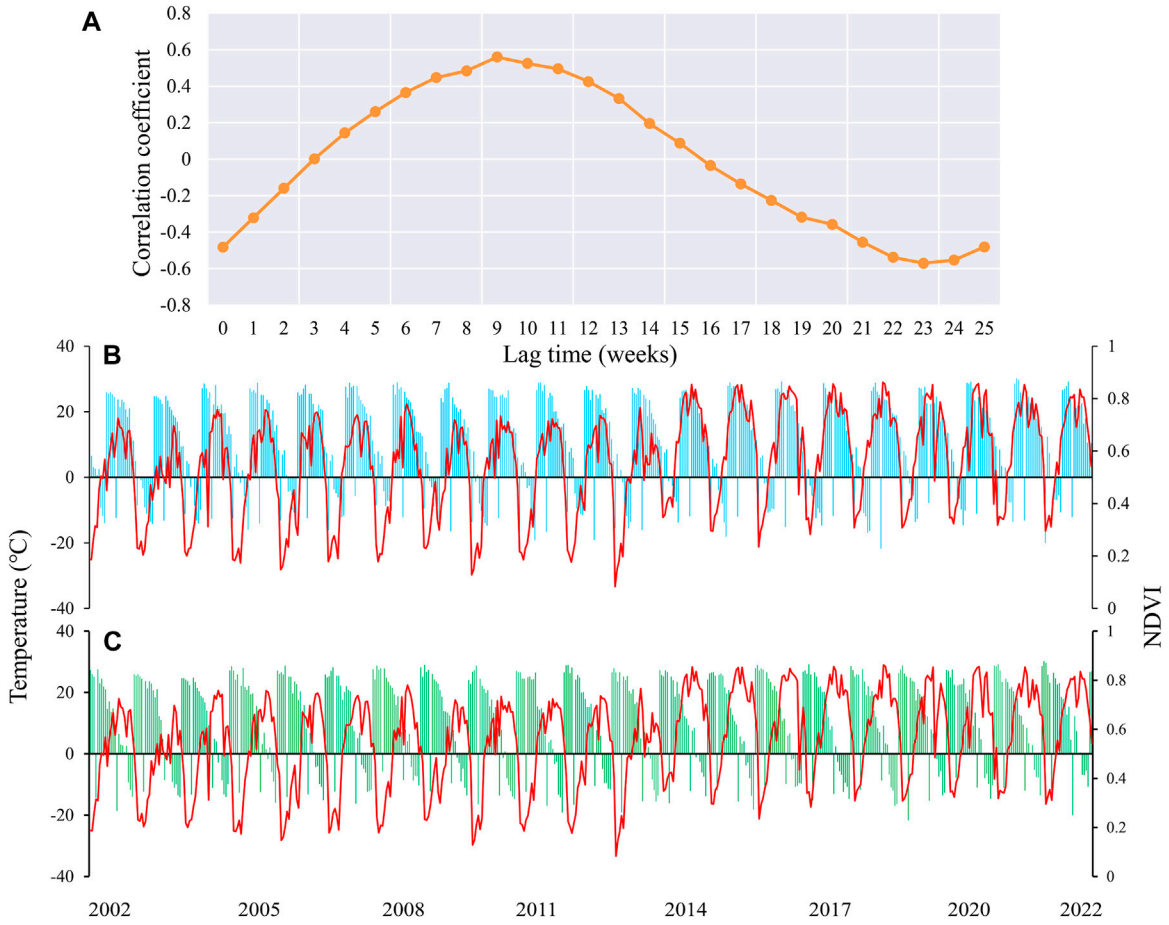

FIGURE 2
Correlation coefficients between NDVI and temperature at different lag times **(A)**, along with changes in NDVI **(B)** and temperature **(C)** at extreme values.

pronounced (Huang et al., 2017). Vegetation will vary in its sensitivity to temperature with different lag times, especially during the growing season period of vegetation (Wu et al., 2015). Figure 2A shows the variation of correlation coefficients between vegetation and temperature changes in HLJ at different weekly time scales. It is apparent that the maximum positive correlation ($r = 0.56$, $p < 0.01$) and the minimum negative correlation ($r = -0.57$, $p < 0.01$) are achieved at 9 weeks and 23 weeks, respectively. Figures 2B,C show in detail the changes of NDVI *versus* temperature in Heilongjiang Province with a lag of 9 and 23 weeks. In the period of positive correlation, NDVI shows a synchronous and stable trend as the temperature increases and decreases. The negative correlation period shows the opposite change. Relative to changes in temperature, the variations in NDVI were more pronounced around the year 2014, beginning with a notable increase from that year onward.

On the spatial scale, the positive and negative correlation two periods (Figures 3A,B) showed significance at the 0.05 level for almost all image elements. They exhibit similar spatial distribution characteristics, with lower correlation coefficients (regardless of the direction of correlation) in the central region of HLJ. In the western and eastern regions, there is a higher level of correlation (direction of correlation not considered). However, the differences in lag times are more pronounced. During the period of positive correlation (Figure 3C), most of the lag times are concentrated within 10 weeks. In contrast, during the period of negative correlation (Figure 3D), most lag times exceed 20 weeks, with a noticeable acceleration in lag as latitude increases. Furthermore, the strong sensitivity between NDVI and temperature forms the foundation for constructing bivariate Copula functions, where the direction of correlation directly influences the outcomes of vegetation loss risk under various temperature stresses. Therefore, the changes in correlations illustrated in Figures 2, 3 also provide a good opportunity to explore the risk of vegetation loss under different warming and cooling scenarios.

3.2 Risk assessment of vegetation loss under different levels of temperature stress

Given the complexity and stochastic nature of risk loss (Blauhut, 2020), we have conducted detailed analyses of the probabilities of vegetation loss at various levels under different temperature stresses during periods of both positive and negative correlation. During the period of positive correlation, changes in the probability of vegetation loss risk as temperatures decrease are displayed

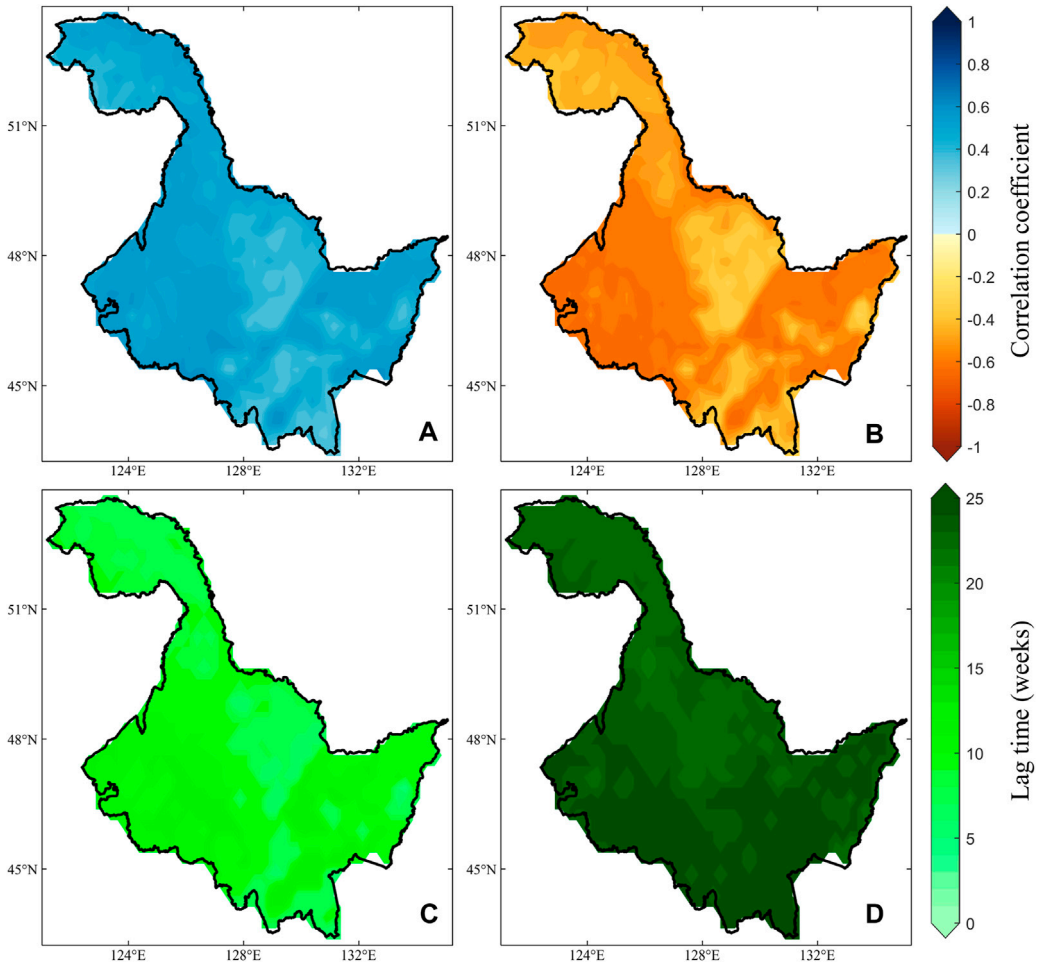

FIGURE 3
Correlation coefficients between NDVI and temperature under periods of positive **(A, C)** and negative correlation **(B, D)** and their spatial variation in lag time.

(Figure 4). It can be observed that as the degree of temperature reduction intensifies, the risk probability of vegetation loss at the 40th percentile exhibits a significant increasing trend, with the color deepening to dark red. On the other hand, when the degree of vegetation loss was at the 10th percentile, it increased with temperature stress. Although the probability of risk also tended to increase, it was significantly lower than the probability at the 40th percentile. Overall, the spatial distribution of risk probabilities under different scenarios shows a high degree of consistency during the period of positive correlation. In particular, it tends to have higher probability values in the eastern and western parts of HLJ, and lower probability values in the northwestern and central parts of HLJ.

During periods of negative correlation, an increase in temperature will inhibit vegetation growth. For this reason, we also discussed the changes in the risk probabilities of vegetation loss due to increases in temperature (Figure 5). Similar to the results during the period of positive correlation, as the degree of temperature stress intensifies, the risk probability of vegetation loss shows an increasing trend. Moreover, the higher the extent of vegetation loss, the lower the risk probability becomes. Additionally, the risk probability values across different scenarios exhibit a high degree of spatial similarity, mirroring the spatial variations observed in Figures 3A,B. This suggests that in areas where vegetation is more sensitive to temperature changes, the risk of loss due to temperature stress is greater. When we further compare the risk probabilities between the two periods, it is evident that cooling has a more substantial impact on vegetation than warming, and the extent of this impact intensifies as the level of temperature stress increases. Particularly, when cooling reaches the 10th percentile and warming reaches the 90th percentile, the average difference in the risk probability of vegetation loss at the 10th percentile is as high as 17%. Risk probability values are greater than 50% for eastern and western HLJ during cooling. As a result, vegetation growth conditions in the region are significantly affected by temperature, warranting increased attention and heat prevention in the area.

3.3 Effects of warming and cooling changes on ecosystems

In fact, although Figures 4, 5 provide detailed representations of vegetation loss risk under various scenarios. However, for government officials and farmers, they might be more concerned

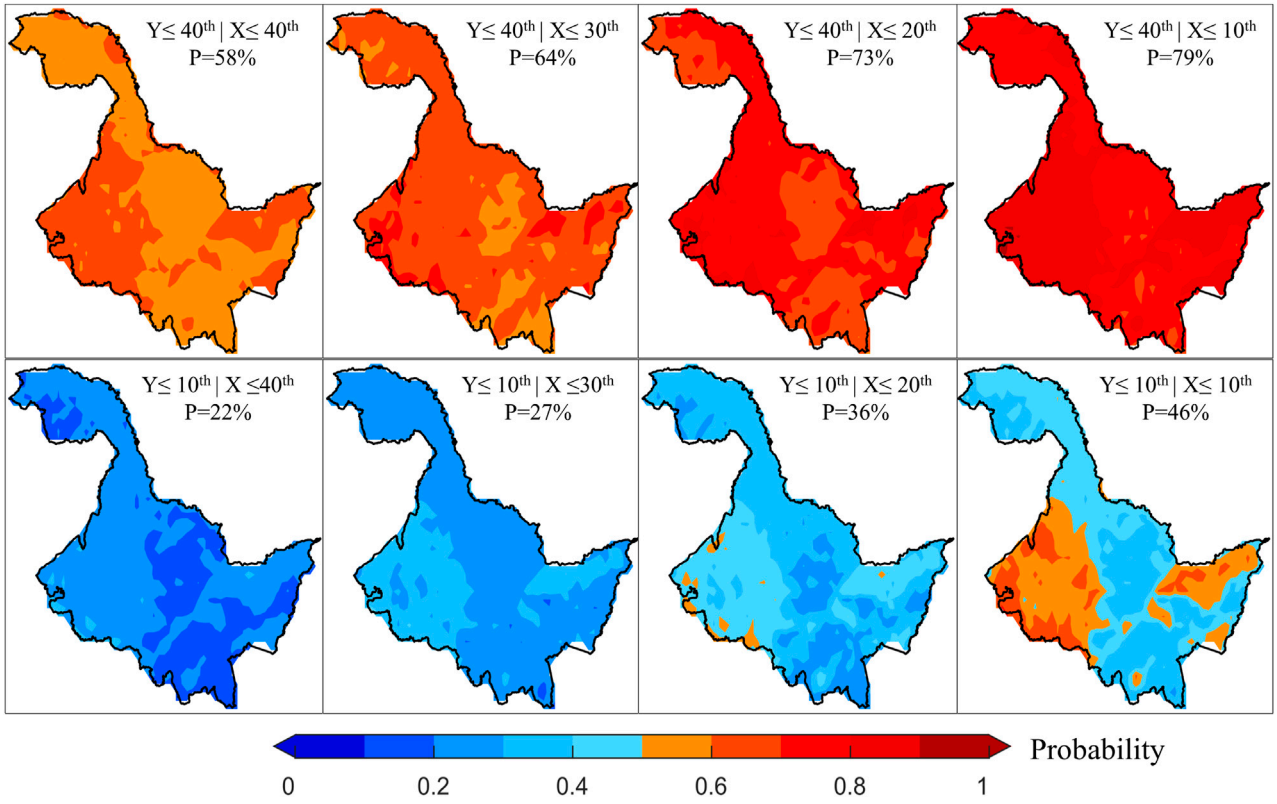

FIGURE 4
Changes in risk probability of causing different levels of vegetation loss under different levels of temperature stress during the positive correlation period. Here, X and Y represent temperature and NDVI, respectively, and P denotes the average risk probability value.

about the specific magnitude of temperature changes and their impact on vegetation. Therefore, we further quantified the risk changes of vegetation loss at the 40th percentile within each pixel, when temperatures increase or decrease by 1°C–4°C based on the mean temperature change (Figure 6). For each 1°C increase in temperature, the average risk probability increases by approximately 0.5%, while each 1°C decrease in temperature reduces the risk by about 0.7%. This indicates that cooling has a greater impact on vegetation than warming. Furthermore, the areas most affected by both warming and cooling are on the eastern and western sides of the study area, with the smallest impact observed in the northwest and central regions. These findings are highly consistent with earlier conclusions and serve to indirectly validate the accuracy and reliability of this study.

Moreover, we conducted detailed risk analyses for farmland, forest, grassland and wetland ecosystems separately (Figure 7). Pixel counts for remaining ecosystem types constitute only about 5% of the total in the study area, and hence were not considered in this analysis. In both scenarios, distinct differences in the risk of loss due to temperature stress are evident across different ecosystems, exhibiting highly consistent patterns. Among these, the sensitivity to temperature changes ranked from highest to lowest is farmland, wetlands, grasslands, and forests. The risk probabilities for each ecosystem increase in a linear fashion. Simultaneously, this indicates that farmland has the lowest resilience to temperature stress, while forests exhibit the highest resilience. It has been shown that farmland ecosystems tend to have low carbon sequestration capacity and biodiversity, and a relatively weak resilience in the face of extreme climate events (Seddon et al., 2021). In contrast, systems such as forests have a higher carbon sequestration capacity and richer biodiversity. They are more resilient to climate change, especially in terms of climate and water regulation (Roy et al., 2022), and thus relatively less exposed to risk. These difference not only reveals the vulnerability of different ecosystems to future climate change, but emphasizes the need to consider the characteristics of different ecosystems when proposing measures or strategies such as climate change adaptation.

3.4 Reliability and limitations of the risk assessment framework

Traditional methods of assessing vegetation risk are common, but they often rely on deterministic approaches and single-scenario methods. In contrast to other natural variables such as soil moisture, runoff, and groundwater, vegetation dynamics are severely dependent on unilateral changes in precipitation or temperature. For example, lower precipitation and higher temperatures tend to cause a decrease in the above variables, thus exacerbating the risk (Han et al., 2021; Han et al., 2023b). However, vegetation can adjust its state in response to environmental changes, thus adapting to the evolution of natural conditions. To this end, this study proposes a model for assessing the risk probability of vegetation loss from warming and cooling changes. The risk probability of causing a certain level of vegetation loss under any temperature stress can be accurately quantified.

Further, we randomly selected a pixel (123.875°E, 46.375°N) and assessed the reliability of the framework by applying Gaussian and

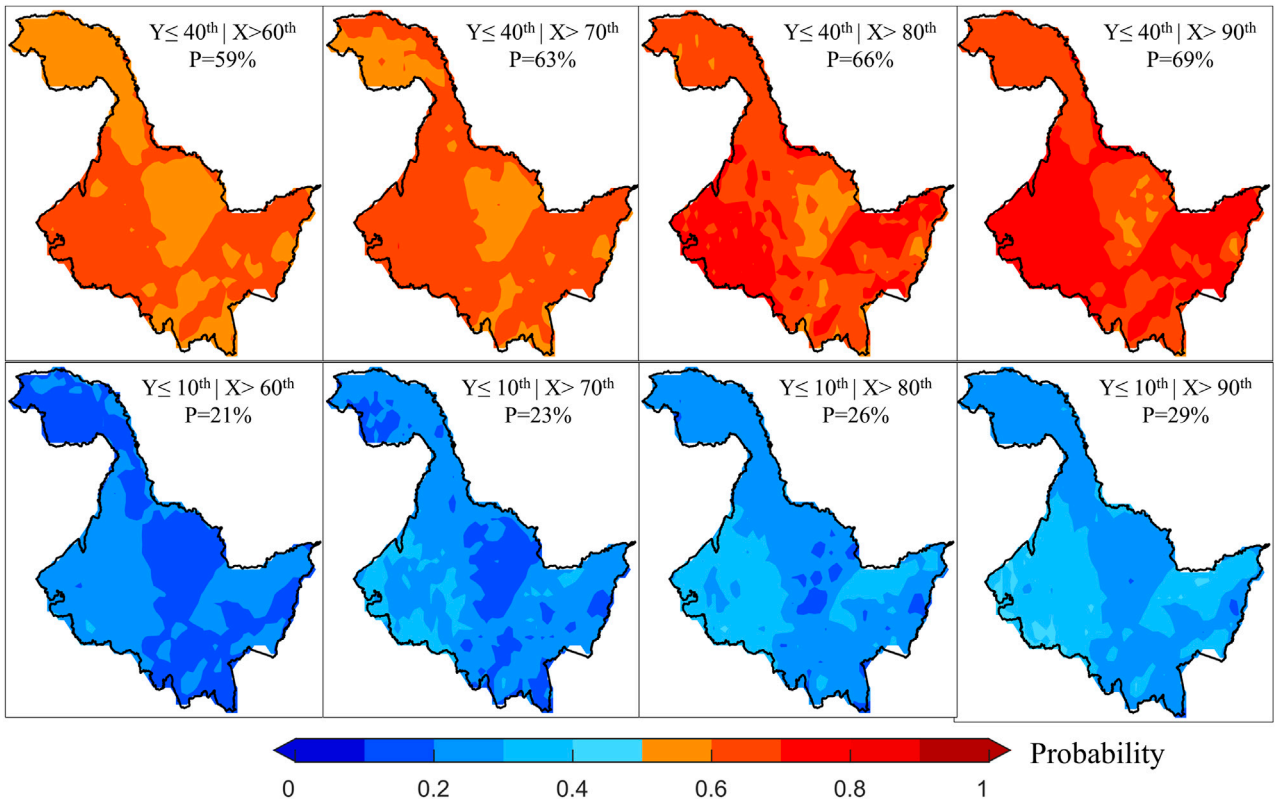

FIGURE 5
Changes in the risk probabilities of vegetation loss at various degrees under different temperature stresses during periods of negative correlation.

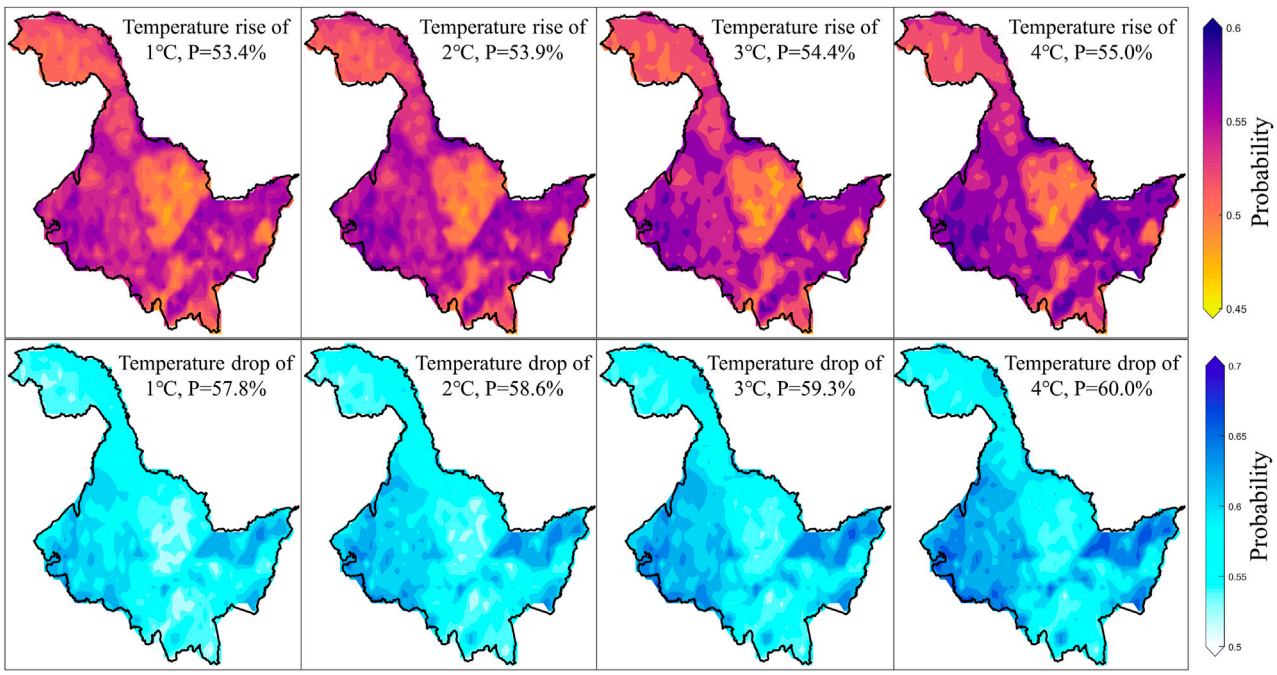

FIGURE 6
Changes in risk at the 40th percentile of vegetation loss for warming and cooling of 1°C–4°C compared to average temperatures.

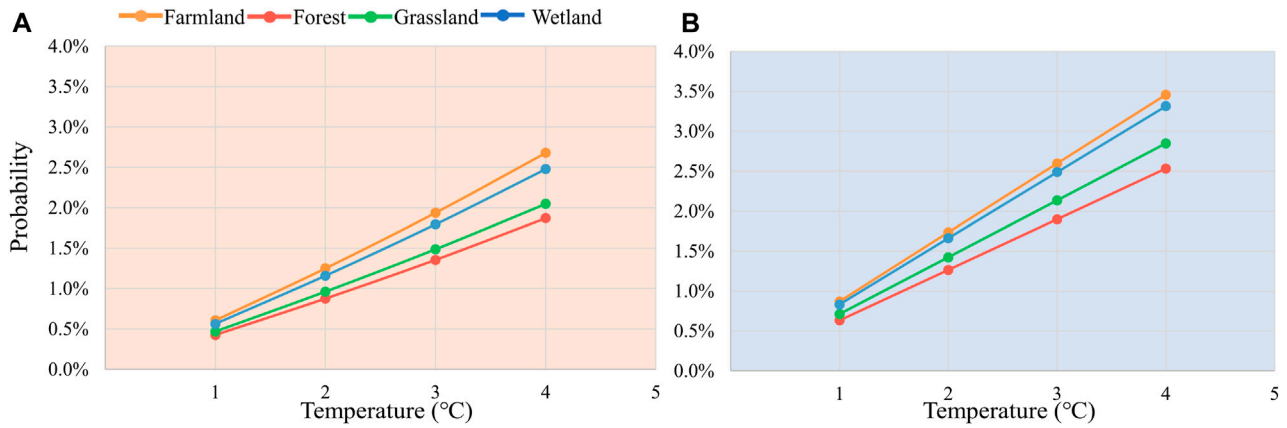

FIGURE 7
Changes in risk at the 40th percentile of ecosystem loss for different ecosystems for warming **(A)** and cooling **(B)** 1°C–4°C.

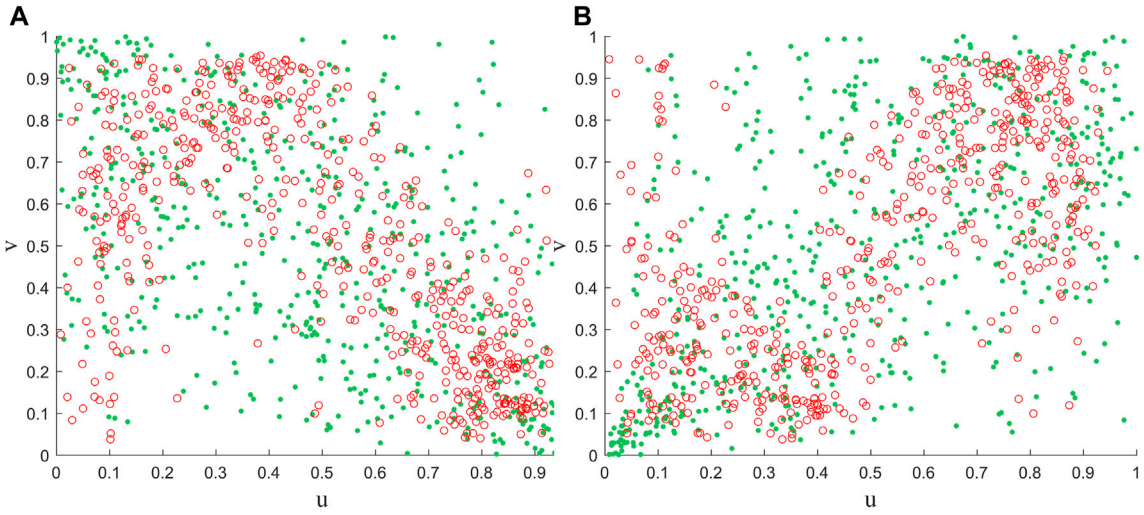

FIGURE 8
Comparison of observed combinations of air temperature and NDVI with simulated random variables using Gaussian **(A)** and Clayton copula **(B)**, respectively. Where the red circles and green dots indicate the results of observations and simulations, respectively.

Clayton copulas to the NDVI and vegetation for both periods (Figure 8). It can be seen that the distribution of most observations and simulations results is more consistent, i.e., during periods of positive (negative) correlation, the modelled point changes also show positive (negative) correlation. More importantly, based on the properties of the copula function, it can be seen that the Calyton copula function has a more sensitive lower tail characteristic. Thus, the loss of vegetation under the cooling scenario can be better captured (Figure 8B). However, several limitations must also be acknowledged in this study. Firstly, although we chose different copula functions for different scenarios. However, the uncertainty inherent in the copula model itself also affects and is passed on to the assessment of the probability of risk (Leng and Hall, 2019). Secondly, we will only focus on the effect of temperature on vegetation and lack of consideration of other environmental factors. Therefore, more environmental factors as well as more appropriate methods can be considered in future studies.

Overall, this study quantifies in detail the effects of warming and cooling on vegetation loss. It also explores the variability in the response of different ecosystems to changes in temperature. These provide new insights into the status of vegetation loss under temperature stress.

4 Conclusion

In this study, two copula functions with Bayesian conditional probabilities were used to assess the probability of risk to different vegetation losses under temperature stress in HLJ. While accounting for lag effects, this study quantified the impact of temperature increases and decreases of 1°C–4°C on vegetation loss across different ecosystems. The research identified that lag effects play a critical role in the risk of vegetation damage, with varying lag times leading to different

sensitivities and risks of vegetation loss due to temperature changes. This study shows that at around 9 weeks and 23 weeks of lag, there is a maximum positive correlation and a minimum negative correlation with temperature, respectively. The correlation and risk loss scenarios in HLJ have a similar spatial distribution. The eastern and western parts of the province are the most sensitive areas in terms of vegetation response to temperature and are also at high risk of loss. Further analysis of the risk changes under warming and cooling stresses indicates that cooling has a greater impact on vegetation than warming. Different ecosystems exhibit varied probabilities of risk under temperature stress, with agricultural ecosystems showing lower resistance to temperature stress, while forest ecosystems demonstrate higher resilience.

These findings emphasize the practical importance of integrating the lagged effects of temperature stress for accurate assessment of vegetation damage in the context of global climate change. Additionally, future research should delve deeper into the interactions between different types of vegetation and their intrinsic mechanisms for climate adaptability. This would enable a more comprehensive understanding and prediction of vegetation responses to temperature stress. Such efforts will provide a scientific basis for the sustainable management and conservation of ecosystems.

Data availability statement

The original contributions presented in the study are included in the article/Supplementary material, further inquiries can be directed to the corresponding authors.

Author contributions

CF: Writing–original draft. HH: Validation, Writing–review and editing. TL: Formal Analysis, Writing–review and editing. YL: Supervision, Writing–review and editing. FY: Funding acquisition, Writing–original draft.

Funding

The author(s) declare financial support was received for the research, authorship, and/or publication of this article. This research was supported by the Foundation of Important Science and Technology Specific Projects of Ordos (ZD20232301).

Conflict of interest

The authors declare that the research was conducted in the absence of any commercial or financial relationships that could be construed as a potential conflict of interest.

Publisher's note

All claims expressed in this article are solely those of the authors and do not necessarily represent those of their affiliated organizations, or those of the publisher, the editors and the reviewers. Any product that may be evaluated in this article, or claim that may be made by its manufacturer, is not guaranteed or endorsed by the publisher.

References

Becklin, K. M., Anderson, J. T., Gerhart, L. M., Wadgymar, S. M., Wessinger, C. A., and Ward, J. K. (2016). Examining plant physiological responses to climate change through an evolutionary lens. *Plant physiol.* 172 (2), 635–649. doi:10.1104/pp.16.00793

Bhattacharya, A. (2022). "Effect of low temperature stress on photosynthesis and allied traits: a review," in *Physiological processes in plants under low temperature stress* (Springer Nature), 199–297.

Blauhut, V. (2020). The triple complexity of drought risk analysis and its visualisation via mapping: a review across scales and sectors. *Earth-Science Rev.* 210, 103345. doi:10.1016/j.earscirev.2020.103345

De Boeck, H. J., Dreesen, F. E., Janssens, I. A., and Nijs, I. (2011). Whole-system responses of experimental plant communities to climate extremes imposed in different seasons. *New Phytol.* 189 (3), 806–817. doi:10.1111/j.1469-8137.2010.03515.x

Fu, Y. H., Piao, S., Zhao, H., Jeong, S. J., Wang, X., Vitasse, Y., et al. (2014). Unexpected role of winter precipitation in determining heat requirement for spring vegetation green-up at northern middle and high latitudes. *Glob. change Biol.* 20 (12), 3743–3755. doi:10.1111/gcb.12610

Gillison, A. N. (2019). Plant functional indicators of vegetation response to climate change, past present and future: I. Trends, emerging hypotheses and plant functional modality. *Flora* 254, 12–30. doi:10.1016/j.flora.2019.03.013

Han, Z., Huang, S., Huang, Q., Leng, G., Liu, Y., Bai, Q., et al. (2021). GRACE-based high-resolution propagation threshold from meteorological to groundwater drought. *Agric. For. Meteorology* 307, 108476. doi:10.1016/j.agrformet.2021.108476

Han, Z., Huang, S., Peng, J., Li, J., Leng, G., Huang, Q., et al. (2023b). GRACE-based dynamic assessment of hydrological drought trigger thresholds induced by meteorological drought and possible driving mechanisms. *Remote Sens. Environ.* 298, 113831. doi:10.1016/j.rse.2023.113831

Han, Z., Huang, S., Zhao, J., Leng, G., Huang, Q., Zhang, H., et al. (2023a). Long-chain propagation pathways from meteorological to hydrological, agricultural and groundwater drought and their dynamics in China. *J. Hydrology* 625, 130131. doi:10.1016/j.jhydrol.2023.130131

Hoover, D. L., Hajek, O. L., Smith, M. D., Wilkins, K., Slette, I. J., and Knapp, A. K. (2022). Compound hydroclimatic extremes in a semi-arid grassland: drought, deluge, and the carbon cycle. *Glob. Change Biol.* 28 (8), 2611–2621. doi:10.1111/gcb.16081

Huang, M., Piao, S., Janssens, I. A., Zhu, Z., Wang, T., Wu, D., et al. (2017). Velocity of change in vegetation productivity over northern high latitudes. *Nat. Ecol. Evol.* 1 (11), 1649–1654. doi:10.1038/s41559-017-0328-y

Jia, G., Hu, W., Zhang, B., Li, G., Shen, S., Gao, Z., et al. (2022). Assessing impacts of the ecological retreat project on water conservation in the yellow river basin. *Sci. Total Environ.* 828, 154483. doi:10.1016/j.scitotenv.2022.154483

Khan, M. I. R., Asgher, M., and Khan, N. A. (2013). Rising temperature in the changing environment: a serious threat to plants. *Clim. Change Environ. Sustain.* 1 (1), 25–36. doi:10.5958/j.2320-6411.1.1.004

Leng, G., and Hall, J. (2019). Crop yield sensitivity of global major agricultural countries to droughts and the projected changes in the future. *Sci. Total Environ.* 654, 811–821. doi:10.1016/j.scitotenv.2018.10.434

Liu, Z., and Li, J. (2024). Responses of temporal and spatial changes of vegetation to climate factors in Heilongjiang Province from 2000 to 2020. *For. Eng.* 40 (1), 85–97.

Lu, Q., Jiang, T., and Liu, D. (2020). The response characteristics of NDVI with different vegetation cover types to temperature and precipitation in China. *Ecol. Environ. Sci.* 29 (1), 23–34.

National Research Council, Division of Behavioral, Policy Division, Board on Environmental Change, Committee on the Human Dimensions of Global Change, and Committee on Global Change Research (1999). *Human dimensions of global environmental change: research pathways for the next decade*. Washington, DC: National Academies Press.

Nelsen, R. B. (2006). *An introduction to copulas*. Springer.

Pan, D., Jiang, F., and Liu, W. (2018). On the grain production capacity and safeguard measures of Heilongjiang province. *Mod. Agric. Res.* (05), 11–13.

Rani, G., Kaur, J., Kumar, A., and Yogalakshmi, K. (2020). "Ecosystem health and dynamics: an indicator of global climate change," in *Contemporary environmental issues and challenges in era of climate change* (Springer Nature), 1–32.

Reyer, C. P., Leuzinger, S., Rammig, A., Wolf, A., Bartholomeus, R. P., Bonfante, A., et al. (2013). A plant's perspective of extremes: terrestrial plant responses to changing climatic variability. *Glob. change Biol.* 19 (1), 75–89. doi:10.1111/gcb.12023

Roy, P. S., Ramachandran, R. M., Paul, O., Thakur, P. K., Ravan, S., Behera, M. D., et al. (2022). Anthropogenic land use and land cover changes—a review on its environmental consequences and climate change. *J. Indian Soc. Remote Sens.* 50 (8), 1615–1640. doi:10.1007/s12524-022-01569-w

Seddon, N., Smith, A., Smith, P., Key, I., Chausson, A., Girardin, C., et al. (2021). Getting the message right on nature-based solutions to climate change. *Glob. change Biol.* 27 (8), 1518–1546. doi:10.1111/gcb.15513

Sklar, M. (1959) *Fonctions de répartition à n dimensions et leurs marges*, 229–231.

Wang, L., Huang, S., Huang, Q., Leng, G., Han, Z., Zhao, J., et al. (2021). Vegetation vulnerability and resistance to hydrometeorological stresses in water-and energy-limited watersheds based on a Bayesian framework. *Catena* 196, 104879. doi:10.1016/j.catena.2020.104879

Wu, D., Zhao, X., Liang, S., Zhou, T., Huang, K., Tang, B., et al. (2015). Time-lag effects of global vegetation responses to climate change. *Glob. change Biol.* 21 (9), 3520–3531. doi:10.1111/gcb.12945

Zhao, L., Dai, A., and Dong, B. (2018). Changes in global vegetation activity and its driving factors during 1982–2013. *Agric. For. Meteorology* 249, 198–209. doi:10.1016/j.agrformet.2017.11.013

Zhou, L.-q., and Cheng, Y.-q. (2015). Spatio-temporal pattern and its driving factors of grain production in Heilongjiang Province. *J. Nat. Resour.* 30 (3), 491–501.

frontiers | Frontiers in Environmental Science

TYPE Original Research
PUBLISHED 31 May 2024
DOI 10.3389/fenvs.2024.1410037

OPEN ACCESS

EDITED BY
Jing Zhao,
Xi'an University of Technology, China

REVIEWED BY
Shuixia Zhao,
China Institute of Water Resources and Hydropower Research, China
Hui Huo,
Xiamen University of Technology, China

*CORRESPONDENCE
Chengfu Zhang,
ch893169@dal.ca
Teng Wang,
wangtengnjsy@126.com

RECEIVED 31 March 2024
ACCEPTED 03 May 2024
PUBLISHED 31 May 2024

CITATION
Fan C, Guo J, Li X, Zhang C and Wang T (2024), Effects of enclosure measures on soil water infiltration and evaporation in arid and semi-arid grassland in northern China.
Front. Environ. Sci. 12:1410037.
doi: 10.3389/fenvs.2024.1410037

Effects of enclosure measures on soil water infiltration and evaporation in arid and semi-arid grassland in northern China

Cairui Fan[1,2], Jinyan Guo[3], Xiu Li[2], Chengfu Zhang[1]* and Teng Wang[2]*

[1]College of Desert Science and Engineering, Inner Mongolia Agricultural University, Hohhot, Inner Mongolia, China, [2]College of Geographic and Planning, Jining Normal University, Ulanqab, Inner Mongolia, China, [3]College of Water Conservancy and Civil Engineering, Inner Mongolia Agricultural University, Hohhot, Inner Mongolia, China

Soil infiltration and evaporation are the main factors affecting the water cycle in arid and semi-arid areas, and the sealing measures determine the soil water storage capacity by affecting the evaporation and infiltration process of grassland soil water, which is the key to the ecological environment restoration of arid and semi-arid grassland. This study taking the enclosure time of Hulunbuir grassland for 3 years, 7 years, 10 years and the grazing control grassland as the research objects by using small evaporation instrument and double-ring infiltration instrument.To study the effects of enclosure measures on soil water distribution, soil infiltration and evaporation, and to evaluate the applicability of the main soil evaporation and infiltration models in enclosed grassland. The results show that (1) the enclosure measures can effectively improve the soil water content. In the vertical direction, the soil water content shows a trend of increasing first and then decreasing. (2) The initial infiltration rate and stable infiltration rate of grassland at different enclosure time are significantly different ($P<0.05$), and the soil infiltration rate and evaporation rate were in the order of EN10 >EN7 >EN3 >CK. (3) Using three infiltration process models to simulate the grassland infiltration process at different enclosure times, the Horton model is able to better model the inflection points of the infiltration process, and the fit accuracy is higher than that of the Philip and Kostiakov models. (4) The cumulative evaporation process of grassland at different closure times was simulated by using Black, Ross, and Power function models.The simulation values calculated by the Rose model are the closest to the measured value, and the simulation accuracy is the highest.The comprehensive analysis shows that the hydrological characteristics of grassland soil change significantly in the early stage of enclosure phase, and the soil properties have reached a good state for 3 to 7 years.With the continuous increase of enclosure time, the change of soil hydrological characteristics is not obvious. The results are helpful for soil and water conservation and ecological environment management in arid and semi-arid grassland.

KEYWORDS

enclosure measures, soil water infiltration, soil evaporation, model, arid and emi-arid grassland

Introduction

Water is the key controlling factor of vegetation growth, which directly affects the growth and development of vegetation (Chamizo et al., 2013). Soil infiltration and evaporation is not only an important part of the surface water cycle in semi-arid regions, but also a link between surface water, underground water and atmospheric water. The magnitude of soil water infiltration rate and the strength of evaporation capacity directly affect the soil water content (Guan and Cao, 2019). In semi-arid grassland areas, precipitation is small, evaporation is large, and available water for vegetation is limited. The growth of vegetation mainly depends on the water entering into the soil, and the soil evaporation capacity and infiltration performance directly affect the amount of soil water, and then indirectly control the growth trend of grassland vegetation (Zhang, 2021). In Hulunbuir grassland, due to the influence of climate change and unreasonable grazing activities, the vegetation coverage, biodiversity and ecological service function of grassland are decreased, and the large area of grassland was degraded as a whole (Nie et al., 2021). Grassland enclosure is a simple and effective way to restore degraded grasslands. In the process of closure and restoration, the growth and development of grassland vegetation is limited by soil water. With the increase of enclosure times, the change of vegetation community structure will alter the soil texture and water supply conditions and further affect soil infiltration and evaporation. Therefore, exploring the effects of enclosure measures on the soil infiltration and evaporation process of grassland, and determining the optimal enclosure period for soil water conservation, is the key to restoring the ecological environment of semi-arid grassland.

The soil water infiltration process determines the ability of precipitation to transform into soil water, while the soil evaporation process determines how much infiltration water can be retained in the surface soil for use. Infiltration and evaporation directly affect soil water content and vegetation water utilization efficiency (Yu et al., 2010; Jiao et al., 2017). In recent years, numerous researchers at home and abroad have studied the process of soil infiltration and evaporation under different environmental conditions, mainly focusing on soil infiltration and evaporation processes under the influence of human factors in agricultural planting environment (Bristow et al., 2020; Cui et al., 2021), among which the use of external additives such as biochar (Sun et al., 2019), fly ash (Yang et al., 2020) and bioactive agent (Saad, 2018) to change the soil texture and affect the movement of soil water. A large number of studies have been carried out to clarify the effects of external additives on soil evaporation and infiltration; At the same time, some researchers discussed the effects of residual agricultural film (De Souza Machado et al., 2018) and soil microplastics (Wan et al., 2019) on soil infiltration and evaporation, and constructed empirical and semi-empirical models to simulate the evaporation infiltration process of agricultural film soil and microplastic soil, and explained the effect of residual film and microplastics on soil water transport by blocking pores (Machado et al., 2019). At present, the research on soil infiltration and evaporation process and its influencing factors is mainly focused on the agricultural planting soil environment in various types of farming areas (Liao et al., 2021). While, there have been relatively few studies of meadow grassland soils in semi-arid regions, where the ecological environment is relatively fragile, the geographic spatial span is distinct, and the ability to resist disturbance is weak. The source of soil water in semi-arid grasslands is single. How to maintain soil water and reduce ineffective evaporation is the key to the healthy growth of grassland vegetation. Through field measurement and indoor simulation.

The Hulun Buir grassland is located in the interior of northern China. Long-term unreasonable grazing activities have led to grassland vegetation degradation, soil desertification and habitat fragmentation. As an effective means of grassland restoration, enclosure measures can improve the structure of vegetation groups, conserve water sources, maintain water and soil, and ensure the healthy growth of grassland vegetation. This paper takes grazing grassland and enclosed grassland in Hulun Buir meadow grassland for 3, 7 and 10 years as the research objects. Through field measurements and indoor simulations, the effects of enclosure period on soil infiltration and evaporation characteristics of grassland were studied, and the simulation processes of main infiltration and evaporation models were evaluated, so as to provide a theoretical basis for soil and water conservation and ecological environment control of meadow grassland in arid and semi-arid areas.

Materials and methods

Overview of the study area

This research area is located in Baodong Sumu, Xinbarhu Banner, Hulun Buir City, Inner Mongolia (N 48°27′54.95″~48°28′33.07″, E 117°11′41.26″~117°16′19.68″). It belongs to the hinterland of the Hulun Buir grassland and is about 30 km nearby Hulun Lake. Located in northeastern Inner Mongolia, it belongs to the semi-arid continental climate zone of the Northern temperate zone. The mean annual temperature ranges from −0.6°C to 1.1°C, and the annual sunshine duration ranges from 2,694 to 3,131 h. The average annual precipitation ranges from 240.5 to 283.6 mm and is mainly concentrated from July to September, accounting for over 60% of the annual precipitation, the annual average evaporation rate ranges from 1455.3 to 1754.3 mm and the annual frost-free period of 110–160 days. The soil composition is mainly sandy soil and sandy loam with loose structure and low fertility (Fan and Wang, 2021). The main plant species in the study area are: Leymus chinensis, Cleistogenes squarrosa, Stipa sareptana, Artemisia frigida and other vegetation (Fan and Wang, 2021).

Sample collection and processing

From July to August 2021, the soil evaporation experiment and infiltration simulation experiment were selected in the research area for 3 years (EN3), 7 years (EN7), 10 years (EN10) and grazing control (CK) grasslands in the research area. Of these, the closed grassland showed severe degradation prior to closure. The grazing intensity of the control grassland is heavy grazing, and the livestock carrying rate is 610~680 sheep/km^2. Following the grid arrangement

TABLE 1 The physical and chemical properties of grassland soil at different confining periods.

Plot	Soil bulk density (g/cm^3)	Soil porosity (%)	Noncapillary poropsity (%)	Capillary porosity (%)	Organic matter ($mg \cdot kg^{-1}$)	Soil type
CK	1.52 ± 0.08a	42.64 ± 0.11a	18.35 ± 0.12a	24.29 ± 0.10a	0.63 ± 0.28a	Sand soil
EN3	1.48 ± 0.03b	44.34 ± 0.06b	12.74 ± 0.11b	31.6 ± 0.09b	1.64 ± 0.37b	Loamy soil
EN7	1.43 ± 0.03c	46.00 ± 0.04c	9.15 ± 0.17c	36.85 ± 0.13b	2.71 ± 0.51c	Loamy soil
EN10	1.42 ± 0.06c	46.34 ± 0.07d	8.32 ± 0.14d	38.02 ± 0.08b	3.11 ± 0.39d	Loamy soil

Note: Different letters in the same column indicate significant differences; The data are expressed as mean ± standard deviation; $n = 27$.

method, grid points were established at intervals of 500 m for closed and controlled grassland, 13 points for EN3 grassland, 12 points for EN7 grassland, 15 points for EN10 grassland and 9 points for heavy grazing grassland, in which soil samples were collected and analyzed. According to the requirements of "soil agrochemical analysis," the sampling points were set up by X distribution method and triangle distribution method at each survey site. 0~30 cm soil samples and ring knife samples were collected in three layers at each sampling point. After soil samples were layered and mixed, 500 g soil samples were retained by quarter method, the soil samples were sifted by 1 mm and 0.25 mm. After screening, put it in a sealed pocket for preservation, and take it back to the laboratory to determine the physical and chemical indicators such as soil texture composition, soil volume, porosity, and organic matter. The basic properties are shown in Table 1. Soil evaporation experiment and double ring infiltration experiment were carried out at three points with similar physical structure in different enclosed grasslands, and the evaporation and infiltration performance of soil was measured. At the same time, a portable small automatic weather station is set up in the study area to observe air temperature, humidity, wind speed, solar radiation, air pressure, soil water content and other meteorological indicators, and automatically record data per 30 min.

Evaporation experiment

In this study, the soil evaporation experiment was carried out by using small lysimeter, which is a PVC sleeve with inner diameter 10 cm and height 15 cm, with a leak-proof yarn net at the bottom, which is a self-developed Chinese national patent (patent number ZL201620486286.3). For the experiment, 28 typical days were selected from 22 July to 18 August 2016 and the soil evaporation was measured at 7:00 and 19:00. Weighing the soil evaporation with a precision of 0.01 g of electron equilibrium, the mass conservation principle is used to calculate the soil evaporation. At the same time, the parameters of soil temperature and the moisture content were measured.

Infiltration experiment

In this study, the soil water infiltration rate was measured by using double-ring infiltration instrument with an inner diameter of 50 cm and an outer diameter of 80 cm. Before the start of the experiment, the grassland was pruned and the topsoil herbaceous plants were cut off, after which the infiltration ring was slowly penetrated into the soil layer with an energy-absorbing hammer to keep the soil from being damaged. Finally, we began the soil infiltration experiment, using Markov bottle to inject water into the infiltration ring, keeping the infiltration head at a constant height of 5 cm, always paying attention to the water level between the two rings, ensuring flattening, and preventing the lateral infiltration of water in the inner ring. The water level scale of the Markov bottle was read at 0, 30, 60, 120, 180 s, 5 min, 7 min, 10 min, 15 min, 25 min, 30 min, and every 10 min after the start of the experiment. The infiltration temperature and salinity were measured simultaneously until the end of the two-hour period. Three sets of repeated experiments were performed at three infiltration test sites in grasslands with different enclosure periods and control grasslands, and the characteristic curves of soil water infiltration were measured in the closed grasslands. At the same time, prior to the start of the infiltration experiment, the soil around the infiltration point was drilled to determine the initial water content, with a sampling range of 0–60 cm.

Evaporation model and infiltration model

Horton model, Philip model and Kostiakov model were used to simulate grassland soil infiltration (Niu et al., 2016), and Black model, Rose model and Power function were used to simulate grassland soil cumulative evaporation (Wang et al., 2017). The effect of the enclosure time on soil infiltration and evaporation is discussed.

(1) The relationship of Horton infiltration model is as follows:

$$f(t) = f_c + (f_0 - f_c)e^{-kt}$$

In the formula, $f(t)$ is the infiltration rate (mm/min); t is the infiltration time (min); f_0 is the hypothetical initial infiltration rate (mm/min); f_c is the hypothetical stable infiltration rate (mm/min); k is the empirical constant.

(2) The relationship of Philip infiltration model:

$$f(t) = St^{-0.5} + A$$

In the formula, $f(t)$ is the infiltration rate (mm/min), t is the infiltration time (min), S is the soil water absorption rate (mm/min), A is the stable infiltration rate (mm/min).

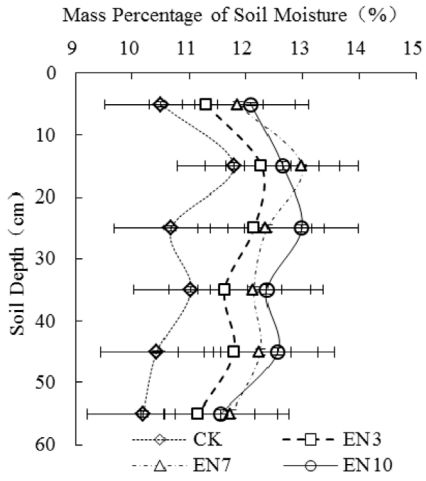

FIGURE 1
The vertical distribution of soil water in grassland with different years of enclosure. Data are the mean ± SD.

(3) The relationship of Kostiakov infiltration model:

$$f(t) = at^{-b}$$

In the formula, $f(t)$ is the infiltration rate (mm/min), t is the infiltration time (min), and a and b is an empirical constant.

(4) The relationship of Black evaporation model:

$$E = F + B\sqrt{t_0}$$

In the formula, E is the cumulative evaporation (mm), t_0 is the evaporation duration (d), F and B are evaporation parameters.

(5) The relationship of Rose evaporation model:

$$E = Ct_0 + D\sqrt{t_0}$$

In the formula, E is the cumulative evaporation (mm), t_0 is the evaporation duration (d), C is the stable evaporation parameter, and D is the water diffusion parameter.

(6) The relationship of power function model:

$$E = A \cdot t_0^{B}$$

In the formula, E is the cumulative evaporation (mm), t_0 is the evaporation duration (d), A and B are evaporation parameters.

Data analysis and processing

Statistical analysis of the measurements was performed using excel2010 and SPSS20.0 software. Relative root mean square error (RRMSE), mean absolute error (MAE), group residual coefficient (CRM) and determination coefficient (R^2) are used as the evaluation index of the simulation effect of the model. The smaller the RRMSE, MAE and CRM values are, the closer R^2 is to 1, and the better the model simulation effect is.

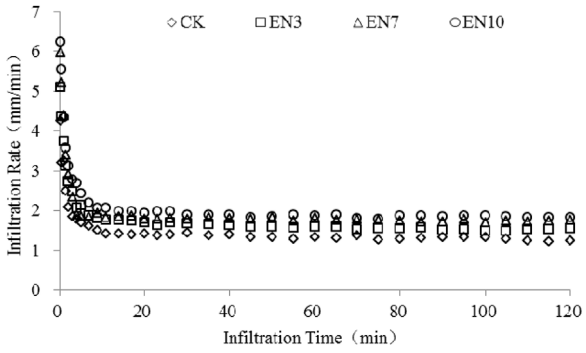

FIGURE 2
Soil infiltration rate curve of grassland with different enclosure time.

Results

Soil water distribution characteristics of different enclosed grasslands

Based on the analysis of the distribution characteristics of soil water in grasslands with different closure periods, Figure 1 shows that the soil water content initially increases and then decreases as the soil depth increases. The soil water content of the CK grassland ranges from 9.36% to 12.72%, with a water variability coefficient of 0.02–0.05. EN3 grassland soil water content ranges from 10.10% to 13.50%, the coefficient of water variation is between 0.02 and 0.07; The soil water content of the EN7 grassland ranges from 10.71% to 13.37%, and the coefficient of water variation is between 0.01 and 0.05; The soil water content of the EN10 grassland ranges from 10.36% to 13.92% and the coefficient of water variation is between 0.02 and 0.07. Except for the EN10 grassland, where the maximum soil water content occurs in layers of 20–30 cm, the maximum soil water content in other grasslands occurs in layers of 10–20 cm, and the minimum soil water content occurs in layers of 50–60 cm. The vertical distribution of soil water in the grassland showed significant differences under different disturbance measures, with enclosure measures having a large impact on the soil water content. Compared with grazing grassland, the soil water content in enclosed grassland was significantly higher than that in grazing grassland ($p < 0.01$). Compared with CK grassland, the soil water accumulation distribution area of CK grassland is mainly concentrated in10~20 cm, the soil water accumulation distribution area of EN3 and EN7 grassland is 10~30 cm, EN10 grassland soil water accumulation region 20~50 cm, and the soil water content showed as EN10 > EN7 > EN3 > CK.

Soil infiltration process in different enclosed grassland

Double-ring infiltration experiments with a 5 cm water head were performed on enclosed grasslands and grazing grasslands, and the soil infiltration properties of the grasslands were measured under different interference measures, as shown in Figure 2. At the beginning of the infiltration process, the water percolates rapidly

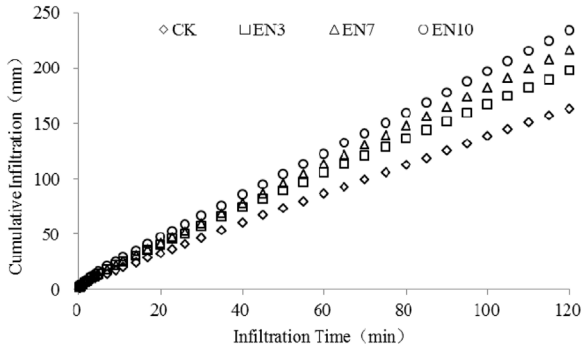

FIGURE 3
Soil cumulative infiltration curve of grassland with different enclosure time.

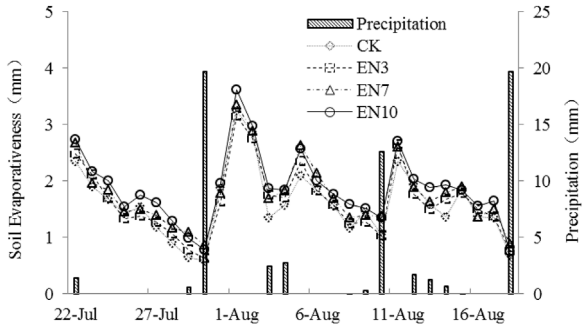

FIGURE 4
Soil evaporation of grassland with different enclosure time.

and the soil water infiltration rate rapidly decreases to 40% of the initial infiltration rate within 3–5 min. As the infiltration time increases, the downward trend of the infiltration rate slows down and gradually stabilizes at 14–20 min. The shift law is the same for soil infiltration rates in closed and grazing grasslands. There was no significant difference in initial soil infiltration rate between EN10 grassland and EN7 grassland under the same water head ($p > 0.05$), but there was significant difference in stable infiltration rate among different treatments ($p < 0.01$). By comparing the initial infiltration rate and stable infiltration rate of EN3, EN7, NE10 and CK, it was found that there were significant differences ($p < 0.05$) in initial infiltration rate and stable infiltration rate of different closed time grasslands under the same infiltration head. The overall results show that EN10 grassland is the largest, EN7 grassland is the second largest and EN3 grassland is the smallest. The initial infiltration rate of EN3 grassland was 5.10 ± 0.12 mm/min, and the stable infiltration rate was 1.57 ± 0.21 mm/min, which was 20.3% and 19.7% higher than that of CK grassland, respectively. The initial infiltration rate of EN7 grassland was 5.95 ± 0.17 mm/min, and the stable infiltration rate was 1.76 ± 0.28 mm/min, which was 40.5% and 33.9% higher than that of CK grassland, respectively. The initial infiltration rate of EN10 grassland was 6.23 ± 0.11 mm/min, and the stable infiltration rate was 1.88 ± 0.23 mm/min, which was 47.1% and 43.4% higher than that of CK grassland, respectively. The closure measures can effectively increase the infiltration rate of the grassland soil and accelerate the supply of water to this area.

Cumulative infiltration is the total amount of infiltrated water per unit area of the surface over a certain period of time, and the cumulative infiltration of grassland with different disturbance measures has been analyzed and can be seen in Figure 3. There was a significant difference in cumulative infiltration between different closure periods and grazing grasslands under the same water head ($p < 0.05$). The cumulative infiltration amount of EN10 grassland was considerably higher than that of other closed time grasslands, which was 233.41 ± 3.27 mm, 1.43 times of CK grassland, 216.44 ± 5.73 mm of EN7 grassland, 1.33 times of CK grassland, 197.23 ± 5.14 mm of EN3 grassland, 1.21 times of CK grassland. Enclosing can be effective in increasing soil water infiltration and improving water supply conditions for grassland vegetation, but the rate of increase in grassland water infiltration decreases with the length of enclosure. Therefore, grazing grasslands can alter the soil infiltration status and restore soil infiltration capacity with appropriate enclosure measures.

Evaporation process of different enclosed grassland

Soil evaporation was analyzed in grasslands and grazing grasslands with different enclosure periods from July 22 to August 18. As shown in Figure 4, the change law of soil evaporation of the grassland with different disturbance measures was the same, showing a fluctuating state, and the soil evaporation rate showed EN10 > EN7 > EN3 > CK. The cumulative soil evaporation in EN10 grassland was the highest at 52.19 mm, which was 1.05, 1.14, and 1.17 times higher than that of EN7 grassland, EN3 grassland, and CK grassland respectively. The cumulative soil evaporation of EN3 grassland was close to that of CK grassland, which was 45.91 mm and 44.65 mm, respectively, and the difference was not significant ($p > 0.05$). During the observation period, there were four peaks in daily soil evaporation in the grassland, all of which occurred after rainfall events, with the largest daily evaporation occurring on 1 August, which could reach 3.15–3.62 mm/d. It can be seen that this phase is primarily a control phase of atmospheric evaporation. As a result of the rainfall on 30 July, the soil water content increased substantially and approached saturation. The coefficient of variation for soil evaporation in each enclosed grassland exceeds 0.3, with the CK grassland exhibiting the highest coefficient of variation at 0.39. Additionally, EN3 grassland shows a coefficient of variation of 0.37, while EN7 and EN10 grasslands exhibit coefficients of variation of 0.34 each. These findings indicate that different treatments applied to the grasslands are significantly influenced by external factors, resulting in greater variability and diversity in soil evaporation patterns, aligning with the general principles governing soil evaporation.

Simulation of soil infiltration and evaporation in different enclosed grasslands

The calculated parameters of the model are given in Table 2. In the simulation of the infiltration process, the Horton model

TABLE 2 The fitting parameters of infiltration model and evaporation model.

Infiltration simulation	Horton model				Philip model			Kostiakov model		
	f_0	f_c	k	R^2	S	A	R^2	a	b	R^2
CK	4.70	1.32	0.63	0.91	1.48	1.09	0.91	2.26	0.14	0.80
EN3	5.18	1.58	0.51	0.93	2.03	1.30	0.92	3.07	0.17	0.85
EN7	5.82	1.76	0.76	0.94	2.25	1.45	0.88	3.19	0.15	0.74
EN10	7.09	1.89	0.72	0.93	2.36	1.52	0.92	3.48	0.15	0.81
Evaporation simulation	**Black Model**				**Rose Model**			**Power Function Model**		
	F		B	R^2	C	D	R^2	A	B	R^2
CK	−17.75		11.35	0.91	1.58	0.28	0.93	1.73	0.98	0.93
EN3	−18.10		11.57	0.90	1.66	0.11	0.93	1.73	0.98	0.93
EN7	−20.15		12.62	0.91	1.81	0.04	0.93	1.79	1.01	0.93
EN10	−20.38		13.06	0.91	1.85	0.34	0.93	2.03	0.98	0.93

parameter f_0 represents the initial infiltration rate, which ranges from 4.7 to 7.09. f_c are stable infiltration rates, ranging from 1.32 to 1.89. The value of k, a soil characteristic parameter, varies widely among closed grasslands, with a coefficient of determination R^2 ranging from 0.91 to 0.94. The parameter A in the Philip model represents the steady infiltration rate, and S represents the initial infiltration rate. Affected by the initial water content in the soil, the initial water content of each closed grassland is significantly different ($p < 0.05$), and the determination coefficient R^2 is between 0.92 and 0.99. In Kostiakov model, parameter a represents the speed of infiltration rate decay, EN10 grassland infiltration rate attenuates fastest and reaches stability at first, b represents the trend of soil infiltration rate changing with time, its variation range is 0.14~0.17, the variation range is tiny, and the determination coefficient R^2 is between 0.74 and 0.85. In the simulations of the cumulative evaporation process, the Black model F is the regulation coefficient and B represents the rate of soil evaporation, which ranges from 11.35 to 13.06. CK and EN3 grasslands have smaller values of B, and EN10 grasslands have rapid changes in soil evaporation. The coefficient of determination R^2 for this model is between 0.90 and 0.91. The Ross model parameter C represents the steady evaporation rate and D represents the water diffusion rate. The stable evaporation dimension of grassland at different enclosure periods is 1.58–1.85 and the difference in water diffusion is large. The EN7 grassland has the smallest water diffusion rate, with a determination coefficient R^2 of 0.93. The parameters A and B of the Power function model are varied by one bit, and the coefficient of determination R^2 of the model is also 0.93. Further evaluation of the simulation effects of the two models is needed.

The fit effects of the three infiltration models are analyzed. As shown in Figure 5, the measured values of the soil infiltration process are compared with the calculated values of the three infiltration models. The simulation effect of Horton model on water infiltration process of three kinds of enclosed grassland and grazing grassland is excellent, the initial infiltration rate and stable infiltration rate are close to the measured values, the relative error of initial infiltration rate is less than 0.76%, and the relative error of stable infiltration rate is less than 0.94%. The Horton model is able to better model the inflection point of the infiltration process during the infiltration transient phase. The Philip model is second only to the Horton model for the simulation of the initial infiltration rate and the steady infiltration rate, with relative errors of less than 5.01 percent and 1.94 percent, respectively, but the transient inflection point model performs poorly. The Kostiakov model has a poor simulation for the initial infiltration rate, with a relative error of more than 23.9 percent for the initial infiltration rate, and a relatively good simulation for the steady infiltration rate, with a relative error of less than 2.1 percent. The simulation results of the three models are close to those of the steady infiltration and can better simulate the steady infiltration phase.

We analyze the effect of fitting the three evaporation models. It can be seen in Figure 6 that the measured values of the cumulative evaporation process of the soil are compared with the calculated values of the three evaporation models. The Black model exhibits some bias in simulating cumulative evaporation for enclosed grasslands and grazing grasslands, with a downward shift in the starting point and a relative error ranging from 5.27% to 6.67%. In contrast, both the Rose model and Power function model provide relatively more favorable simulations, accurately capturing initial evaporation rates and final accumulation values of cumulative evaporation. The error between simulated and measured values for the Rose model ranges from 2.67% to 3.08%, while that for the Power function model is between 0.15% and 3.52%.

Three infiltration models and three evaporation models can simulate the evaporation process and infiltration process of grassland soil in arid and semi-arid areas, but there are certain differences in the final simulation effect. The simulation effect of some models is relatively close, and it is impossible to judge the advantages and disadvantages of the model intuitively. Therefore, the simulation effect of the infiltration model and evaporation model is evaluated by using the relative mean square root error RRMSE, average absolute error MAE and the whole group residual coefficient CRM. As can be seen from Table 3, the RRMSE of the Horton model is lower than the Philip model and the Kostiakov model in the three enclosure time grasslands, and only higher than the Philip model in the grazing grassland, but lower than the Kostiakov model;

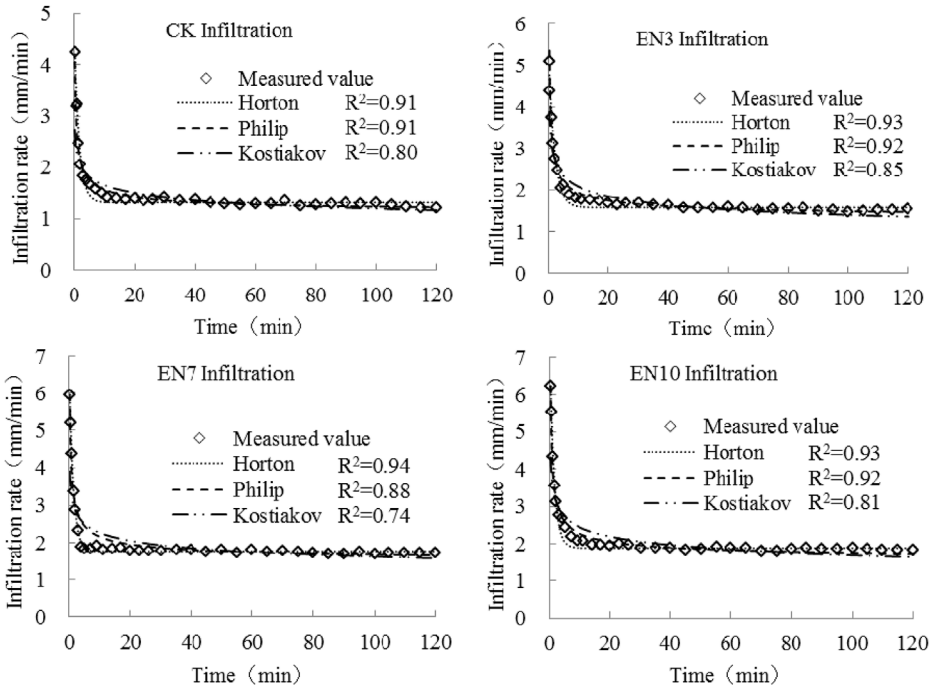

FIGURE 5
The effect of infiltration model simulation.

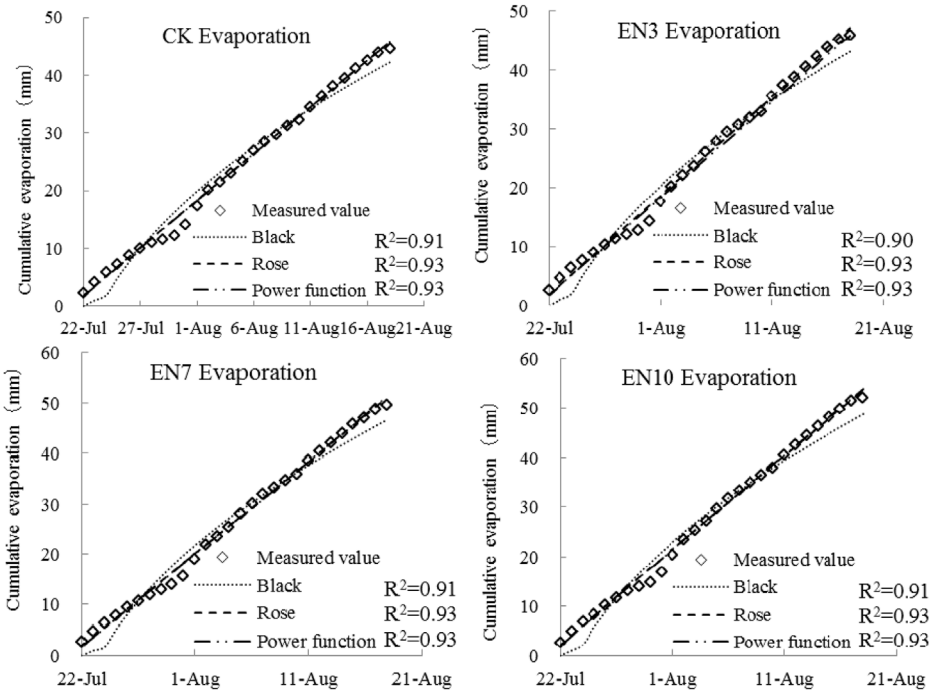

FIGURE 6
The effect of evaporation model simulation.

MAE in the grazing grassland and the enclosure 3-year grassland is higher than the Philip model, but lower than the Kostiakov model, which is the lowest in both 7 years of enclosed grasslands and 10 years of enclosed grasslands; the Horton model is lower than 0.1 in the CRM of CK and EN7 grassland, with a maximum value of 0.2, while the Philip model is only lower in EN3 grassland, the maximum value is 0.27. And

TABLE 3 Error analysis of infiltration model and evaporation model.

Infiltration model	Horton model			Philip model			Kostiakov model		
	RRMSE	MAE	CRM	RRMSE	MAE	CRM	RRMSE	MAE	CRM
CK	0.086	0.089	0.002	0.081	0.072	0.010	0.212	0.168	0.045
EN3	0.060	0.087	0.017	0.060	0.074	0.002	0.162	0.193	0.027
EN7	0.030	0.045	0.003	0.122	0.167	0.027	0.258	0.320	0.020
EN10	0.061	0.087	0.020	0.074	0.111	0.010	0.209	0.273	0.035
Evaporation Model	**Black Model**			**Rose Model**			**Power Function Model**		
	RRMSE	MAE	CRM	RRMSE	MAE	CRM	RRMSE	MAE	CRM
CK	0.091	1.829	0.005	0.040	0.611	0.011	0.040	0.618	0.009
EN3	0.093	1.886	0.013	0.039	0.658	0.006	0.045	0.951	0.018
EN7	0.089	1.935	0.017	0.037	0.696	0.006	0.037	0.696	0.006
EN10	0.090	2.041	0.024	0.035	0.641	0.008	0.035	0.648	0.009

the CRM value of the Kostiakov model is greater than 0.2. For the simulation of soil cumulative evaporation process of the three models, the RRMSE and MAE of the Black model are higher than the Rose model and the Power function model, and the RRMSE and MAE of the Rose model are less than or equal to the Power function model. Except for grazing grassland, the CRM of the Black model is higher than the Rose model and the Power function model. The CRM of the Rose model in CK is higher than the Power function model, and the rest is lower than the Power function model. The simulated value of soil water infiltration process calculated by Horton model is the closest to the measured value, and the simulation accuracy is the highest. The simulation value of the soil water accumulation evaporation process calculated by the Rose evaporation model is the closest to the actual measured value, and the simulation accuracy is the highest.

Discussion

The soil water content of grasslands in arid and semi-arid regions is a major factor affecting the ecological environment of grasslands. Human activities such as over-grazing contribute to grassland degradation by affecting water supply and nutrient transport through the topsoil. For the restoration and improvement of degraded grassland, closure measures also make use of long-term vegetation decay and decay to form aggregates, improve soil texture, optimize soil water storage conditions, improve water use efficiency, and support grassland vegetation recovery and growth (Zhang et al., 2012). Hulunbuir Grassland is located in the arid and semi-arid climate zone in northern China, with little precipitation and large evaporation, and poor anti-interference ability of grassland ecological environment. Due to the influence of grazing activities, a large area of grassland has been degraded. The use of enclosure measures to restore the growth and development of grassland vegetation has effectively alleviated the grassland degradation caused by overgrazing to a great extent (Zhao and Yang, 2010). There are differences in soil water storage in grassland with different sealing time. The effect of enclosure time on grassland soil was significant in the early stage of enclosure, and the depth of soil water storage area gradually expanded with the increase of enclosure time, but the increase of water storage area became slow when the enclosure time increased to a certain value. This result is consistent with the study of soil water and vegetation community structure of grassland by different disturbance methods conducted by Wang et al. (2020) in desert steppe of Ningxia. Closure measures can increase the activity of soil water and change the depth of water storage area.

The soil infiltration process of grassland was mainly affected by vegetation cover, soil texture, bulk density, porosity, initial water content and other factors, in addition to the intensity of water supply. At the initial infiltration stage, influenced by matrix potential, soil water content was the main controlling factor, and the infiltration rate gradually decreased with the increase of infiltration time (Sochorec et al., 2015). The enclosed grassland indirectly affects soil texture structure and changes soil porosity through vegetation growth alternations, thus affecting the infiltration process of the grassland soil. The soil permeability and soil water storage energy of the enclosed grassland for 10 years and 7 years were significantly higher than those of the enclosed grassland for 3 years and grazing grassland. Mainly due to the long closure restoration, the vegetation cover of the grassland increased significantly. Every year vegetation grows and dies, and the litter is converted into humus to provide more organic matter to improving soil structure. At the same time, long-term closed grassland will grow surface vegetation with lush roots, and a large number of capillary heels will increase soil pore diameter during the growth process, and enhance soil infiltration and moisture retention ability. This situation is consistent with the results of Lu et al. (2018) research on soil infiltration characteristics of different vegetation communities in the northwest wind-blown sand region, both of which concluded that the better the vegetation growth status of grassland, the stronger the soil infiltration performance. With the increase of enclosure time, the soil infiltration performance of the grassland was limited, indicating that the extension of enclosure time did not improve the overall quality of the grassland after the grassland was restored from degradation to normal state. This result is consistent with the

research of Xu et al. (2020) on grassland productivity in meadow steppe. The main reason is that long sealing time will lead to serious accumulation of ground litter, and a large amount of litter will inhibit the growth of vegetation seedlings and delay the regeneration rate of grassland (Nie et al., 2022), thus affecting the soil infiltration rate.

Soil evaporation is not only an important link of groundwater return to the atmosphere, but it is also a major way of soil water loss. In arid and semi-arid areas, the soil water supply comes primarily from precipitation, the vegetation growth of grassland is mainly controlled by soil water content. Therefore, inhibiting ineffective evaporation and improving the water use efficiency of grassland vegetation are of great significance for ecological restoration of grazing grassland. The process of soil evaporation is affected by the external natural environment and soil water content. When the water content is saturated, soil evaporation is carried out at the evaporation rate of water surface. With the decrease of soil water content, soil water supply is transformed into capillary water supply and finally into water vapor diffusion (Dam et al., 2022). Soil evaporation is the main link of soil water loss in arid and semi-arid areas, and effective suppression of evaporation can alleviate soil water shortage to a greater extent. On the basis of improving the characteristics of grassland vegetation community, enclosure measures affect soil structure and soil water storage function through vegetation growth, and enclosure of grassland surface vegetation cover can also effectively slow down soil water evaporation (Liu et al., 2019). In this study, the soil evaporation of the enclosed grassland for 10 years was greater than that of the grassland with other disturbance measures, and the result was different from the soil evaporation characteristics measured by Liu et al. (2019) in the alpine steppe of the Tibetan Plateau. Liu et al. (2019) believed that the greater the surface cover biomass, the lower the evaporation. The reason for this difference is that, in the process of measuring soil evaporation of grassland with different enclosure periods, the surface covering vegetation and litter were artificially removed, and the bare soil evaporation experiment was conducted under different disposal measures, mainly to identify the differences in soil evaporation caused by enclosure measures on soil structure and eliminate the influence of vegetation cover on soil evaporation. Grazing forbedden and enclosure can improve soil porosity, increase soil water transfer capacity and water conservation capacity of grassland. The initial effect of sealing was obvious and reached the peak in 3 ~ 7 years. With the further increase of sealing time, the soil hydrological characteristics did not change significantly. This result is consistent with the results of Zhang's research on the soil water characteristics of the alpine meadow in the source of the Yellow River (Zhang et al., 2023). Proper closure is conducive to the restoration of the grassland ecosystem, but long-term closure cannot achieve a good grassland ecosystem.

Conclusion

(1) Grassland enclosure measures can effectively improve soil water content, and the overall soil water content shows that the grassland with 10 years of enclosure > the grassland with 7 years of enclosure > the grassland with 3 years of enclosure > the grazing grassland. In the vertical direction, the soil water content increased first and then decreased. Compared with grazing grassland, the soil water storage depth could be widened by increasing the time of enclosure.

(2) The changes of initial infiltration rate and stable infiltration rate of grassland with different sealing time were significant ($p < 0.05$). The highest was found in the grassland with 10 years of sealing, followed by the grassland with 7 years of sealing, and the lowest was found in the grassland with 3 years of sealing. The variation of soil evaporation in different enclosed grasslands was consistent, the soil evaporation rate was the grassland with 10 years of enclosure > the grassland with 7 years of enclosure > the grassland with 3 years of enclosure > the grazing grassland. The soil hydrological characteristics of grassland changed significantly in the early stage of enclosure, and reached the peak in 3–7 years. With the increasing of enclosure time, the soil hydrological characteristics did not change significantly.

(3) The Horton model, the Philip model and the Kostiakov model can be used to model the infiltration process in grasslands at different closure times. The Horton model is able to better model the inflection point of the infiltration process, and the fit accuracy is higher than that of the Philip and Kostiakov models. Black model, Rose model and Power function model simulated the cumulative evaporation process of grassland soil at different sealing times. The simulated value calculated by Rose model was the closest to the measured value, and the simulation accuracy was the highest.

Data availability statement

The original contributions presented in the study are included in the article/Supplementary Material; futher inquiries can be directed to the corresponding authors.

Author contributions

CF: Writing–original draft. JG: Data curation, Writing–review and editing. XL: Investigation, Writing–review and editing. CZ: Writing–review and editing. TW: Writing–review and editing, Conceptualization, Investigation, Methodology.

Funding

The authors declare that financial support was received for the research, authorship, and/or publication of this article. The present study was funded by the Postdoctoral Science Foundation of China (Grant No. 2020M673548XB), the Natural Science Foundation of Inner Mongolia Province (Grant Nos 2021MS04005, 2024MS05053), the Doctor Innovation Fund project of Jining Normal University (Grant Nos jsbsjj2324, jsbsjj 1802), the Basic research project of Ulanqab (Grant No. 2021JC322).

Conflict of interest

The authors declare that the research was conducted in the absence of any commercial or financial relationships that could be construed as a potential conflict of interest.

Publisher's note

References

Bristow, K. L., Imnek, J., Helalia, S. A., and Siyal, A. A. (2020). Numerical simulations of the effects furrow surface conditions and fertilizer locations have on plant nitrogen and water use in furrow irrigated systems. *Agric. Water Manag.* 232, 106044–106055. doi:10.1016/j.agwat.2020.106044

Chamizo, S., Cantón, Y., Domingo, F., and Belnap, J. (2013). Evaporative losses from soils covered by physical and different types of biological soil crusts. *Hydrol. Process.* 27 (3), 324–332. doi:10.1002/hyp.8421

Cui, Z., Huang, Z., Luo, J., Qiu, K., López-Vicente, M., and Wu, G. L. (2021). Litter cover breaks soil water repellency of biocrusts, enhancing initial soil water infiltration and content in a semi-arid sandy land. *Agric. Water Manag.* 255, 107009–106999. doi:10.1016/j.agwat.2021.107009

Dam, B. R. V., Lopes, C. C., Polsenaere, P., Price, R. M., Rutgersson, A., Fourqurean, J. W., et al. (2021). *Water temperature control on CO2 flux and evaporation over a subtropical seagrass meadow revealed by atmospheric eddy covariance* (Hoboken, New Jersey, United States: Wiley).

De Souza Machado, A. A., Lau, C. W., Till, J., Kloas, W., Lehmann, A., Becker, R., et al. (2018). Impacts of microplastics on the soil biophysical environment. *Environ. Sci. Technol.* 52 (17), 9656–9665. doi:10.1021/acs.est.8b02212

Fan, C. R., and Wang, T. (2021). Soil health assessment of typical grasslands differing in grazing intensity. *Ecol. Sci.* 40 (05), 140–148. doi:10.14108/j.cnki.1008-8873.2021.05

Guan, H. J., and Cao, R. J. (2019). Effects of biocrusts and rainfall characteristics on runoff generation in the Mu US desert, Northwest China. *Hydrology Res.* 50 (5), 1410–1423. doi:10.2166/nh.2019.046

Jiao, J. Y., Zhang, Y., and Zhu, J. T. (2017). Direct hydraulic parameter and function estimation for diverse soil types under infiltration and evaporation. *Transp. Porous Media* 116, 797–823. doi:10.1007/s11242-016-0801-0

Liao, Y. C., Liu, H. X., Li, X., Hu, Q. Y., and Xue, W. K. (2021). By increasing infiltration and reducing evaporation, mulching can improve the soil water environment and apple yield of orchards in semiarid areas. *Agric. Water Manag.* 253 (1), 106936–106948. doi:10.1016/j.agwat.2021.106936

Liu, Z. W., Li, S. G., Zhang, Y. S., Guo, Y. H., Wei, W., Wang, K. X., et al. (2019). Evaporation characteristics of alpine meadow in Tibetan Plateau and the influencing factors. *J. Arid Land Resour. Environ.* 33 (9), 87–93. doi:10.13448/j.cnki.jalre.2019.270

Lu, G., Zhai, J. X., Li, Y. X., Wang, L., and Wang, Y. (2018). Soil infiltration characteristics of different plant community in sandy land of northwestern Liaoning. *Agric. Res. Arid Areas* 36 (04), 133–139. doi:10.7606/j.issn.1000-7601.2018.04.19

Machado, A. A. D. S., Lau, C. W., Kloas, W., Bergmann, J., Bachelier, J. B., Faltin, E., et al. (2019). Microplastics can change soil properties and affect plant performance. *Environ. Sci. Technol.* 53 (10), 6044–6052. doi:10.1021/acs.est.9b01339

Nie, Y. Y., Chen, J. Q., Xin, X. P., Xu, J. J., Yang, G. X., Wang, X., et al. (2021). Responses of niche characteristics and species diversity of main plant populations to duration of enclosure in the Hulun Buir meadow steppe. *Acta Prataculturae Sin.* 30 (10), 15–25. doi:10.11686/cyxb2021127

Nie, Y. Y., Xin, X. P., Xu, L. J., and Yang, G. X. (2022). Effects of enclosure measures on grassland and productivity in Hulunbeier meadow steppe. *Chin. J. Agric. Resour. Regional Plan.* 43 (8), 74–82. doi:10.7621/cjarrp.1005-9121.20220808

Niu, W. Q., Zou, X. Y., Liu, J. J., Zhang, M. Z, Lü, W., Gu, J., et al. (2016). Effects of residual plastic film mixed in soil on water infiltration, evaporation and its uncertainty analysis. *Trans. Chin. Soc. Agric. Eng.* 32 (14), 110–119. doi:10.11975/j.issn.1002-6819.2016.14.016

Saad, A. F. (2018). Recycling rice straw as an amendment for improving soil evaporation and infiltration rates in sandy soils. *Alexandria Sci. Exch. J.* 39 (2), 370–378. doi:10.21608/ASEJAIQJSAE.2018.9269

Sochorec, M., Jandák, J., Raus, J., Kvasnovský, M., and Knot, P. (2015). Influence of different grassland management on water infiltration and soil physical properties. *Bulg. J. Agric. Sci.* 21 (3), 573–578. doi:10.1016/0959-8049(93)91355-O

Sun, Z., Yang, J. N., Zhu, R. Y., Zhou, C., Yang, M., Pan, Y., et al. (2019). Contrasting effects of corn straw biochar on soil water infiltration and retention at tilled and compacted bulk densities in the Yellow River Delta. *Can. J. Soil Sci.* 99 (4), 357–366. doi:10.1139/cjss-2019-0004

Wan, Y., Wu, C., Xue, Q., and Hui, X. (2019). Effects of plastic contamination on water evaporation and desiccation cracking in soil. *Sci. Total Environ.* 654, 576–582. doi:10.1016/j.scitotenv.2018.11.123

Wang, Z. C., Li, X. Y., Shi, H. B., Zhang, D. L., and Xu, P. C. (2017). Effects of residual plastic film on infiltration and evaporation for sandy loam and sandy soil. *Trans. Chin. Soc. Agric. Eng.* 48 (1), 198–205. doi:10.6041/j.issn.1000-1298.2017.01.026

Wang, Z. J., Jiang, Q., Wu, X. D., Yu, H. Q., Ji, B., He, J. L., et al. (2020). Effects of different disturbance modes on soil moisture and vegetation community in desert steppe of Ningxia. *Heilongjiang Animal Husb. Veterinary Med. China* (24), 103–107. doi:10.13881/j.cnki.hljxmsy.2020.04.0464

Xu, L., Nie, Y., Chen, B., Xin, X., Yang, G., Xu, D., et al. (2020). Effects of fence enclosure on vegetation community characteristics and productivity of a degraded temperate meadow steppe in northern China. *Appl. Sci.* 10 (8), 2952. doi:10.3390/app10082952

Yang, K., Tang, Z., and Feng, J. (2020). Effect of Co-use of fly ash and granular polyacrylamide on infiltration, runoff, and sediment yield from sandy soil under simulated rainfall. *Agronomy* 10 (3), 344–354. doi:10.3390/agronomy10030344

Yu, Z., Lue, H., Zhu, Y., Drake, S., and Liang, C. (2010). Long-term effects of revegetation on soil hydrological processes in vegetation-stabilized desert ecosystems. *Hydrol. Process.* 24 (1), 87–95. doi:10.1002/hyp.7472

Zhang, A. K. W., Zhao, W., Li, X., Jia, A., and Kang, W. (2021). Contribution of soil macropores to water infiltration across different land use types in a desert-oasis ecoregion. *Land Degrad. Dev.* 32 (4), 1751–1760. doi:10.1002/ldr.3823

Zhang, D., Zhou, Z., Zhang, B., Du, S., and Liu, G. (2012). The effects of agricultural management on selected soil properties of the arable soils in Tibet, China. *Catena* 93, 1–8. doi:10.1016/j.catena.2012.01.004

Zhang, M. Y., Li, X. J., Yang, Y. S., Wang, B. J., and Yang, L. (2023). Effects of forbidden grazing and enclosure on vegetation community structure and soil moisture characteristics in alpine meadow of the Yellow River source. *Acta Bot. sin.* 43 (7), 1185–1197. doi:10.7606/j.issn.1000-4025.2023.07

Zhao, P., Yang, H., Zhang, X., Xu, X., Zhou, C., and Yang, W. (2010). Spatial variability of soil moisture at typical alpine meadow and steppe sites in the Qinghai-Tibetan Plateau permafrost region. *Environ. Earth Sci.* 63, 477–488. doi:10.1007/s12665-010-0716-y

frontiers | Frontiers in Environmental Science

TYPE Original Research
PUBLISHED 24 June 2024
DOI 10.3389/fenvs.2024.1428058

OPEN ACCESS

EDITED BY
Zhiming Han,
Northwest A&F University, China

REVIEWED BY
Wang Junjie,
Ocean University of China, China
Xinchen Gu,
Tianjin University, China
Dian Yuan,
Nanjing University of Information Science and Technology, China

*CORRESPONDENCE
Hanyu Lu,
teesn463@gues.edu.cn

RECEIVED 06 May 2024
ACCEPTED 30 May 2024
PUBLISHED 24 June 2024

CITATION
Ren J, Dong Y, He P and Lu H (2024), Spatial-temporal changes of landscape ecological risk in the Liuchong river basin from the perspective of production-life-ecological space.
Front. Environ. Sci. 12:1428058.
doi: 10.3389/fenvs.2024.1428058

Spatial-temporal changes of landscape ecological risk in the Liuchong river basin from the perspective of production-life-ecological space

Jintong Ren[1,2], Yanqin Dong[3], Panxing He[4] and Hanyu Lu[1,2]*

[1]School of Ecological Engineering, Guizhou University of Engineering Science, Bijie, China, [2]Guizhou Province Key Laboratory of Ecological Protection and Restoration of Typical Plateau Wetlands, Bijie, China, [3]School of Civil and Surveying Engineering, Jiangxi University of Science and Technology, Ganzhou, China, [4]Ministry of Education Key Laboratory for Biodiversity Science and Ecological Engineering, School of Life Sciences, Fudan University, Shanghai, China

Promoting the construction of ecological civilization and sustainable development in karst mountainous areas by analyzing the spatial and temporal changes of landscape ecological risks is critical in karst mountainous watersheds. In this study, the land use transfer matrix, landscape ecological risk evaluation model, ecological contribution rate of land use change, and spatial autocorrelation analysis were combined to quantitatively analyze the land use and landscape ecological risk of a typical karst watershed, Liuchong River Basin, over the past 20 years. The results revealed that: 1) From 2000 to 2020, the functional classification of land use in the Liuchong River Basin was dominated by the woodland ecological space, and the most significant shifting characteristics were the increase in the area of watershed ecological space and industrial production space and the decrease in woodland ecological space, with shifts in the middle reaches of the Liuchong River being the most drastic; 2) Generally, the change of the regional landscape pattern was related to the transformation of the land use function type of "production-life-ecological space," and the spatial aggregation of ecological risk level showed a gradual weakening trend. 3) The conversion of the watershed ecological space to the grassland ecological and agricultural production spaces, the conversion of urban living space to the agricultural production space, and the conversion of the rural living space to the agricultural production space were the dominant factors affecting ecological improvement, whereas the conversion of the woodland ecological space to the grassland ecological space, the woodland ecological space to the agricultural production space, and the grassland ecological space to the agricultural production space contributed to ecological degradation. The study findings can be used as a reference for the coordinated development of "production-life-ecological space" in karst watersheds and provide a scientific basis for ecological environmental protection and sustainable utilization.

KEYWORDS

landscape ecological risk, production-life-ecological space, spatial and temporal changes, Liuchong river basin, ecological risk

1 Introduction

Ecological risk is the amount of risk an ecosystem and its components are exposed under natural or anthropogenic disturbances (Yu et al., 2022). Landscape ecological risk assessment can reflect the effect of landscape patterns on ecological processes and functions (Liu et al., 2022; Ran et al., 2022). Urban growth patterns in China exhibit a trend of sprawling expansion, which has led to a considerable increase in the level of urbanization and a drastic expansion in the scale of land use. However, urbanization has caused several problems, including encroachment on productive agricultural and ecological land, deepening landscape fragmentation, and ecological pollution. These problems have resulted in an imbalance in the ratio of the production-life-ecology spatial structure (Bai et al., 2019; Qi, 2020; Zhang et al., 2021; Lu et al., 2022). Especially in the karst mountainous areas of southwest China, the frequent natural and human activities and the increasing level of economic development and urbanization have exerted a considerable ecological and environmental pressure on the ecologically fragile and environmentally change-sensitive karst mountain belt. In this context, the 18th Party Congress proposed ecological civilization construction to control the development intensity and adjust the spatial structure and balance population, resources and environment, and unify economic, social and ecological benefits, for promoting intensive and efficient production space, livable and moderate living space, and beautiful ecological space, with nature restoration, good land for agriculture, and a beautiful home with blue sky, green land, and clean water for future generations. Thus, the construction of ecological civilization has gradually become the prime focus of national land space development.

By providing novel perspectives for regional ecological risk research, the landscape pattern index method has become a research hotspot (Guo and Guo, 2022; Li et al., 2023). To construct landscape ecological risk evaluation models, corresponding parameters are chosen according to the specificity of landscape patterns in various research regions. This approach has been applied in many risk control regions, yielding excellent results. For example, Hayes et al. used a relative risk model to assess regional ecological risk in the near-coastal marine environment of northwest Washington and identified ship traffic, mountainous urban, and agricultural land use, and shoreline recreational activities as the ecological risk factors in the marine nearshore area (Hayes and Landis, 2004). Ayre analyzed (Ayre and Landis, 2012) a forested landscape in northeastern Oregon from a landscape disturbance, habitat, and ecological resource perspective based on a Bayesian network model with an ecological risk assessment framework. Paukert conducted a landscape-scale ecological risk assessment of land use, waterway development and diversion, and human development in the lower Colorado River basin at four watershed scales (Paukert et al., 2011). Studies in China have investigated the factors affecting landscape ecological risk (LER) from the perspective of landscape ecology and elucidated the dynamics of LER and its spatial and temporal patterns. Kang constructed a LER index for the Manas River basin from the proportion of landscape components during 2000–2015 and then compared the distribution of various levels of LER and spatial and temporal distribution in the region (Kang et al., 2020). Based on the landscape ecological risk index and geographically weighted regression model, Wang revealed the interconnection between the levels of LER and urban expansion in Yuanzhou district from 2000 to 2018 (Wang et al., 2021). Liu constructed an ecological risk evaluation model from the watershed scale and water source protection zone scale to examine the spatial and temporal changes of ecological risk in the Miyun Reservoir watershed during 1990–2018 (Liu et al., 2023). Lan evaluated the spatial and temporal evolution characteristics of ecological risk in Guilin city at the overall and county scales based on the spatial correlation between land use and ecological risk in the city during 2000–2020 (Lan et al., 2023). Although studies on LER evaluation are relatively mature, limited research has been conducted on LER in karst mountains (Wang et al., 2022a). In addition, most studies have focused on a single land use type, and fewer studies have analyzed LER from the perspective of "production-life-ecological space" (Su et al., 2020; Wang et al., 2022b).

The continuous development of the global economy, technology, and population has further strengthened the effect of human activities on the natural environment. The karst region has considerably higher ecosystem fragility and environmental vulnerability than other regions because of its unique geological and climatic conditions. Being an important region, effectively promoting the healthy development of ecological environment in the watershed is a concern. Therefore, this study analyzed the spatial and temporal evolution patterns of ecological risk in the Liuchong River Basin from the spatial perspective of "three lives," based on the land use data of 2000, 2010, and 2020. Furthermore, by integrating the results with geographical information system (GIS) spatial analysis and LER index, the spatial evolution of production-ecology in the context of rapid socio-economic development was clarified. The spatial evolution process of life ecology and LER in the context of rapid socio-economic development was considered to provide a reference for ecological risk management and landscape pattern optimization in typical karst mountainous basins.

2 Materials and methods

2.1 Study area

Liuchong River is the largest first-order tributary of the Wujiang River system, with a total length of 273.4 km and a natural drop of 1,243 m. Because of geomorphology and hydrogeology constraints, the river is tortuous, with deep valley, narrow surface and large drop. The Liuchong River Basin is located in Bijie City, northwestern Guizhou Province and southwestern Zhenxiong County, Yunnan Province, with longitude and latitude ranges of 104°20′-160°07′E and 26°31′-27°30′N, respectively. The total area of the basin is 10,874 km^2 (Figure 1). The basin is a typical karst mountainous watershed with karst landform development and complex topography. The watershed belongs to a subtropical cool and humid monsoon climate, with moderate water and heat resources. The annual average temperature is approximately 18 °C, and the precipitation is concentrated in May-September, with an annual average precipitation of 848.6–1394.4 mm. Because of the fragile ecological environment in the watershed, the ecological landscape security in the watershed is has attracted considerable research attention because of the continuous

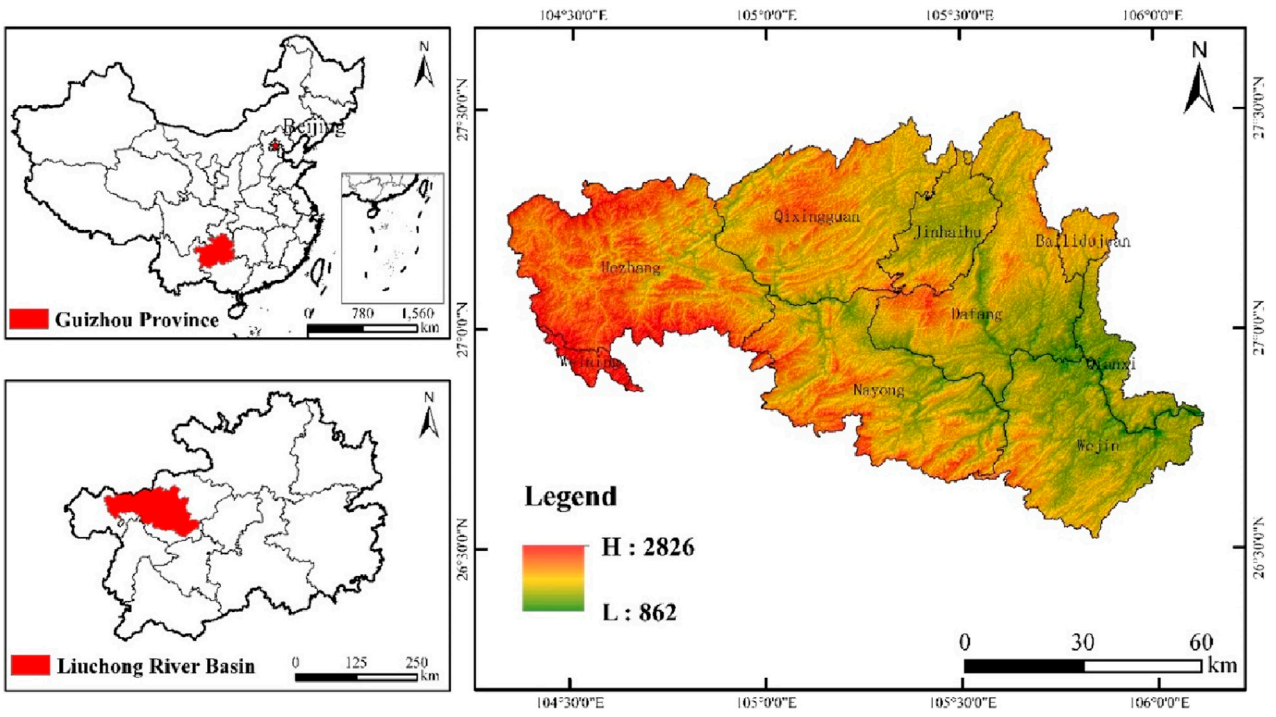

FIGURE 1
Location map of the study area.

TABLE 1 Classification of dominant land use functions.

Primary functional classification	Secondary functional classification	Tertiary land classification
Production space	Agricultural space	11 (paddy field), 12 (dry land)
	Industrial space	53 (industrial and mining construction land)
Living space	Urban space	51 (urban residential land)
	Rural space	52 (rural residential land)
Ecological space	Forested space	21 (forested land), 22 (shrub land), 23 (open forest land), and 24 (other forest lands)
	Grass space	31 (high-cover grassland), 32 (medium-cover grassland), and 33 (low-cover grassland)
	Water space	41 (rivers and canals), 42 (lakes), 43 (reservoir ponds), 44 (permanent glaciers), 45 (mudflats), 46 (mudflats)
	Other spaces	61 (sandy land), 62 (Gobi), 63 (saline land), 64 (marshland), 65 (bare land), 66 (bare rocky gravel land)

urbanization and accelerated comprehensive development and utilization of the watershed in the past 20 a.

2.2 Data

Land use data of the Liuchong River Basin for three periods from 2000 to 2020 (2000, 2010, 2020) were obtained from the Resource and Environment Science Data Center of the Chinese Academy of Sciences (http://wwwresdc.cn), with the spatial resolution of 30 m. Using ArcGIS 10.6, the land use data were projected and transformed, spliced, and cropped. Based on the development objective of building the efficient production space (PS), livable space (LS), and beautiful ecological space proposed by the government and the actual situation of the watershed and according to the land use classification system, PLES was classified into eight secondary categories, namely agricultural production space, industrial production space, urban living space, rural living space, forest ecological space, grassland ecological space, water ecological space, and other ecological spaces (Table 1).

TABLE 2 Calculation method for the landscape pattern index and its ecological meaning.

Landscape pattern index	Formula and its ecological meaning
Landscape fragmentation	$C_i = n_i/A_i$; where n_i is the number of patches of landscape type i; and A_i is the total area of landscape type i. Landscape fragmentation characterizes the degree of fragmentation of landscape types, reflecting the complexity of landscape spatial structure, which is caused by natural or man-made disturbance of the landscape from a single, homogeneous, and continuous whole tends to complex, heterogeneous, and discontinuous patch mosaic process
Landscape Separation	$N_i = \frac{1}{2}\sqrt{n_i/A} \cdot P_i$, $P_i = A/A_i$; where A indicates the proportion of the total area of the landscape patches. The degree of landscape separation characterizes the degree of separation of various elements or individual distribution of patches in a landscape type, and the greater the degree of separation is, the more dispersed the landscape is in terms of geographical distribution and the more complex the landscape distribution is
Number of landscape sub-dimensions	$F_i = 2\ln(p_i/4)/\ln A_i$, where p_i is the perimeter of the landscape type and indicates the complexity of shape and spatial stability of the landscape patches
Landscape disturbance degree	$U_i = aC_i + bF_i + cD_i$; where: a, b, and c denote the corresponding weights of landscape fragmentation, separation, and dominance, respectively, based on a previous study (Zhan et al., 2009), and are assigned the corresponding weights of 0.5, 0.3, and 0.2, with a + b + c = 1. The landscape disturbance degree indicates the degree to which the ecosystems represented by various landscape types are disturbed by human activities
Landscape fragility	The landscape vulnerability index is a critical quantitative index that indicates the stability of the landscape to maintain its physical and chemical properties under the influence of external factors, also called the landscape external disturbance resistance, with reference to existing research results (Chen et al., 2022a), and combined with the actual situation of the study area. The eight secondary land categories in the study area were assigned values from low to high: urban living space, 1; rural living space, 2; woodland ecological space, 3; grassland ecological space, 4; agricultural production space, 5; watershed ecological space, 6; industrial production space, 7; and other ecological spaces, 8, with normalized sizes of 0.03, 0.06, 0.08, 0.11, 0.14, 0.14, 0.17, 0.19, and 0.22, respectively
Landscape loss degree	$R_i = U_i \times S_i$; R_i indicates the degree of loss of natural attributes of the ecosystems represented by various landscape types when subjected to natural and anthropogenic disturbances

2.3 Methods

2.3.1 Division of the LER assessment unit

To make the LER index reflect the ecological risk status caused by landscape changes in a certain area, a quantitative expression was used to portray the degree of spatial ecological risk, according to the basic requirements and principles of landscape ecology, and using 2–5 times the average patch area for the grid is appropriate, considering the study area and landscape spatial heterogeneity. After repeated debugging, a square grid of 3 km × 3 km was selected as the study area. The center point of each grid was considered to be the sampling point, totaling 1240 sampling points. The ecological risk index was calculated for each of the 1240 cells in the study area based on this grid division and used as the ecological risk value of the sample area center point for spatial interpolation analysis.

2.3.2 The LER assessment model

To examine the spatial and temporal variability and characteristics of landscape ecological risk in the Liuchong River Basin, a landscape ecological risk evaluation model was constructed using the calculation of the LER from previous studies (Su et al., 2020).

$$ERI_k = \sum_{i=1}^{n} \frac{A_{ki}}{A_k} \times R_i \quad (1)$$

Here, ERI_k denotes the regional LER index of the k-th sampling area, n denotes the total number of landscape types, Ak_i denotes the area of landscape type i in the k-th plot, A_k denotes the total area of the k-th plot, and R_i denotes the landscape loss degree index, which is obtained by the product operation of landscape fragility S_i and landscape disturbance U_i. The formula and ecological meaning of the corresponding calculation of landscape pattern index are presented in Table 2.

2.3.3 Ecological contribution rate of PLES land use transformation (LEI)

LEI refers to the land use types leading to ecological risk changes. Quantifying the impact of land use type shifts on the ecological environment from both positive and negative aspects can help in discriminating between the land use types that affect changes in regional ecological quality and identifying the dominant factors for changes in the regional ecological environment (Liang et al., 2022). It is calculated using the following formula:

$$LEI = (LE_{t1} - LE_{t0})LA/TA \quad (2)$$

where LEI indicates the ecological contribution of the regional land use transformation type. The value of LEI ranges from −1 to 1, with a positive number indicating a positive contribution that increases the ecological risk, and a negative number indicating a negative contribution that decreases the ecological risk. LEt1 and LEt0 refer to the ecological risk index of a specific land type before and after transformation, respectively; LA is the area of that change type; TA is the total area of the study area.

3 Results

3.1 Quantitative change and type shift of land use in the PLES

The changes of PLES area and the proportion of PLES in the Liuchong River Basin for 3 years are presented in Table 3, revealing

TABLE 3 Area and change of land use types in the Liu Chong River Basin from 2000 to 2020.

Land use Functional classification	Area/km²			Area of change/km²	
	2000	2010	2020	2000–2010	2010–2020
Forest ecological space	93629.73	95618.42	93202.41	1988.69	−2416.01
Grass Ecological Space	31878.41	29584.88	31331.05	−2293.53	1746.16
Water Ecological Space	406.02	687.99	1046.64	281.97	358.64
Other Ecological Spaces	40.25	29.73	30.39	−10.51	0.66
Urban Living Space	251.95	358.33	681.24	106.38	322.90
Rural Living Space	240.57	270.24	310.16	29.68	39.91
Industrial production space	106.62	244.18	1167.96	137.56	923.78
Agricultural production space	49624.98	49386.65	48403.52	−238.33	−983.13

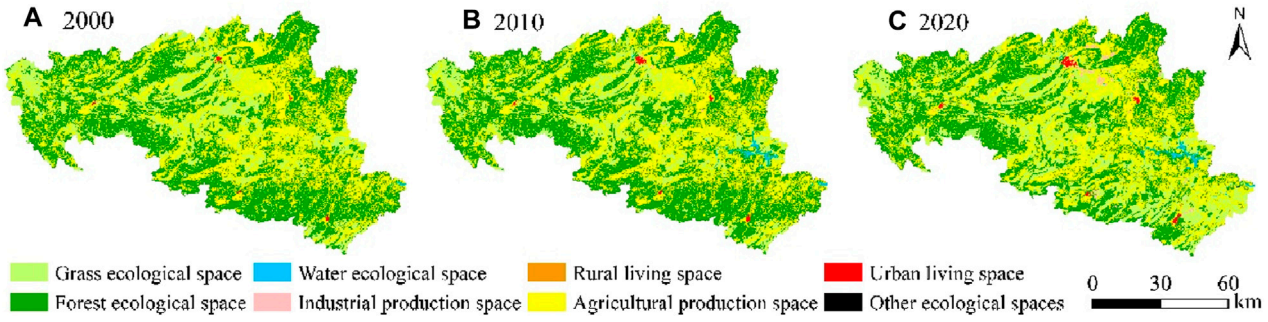

FIGURE 2
PLES distribution pattern in the Liuchong River Basin in 2000 **(A)**, 2010 **(B)**, 2020 **(C)**.

that the area of "production-life-ecological space" in the Liuchong River Basin varied greatly from 2000 to 2020, and the land use function classification in 2000–2020 is woodland ecological space, followed by an agricultural production space. During the study period, the area of woodland and grassland ecological spaces exhibited an overall decrease, with the woodland ecological space of 93629.73 km² in 2000 decreasing to 93202.41 km² in 2020, grassland ecological space shrinking from 31878.41 km² in 2000–31331.05 km² in 2020, and the agricultural production space shrinking from 49624.98 km² in 2000–48403.52 km² in 2020. The area of the water ecological space showed an increasing trend, from 406.02 km² in 2000 to 1046.64 km² in 2020, whereas the area of other ecological spaces did not significantly change. From the perspective of the living space, the area of urban living space and rural living space increased from 251.95 to 240.57 km² in 2000 to 681.24 and 310.16 km² in 2020, respectively. From the perspective of the production space, the area of the industrial production space continued to increase from 106.62 km² in 2000 to 1167.96 km² in 2020, whereas the area of the agricultural production space exhibited a slightly decreasing trend from 49,624.98 km² in 2000 to 48,403.52 km² in 2020.

According to the change patterns in the distribution of PLES in the study area from 2000 to 2020 (Figure 2), the industrial production space underwent the most rapid expansion, the area of urban living, rural living, and watershed ecological spaces exhibited a gradual increase, corresponding to a gradual reduction in the area of agricultural production space, and the woodland ecological space and grassland ecological space exhibited a slight change. Although the area of industrial production space decreased in 2000, which was only sporadically distributed around the urban living space, by 2020, a large expansion was observed along the perimeter of the city, with significant changes in the area.

PLES land use area, in addition to the quantitative increase or decrease, also shows distinct types of transfer. Figure 3 reveals that during the 20-year period, the area transferred out of woodland ecological space was 3667.46 km², reaching the historical maximum, of which 655.33 km² was transformed into the grassland ecological space, and 160.90 km² was transformed into the agricultural production space. The amount of transfer in was only 319.34 km², whereas the amount of transfer out was considerably larger than the amount of transfer in, which indicated that the area of woodland ecological space decreased during the study period. Second, the amount of the agricultural production space transferred out was 3459.94 km², mainly to the woodland ecological and grassland ecological spaces, with an area of 222.91 km², and the amount of transfer in was 280.11 km², converted from the grassland ecological and woodland ecological spaces, with an area of

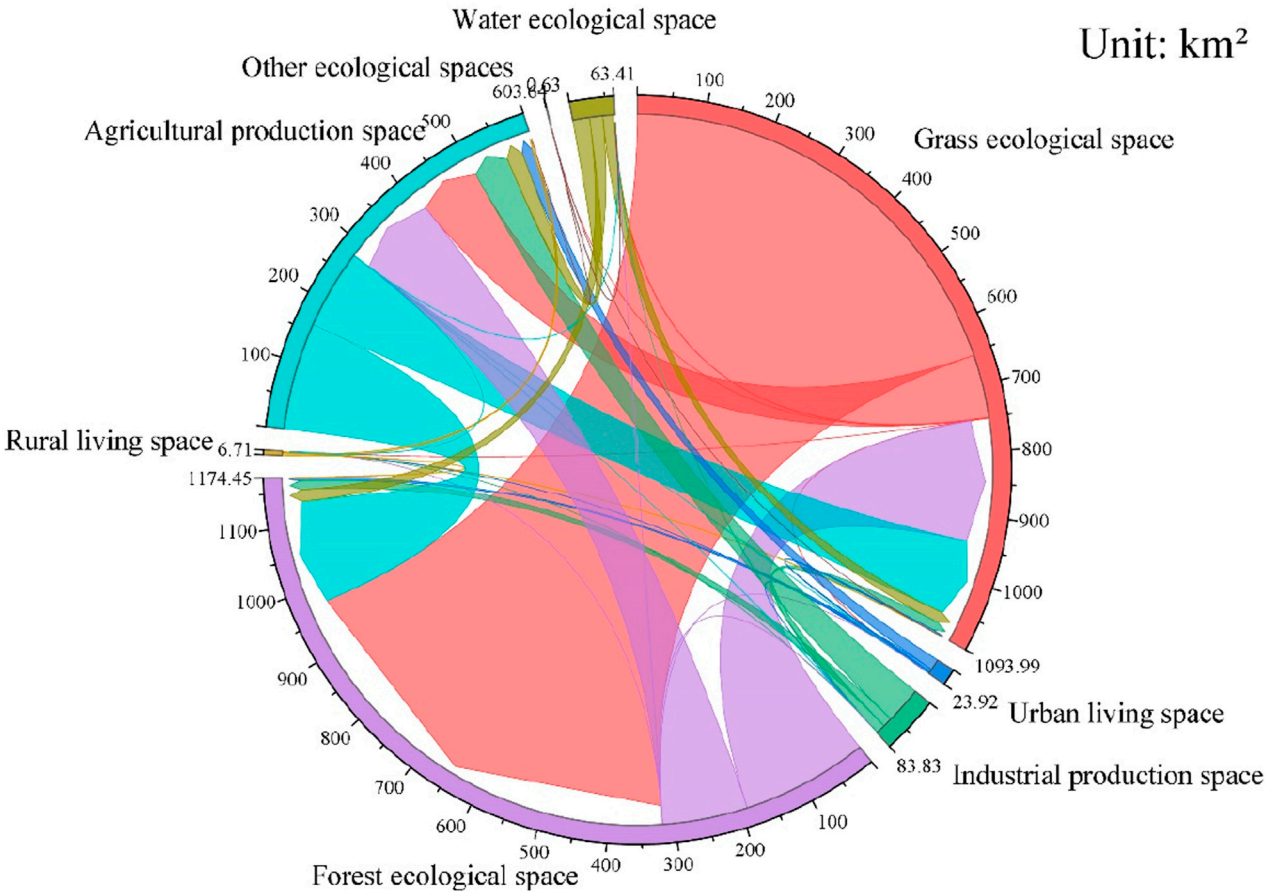

FIGURE 3
PLES land use transfer in the Liuchong River Basin.

279.30 km^2. The grassland ecological space was the type with the most amount of land transfer in, and the area converted from woodland ecological and grassland. The area transformed from woodland ecological space and grassland ecological space amounted to 750.09 km^2.

3.2 Temporal variation in ecological risk in PLES landscapes

Based on the PLES land use raster data of 2000, 2010, and 2020 in the Liuchong River Basin, the ecological risk indexes of each landscape were calculated using Fragstats 4.2 software and combined with the formula 1 and formulas in Table 2; subsequently, the results were compiled (Table 4). As depicted, for over 20 years, the index of fragmentation of agricultural production space remained unchanged; the degree of separation first decreased and subsequently increased, indicating that the aggregation of its landscape type has increased; the fragmentation and separation of industrial production space and rural living space were high, and the values decreased year by year, indicating that their distribution in space is highly dispersed; and the ecological stability increased considerably with the increase in the area. The increase in the area of the urban living space covered the surrounding small patches, resulting in a decrease in fragmentation and separation of the urban living space annually. The fragmentation of the woodland ecological space increased, whereas the fragmentation and separation of grassland, water, and other ecological spaces continued to decline, with the decline for other ecological spaces being linear. Second, the values of the sub-dimension of each landscape type in the Liuchong River Basin were low and exhibited a decreasing trend, indicating that the shape of the landscape types in the study area tended to be simple and the intensity of disturbance by human activities was decreasing. The change trend of the disturbance index of each landscape type was similar to that of the sub-dimension; however, the disturbance index of rural living space and other ecological space was large, with both reached the historical peak at the beginning of the study, indicating that the disturbance index of human activities on rural living space and other ecological space was large in 2000, which reached the historical minimum in 2020, indicating a decrease in the disturbance of human activities on the landscape.

3.3 Analysis of spatial and temporal changes in LER

The ecological risk distribution maps of the study area in 2000, 2010, and 2020 were obtained through kriging interpolation. According to the natural breakpoint method, the

10.3389/fenvs.2024.1428058

TABLE 4 Land Use Transfer Matrix for production-life-ecological space in the Liuchong River Basin (Unit: km²).

Type	Year	Fragmentation degree	Separation degree	Separation dimension	Interference degree	Loss degree
Rural Living Space	2000	0.014	0.1	0.396	0.117	0.016
	2010	0.014	0.097	0.396	0.115	0.016
	2020	0.014	0.1	0.002	0.038	0.005
Industrial production space	2000	0.07	9.608	0.293	2.976	0.565
	2010	0.045	2.81	0.339	0.933	0.177
	2020	0.035	1.008	0.004	0.321	0.061
Urban Living Space	2000	0.004	0.937	0.354	0.354	0.011
	2010	0.003	0.547	0.375	0.24	0.007
	2020	0.002	0.348	0.006	0.106	0.003
Rural Living Space	2000	0.113	7.082	0.308	2.243	0.135
	2010	0.087	4.838	0.321	1.559	0.094
	2020	0.082	4.503	0.007	1.393	0.084
Forest ecological space	2000	0.004	0.049	0.411	0.099	0.008
	2010	0.004	0.048	0.412	0.099	0.008
	2020	0.005	0.059	0.002	0.021	0.002
Grass Ecological Space	2000	0.009	0.104	0.398	0.115	0.013
	2010	0.009	0.112	0.396	0.117	0.013
	2020	0.008	0.088	0.003	0.031	0.003
Water Ecological Space	2000	0.041	3.485	0.329	1.132	0.192
	2010	0.008	0.574	0.374	0.251	0.043
	2020	0.007	0.506	0.005	0.156	0.027
Other Ecological Spaces	2000	0.063	31.581	0.221	9.55	2.101
	2010	0.06	29.713	0.225	8.989	1.978
	2020	0.039	11.157	0.015	3.369	0.741

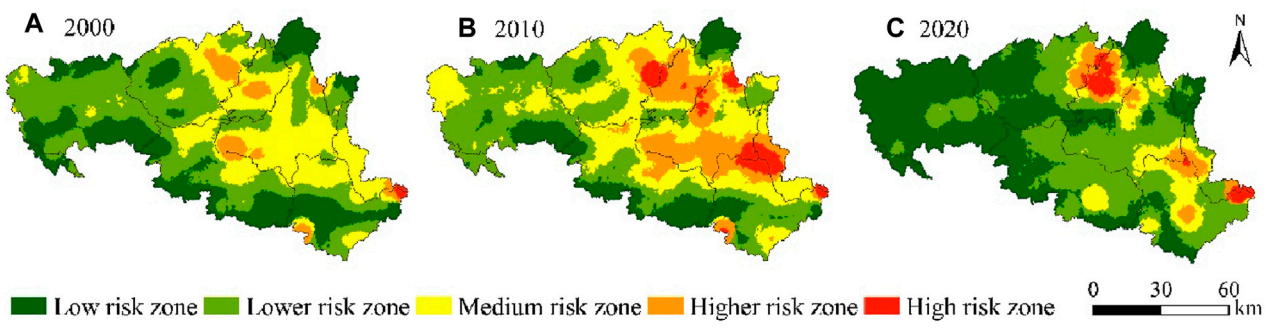

FIGURE 4
LER class distribution for 2000 **(A)**, 2010 **(B)**, 2020 **(C)**.

ecological risk of the study area landscape was classified into low, lower, medium, higher, and high ecological risk zones (Figure 4).

The distribution of the ecological risk level of the landscape strongly correlated with the distribution of PLES land types, with high-risk and medium-high-risk areas in the northeast and southeast

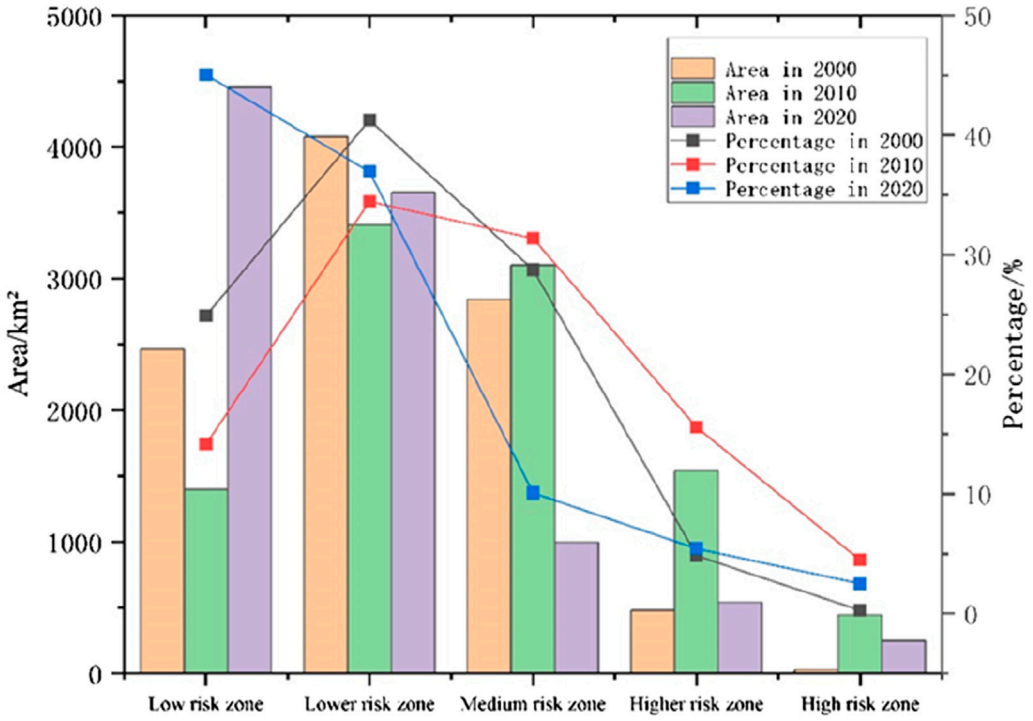

FIGURE 5
. Proportion and change of area of the ecological risk class area.

regions exhibiting a trend of "scattering-clustering" from 2000 to 2020, and expanding outward by 2020. The aforementioned areas are dominated by the industrial production and urban living space, and the strong human activities lead to the instability of the ecosystem. High landscape separation and sub-dimension number considerably influence the formation of the landscape pattern and are sensitive to external disturbances. For the medium-risk areas, the aggregation areas located in the central-western and south-central regions gradually declined. Furthermore, lower-risk areas were concentrated in the periphery of medium-risk areas, including the woodland ecological and grassland ecological spaces, with low landscape fragmentation and weak human activities. During 2010–2020, this space increased considerably, and most medium-risk areas converted into lower-risk areas. The low ecological risk areas were concentrated in the peripheral areas, and in 2020, a large distribution in the northwest of the watershed, mostly the woodland ecological space, with low population density and complex and diverse topography, was observed. These low-risk areas are not easily disturbed by human activities, leading to the predominance of these areas.

The area and proportion of each risk level area were counted to analyze the changes in increase and decrease of the ecological risk (Figure 5). From the temporal perspective, in 2000, the ecological risk was dominated by low-risk, lower-risk, and medium-risk areas, among which the lower-risk area occupied the largest area, reaching 4078.91 km^2, which was 41.25% of the total study area. The ecological risk situation deteriorated from 2000 to 2010 and improved considerably from 2010 to 2020. This phenomenon indicates that the ecological environment quality improved and the ERI level decreased during the study period.

3.4 Spatial autocorrelation analysis of ecological risk in the landscape

The global Moran's I value of ERI in the study area in 2000, 2010, and 2020 were 0.3881, 0.3456, and 0.3100, respectively, all of which are greater than 0, indicating that ERI is positively correlated in space and exhibits a certain spatial convergence. Furthermore, the global Moran's I value from 2000 to 2020 exhibited an overall decreasing trend, reflecting the weakening of the ERI and spatial convergence. Compared with the global Moran's I, the local Moran's I accurately reflects the spatial distribution of ecological risk values in the landscape. As displayed in Figure 6, high-high (HH) and low-low (LL) clustering dominated ecological risk values in the three periods, as presented in the LISA clustering of ecological risk indices in the Liuchong River Basin from 2000 to 2020 (Figure 6), with the high concentration exhibiting a northeast-southeast trend. By 2020, the HH agglomeration declined and part of the internal grid became nonsignificant. By contrast, LL agglomerations were distributed around the study area and were dispersed. The agglomerated areas exhibited a gradual convergence, whereas the dispersed areas showed gradual dispersion. High-low (HL) and low-high (LH) phenomena are rare and discrete in distribution. Quantitatively, both the spatial autocorrelation and the number of grids in the HH clustered areas declined over time, and the number of positively correlated grids that passed the significance test ($p > 1$) decreased. Therefore, the spatial clustering characteristics of ERI in the Sixchon River basin are weakening.

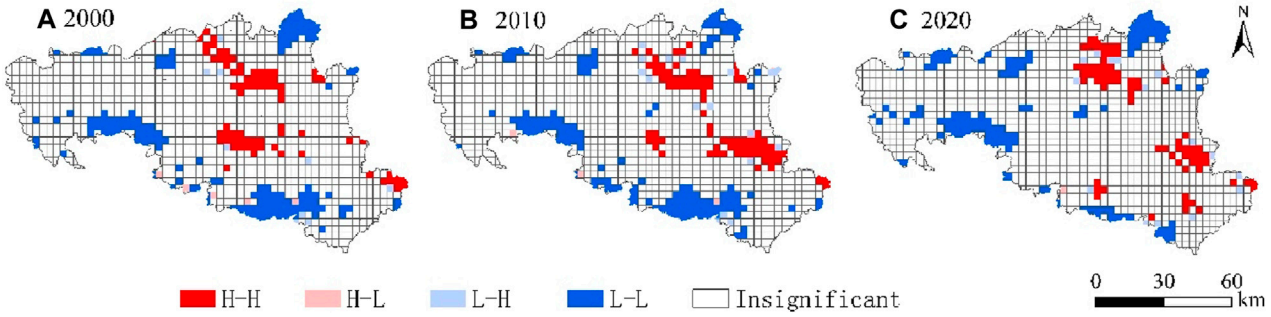

FIGURE 6
LISA cluster map of land use ecological risk index in the Liuchong river basin in 2000 **(A)**, 2010 **(B)**, 2020 **(C)**.

TABLE 5 Landscape index calculation results of production-life-ecological space.

Transformation of "production-life-ecological space" (leading to improvement of ecological environment)	Index change	Contribution share (%)	Transformation of the "production-life-ecological space" (leading to ecological degradation)	Index change	Contribution share (%)
III -VI	0.000000000043	2.05	VI-V	−0.0000003654	8.25
III - I	0.000000000202	9.65	VI-I	−0.0000000799	1.80
II -VI	0.000000000079	3.76	V-VI	−0.0000017575	39.69
IV-II	0.000000000055	2.62	V-I	−0.0000002609	5.89
IV-V	0.000000000085	4.07	VI-I	−0.0000004836	10.92
IV - I	0.000000000612	29.19	I-III	−0.0000000980	2.21
VII -VI	0.000000000590	28.15	I-II	−0.0000003156	7.13
VII -V	0.000000000068	3.25	V-I	−0.0000006928	15.65
VII - I	0.000000000343	16.38	I-VII	−0.0000001495	3.38

Note: I is agricultural production space; II, is industrial production space; III, is urban living space; IV, is rural living space; V is woodland ecological space; VI, is grassland ecological space; VII, is water ecological space.

3.5 Effect of PLES land use conversion on ecological risk

In terms of the contribution of the dominant PLES land use conversion (Table 5), the dominant factors affecting ecological improvement are the conversion of the watershed ecological space to the grassland ecological and agricultural production spaces, the conversion of the urban living space to the agricultural production space, and the conversion of the rural living space to the agricultural production space in the Liuchong River Basin from 2000 to 2020, with a combined contribution of 83.37%. By contrast, the conversion of the woodland ecological space to the grassland ecological space, the woodland ecological space to the agricultural production space, and the grassland ecological space to the agricultural production space were the dominant factors leading to ecological degradation, with a combined contribution of 63.26%. The expansion of the urban living space during the study period was attributed mainly to the reduction of the agricultural production space. The transformation of the agricultural production space to the urban living space indirectly changes landscape fragmentation, landscape separateness, and landscape fractional dimension index, eventually increasing the regional ecological risk.

4 Discussion

Examining the interactions between PLES land use changes and landscape patterns in the Liuchong River Basin, a typical karst basin, can help analyze the correlation at the macro level. In this study, we investigated the land use and LER changes in the Liuchong River Basin from the perspective of PLES. We constructed a LER assessment model by referring to existing studies (Yang et al., 2018; Qi, 2020; Chen and Shi, 2021; Chen et al., 2022b; Wang et al., 2022c; Guo and Guo, 2022; Li and Wu, 2022; Liang et al., 2022). Furthermore, by using land use change ecological contribution ratio and spatial autocorrelation analysis, we quantitatively analyzed the LER of the Liuchong River Basin in karst areas. By comparing data of different years, we summarized the spatial and temporal change patterns of LER in the region in the past 20 years. The results revealed that, first, the stability of

the ecosystem in the karst region was severely disturbed by human activities. In this study, the functional classification of land use in the Liuchong River Basin in the past 20 years was dominated by the woodland ecological space, but a trend of decreasing woodland ecological space was observed, whereas the area of the industrial production space increased. This phenomenon indicates that the impact of current human activities on the karst ecosystem is intensifying, and effective measures are required to protect and restore the ecosystem. Second, the distribution of high and low ecological risk levels in the landscape is strongly correlated with the distribution of PLES land types. The high-risk and medium-high-risk areas are distributed in the northeast and southeast regions, which are dominated by the agricultural production, industrial production, and urban living spaces and are disturbed by human activities. Although the lower and low-risk areas are mostly in the periphery of the medium-risk area, including the woodland ecological and grassland ecological spaces. Therefore, targeted measures should be enacted to protect high-risk and medium-high-risk areas. Moreover, coordinated management with agriculture, industry, and towns should be conducted to ensure environmental quality and ecosystem stability. Finally, the conversion of the watershed ecological space to the grassland ecological and agricultural production spaces, the conversion of the urban living space to the agricultural production space, and the conversion of the rural living space to the agricultural production space are the dominant factors affecting ecological improvement. This phenomenon indicates that the agricultural production and grassland ecological spaces should be protected and restored to ensure ecological environmental protection in karst areas. Further, to promote agricultural modernization and sustainable development, the occupation of land resources by urban and rural living spaces should be reduced and transformed into the agricultural production space as much as possible.

This study has some shortcomings. First, LER assessment is a complex process requiring the consideration of multiple uncertainties. These factors determine the comprehensive evaluation results. When assessing ecological risks, these factors determine the integrated evaluation results. In the LER assessment of complex karst areas, the method and process should be improved. Second, this study selected only the Liuchong River Basin as the study object and did not cover other regions. In the future, more study sites can be selected for cross-sectional comparative analysis to improve the generalizability and reliability of the results. Finally, we did not consider the differences in human activities and influence, especially under different topographic conditions, human production, living, and other activities. These factors considerably influence the evolutionary process of PLES land use, spatial and temporal patterns, and the extent of their effect on the ecosystem. Therefore, these factors were not included to elucidate the complexity and diversity of land use and its ecological environment in the Liuchong River Basin. Future research should use improved methodology and advanced technologies in land use analysis and ecological risk evaluation, and expand the scope of the study area to achieve effective protection and management of karst watershed ecosystems.

5 Conclusion

In this study, the land use classification system was constructed from the perspective of PLES based on the land use cover data in 2000, 2010, and 2020. Using GIS spatial analysis technology and Fragstats 4.2 software, the land use transfer matrix, LER evaluation model, ecological contribution rate of land use flow, and spatial autocorrelation analysis were combined. Furthermore, the spatial and temporal patterns of PLES land use and its LER in the Liuchong River Basin over the past 20 years were quantitatively analyzed. The conclusions are as follows:

(1) From 2000 to 2020, the functional classification of land use in the Liuchong River Basin was dominated by the woodland ecological space, accounting for more than 53% of the total area, and the industrial production space underwent the most rapid expansion. The most significant transfer characteristics of PLES land use were the increases in the ecological space of watershed and the area of industrial production space and a decrease in the woodland ecological space; the transfer was the most drastic in the middle reaches of the main stream of the Liuchong River, whereas the surrounding areas of Hezhang County are stable ecosystems due to higher altitude and less disturbance by human activities.
(2) The distribution of high and low LER levels correlated strongly with the distribution of PLES land types, with high-risk and medium-high-risk areas distributed in the northeast and southeast regions, and medium-risk areas clustered in the west-central and south-central regions of the basin and exhibiting a gradual decrease. Furthermore, the lower and lowest risk areas were concentrated in the periphery of the medium-risk areas, including the woodland ecological and grassland ecological spaces, with low landscape fragmentation and weakly affected by human activities.
(3) The spatial aggregation characteristics of ecological risk levels gradually weakened from 2000 to 2020. HH and LL are concentrated in distribution, HL and LH phenomena are rare and discrete in distribution, and the clustering of HH and LL is obvious in local areas, showing a northeast-southeast trend and a strip-like distribution in space. These areas predominately comprise the agricultural production space, industrial production space, and urban living space and are strongly affected by anthropogenic activities.
(4) The conversion of the watershed ecological space to the grassland ecological and agricultural production spaces, urban living space to the agricultural production space, and rural living space to agricultural production space were the predominant factors contributing to ecological improvement, with a combined contribution of 83.37%. By contrast, the conversion of woodland ecological space to grassland ecological space, woodland ecological space to agricultural production space, and the grassland ecological space to the agricultural production space were the factors contributing to ecological degradation.

Data availability statement

The original contributions presented in the study are included in the article/supplementary material, further inquiries can be directed to the corresponding author.

Author contributions

JR: Conceptualization, Data curation, Project administration, Writing–original draft, Writing–review and editing. YD: Data curation, Formal Analysis, Methodology, Project administration, Writing–original draft, Writing–review and editing. PH: Methodology, Writing–original draft. HL: Data curation, Methodology, Writing–original draft.

Funding

The author(s) declare that financial support was received for the research, authorship, and/or publication of this article. This study was made possible through financial support from the National Natural Science Foundation of China (42361074), Guizhou Bijie United Fund Project, Bike United [No. (2023)8]; "Karst Plateau Resources and Environment Remote Sensing Talent Team", Office of the Talent Work Leading Group of the Bijie Municipal Committee of the Communist Party of China, Project No.: BWRLT (2023) No. 14, (2021) No. 12; Discipline Construction Project of Guizhou University of Engineering Science.

Conflict of interest

The authors declare that the research was conducted in the absence of any commercial or financial relationships that could be construed as a potential conflict of interest.

Publisher's note

References

Ayre, K. K., and Landis, W. G. (2012). A Bayesian approach to landscape ecological risk assessment applied to the Upper Grande Ronde Watershed, Oregon. *Hum. Ecol. Risk Assess. An Int. J.* 18, 946–970. doi:10.1080/10807039.2012.707925

Bai, L. M., et al. (2019). Ecological risk assessment for Changchun based on land use change. *Ecol. Sci.* 38, 26–35. doi:10.14108/j.cnki.1008-8873.2019.03.004

Chen, B., et al. (2022a). Evaluation and coupling coordination analysis of landscape ecological security of Yichang from the perspective of production-life-ecological space. *Res. Soil Water Conserv.* 29, 344–351. doi:10.13869/j.cnki.rswc.2022.04.011

Chen, D., and Shi, L. (2021). The landscape ecological risk assessment and prediction for xiong'an new area based on land use change. *Ecol. Econ.* 37, 224–229.

Chen, Z., and Liu, Y. (2022b). Comprehensive eco-environmental effects caused by land use transition from the perspective of production-living-ecological spaces in a typical region: a case study of the guangxi Zhuang autonomous region, China. *Land* 11, 2160. doi:10.3390/land11122160

Guo, Y., and Guo, W. (2022). Landscape ecological risk analysis of urban agglomeration in the central basin of Shanxi from the perspective of "production-living-ecological spaces". *Chin. J. Ecol.* 41, 1813–1824. doi:10.13292/j.1000-4890.202206.015

Hayes, E. H., and Landis, W. G. (2004). Regional ecological risk assessment of a near shore marine environment: cherry Point, WA. *Hum. Ecol. Risk Assess.* 10, 299–325. doi:10.1080/10807030490438256

Kang, Z., et al. (2020). Landscape ecological risk assessment in Manas River Basin based on land use change. *Acta Ecol. Sin.* 40, 6472–6485.

Lan, Y., Chen, J., Yang, Y., Ling, M., You, H., and Han, X. (2023). Landscape pattern and ecological risk assessment in Guilin based on land use change. *Int. J. Environ. Res. Public Health* 20, 2045. doi:10.3390/ijerph20032045

Li, C., and Wu, J. (2022). Land use transformation and eco-environmental effects based on production-living-ecological spatial synergy: evidence from Shaanxi Province, China. *Environ. Sci. Pollut. Res.* 29, 41492–41504. doi:10.1007/s11356-022-18777-z

Li, S., He, W., Wang, L., Zhang, Z., Chen, X., Lei, T., et al. (2023). Optimization of landscape pattern in China Luojiang Xiaoxi Basin based on landscape ecological risk assessment. *Ecol. Indic.* 146, 109887. doi:10.1016/j.ecolind.2023.109887

Liang, T., Yang, F., Huang, D., Luo, Y., Wu, Y., and Wen, C. (2022). Land-use transformation and landscape ecological risk assessment in the Three Gorges Reservoir region based on the "production-living-ecological space" Perspective. *Land* 11, 1234. doi:10.3390/land11081234

Liu, H., Hao, H., Sun, L., and Zhou, T. (2022). Spatial-temporal evolution characteristics of landscape ecological risk in the agro-pastoral region in western China: a case study of ningxia hui autonomous region. *Land* 11, 1829. doi:10.3390/land11101829

Liu, K., et al. (2023). Optimization of landscape pattern in China Luojiang Xiaoxi Basin based on landscape ecological risk assessment. *Acta Ecol. Sin.* 43, 105–117.

Lu, C., et al. (2022). Spatial-temporal pattern and influencing factors of the "production-living-ecological" functional space of the Yellow River Basin at county level in Gansu, China. *Sci. Geogr. Sin.* 42, 579–588.

Paukert, C. P., Pitts, K. L., Whittier, J. B., and Olden, J. D. (2011). Development and assessment of a landscape-scale ecological threat index for the Lower Colorado River Basin. *Ecol. Indic.* 11, 304–310. doi:10.1016/j.ecolind.2010.05.008

Qi, J. (2020). Spatial function identification and pattern evolution of "production-living-ecology" in fast-going urbanization areas—a sampling case study of Xinzheng City, Henan. *J. Saf. Environ.* 20, 1588–1595.

Ran, P., Hu, S., Frazier, A. E., Qu, S., Yu, D., and Tong, L. (2022). Exploring changes in landscape ecological risk in the Yangtze River Economic Belt from a spatiotemporal perspective. *Ecol. Indic.* 137, 108744. doi:10.1016/j.ecolind.2022.108744

Su, Y., et al. (2020). Ecological risk assessment in Yongchuan District of Chongqing city based on landscape pattern. *Bull. Soil Water Conserv.* 40 (03), 195–201+215. doi:10.13961/j.cnki.stbctb.2020.03.028

Wang, A., Liao, X., Tong, Z., Du, W., Zhang, J., Liu, X., et al. (2022a). Spatial-temporal dynamic evaluation of the ecosystem service value from the perspective of "production-living-ecological" spaces: a case study in Dongliao River Basin, China. *J. Clean. Prod.* 333, 130218. doi:10.1016/j.jclepro.2021.130218

Wang, H., Liu, X., Zhao, C., Chang, Y., Liu, Y., and Zang, F. (2022b). Spatial-temporal pattern analysis of landscape ecological risk assessment based on land use/land cover change in Baishuijiang National nature reserve in Gansu Province, China. *Ecol. Indic.* 124, 107454. doi:10.1016/j.ecolind.2021.107454

Wang, J. Y., et al. (2021). Coupling relationship between urban spatial expansion and landscape ecological risk—a case study of Yuanzhou District in Jiangxi Province. *Res. Soil Water Conservation* 28, 142–151. doi:10.13869/j.cnki.rswc.2021.05.017

Wang, S., et al. (2022c). GIS-based ecological risk assessment and ecological zoning in the Three Gorges Reservoir area. *Acta Ecol. Sin.* 42, 4654–4664. doi:10.5846/stxb202104080909

Yang, Q. K., et al. (2018). Land use transformation based on ecological-production-living spaces and associated eco-environment effects: a case study in the Yangtze River Delta. *Sci. Geogr. Sin.* 38, 97–106. doi:10.13249/j.cnki.sgs.2018.01.011

Yu, J., et al. (2022). Landscape ecological risk assessment and ecological security pattern construction in landscape resource-based city: a case study of Zhangjiajie City. *Acta Ecol. Sin.* 42, 1290–1299. doi:10.5846/stxb202012313341

Zhan, H. X., et al. (2009). Suggestion on reasons and countermeasures for fishery resources to decline of Liuchong River. *J. Hydroecology* 30, 147–149.

Zhang, X., Du, H., Wang, Y., Chen, Y., Ma, L., and Dong, T. (2021). Watershed landscape ecological risk assessment and landscape pattern optimization: take Fujiang River Basin as an example. *Hum. Ecol. Risk Assess. An Int. J.* 27, 2254–2276. doi:10.1080/10807039.2021.1970511

frontiers | Frontiers in Environmental Science

TYPE Original Research
PUBLISHED 02 August 2024
DOI 10.3389/fenvs.2024.1428828

OPEN ACCESS

EDITED BY
Song Feng,
University of Arkansas, United States

REVIEWED BY
Dong Wang,
Henan University, China
Yujie Shi,
Northeast Normal University, China

*CORRESPONDENCE
Zhiguo Li,
nmndlzg@163.com

RECEIVED 07 May 2024
ACCEPTED 15 July 2024
PUBLISHED 02 August 2024

CITATION
Meng B, Gao C, Lv S, Han G, Li Z, Li J, Wu Q and Zhang F (2024), The effects of grazing and the meteorologic factors on wind-sand flux in the desert steppe.
Front. Environ. Sci. 12:1428828.
doi: 10.3389/fenvs.2024.1428828

The effects of grazing and the meteorologic factors on wind-sand flux in the desert steppe

Biao Meng[1], Cuiping Gao[1], Shijie Lv[1], Guodong Han[1], Zhiguo Li[1]*, Junran Li[2], Qian Wu[1] and Feng Zhang[1]

[1]Key Laboratory of Grassland Resources of the Ministry of Education, Key Laboratory of Forage Cultivation, Processing and High Efficient Utilization of the Ministry of Agriculture and Rural Affairs, Inner Mongolia Key Laboratory of Grassland Management and Utilization, College of Grassland, Resources and Environment, Inner Mongolia Agricultural University, Hohhot, China, [2]Department of Geography, The University of Hong Kong, Hong Kong, Hong Kong SAR, China

Introduction: Affected by global climate warming and changing rainfall patterns, the degree of soil desiccation in arid grasslands has increased and soil wind erosion has become a major environmental concern. Understanding and controlling the characteristics of sand flux and wind erosion caused by the degradation of grassland vegetation, as well as their changing patterns, has become a top priority in combating grassland degradation. Therefore, the aim of this study is to clarify the extent of wind erosion in desert grasslands and its influencing factors in order to provide a theoretical basis and data support for the restoration of grassland vegetation and the sustainable development of grassland livestock production.

Methods: Use of SAS and Origin statistical software to perform multifactorial analysis of variance on variables such as year, stocking rate, meteorological conditions and wind-sand flux to determine the degree of influence of different factors on sand flux and the magnitude of interactions among different factors.

Results and discussion: The results showed that wind-sand flux was higher when rainfall was low and stocking intensity was high. Specifically, the wind-sand flux increased by 50.3% and 83.6% in the moderate and high grazing treatments, respectively, compared to the control. The data obtained also showed that there was a significant interaction between climate and grazing intensity, suggesting that an increase in one factor may attenuate the differences in wind-sand flux at different levels of other factors. There is likely to be a threshold effect of stocking rate of moderate grazing on the variation of wind-sand flux influenced by different factors. In summary, the factors affecting wind-sand flux in the arid desert steppe are numerous and complex, with stocking rates below moderate grazing being key to reducing wind-sand flux.

KEYWORDS

interactions, environmental characteristics, stocking rate, desert steppe, wind-sand flux

1 Introduction

The increasing aridity of grassland soils in dryland zones, driven by global warming and altered rainfall patterns, has intensified soil wind erosion. This pervasive issue has led to a decline in grassland vegetation, exposing bare soil, heightening susceptibility to wind erosion, and exacerbating land sandification. Such degradation not only severely impacts grassland ecology but also poses substantial challenges to ecological security and human settlement in these arid regions (Liu J et al., 2021; Zhang et al., 2021). Consequently, understanding the characteristics of wind-sand flux and the dynamics of wind erosion, precipitated by vegetation deterioration, has become essential in addressing grassland degradation and developing management plans.

The Inner Mongolia Autonomous Region, situated on the Mongolian Plateau, straddles semi-arid and arid climates and is primarily afflicted by wind erosion as the predominant form of soil degradation (Caiyun et al., 2021). The central and western areas of Inner Mongolia, characterized by desert grasslands with thin, loose soil layers, are highly vulnerable to external disturbances. The region endures severe desertification, accounting for 90% of China's desertified grasslands (An et al., 2022). The region is also plagued by frequent and intense dust storms, largely due to its sparse vegetation and friable soil (Piao et al., 2017). Overgrazing is a principal causal agent in grassland degradation, accentuating soil erosion and vegetation decline, thereby underscoring the critical issue of grassland wind erosion (Tao et al., 2015). The interplay of grassland grazing and climate change on soil wind erosion unfolds as follows: Overgrazing results in excessive consumption of pasture vegetation, which in turn reduces the soil's resistance to wind erosion, thereby exacerbating the issue (Chen et al., 2008; Zhang et al., 2020; Hao et al., 2022). Furthermore, grazing damage to pasture plants and soil compaction from trampling can lead to increased soil erodibility and structural loosening, fostering wind erosion (Zhang et al., 2023). Thus, climatic conditions and overgrazing collectively heighten the risk of wind erosion through their impact on vegetation composition, above- and below-ground biomass, soil structure, and soil crust cover (Piao et al., 2017).

To address these concerns, this study makes use of the long-term grazing experimental platform in Inner Mongolia (established in 2004) to analyze wind-sand fluxes in desert grasslands under different grazing intensities (Zhang et al., 2023). Amidst the combined effects of climate and grazing on grassland wind erosion, we sought to answer the following questions: 1) How does interannual variation in climate and stocking rate influence wind-sand flux in desert grasslands? 2) Is there an interaction between climate and stocking rate that affects wind-sand flux? 3) Which climatic factors contribute to interannual differences in wind-sand fluxes?

Addressing these questions will not only illuminate the extent of wind erosion in desert grasslands but also identify contributing factors, providing a theoretical framework and empirical support for the restoration of grassland vegetation and the sustainable management of grassland animal husbandry.

2 Material and methods

2.1 Physical and geographic overview of the study area

The research site was located in Wangfu 1, Siziwangqi, Ulanqab City, within the Inner Mongolia Autonomous Region (41°47′17″N, 111°53′46″E). The site's elevation is 1,450 m, and it is situated 30 km from the governmental center of Siziwangqi, Wulanhua (Zhang et al., 2023).

The topography of Siziwangqi is varied, comprising 4% mountains, 39% plateaus, and 66% hills, with a relative elevation difference of 1,100 m between the lowest and highest points, which range from 1,000 to 2,100 m. Its location on the southern edge of the Inner Mongolia Plateau makes it susceptible to persistent winds throughout the year. Predominant winds are westerly and northwesterly during the spring and winter, while southerly and southeasterly winds prevail in the summer and autumn. The average annual wind speed exceeds 4.4 m/s.

The region experiences significant thermal variation, with an annual temperature range of 34°C–37°C and daily temperature fluctuations of approximately 13°C–14°C. The temperature gradient aligns with the terrain, descending from north to south; summers are relatively short and warm, while winters are extended and notably cold, with January being the coldest month. Spring temperatures rise swiftly, with substantial variability from March to May. July records the highest temperatures, and autumn witnesses a rapid decline in temperature starting in the latter half of September, averaging a 2°C drop every 5 days. The area typically enjoys a brief frost-free period averaging 108 days annually. The longest recorded frost-free period was in 2,000, lasting 142 days, whereas the shortest spanned only 78 days in 1965.

The average weather indicators for the growth seasons from 2019 to 2021 in the test area are provided below.

The study area is located in a dry, semi-arid region of inland high latitudes, receiving an average annual precipitation ranging from 110 to 350 mm. Despite the ample sunlight, the region suffers from insufficient rainfall. The predominant soil type at the test site is compact, light chestnut calcic soil, characterized by low water permeability and poor aeration. This often results in noticeable surface runoff following precipitation events. The vegetation is sparse, typically reaching heights of 10–15 cm, and consists mainly of short-flowered needlegrass (*Stipa breviflora* Griseb.), indicative of the desert grassland zonal vegetation typical of the region.

2.2 Experimental design

This study was based on a sheep grazing experiment platform with a grazing intensity gradient established in 2004. A completely randomized block design was used to divide 12 fenced grazing plots (each covering an area of 4.4 hm^2) into three blocks, and four different stocking rate levels were randomly arranged within each block: control (CK), light stocking rate (LG), moderate stocking rate (MG), and heavy stocking rate (HG). Stocking rates were set at 0 (CK), 0.91 (LG), 1.82 (MG), and 2.71 (HG) sheep hm^{-2}·$year^{-1}$

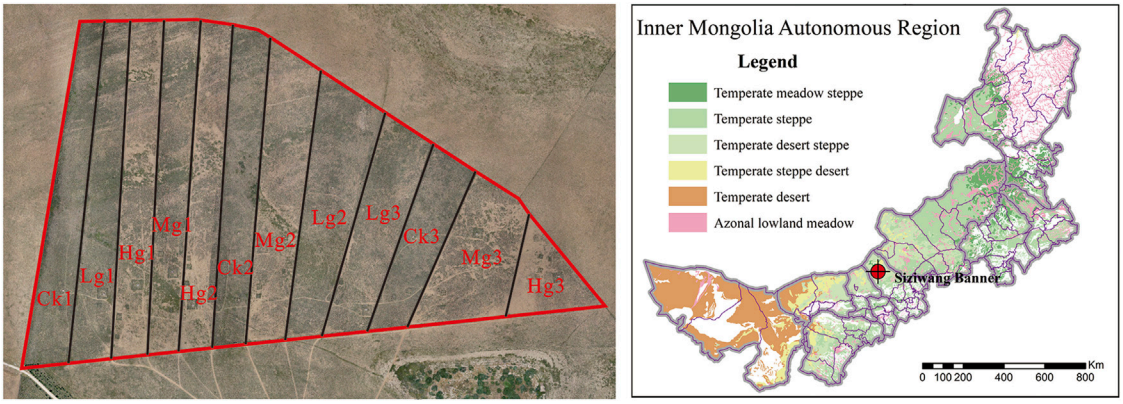

FIGURE 1
The map of the location of research objects and experimental plots.

FIGURE 2
BSNE dust sampler field photo.

during the grazing season (early June to late November), and the actual number of sheep grazed were 4, 8 and 12 in the light, moderate and heavy grazing areas, respectively (Figure 1).

We placed a BSNE (Big Spring Number Eight) dust sampler (Custom Products, United States) in the center of every grazing plot (Figure 2). These sand and dust sampler sets feature adjustable-height samplers within their support bars. The samplers are equipped with rotatable shafts and wind blades and can be positioned at various heights along the bar. Each sampler includes a sand trap measuring 2 cm in width by 5 cm in height, boasting a sand collection efficiency exceeding 90% within the BSNE system. Air carrying sand particles enters the trap, where it is collected. Mounted on each 1.5 m tall BSNE support rod are four sets of BSNE, with seven sand-collecting boxes at different heights (0, 0.1, 0.3, 0.5, 0.7, 1.0, and 1.2 m). Across all plots, there were 19 sand-collection boxes per plot, with a total of 228 boxes for the entire study area (Zhang et al., 2023).

2.3 Wind-sand flux calculations

The wind-sand flow is an airflow that carries sand particles; it can be created by wind that is blowing up and migrating fine particles close to the ground. The horizontal flux of sand flow (Q), defined as the

TABLE 1 Growing season averages of climate factors in the test area, 2019–2021.

Year	Temperature (°C)	Average annual precipitation (mm)	Relative humidity (%)	Wind speed (m/s)
2019	14.72	249.20	42.34	3.24
2020	13.54	171.10	52.36	2.97
2021	14.56	178.06	52.25	2.93

TABLE 2 ANOVA table for 3 factors affecting wind-sand fluxes.

Source	DF	SS	MS	F value	Pr > F
Model	47	13.21	0.28	31.82	<0.0001
Year	2	2.90	1.45	163.97	<0.0001
Stocking rates	3	1.17	0.39	44.21	<0.0001
Height	6	7.28	1.21	137.43	<0.0001
Year × stocking rate	6	0.12	0.02	2.21	0.0439
Year × height	12	1.10	0.09	10.39	<0.0001
Stocking rate × height	18	0.64	0.04	4.03	<0.0001
Error	204	1.80	0.01		
Total	251	15.01			

mass of sand and dust per unit time per unit breadth at a specific height perpendicular to the wind direction, is made up of sand flow *q[z]* at various heights from the ground. Since the horizontal fluxes *q[z]* per unit area at different heights satisfy the following relationship, *Q* can be composed of wind-sand flow *q[z]* at different heights. *Q[z]* is obtained by using the fitting method to obtain different sets of equations:

$$q(z) = ce^{(az^2+bz)} \quad (1)$$

where *z* is the height of the sand collecting opening (m), *a*, *b*, and *c* are the fitting parameters, and both sides of the equation are calculated logarithmically, that is to say:

$$lnq[z] = az^2 + bz + lnc \quad (2)$$

We used SPSS 13.0 (Zhang et al., 2023) to fit a polynomial to Eq. 1, to provide the three constant terms, *a*, *b*, and *c*. Additionally, the height of the sand collection *z* and the horizontal fluxes *q* at various vertical heights can be related by establishing the equation *q[z]* using the quadratic polynomial function.

2.4 Statistics and analysis of data

We considered the following three factors that might influence wind-sand flux: year (2019, 2020, 2021), height above ground (0, 0.1, 0.3, 0.5, 0.7, 1.0, and 1.2 m), and stocking rate (control, low, medium, high). We analyzed these variables using a 3-factor ANOVA model and transformed the variables X and Y using the SQRT (Ln(X + 1)) to better approach normality.

We calculated average temperature, average precipitation, average relative humidity, and average wind speed for each growing season (May-October) of each year. The intervals were categorized based on the average results; a year with a value of 1 was assigned to be greater than the mean, and a year with a value of 0 was assigned to be less than the mean value. The average wind speed for the 3-year period coincided with the same amount of precipitation (Table 1), so in 2019 the wind speed (precipitation) is assigned a value of 1, 2020 and 2021 a value of 0, just as the average temperature is assigned a value of 1, 0 and 1, and the average relative humidity a value of 0, 1 and 1. In this case, the stocking rates and height above ground were considered in conjunction with the analysis of variance (ANOVA) of the four factors (temperature, precipitation, stocking rates, and height), which resulted in the retention of only the two factors of temperature and precipitation. This constructed multifactorial influence on the wind-sand homogeneity was caused by the fact that the relative humidity and wind speed were implicitly included in the precipitation variable, and that both the precipitation and wind speed elements were assigned the same value.

The ANOVA procedure was used, followed by Duncan's multiple range test on all main effect means. We used SAS 9.21 for statistical analysis, Excel 2019 to summarize the data tables, and Origin 2022 for charting.

3 Results

3.1 Effect of different influences on wind-sand fluxes

All three factors (year, stocking rate, and sampling height) showed significant differences in wind-sand flux (Table 2). Moreover, wind-sand flux varied significantly with height across years and with height across stocking rate, but there was no significant interaction between stocking rate and year (Table 2). Sampling height contributed most to the variance (48.5%), followed by year (19.3%) and stocking rate (7.8%), with the interactions year × height (7.3%), stocking rate × height (4.3%), and year × stocking rate (0.8%) the lowest and exerting the least influence on wind-sand fluxes. The cumulative variance contribution of these factors was 88.0%, indicating that the ANOVA model closely fits the original data and that the results were both statistically significant and indicative. Height is the factor with the highest contribution rate, which indicates a significant difference in the wind-blown sand flux collected at different heights. This may be due to the obstructive effect of vegetation or the migration effect of wind-blown sand on the surface.

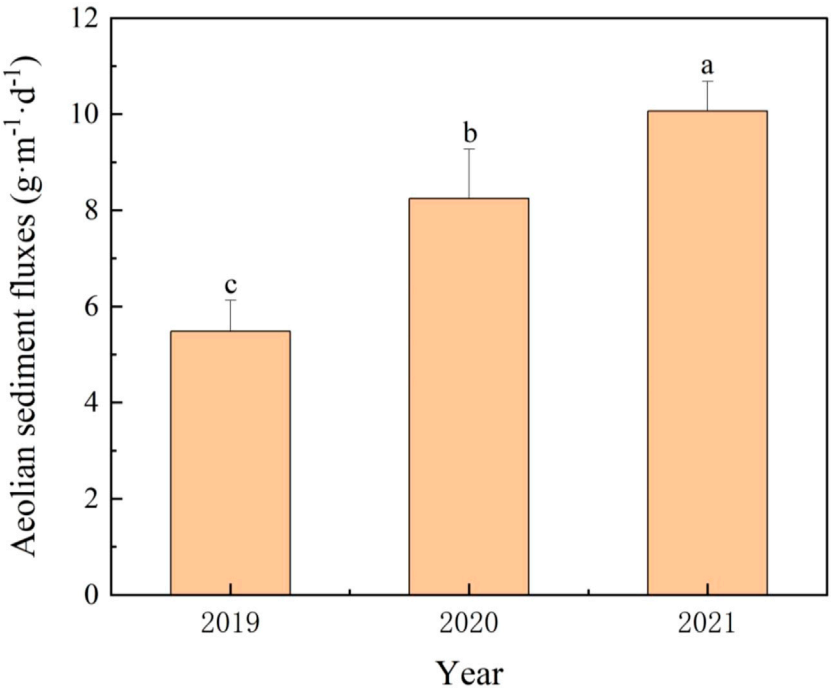

FIGURE 3
Differences in wind-sand flux between different years.

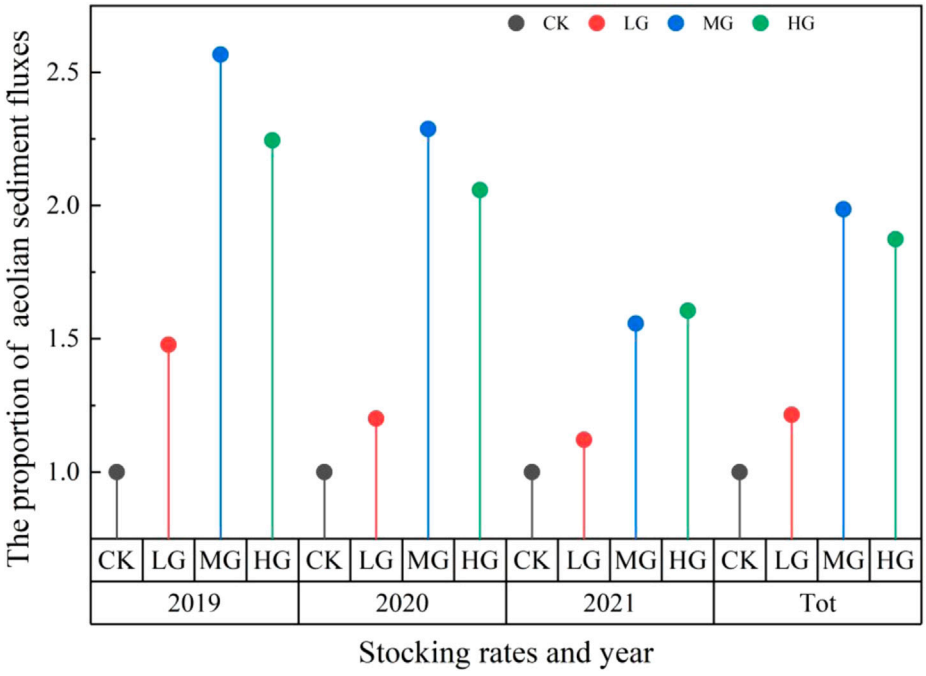

FIGURE 4
The impact of interannual variations and grazing intensity on wind-sand flux.

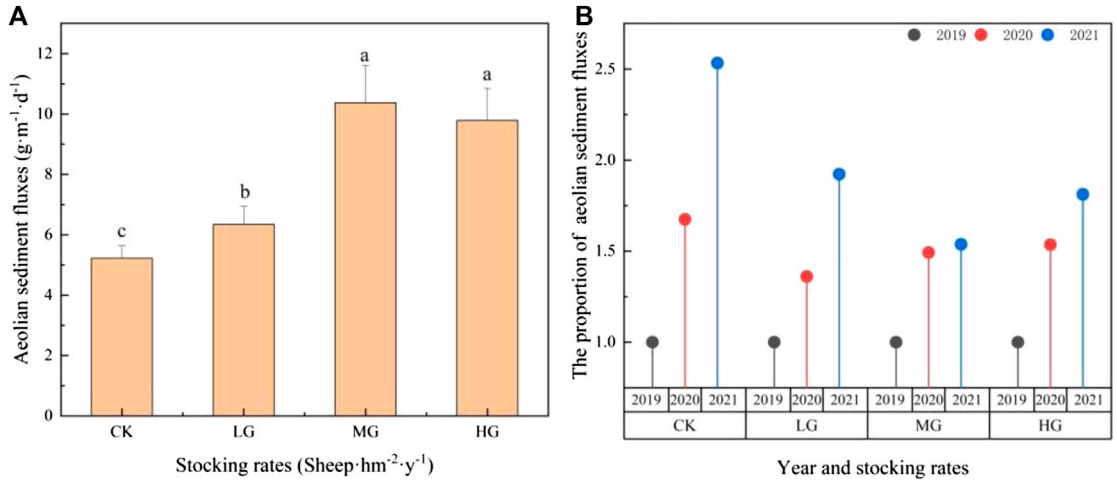

FIGURE 5
Differences in wind-sand fluxes under control (CK), low (LG), medium (MG), and high (HG) stocking rate **(A)**, and variation in wind-sand fluxes between stocking rates and year **(B)**.

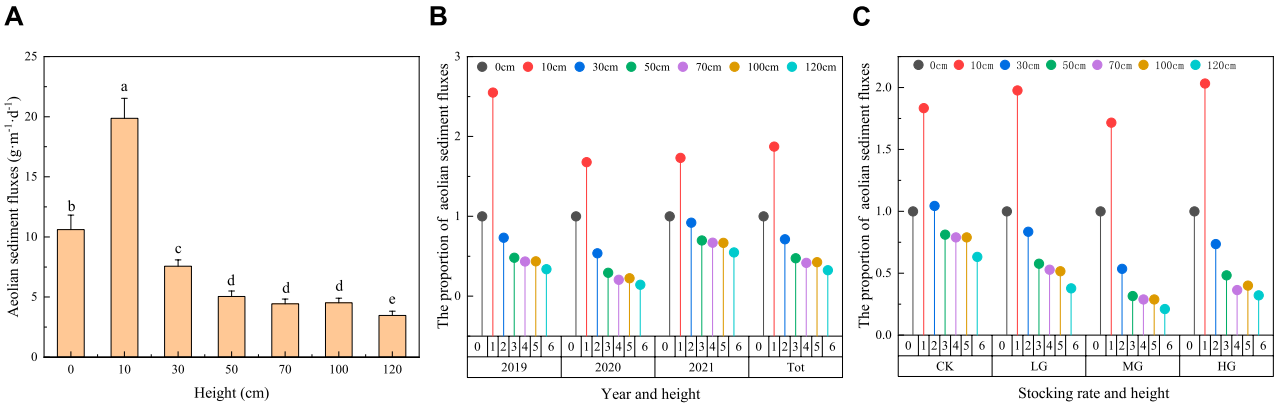

FIGURE 6
Wind-sand fluxes at different heights from the ground **(A)**, and the interacting effects of height and year **(B)** and height and stocking rate **(C)** on wind-sand fluxes.

3.2 Comparison of wind-sand fluxes in desert grasslands between years

During the 3-year study period, wind-sand fluxes showed a year-over-year increasing trend (Figure 3). During the annual growing season, the wind-sand flux gradually increased, while the difference in fluxes between different stocking rates decreased (Figure 4). It is worth noting that the MG treatment area consistently exhibited a relatively large proportion compared to the CK, and over the 3 years, there was a pattern of mutual growth and decline between the MG and HG treatment areas, indicating a potential threshold effect of wind-sand flux in the gradient of stocking rates. When the grazing intensity reaches the level of the MG test area, the protective effect of vegetation against wind erosion is almost eliminated. The increase in wind-sand flux in 2021 and the reduced variation in fluxes among different stocking rates implies that years with higher wind-sand fluxes may also experience smaller variations in fluxes among different stocking rates.

3.3 Effects of stocking rate on wind-sand fluxes

Overall, wind-sand fluxes were greater in higher stocking rates (Figure 5A), up to the medium rate. At low stocking rates, a marked difference in wind-sand fluxes was noted among the years (Figure 5B). The rate of change between the CK and LG treatments was significantly greater than that in the MG and HG treatments (Figure 5B). Notably, even when wind-sand fluxes were substantially higher in the year 2021 than year 2020, the MG treatment area remained consistent. This observation suggests that areas with high

TABLE 3 Response of wind-sand fluxes to meteorological factors, stocking rate and height above ground level.

Source	DF	SS	MS	F value	Pr > F
Model	47	14.408	0.307	104.16	<0.0001
Temperature	1	0.147	0.147	49.98	<0.0001
Precipitation (Wind speed OR Relative humidity)	1	1.548	1.548	525.91	<0.0001
Stocking rate	3	1.171	0.390	132.66	<0.0001
Height	6	7.282	1.214	412.37	<0.0001
Stocking rate × height	18	0.640	0.036	12.08	<0.0001
Temperature × height	6	0.811	0.135	45.94	<0.0001
Temperature × precipitation (Ws OR Rh) × height	6	1.491	0.248	84.43	<0.0001
Temperature × precipitation (Ws OR Rh) × stocking rate	6	1.318	0.220	74.64	<0.0001
Error	204	0.600	0.003		
Total	251	15.008			

stocking rates may diminish the interannual variability of wind-sand fluxes. Moreover, in years with lower wind-sand fluxes, the vegetation above ground might not effectively protect the soil from wind erosion.

3.4 Effect of height on wind-sand fluxes

Wind-sand flux was the highest at 10 cm above the ground (Figure 6A), reaching 19.87 g m^{-2} d^{-1}. The next highest flux was at ground level (0 cm), at 10.61 g m^{-2} d^{-1}, and the minimum wind-sand flux was at 120 cm above the ground, at only 3.47 g m^{-2} d^{-1}. Due to the interactions between wind-sand flux at different heights and the variables of year and stocking rate, high wind-sand flux years weakened the differences in wind-sand flux between different heights (Figure 6B), and high stocking rate treatment areas weakened the differences in wind-sand flux between different heights (Figure 6C). A high level of any factor weakens the variability in wind-sand flux between different levels of other factors.

3.5 Effects of interannual climatic factors on wind-sand fluxes

Temperature, precipitation, livestock load, and heights all show significant differences in wind-sand flux during the observation period ($p < 0.001$). There were significant two-way interactions between livestock load and height, temperature and height, and significant three-way interactions among temperature, precipitation and height, as well as temperature, precipitation, and livestock load (Table 3).

The variance contributions of height, precipitation, (temperature*precipitation) and livestock load, temperature, livestock load and height, (temperature*precipitation) and height, temperature and height, livestock load are 48.5%, 10.3%, 9.9%, 8.8%, 7.8%, 5.4%, 4.3%, 1.0% respectively. Therefore, differences in wind-sand flux were greatest at different heights from the ground, and the effect of temperature had the smallest impact on wind-sand flux. The combined effect of temperature and precipitation on wind-sand flux reached 18.7%. The total variance contribution of all factors was 96.0%, suggesting that the variance analysis model fits the original data well. The results indicate that precipitation has the highest contribution among meteorological elements, followed by temperature. This suggests that precipitation reduces the dust density in the air, increases soil moisture, and increases the threshold wind speed to reduce wind erosion, with its impact on wind erosion being greater than temperature.

4 Discussion

4.1 Influence of meteorological factors on wind-sand fluxes

While grazing can influence the dynamics of wind-sand fluxes in grasslands, it is the climatic conditions that fundamentally drive these changes. Key meteorological factors such as temperature, wind speed, precipitation, and relative humidity significantly impact these fluxes, often in complex interplays (Wiesmeier et al., 2015; Han et al., 2021; Zhao et al., 2022). The desert grassland has a dry climate, low vegetation cover, and the soil is more prone to weathering and erosion, so this paper chooses precipitation, temperature, humidity, and wind speed (four meteorological factors, precipitation and wind speed, have the same value, and relative humidity is exactly the opposite of its value, so only temperature and precipitation are retained, and relative humidity and wind speed are implied in precipitation variables) as the four representative indicators to be analyzed as climate factors.

Temperature and precipitation ultimately drive wind erosion in their effects on aboveground and belowground net primary productivity, vegetation recovery and compensatory capacity, abundance of perennial species, belowground biomass, and root

distribution (Zhang et al., 2017; Zhongju et al., 2018; Niu, 2020; Qu et al., 2023). Warmer wetter areas tend to have more vegetation that protects against erosion.

However, temperature and rainfall also have proximate effects as well. The high rainfall in 2019, lower rainfall in 2021, and the occurrence of consecutive droughts, led to an increase in the wind-sand flux over the 3 years of our study. Precipitation had a much greater independent effect than temperature at our site. As temperatures rise, surface water evaporation increases, leading to drier soil surfaces, which in turn can result in increased wind-sand flux. In areas with low precipitation, the surface temperature rises more rapidly than in surrounding areas, intensifying convection with cold air, leading to more severe wind effects on the surface, and ultimately increasing wind-sand flux. Different regions show varying responses of wind-sand flux to climatic factors (Ren et al., 2018; Yang et al., 2018). In the northeast region of China, the main meteorological factors affecting soil erosion during the non-growing season are wind speed and temperature, with the contribution of precipitation increasing during the growing season while the contributions of wind speed and temperature decrease (Zhu et al., 2012). In the alpine meadow region, wind speed and moisture content are the main factors affecting wind-sand flux (Munkhtsetseg et al., 2017).

Climate factors often do not act alone, but may have synergistic effects with each other, or with other factors (Tabeni et al., 2014). We found that the combined contributions of temperature and precipitation, in conjunction with other factors, was greater than 25% of variance explained in the models. The impact of temperature and precipitation on soil erosion is a complex physical process, and wind-sand flux varies under different temperature and precipitation conditions (Schönbach et al., 2011; Zhang et al., 2015; Liu X et al., 2021). Under extreme weather conditions, climate factors lead to a decrease in vegetation recovery capacity, exacerbating grassland wind erosion and causing more severe damage to grassland productivity (Miri et al., 2019).

4.2 Effects of grazing on the wind-sand flux

Grazing is one of the significant factors exacerbating soil wind erosion. Desert grasslands, due to their unique geographical factors, exhibit noticeable variation in wind-sand fluxes under different grazing intensities (Du et al., 2019; Li et al., 2020). Grazing affects soil wind erosion primarily through the degradation of vegetation, reduced protection of soils, and physical disruption of the soil structure by livestock trampling (Li et al., 2017; Hou et al., 2019). Our results show wind-sand flux was greater in plots with more livestock. Interestingly, in the moderately grazed treatment, the proportion remained consistent even when wind-sand fluxes were significantly higher in the 2021 compared to 2020, indicating that intense grazing diminishes the year-to-year variability in wind-sand flux.

Grazing directly impacts soil structure through animal foraging, leading to increased wind erosion and dust storms, and indirectly affects plant community composition and structure. Surface characteristics such as soil crust, bare ground ratio, and gravel cover also influence wind-sand fluxes (Chen et al., 2013; Bösing et al., 2014; Ren et al., 2016). Further studies in the same experimental area have demonstrated that in control and lightly grazed zones, the existing plant community and litter play a crucial role in reducing wind erosion, while plant community height and coverage have a more significant impact in the moderate and heavily grazed areas (Gao et al., 2013). This suggests that the observed threshold effect in the moderate treatment area may be due to lower vegetation and litter levels caused by high grazing pressure, reducing the protective effects on the soil.

In terms of height, the maximum wind-sand flux occurs at a height of 10 cm, with the flux decreasing as height increases. Due to the interaction between wind-sand flux at different ground heights and the year and stocking rate, high wind-sand flux years and high stocking rates both have a weakening effect on the differences in wind-sand flux at different heights. Prior research indicates that typically 92.2%–95.6% of sand transport occurs at heights of 0–21 cm, and the wind-sand flux at the same collection height shows an increasing trend with stocking rate, while the wind-sand flux decreases with elevation above ground level (Reiche et al., 2015). Earlier research on desert grasslands has yielded similar conclusions, with the wind-sand flux in each grazing plot decreasing monotonically with elevation above ground level as a negative power function, while nutrient levels increase with height (Zhang et al., 2023).

We found a significant interaction between year, grazing intensity and measurement height on wind-sand flux. The year and stocking rate seem to mutually weaken each other, and the process of mutual weakening actually reflects the unaffected nature of the wind-sand flux, indicating more severe wind-induced soil erosion in grasslands. This suggests that changes in stocking rate and climate over the years influence wind-sand flux, with complex interactions among these three factors. Thus, annual fluctuations in climate appear to be the primary factor influencing wind-sand flux, moderated by grazing intensity.

This study is based on observational data from 2019 to 2021. Due to limitations in sample size and observation conditions, there is still a lack of in-depth exploration into the interactions among meteorological factors, the specific elements affected by each factor leading to changes in wind erosion, and the reasons for significant differences in wind-sand flux collected at different heights. Further investigation is needed in these areas.

5 Conclusion

(1) In a long-term grazing experimental platform in the steppes of Inner Mongolia, we found that grazing intensity and climate significantly increased wind-sand flux over the 3-year study period. Moreover, an increase in either of these factors led to a reduction in the variability of wind-sand flux across the varying levels of the other.

(2) Among the climate variables, precipitation exerts the most considerable influence on wind-sand flux, followed by temperature.

(3) Moderate grazing acts as a critical threshold in the relationship between stocking rate and wind-sand flux under different climatic conditions.

Data availability statement

The original contributions presented in the study are included in the article/Supplementary Material, further inquiries can be directed to the corresponding author.

Author contributions

BM: Writing–original draft. CG: Writing–review and editing. SL: Writing–review and editing. GH: Writing–review and editing. ZL: Writing–review and editing. JL: Writing–review and editing. QW: Writing–review and editing. FZ: Writing–review and editing.

Funding

The author(s) declare financial support was received for the research, authorship, and/or publication of this article. This work was supported by the National Science Foundation of China (32060384), the Project of the Ministry of Science and Technology (G2022005006L), and the Research Program of Science and Technology at Universities of Inner Mongolia Autonomous Region (2020GG0100).

Acknowledgments

The authors are grateful to a large number of individuals who helped with the field sampling in the 3 years of this study. We acknowledge Inner Mongolia Academy of Agriculture and Animal Husbandry Sciences for providing us with permission to enter the research site.

Conflict of interest

The authors declare that the research was conducted in the absence of any commercial or financial relationships that could be construed as a potential conflict of interest.

Publisher's note

References

An, M., Han, Y., Zhao, C., Qu, Z., Xu, P., Wang, X., et al. (2022). Effects of different wind directions on soil erosion and nitrogen loss processes under simulated wind-driven rain. *Catena* 217, 106423. doi:10.1016/j.catena.2022.106423

Bösing, B. M., Susenbeth, A., Hao, J., Ahnert, S., Ohm, M., and Dickhoefer, U. (2014). Effect of concentrate supplementation on herbage intake and live weight gain of sheep grazing a semi-arid grassland steppe of North-Eastern Asia in response to different grazing management systems and intensities. *Livest. Sci.* 165, 157–166. doi:10.1016/j.livsci.2014.03.026

Caiyun, G., Dongsheng, Z., Du, Z., and Yu, Z. (2021). Effects of grazing on the grassland vegetation community characteristics in Inner Mongolia. *J. Resour. Ecol.* 12 (3), 319–331. doi:10.5814/j.issn.1674-764x.2021.03.002

Chen, W., Zheng, X., Chen, Q., Wolf, B., Butterbach-Bahl, K., Bruu ® ggemann, N., et al. (2013). Effects of increasing precipitation and nitrogen deposition on CH4 and N2O fluxes and ecosystem respiration in a degraded steppe in Inner Mongolia, China. *Geoderma* 192, 335–340. doi:10.1016/j.geoderma.2012.08.018

Chen, N., Zhao, G., Chen, Y., et al. (2008). Response of sandstorm transformation to climate and eco-environment change in east part of northwest China. *J. Desert Res.* 28 (4), 717–723. doi:10.3724/SP.J.1011.2008.00323

Du, H., Zuo, X., Li, S., Wang, T., and Xue, X. (2019). Wind erosion changes induced by different grazing intensities in the desert steppe, Northern China. *Agric. Ecosyst. Environ.* 274, 1–13. doi:10.1016/j.agee.2019.01.001

Gao, Y. Z., Giese, M., Gao, Q., Brueck, H., Sheng, L. X., and Yang, H. J. (2013). Community level offset of rain use-and transpiration efficiency for a heavily grazed ecosystem in inner Mongolia grassland. *Plos one* 8 (9), e74841. doi:10.1371/journal.pone.0074841

Han, J., Dai, H., and Gu, Z. (2021). Sandstorms and desertification in Mongolia, an example of future climate events: a review. *Environ. Chem. Lett.* 19, 4063–4073. doi:10.1007/s10311-021-01285-w

Hao, Y., Liu, Y., Li, Y., and Gao, F. (2022). Energy consumption and erosion mechanism of polyester fiber reinforced cement composite in wind-blown sand environments. *J. Wuhan Univ. Technology-Mater. Sci. Ed.* 37 (4), 666–676. doi:10.1007/s11595-022-2581-4

Hou, J., Zhang, Y., Tong, Y., Guo, K., Qi, W., and Hinkelmann, R. (2019). Experimental study for effects of terrain features and rainfall intensity on infiltration rate of modelled permeable pavement. *J. Environ. Manag.* 243, 177–186. doi:10.1016/j.jenvman.2019.04.096

Li, J., Tong, J., Xia, C., Hu, B. X., Zhu, H., Yang, R., et al. (2017). Numerical simulation and experimental study on farmland nitrogen loss to surface runoff in a raindrop driven process. *J. Hydrology* 549, 754–768. doi:10.1016/j.jhydrol.2017.01.035

Li, Y., Feng, G., Tewolde, H., Yang, M., and Zhang, F. (2020). Soil, biochar, and nitrogen loss to runoff from loess soil amended with biochar under simulated rainfall. *J. Hydrology* 591, 125318. doi:10.1016/j.jhydrol.2020.125318

Liu, J., Kimura, R., Miyawaki, M., and Kinugasa, T. (2021a). Effects of plants with different shapes and coverage on the blown-sand flux and roughness length examined by wind tunnel experiments. *Catena* 197, 104976. doi:10.1016/j.catena.2020.104976

Liu, X., Kang, Y., Chen, H., et al. (2021b). *Analysis of dust flux and sand collection efficiency of wind erosion near surface based on field observations*.

Miri, A., Dragovich, D., and Dong, Z. (2019). Wind-borne sand mass flux in vegetated surfaces–Wind tunnel experiments with live plants. *Catena* 172, 421–434. doi:10.1016/j.catena.2018.09.006

Munkhtsetseg, E., Shinoda, M., Ishizuka, M., Mikami, M., Kimura, R., and Nikolich, G. (2017). Anthropogenic dust emissions due to livestock trampling in a Mongolian temperate grassland. *Atmos. Chem. Phys.* 17 (18), 11389–11401. doi:10.5194/acp-17-11389-2017

Niu, S. (2020). *Faculty Opinions recommendation of Diversifying livstock promotes multidiversity and multifunctionality in managed grasslands*. Faculty Opinions-Post-Publication Peer Review of the Biomedical Literature.

Piao, J., Chen, W., Wei, K., Liu, Y., Graf, H. F., Ahn, J. B., et al. (2017). An abrupt rainfall decrease over the Asian inland plateau region around 1999 and the possible underlying mechanism. *Adv. Atmos. Sci. Engl. Ed.* 34 (004), 456–468. doi:10.1007/s00376-016-6136-5

Qu, J., Wang, T., Niu, Q., Liu, B., Tan, L., Han, Q., et al. (2023). Mechanisms of the formation of wind-blown sand hazards and the sand control measures in Gobi areas under extremely strong winds along the Lanzhou-Xinjiang high-speed railway. *Sci. China Earth Sci.* 66 (2), 292–302. doi:10.1007/s11430-021-1000-6

Reiche, M., Funk, R., Hoffmann, C., Zhang, Z., and Sommer, M. (2015). Vertical dust concentration measurements within the boundary layer to assess regional source–sink

relations of dust in semi-arid grasslands of Inner Mongolia, China. *Environ. Earth Sci.* 73, 163–174. doi:10.1007/s12665-014-3404-5

Ren, H., Eviner, V. T., Gui, W., Wilson, G. W. T., Cobb, A. B., Yang, G., et al. (2018). Livestock grazing regulates ecosystem multifunctionality in semi-arid grassland. *Funct. Ecol.* 32 (12), 2790–2800. doi:10.1111/1365-2435.13215

Ren, H., Han, G., Schönbach, P., Gierus, M., and Taube, F. (2016). Forage nutritional characteristics and yield dynamics in a grazed semiarid steppe ecosystem of Inner Mongolia, China. *Ecol. Indic.* 60, 460–469. doi:10.1016/j.ecolind.2015.07.027

Schönbach, P., Wan, H., Gierus, M., Bai, Y., Müller, K., Lin, L., et al. (2011). Grassland responses to grazing: effects of grazing intensity and management system in an Inner Mongolian steppe ecosystem. *Plant Soil* 340, 103–115. doi:10.1007/s11104-010-0366-6

Tabeni, S., Garibotti, I. A., Pissolito, C., and Aranibar, J. N. (2014). Grazing effects on biological soil crusts and their interaction with shrubs and grasses in an arid rangeland. *J. Veg. Sci.* 25 (6), 1417–1425. doi:10.1111/jvs.12204

Tao, S., Fang, J., Zhao, X., et al. (2015). Rapid loss of lakes on the Mongolian Platform. *Proc. Natl. Acad. Sci. U. S. A.*, 112–117. doi:10.1371/journal.pone.0123160

Wiesmeier, M., Munro, S., Barthold, F., Steffens, M., Schad, P., and Kögel-Knabner, I. (2015). Carbon storage capacity of semi-arid grassland soils and sequestration potentials in northern China. *Glob. Change Biol.* 21 (10), 3836–3845. doi:10.1111/gcb.12957

Yang, X., Shen, Y., Liu, N., Wilson, G. W. T., Cobb, A. B., and Zhang, Y. (2018). Defoliation and arbuscular mycorrhizal fungi shape plant communities in overgrazed semiarid grasslands. *Ecology* 99 (8), 1847–1856. doi:10.1002/ecy.2401

Zhang, B., Qu, Z., Lv, S., Gao, C., Wilkes, A., et al. (2023). Grazing effects on total carbon and nitrogen content of wind-eroded soils in desert steppe. *Land Degrad. Dev.* 34 (17), 5328–5342. doi:10.1002/ldr.4847

Zhang, H., Peng, J., Zhao, C., Xu, Z., Dong, J., and Gao, Y. (2021). Wind speed in spring dominated the decrease in wind erosion across the Horqin Sandy Land in northern China. *Ecol. Indic.* 127, 107599. doi:10.1016/j.ecolind.2021.107599

Zhang, H., Wu, C., Chen, W., and Huang, G. (2017). Assessing the impact of climate change on the waterlogging risk in coastal cities: a case study of Guangzhou, South China. *J. Hydrometeorol.* 18 (6), 1549–1562. doi:10.1175/jhm-d-16-0157.1

Zhang, P., Jeong, J. H., Yoon, J. H., Kim, H., Wang, S. Y. S., Linderholm, H. W., et al. (2020). Abrupt shift to hotter and drier climate over inner East Asia beyond the tipping point. *Science* 370 (6520), 1095–1099. doi:10.1126/science.abb3368

Zhang, T., Guo, R., Gao, S., Guo, J., and Sun, W. (2015). Responses of plant community composition and biomass production to warming and nitrogen deposition in a temperate meadow ecosystem. *PLoS One* 10 (4), e0123160. doi:10.1371/journal.pone.0123160

Zhao, Y., Gao, G., Ding, G., et al. (2022). Learning the influencing factors of soil susceptibility to wind erosion: a wind tunnel experience with a machine learning and model-agnostic interpretation application. *Catena Interdiscip. J. Soil Sci. Hydrology-Geomorphology Focus. Geoecology Landsc. Evol.* (215-), 215. doi:10.1016/j.catena.2022.106324

Zhongju, M., Xiaohong, D., Yong, G., et al. (2018). Interactive effects of wind speed, veegation cover and soil motion in controlling wind erosion in a temperature desert steppe, Inner Mongolia of China. *J. Arid Land* 10 (2), 1–14. doi:10.1007/s40333-018-0059-1

Zhu, H., Wang, D., Wang, L., Bai, Y., Fang, J., and Liu, J. (2012). The effects of large herbivore grazing on meadow steppe plant and insect diversity. *J. Appl. Ecol.* 49 (5), 1075–1083. doi:10.1111/j.1365-2664.2012.02195.x

frontiers | Frontiers in Environmental Science

TYPE Original Research
PUBLISHED 03 September 2024
DOI 10.3389/fenvs.2024.1417199

OPEN ACCESS

EDITED BY
Jing Zhao,
Xi'an University of Technology, China

REVIEWED BY
Germano Costa-Neto,
Syngenta, United States
A. Amarender Reddy,
National Institute of Agricultural Extension Management (MANAGE), India

*CORRESPONDENCE
Gajanan L. Sawargaonkar,
gajanan.sawargaonkar@icrisat.org

RECEIVED 14 April 2024
ACCEPTED 02 August 2024
PUBLISHED 03 September 2024

CITATION
Sawargaonkar GL, Davala MS, Rakesh S, Kamdi PJ, Khopade RY, Nune R, Pasumarthi R, Choudhari P, Datta A, Akuraju VR, Dixit S, Singh R and Jat ML (2024) Envirotyping helps in better understanding the root cause of success and limitations of rainfed production systems. *Front. Environ. Sci.* 12:1417199. doi: 10.3389/fenvs.2024.1417199

Envirotyping helps in better understanding the root cause of success and limitations of rainfed production systems

Gajanan L. Sawargaonkar*, Moses Shyam Davala, S. Rakesh, Prasad J. Kamdi, Rohan Y. Khopade, Rajesh Nune, Rajesh Pasumarthi, Pushpajeet Choudhari, Aviraj Datta, Venkata Radha Akuraju, Sreenath Dixit, Ramesh Singh and Mangi Lal Jat

International Crops Research Institute for the Semi-Arid Tropics (ICRISAT), Patancheru, Telangana, India

The current diagnostic agronomy study of the Bankura region of West Bengal, India, examined the variations in crop yields through a socio-ecological analysis of multiple production system components. Envirotyping for root cause analysis was employed to delve into the variables that affect the performance of rainfed production systems. Mother Earth, man, machine, management, and materials (5Ms concept) were the five indicators under which the variables were grouped. Findings demonstrated the fragility of the region's soils due to its undulating terrain, unpredictable rainfall patterns, and frequent drought scenarios. The LULC's NDVI showed that the agricultural area is about 60% and 43% of the total geographical area in the Hirbandh and Ranibandh blocks, respectively. Soils are acidic and diagnosed with deficiency of both macro and micronutrients (phosphorous, sulfur, and boron) having poor water holding capacity (35 to 55 mm for a 50 cm soil depth). The sand and soil organic carbon contents ranged between 43.04%–82.32% and 0.17%–1.01%, respectively with a low bacterial population. These factors are the root cause for low cropping intensity (106%) and low paddy productivity (3,021 kg/ha). Overall, the study contributes to designing and scaling-up of sustainable landscape management practices that could ensure higher cropping intensity and system productivity in similar agro-ecologies with limited evidence.

KEYWORDS

envirotyping, soil health, rainfed agriculture, soil degradation, climate-resilient agriculture, crop productivity

1 Introduction

Considering that 17.4% of India's GDP comes from agriculture and related industries, which employ 54.6% of the nation's workforce, agriculture is a key sector of the economy. It is desirable to use cultivable land as intensively as possible to maximize agricultural output since there is an inelastic supply of land for cultivation in a country like India, where there is demand from a high and expanding population for cultivable land. Nonetheless, since the country's independence, its net sown area has increased roughly by 20% and has reached a point where further growth is not currently feasible. There are only two ways to use land to meet the nation's growing population's needs for food and other necessities: either increasing

the net area under cultivation or intensifying cropping over the current area. Increasing cropping intensity is one of the tried-and-true methods for raising agricultural productivity and creating jobs in rural areas. Nonetheless, the degree of cropping intensity is mostly determined by the agroecological conditions and the inputs used in agriculture (Mondal and Sarkar, 2021).

In India, there are many different cropping systems under various agroclimatic zones, which are primarily determined by soil type, rainfall, climate, technology, policies, and the socioeconomic status of the farming community (Gulati and Juneja, 2022). All these factors have a significant impact on crop productivity and intensity. Bankura is the western district of West Bengal, India, and much of the terrain is undulating, having soils with low available moisture capacity (National Bureau of Soil Survey and Land Use Planning, 2013). The soils in Bankura are of inherently poor quality due to erosion and warm climate. Soil degradation is exacerbated by the conversion of land uses, such as forests to croplands, and poor farmland management (De et al., 2022). Due to unpredictable rainfall patterns, rainfed crops are typically grown with low nutrients, and the farmers in these areas tend to be resource-poor (Srinivasarao et al., 2013). As a result, these soils frequently have nutrient deficits, which make it difficult for crops to produce desirable yields. Long-term fertilizer studies spanning approximately 30 years showed that organic manures are essential for maintaining agricultural yield in addition to enhancing soil organic carbon stock (Srinivasarao et al., 2009). However, high temperatures oxidize soil organic matter (SOM); hence, the conservation and maintenance of SOM in tropical regions is the biggest challenge. Consequently, there is a multi-nutrient deficiency in these soils.

The four different types of drought situations that can occur in Bankura are meteorological drought, hydrological drought, agricultural drought, and socio-economic drought, which affects human activities (Wilhite and Glantz, 1985; Wilhite, 2000; AMS, 2004; Parry et al., 2007; Bera and Bandyopadhyay, 2017; District Disaster Management Cell, 2017). Drought coupled with the high runoff rate of rainwater, inadequate storage facilities, high surface runoff, and low water holding capacity of the soil exacerbates the situation during the post-rainy season (Rahim et al., 2011; District Disaster Management Cell, 2021). The development of sustainable cropping systems is significantly becoming important in the current scenario with increased vulnerability to climate change. The UN Sustainable Development Goals (SDGs) such as #SDG13 and #SDG15 focus on climate action, and the life on land can be effectively achieved by the adoption of sustainable agriculture practices. Consequently, we can achieve land degradation neutrality (LDN) and climate mitigation.

Large yield gaps between potential, on-station, and farm yields (Srinivasarao et al., 2010) are attributable to many factors, which include a range of management techniques that affect crop yield, in addition to having a high correlation with certain socioeconomic aspects. "Envirotyping" is an approach proposed by Xu (2016) which considers all environmental factors in order to determine the impact of climate change on the growth and production of plants. Batan (2017) and Xu (2016) classified the envirotyping factors into five major groups, namely, soil, climate, crop canopy, companion organisms, and crop management, and these components are important environmental factors affecting plant growth. However, the human element (i.e., man) was not considered in the envirotyping framework, like the role of socio-economic factors, which greatly influence the decision-making process and adaptation strategies of the farmer to climate change. The land tenancy system, farm size, skilled (young) labor, capital (agricultural credit), market and product price, farm mechanization, access to and knowledge of IT, farm subsidies, resource management, farm risk, awareness, age of the farmers, population, rural development, government policies, and religion are some of the notable socioeconomic barriers that numerous studies have reported (Roy and Kaur, 2015). As the budgetary payments to farmers did not counteract the price-depressing effects of intricate domestic marketing rules and trade policy measures, it inevitably affected the farmers' net income and, consequently, the subsequent investments in agriculture. This led to the dependency of farmers, particularly small and marginal farmers, on government schemes and support. Hence, the reasons for low productivity or cropping intensity cannot be attributed to one single factor, but it is a complex relationship between tangible and intangible factors and needs a thorough understanding of inter-relationship.

In the present investigation, we contributed to answering these questions by analyzing a case study of the Bankura region of West Bengal, India, with the objectives (i) to characterize the existing ecosystem complemented with socio-economic analysis, (ii) to analyze the root cause for low agricultural productivity and cropping intensity, and (iii) to recommend site-specific interventions to address the challenges.

2 Material and methods

2.1 Root cause analysis

Root cause analysis (RCA) was carried out in a small focus group of about six to eight people in each of the 10 villages using a flip chart paper, and as the conversation progressed, important factors were added. The first step is to discuss and agree on the problem or issue to be analyzed. The broader topic was further broken down with the help of a tree. The problem or issue is written in the center of the flip chart, which becomes the "trunk" of the tree representing the "focal problem." The next step is to identify the causes of the focal problem, which become the roots, and then identify the consequences, which become the branches. As the study involves envirotyping, the measurements include both field and laboratory activities such as planning, sample collection, laboratory tests and analysis, and data handling (Worthington et al., 2024). To meticulously understand the concepts of cropping systems in rainfed regions and the root cause determination (Alpha et al., 2021) behind each of the 5Ms, the authors attempted to generate a research-based fishbone concept framework (Kaoru Ishikawa diagram) for the underlying causes of an event with proper corrective measures and further prevent any recurrences (Murumbi, 2014).

2.2 Five M's concept

The present investigation was outlined under the framework of five M's, e.g., Mother Earth, man, machine, management, and

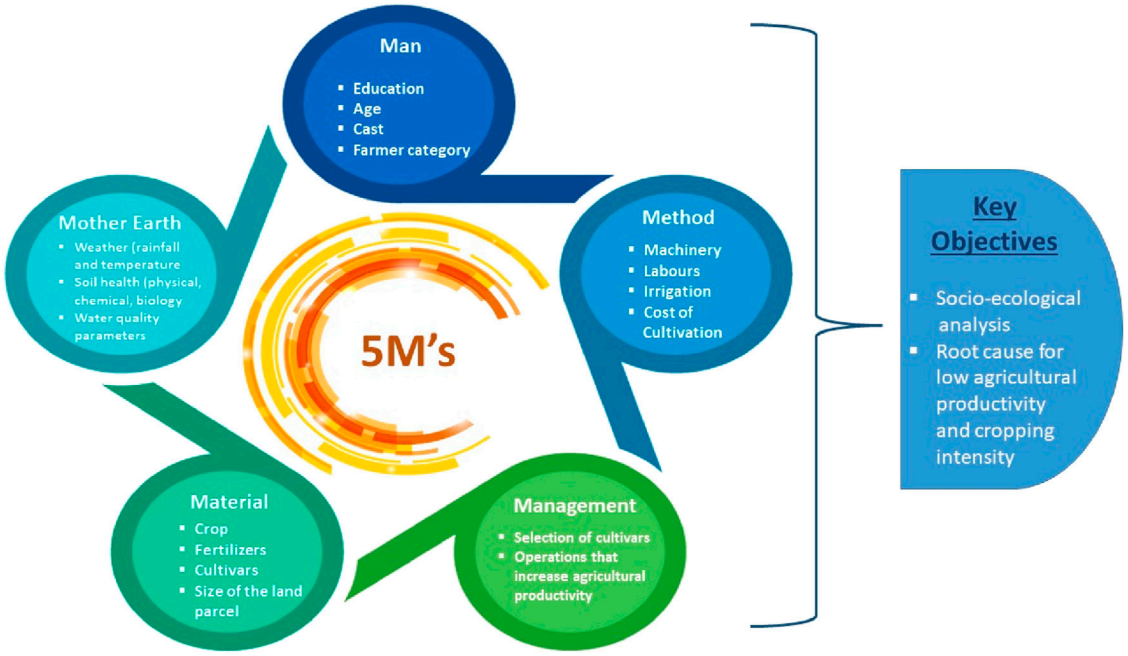

FIGURE 1
5M concept of the study.

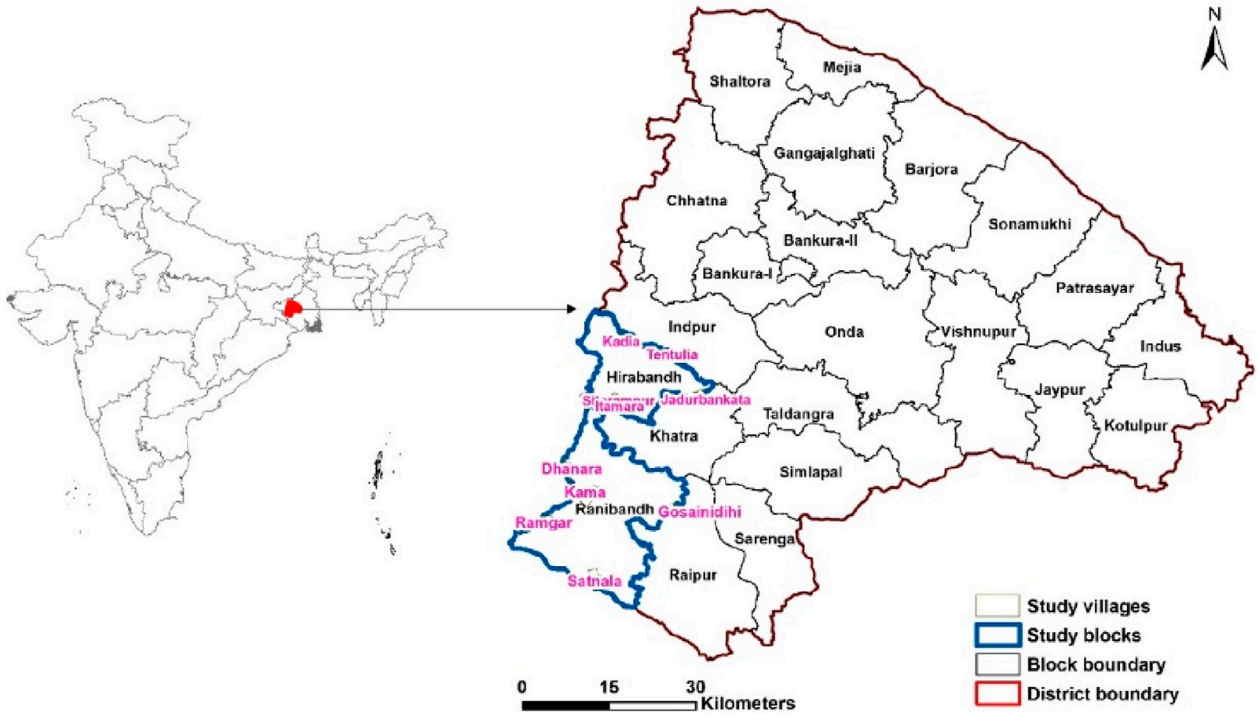

FIGURE 2
Location of the experimental area.

materials (Zielińska-Chmielewska et al., 2021). Several other methods (Chaudhary et al., 2015; Rao et al., 2019; Reddy et al., 2021) have also studied vulnerability indicators using different quantifying methodologies/approaches, but the 5M's approach unveiled the opportunities to identify the key root causes of each problem in the present study. We used this approach to

critically focus on the 5Ms and discuss several sub-elements (Figure 1) under each M to come up with salient features of the studied regions. To identify a research problem's primary reason or causes, a "five whys" approach was used. Any question will serve as the starting point and basis for the subsequent question in this manner. Quality professionals rank fifth for repeating the inquiry based on their experience and field studies. This approach's primary objective was to identify the underlying source of an issue by asking "why?" a lot.

2.3 Site description

The study area comprises Ranibandh (22.8661°N and 86.7831°E) and Hirbandh (23.0616°N and 86.8145°E) blocks of the Bankura district (Figure 2) of the south-western part of West Bengal, India, which is bordered by the Mukutmanipur reservoir. The geographical areas of the Hirbandh and Ranibandh blocks are 199 and 418 sq. km, respectively. There are about 119 villages in Hirbandh and about 184 villages in the Ranibandh block with diverse socio–agro–economic characteristics. All the villages in both blocks were clustered based on the demographic and socio-economic criteria (Supplementary Table S1), and five representative villages from each block were selected (Figure 2). The villages, namely, Tentulia, Sitarampur, Jadurbankata, Kadia, and Itamara from the Hirbandh block, while Satnala, Gosainidihi, Dhanara, Ramgarh, and Kama from the Ranibandh block were selected for the study.

2.3.1 Selection of samples based on landforms

As the topography influences the cropping pattern and productivity (Kumhálová et al., 2011), 30 farmers from each village were randomly selected and classified into four categories: uplands, mid-uplands, mid-lowlands, and lowlands (Jana SK, 2011A). The uplands consist of a mix of non-arable wasteland and cultivable land with thin topsoil and low water-holding capacity. The mid-uplands are sandy to sandy loam and shallow with low organic matter and moisture holding capacity. The mid-lowlands are loamier than the mid-uplands and are lower than mid-uplands but higher than lowlands (Sugata et al., 2017). Low-lying arable land is best suited for paddy cultivation as water from uplands collects in these types of plots.

2.4 Soil and water sampling

To analyze the nutrient status and physical and soil biological properties, 20 composite soil samples were collected from each of the 10 villages using a stratified soil sampling method (up-, mid-, and lowlands). Water samples were collected from drinking water wells, community ponds near the households used for washing, and from the main irrigation sources in each of the 10 villages for its quality assessment. Overall, the sample design comprises 300 household samples, 200 soil samples, and 30 water samples (Supplementary Table S2).

2.5 Laboratory analysis

Table 1 shows the brief methodology used to analyse various parameters of soil and water:

TABLE 1 Laboratory protocol used for testing soil and water samples and please add the right hand border.

Parameter measured	Method	Reference
Chemical properties		
pH	Soil pH was measured by a glass electrode using a soil–water suspension ratio of 1:2	Rhoades (1996)
EC	Soil electrical conductivity (EC) was measured by a calomel electrode using a soil–water suspension ratio of 1:2 after settling the sample overnight using an EC meter	Rhoades (1996)
Organic carbon	Soil samples were ground to pass through a 0.25-mm sieve for organic carbon analysis by the Walkley–Black method	Nelson and Sommers (1996)
Exchangeable bases	Exchangeable bases, e.g., K, Ca, and Mg, were determined using the neutral normal ammonium acetate method	Okalebo et al. (1993)
Available P	Available P in acidic soils was estimated by using Bray's extractant no 1- 0.03*M* NH_4F in 0.025*M* HCl Available P in alkaline soils was estimated by using sodium bicarbonate ($NaHCO_3$) of pH 8.5 as an extractant for soils, respectively	Bray and Kurtz (1945) Olsen (1982)
Available micronutrients	Available micronutrients, e.g., Fe, Cu, Mn, and Zn, were extracted by the DTPA reagent of pH 7.3	(Lindsay and Norvell, 1978)
Available boron	Available boron was extracted from hot water	Keren (1996)
Available S	Measured using 0.15% calcium chloride ($CaCl_2$) as an extractant	Tabatabai (1996), Sahrawat et al., (2009)
Inductively coupled plasma-optical emission spectroscopy (ICP-OES) was used to detect sulfur and boron, whereas microwave plasma atomic emission spectroscopy MP-AES was used to quantify macro and micronutrients		
Physical properties The soil samples collected were analyzed for the parameters, viz., water holding capacity at 0.33 bar (upper limit); permanent wilting point at 15 bar (lower limit), plant available water (derived value), and profile water storage capacity (derived value) using standard protocols. This analysis helps us to know the plant available moisture content and to assess profile water storage capacity		
Microbial properties Microbial biomass count (bacteria, fungi, actinomycetes, nitrogen-fixing bacteria, and phosphate-solubilizing bacteria) was estimated using 1 g of each soil sample, which was subjected to serial dilution in 0.9% of sterile saline solution and spread on nutrient agar medium, potato dextrose medium, actinomycetes isolation agar, and Jensen's medium, respectively (Sanders, 2012). The soil respiration rate was estimated by the alkali trap method (Anderson, 1982)		
Water Water samples were analyzed for presence of nitrates, carbonates, Chemical Oxygen Demand (COD), and heavy metals using standard protocols.		

2.6 Land use and land cover (LULC)

Detection of changes in land use/land cover patterns is a good indicator of land degradation and, hence, an essential task for sustainable natural resources management planning. This section analyses the changes in land use/land cover for the years 2005–06 and 2020–21 in Hirbandh and Ranibandh blocks. To analyze changes in land use in the study area, time-series satellite data from 2005–06 and 2020–21 were used. Monthly IRS-P6 AWiFs images were utilized, with digital numbers converted to reflectance values to normalize multi-date effects. Top-of-atmosphere (TOA) reflectance was calculated using a reflectance model built in ERDAS Imagine (Thenkabail et al., 2004; Velpuri et al., 2009), and normalization was based on available metadata in header files. A hybrid approach, including decision tree or supervised MXL or both, was used to classify the data and extract information on land use/land cover classes and agricultural seasons. This allowed for regular process repetition at set time intervals. All classes were reclassified into major classes such as built-up, rainy season (June to November), post-rainy (December to March), double crop, fallow land, forest, wasteland, and waterbodies.

2.7 Cropping intensity and diversification index

The cropping intensity of the region was estimated to understand the present utilization efficiency of the land, which is the ratio between the gross cropped area (GCA) and net cropped area (NCA) (Brahmanand et al., 2021). The GCA represents the total area sown once, twice, or more in a specific year; hence, in GCA, an area is counted twice when a crop is sown twice on the same plot of land, while the NCA is the crop-planted area that was only counted once. Crop diversity is calculated using the Simpson index of diversification (Simpson, 1949), which measures the diversity by considering both the total number of species and the relative abundance of each species.

Simpson index of diversification (SID) = $1 - \sum_{i=1}^{k} p_i^2$ where

$$p_i = \left(A_i \middle| \sum_{i=1}^{k} A_i \right).$$

Here, A_i is the amount of land allocated to each i^{th} crop, and $\sum_{i=1}^{k} A_i$ is the total amount of land area cultivated by a farmer for all his crops.

2.8 Statistical analysis

The standard deviation and the standard error mean of the samples of different villages under two different blocks were computed using SPSS software- version: 17.0.

3 Results and discussion

3.1 Agronomical challenges in the selected villages of Hirbandh and Ranibandh

The variation in cropping intensity (CI) has been noticed in the sample locations (Figure 3A). Jadurbankata and Itamara have a higher CI, which is around 200%. On the other hand, Sitamara and Kamo Gora have a lower CI (<100%). The average CI of all the 10 villages was 121%, whereas after the exclusion of the two villages (viz, Jadurbankata and Itamara), the CI for the rest of the villages was 106%, thus indicating the low land use efficiency of the study region (Mondal, 2019). Due to low rainfall and excess draining out of water, there is less residual soil moisture availability in these areas during the post-rainy season, thereby making farmers unable to cultivate multiple crops, and thus, the region witnesses low CI.

Diversified cropping systems, in general, tend to be more agronomically stable and resilient (Makate et al., 2016). The average Simpson diversification index (SDI) score was <0.5, indicating moderate diversification across the villages (Figure 3B). The highest SDI was observed at Jadurbankata (0.30), indicating diversification from subsistence crops to more commercial crops. Studies proved that crop diversification has a significant and positive impact on the farm income of households (Lama, 2016), and as these areas have low cropping system diversification and low CI, the agricultural income is very meager to sustain the livelihoods of small and marginal farmers in the area. Hence, it is very important to understand the socio-ecological reason for low CI.

3.2 Status of Mother Earth, man, machine, management, and materials (5Ms)

The team has brainstormed along with farmers and scientists about many possible causes and their effects that lead to low intensity and productivity and are represented in a cause-and-effect diagram or a fishbone diagram (Figure 4). The factors are classified into five main groups: Mother Earth, man, material, methods, and management.

Each node in the framework represents the causes that affect it. Each cause has its opportunities for improvement and needs to be analyzed separately. Based on the judgment of the expert team, the problem is assigned to the pre-described root cause (5M's). Table 2 shows the important controllable causes of this problem.

3.2.1 Mother Earth

Mother Earth encapsulates the environmental elements such as weather, soil, water, and other uncontrollable events that fall into this category. The present study includes weather (rainfall and temperature), soil health (physical, chemical, and biological), and water quality parameters under this category.

3.2.1.1 Land use and change detection

A total of eight classes were generated to understand LULC in Hirbandh and Ranibandh blocks for the year 2020–21 (Figure 5). Time-series satellite data for the years 2005–06 and 2020–21 were used to analyze the land use change in the study area. The changes in land use/land cover classes for the period 2005 to 2020 were analyzed as a percent difference. Remote-sensing analysis showed that the agricultural area is about 60% and 43% of the total geographical area in the Hirbandh and Ranibandh blocks, respectively. This shows that both blocks are agriculture-dominant. About 54% and 37% of areas are under the rainy season, and negligible areas are under the post-rainy season in Hirbandh and Ranibandh blocks (Table 3). The area under built-up,

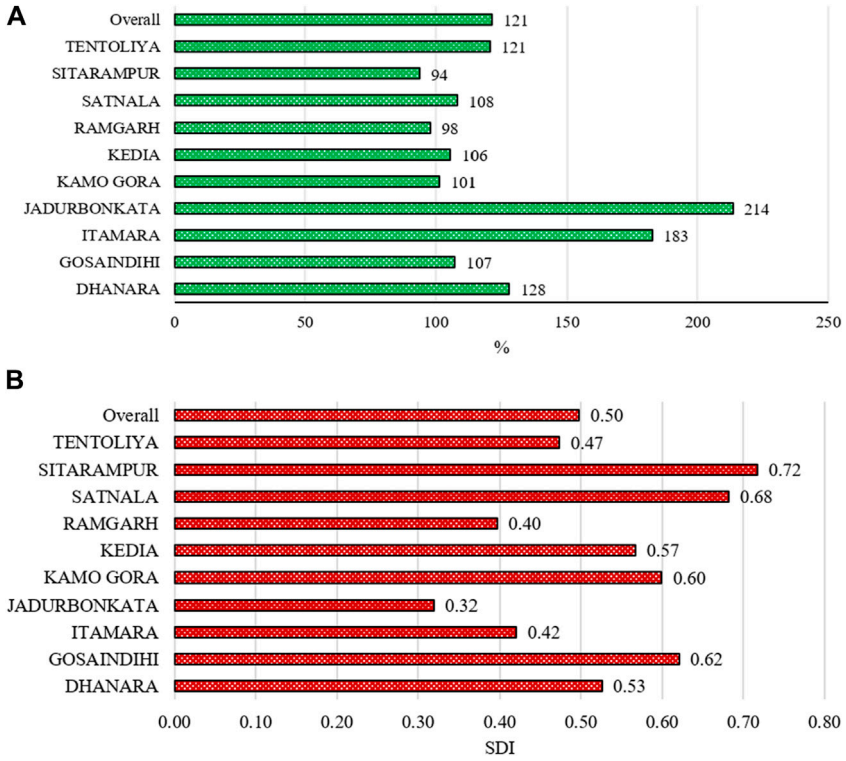

FIGURE 3
(A) Cropping intensity of the study area and **(B)** Simpson diversity index of the study villages.

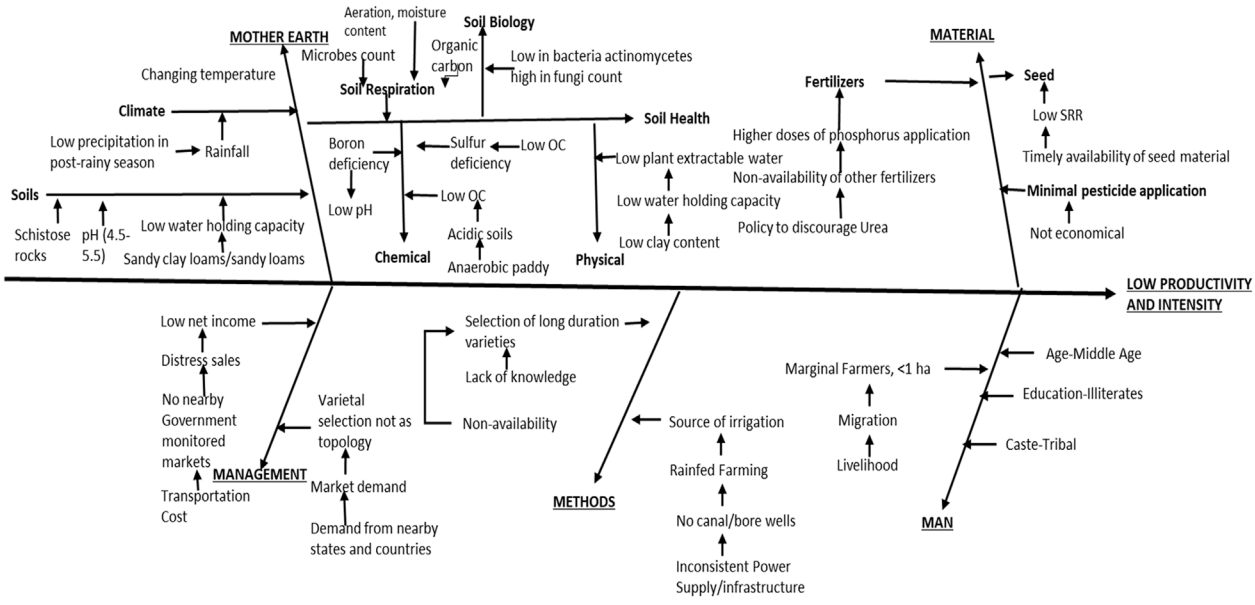

FIGURE 4
Fishbone conceptual framework.

post-rainy, forest, and water bodies has not changed significantly (<1%) in the Hirbandh block. The area under the rainy season has increased by 18% due to the conversion of 5.5% of fallow land, 9.5% of double crop land, and 3.5% of wasteland.

Analysis showed that the areas under built-up, post-rainy, forest, and waterbodies have not changed significantly (<1%) in the Ranibandh block. However, only the rainy season area increased by 13.4% due to the conversion of 7.5% of fallow

TABLE 2 Controllable root causes of the problem.

Problem	Main root cause	Assigned M
Low productivity	Boron, sulfur, and phosphorous deficiency	Mother Earth
	Low varietal and seed replacement	Material
	Selection of varieties according to topography	Management
	Pest management	
Low intensity	Low water holding capacity	Mother Earth
	Low in beneficial bacteria	Mother Earth
	Low in organic content	Mother Earth
	Low economic returns from rainy season crop	Management/man
	Migration	Man

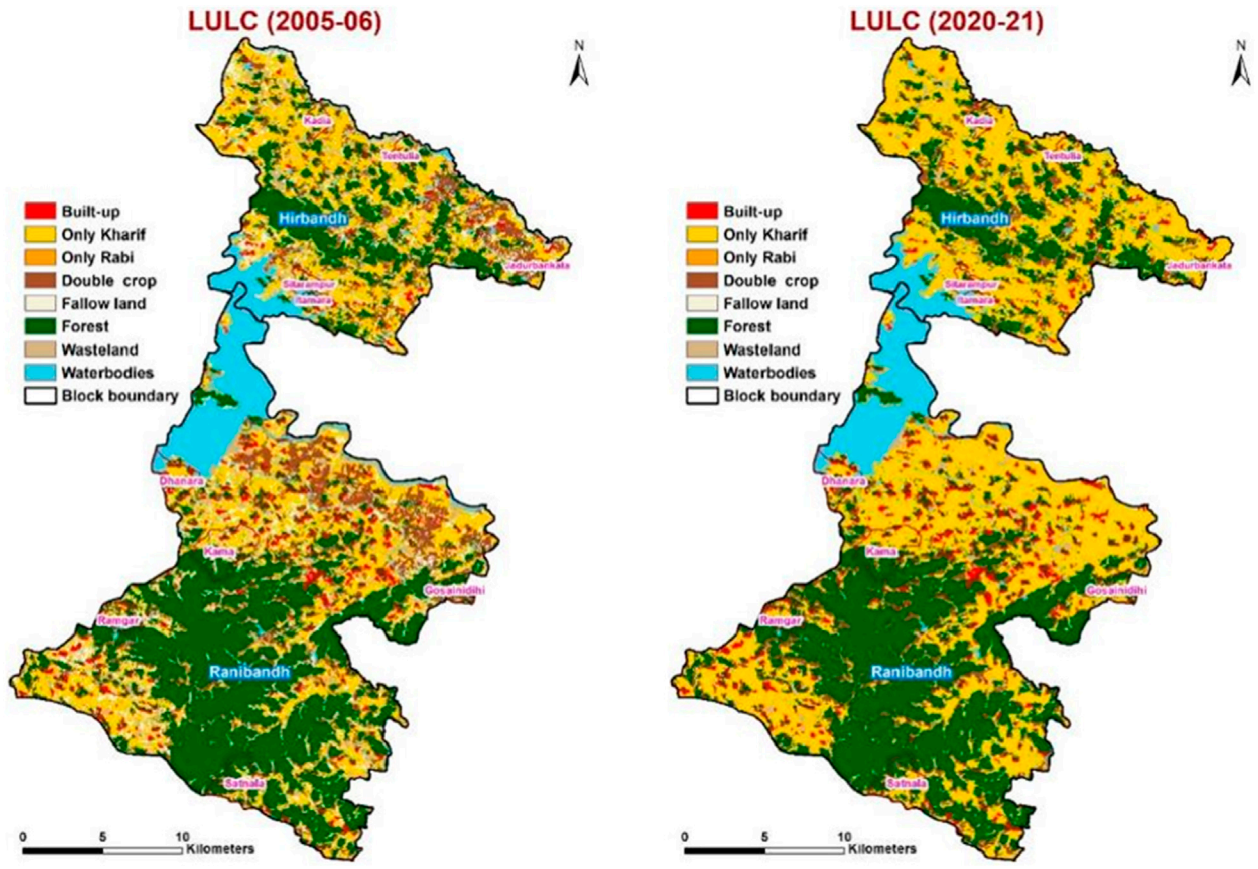

FIGURE 5
LULC of Hirbandh and Ranibandh blocks for 2005–06 and 2020–21.

land, 3.5% of the double crop land, and 2.5% of wasteland. Overall, Hirbandh and Ranibandh blocks experienced a similar type of conversion from one land use class to other classes. The existing cropping pattern in the region is presented in Supplementary Table S3, and it shows that paddy cultivation occupies 99% of the cropped area in the rainy season and only 6% in the post-rainy season. The post-rainy season was dominated by mustard (54%), followed by potato (18%) and watermelon 10%. Vegetables (other than potato) occupy only 6.4% of the cropped area as they are majorly grown from self-consumption rather than for the market. The post-rainy area occupies only 52% of the rainy season area (Supplementary Table S3), highlighting that farming during the post-rainy season is under constrained conditions. As paddy cultivation occupies

TABLE 3 Percentage of land use/land cover classes of the study area during 2020–21.

Class name	Hirbandh		Ranibandh	
	Area (sq.km)	Percentage	Area (sq.km)	Percentage
Built-up	5.84	2.92	22.87	5.46
Rainy	108.32	54.22	155.59	37.18
Post-rainy	0.18	0.09	0.07	0.02
Double crop	14.20	7.11	23.25	5.56
Fallow	0.40	0.20	0.31	0.07
Forest	51.53	25.79	173.68	41.50
Wasteland	3.75	1.88	7.76	1.85
Waterbodies	15.58	7.80	35.00	8.36
Total	199.80	100	418.53	100

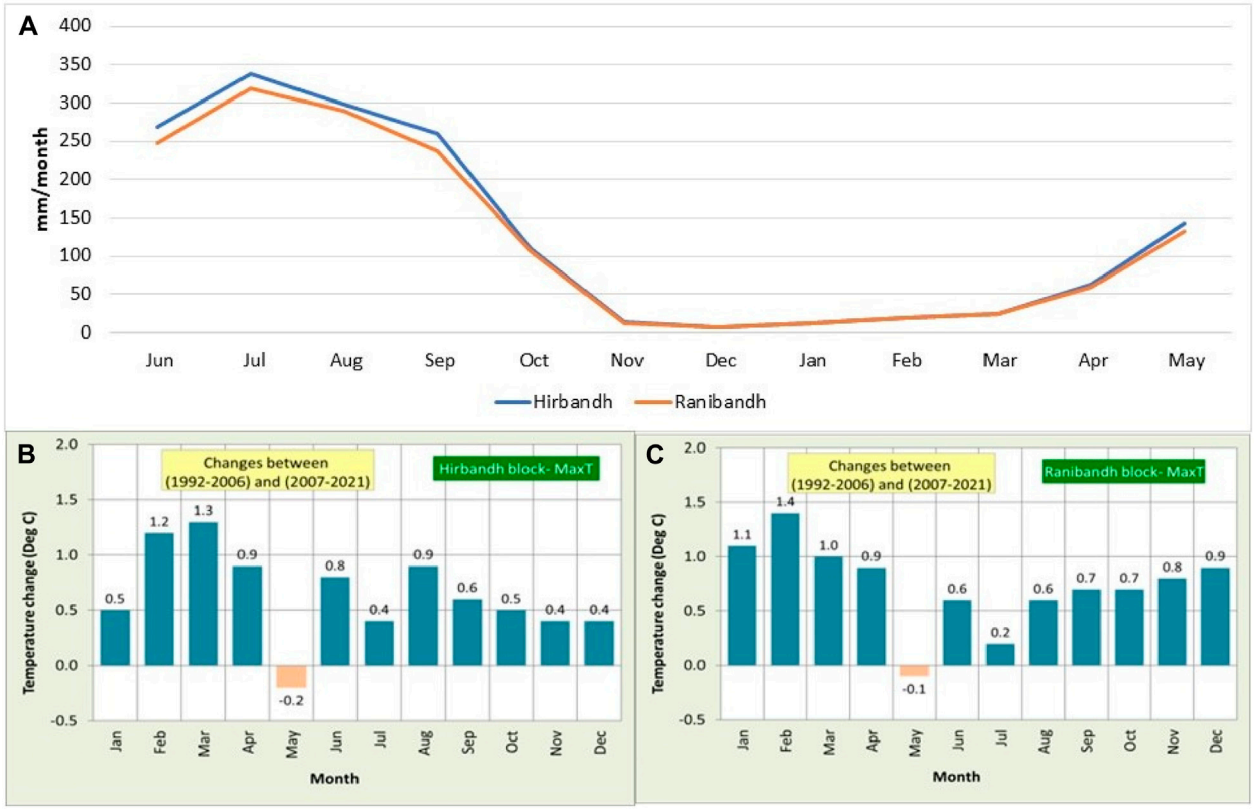

FIGURE 6
(A) Seasonal patterns of monthly rainfall in Hirbandh and Ranibandh blocks **(B)** and **(C)** long-term temperature changes in Hirbandh and Ranibandh blocks, respectively, calculated as mean (1992–2006) monthly averages–mean (2007–2021) monthly averages.

major portion of the land, the study primarily focuses on paddy cultivars and the related factors of production.

3.2.1.2 Climate

3.2.1.2.1 Rainfall. The selected blocks fall under the "hot, dry, sub-humid ecological hub region" with the length of the rainfed crop-growing period (LGP) being approximately 150–180 days. The normal rainfall of the blocks was 1,556 mm/annum and 1,464 mm/annum, and nearly 75% of the total rainfall is received between June and September (Figure 6) and nearly 15% during the months of March–May. The post-rainy season receives only 8%–10% of the rainfall, which could be the main reason for the very low CI. High rainfall variability was observed during the monsoon season (high: 7%–8%) in the Hirbandh block, which led to decreased runoff

TABLE 4 Soil physicochemical and biological properties of the selected villages under Hirbandh and Ranibandh.

Block	Village	Topography	Sand (%)	Silt (%)	Clay (%)	Textural class	Volumetric water content at FC (cm^3/cm^3)	Volumetric water content at PWP (cm^3/cm^3)	Plant extractable water in 50-cm depth (mm)	Plant extractable water in 100-cm depth (mm)	pH	OC	Soil respiration rate (mg CO_2/g soil)	Bacteria (CFU/g)	Fungi (CFU/g)	Actinomycetes (CFU/g)
Hirbandh	Sitarampur	Upper	74.93	13.79	11.28	SL	0.22	0.08	69	138	5.09	0.52	18.15	1.2×108	0.57×105	0.75×106
	Kendiya		78.65	8.79	12.56	SL	0.14	0.07	38	75	5.69	0.38	23.65	0.41×10^9	0.81×10^5	0.65×10^6
	Itamara		59.82	27.62	12.56	SL	0.28	0.09	94	187	5.12	0.6	14.85	VL	0.31×10^5	VL
	Tentulia		64.71	13.86	21.43	SCL	0.28	0.13	72	145	4.94	0.65	23.65	VL	0.29×10^6	0.19×10^6
	Jadurbankata		67.35	12.56	20.09	SCL	0.27	0.1	85	170	5.3	0.2	22.55	0.31×108	1.1×10^5	0.84×10^5
Ranibandh	Ramgarh		62.18	20.17	17.65	SL	0.28	0.13	73	146	5.51	0.86	18.94	0.15×106	0.41×10^6	0.78×10^5
	Satnala		46.98	25.25	27.77	SCL	0.43	0.23	97	194	5.65	1.01	24.75	VL	0.26×10^5	0.27×10^6
	Dhanara		54.72	23.9	21.38	SCL	0.34	0.14	102	203	5.26	0.57	12.65	VL	0.41×10^5	0.19×10^6
	Kama		62.05	17.71	20.24	SCL	0.31	0.14	86	172	4.99	0.41	21.46	0.12×107	0.84×10^6	VL
	Gosainidihi		82.32	7.58	10.1	LS	0.21	0.08	65	130	4.72	0.17	25.85	VL	0.95×10^5	0.68×10^6
Average			65.371	17.123	17.51	—	0.276	0.119	78.1	156	5.22	0.513	20.7625	—	—	—
SD			10.87	6.95	5.70	—	0.08	0.05	18.91	37.78	0.33	0.27	4.92	—	—	—
SEM			3.44	2.20	1.80	—	0.02	0.01	5.98	11.95	0.10	0.09	1.55	—	—	—
Hirbandh	Tentulia	Middle	47.03	20.18	32.79	SCL	0.34	0.19	77	153	5.76	0.61	32.45	VL	0.29×10^5	0.25×10^6
	Sitarampur		69.86	8.79	21.35	SCL	0.26	0.14	60	120	5.01	0.59	20.35	VL	0.47×10^5	0.44×10^6
	Jadurbankata		64.81	12.57	22.62	SCL	0.3	0.12	93	186	5.62	0.49	22.55	VL	0.56×10^5	0.43×10^5
	Kendiya		67.24	12.6	20.16	SCL	0.24	0.11	62	125	5.43	0.53	25.85	0.22×107	0.69×10^5	0.21×10^6
	Itamara		57.27	17.59	25.14	SCL	0.32	0.16	78	157	5.3	0.54	21.45	VL	0.32×10^5	VL
Ranibandh	Satnala		63.38	18.94	17.68	SL	0.34	0.14	98	196	4.88	0.71	29.15	0.21×105	0.29×10^6	VL
	Gosainidihi		69.74	12.61	17.65	SL	0.28	0.12	83	167	5.07	0.54	6.05	0.61×107	1.02×10^5	0.34×10^7
	Dhanara		69.69	12.63	17.68	SL	0.31	0.13	87	175	5.12	0.54	24.75	VL	0.28×10^5	VL
	Ramgarh		54.28	17.78	27.94	SCL	0.36	0.18	86	172	4.79	0.61	23.41	VL	0.71×10^5	VL
	Kama		48.88	17.89	33.23	SCL	0.39	0.23	80	160	5.01	0.58	21.68	VL	0.61×10^6	VL
Average			61.863	14.521	23.62	—	0.314	0.152	80.4	161.1	5.27	0.569	22.825	—	—	—
SD			8.76	3.75	5.98	—	0.05	0.04	12.12	24.18	0.31	0.07	7.88	—	—	—
SEM			2.77	1.19	1.89	—	0.01	0.01	3.83	7.65	0.10	0.02	2.49	—	—	—
Hirbandh	Sitarampur	Lower	69.83	12.57	17.6	SL	0.31	0.12	94	189	4.79	0.51	24.75	L	0.54×10^6	0.64×10^6
	Itamara		74.86	12.57	12.57	SL	0.29	0.1	92	184	5.19	0.56	15.95	VL	0.32×10^5	VL

(Continued on following page)

10.3389/fenvs.2024.1417199

TABLE 4 (*Continued*) Soil physicochemical and biological properties of the selected villages under Hirbandh and Ranibandh.

Block	Village	Topography	Sand (%)	Silt (%)	Clay (%)	Textural class	Volumetric water content at FC (cm^3/cm^3)	Volumetric water content at PWP (cm^3/cm^3)	Plant extractable water in 50-cm depth (mm)	Plant extractable water in 100-cm depth (mm)	pH	OC	Soil respiration rate (mg CO_2/g soil)	Bacteria (CFU/g)	Fungi (CFU/g)	Actinomycetes (CFU/g)
	Jadurbankata		46.68	16.5	36.82	SC	0.34	0.2	71	142	7.13	0.86	13.75	0.54×10^8	0.63×10^5	0.42×10^6
	Kendiya		69.79	10.07	20.14	SCL	0.22	0.09	65	129	5.26	0.28	11.55	1.6×10^7	0.7×10^5	0.75×10^6
	Tentulia		43.74	20.46	35.8	CL	0.36	0.19	82	165	5.04	0.78	22.55	VL	0.16×10^6	0.29×10^6
Ranibandh	Ramgarh		54.52	17.69	27.79	SCL	0.31	0.17	69	138	5.49	0.79	16.98	0.67×10^5	0.84×10^6	0.36×10^6
	Dhanara		54.69	27.69	17.62	SL	0.3	0.13	84	169	5.16	0.6	8.25	VL	0.27×10^5	VL
	Satnala		81.15	7.54	11.31	LS	0.19	0.08	54	108	5.16	0.56	17.05	VL	0.19×10^6	0.19×10^6
	Gosainidihi		59.14	12.77	28.09	SCL	0.39	0.19	103	207	5.32	0.73	20.35	0.44×10^5	1.04×10^5	0.98×10^6
	Kama		43.04	19.42	37.54	CL	0.48	0.26	110	219	4.97	0.85	15.98	VL	0.74×10^5	0.46×10^6
Average			56.594	16.518	26.89	—	0.319	0.153	82.4	165	5.38	0.61	16.775	—	—	—
SD			13.53	5.88	10.02	—	0.08	0.06	17.75	35.65	0.72	0.18	5.60	—	—	—
SEM			4.28	1.86	3.17	—	0.03	0.02	5.61	11.27	0.23	0.06	1.77	—	—	—

Note: SL, sandy loam; SCL, sandy clay loam; CL, clay loam; LS, loamy sand; L, less; VL, very less.

10.3389/fenvs.2024.1417199

during the monsoon season (2007–2021). The rainfall variability in the Ranibandh block is observed low (2%) during the monsoon season.

3.2.1.2.2 Temperature. Although the period between May and June is the hottest with temperature as high as 45°C, the onset of southeast monsoons brings down temperature. The winter (November–January) temperature is between 22°C and 25°C (Figure 6), and this period is most suited for the cultivation of a variety of good quality vegetables. The meteorological data obtained from the local meteorological department indicate that the maximum temperature in Hirbandh and Ranibandh during the monsoon season increased by 0.20°C–0.40°C (winter) and 1.30°C–1.40°C (summer) (February/March), respectively. However, there was a decreasing trend in temperatures in May in both the blocks.

3.2.1.3 Soil health

3.2.1.3.1 Soil physical properties. The sand content of 30 soil samples ranged from 43.04% to 82.32%, silt content ranged from 7.54% to 27.69%, and clay content ranged from 10.10% to 37.54% (Table 4). Light textured soils (high sand) have a low water holding capacity and require frequent rains or irrigations, as compared to heavy textured soils (high clay) which have a high water holding capacity (Pathak et al., 2009). The upland soils are light textural soils, and lowland soils are heavy textural soils as the clay content is comparatively higher (Table 4). Simple water budgeting obtained from model simulations (Supplementary Table S4) showed that 30%–44% of the runoff generated in these blocks is already captured by existing water storage structures (waterbodies). Although the soil moisture holding capacity of soils in the Ranibandh block is higher than that in Hirbandh block, the average water holding capacities of both soils are poor (35 mm–55 mm for a 50-cm depth of soil). Similarly, groundwater recharge was found high (9%) due to sandy loamy soils in both the blocks.

Water retention of Bankura soils at 0.33 bar field capacity (FC) varies from 0.14 to 0.48 cc/cc, whereas at 15 bar, permanent wilting point (PWP) varies from 0.07 to 0.26 cc/cc (Table 4). Alfisols are highly variable in depth, texture, bulk density, and stoniness; their water retention and transmission properties are very site-specific and must be judiciously evaluated for the specific areas in which quantitative studies of soil–plant–water relations are conducted (El-Swaify et al., 1985). Water availability to crops is affected by their rooting characteristics and soil physical properties (El-Swaify et al., 1985). The value of plant extractable water (PEW) for the Bankura soils in the top 50-mm layer varies from 38 mm to 110 mm, whereas, in the top 100 cm, depth varies from 75 mm to 219 mm (Table 4). Crop water requirements of various crops are wheat and maize, 500 to 600 mm; groundnut, 500 to 550 mm; sorghum/millets, 350 to 500 mm; sunflower, 400 to 500 mm; finger millet, 400 to 450 mm; chickpea, green gram, and black gram, 350 to 400 mm; mustard, 400 to 450 mm; safflower, 250 to 300 mm; and sesame, 200 to 250 mm. Since the plant extractable water of Bankura soils ranges from 75 to 219 mm in the top 100-cm layer (Table 4), we have to provide supplemental irrigations during critical crop growth stages during the post-rainy season to grow these crops successfully without any risk. Even though there is some rainfall during the post-rainy season but not enough to cover the water needs of the crops, irrigation water must supplement the rainwater in such a way that the rainwater and the irrigation water together cover the water needs of the crop (Brouwer and Heibloem, 1986). The analysis of physical properties indicates that due to the high sand content, the saturation capacity of both block soils is 40%–60% of their volumetric content, water holding capacity is low (6%–10%) due to low clay content, and the drainable limit is good (0.28%–40%), which leads to better groundwater recharge (Figure 7).

3.2.1.3.2 Soil chemical properties. The soil pH of both blocks ranged between 4.72 and 7.13, with an average soil pH of 5.29 (Table 4). The soil pH of Hirbandh and Ranibandh blocks was found to be acidic in reaction, and this might be due to granite being the parent material, sloppy land, and heavy rainfall, which cause leaching losses of basic cations, and the laterization process causes the accumulation of iron and aluminum oxide. More than 50% of soil samples are deficient in available phosphorus (P) (61.90%), sulfur (S) (70.48%), and boron (B) (94.29%) in the Hirbandh block (Figure 8). In the Ranibandh block, more than 50% of soil samples are deficient in available calcium (Ca) (68.57%), S (82.86%), and B (97.14%) (Figure 8). The soil organic carbon content (SOC) in Hirbandh and Ranibandh blocks varied from 0.17 to 1.01% and was categorized as low-to-high in the range. Furthermore, the highest SOC content was observed in Satnala village. Low SOC was observed in the Sitarampur and Jadurbankata villages of the Hirbandh block. The available potassium is less in the Sitarampur village (Figure 8).

3.2.1.3.3 Soil biological properties. The bacterial population was noticeably lower (Table 4) in most of the samples, irrespective of terrain (upper, middle, and lower), which might be due to the low-to-medium organic carbon content of the soil and the acidic nature of the soil. The fungal population (colony-forming units: CFU/g) was high compared to bacteria, which might be attributed to the acidic nature of the soil (Rousk et al., 2008). A study was conducted by Rousk et al., (2010) on the influence of soil pH on bacterial and fungal communities. The quantitative polymerase chain reaction (qPCR) results based on 16S rDNA revealed that the abundance of bacteria was increased four-fold with an increase in pH from 4 to 9, and no significant influence of pH was observed on fungal abundance. Similar results were also observed by Wang et al. (2022).

In the present study, we observed that sample BN-55 (L) from Jadurbankata village has a high SOC, i.e., 0.86%, which is the reason for the comparatively high microbial population (bacteria, fungi, and actinomycetes), compared to other samples. Therefore, field bunding in this region is an important intervention that could help retain moisture, which creates favorable conditions for microbial growth, resulting in an increase in the microbial population (Van et al., 2014). One of the most important biological indicators of soil health, indicating the presence of living organisms and their activities, is soil respiration. Although soil organic carbon (SOC) was reported to have a positive correlation with soil respiration, soil respiration is also influenced by factors like temperature, moisture, porosity, and soil type (Duan et al., 2021). In the present study, not all the samples tested for soil respiration had a positive correlation with SOC, which might be due to the presence of labile carbon (active carbon pool) that contributes to microbial activity and

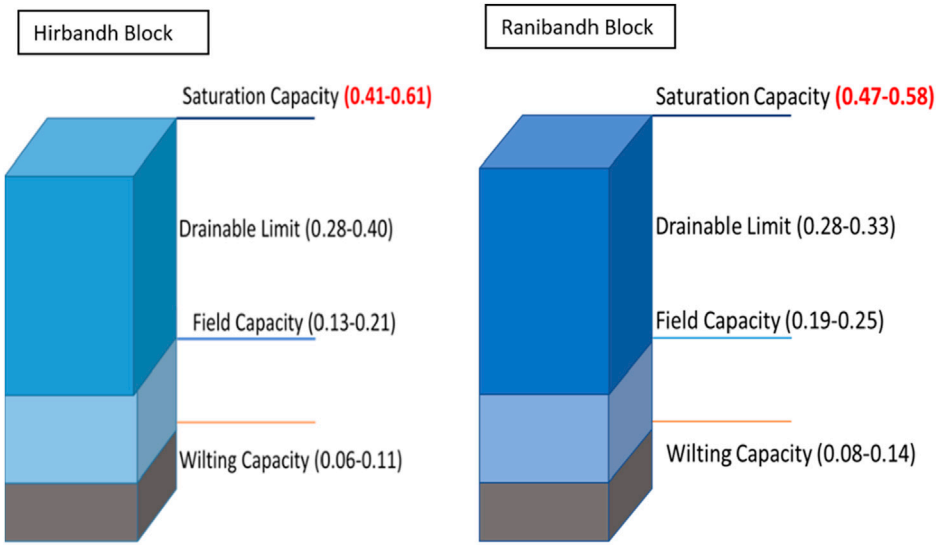

FIGURE 7
Water retention capacity of the soil.

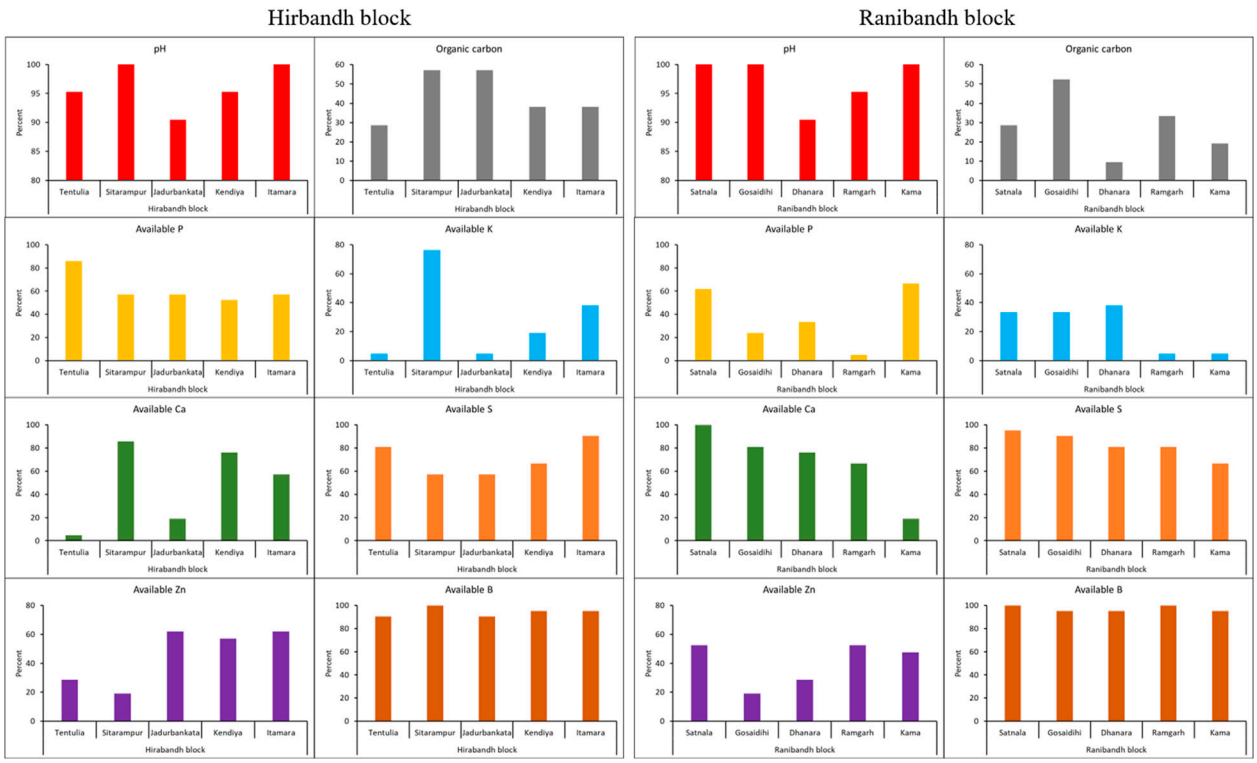

FIGURE 8
Village-wise percent-deficient soil samples in Hirbandh and Ranibandh blocks, Bankura, West Bengal.

respiration (Cleveland et al., 2007). The samples were observed to have low-to-medium organic carbon and fewer bacteria compared to fungi.

As per the total microbial biomass, e.g., bacteria, fungi, and actinomycetes, it has been observed that the bacterial count was less in the samples. Soil acidity and low organic carbon content are contributing to the low microbial activity and less productivity of the soil. To improve the SOC content, practices like composting and incorporation of crop stubble into soil can be practiced. Vermicomposting and aerobic

TABLE 5 Chemical analysis of water.

Village	Drinking water	Irrigation water	Pond water
Tentulia	Chemical oxygen demand (COD) level of 32 mg/L Arsenic–0.01 mg/L	$CaCO_3$ – <100 mg/L pH < 6-alkaline soils	COD–22.40 mg/L
Sitarampur	Safe	Safe	COD–19.2 mg/L Arsenic–0.01 mg/L
Jadurbankata	COD–12.80 mg/L	Safe	Safe
Kedia	Presence of magnesium sulfate Arsenic–0.02 mg/L	$CaCO_3$ – <100 mg/L	COD–12.8 mg/L Arsenic–0.02 mg/L
Itamara	Arsenic–0.02 mg/L	COD–41.6 mg/L Arsenic–0.03 mg/L	Arsenic–0.02 mg/L Potassium levels–23.12 mg/L
Satnala	COD–57.60 mg/L Arsenic–0.02 mg/L	Arsenic–0.02 mg/L	Arsenic–0.02 mg/L
Gosainidihi	Arsenic–0.03 mg/L	Arsenic–0.03 mg/L	Safe
Dhanara	Arsenic–0.04 mg/L	Arsenic–0.03 mg/L	Arsenic–0.03 mg/L
Ramgarh	Arsenic–0.05 mg/L	Arsenic–0.03 mg/L	High COD Arsenic–0.03 mg/L
Kama gora	Arsenic–0.06 mg/L High Mg concentration–91.90 mg/L (BIS desired safe limit is 30 mg/L)	Arsenic–0.04 mg/L	Arsenic–0.04 mg/L

composting are two proven methods to practice composting at the rural level. Agroforestry practices and the presence of vegetation on bunds contribute to the accumulation of plant residues, fallen leaves, and other organic materials. These organic inputs gradually decompose, enriching the soil with organic carbon (Sarvade et al., 2014). The flora diversity found in agroforestry systems fosters the growth of soil microorganisms, which are essential for the breakdown of litter and the release of nutrients (Kumar, 2011).

3.2.1.4 Water characteristics

The chemical analysis of water samples (Table 5) showed that water is not safe for drinking as arsenic levels are high. Arsenic (As) contamination poses a serious risk to human health. As per the World Health Organization (WHO), the minimum permissible safe limit of As in drinking water is 10 μg L^{-1}, and as per the US Environmental Protection Agency (USEPA), the approved safe limit of As in soil is 24 mg kg^{-1}. Drinking water contaminated with arsenic is the most common route of human exposure to arsenic contamination (Tandukar and Neku, 2002). The presence of As in paddy cultivation, if irrigated with arsenic-contaminated water, may vary depending on the cultivation method, cooking, irrigation methods, and fertilizer application practices. The immediate adverse impact of arsenic stress appears through up- or downregulation of the expression of transporters. Moreover, arsenic stress causes phytotoxic and genotoxic effects on plants by escalating lipid peroxidation levels, affecting the permeability of cell membranes. Arsenic stress reduces seed germination and growth of seedlings through the lower uptake of water and lowered amylase activity (Moulick et al., 2018). Grain quality and yield of rice decrease due to arsenic stress because of the decreased uptake of essential nutrients and alterations of physicochemical and biochemical properties of plants (Shri et al., 2019). The straighthead disease of rice is also caused due to arsenic stress, which manifests through the presence of distorted husks, sterile spikelets, unfilled grains, etc.

3.2.2 Material

For site-specific management, a thorough understanding of soil variability and landscape properties, as well as their effects on crop yield, is very critical (Jiang and Thelen, 2004). In the two blocks of the study area, the suitable land for cultivation (midland) is 61%, which is distributed mostly in the mid-upland and mid-lowland (Figure 9A), whereas the remaining land (39%) is less productive due to poor water holding capacity and low fertility (Jana SK, 2011). The less productive lands are around 40%–50%, which is a major concern contributing to low cropping intensity and low system productivity in the study area. Most households in the region are marginal, with the average land holding below 0.5 ha (Figure 9B).

The average land holding was 0.53 ha/HH, with the highest in Kamo Gora (0.73 ha/HH) and lowest in Tentulia (0.34 ha/HH). This indicates the existence of marginalized communities across the villages, which are exposed to a variety of risks at the individual or household level (Mahendra, 2012). Studies proved that the farm size is positively related to technology adoption (Shang et al., 2021); thus, it depicts the reason for the subsistence level of farming in these two blocks. As the low size of land holding is not economical, the returns are affecting the reinvestment on the second crop. With respect to the paddy cultivars cultivated by the farmers, Swarna variety was cultivated by 24% of the farmers (Figure 9C), followed by Lolat (21%) and Khandagiri (14%), constituting about 59% of the land area under paddy cultivation (IET-10396). The cultivated paddy cultivars were short-duration cultivars like Lolat, Sindhu, Bullet, and IR-64, which occupy 31% of the cropped area, and the remaining cultivars occupy 69%. The varietal adoption pattern indicates that farmers are continuing the older varieties which were notified 20–30 years ago. Khandagiri (IET-10396) was notified in the year 1994 (DRD, Patna), Lolat was prior to it, and

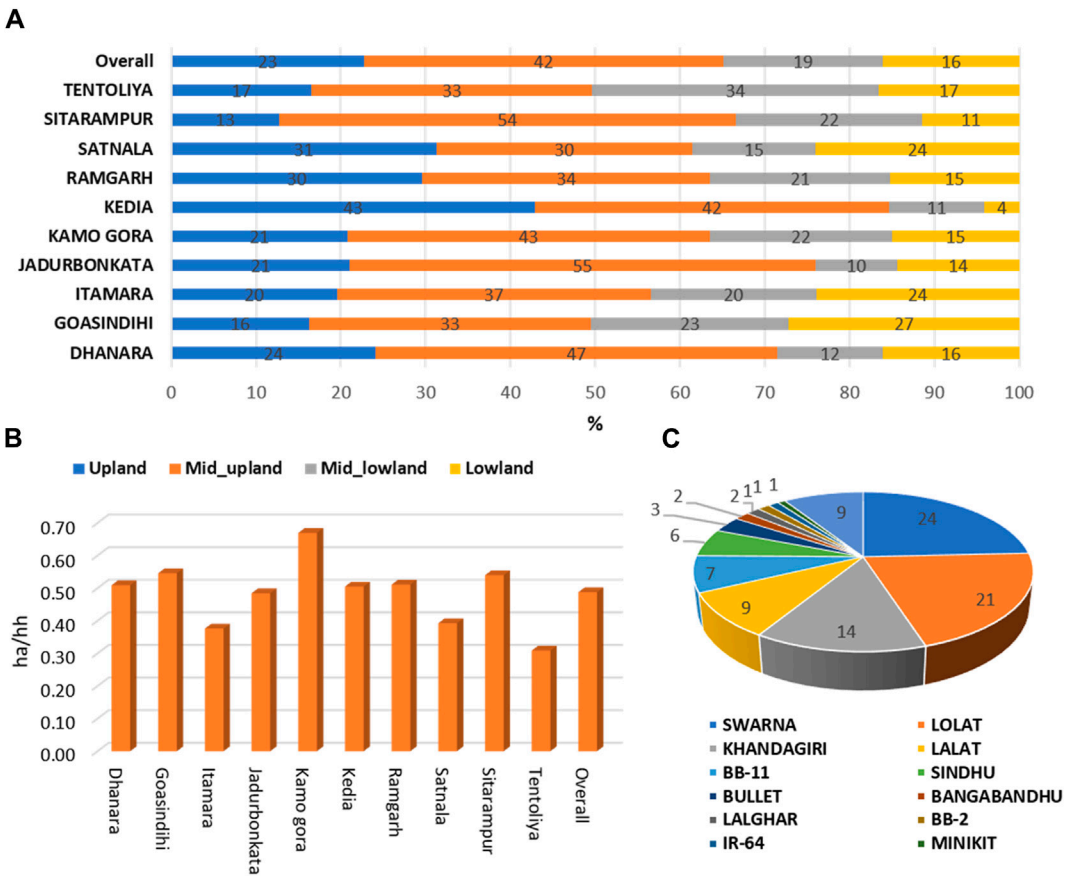

FIGURE 9
(A) Cropped area distribution by topology; **(B)** average size of land holding; and **(C)** share of paddy cultivars in the study area.

Swarna Sub-1 in 2009. Even though Swarna Sub-1 was a better variety under submergence/lowland conditions, because of its duration, the variety cannot sustain the terminal stress during the critical stages of growth. This shows that the farmers are not adopting the climate-resilient cultivars suitable for the region, and the topography might be due to non-availability in the study area or demand from the market. For example, Pushpa (notified in 2015) is a non-lodging, non-shattering, drought-tolerant early variety with 50% flowering in 79 days and seed-to-seed of 105 days during rainy season. Its average yield ranged from 4,500 to 5,000 kg ha^{-1}, and its productivity was 8,216 kg ha^{-1} (Mallick et al., 2013). Hence, the extension activities with seed availability and market infrastructure need to be developed. The data on fertilizer (NPK) use pattern across the villages (Supplementary Table S5) infer that the application of phosphate fertilizers (e.g., DAP) was found to be high. The application of nitrogen fertilizers was less than the recommended dosage of 80 kg/ha in the majority of villages.

3.2.3 Management

Most of the cultivars grown were old-ranging and cultivated irrespective of their suitability to the topology. Usually, short-duration varieties were in the uplands due to water deficit, medium-duration varieties in mid-lands, and long-duration varieties in the lowlands. However, the cultivars were grown irrespective of their suitability to topology (Figure 10A). This is mainly because of market demand for the varieties from neighboring districts like Assam, Jharkhand (SEMA, 2023), and Odisha and international demand from Bangladesh. Most of the previous studies employed aerobic or upland rice cultivars, whereas modern lowland cultivars typically exhibit longer growth durations and higher yield potential, particularly the super hybrid cultivars that are sensitive to unfavorable conditions and suitable for intensive cultivation (Bouman et al., 2006; Liu et al., 2019). We observed that in the uplands, short-duration crop varieties were typically found due to water scarcity, while medium-duration crop cultivars were found in the midlands and long-duration crop cultivars in the lowlands. This suggests that lowland rice cultivars, with their longer growth duration and higher growth potential, could benefit more from rainfall (Liu et al., 2019). In upland cultivation, rainfall accounted for 60%–85% of total water use during the growing season. Upland cultivars are bred with the specialty of shorter growth duration and lower aboveground biomass accumulation, which accounts for their lower yield performance under aerobic cultivation in Central China when compared to lowland cultivars (Zhao et al., 2010).

3.2.4 Methods

Scale-appropriate farm mechanization holds a key to the successful management of the farmland. Tractors and the associated machinery are primarily used during land preparation

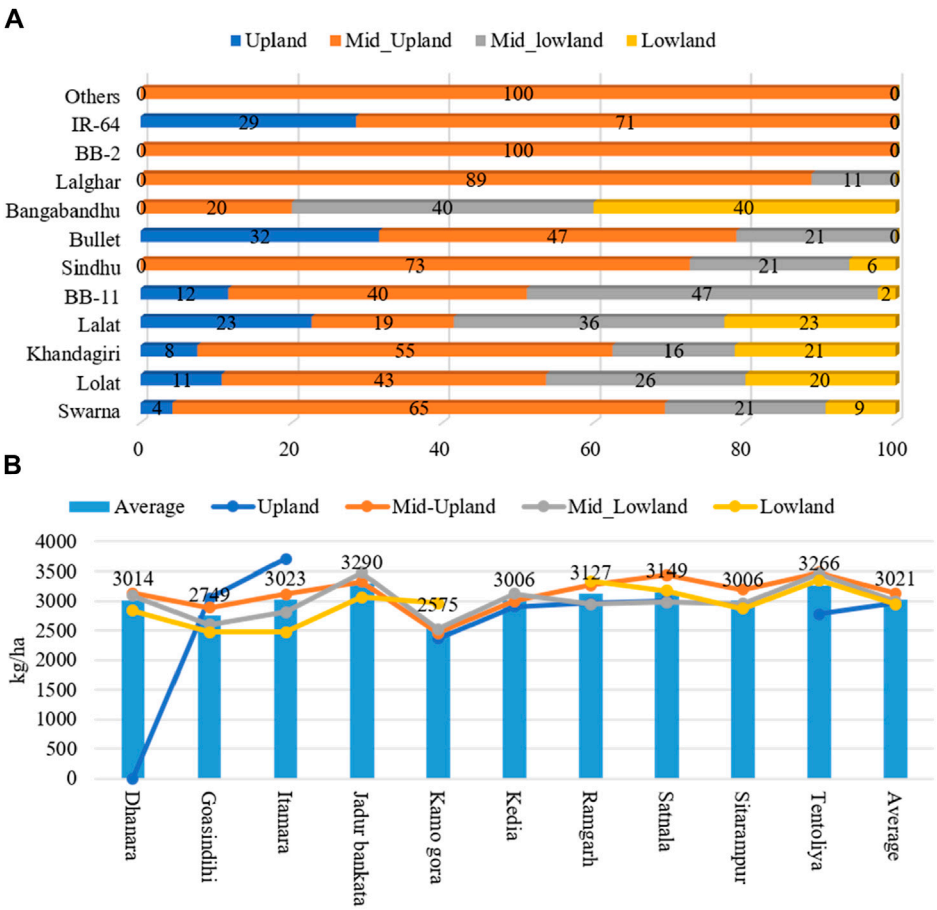

FIGURE 10
(A) Varietal selection across the topography and **(B)** paddy productivity by topology.

and seeding, whereas other machineries are less important during crop growth (Supplementary Figure S1). A study on the impact of farm mechanization on foodgrain productivity revealed that foodgrain productivity is higher in the states where farm power availability is high (Buragohain, 2021), which proves the need for introducing farm power through customer hiring centers (CHCs). The study revealed that most of the farm operations are carried out by labor, mostly family labor. The farmers are realizing low economic returns from the rainy season paddy cultivation.

The net returns observed were negative in many cases when the cost of family labor was included (Table 6) while calculating the total cost of cultivation (CoC). The results imply that economic returns are more relevant as the low net returns from rainy season paddy cultivation might be one of the essential factors affecting low investment in post-rainy cultivation. The study observed that because of low income from rainy season crops, the young members of the households tend to migrate to nearby towns, creating acute labor shortage during the post-rainy season. The average productivity of the existing varieties is 3,021 kg/ha, which is significantly on the lower side, as compared to the recently introduced variety, namely, Pushpa. The study further revealed that the farmers are realizing low economic returns from the rainy season paddy cultivation. The major reasons are low-yielding crop cultivars, low seed replacement rate, generalized selection of rice cultivars at all the typologies (for example, lowland, midland, and upland), imbalanced use of inorganic fertilizers, and unavailability of nutrients primarily secondary and micronutrients. The negative net returns in many cases reduce the capacity of farmers to invest not only for post-rainy crops but for next year's rainy season crops.

3.2.5 Man

Most of the farmers were from the middle age group (<45 years). The average age of the surveyed farmers was 42 years; the youngest (~35 years) was observed in Satnala and Jadurbankata, whereas the oldest (~50 years) was observed in Kadia and Ramgarh (Supplementary Figure S2). Most farmers were uneducated (40%), and only 3% of the respondents had completed their graduation (Supplementary Figure S3). About 50% of illiterates were observed at Satnala and Tentulia. The lowest level of illiteracy was found in Ramgarh (28%). The low levels of education could be attributed to high poverty levels and a lack of motivation to pursue higher education (Mwango, 2010). Moreover, low levels of education might affect the farming skills and productive capabilities of the farmers (Paltasingh and Goyari, 2018). Agriculture systems should adapt to uncertain climatic conditions by building sustainable resilience systems which require a dynamic understanding of agricultural systems and their interaction with

TABLE 6 Cost of cultivation of paddy.

Operation	Kedia	Tentulia	Itamara	Jadurbankata	Sitarampur	Kamo gora	Ramgar	Dhanara	Gosainidihi	Satnala
Land preparation	1,200	1,200	1,200	1,100	1,200	1,000	1,500	1,500	1,000	1,200
Seed	200	150	200	300	350	200	300	320	320	300
Transplanting	600	750	750	800	650	900	700	800	750	750
Fertilizers	500	300	300	150	300	300	200	150	350	300
Pesticide	600	500	500	500	1,000	400	800	600	1,000	1,000
Inter-cultivation + weeding	600	500	500	500	600	400	400	500	600	500
Harvesting	600	1,000	600	1,000	1,200	500	1,200	1,600	750	1,000
Transport	600	600	500	600	600	600	500	500	500	600
Others	350	400	300	400	400	300	300	300	400	300
Total cost	4,900	5,000	4,550	4,950	5,900	4,300	5,600	5,970	5,270	5,650
Cost of family labor (3 + 6 + 7 + 9)	2,150	2,650	2,150	2,700	2,850	2,100	2,600	3,200	2,500	2,550
COC (excluding cost of family labor)	2,750	2,350	2,400	2,250	3,050	2,200	3,000	2,770	2,770	3,100
Gross revenue	4,902	5,175	5,226	6,281	5,130	4,702	5,484	5,655	4,198	5,902
Net revenue (including the family labor cost)	2	175	676	1,331	−770	402	−116	−315	−1,072	252
Net revenue (excluding the family labor cost)	2,752	2,525	3,076	3,581	2,280	2,602	2,884	2,455	1,698	3,352

(INR/decimal* of land); *1 decimal = 0.004046483 ha [Source: Focus Group Discussion (FGD)].

10.3389/fenvs.2024.1417199

climate and practices (Abhilash et al., 2021). The adoption of contemporary paddy varieties and, consequently, the farm production of adopters have been found to be considerably influenced by a minimum threshold level of education, according to Paltasingh and Goyari's (2018) study on the impact of farmer education on farm productivity. The likelihood of applying agricultural inputs rises dramatically with higher education levels but falls with farmers' ages (Sagar et al., 2022). Considering that the age group (>42 years) with low literacy rates is majorly engaged in rainfed farming, they are less receptive to the adoption of improved cultivars (Pushpa, MTU1140 TARANGINI, and MTU1001) over the early 1970s' traditional varieties (Lolat, Swarna, and Khandagiri) and climate-smart agricultural technologies.

4 Strategies to enhance 5Ms by farmers through government schemes

We have determined the primary underlying causes of every issue that the farming communities who are most at risk are dealing with, and we have also talked about the best ways to address each of the 5Ms. Government programs must, however, play a crucial role in helping farming communities that are most vulnerable to changes in the climate, the availability of resources, and other factors that affect sustainable agriculture. Even with numerous government initiatives designed to assist small and marginal farms, awareness building is still necessary.

Low rainfall and excess draining out of water are resulting in low cropping intensity and low system productivity in the studied regions of West Bengal. Farmers need to enhance crop diversification by cultivating multiple crops that positively impact the farm income of households of small and marginal farmers (Lama, 2016). There are several schemes initiated by the Indian government for the benefit of small and marginal farmers in order to enhance crop productivity. The national scheme, i.e., Rainfed Area Development (RAD) was launched to support integrated farming systems (IFS), which emphasize intercropping, rotational cropping, mixed cropping, and other related practices. The Pradhan Mantri Kisan Samman Nidhi (PMKISAN) was launched to help land-holding farmers meet their financial needs, the Pradhan Mantri Kisan Maan Dhan Yojana (PMKMY) was launched to provide stability and financial assistance to the most vulnerable farming households; and the Pradhan Mantri Fasal Bima Yojana (PMFBY) was launched to offer farmers a straightforward and reasonably priced crop insurance solution that would guarantee full crop risk coverage against all unavoidable natural hazards from planting to harvest, as well as a sufficient claim amount, and the minimum support price (MSP) for all required commercial crops with a minimum 50% return, including rainy and post-rainy seasons.

Due to low soil organic carbon, there are multi-nutrient deficiencies and poor water holding capacity and, as a result, declined crop productivity in the dryland farming soils of studied regions. Hence, there is a great necessity for improving SOC in these areas to deal with moisture stress and nutrient deficiencies. The Indian government has taken several initiatives for soil carbon and water storage specifically in drylands. The Mahatma Gandhi National Rural Employment Guarantee Act (MGNREGA) and the National Mission for Sustainable Agriculture (NMSA) were launched to maintain agricultural productivity by conserving natural resources like water and soil while also advancing rainfed agriculture in India. The Soil Health Card (SHC) mission is to enhance the soil fertility status by providing fertilizer recommendations based on soil tests. However, 82% of the farmers were aware of the SHC plan, only 66% of them could grasp the guidelines, and only 48% of them applied fertilizer at the prescribed rate (Reddy, 2019). Hence, it is high time to create awareness about the SHC among the farmers. The Rashtriya Krishi Vikas Yojana (RKVY) supports the overall growth of agriculture and related industries by conserving water and soil, enhancing farmer effort, reducing risk, and encouraging agribusiness entrepreneurship.

Farm mechanization and potential management practices are other major problems that are noticed in the studied regions. In the investigated areas, the majority of small and marginal farmers lack formal education; nonetheless, they can still receive assistance and benefit from government programs. The Sub-Mission on Agriculture Automation (SMAM) has been launched by the Indian government to employ drones to apply fertilizer and pesticides in public areas, as well as to expand the use of farm automation to small and marginal farmers. The Indian government has made funds available for plant protection equipment, tractors, power tillers, self-propelled machinery, custom hiring centers, hi-tech hubs, and farm machinery banks under this program. The Per Drop More Crop (PDMC) scheme uses micro-irrigation technology, such as sprinkler and drip irrigation systems, to improve farm-level water consumption efficiency. Furthermore, the scheme Mission for Integrated Development of Horticulture (MIDH) was launched for the holistic growth of the horticultural industry.

The global commitments/agreements such as the Paris Climate Change Agreement and the 4 per mille concept are also committed by India to the mitigation of GHG emissions and enhance soil carbon sink. Achieving these goals would immensely contribute to the overall succession of sustainable development goals (SDGs) such as #SDG-1: no poverty; #SDG-2: zero hunger; #SDG-13: climate action; and #SDG-15: life on land, and also help in achieving the land degradation neutrality (LDN) in the global dryland farming soils. However, there is no "one-size-fits-all" solution to the complex problems, primarily pertaining to dryland farming systems. Taking into account the current situation as identified under the 5M approach, building soil carbon, increasing cropping system diversification, improvising farm mechanization, and raising farmer community awareness of the benefits of various government schemes are some of the "win–win" strategies to unlock the potential of dryland soils. These initiatives are required to be scaled through various national and state government initiatives, which are present in every developing country.

5 Conclusion

Envirotyping of agroecology using the 5M concept not only helps in characterizing and quantifying the environmental factors

but also complements in achieving system profitability through tailored advocacy of climate-resilient landscape-specific technologies, particularly in rainfed agro-ecologies like Bankura, West Bengal, India. In conditions like low cropping intensity, the root causes are low organic carbon and soil microbial population, particularly bacteria and actinomycetes in soils. Farmers need to be encouraged and facilitated to apply bacterial inoculum/culture comprising *Azospirillum*/*Rhizobium*, phosphate-solubilizing bacteria (PSB), and vesicular arbuscular mycorrhiza (VAM). Climate-resilient agriculture practices like cropping system diversification, cover crops, soil mulching, zero-tillage, biochar, green manuring, and agroforestry, need to be promoted to build soil organic carbon and retain the residual soil moisture levels. Sandy soils with low pH tends to have sulfur deficiency, and soils rich in iron and bauxites shows boron deficiency due to the chemical interaction between iron and bauxite and subsequent leaching of boron. Hence, a basal application or foliar application of boron is recommended, and sulfur deficiency can be addressed by replacing urea with ammonium sulfate. Economic returns can be maximized by forming farmer collectives. Climate-resilient and topography-suitable varieties need to be promoted through farmer collectives for the efficient utilization of available soil moisture regime and thereby enhancing cropping intensity. Farmer collectives need to encourage where the land holding is small and net income realization is low. In a nutshell, the present agronomic diagnostic study could be referred as a model to help development agencies, government institutions and policy makers understand the root cause analysis of the pertinent problems and design suitable interventions/policy frameworks in a short period for similar agro-ecologies.

The limitation to the study was that the role of government or enabling systems was not covered by the research team, which is important for policy advocacy and scaling the recommendations at landscape level. The diagnostic study was limited to soils with high sand content where available soil moisture was low for the second season. The study emphasized more on the scientific evidence, and the human interaction with the environment was not properly explored due to the time and budgetary constraints.

Data availability statement

The original contributions presented in the study are included in the article/Supplementary Material, further inquiries can be directed to the corresponding author.

Author contributions

GS: conceptualization, methodology, project administration, supervision, writing–original draft, and writing–review and editing. MD: conceptualization, data curation, formal analysis, methodology, supervision, validation, writing–original draft, and writing–review and editing. SR: data curation, formal analysis, methodology, validation, and writing–review and editing. PK: formal analysis, validation, and writing–review and editing. RK: conceptualization, methodology, supervision, and writing–review and editing. RN: data curation, formal analysis, and writing–review and editing. RP: data curation, formal analysis, methodology, validation, and writing–review and editing. PC: data curation, formal analysis, methodology, and writing–review and editing. AD: data curation, formal analysis, methodology, and writing–review and editing. VA: data curation, formal analysis, methodology, and writing–review and editing. SD: conceptualization, methodology, supervision, and writing–review and editing. RS: supervision, writing–review and editing. MJ: supervision, writing–review and editing.

Funding

The authors declare that financial support was received for the research, authorship, and/or publication of this article. This study was funded by the consortium led by Professional Assistance for Development Action (PRADAN), India, which was supported by Hindustan Unilever Foundation (HUL), India, as a part of a project on "Agronomic Diagnostics Study of Bankura region in West Bengal."

Acknowledgments

The authors would like to gratefully acknowledge financial support from PRADAN and Hindustan Unilever Foundation (HUL), India. They would also like to thank the staff of PRADAN and the farmers of the Bankura region for their active support during the agronomy diagnostic study.

Conflict of interest

The authors declare that the research was conducted in the absence of any commercial or financial relationships that could be construed as a potential conflict of interest.

Publisher's note

Supplementary material

The Supplementary Material for this article can be found online at: https://www.frontiersin.org/articles/10.3389/fenvs.2024.1417199/full#supplementary-material

References

Abhilash, S. C., Rani, A., Kumari, A., Singh, R. N., and Kumari, K. (2021). "Climate-smart agriculture: an integrated approach for attaining agricultural sustainability," in *Climate change and resilient food systems: issues, challenges, and way forward* (Singapore, Singapore: Springer), 141–189.

Alpha, M. M., Patience, S., and Paidamoyo, P. C. (2021). Root cause analysis of factors associated with high cost of dairy feed under the Zimbabwean stock feed manufacturing sector. *World Acad. J. Manag.* 9 (3), 37–44.

AMS (2004). Statement on meteorological drought. *Bull. Am. Meteorological Soc.* 85, 771–773.

Anderson, J. P. E. (1982). "Soil respiration," in *Methods of soil analysis: part 2 chemical and microbiological properties*. Editor A. L. Page (Madison: Agronomy Monograph, ASA and SSSA), 831–871.

Batan, E. L. (2017). New environmental analysis method improves crop adaptation to climate change. August 15, Mexico (*CIMMYT*). Available at: https://www.cimmyt.org/news/new-publications-new-environmental-analysis-method-improves-crop-adaptation-to-climate-change/.

Bera, K., and Bandyopadhyay, J. (2017). Drought analysis for agricultural impact through geoinformatic based indices, A case study of Bankur district, West Bengal, India. *J. Remote Sens. GIS* 6 (209), 2. doi:10.4172/2469-4134.1000209

Bouman, B. A. M., Yang, X., Wang, H., Wang, Z., Zhao, J., and Chen, B. (2006). Performance of aerobic rice varieties under irrigated conditions in North China. *Field Crop. Res.* 97, 53–65. doi:10.1016/j.fcr.2005.08.015

Brahmanand, P. S., Behera, B., Srivastava, S. K., Singandhupe, R. B., and Mishra, A. (2021). Cultivated land utilization index vis-a-vis cropping intensity for crop diversification and water resource management in Odisha, India. *Curr. Sci.* 120 (7), 1217. doi:10.18520/cs/v120/i7/1217-1224

Bray, R. H., and Kurtz, L. T. (1945). Détermination du phosphoreorganique total et des formesdisponibles dans les sols. *Soil. Sci.* 59, 39–46. doi:10.1097/00010694-194501000-00006

Brouwer, C., and Heibloem, M. (1986). Irrigation water management: irrigation water needs. *Train. Man.* 3, 1–5.

Buragohain, T. (2021). Impact of farm mechanisation on foodgrain productivity in India. *Agric. Situat. India* LXXVII, 13–19.

Chaudhary, A., Verones, F., De Baan, L., and Hellweg, S. (2015). Quantifying land use impacts on biodiversity: combining species–area models and vulnerability indicators. *Environ. Sci. Technol.* 49, 9987–9995. doi:10.1021/acs.est.5b02507

Cleveland, C. C., Nemergut, D. R., Schmidt, S. K., and Townsend, A. R. (2007). Increases in soil respiration following labile carbon additions linked to rapid shifts in soil microbial community composition. *Biogeochemistry* 82, 229–240. doi:10.1007/s10533-006-9065-z

De, P., Deb, S., Deb, D., Chakraborty, S., Santra, P., Dutta, P., et al. (2022). Soil quality under different land uses in eastern India: evaluation by using soil indicators and quality index. *PLoS One* 17 (9), e0275062. doi:10.1371/journal.pone.0275062

District Disaster Management Cell (2017). *District disaster management plan*. Bankura, West Bengal: District Disaster Management Cell.

District Disaster Management Cell (2021). *District disaster management plan*. Bankura, West Bengal: District Disaster Management Cell.

Duan, L., Liu, T., Ma, L., Lei, H., and Singh, V. P. (2021). Analysis of soil respiration and influencing factors in a semiarid dune–meadow cascade ecosystem. *Sci. Total Environ.* 796, 148993. doi:10.1016/j.scitotenv.2021.148993

El-Swaify, S. A., Pathak, P., Rego, T. J., and Singh, S. (1985). Soil management for optimized productivity under rainfed conditions in the semi-arid tropics. *Adv. Soil Sci.* 1, 1–64. doi:10.1007/978-1-4612-5046-3_1

Gulati, A., and Juneja, R. (2022). "Transforming Indian agriculture," in *Indian agriculture towards 2030. India studies in business and economics*. Editors R. Chand, P. Joshi, and S. Khadka (Singapore, Singapore: Springer). doi:10.1007/978-981-19-0763-0_2

Jana, S. K. (2011). Sustainable small scale irrigation experiment in the dry zones: a case study on happa (small tank) model in the state of West Bengal, India, mpra paper No. 29553. Available at: https://mpra.ub.uni-muenchen.de/29553/.

Jiang, P., and Thelen, K. D. (2004). Effect of soil and topographic properties on crop yield in a North-Central corn–soybean cropping system. *Agron. J.* 96 (1), 252–258. doi:10.2134/agronj2004.0252

Keren, R. (1996). Boron. Methods of soil analysis: Part 3. *Chem. Methods* 5, 603–626.

Kumar, B. M. (2011). Quarter century of agroforestry research in Kerala: an overview. *J. Trop. Agric.* 49 (1-2), 1–18.

Kumhálová, J., Kumhála, F., Kroulík, M., and Matějková, Š. (2011). The impact of topography on soil properties and yield and the effects of weather conditions. *Precis. Agric.* 12, 813–830. doi:10.1007/s11119-011-9221-x

Lama, M. (2016). Crop diversification and farm income in the hills of North East India: a Case study of Arunachal Pradesh. *Int. J. Food Agric. Vet. Sci.* 6 (2), 15–21.

Lindsay, W. L., and Norvell, W. A. (1978). Development of a DTPA soil test for zinc, iron, manganese, and copper. *Soil Sci. Amer. J.* 42, 421–428. doi:10.2136/sssaj1978.03615995004200030009x

Liu, H., Zhan, J., Hussain, S., and Nie, L. (2019). Grain yield and resource use efficiencies of upland and lowland rice cultivars under aerobic cultivation. *Agronomy* 9 (10), 591. doi:10.3390/agronomy9100591

Mahendra, D. S. (2012). *Small farmers in India: challenges and opportunities, WP-2012-014*. Mumbai, India: Indira Gandhi Institute of Development Research. Available at: http://www.igidr.ac.in/pdf/publication/WP-2012-014.pdf.

Makate, C., Wang, R., Makate, M., and Nelson, M. (2016). Crop diversification and livelihoods of smallholder farmers in Zimbabwe: adaptive management for environmental change. *Springer Plus* 5, 1135. doi:10.1186/s40064-016-2802-4

Mallick, G. K., Mondal, M., Jana, K., Ghosh, A., and Biswas, A. (2013). PUSPA–a new rice variety alternative to Annada, released for upland areas of West Bengal, India. *Ecol. Environ. Conserv.* 19 (4), 1127–1129.

Mondal, A. (2019). Land capability classification of Bankura district, West Bengal. *Indian J. Spat. Sci.* 10 (1), 87–91.

Mondal, T. K., and Sarkar, S. (2021). Analysis of cropping intensity and irrigation intensity in North Twenty Four Parganas district, West Bengal, India. *Misc. Geogr.– Regional Stud. Dev.* 25 (4), 246–258. doi:10.2478/mgrsd-2020-0063

Moulick, D., Chandra Santra, S., and Ghosh, D. (2018). Rice seed priming with Se: a novel approach to mitigate as induced adverse consequences on growth, yield and as load in brown rice. *J. Hazard. Mater.* 355, 187–196. doi:10.1016/j.jhazmat.2018.05.017

Murumbi, F. (2014). "Root cause analysis in horticulture exporting firms in Kenya,". Doctoral dissertation (Nairobi, Kenya: University of Nairobi).

Mwango, N. H. (2010). "Community traditional knowledge, perceptions and response to flood risks in nyando basin, western Kenya,". A Thesis submitted in partial fulfilment for the award of the Degree of Master of Public Health in the School of Health Sciences (Nairobi, Kenya: Kenyatta University).

National Bureau of Soil Survey and Land Use Planning (2013). *Soils of Bankura district, (West Bengal) for land use planning*. Nagpur, Maharashtra: NRM-NBSSLUP-Publication, 1–122.

Nelson, D. W., and Sommers, L. E. (1996). Total carbon, organic carbon, and organic matter. *Methods soil analysis part 3 Chemical methods*. Madison, WI: SSSA Book Series No. 5, SSSA and ASA vol 5, 961–1010. doi:10.2136/sssabookser5.3.c34

Okalebo, J. R., Gathua, K. W., and Woomer, P. L. (1993). *Laboratory methods of soil and plant analysis: a working manual–KARI*. Nairobi, Kenya: UNESCO–ROSTA, 88.

Olsen, S. R. (1982). Anion resin extractable phosphorus. *Meth. Soil Anal.* 2, 423–424.

Paltasingh, K. R., and Goyari, P. (2018). Impact of farmer education on farm productivity under varying technologies: case of paddy growers in India. *Agric. Econ.* 6, 7. doi:10.1186/s40100-018-0101-9

M. L. Parry, O. F. Canziani, J. P. Palutikof, P. J. van der Linden, and C. E. Hanson (2007). *Climate change 2007: impacts, adaptation and vulnepost rainylity. Contribution of working group II to the fourth assessment report of the Intergovernmental Panel on Climate Change* (Cambridge, Uinted Kingdom: Cambridge University Press).

Pathak, P., Sahrawat, K. L., Wani, S. P., Sachan, R. C., and Sudi, R. (2009). "Opportunities for water harvesting and supplemental irrigation for improving rainfed agriculture in semi-arid areas," in *Rainfed agriculture: unlocking the potential* (Wallingford, Uinted Kingdom: CABI), 197–221.

Rahim, K. M. B., Majumder, D., and Biswas, R. K. (2011). *Determinants of stagnation in productivity of important crops in West Bengal*. India: Agro-Economic Research Centre Visva-Bharati Santiniketan.

Rao, C. S., Kareemulla, K., Krishnan, P., Murthy, G. R. K., Ramesh, P., Ananthan, P. S., et al. (2019). Agro-ecosystem based sustainability indicators for climate resilient agriculture in India: a conceptual framework. *Ecol. Indic.* 105, 621–633. doi:10.1016/j.ecolind.2018.06.038

Reddy, A. A. (2019). The soil health card Scheme in India: lessons learned and challenges for replication in other developing countries. *J. Nat. Resour. Policy Res.* 9 (2), 124–156. doi:10.5325/naturesopolirese.9.2.0124

Reddy, A. A., Bhattacharya, A., Reddy, S. V., and Ricart, S. (2021). Farmers' distress index: an approach for an action plan to reduce vulnerability in the drylands of India. *Land* 10 (11), 1236. doi:10.3390/land10111236

Rhoades, J. D. (1996). "Salinity: electrical conductivity and total dissolved solids," in *Methods of soil analysis: Part 3 Chemical methods, 5* (Madison, USA: Soil Science Society of America), 417–435.

Rousk, J., Bååth, E., Brookes, P. C., Lauber, C. L., Lozupone, C., Caporaso, J. G., et al. (2010). Soil bacterial and fungal communities across a pH gradient in an arable soil. *ISME J.* 4 (10), 1340–1351. doi:10.1038/ismej.2010.58

Rousk, J., Demoling, L. A., Bahr, A., and Bååth, E. (2008). Examining the fungal and bacterial niche overlap using selective inhibitors in soil. *FEMS Microbiol. Ecol.* 63 (3), 350–358. doi:10.1111/j.1574-6941.2008.00440.x

Roy, P., and Kaur, M. (2015). Status and problems of paddy straw management in West Bengal. *Int. J. Agric. Environ. Eng.* 1, 44–48.

Sagar, G. G. M., Khan, M., and Blay, J. K. (2022). Factors determining adoption of bhoochetana scheme by farmers in rainfed agriculture of Karnataka: a probit analysis. *Econ. Aff. New Delhi* 67, 43–48. doi:10.46852/0424-2513.1.2022.9

Sahrawat, K. L., Murthy, K. V. S., and Wani, S. P. (2009). Comparative evaluation of Ca chloride and Ca phosphate for extractable sulfur in soils with a wide range in pH. *J. Plant. Nutr. Soil Sci.* 172 (3), 404–407. doi:10.1002/jpln.200800005

Sanders, E. R. (2012). Aseptic laboratory techniques: plating methods. *J. Vis. Exp.* 63, e3064. doi:10.3791/3064

Sarvade, S., Singh, R., Prasad, H., and Prasad, D. (2014). Agroforestry practices for improving soil nutrient status. *Pop. Kheti* 2 (1), 60–64.

SEMA (2023). *Report on Assam and Jharkhand rice value chain*. India: SEMA Equipment and Energy Private Limited. Available at: https://selcofoundation.org/wp-content/uploads/2023/06/Report-Rice-Value-Chain-Assam-Jharkhand-01-05-2023-merged.pdf.

Shang, L., Heckelei, T., Gerullis, M. K., Börner, J., and Rasch, S. (2021). Adoption and diffusion of digital farming technologies-integrating farm-level evidence and system interaction. *Agri. Sys.* 190, 103074. doi:10.1016/j.agsy.2021.103074

Shri, M., Singh, P. K., Kidwai, M., Gautam, N., Dubey, S., Verma, G., et al. (2019). Recent advances in arsenic metabolism in plants: current status, challenges and highlighted biotechnological intervention to reduce grain arsenic in rice. *Metallomics* 11, 519–532. doi:10.1039/C8MT00320C

Simpson, E. H. (1949). Measurement of diversity. *Nature* 163, 688. doi:10.1038/163688a0

Srinivasarao, C., Venkateswarlu, B., Wani, S. P., Sahrawat, K. L., Dixit, S., Kundu, S., et al. (2010). Productivity enhancement and improved livelihoods through participatory soil fertility management in tribal districts of Andhra Pradesh. *Indian J. Dryland Agric. Res.* 25 (2), 23–32.

Srinivasarao, C., Venkateswarlu, B., Lal, R., Singh, A. K., and Kundu, S. (2013). Sustainable management of soils of dryland ecosystems of India for enhancing agronomic productivity and sequestering carbon. *Adv. Agron.* 121, 254–329. doi:10.1016/B978-0-12-407685-3.00005-0

Srinivasarao, Ch., Vittal, K. P. R., Venkateswarlu, B., Wani, S. P., Sahrawat, K. L., Marimuthu, S., et al. (2009). Carbon stocks in different soil types under diverse rainfed production systems in tropical India. *Commun. Soil Sci. Plant Anal.* 40 (15), 2338–2356. doi:10.1080/00103620903111277

Sugata, H., Sabita, R., and Sujit, M. (2017). *Enhancing adaptive capacity and increasing resilience of small and marginal farmers of purulia and Bankura districts, West Bengal to climate change*. Kolkata, India: School of Oceanographic Studies Jadavpur University.

Tabatabai, M. A. (1996). "Sulfur," in *Methods of soil analysis, part 3: chemical methods*. Editor D. L. Sparks (Madison, Wisconsin: SSSA and ASA), 921–960. Soil Science Society of America Book Series No. 5.

Tandukar, N., and Neku, A. (2002). "Arsenic contamination in groundwater in Nepal - an overview," in Fifth International Conference on Arsenic Exposure and Health Effects, San Diego, July 14-18, 2002.

Thenkabail, P., Enclona, E. A., Legg, C., and De Dieu, M. J. (2004). Hyperion, IKONOS, ALI, and ETM+ sensors in the study of African rainforests. *Remote Sens. Environ.* 90 (1), 23–43. doi:10.1016/j.rse.2003.11.018

Van, D. J., Okie, J. G., Buelow, H. N., Gooseff, M. N., Barrett, J. E., and Takacs-Vesbach, C. D. (2014). Soil microbial responses to increased moisture and organic resources along a salinity gradient in a polar desert. *Appl. Environ. Microbiol.* 80 (10), 3034–3043. doi:10.1128/aem.03414-13

Velpuri, N. M., Thenkabail, P. S., Gumma, M. K., Biradar, C. M., Dheeravath, V., Noojipady, P., et al. (2009). Influence of resolution in irrigated area mapping and area estimation. *Photogramm. Eng. Remote Sens.* 75 (12), 1383–1395. doi:10.14358/pers.75.12.1383

Wang, T., Cao, X., Chen, M., Lou, Y., Wang, H., Yang, Q., et al. (2022). Effects of soil acidification on bacterial and fungal communities in the Jiaodong peninsula, Northern China. *Agronomy* 12 (4), 927. doi:10.3390/agronomy12040927

Wilhite, D. A. (2000). *Drought as a natural hazard: concepts and definitions. Drought: a global assessment*. London, United Kingdom: Routledge Publishers, 16.

Wilhite, D. A., and Glantz, M. H. (1985). Understanding: the drought phenomenon: the role of definitions. *Water Inter.* 10 (3), 111–120. doi:10.1080/02508068508686328

Worthington, J., Dockum, S., and Smith, A. (2024).Root cause analysis as a problem solving tool for leaders and managers: application to environmental measurement systems, 2014 national environmental monitoring conference. Washington, DC. August 4–8, 2014.

Xu, Y. (2016). Envirotyping for deciphering environmental impacts on crop plants. *Theor. Appl. Genet.* 129, 653–673. doi:10.1007/s00122-016-2691-5

Zhao, D. L., Amante, M., Cruz, M. T. S., Atlin, G. N., and Kumar, A. (2010). Developing aerobic rice cultivars for water-short irrigated and drought-prone rainfed areas in the tropics. *Crop. Sci.* 50, 2268–2276. doi:10.2135/cropsci2010.10.0028

Zielińska-Chmielewska, A., Mruk-Tomczak, D., and Wielicka-Regulska, A. (2021). Qualitative research on solving difficulties in maintaining continuity of food supply chain on the meat market during the COVID-19 pandemic. *Energies* 14 (18), 5634. doi:10.3390/en14185634

frontiers | Frontiers in Environmental Science

TYPE Original Research
PUBLISHED 15 October 2024
DOI 10.3389/fenvs.2024.1420078

OPEN ACCESS

EDITED BY
Jing Zhao,
Xi'an University of Technology, China

REVIEWED BY
Milu Rani Das,
University of Science and Technology, India
Alpha Kamara,
International Institute of Tropical Agriculture (IITA), Nigeria

*CORRESPONDENCE
Vivekananda M. Byrareddy,
vivekananda.mittahallibyrareddy@unisq.edu.au
U. Surendran,
u.surendran@gmail.com

†PRESENT ADDRESS
U. Surendran,
ICAR- National Bureau of Soil Survey and Land Use Planning (NBSS&LUP), Nagpur, India

RECEIVED 19 April 2024
ACCEPTED 05 September 2024
PUBLISHED 15 October 2024

CITATION
Marimuthu S, Byrareddy VM, Dhanalakshmi A, Mushtaq S and Surendran U (2024) Strategic cultivar and sowing time selection for weed management and higher redgram productivity in semi-arid Indian regions.
Front. Environ. Sci. 12:1420078.
doi: 10.3389/fenvs.2024.1420078

Strategic cultivar and sowing time selection for weed management and higher redgram productivity in semi-arid Indian regions

S. Marimuthu[1,2], Vivekananda M. Byrareddy[2]*, A. Dhanalakshmi[3], Shahbaz Mushtaq[2] and U. Surendran[4]*†

[1]National Pulses Research Centre, Tamil Nadu Agricultural University, Pudukkottai, India, [2]Centre of Applied Climate Sciences, University of Southern Queensland, Toowoomba, Australia, [3]Department of Physics, Kalaingar Karunanithi Government Arts College for Women (A), Pudukkottai, India, [4]Centre for Water Resources Development and Management (CWRDM), Kerala, India

Introduction: Redgram (*Cajanus cajan* L. Mill sp.), a leguminous crop commonly grown in tropical and subtropical climates, is highly valued for its high protein content (21%), which contributes significantly to food and nutritional security. However, its production faces challenges primarily due to terminal dryness experienced during critical growth stages because of changing rainfall patterns. To overcome this, adaptive techniques become imperative as the productivity of this crop is intricately linked to environmental factors and the crop's growth cycle.

Methods: Hence, the field experiment was conducted at the National Pulses Research Centre, Vamban, Pudukkottai, Tamil Nadu, in South India under rainfed condition, during the kharif (monsoon) seasons of 2017–18 and 2018–19. The primary objectives were to determine the optimal sowing time and identify suitable redgram cultivars, especially in the context of the late onset of the monsoon in Tamil Nadu, a common issue under changing climate conditions. The experiments tested six different sowing dates with three redgram cultivars.

Results and discussion: The findings highlighted the substantial influence of different redgram cultivars and sowing times on the crop's growth characteristics and yield. Among the six sowing dates tested, planting in later half of June (S_6) resulted in notably higher plant height (201 cm), a greater number of pods per plant (287), a seed yield of 1,112 kg ha–1, and a benefit-cost ratio of 2.61 Notably, this sowing period (S_6) demonstrated comparable performance with the treatment of redgram sowing in the latter part of September (S_4). CO 6 (V_1) is the most productive of the three redgram cultivars, with the highest mean pant height (200 cm), number of pods per plant (237), grain yield (1,017 kg ha–1), and benefit cost ratio (2.38). Extended phenological phases along with extra days to reach phenological stages could account for the increased yield in comparison to the other cultivars. Among the two short-duration cultivars, VBN (Rg) 3 (V_3) had a significantly higher mean grain yield of 958 kg ha–1 with the benefit-cost ratio of 2.24. Even though CO 6 (V_1) obtained a higher yield due to its long duration nature, it matured in 187 days whereas VBN (Rg) 3 (V_3) matured within 129 days. Consequently, the short-duration redgram cultivars emerge as highly suitable choices for integrating into crop sequences, thereby augmenting farm cropping intensity.

KEYWORDS

redgram cultivars, time of sowing, weed growth, yield, economics

1 Introduction

Global crop production must increase by 60% by 2050 to satisfy an increasing demand for food, driven by population growth and rising *per capita* incomes (Fischer et al., 2014). This challenge is further compounded by the impacts of climate change, which threaten agricultural productivity and necessitate the adoption of resilient and adaptive farming practices. (Surendran et al., 2021). Climate plays a crucial role in crop adaptation, influencing farmers' decisions on which crops to cultivate based on their suitability for the local environment. Approximately 67% of the fluctuations in crop production over a season can be attributed to weather, which significantly impacts crop growth and development. The remaining variations in production are due to agronomic factors such as soil and nutrient management (Sasane, 2017; Grigorieva et al., 2023). In dryland environments, instability in crop production is primarily caused by an imbalance between rainfall distribution and crop water demand. This issue is particularly pronounced in dryland agriculture, where soil moisture levels during the crop season are highly variable and largely dependent on the amount and distribution of rainfall (Pawar et al., 2020). In India, the activity of the South-West monsoon and the associated weather patterns are critical determinants of agricultural success. Agroclimatic conditions strongly influence crop selection, yield, and sustainability, underscoring the need for strategies that account for the variability and unpredictability of weather in dryland farming systems (Ravi et al., 2022). In the semi-arid regions of India, agricultural productivity is heavily influenced by climatic variability, particularly the distribution and timing of rainfall. Redgram (*Cajanus cajan* L. Mill sp.), a vital leguminous crop, plays a crucial role in providing food and nutritional security due to its high protein content. However, its cultivation faces significant challenges owing to terminal dryness during critical growth stages, exacerbated by the erratic nature of monsoons.

Redgram is one of the most important tropical legumes in India playing a crucial role in the diet and agriculture of the region. Redgram is made by splitting and boiling grains, and redgram green pods are used as vegetables. It is a significant protein rich component of our regular vegetarian diet and has 22 percent protein content, with an average cooked protein digestibility of 70 percent (Reed et al., 1989; Mallikarjuna and Devaraja, 2023). Furthermore, it is adaptable to many cropping systems without altering the main oilseed and cereal crops, and enhances soil health through biological nitrogen fixation. Residual plant parts provide good fodder (Patel et al., 2019). Understanding plant-environment interactions is essential for improving crop yield. Optimum sowing time and the selection of appropriate cultivars play a crucial role in harnessing the yield potential of crops under complex agro-climatic conditions. The sowing date has been proven to be one of the most significant non-monetary factors affecting pulse yields. Suboptimal thermal conditions during the growing season can significantly affect crop productivity. Therefore, determining the optimum sowing time is vital to maximize production by exploiting favourable environmental conditions during the growth of pulses.

Because of its distinctive morphological characteristics that encourage deep roots and drought endurance, redgram is suited to a wide range of unfavourable growing conditions, including varied soil depth and irregular rainfall (Islam et al., 2008). Rainfed cultivations are the primary growing conditions in Tamil Nadu. Most oilseeds, millets, and pulses (80–90%) are restricted to dryland habitats. Dryland habitat is characterized by small and marginal farmers, lack of resources, poor infrastructure, and little investment in inputs and technologies. The main cause of this region's declining redgram grain production is erratic rainfall, which severely impacts the timing of planting. Developing the right time of sowing and identifying suitable redgram cultivars can assist these financially constrained farmers in avoiding crop failure, as they are unable to invest additional costs (Sunil Kumar et al., 2020). Due to its photo-sensitivity redgram growth, including plant height, number of branches, the height at which branching begins, flowering, and pod formationis influenced by the sowing time. Consequently, Channabasavanna et al. (2015) discovered that planting time significantly affects redgram vegetative and reproductive growth stages. The growth, development, and yield of redgram crops were mostly determined by cultivars and the sowing date. Since the planting date determines the types of climates to which the crop's difficult phenological stages are exposed, it has a major impact on crop performance (Kumar et al., 2023). To maximize the benefits of all available natural resources, such as nutrients, sunlight, and soil moisture, as well as to ensure a sufficient yield, it is essential to maintain a desired plant population by optimizing the sowing date as well the cultivars. Developing the right time of sowing and identifying suitable redgram cultivars can assist these financially constrained farmers in avoiding crop failure, as they are unable to invest additional costs. Crop environments affect yield and yield components, according to Sharifi et al. (2009). Delays in sowing cause more harm to redgram (Padhi, 1995). A significant decrease in the number of branches per plant and dry weight per plant at harvest occurs when delayed planting is done in contrast to regular sowing. (Reddy et al., 2012). In contrast to early sowing, late seeding shortened the time required to reach harvest maturity (Ram et al., 2011). Delays in sowing cause more harm to redgram, as crop environments affect yield and yield components. Maintaining optimum plant population under poor soil moisture conditions is very difficult, given the significant role plant population plays in determining crop yield. Delayed sowing, compared to regular sowing, leads to a significant decrease in the number of branches and dry weight per plant at harvest, while also shortening the time to reach harvest maturity. Regular efforts are being undertaken to shorten the redgram growth season, and as a result, cultivars with medium (155–170 days) and short (120 days) durations are being produced. Additionally, short-duration cultivars are noted for their seamless integration into intensive cropping areas year-round, attributed to their thermo- and photo-insensitivity (Aruna and Sunil Kumar, 2023). Selecting the optimal sowing date for each genotype is a crucial decision in agricultural production, especially when aiming to maximize the genetic potential of crops (Krsti et al., 2023).

Redgram holds a significant position in the global agricultural economy, cementing its status as one of the most important pulse crops worldwide. However, the crop's duration and genotype vigour are crucial factors influencing its success. In recent years, unpredictable and delayed rainfall has challenged redgram cultivation, particularly when planting occurs after its optimal period. Therefore, this study aims to standardize the sowing date

TABLE 1 Treatment structure of the experiment.

Factor A: Sowing schedule	Factor B: Cultivars
S_1: 1–14thAugust (1st fortnight) S_2: 15–30thAugust (2nd fortnight) S_3: 1–14thSeptember (1st fortnight) S_4: 15–30thSeptember (2nd fortnight) S_5: 1–14thOctober (1st fortnight) S_6: 15 to 30thJune (2nd fortnight) (Control)	V_1:CO 6 V_2: CO(Rg)7 V_3: VBN (Rg) 3

for the late advent of the monsoon in the southern zone of Tamil Nadu by utilizing potential redgram genotypes from this region. By addressing the timing and selection of genotypes, this research aims to enhance redgram productivity under changing climatic conditions, offering valuable insights for improving agricultural resilience and sustainability in semi-arid regions.

2 Materials and methods

A field experiment was carried out at the National Pulses Research Centre, Vamban, Pudukkottai, Tamil Nadu, part of Tamil Nadu Agricultural University, during the *kharif* seasons of 2017–18 and 2018–19. The main objectives were to find out the optimum time of sowing and the suitable redgram cultivars during the late onset of the monsoon in Tamil Nadu under rainfed condition and to assess the weed growth due to different sowing dates and redgram cultivars. The experiment site is located at 8 ^{0} 30′ to 10 ^{0} 40′ N latitude and 78,^{0}24′to 79^0 4′ E longitude, with an altitude of 120 m above the mean sea level of Pudukkottai district in TamilNadu, South India. The weather data collected from the National Pulses Research Centre in Vamban, Pudukottai, is available from a B-class meteorological observatory. In this observatory, weather parameters were collected regularly during the cropping period. The average annual rainfall was 940 mm, with 52 rainy days and 38.74°C and 22.14°C mean annual maximum and minimum temperatures, respectively. The soil characteristics of the experimental site were sandy clay loam, a mean pH of 6.55, EC of 0.21 dsm^{-1},organic carbon of 0.3 percent, and 220, 33.5, and 159.5 kg ha^{-1} of available N, P, and K respectively. The experiment was laid out in a factorial randomized complete block design and replicated three times with the following treatments: factor 'A' comprising of six dates of sowing schedule and factor 'B' consisting of three redgram cultivars are given in Table 1.

Redgram VBN (Rg) 3 (110–120 days) and CO (Rg) 7 (130 days) are short-duration cultivars, and CO6 is a long-duration (180 days) cultivar. Both years of study, the recommended seed rates of 15 kg ha^{-1} for CO (Rg) 7 and VBN (Rg) 3 and 8 kg ha^{-1} for CO 6 were used for this study. Seeds were treated with *rhizobium* and *phosphobacteria* at the rate of 600 g per hectare using rice gruel. The sowing was taken on 11.8.2017, 24.8.2017, 09.9.2017, 29.9.2017, 6.10.2017, and 30.6.2017 during the first year, and 10.8.2018, 22.8.2018, 06.9.2018, 19.9.2018, 05.10.2018, and 21.6.2018 in the second year of the experiment, respectively. The spacing of 60 × 25 cm was adopted for short-duration redgram var. CO (Rg) 7 and VBN (Rg) 3, and 90 × 30 cm for long-duration redgram var. CO 6. The recommended dose of 12.5: 25: 12.5: 10 kg ha^{-1} of nitrogen through urea, phosphorus through single super phosphate, potassium through muriate of potash, and sulphur through gypsum, respectively, at basal. The crop was harvested from 09.11.2017 to 17.03.2018 and 01.11.2018 to 15.3.2019 in first- and second-year experiments, respectively.

Weed counts, namely, weed density (nos/m^2) and weed dry matter (g/m^2) were recorded 30 days after sowing (DAS). The weed count was assessed using quadrat method and the size of the quadrat was 0.25 m^2. The collected weeds were first air-dried and subsequently oven-dried at 75°C ± 2°C until a constant weight was achieved using an electronic balance, and then expressed in kilograms per hectare. Prior to statistical analysis, weed dry weight and weed density data underwent transformation using the square root method ($\sqrt{x+0.5}$).

To calculate Weed Control Efficiency (WCE) at both 30 and 45 days after sowing (DAS), the following formula was employed:

$$WCE = \frac{X\ (X - Y)}{X} x\ 100$$

Where: X = Number or dry weight of weeds in the unweeded plot Y = Number or dry weight of weeds in the treated plot.

Ten plants were randomly chosen and marked with waxy-coated labels in each treatment to monitor growth and yield parameters. At the time of maturity, observations were made on plant height, number of branches per plant, and yield parameters such as pod count per plant, number of seeds per pod and 100-grain weight. The matured pods were harvested plot-wise using a sickle, cut above the soil surface, bundled according to treatment, and transported to the threshing floor. The harvested produce was left to sun dry for 3 days, then beaten with bamboo sticks to separate grains, and dried again to facilitate winnowing. The produce continues drying until it reaches a moisture content of 12 percent. The total plot yield was weighed according to treatment. To convert this weight to kilograms per hectare, the measured weight was multiplied by a conversion factor based on the net plot size.

Based on the local market price cost incurred for this experiment, gross and net income and benefit cost ratios were worked out. The costs associated with the application of organic matter, major and micronutrients, and plant growth regulators were calculated using current market prices of inputs and redgram seeds. The cost of cultivation encompasses expenses from field preparation to harvest, expressed in Indian rupees (₹.) per hectare. Gross return is determined by calculating the crop yield per hectare and multiplying it by the prevailing minimum market rate at the time of the study, which was 60 ₹. per kilogram of redgram. Net return is then calculated by subtracting the cost of cultivation from the gross return for each treatment: Net return = Gross return (₹./hectare) - Cost of cultivation (₹./hectare). Finally, the Benefit-Cost (B: C) ratio is calculated using the formula: B: C ratio = Gross return (₹./hectare)/Total cost of cultivation (₹./hectare).

2.1 Statistical analysis

The collected data were subjected to R studio statistical analysis and tabulation. Statistical scrutiny was conducted following the methods suggested by Gomez and Gomez (1984). Fisher's Least Significant Difference was employed to test for significant differences between means at a probability level of $p \leq 0.05$ via ANOVA. The analysis focused on the impact of different sowing dates and redgram cultivars as independent variables on the growth and yield parameters of redgram,

10.3389/fenvs.2024.1420078

TABLE 2 Effect of different date of sowing and redgram varieties on growth, yield attributes and grain yield.

Treatments	Plant height (cm)	No. of branches/plant	No. of pods/Plant	No. of seeds/pod	100 seed weight (g)	Grain yield (kgha^{-1})	B:C ratio
Factor A: Sowing schedule							
S_1: August 1st fortnight	190	9.82	204	3.98	9.04	926	2.17
S_2: August 2nd fortnight	178	8.43	200	3.96	8.95	917	2.15
S_3: September 1st fortnight	182	9.07	223	4.02	8.98	967	2.27
S_4: September 2nd fortnight	179	10.25	259	4.11	8.82	1,045	2.45
S_5: October 1st fortnight	155	8.71	155	3.91	8.82	773	1.81
S_6: June 2nd fortnight	201	11.82	287	4.00	8.97	1,112	2.61
S: SE	2.59	0.33	6.90	0.16	0.16	26.20	-
CD (p = 0.05)	8.15	1.03	21.73	0.50	NS	82.56	-
Factor B: Variety							
V_1:CO 6	200	10.90	237	3.98	8.94	1,017	2.38
V_2: CO(Rg)7	171	8.23	201	4.09	8.91	892	2.10
V_3:VBN (Rg) 3	173	9.92	226	3.92	8.93	958	2.24
V: SE	2.04	0.21	3.85	0.07	0.10	9.82	-
CD (p = 0.05)	5.96	0.63	11.24	NS	NS	28.64	-
Interaction S x V: SE	5.00	0.53	9.43	0.18	0.23	24.04	-
CD (p = 0.05)	14.59	NS	NS	NS	NS	70.15	-
CV (%)	7.94	9.44	7.38	5.27	4.58	8.22	-

with a one-way ANOVA conducted using Tamil Nadu Agricultural University AGRES Statistical softwarev 7.01. Non-significant treatment differences were denoted as "NS."

3 Results

During the cropping period, a total of 415.1 and 556.9 mm of rainfall were recorded over 30 and 34 rainy days during 2017–18 and 2018–19, respectively (Figure 1). The mean maximum and minimum temperatures during these seasons were 33.96°C and 32.84°C, and 24.38 °C and 23.06°C, respectively. In 2018–19, a 25.5% increase in rainfall with a more uniform distribution was observed during the cropping period.

3.1 Influence of treatments on growth parameters

The result of the present experiment revealed that redgram cultivars and different dates of sowing significantly influenced growth characteristics namely, plant height and number of branches per plant. Among the six different dates of sowing, crop sown during the 15 to 30thof June (S_6) recorded a significantly higher plant height of 201 cm and a number of branches of 11.82 per plant (Table 2). Sowing redgram during the 1to 14thof September (S_3) resulted in favourable plant height, which was statistically comparable to sowing in the 15 to 30th of September (S_4) and the 15 to 30th of August (S_2) in both years of the study. The lowest plant height (155 cm) was recorded in the 1 to 14th of October (S_5) sown redgram crop. From the three redgram cultivars, var. CO 6 (V_1) recorded a significantly higher plant height of 200 cm and a number of branches of 10.90 per plant. Among the two short-duration cultivars, VBN (Rg) 3 (V_3) registered significantly higher plant height (173 cm), which was on par with CO (Rg) 7 and the number of branches (9.92 per plant). The interaction effect between different dates of sowing and redgram cultivars on plant height was found to be significant. Sowing of CO6, in 15 to 30th the 2nd fortnight of June (V_1S_6), exhibited the tallest plant height at 234 cm among the six sowing dates and three redgram cultivars. Following closely was CO 6 sown in the 1st fortnight of September (1–14) (V_1S_3), which reached a height of 206 cm.

3.2 Influence of treatments on yield parameters

Among the six different dates of sowing, crop sown during the 15 to 30th of June (S_6) recorded the significantly highest number of

10.3389/fenvs.2024.1420078

TABLE 3 Effect of different date of sowing and redgram varieties on weed density and weed dry matter on 30 DAS.

Treatments	Weed density (nos/m^2)	Weed dry matter (g/m^2)
Factor A: Sowing schedule		
S_1: August 1st fortnight	8.29	11.84
	(64.83)	(141)
S_2: August 2nd fortnight	7.98	11.12
	(71.83)	(124)
S_3: September 1st fortnight	7.86	10.76
	(60.17)	(116)
S_4: September 2nd fortnight	7.82	10.52
	(66.83)	(111)
S_5: October 1st fortnight	7.87	10.47
	(61.67)	(110)
S_6: June 2nd fortnight	8.16	12.26
	(66.67)	(142)
S: SE	0.08	0.24
CD (p = 0.05)	0.24	0.76
Factor B: Variety		
V_1:CO 6	7.80	10.49
	(63.33)	(111)
V_2: CO(Rg)7	8.29	11.96
	(67.33)	(140)
V_3:VBN (Rg) 3	7.90	11.03
	(65.33)	(122)
V: SE	0.10	0.12
CD (p = 0.05)	0.29	0.36
Interaction S x V: SE	0.25	0.30
CD (p = 0.05)	0.72	0.88
CV (%)	5.35	4.67

Note: Square root log transformed value and Figures in parenthesis indicate original values.

pods per plant of 287, followed by the sowing of redgram during 15 to 30thof September (S_4), which recorded 259 pods per plant. Crops grown during 1 to 14th of October (S_5) recorded the lowest number of 155 pods per plant. Among the three redgram cultivars, var. CO 6 (V_1) recorded the significantly highest number of 237 pods per plant. Of the two short-duration cultivars, VBN (Rg) 3 (V_3) registered the significantly highest number of 226 pods per plant. The number of seeds per pod and 100 seed weight were not significantly influenced by the treatments (Table 2; Figure 2). The interaction effect between various sowing dates and redgram cultivars on yield attributes, including the number of pods per plant, number of seeds per pod, and 100-seed weight, did not show statistical significance.

3.3 Influence of treatments on grain yield

The treatments exerted a significant influence on grain yield (Table 2; Figure 3). Among the six different sowing dates, a higher mean redgram seed yield of 1,112 kg ha^{-1} was recorded in crops sown during 15 to 30th of June (S6), which was comparable to the yield obtained from redgram sown during 15 to 30thof September (S_4). Sowing of redgram at September 1 to 14th (S_3) was on par with 1-14thofAugust (S_1) and 15–30thofAugust (S_2). The lowest seed yield of 773 kg ha^{-1}was recorded for the sowing of redgram on October 1 to 14th (S_5). From the three redgram cultivars, CO 6 (V_1) recorded a significantly higher mean grain yield of 1,017 kg ha^{-1}. Among the two short-duration cultivars, VBN (Rg) 3 (V_3) had a significantly

TABLE 4 Effect of different date of sowing and redgram varieties on economics.

Treat	Cost of cultivation (Rs. ha^{-1})	Gross income (Rs. ha^{-1})	Net income (Rs. ha^{-1})
S_1	32,000	69,485	37,485
S_2	32,000	68,782	36,782
S_3	32,000	72,491	40,491
S_4	32,000	78,381	46,381
S_5	32,000	57,938	25,938
S_6	32,000	83,433	51,433
V_1	32,000	76,252	44,252
V_2	32,000	67,252	35,252
V_3	32,000	71,751	39,751

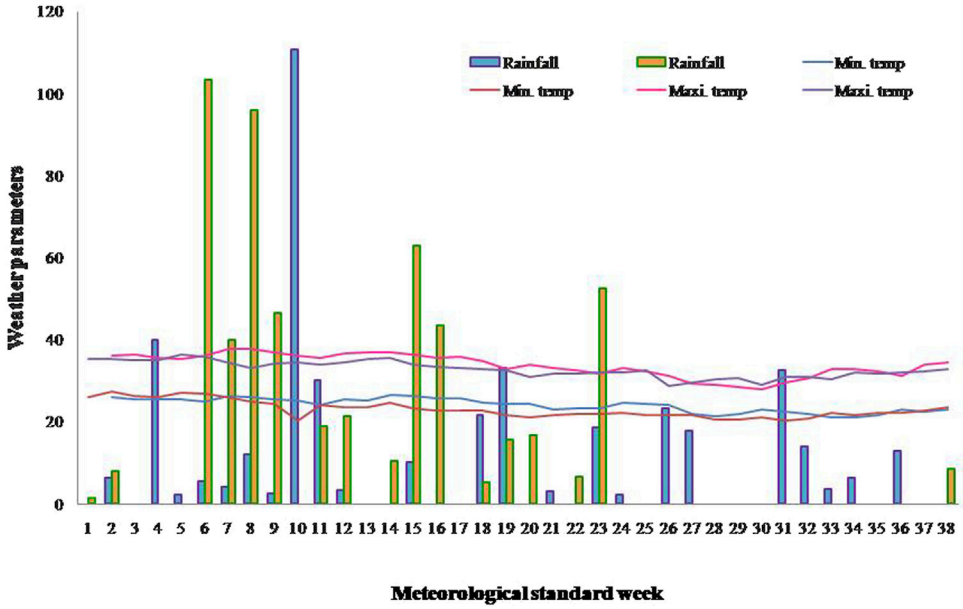

FIGURE 1
Meteorological parameters observed during the experimental period for both years.

higher mean grain yield of 958 kg ha^{-1}. Even though CO 6 (V_1) obtained a higher yield due to its long duration nature, it matured in 187 days, whereas VBN (Rg) 3 (V_3) matured within 129 days. According to the experimental results, the redgram cultivar CO6 produced the highest yield during the second fortnight of June, while the short-duration redgram cultivarVBN (Rg) 3 demonstrated the highest yield during 15 to 30thof September. The results revealed that redgram seed yield was significantly affected by the combination of sowing time and cultivar. Redgram CO 6, sown during 15 to 30thof June (V_1S_6), yielded the highest grain yield of 1,161 kg ha^{-1} among the six sowing dates and three redgram cultivars. Close behind was CO 6 sown in 15 to 30thof September (V_1S_4), which produced a grain yield of 1,105 kg ha^{-1}.

3.4 Weed density (no/m^2) and weed drymatter production (g/m^2)

The weed population in the experimental field was varied and included broadleaved, sedge, and grass weeds. *Dactyloctenium aegyptium* and *Chloris barbata* were the most common grass-related weed species, while *Cyperus rotundus* was the most common sedge-related weed. The broadleaved weeds included *Flaveria australica*, *Cleome gynandra*, *Eclipta alba*, *Convolvulus arvensis*, *Digera arvensis*, *Vicia* spp., and *Celosia argentea*. The result revealed that, among the six different dates of sowing, crops sown at15-30th of September (S_4) registered significantly lower weed density and weed dry matter production of 7.82 nos m^{-2} and 10.52 g m^{-2} respectively, followed by the 1–14thof September (S_3)

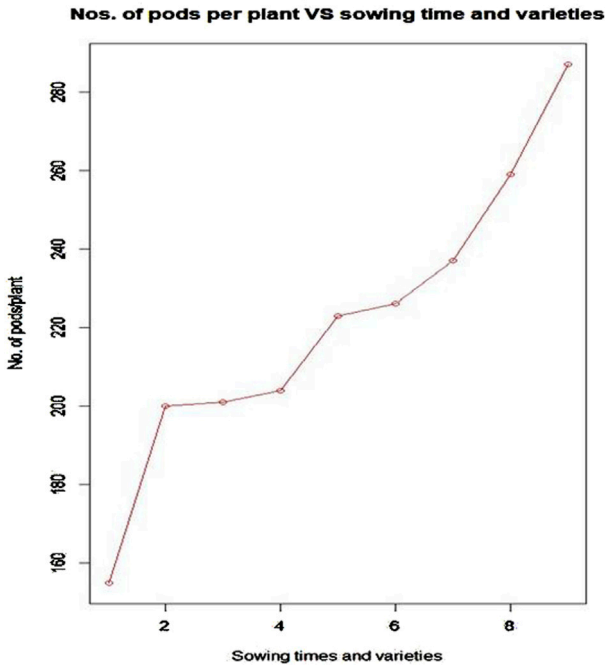

FIGURE 2
Effect of sowing times and varieties on the number of redgram pods per plant at harvest.

(Table 3; Figure 4). The highest weed density and weed dry matter production of 8.29 nos m^{-2} and 11.84 g m^2 respectively, registered the crop sown on August 1 to 14th. Among the three redgram cultivars, CO 6 (V1) exhibited significantly the lowest weed density and weed dry matter production, with values of 7.80 nos. m^{-2} and 10.49 g m^{-2}, respectively, followed by VBN (Rg) 3 (V_3). The weed density and weed dry matter production was significantly influenced by interaction between redgram cultivars and sowing time. Among the six sowing dates and three redgram cultivars. CO 6, sown during the 15 to 30th the 2nd fortnight of June (V_1S_4), yielded the highest grain yield of 7.51 No. m^{-2} and Weed dry matter 9.61 g m^{-2}) on 30 DAS. It was followed by redgram CO 6 sown in the 1 to 14thof September (V_1S_3).

3.5 Economics

Sowing of redgram during the 15 to 30th of June (S_6) recorded the highest gross and net income of ₹. 83,433 and 51,433 ha^{-1}, respectively, and a B: C ratio of 2.61, followed by the September 15 to 30th (S_4) 2.45 (Table 4). Among the three redgram cultivars, CO 6 (V_1) recorded higher gross and net income of ₹. 76,252 and 44,252 ha^{-1} respectively, and a B: C ratio of 1: 2.38, followed by VBN (Rg) 3 (V_3) at 2.24.

4 Discussion

4.1 Influence of time of sowing

The sowing of long-duration redgram during the second week of July notably enhanced plant height and the number of branches per plant in both study years. Unlike other planting dates, seeds sown early in the second week of July resulted in significantly larger plants. One plausible explanation for this observation could be that the crop had sufficient time to mature and capitalize on favourable environmental conditions for vegetative growth and development, leading to increased accumulation of photosynthates during the early stages of crop growth. Similar results were found in studies by Sandeep et al. (2022) and Dahariyaet al. (2018) about the largest plant height. Flowering time dictates how long the vegetative phase lasts, marks the beginning of the reproductive phase, and thus influences the climatic conditions affecting crop growth thereafter. As the season progresses, photoperiod ceases to be a limiting factor, with temperature and soil moisture becoming the primary climatic variables affecting the rate of progress from flowering to physiological maturity. Later sowings in the first fortnight of October accelerated the time to reach physiological maturity and shortened the duration of vegetative, flowering, and podding growth phases compared to the second fortnight of September as earlier sowing dates. These findings are consistent with prior research indicating the substantial impact of temperature on (Soybean by Kundu et al., 2016 and in Chickpea by Richards et al., 2020; 2022) development and the length of growth stages.

The phenology of redgram crop aligns with the resources available in the production environment, including water, nutrients, light, and space, as well as with the genetic variability among redgram cultivars reported by Patel et al. (2000). When crops were sown early, their leaf area index was higher than when they were sown later. Planting a high-yielding cultivar at the optimal time can effectively utilize all production inputs which leads to better plant growth, leaf area index and maximize yield was reported by Kittur and Guggari (2017). Positive weather conditions such as light, temperature, and precipitation may have aided in greater development, and the genetic composition of the cultivar may have provided higher growth parameters and yield-related qualities like the number of pods per plant. It may be the result of the maximum transfer of photosynthates into seed growth in crops sown early (Sandeep et al., 2022). The lowest weed density and dry matter were observed in the sowing of redgram CO6 during the second week of September. The reasons might be the crop's accelerated vegetative and reproductive growth may have resulted from a combination of favourable weather conditions, including higher soil moisture content from adequate rainfall from third week of July to the second week of September in both the years of study (Subbulakshmi,2021).

4.2 Influence of redgram genotypes

The extended duration redgram cultivar CO6 required 43 days more for flowering to maturity compared to VBN(Rg)3, which took 17 days less. CO6, the prolonged-duration cultivar, stood 27 cm taller and produced 12.3 percent more than the early maturing cultivar CO(Rg)7, while VBN(Rg)3 exhibited a 7.0 percent increase among the early maturing cultivars, in contrast to CO(Rg)7. These differences in blooming time, maturity time, plant height, and seed yield were attributed to variations in the genetic composition and characteristics of the plants. Consistent with findings from Kithan et al. (2020), cultivars characteristics in redgram production

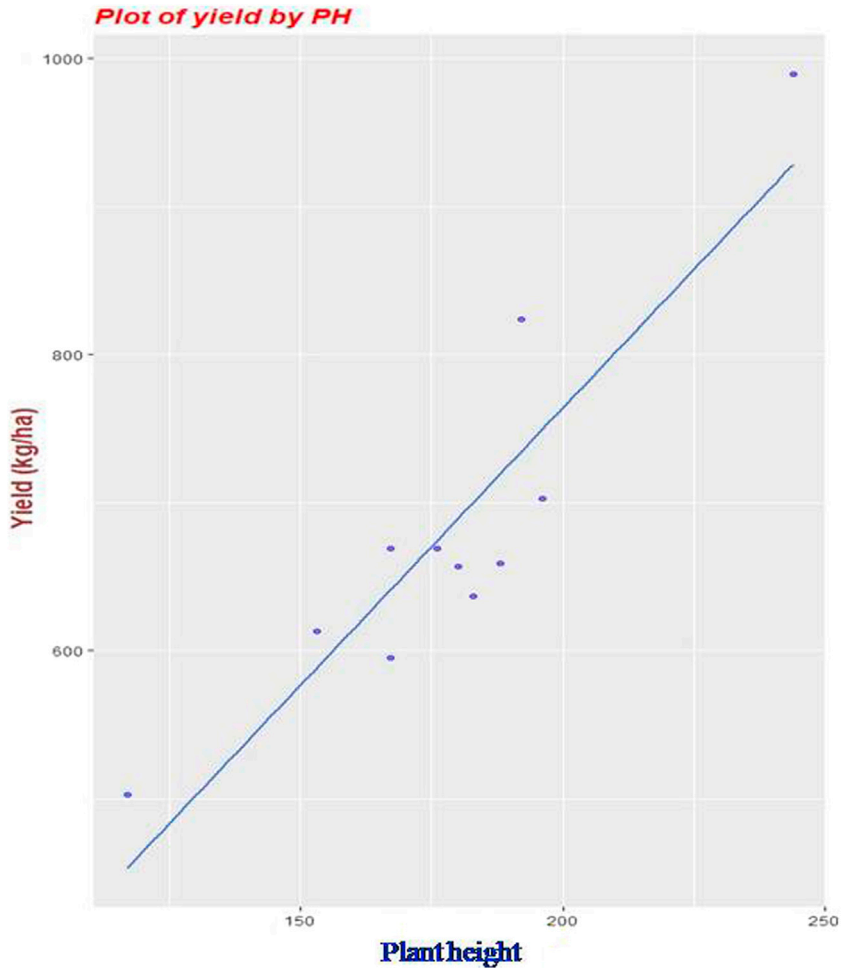

FIGURE 3
Scatter plot of sowing times and varieties on the plant height and grain yield of redgram.

influenced differences in flowering and ripening days, plant height, and seed yield. For instance, they noted that the yield of cultivar UPAS 120 was higher (969 kg ha^{-1}) among the three categories tested. Similarly, Kuri et al. (2018), Chawhan et al. (2019), and Rani and Reddy (2010) observed varietal differences contributing to yield variance in redgram in their investigations. Singh (2000) also highlighted the influence of environmental factors on the source-sink relationship and its impact on redgram seed yield.

Early-maturing or short-duration cultivars tend to be small in stature due to their short vegetative growth period, while late-maturing or long-duration cultivars are typically taller owing to their extended vegetative phase, as noted by Anil et al. (2023). In both years of the study, primary branches/plants were greater in extended-duration redgram cultivars (Reddy, 1990). The interaction between grain yield and plant height was found to be significant in both research years, consistent with reports by several researchers (Mligo and Craufurd, 2005; Reddy et al., 2006; Singh, 2006; Egbe and Vange, 2008) indicating genetic variation in growth and yield.

Among the various factors influencing redgram production, sowing time is considered a crucial non-monetary input. Cultivar choice and planting time are the two most critical elements in redgram production. Sowing a high-yielding cultivar at the proper time is a key strategy for optimizing production input consumption and achieving the best yield. Based on our research, it was concluded that the best time to sow redgram cultivar CO6 is 15 to 30thof June for a long-duration crop and in 15 to 30thof September for the short-duration cultivar VBN (Rg) 3. Although CO6 achieved a higher yield, VBN (Rg) 3 (V_3) matured 58 days earlier than CO6. Hence, the sowing of redgram cultivar VBN (Rg) 3 during 15 to 30thof September is suitable for the southern zone of Tamil Nadu.

4.3 Weed growth

The slow initial growth of redgram encourages rapid weed growth, resulting in intense competition that ultimately reduces crop yield (Channappagoudar and Birdar, 2007). Early sown led to stronger crop growth and canopy, which controlled weeds better than late planting. This early sowing also boosted crop vitality and faced less weed competition, resulting in higher productivity (Malik and Yadav, 2014). Lateral expansion of the canopy resulted in reduced weed density and dry weight, consequently boosting chickpea grain yield (Dhiman, 2007). Leaves shaded deeper within the canopy receive diminished levels of photosynthetically

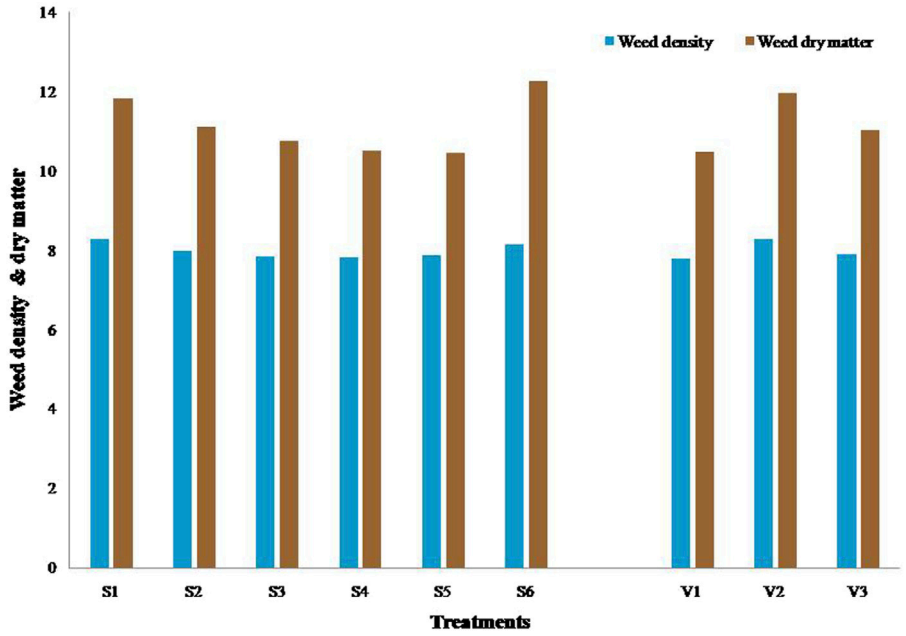

FIGURE 4
Effect of sowing times and redgram varieties on weed density and weed dry matter on 30 DAS.

active radiation and a lower ratio of red to far-red light leads to poor weed growth (Olabode et al., 2007; Rajesh and PaulPandi, 2015). The growth and yield of pulse crops are directly influenced by the sowing date. Sowing at the wrong time in the season can have several negative effects. If sowing occurs either too early or too late, it can result in reduced seed germination and poor growth. Additionally, there may be fewer branches and a smaller crop canopy, allowing more light to penetrate the ground. This increased light can lead to higher weed seed germination, further reducing crop yield. Early sowing may expose young seedlings to frost damage, whereas late sowing could expose plants to heat stress during important growth phases, both of which can significantly impact overall crop productivity. Earlier sowing resulted in significantly lower weed populations and reduced weed dry weight compared to delayed sowing. This is likely due to more favourable environmental and weather conditions that promoted optimal germination and early establishment of plants, leading to a denser canopy that effectively suppressed weeds. This enhanced weed control allowed crops to utilize natural resources more efficiently, with reduced light transmission at the surface inhibiting weed seed germination and growth (Chaudhary et al., 2023). The timing of pea sowing significantly impacts their growth, flowering, and fruiting, ultimately affecting yield per hectare. Optimal sowing dates vary based on local climatic conditions and the specific pea cultivar (Kaur et al., 2024). Pulses sown earlier may undergo a longer vegetative phase, allowing for more branch development. Conversely, late sowing may result in shorter vegetative phases, limiting branch formation (Doraiswamy and Singh, 2001). This is probably because plants sown early benefit from an extended growing season and more favourable temperature and light conditions, which promote pod development. Conversely, late sowing may expose plants to higher temperatures and during critical pod development stages, resulting in shorter pods (Al-Asadi and Kopytko, 2019).

4.4 Yield

The key to maximizing redgram production lies in selecting the right cultivar and sowing it at the optimal time. By choosing a high-yielding cultivar and planting it at the correct time, farmers can effectively utilize production inputs and achieve the highest possible yield (Anil et al., 2023). The combination of sowing time and cultivar significantly influenced redgram seed yield. Commencing from the second half of July, a combination of favourable growth conditions and yield traits contributed to an increase in seed production. Early sowing establishes conditions conducive to robust growth and development, facilitating the formation of larger leaf areas and increased biomass accumulation, ultimately leading to higher seed yield. These outcomes could be attributed to variations in precipitation and temperature over the 2-year period. (Figure 1). The sowing dates and cultivar selections in modern farming reflect the gradual adaptation and fine-tuning of cropping systems to suit local conditions and respond to incremental changes in climate (Minoli et al., 2022).

The decrease in grain yield observed when sowing *kharif* mungbean later, from July 5 to August 5, as reported by Singh et al. (2010), may be attributed to various factors including the genetic makeup of the cultivar, favourable meteorological conditions, and physiological processes could be the highest translocation of photosynthates toward seed development in redgram. The earlier sowing allowed for optimal growth parameters and yield-enhancing characteristics such as increased pod count, facilitated by ideal meteorological conditions including temperature, light, and precipitation, which promoted better growth.

(Sandeep et al., 2022). Moreover, early sowing provides the crop with sufficient time and favourable weather conditions—adequate light, warmth, and developmental cues—for optimal growth, development, and maturation stages. These findings are consistent with those of Fukugawa and Zhenga (1999), who observed significant increases in blooms following vegetative growth in early-planted crops.

In contrast, late sowing of redgram can impact seed germination and yield due to decreased temperatures during the reproductive and maturity periods, along with increased soil moisture (Dhanoji and Patil, 2011; Kumar et al., 2008). Similarly, when redgram is sown later, it often results in shorter plants, longer flowering and maturity periods, and lower yields compared to earlier sowing conditions (Kuri et al., 2018; Kittur and Guggari, 2017; Chawhan et al., 2019). The study findings align with previous research by Kithan et al. (2020) and Kumar et al. (2008), which demonstrated superior production and growth characteristics with the 15 to 30th of September sowing.

The reduction in yield associated with later sowing dates can be attributed to shortened timeframes for flowering, maturity, and dry matter production, as evidenced by Arunkumar and Meena (2018). Interactions between environmental factors and morphological or physiological characteristics throughout the pre- and post-flowering phases contribute to variations in grain legume production. Notably, crops sown in the second and third weeks of July exhibited increased main and subsidiary branches, resulting in higher pod production per plant and overall seed yield. Conversely, delayed seeding led to earlier flowering, reduced vegetative growth, and premature maturity, all of which negatively impacted seed production. These observations align with the findings of Nene and Sheila (1990) and Reddy et al. (2015), indicating that delays in redgram sowing result in reduced branching per plant and lower dry weight at harvest compared to timely sowing (Kumar et al., 2023).

5 Conclusion

The inherent challenges faced in pulse production, particularly the impact of climate variability resulting from shifting rainfall patterns, necessitates adaptive techniques to ensure sustainable productivity. With this background, field experiments were conducted at the National Pulses Research Centre, Vamban, Pudukkottai, Tamil Nadu, South India, during the *kharif* seasons of 2017–18 and 2018–19, focused on optimizing sowing times and identifying suitable redgram cultivars, especially in the face of delayed monsoons in Tamil Nadu. The exploration of six distinct sowing dates alongside three redgram cultivars resulted in a clear correlation between varied sowing times and redgram's growth characteristics and yield. Results showed that the crop sown in 15 to 30th of June showcased remarkable success, with higher plant growth and yield attributes and also a profitable B:C ratio. This sowing period exhibited comparable success to later sowing dates, highlighting its viability even amidst challenging conditions. Among the redgram cultivars, CO 6 emerged as the most productive among the redgram cultivars, attributed to its prolonged phenological phases and extended days to reach critical growth stages, leading to amplified yields compared to other cultivars. However, the shorter duration redgram cultivar, VBN (Rg) 3, despite its lower yield compared to CO 6, matured significantly faster, within 129 days, offering an advantage for crop sequencing and enhancing overall cropping intensity of the farm and also sustain the profitability in harsh climate situations such as drought and erratic rainfall. The research outcome suggests the need for strategic crop cultivar selection and timely sowing practices to mitigate the impact of adverse environmental conditions in changing climatic scenario, ultimately ensuring sustained redgram productivity in rainfed agricultural systems.

Data availability statement

The original contributions presented in the study are included in the article/supplementary material, further inquiries can be directed to the corresponding authors.

Author contributions

SMM: Conceptualization, Formal Analysis, Investigation, Methodology, Supervision, Resources, Validation, Visualization, Writing–review and editing, Writing–original draft. VB: Funding acquisition, Resources, Writing–review and editing. AD: Investigation, Validation, Visualization, Conceptualization, Formal Analysis, Methodology, Supervision, Writing–review and editing. SM: Funding acquisition, Visualization, Resources, Writing–review and editing. US: Funding acquisition, Visualization, Conceptualization, Formal Analysis, Investigation, Methodology, Supervision, Resources, Writing–review and editing, Writing–original draft.

Funding

The author(s) declare that no financial support was received for the research, authorship, and/or publication of this article.

Acknowledgments

Authors would like to acknowledge the respective head of the institute for their support and encouragement during the course of thestudy. The authors gratefully acknowledge the ICAR-AICRP on Pigeonpea for providing financial support and assistance with project formulation. We gratefully acknowledge the support provided by Tamil Nadu Agricultural University for the smooth conduct of the experiments and other logistic support provided. We gratefully acknowledge the funding received from the Australian Government Department of Foreign Affairs and Trade through the Australia-India Strategic Research Fund (AISRF) Round 12 project.

Conflict of interest

The authors declare that the research was conducted in the absence of any commercial or financial relationships that could be construed as a potential conflict of interest.

Publisher's note

References

Al-Asadi, M. S., and Kopytko, P. (2019). Effect of row spacing and planting density on yield and yield components of pea (*Pisum sativum* L.). *J. Environ. Biol.* 40 (4), 821–826.

Anil, P., Sarita, M., and Dangi, S. R. (2023). Effect of sowing date and variety on pigeonpea production in Nepal. *Asian J. Res. Crop Sci.* 8 (3), 173–178. doi:10.9734/ajrcs/2023/v8i3177

Aruna, E., and Sunil Kumar, K. (2023). Influence of sowing time on varied duration redgram genotypes in YSR kadapa district. *Int. J. Plant Soil Sci.* 35 (18), 1983–1988. doi:10.9734/ijpss/2023/v35i183483

Arunkumar, M. M., Dhanoji., and Meena, M. K. (2018). Phenology and productive performance of pigeon pea as influenced by date of sowing. *J. Pharmacogn. Phytochemistry* 7 (5), 266–268.

Channabasavanna, A. S., Kitturmath, M. S., and Rajakumar, H. (2015). Standardization of sowing date and genotypes of pigeonpea [*Cajanus cajan* (L.) Mill sp.] under erratic rainfall conditions in northern dry zone of Karnataka. *Karnataka J. Agric. Sci.* 28 (4), 604–605.

Channappagoudar, B. B., and Birdar, N. R. (2007). Physiological approaches in weed management in soybean and redgram (4:2 rp) intercropping system. *Karnataka J. Agric. Sci.* 20, 241–244.

Chaudhary, A., Venkatramanan, V., Kumar Mishra, A., and Sharma, S. (2023). Agronomic and environmental determinants of direct seeded rice in South Asia. *Circ. Econ. Sustain.* 3, 253–290. doi:10.1007/s43615-022-00173-x

Chawhan, R. G., Chahande, R. V., and Deshmukh, H. S. (2019). Effect of sowing date on seed quality of pigeonpea [*Cajanus cajan*(L.) Mill sp.]. *Pharma Innovation J.* 8 (7), 784–789.

Dahariya, L., Chandrakar, D. K., and Chandrakar, M. (2018). Effect of dates of planting on the growth characters and seed yield of transplanted pigeonpea (*Cajanus cajan*L. Mill Sp.). *Int. J. Chem. Stud.* 6 (1), 2154–2157.

Dhanoji, M. M., and Patil, J. R. (2011). Effect of date of sowing on potential source and sink realization in pigeon pea. *Environ. Ecol.* 29 (3), 1003–1005.

Dhiman, M. (2007). Techniques of weed management in chickpea. *Agric. Rev.* 28 (1), 34–41.

Doraiswamy, P. C., and Singh, N. P. (2001). Effects of sowing dates on growth, yield and quality of early maturing cultivars of pea (*Pisum sativum* L.) under semi-arid conditions. *Indian J. Agrl. Sci.* 71 (3), 210–212.

Egbe, O. M., and Vange, T. (2008). Yield and agronomic characteristics of 30 pigeonpea genotypes at Otobi in Southern Guinea Savanna of Nigeria. *Life Sci. J.* 5, 70–80.

Fischer, T., Byerlee, D., and Edmeades, G. (2014). Crop yields and global food security. *ACIAR Canberra*, 8–11.

Fukugawa, Y., and Zhenga, S. U. H. (1999). Growth response to sowing dates of pigeonpea in northern kyusha of Japan. *Jpn. J. Crop Sci.* 68, 33–38.

Gaikwad, S. V., Mahude, S. V., and Jadhav, S. S. (2023). Effect of dates of sowing on Pigeon pea varieties under varied weather conditions. *Pharma Innovation J.* 12 (12), 320–322.

Grigorieva, E., Livenets, A., and Stelmakh, E. (2023). Adaptation of agriculture to climate change: a scoping review. *Climate* 11, 202. doi:10.3390/cli11100202

Islam, S., Nanda, M. K., and Mukherjee, A. K. (2008). Effect of date of sowing and spacing on growth and yield of *rabi* pigeon pea (*Cajanus cajan*(L.) Millsp.). *J. Crop Weed* 4 (1), 7–9.

Kaur, R., Kondal, P., Singh, N., Maurya, V., Sharma., A., and Kumar, R. (2024). Effect of spacing and sowing dates on growth, yield and quality of pea (*Pisum sativum* L.). *Int. J. Res. Agron.* 7 (2), 238–251. doi:10.33545/2618060X.2024.v7.i2d.312

Kithan, L., Sharma, M. B., and Longchar, A. (2020). Efrformance of promising pigeonpea genotypes under NEHZ. *Int. J. Econ. Plants* 7, 6–8.

Kittur, C. N., and Guggari, A. K. (2017). Effect of sowing time and planting geometry on the growth and yield of pigeonpea in Northeren Dry Zone (Zone 3) of Karnataka. *J. Farm Sci.*, 334–337.

Krsti, ´C. M., Mladenov, V., Banjac, B., Babec, B., Dunđerski, D., C´ uk, N., et al. (2023). Can modification of sowing date and genotype selection reduce the impact of climate change on sunflower seed production? *Agriculture* 13, 2149. doi:10.3390/agriculture13112149

Kumar, N., Gopinath, K. A., Srivastva, A. K., and Mahajan, V. (2008). Performance of pigeonpea (*Cajanus cajan*L. Millsp.) at different sowing dates in the mid-hills of Indian Himalaya. *Archives Agron. Soil Sci.* 54, 507–514. doi:10.1080/03650340802287018

Kumar, R., Niwas, R., Khichar, M. L., and Leharwan, M. (2023). Assessment of sowing time and cultivars on growth, development and yield parameters of pigeonpea. *Legume Res.* 46 (5), 604–608. doi:10.18805/LR-4380

Kundu, P. K., Roy, T. S., Khan, S. H., Parvin, K. ., and Mazed, H. E. M. K. (2016). Effect of sowing date on yield and seed quality of soybean. *J.Agric. Ecol. Res. Int.* 9, 1–7. doi:10.9734/jaeri/2016/29301

Kuri, S., Shivaramu, H. S., Thimmegowda, M. N., Yogananda, S. B., Prakash, S. S., and Murukannappa, S. M. (2018). Effect of row spacing, varieties and sowing dates on growth and yield of pigeonpea. *Int. J. Cur. Microbio. App. Sci.* 7 (8), 1125–1128. doi:10.20546/ijcmas.2018.708.127

Malik, R. S., and Yadav, A. (2014). Effect of sowing time and weed management on performance of pigeonpea. *Indian J. Weed Sci.* 46 (2), 132–134.

Mallikarjuna, B. O., and Devaraja, T. N. (2023). Frontline demonstration A tool to study drought tolerant and high yielding red gram variety for davanagere district, India. *Int. J. Curr. Microbiol. App. Sci.* 12 (08), 100–105. doi:10.20546/ijcmas.2023.1208.012

Minoli, S., Jägermeyr, J., Asseng, S., Urfels, A., and Müller, C. (2022). Global crop yields can be lifted by timely adaptation of growing periods to climate change. *Nat. Commun.* 13, 7079. doi:10.1038/s41467-022-34411-5

Mligo, J. K., and Craufurd, P. Q. (2005). Adaptation and yield of pigeonpea in different environments in Tanzania. *Field Crops Res.* 94, 43–53. doi:10.1016/j.fcr.2004.11.009

Nene, Y. L., and Sheila, V. K. (1990). "Pigeonpea: geography and importance," in *The pigeonpea*. Editors Y. L. Nene, S. H. Hall, and V. K. Sheila (Wellingford, U.K: CAB International), 1–14.

Olabode, O. S., Ogunyemi, S., and Adesina, G. O. (2007). Response of okra (*Abelmoschus esculentus* (L.)Moench.) to weed control by mulching. *Food Agric. Environ.* 5 (3-4), 324–326.

Padhi, A. K. (1995). Effect of sowing date and planting geometry on yield of redgram (*Cajanus cajan*) genotypes. *Indian J. Agron.* 40 (1), 72–76.

Patel, H. P., Gurjar, R., Patel, K. V., and Patel, N. K. (2019). Impact of sowing periods on incidence of insect pest complex in Pigeon pea. *J. Entomology Zoology Stud.* 7 (2), 1363–1370.

Patel, N. R., Mehta, A. N., and Shekh, A. M. (2000). Radiation absorption, growth and yield of pigeon pea cultivars as influenced by sowing dates. *Exp. Agric.* 36, 291–301. doi:10.1017/s001447970000301x

Pawar, G. R., Gokhale, D. N., and Mirza, I. A. B. (2020). Performance of different sowing dates and cropping systems on yield attributes and yield of pigeonpea (*Cajanus cajan*L.) under rainfed condition. *Int. J. Curr. Microbiol. App. Sci.* 11, 63–73.

Rajesh, N., PaulPandi, V. K., and Duraisingh, R. (2015). Enhancing the growth and yield of pigeon pea through growth promoters and organic mulching- A review. *Afr. J. Agric. Res.* 10 (12), 1359–1366. doi:10.5897/ajar2014.8736

Ram, H., Singh, G., Sekhon, H. S., and Khanna, V. (2011). Effect of sowing time on the performance of pigeonpea genotypes. *J. Food Legumes* 24, 207–210.

Rani, B. P., and Reddy, R. D. (2010). Performance of pigeonpea in sole and intercropping system in vertisols of Krishna - godavari zone in Andhra Pradesh. *Indian J. Agric. Res.* 44 (3), 225–228.

Ravi, D., Patil, B. L., Manjunatha, B. L., and Patil, S. L. (2022). Climate change mitigation and adaptation strategies in drylands of Northern Karnataka. *Indian J. Agric. Sci.* 92 (1), 80–84. January 2022/Article. doi:10.56093/ijas.v92i1.120844

Reddy, G. K., Reddy, P. M., Kumari, P. L., and Krishna, T. G. (2015). Response of Pigeonpea varieties to time of sowing during rabi season. *J. Agric. Veterinary Sci.* 8 (2), 12–15.

Reddy, L. J. (1990). "Pigeonpea: morphology," in *The pigeonpea*. Editors Y. L. Nene, S. D. Hall, and V. K. Sheila (Wallingford,UK: CAB International), 47–86.

Reddy, M. M., Padmaja, B., and Malathi, S. (2012). Evaluation of pigeonpea genotypes for delayed Sowing in Telangana region of Andhra Pradesh under rainfed conditions. *Indian J. Dry land Agrl. Res. Dev.* 27 (2), 59–62.

Reddy, M. M., Padmaja, B., and Rao, L. J. (2006). Agronomic management for improving productivity of pigeonpea-based intercropping system under rainfed conditions in vertisols. *Indian J. Pulses Res.* 19, 219–221.

Reed, W., Lateef, S. S., Sithananthan, S., and Pawar, C. S. (1989). *Pigeonpea and chickpea insect identification handbook international crops research institute for the semi-AridTropics (ICRISAT), patancheru, Andhra Pradesh*. India, 120.

Richards, M. F., Maphosa, L., and andPreston, A. L. (2022). Impact of sowing time on chickpea (*Cicer arietinum* L.) biomass accumulation and yield. *Agronomy* 12, 160. doi:10.3390/agronomy12010160

Richards, M. F., Preston, A. L., Napier, T., Jenkins, L., and Maphosa, L. (2020). Sowing date affects the timing and duration of key Chickpea (*Cicer arietinum* L.) growth phases. *Plants* 9, 1257. doi:10.3390/plants9101257

Sandeep, G., Vijaya Bhaskar Reddy, U., Ramesh Babu, P. V., Kavitha, P., and Srinivasa Reddy, M. (2022). Cultivar and sowing date effect on growth attributes and yield of redgram (*Cajanus cajan*L.). *Pharma Innovation J.* 11 (7), 2476–2479.

Sasane, S. (2017). "Impact of south west monsoon on crop yield: a statistical analysis," in *International interdisciplinary seminar on geographical and historical perspective of global problems, 1-10, 2017*. Kolhapur, India: Department of Geography, D.P. Bhosle College.

Sharifi, R. S., Sedghi, M., and Gholipouri, A. (2009). Effect of plant population density and yield attributes of maize hybrids. *Res. J. Biol. Sci.* 4 (4), 375–379.

Singh, G., Sekhon, H. S., Ram, H., Gill, K. K., and Sharma, P. (2010). Effect of date of sowing on nodulation, growth, thermal requirement and grain yield of kharif mungbean genotypes. *J. Food Legumes* 23, 132–134.

Singh, I. (2000). Flowering and podding behavior in determinate and indeterminate pigeonpea genotypes. *Indian J. Agrl. Res.* 34 (1), 67–70.

Singh, R. S. (2006). Performance of late duration pigeonpea varieties under delayed planting. *Indian J. Pulses Res.* 19, 255–256.

Subbulakshmi, S. (2021). Effect of sowing dates and weed control treatments on weed management and grain yield of greengram under rainfed condition. *Indian J. Weed Sci.* 53 (2), 191–194. doi:10.5958/0974-8164.2021.00036.8

Sunil Kumar, D. U., Rao, M., Pratibha, T., and Kale, P. (2020). Small and marginal farmers of Indian agriculture: prospects and extension strategies. *Indian Res. J. Ext. edu.* 20 (1).

Surendran, U., Raja, P. M. J., Rama Subramoniam, S., and Subramoniam, S. R. (2021). Use of efficient water saving techniques for production of rice in India under climate change scenario: a critical review. *J. Clean. Prod.* 309, 127272. doi:10.1016/j.jclepro.2021.127272

frontiers | Frontiers in Environmental Science

TYPE Original Research
PUBLISHED 24 January 2025
DOI 10.3389/fenvs.2024.1535193

OPEN ACCESS

EDITED BY
Xiaoping Wang,
Northwest A&F University, China

REVIEWED BY
Chenfeng Wang,
Chinese Academy of Sciences (CAS), China
Meng Wang,
Chaozhou Environmental Information Center, China

*CORRESPONDENCE
Zhongju Meng,
mengzhongju@126.com

RECEIVED 27 November 2024
ACCEPTED 27 December 2024
PUBLISHED 24 January 2025

CITATION
Yang Y, Meng Z, Li H, Gao Y, Li T and Qin L (2025) Soil porosity as a key factor of soil aggregate stability: insights from restricted grazing.
Front. Environ. Sci. 12:1535193.
doi: 10.3389/fenvs.2024.1535193

Soil porosity as a key factor of soil aggregate stability: insights from restricted grazing

Yi Yang[1,2,3], Zhongju Meng[1,2,3]*, Haonian Li[1,2,3], Yue Gao[1,2,3], Tianyang Li[1,2,3] and Lei Qin[4]

[1]College of Desert Control Science and Engineering, Inner Mongolia Agricultural University, Hohhot, China, [2]Key Laboratory of Aeolian Physics and Desertification Control Engineering from Inner Mongolia Autonomous Region, Inner Mongolia Agricultural University, Hohhot, China, [3]Key Laboratory of Desert Ecosystem Conservation and Restoration, State Forestry and Grassland Administration of China, Inner Mongolia Agricultural University, Hohhot, China, [4]Inner Mongolia Water Conservancy Development Center, Hohhot, China

Overgrazing leads to steppe degradation and soil structure deterioration, which is common in desert steppes. Restricted grazing is a sustainable practice, but the mechanisms by which soil structure responds to restricted grazing have received little attention. This study examined the effects of two different grazing management strategies, namely, restricted grazing and free grazing (CK), on soil structure indicators in the desert steppe. The restricted grazing further included grazing exclusion (GE) and seasonal grazing (SG). Additionally, a preliminary exploration was conducted to identify the main factors affecting the soil aggregate stability. Our results demonstrated that GE significantly increased clay (<0.002 mm) and silt (0.002–0.02 mm) in the 0–10 cm and 10–20 cm layers by an average of 71.27% and 70.64%, respectively. Additionally, SG significantly increased clay (<0.002 mm), silt (0.002–0.02 mm), and macroaggregates (>0.25 mm) in the 0–10 cm layer. GE significantly increased soil organic carbon in the 0–10 cm and 10–20 cm layers by 7.02 g/kg and 7.45 g/kg, respectively. In addition, SG had no significant effect on soil organic carbon. The findings obtained from the computations using the boosted regression tree (BRT) demonstrated that, within the study period, soil porosity significantly affects soil aggregate stability compared to other factors. Moreover, it possessed an average explanatory power that surpassed 45%. Overall, the soil structure is better under GE than under SG, and GE is the key to improving the soil structure of desert steppe. The research will contribute to a more profound comprehension of the impact of grazing on soil structure. Therefore, it is recommended that grazing closures be prioritized in desert grasslands to promote coordination between grassland restoration and livestock development.

KEYWORDS

soil aggregate stability, desert steppe, soil organic carbon, grazing exclusion, soil porosity

1 Introduction

Steppe ecosystems are a vital component of the natural environment, covering approximately 40% of the total land area and serving numerous ecological and productive roles (Tian et al., 2021; Liu et al., 2023). These ecosystems predominantly exist in arid and semiarid regions susceptible to global environmental changes,

characterized by fragile ecosystems and a high risk of soil erosion. Soil dispersion and water permeability properties significantly contribute to soil erosion vulnerability. Good soil structure is critical for enhancing soil stability and effectively combating erosion (Abu-Hamdeh et al., 2006; Kinnell, 2018; Gao et al., 2024). The dual nature of soil structure can be delineated as the unity of aggregates and pores. In the long run, soil aggregates have a more comprehensive range of functions than pore space alone (Yudina and Kuzyakov, 2023). Soil aggregate formation increases soil cohesion and reduces soil erosion (Yudina and Kuzyakov, 2019; Phefadu and Munjonji, 2024). Also, soil aggregates have comparable water-holding and aerated pore space, and the soil is highly permeable, which also favors erosion resistance (Ferreira et al., 2023). As early as 1983, it was pointed out that soil aggregate stability indicates the indices of soil erodibility (Egashlra et al., 1983). In the Water Erosion Prediction Project (WEPP) model, Agglomerate stability is also recognized as one of the most critical soil indicators for soil erosion (Karlen and Stott, 2015; Xiao et al., 2017; Zhu et al., 2018).

The utilization of steppe ecosystems for grazing represents a pivotal aspect of their management, exerting a considerable influence on the configuration and functionality of these ecosystems (Reinhart et al., 2021). Soil erosion and degradation of grassland ecosystem services and functions caused by inappropriate grazing have become a global problem (Zhang et al., 2018; Bardgett et al., 2021). It is estimated that the degraded grassland area in China has reached 90% (Zhu et al., 2021). It is imperative to identify suitable grazing practices that can alleviate grassland degradation and ensure the long-term stability of grassland ecosystems (Rojas-Briales, 2015).

Since the 1960s, grassland privatization has led to the loss of self-recovery of desert steppe in northern China and reduced soil productivity (Conte and Tilt, 2014; Ye et al., 2023). This severe consequence has prompted the government to prioritize this issue. In 2003, a 'Returning Grazing Land to Grassland' policy was introduced to restore degraded steppe, including grazing bans and seasonal grazing (Li et al., 2013). The objective of these measures is twofold: firstly, to enhance plant diversity and, secondly, to restore the functioning of steppe ecosystems by improving soil structure through a series of reciprocal mechanisms (Franzluebbers et al., 2012; Enriquez et al., 2021; Nael et al., 2024; Blanco-Sepúlveda et al., 2024). Different grazing patterns affect the degree of soil disturbance, which in turn causes dynamic changes in soil structure indicators (Blanco and Lal, 2023). Therefore, research on grassland restoration should focus on the response of soil structure indicators to changes in grazing patterns (De Boer et al., 2018; Lai and Kumar, 2020). Conversely, the evidence suggests that moderate grazing can help offset these impacts, although this approach does result in a corresponding decrease in soil organic carbon (Lai and Kumar, 2020). A reduction in grazing levels results in a notable decrease in soil compaction, primarily caused by livestock trampling (Romero-Ruiz et al., 2023). A systematic framework has been developed to predict changes in soil structural properties associated with livestock-induced soil compaction (Romero-Ruiz et al., 2023). Seasonal grazing promotes sustained restoration of grassland soils by reducing the duration of grazing, but scientists have paid little attention to it (Chen and Baoyin, 2024). One of the few examples is a study in a typical steppe in China, which demonstrated that seasonal grazing can reduce the adverse effects of grazing on pore characteristics (Yang et al., 2024).

Many studies have been conducted on the effects of grazing on grassland soil aggregates. These studies have shown that grazing exclusion significantly increases the number and stability of soil aggregates, as well as the erosion resistance of soils. These studies have attributed the improved stability of soil aggregates to increased organic carbon (Deng et al., 2018; Dong et al., 2022). Other studies point out that soil texture controls the formation of specific aggregates, where larger-diameter aggregates are positively correlated with increased clay content (Schweizer et al., 2019). Some other studies have shown a significant positive correlation between porosity and soil aggregate stability. During the decomposition of plant residues by microorganisms, phenolic acids are released. At the same time, the decomposition of amino acids in the residues triggers an instantaneous stabilization of the aggregates. The interaction of phenolic acids with the instantly formed aggregates further enhances the soil aggregates stability (Martens, 2000). The contradictory results of these studies prompted us to explore the main factors affecting the soil aggregate stability.

This study utilizes a 20-year-long field experiment to fill this gap in the mechanisms by which soil structure indicators respond to restricted grazing and to explore differences in scores of factors influencing soil aggregate stability in a desert steppe. Three field observation sites were established using fences to desert steppe in Inner Mongolia, these were designated as grazing exclusion (GE), seasonal grazing (SG), and free grazing (CK), each defined by fenced boundaries. Therefore, the research objectives of this study were defined as follows: (1) To assess the effects of different grazing practices on soil structure indicators, quantitatively evaluate soil particle size composition, soil bulk density, soil aggregate composition, soil aggregate stability, and soil organic carbon under varying grazing practices; and (2) To explore the primary factors influencing changes in soil aggregate stability. The results of this experiment aim to provide a theoretical foundation for the adaptive management of steppe ecosystems and contribute to efforts to slow down or reverse steppe degradation.

2 Materials and methods

2.1 Overview of the Study area

The study area is in Baotou, Inner Mongolia, within the southeastern portion of Darhan Muminggan United Banner (coordinates: 41° 21′3.96″N, 111° 12′35.79″E) (Figure 1). It is at approximately 1600 m and has a semiarid continental climate. The annual mean temperature is 3.4°C, the annual mean rainfall is 282 mm, and the annual mean evapotranspiration is 2,225 mm. The soil in this area is calcareous, with a thin humus layer and low organic matter content, and the soil layer is about 40 cm deep. The dominant plant taxa are *Stipa grandis, Leymus chinensis*, *Agropyron cristarum*, and *Cleistogenes squarrosa*.

2.2 Experimental design and soil sampling

The experiment was conducted at the Yinshanbeilu Grassland Eco-hydrology National Observation and Research Station

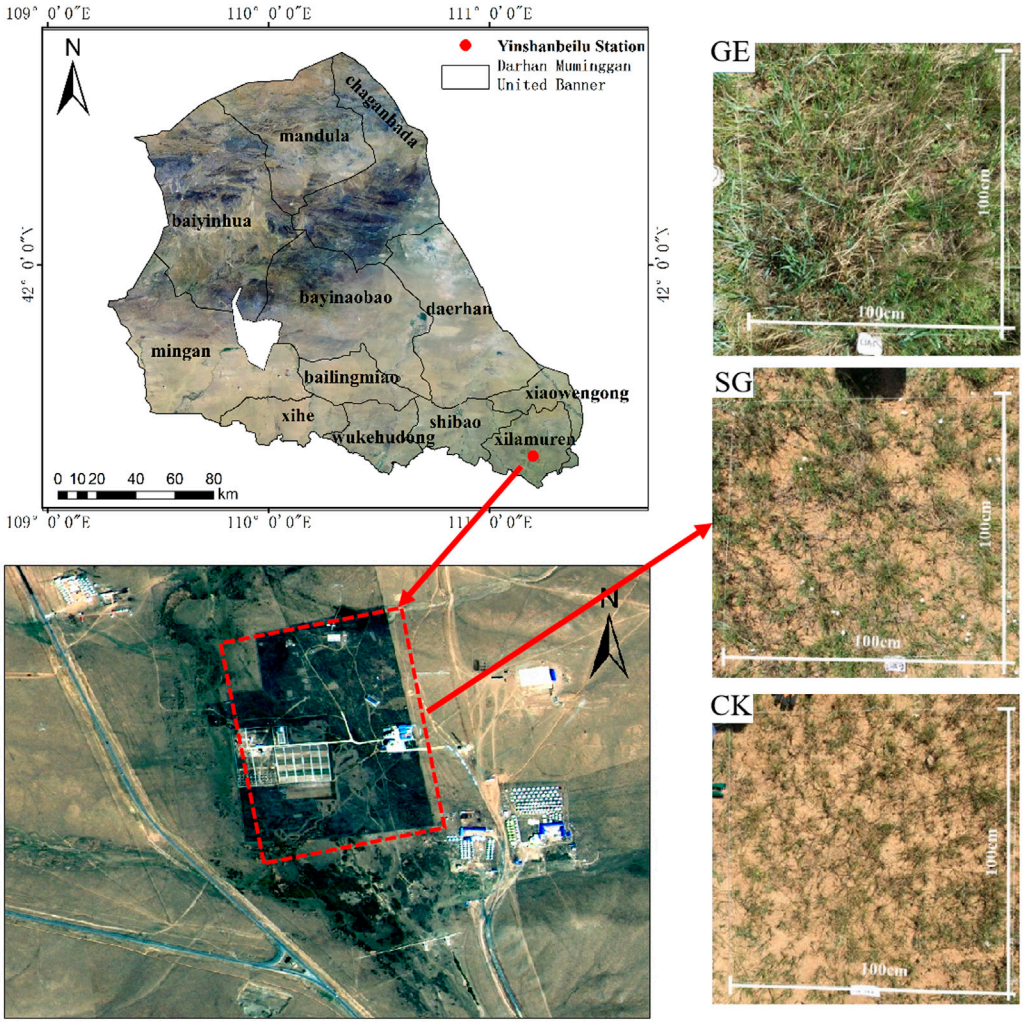

FIGURE 1
Study area. NOTE:GE: grazing exclusion; SG: seasonal grazing; CK: free grazing.

(Yinshanbeilu Station). Three grazing plots were established: restricted grazing (GE and SG) plots were set up on flat terrain under similar natural conditions, and CK in the periphery was set as a control. According to the Yinshanbeilu Station records, the area has been grazed since 1960. The three plots were adjacent and at the same altitude to prevent climate and other factors from influencing the experimental results.

To ensure the greatest possible consistency in grazing intensity, the specifications of plots were varied. Among them: (1) The GE plot has been closed to grazing since 2002, using a 2.0 m wire mesh fence to exclude livestock. The sample plot size was 400 m × 300 m, with no grazing activities, and the vegetation coverage is approximately 92.10%. (2) The SG plot, seasonal grazing (November to April), was introduced in 2002 and enclosed with a 2.0 m barbed wire fence. The sample plot size was 300 m × 250 m, with a grazing intensity of 0.5-1 sheep ha^{-1}, and the vegetation coverage is approximately 60.10%. (3) The CK plot has been fenced off with barbed wire since 2002 and has been under continuous grazing by local herders. The size of the sample plot was 400 m × 200 m. The grazing intensity ranges from 0.5 - 1 sheep ha^{-1} between November and April and 1–1.5 sheep ha^{-1} from May to October, and the vegetation coverage is approximately 48.80%. Each plot adopts the same grazing system as the local herders, feeding from 7:00 to 19:00 and driving back to the sheepfolds to rest in the evening. Three 20 m × 20 m test plots were randomly established as replicates within each grazing method sample plot.

Three 1 m × 1 m sample plots were randomly picked from each grazing area, swith a slope of 2.2°–3.0°. Subsequently, the soil samples were collected in layers from different depths, including 0–10 cm, 10–20 cm, 20–30 cm, and 30–40 cm, by utilizing a 100 cm^3 sampling ring. It is worth noting that no rainfall occurred during the initial 10 days at the sampling locations, nullifying any potential influence that rain could have exerted on the soil characteristics.

2.3 Analysis of soil samples

The mechanical composition of the soil was determined as follows: First, the air-dried soil was crushed, and any foreign matter was removed. Then, the resulting material was passed

through a 2 mm sieve. After that, a Malvern Mastersizer-3000 (Malvern Instruments Ltd., Malvern, UK) model laser particle sizer was used to determine the soil particle size composition for further analysis. Finally, the results were classified by the International Standard Classification of Soils (ISCS). SOC was measured with $K_2Cr_2O_7$-H_2SO_4 (Noulèkoun et al., 2021). The samples collected by the ring knife (V = 100 cm^3) were divided into two groups. A group of soil samples was placed in an oven at a temperature of 105°C ± 2°C, dried to a constant weight, and then weighed (G_s, g). The other set of soil samples was divided into two, weighed and soaked in static water for 1–2 h and 6 h and taken out for weighing respectively. Based on the above measurement, soil bulk density (BD), total porosity (TP), capillary porosity (CP), and non-capillary porosity (NCP) were calculated by Equations 1–4.

$$BD = G_s/V \quad (1)$$

$$TP = (W_{6H} - W_1 - W_D)/V \quad (2)$$

$$CP = (W_{2H} - W_1 - W_D)/V \quad (3)$$

$$NCP = TP - CP \quad (4)$$

Where: W_1:weight of ring cutter(g); W_{6H} is weight of ring cutter with soil after 6 h of water absorption (g); W_{2H} is weight of ring cutter with soil after 2 h of water absorption (g).

The soil clumps within the soil samples were manually fragmented into pieces with a diameter of approximately 10 mm. After air-drying, extraneous substances were meticulously removed with the assistance of tweezers. Subsequently, a 50 g sample was procured and placed into the sieve set of the DIK-2012 Aggregate Analyzer. The sieve set is configured with apertures of 2 mm, 1 mm, 0.5 mm, and 0.25 mm. Distilled water was gradually added along the bucket's rim until it covered the soil samples completely. Following a stationary period of 2 min, the shaking process was initiated at 30 oscillations per minute with a shaking amplitude of 38 mm. The shaking operation was concluded after 5 min. The remaining soil particles in the various sieves were then dried to a constant weight on an electric hot plate maintained at 60°C. They were subsequently weighed, and the proportions of water-stable aggregates of different particle sizes were accurately calculated. The soil aggregates were weighed and used to calculate soil aggregate fractions. To assess the aggregate stability, three metrics, $WSA_{>0.25}$(water-stable aggregate >0.25 mm), MWD (mean weight diameter), and GMD (geometric mean diameter), were calculated. Calculations were made by means of Equations 5–7.

$$WSA_{>0.25} = \frac{M_s}{M_t} \quad (5)$$

Where: M_s is the amount of >0.25 mm water stable aggregates (g), and M_t is the total amount of aggregate before wet sieving (g).

$$MWD = \sum_{i=1}^{n} (\overline{x_i} W_i) \Big/ \sum_{i}^{n} W_i \quad (6)$$

Where: x_i is the average diameter of aggregate of particle size i and ω_i is the percentage content of aggregate of particle size i.

$$GMD = \exp\left(\sum_{i=1}^{n} \omega_i \ln \overline{x_i} \Big/ \sum_{i}^{n} \omega_i \right) \quad (7)$$

Where: x_i is the average diameter (mm) of aggregate of particle size i, and ω_i is the percentage content (%) of particle size i.

2.4 Statistics and analysis of data

Before conducting an Analysis of Variance (ANOVA), the data's normal distribution and homogeneity of variance were tested. Least Significance Difference (LSD) and Duncan tests are employed for multiple comparisons to analyze the differences among different grazing practices. The significance of all differences is tested using SPSS version 25.0 at a significance level of $p < 0.05$.

The relative effects of the factors on overall stability were quantitatively assessed using a Boosted Regression Tree (BRT) model by selecting parameter combinations that ensured an R^2 greater than 0.8 and a Mean Squared Error (MSE) less than 0.1. The specific parameters are "distribution = gaussian,trees = 5000,interaction.depth = 1,shrinkage = 0.06, bag.fraction = 0.8" (Sidhu et al., 2023). The BRT model was implemented using the Dismo package in R version 4.2.3.

3 Results

3.1 Soil particle size composition and soil texture characteristics

The soil particle size composition for different grazing regimes is shown below (Table 1). The composition of the soil particle size of the soil (excluding 20–30 cm) differed significantly ($p < 0.05$) among the three grazing methods. The percentages of the total volume of different grain sizes in the sample graphs for the grazing methods showed the same pattern: sand > silt > clay. Under GE and SG, the volume distribution of soil grain sizes decreased in the sand and increased in silt and clay compared with the CK ($p < 0.05$). At 0–10 cm, the sand in GE and SG was significantly lower than in CK ($p < 0.05$). The reduction in sand in SG (72.85% ± 2.36%) was more significant than that in GE (75.66% ± 4.64%). Similarly, the clay and silt were significantly increased, and the increase in SG was higher than that in GE ($p < 0.05$). Nevertheless, at depths of 10–20 cm and 30–40 cm, the impact of the reduction in sand and the increase in silt and clay was more pronounced in GE than in SG. Conversely, at a depth of 20–30 cm, no statistically significant difference was observed in the sand, silt, and clay among GE, SG, and CK ($p > 0.05$). Nevertheless, it is worth noting that the soil texture within the GE and SG plots has improved when juxtaposed with that of the CK plot (Figure 2).

3.2 Soil bulk density and porosity characteristics

Table 2 summarizes the BD, TP, CP, and NCP for the three different grazing management practices at various soil depths. At 0–10 cm, BD and TP showed no statistically significant differences among GE, SG, and CK ($p > 0.05$). At 10–20 cm, 20–30 cm, and 30–40 cm, BD in GE was significantly lower than in CK, with an average of 11.92%, while TP in GE was significantly higher than in

TABLE 1 Characteristics of the soil mechanical composition under different grazing regimes.

Soil depth cm	Grazing practices	Sand (0.02–2 mm) %	Silt (0.002–0.02 mm) %	Clay (<0.002 mm) %
0–10	GE	75.66 ± 4.54B	18.92 ± 3.64A	5.39 ± 0.91A
	SG	72.85 ± 2.36B	21.42 ± 1.82A	5.71 ± 0.55A
	CK	84.65 ± 1.40A	11.84 ± 1.14B	3.49 ± 0.30B
10–20	GE	70.45 ± 6.42B	23.21 ± 5.04A	6.32 ± 1.38A
	SG	83.34 ± 2.22A	13.13 ± 1.91B	3.49 ± 0.31B
	CK	83.82 ± 1.85A	12.79 ± 1.27B	3.36 ± 0.59B
20–30	GE	78.17 ± 1.79A	17.42 ± 1.48A	4.37 ± 0.30A
	SG	77.33 ± 7.22A	18.14 ± 6.13A	4.49 ± 1.08A
	CK	81.56 ± 4.55A	14.22 ± 3.33A	4.18 ± 1.25A
30–40	GE	73.86 ± 2.65B	20.94 ± 1.94A	5.17 ± 0.82A
	SG	76.9 ± 4.31B	18.48 ± 3.37A	4.58 ± 0.93A
	CK	85.58 ± 1.40A	11.18 ± 1.48B	3.22 ± 0.13B

Note: Different letters represent significant differences at $p < 0.05$. GE, grazing exclusion; SG, seasonal grazing; CK, free grazing.

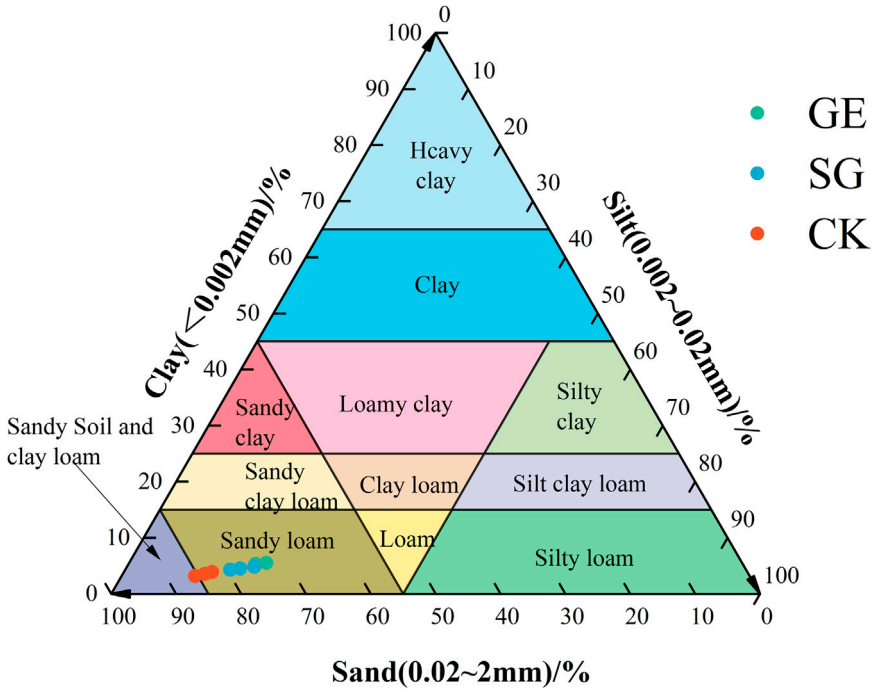

FIGURE 2
Triangular map of soil texture classification. NOTE: SG: seasonal grazing; CK: free grazing.

CK, with an average of 16.09% ($p < 0.05$). In all four soil horizons, CP in GE was significantly higher than in CK, with an average of 27.42% ($p < 0.05$), and SG and CK had no statistically significant difference ($p > 0.05$). A significant difference in NCP at 0–10 cm was only found between GE and CK($p < 0.05$). NCP showed no statistically significant differences among GE, SG, and CK in the remaining three soil horizons ($p > 0.05$).

3.3 Soil aggregate composition distribution and stability characteristics

As shown in Figure 3, grazing practices significantly influenced soil aggregate composition. In the GE and SG, the >2 mm fraction was predominant (accounting for 43.36% and 36.57%, respectively), while in the CK, the <0.25 mm fraction was predominant (35.59%). The >2 mm

TABLE 2 Characteristics of soil bulk density and porosity under different grazing practices.

Soil depth cm	Grazing practices	BD g/cm^3	TP %	CP %	NCP %
0–10	GE	1.46 ± 0.05A	45.69 ± 1.57A	29.75 ± 2.20A	15.94 ± 0.73B
	SG	1.51 ± 0.05A	44.06 ± 1.67A	27.42 ± 1.57AB	16.64 ± 0.37AB
	CK	1.55 ± 0.04A	42.67 ± 1.46A	25.14 ± 2.19B	17.53 ± 0.56A
10–20	GE	1.44 ± 0.08B	46.42 ± 2.53A	31.18 ± 4.12A	15.24 ± 1.62A
	SG	1.54 ± 0.02AB	42.89 ± 0.68AB	26.35 ± 0.65AB	16.55 ± 0.52A
	CK	1.67 ± 0.09A	38.71 ± 2.94B	22.20 ± 3.18B	16.51 ± 0.29A
20–30	GE	1.40 ± 0.08B	47.86 ± 2.71A	32.29 ± 4.21A	15.57 ± 1.54A
	SG	1.48 ± 0.04AB	45.01 ± 1.27AB	29.29 ± 1.65AB	15.72 ± 0.50A
	CK	1.60 ± 0.08A	41.10 ± 2.85B	24.69 ± 2.53B	16.41 ± 0.21A
30–40	GE	1.43 ± 0.09B	46.79 ± 2.83A	30.35 ± 4.16A	16.44 ± 1.39A
	SG	1.45 ± 0.06B	45.12 ± 2.66AB	29.13 ± 3.08A	15.82 ± 0.72A
	CK	1.58 ± 0.02A	41.81 ± 0.78B	25.27 ± 0.83A	16.54 ± 1.33A

Note: Different letters represent significant differences at $p < 0.05$. BD, soil bulk density; TP, soil total porosity; CP, soil capillary porosity; NCP, soil non-capillary porosity; GE, grazing exclusion; SG, seasonal grazing; CK, free grazing.

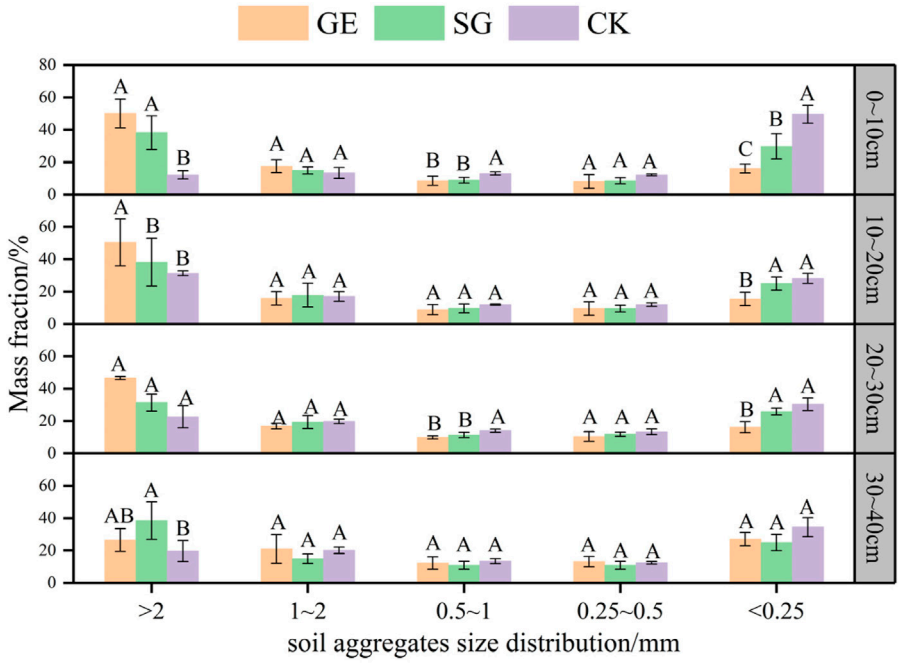

FIGURE 3
Distribution of soil aggregate size under different grazing practices. NOTE: Different letters represent significant differences at $p < 0.05$. GE: grazing exclusion; SG: seasonal grazing; CK: free grazing.

fraction content at 0–10 cm in the GE showed a statistically significant increase of 62.77% compared to the CK ($p < 0.05$). For GE, the content of the >2 mm fraction at a depth of 10–20 cm was significantly higher than that in SG and CK ($p < 0.05$), with the increases being by a factor of 1.32 and 1.61, respectively. Regarding the <0.25 mm fraction at 0–10 cm, 10–20 cm, and 20–30 cm, the values in GE were significantly lower than those in SG and CK ($p < 0.05$), while no statistical difference was detected at 30–40 cm ($p > 0.05$). In particular, for the >2 mm fraction of GE, SG, and CK, there was no statistical difference at 20–30 cm ($p > 0.05$). However, at 30–40 cm, the value for SG was significantly higher than that for CK($p < 0.05$), reaching 1.96 times that of CK.

ANOVA of the water stability of soil aggregates in Figure 4 indicated that soil aggregate stability indicators varied significantly among different grazing methods, yet the stability indicators

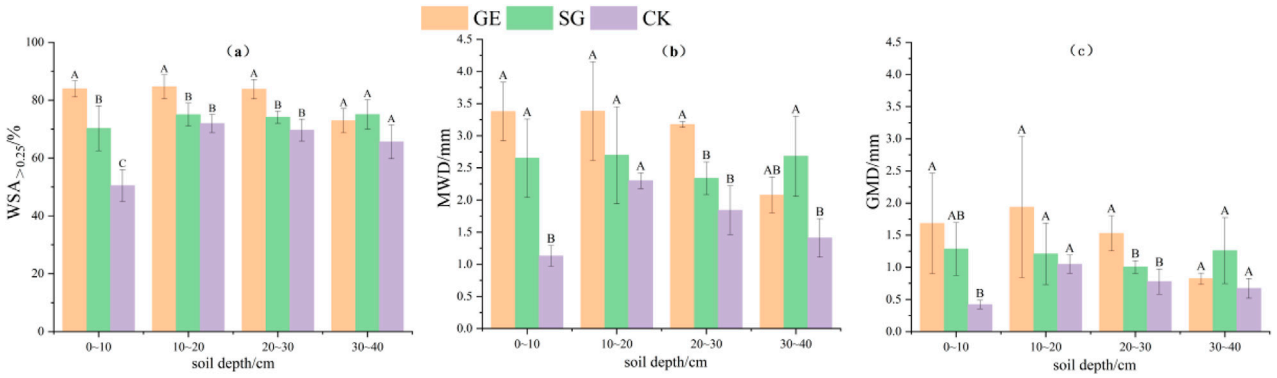

FIGURE 4
Effects of different grazing practices on $WSA_{>0.25}$ **(A)**, MWD **(B)**, GMD **(C)**, water-stability. NOTE: Different letters represent significant differences at $P < 0.05$. $WSA_{>0.25}$: content of soil aggregate >0.25 mm particle size; MWD: mean weight diameter; GMD: geometric mean diameter; GE: grazing exclusion; SG: seasonal grazing; CK: free grazing.

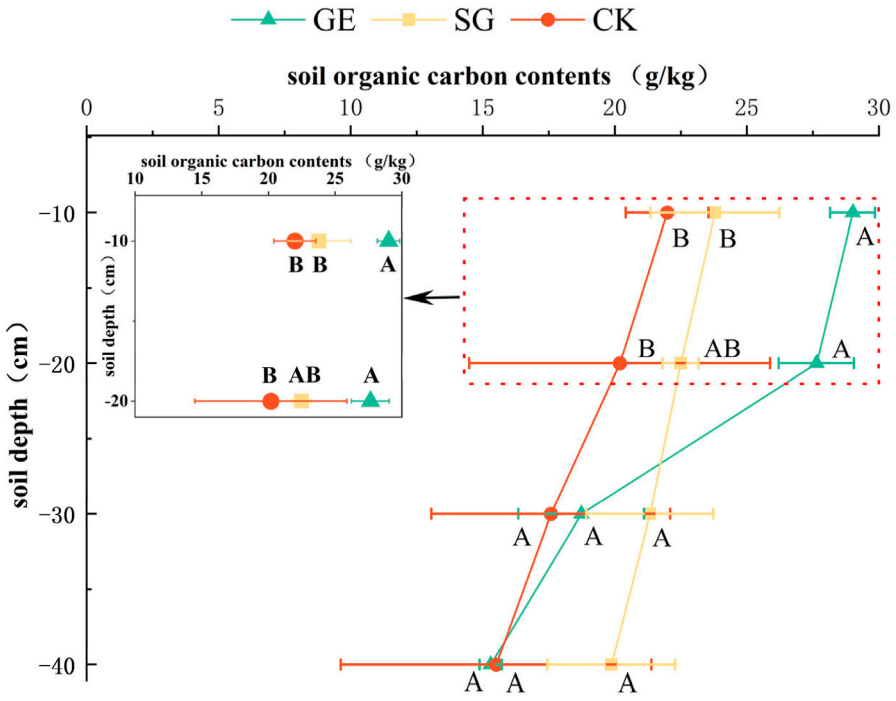

FIGURE 5
Effects of different grazing practices on SOC. NOTE: Different letters represent significant differences at $p < 0.05$. GE: grazing exclusion; SG: seasonal grazing; CK: free grazing; SOC: soil organic carbon.

exhibited a consistent trend. For the 0–30 cm layer, the following results were obtained for $WSA_{>0.25}$, MWD, and GMD: GE > SG > CK. However, at a soil depth of 30–40 cm, the results changed to SG > GE > CK. For GE, the values of $WSA>_{0.25}$, MWD, and GMD were significantly higher than those of CK at soil depths of 0–10 cm and 20–30 cm ($p < 0.05$). For SG, $WSA>_{0.25}$ and MWD values were significantly higher in 0–10 cm than in CK ($p < 0.05$). At a 0–30 cm depth, the $WSA_{>0.25}$ of GE was significantly higher than that of CK ($p < 0.05$). The highest MWD values of GE, SG, and CK were 3.38 mm, 2.70 mm, and 2.30 mm, respectively, and occurred at 10–20 cm. However, they did not reach the significance level between them ($p > 0.05$). At a depth of 30–40 cm, only the MWD of SG was significantly higher than that of CK ($p < 0.05$).

3.4 Characteristics of soil organic carbon changes

The study demonstrated that SOC decreased as soil depth increased (Figure 5). The maximum SOC in the 0–20 cm layer

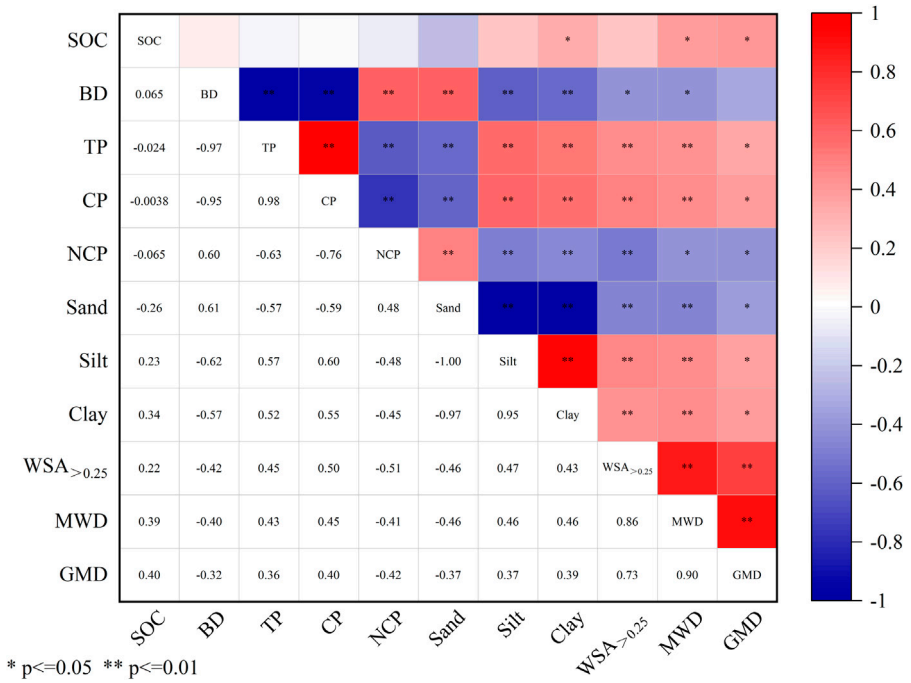

FIGURE 6
Correlation analysis.NOTE:SOC: soil organic carbon; BD: soil bulk density; TP: soil total porosity; CP: soil capillary porosity; NCP: soil non-capillary porosity; $WSA_{>0.25}$: content of soil aggregate >0.25 mm particle size; MWD: mean weight diameter; GMD: geometric mean diameter.

was observed in GE, and the maximum SOC in the 20–40 cm layer was observed in SG. SOC for each grazing method decreased with soil depth. In the GE, the SOC in the 0–10 cm was found to be 1.55 times and 1.81 times that of the 20–30 cm and 30–40 cm. In the SG, the increases in SOC for the 0–10 cm and 10–20 cm in comparison to the 30–40 cm were 19.76% and 13.20%. The mean increase in the 0–10 cm under the CK compared with the 10–20 cm, 20–30 cm, and 30–40 cm was 4.22 g/kg.

At the 0–10 cm and 10–20 cm depths, GE significantly increased SOC by 7.02 mg/kg and 7.45 mg/kg, respectively, compared to the CK ($p < 0.05$). However, there was no statistically significant difference between SG and CK ($p > 0.05$). At the 20–30 cm and 30–40 cm depths, there was no statistical difference among GE, SG, and CK ($p > 0.05$).

3.5 Relationship factors influencing soil aggregate stability

Correlation analyses were performed on eleven factors, including BD, soil porosity (TP, CP and NCP), soil particle size composition (Clay, Silt, and Sand), soil aggregate stability ($WSA_{>0.25}$, MWD and GMD), and SOC (Figure 6). The results showed that most of the selected vital factors significantly impacted soil aggregate stability ($p < 0.05$). Soil porosity and particle size composition showed a significant and positive correlation with all three indicators of soil aggregates ($P < 0.05$). BD exhibited a significant negative correlation with $WSA_{>0.25}$ and MWD ($P < 0.05$). A significant positive correlation was also detected between Clay and SOC.

We used BRT modeling to quantitatively assess other indicators' effects on soil aggregate stability (Figure 7). In the process, we categorized all the relevant indicators into distinct groups. The first group is BD. The second group pertains to soil porosity and is divided into TP, CP, and NCP. The third group involves soil particle size composition consisting of clay, silt, and sand. Then, there is the SOC group. Finally, the soil aggregate stability group is characterized by $WSA_{>0.25}$, MWD, and GMD. The results indicated that porosity was the primary factor affecting soil aggregate stability, with effects of 60.05%, 40.86%, and 38.05% on $WSA_{>0.25}$, MWD, and GMD, respectively. Subsequently, SOC exerted an influence exceeding 20% on MWD and GMD, while its impact on $WSA_{>0.25}$ was limited to 13.87%. Individually, SOC had the most significant impact on MWD and GMD.

4 Discussion

4.1 Effects of grazing practices on soil structure indicators

In studies of the effects of grazing on soil structure, the time span resolves the central variable in the response mechanisms of soil ecosystems. For example, short-term (<5 years) grazing samples showed only minor variations in properties such as soil porosity (Batista et al., 2019), whereas studies of 10-year grazing samples found significant decreases in BD and clay particle fraction, but such changes are still at a more surface stage (Liu J. et al., 2017). In contrast, our observations from sample plots grazed for up to

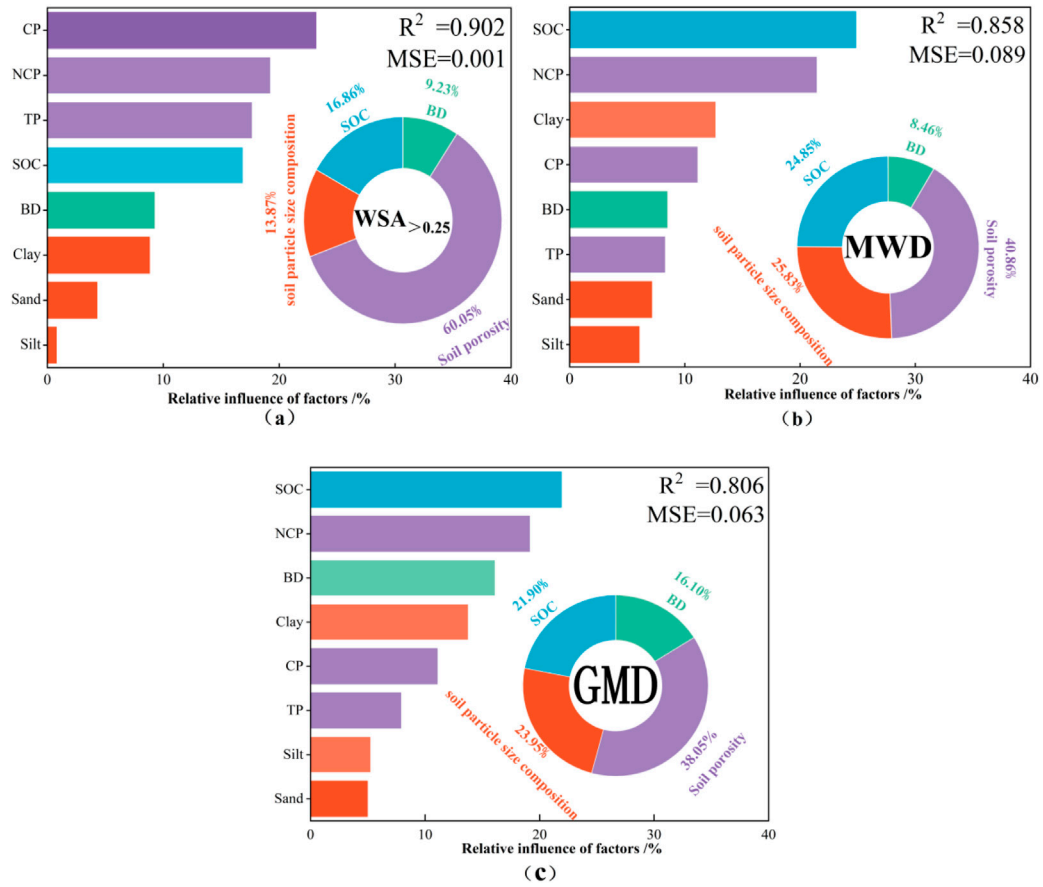

FIGURE 7
Independent effects of factors on $WSA_{>0.25}$ **(A)**, MWD **(B)**, GMD **(C)**. NOTE: BD: soil bulk density; TP: soil total porosity; CP: soil capillary porosity; NCP: soil non-capillary porosity; SOC: soil organic carbon; $WSA_{>0.25}$: content of soil aggregate >0.25 mm particle size; MWD: mean weight diameter; GMD: geometric mean diameter.

20 years are more representative of the evolution of soil structure under long-term grazing. The effects of animal trampling on rangelands are complex and intertwined with other factors that need to be analyzed independently for changes in soil parameters (Bayat et al., 2022).

The influence of grazing on soil structure is mainly due to livestock trampling, which can be divided into three main damage mechanisms: foraging, trampling, and excretion (Mayel et al., 2021). Our study indicated that following 20 years of restricted grazing, the clay of GE and SG increased (mainly from 0 to 10 cm), leading to favorable changes in soil texture (Zhang H. et al., 2019). For BD and soil porosity, we indicated that the average BD from 0 to 40 cm increased from 1.43 g/cm³ (GE) and 1.50 g/cm³ (SG) to 1.60 g/cm³ (CK), while soil porosity decreased from 46.69% to 44.27%–41.07%. The compaction of soil pore space due to trampling is a remarkable phenomenon, leading to CK pastures having the lowest soil porosity (Carrero-González et al., 2012). As hypothesized by Zhang et al., the reduction in porosity resulting from grazing may be mainly due to the disappearance of macropores and larger pores (Zhang B. et al., 2019). Since pores and soil particles are mutually exclusive, the decrease in porosity and the notably corresponding increase in particle volume consequently decrease BD (Mayel et al., 2021). We inferred that this may be due to the cumulative effect of livestock trampling on BD in desert steppe (Negrón et al., 2019). In the 20-year grazing sample plots, each trampling by livestock caused a small compression of the pore space between soil particles. Over time, this compression accumulated, resulting in a significant reduction in soil pore space and a consequent increase in BD.

Additionally, livestock trampling also influences alterations in soil aggregate composition distribution. The level of pressure that livestock apply to soil particles varies depending on the particular grazing practices used. Soil structural function will inevitably deteriorate when the pressure exerted surpasses the soil's pre-compressive stress (Pc) (Dec et al., 2012; Negrón et al., 2019). The main component is large aggregates (>0.25 mm), which suggests that soil aggregation is effective and enhances resistance to livestock trampling pressure (Wang et al., 2020a).

Soil aggregate stability is an essential indicator of soil degradation and soil quality. It is mainly characterized by the following parameters: $WSA_{>0.25}$, MWD, and GMD (Boix-Fayos et al., 2001; Obalum et al., 2019). $WSA_{>0.25}$ reflects soil structure, with higher values indicating better structure; MWD and GMD indicate the proportion and size of soil aggregates, with higher values indicating better stability. The data showed a significant increase in the density of macroaggregates (>0.25 mm) within the 0–20 cm layer following the implementation of GE. MWD and GMD increased by

an average of 1.05 mm in GE and 0.69 mm in SG compared to CK. It is worth noting that SG had the highest values of aggregate stability in 30–40 cm layer, followed by GE and CK, which had the lowest stability values. The GE site has >90% vegetation cover, which reduces the impact of raindrops or livestock on the soil, which in turn contributes to the stabilization of soil aggregates. Vegetation also intercepts soil particles (mainly clay) carried by wind-sand flow, which are bound at the base of the plants by the water lost by the plants and gradually form soil aggregates (Jiang et al., 2022). This may be due to the distribution of desert steppe vegetation roots related to the entanglement of roots and secretion of material that may have facilitated the formation of macroaggregates (>0.25 mm) in the region (Six and Paustian, 2014; Baumert et al., 2018). The formation of soil aggregates is intimately associated with SOC (Xue et al., 2019). The increase in SOC enhanced the generation of macroaggregates (>0.25 mm) and improved their stability, as evidenced by the increase in SOC from the 0–20 cm layer, as demonstrated in our study (Gu et al., 2024). In CK, soil aggregates with a >0.25 mm dominated. This may be associated with increased BD and decreased SOC from livestock trampling on the pastureland (Yao et al., 2019). Disintegration of macroaggregates (>0.25 mm) may also be possible due to dry-wet cycles and freeze-thaw processes (Oztas and Fayetorbay, 2003; Jesús Melej et al., 2024).

This study showed that grazing practices significantly affected surface soil organic carbon, especially at depths of 0–10 cm and 10–20 cm. The GE method significantly enhanced SOC, consistent with the observations reported by Shen (Shen et al., 2023). Macroaggregates (>2 mm) have a strong influence on SOC fixation and are the primary site of SOC storage (Wang et al., 2020b; Xi et al., 2022). Macroaggregates (>2 mm) dominated, effectively storing large amounts of SOC. Grazing had a significant effect on these large aggregates (>2 mm) at depths of 0–10 cm and 10–20 cm, with the SOC gradually dissipating as the macroaggregates (>2 mm) decomposed. The primary reason was that the soil in the desert steppe of this study was more influenced by vegetation. During the grazing period, livestock consumed mainly rhizomatous grasses, resulting in a reduction in above-ground biomass and an increase in the density and complexity of the surface root system (Li et al., 2014; Wang et al., 2014). The growth of roots enhances the conservation of carbon (Yang et al., 2023). However, the effects of grazing on SOC remain controversial, with studies indicating that grazing can increase (Hewins et al., 2018; Shen et al., 2023), decrease (Zhao et al., 2009; Dlamini et al., 2016; Ren et al., 2024) or leave SOC unchanged (Derner et al., 2019). This controversy may arise from differences in the climatic zones studied and the negative impact of climate change on livestock production (Ghahramani et al., 2019; Li et al., 2022). The study area is in an arid and semi-arid zone and is severely constrained by water resources. Grazing increases greenhouse gas emissions and turns grasslands into carbon sources, and prolonged drought alters biogeochemical cycles and organic carbon storage (Pinay et al., 2007). Under warm and humid climatic conditions, grazing favors SOC production due to the accelerated decomposition of plant residues and elevated soil microbial carbon (Abdalla et al., 2018). Another possibility is the effect of the stocking rate, where low stocking rate grazing promotes vegetation diversity and increases SOC due to increased above-ground biomass of communities (Gebregergs et al., 2019). Conversely, large aggregations of livestock foraging cause significant vegetation reductions, leading to a reduction in readily decomposable herb litter mediates, ultimately reducing SOC (Liu S. et al., 2017).

4.2 Relationship factors influencing the soil aggregate stability

The correlation analysis and the results of the BRT analysis indicate that soil aggregate stability is mainly dependent on soil porosity (Rabot et al., 2018; Menon et al., 2020; Ajayi et al., 2021). The data indicated that soil porosity contributed 60.05%, 40.86%, and 38.05% to the $WSA_{>0.25}$, MWD, and GMD changes. Pore space accommodates air entering the soil aggregate. The increase in pore volume and connectivity reduces the expansion pressure of the pores, thus increasing the stability of the soil aggregates (Bisdom et al., 1993). Furthermore, the pore space is an active area for soil microorganisms and microfauna communities. Microorganisms metabolize, reproduce, and secrete organic substances in the pore space. Exopolysaccharides secreted by soil microorganisms gel with clay particles to form soil aggregates (Pokharel et al., 2013; Walshire et al., 2024). In addition, the microorganisms carry an electrical charge that promotes soil particle adhesion and facilitates soil aggregates' formation through electrostatic attraction (Coban et al., 2022). Pores are conduits for physicochemical and biological processes ultimately work together to form soil aggregate stability (Yudina and Kuzyakov, 2023).

SOC plays an essential and irreplaceable role in the formation mechanism of soil aggregates and in maintaining soil aggregate stability (Dong et al., 2020; Fei et al., 2021). The outcomes of our research substantiated this claim, with an average impact of SOC on the soil aggregate stability amounting to 21.17%. This result is consistent with the findings in subtropical China that SOC is the driver factor of soil aggregate stability and plays the role of a cementing agent during soil aggregate formation (Xue et al., 2019). A higher content of SOC can increase the negative charge density on the surface of soil particles and promote the repulsive force and attractive force between soil particles to reach a more stable equilibrium state (Yu et al., 2017). This is conducive to maintaining the structural integrity of soil aggregates in the face of disturbances caused by external environmental factors and reduces the risk of disintegration and dispersion (Kan et al., 2022).

5 Conclusion

Following 2 decades of management, Both grazing practices enhanced soil structure, which exhibited variations at different soil depths. SG significantly improved the clay (<0.002 mm), silt (0.002–0.02 mm), macroaggregates (>0.25 mm), aggregate stability, and SOC within the 0–10 cm soil layer. However, for GE, the significant improvement of these indicators extends down to a depth of 20 cm. In particular, after 20 years of restricted grazing, BD decreased, soil porosity increased, and soil texture improved. Thus, soil structure can be enhanced by limiting grazing with optimal improvement in GE, which can be used to restore degraded desert steppe. Soil porosity exerts the most significant

influence on the soil aggregate stability, with an average expanation of more than 45%, with SOC ranking second in terms of influence. Further insights into the interconnection between soil aggregate stability and soil porosity in desert steppe are offered.

Data availability statement

The original contributions presented in the study are included in the article/supplementary material, further inquiries can be directed to the corresponding author.

Author contributions

YY: Data curation, Formal Analysis, Investigation, Writing–original draft. ZM: Conceptualization, Funding acquisition, Methodology, Writing–review and editing. HL: Data curation, Investigation, Visualization, Writing–original draft. YG: Data curation, Investigation, Writing–original draft. TL: Investigation, Writing–original draft. LQ: Investigation, Writing–original draft.

Funding

The author(s) declare that financial support was received for the research, authorship, and/or publication of this article. This research was supported by the National Key Research and Development Project of China (2024YFF1306305), and the Basic Research Funds for Universities-Innovation Team Building-Desert Ecosystem Protection and Restoration Innovation Team (BR22-13-03).

Conflict of interest

The authors declare that the research was conducted in the absence of any commercial or financial relationships that could be construed as a potential conflict of interest.

Generative AI statement

The author(s) declare that no Generative AI was used in the creation of this manuscript.

Publisher's note

References

Abdalla, M., Hastings, A., Chadwick, D. R., Jones, D. L., Evans, C. D., Jones, M. B., et al. (2018). Critical review of the impacts of grazing intensity on soil organic carbon storage and other soil quality indicators in extensively managed grasslands. *Agr. Ecosyst. Environ.* 253, 62–81. doi:10.1016/j.agee.2017.10.023

Abu-Hamdeh, N. H., Abo-Qudais, S. A., and Othman, A. M. (2006). Effect of soil aggregate size on infiltration and erosion characteristics. *Eur. J. Soil Sci.* 57, 609–616. doi:10.1111/j.1365-2389.2005.00743.x

Ajayi, A. E., Faloye, O. T., Reinsch, T., and Horn, R. (2021). Changes in soil structure and pore functions under long term/continuous grassland management. *Agr. Ecosyst. Environ.* 314, 107407. doi:10.1016/j.agee.2021.107407

Bardgett, R. D., Bullock, J. M., Lavorel, S., Manning, P., Schaffner, U., Ostle, N., et al. (2021). Combatting global grassland degradation. *Nat. Rev. Earth Environ.* 2, 720–735. doi:10.1038/s43017-021-00207-2

Batista, P. H. D., De Almeida, G. L. P., De Lima, R. P., Pandorfi, H., Da Silva, M. V., and Rolim, M. M. (2019). Impact of short-term grazing on physical properties of planosols in northeastern Brazil. *Geoderma Reg.* 19, e00234. doi:10.1016/j.geodrs.2019.e00234

Baumert, V. L., Vasilyeva, N. A., Vladimirov, A. A., Meier, I. C., Kögel-Knabner, I., and Mueller, C. W. (2018). Root exudates induce soil macroaggregation facilitated by fungi in subsoil. *Front. Environ. Sci.* 6, 140. doi:10.3389/fenvs.2018.00140

Bayat, H., Sheklabadi, M., Moradhaseli, M., Rastgou, M., and Gregory, A. S. (2022). Grazing management, slope aspect and canopy effects on the compression characteristic of soils of the Gonbad experimental watershed in Hamedan, Iran. *Geoderma* 409, 115641. doi:10.1016/j.geoderma.2021.115641

Bisdom, E. B. A., Dekker, L. W., and Schoute, J. F.Th. (1993). Water repellency of sieve fractions from sandy soils and relationships with organic material and soil structure. *Geoderma* 56, 105–118. doi:10.1016/0016-7061(93)90103-R

Blanco, H., and Lal, R. (2023). "Management of grazing lands," in *Soil conservation and management* (Cham: Springer Nature Switzerland), 443–469. doi:10.1007/978-3-031-30341-8_18

Blanco-Sepúlveda, R., Gómez-Moreno, M. L., and Lima, F. (2024). An approach to the key soil physical properties for assessing soil compaction due to livestock grazing in mediterranean mountain areas. *Sustainability* 16, 4279. doi:10.3390/su16104279

Boix-Fayos, C., Calvo-Cases, A., Imeson, A. C., and Soriano-Soto, M. D. (2001). Influence of soil properties on the aggregation of some Mediterranean soils and the use of aggregate size and stability as land degradation indicators. *Catena* 44, 47–67. doi:10.1016/S0341-8162(00)00176-4

Carrero-González, B., De La Cruz, M. T., and Casermeiro, M. A. (2012). Application of Magnetic Resonance Techniques to evaluate soil compaction after grazing. *J. Soil Sci. Plant Nutr.* 12, 165–182. doi:10.4067/S0718-95162012000100014

Chen, L., and Baoyin, T. (2024). Effects of plant productivity and species on soil carbon and nitrogen sequestration under seasonal grazing in a semi-arid grassland of north China. *Land Degrad. Dev.* 35, 1960–1970. doi:10.1002/ldr.5035

Coban, O., De Deyn, G. B., and Van Der Ploeg, M. (2022). Soil microbiota as game-changers in restoration of degraded lands. *Science* 375, abe0725. doi:10.1126/science.abe0725

Conte, T. J., and Tilt, B. (2014). The effects of China's grassland contract policy on pastoralists' attitudes towards cooperation in an inner Mongolian banner. *Hum. Ecol.* 42, 837–846. doi:10.1007/s10745-014-9690-4

De Boer, H. C., Deru, J. G. C., and Van Eekeren, N. (2018). Sward lifting in compacted grassland: effects on soil structure, grass rooting and productivity. *Soil Tillage. Res.* 184, 317–325. doi:10.1016/j.still.2018.07.013

Dec, D., Dörner, J., Balocchi, O., and López, I. (2012). Temporal dynamics of hydraulic and mechanical properties of an Andosol under grazing. *Soil Tillage. Res.* 125, 44–51. doi:10.1016/j.still.2012.05.018

Deng, L., Kim, D., Peng, C., and Shangguan, Z. (2018). Controls of soil and aggregate-associated organic carbon variations following natural vegetation restoration on the L oess P lateau in C hina. *Land Degrad. Dev.* 29, 3974–3984. doi:10.1002/ldr.3142

Derner, J. D., Augustine, D. J., and Frank, D. A. (2019). Does grazing matter for soil organic carbon sequestration in the western north American great plains? *Ecosystems* 22, 1088–1094. doi:10.1007/s10021-018-0324-3

Dlamini, P., Chivenge, P., and Chaplot, V. (2016). Overgrazing decreases soil organic carbon stocks the most under dry climates and low soil pH: a meta-analysis shows. *Agr. Ecosyst. Environ.* 221, 258–269. doi:10.1016/j.agee.2016.01.026

Dong, L., Zheng, Y., Martinsen, V., Liang, C., and Mulder, J. (2022). Effect of grazing exclusion and rotational grazing on soil aggregate stability in typical grasslands in inner Mongolia, China. *Front. Environ. Sci.* 10, 844151. doi:10.3389/fenvs.2022.844151

Dong, S., Zhang, J., Li, Y., Liu, S., Dong, Q., Zhou, H., et al. (2020). Effect of grassland degradation on aggregate-associated soil organic carbon of alpine grassland ecosystems in the Qinghai-Tibetan Plateau. *Eur. J. Soil Sci.* 71, 69–79. doi:10.1111/ejss.12835

Egashlra, K., Kaetsu, Y., and Takuma, K. (1983). Aggregate stability as an index of erodibility of ando soils. *Soil Sci. Plant Nutr.* 29, 473–481. doi:10.1080/00380768.1983.10434650

Enriquez, A. S., Necpalova, M., Cremona, M. V., Peri, P. L., and Six, J. (2021). Immobilization and stabilization of volcanic ash in soil aggregates in semiarid meadows of Northern Patagonia. *Geoderma* 392, 114987. doi:10.1016/j.geoderma.2021.114987

Fei, C., Zhang, S., Li, J., Liang, B., and Ding, X. (2021). Partial substitution of rice husks for manure in greenhouse vegetable fields: insight from soil carbon stock and aggregate stability. *Land Degrad. Dev.* 32, 3962–3972. doi:10.1002/ldr.4021

Ferreira, T. R., Archilha, N. L., Cássaro, F. A. M., and Pires, L. F. (2023). How can pore characteristics of soil aggregates from contrasting tillage systems affect their intrinsic permeability and hydraulic conductivity? *Soil Tillage. Res.* 230, 105704. doi:10.1016/j.still.2023.105704

Franzluebbers, A. J., Endale, D. M., Buyer, J. S., and Stuedemann, J. A. (2012). Tall fescue management in the piedmont: sequestration of soil organic carbon and total nitrogen. *Soil Sci. Soc. Am. J.* 76, 1016–1026. doi:10.2136/sssaj2011.0347

Gao, H., Song, X., Wu, X., Zhang, N., Liang, T., Wang, Z., et al. (2024). Interactive effects of soil erosion and mechanical compaction on soil DOC dynamics and CO2 emissions in sloping arable land. *Catena* 238, 107906. doi:10.1016/j.catena.2024.107906

Gebregergs, T., Tessema, Z. K., Solomon, N., and Birhane, E. (2019). Carbon sequestration and soil restoration potential of grazing lands under exclosure management in a semi-arid environment of northern Ethiopia. *Ecol. Evol.* 9, 6468–6479. doi:10.1002/ece3.5223

Ghahramani, A., Howden, S. M., Del Prado, A., Thomas, D. T., Moore, A. D., Ji, B., et al. (2019). Climate change impact, adaptation, and mitigation in temperate grazing systems: a review. *Sustainability* 11, 7224. doi:10.3390/su11247224

Gu, W., Wang, Y., Sun, Y., Liu, Z., Wang, W., Wu, D., et al. (2024). Assessing the formation and stability of paddy soil aggregate driven by organic carbon and Fe/Al oxides in rice straw cyclic utilization strategies: insight from a six-year field trial. *Sci. Total Environ.* 951, 175607. doi:10.1016/j.scitotenv.2024.175607

Hewins, D. B., Lyseng, M. P., Schoderbek, D. F., Alexander, M., Willms, W. D., Carlyle, C. N., et al. (2018). Grazing and climate effects on soil organic carbon concentration and particle-size association in northern grasslands. *Sci. Rep.* 8, 1336. doi:10.1038/s41598-018-19785-1

Jesús Melej, M., Acevedo, S. E., Contreras, C. P., Giraldo, C. V., Maurer, T., Calderón, F. J., et al. (2024). Changes in macroaggregate stability as a result of wetting/drying cycles of soils with different organic matter and clay contents. *Geoderma* 448, 116965. doi:10.1016/j.geoderma.2024.116965

Jiang, L., Hu, D., and Lv, G. (2022). The edaphic and vegetational properties controlling soil aggregate stability vary with plant communities in an arid desert region of northwest China. *Forests* 13, 368. doi:10.3390/f13030368

Kan, Z., Liu, W., Liu, W., Lal, R., Dang, Y. P., Zhao, X., et al. (2022). Mechanisms of soil organic carbon stability and its response to no-till: a global synthesis and perspective. *Glob. Change Biol.* 28, 693–710. doi:10.1111/gcb.15968

Karlen, D. L., and Stott, D. E. (2015). "A framework for evaluating physical and chemical indicators of soil quality," in *SSSA special publications*. Editors J. W. Doran, D. C. Coleman, D. F. Bezdicek, and B. A. Stewart (Madison, WI, USA: Soil Science Society of America and American Society of Agronomy), 53–72. doi:10.2136/sssaspecpub35.c4

Kinnell, P. I. A. (2018). Determining soil erodibilities for the USLE-MM rainfall erosion model. *Catena* 163, 424–426. doi:10.1016/j.catena.2018.01.008

Lai, L., and Kumar, S. (2020). A global meta-analysis of livestock grazing impacts on soil properties. *PLOS One* 15, e0236638. doi:10.1371/journal.pone.0236638

Li, C., Han, Q., and Xu, W. (2022). Contribution of climate change and grazing on carbon dynamics in central asian pasturelands. *Remote Sens-Basel* 14, 1210. doi:10.3390/rs14051210

Li, S., Yu, F., Werger, M. J. A., Dong, M., Ramula, S., and Zuidema, P. A. (2013). Understanding the effects of a new grazing policy: the impact of seasonal grazing on shrub demography in the Inner Mongolian steppe. *J. Appl. Ecol.* 50, 1377–1386. doi:10.1111/1365-2664.12159

Li, Y., Zhu, Y., Zhao, J., Li, G., Wang, H., Lai, X., et al. (2014). Effects of rest grazing on organic carbon storage in Stipa grandis steppe in inner Mongolia, China. *J. Integr. Agr.* 13, 624–634. doi:10.1016/S2095-3119(13)60720-0

Liu, J., Wu, J., Su, H., Gao, Z., and Wu, Z. (2017a). Effects of grazing exclusion in xilin gol grassland differ between regions. *Ecol. Eng.* 99, 271–281. doi:10.1016/j.ecoleng.2016.11.041

Liu, S., Yang, X., Ives, A. R., Feng, Z., and Sha, L. (2017b). Effects of seasonal and perennial grazing on soil fauna community and microbial biomass carbon in the subalpine meadows of yunnan, southwest China. *Pedosphere* 27, 371–379. doi:10.1016/S1002-0160(17)60325-4

Liu, Y., Liu, X., Zhao, C., Wang, H., and Zang, F. (2023). The trade-offs and synergies of the ecological-production-living functions of grassland in the qilian mountains by ecological priority. *J. Environ. Manage.* 327, 116883. doi:10.1016/j.jenvman.2022.116883

Martens, D. (2000). Plant residue biochemistry regulates soil carbon cycling and carbon sequestration. *Soil Biol. biochem.* 32, 361–369. doi:10.1016/S0038-0717(99)00162-5

Mayel, S., Jarrah, M., and Kuka, K. (2021). How does grassland management affect physical and biochemical properties of temperate grassland soils? A review study. *Grass Forage Sci.* 76, 215–244. doi:10.1111/gfs.12512

Menon, M., Mawodza, T., Rabbani, A., Blaud, A., Lair, G. J., Babaei, M., et al. (2020). Pore system characteristics of soil aggregates and their relevance to aggregate stability. *Geoderma* 366, 114259. doi:10.1016/j.geoderma.2020.114259

Nael, M., Salarinik, K., and Assadian, G. (2024). Soil quality and vegetation cover characteristics as influenced by diverse grazing regimes and soil disturbance histories in a semi-arid rangeland (Iran). *Arid. Land Res. Manag.* 38, 318–342. doi:10.1080/15324982.2024.2309495

Negrón, M., López, I., and Dörner, J. (2019). Consequences of intensive grazing by dairy cows of contrasting live weights on volcanic ash topsoil structure and pasture dynamics. *Soil Tillage. Res.* 189, 88–97. doi:10.1016/j.still.2018.12.025

Noulèkoun, F., Birhane, E., Kassa, H., Berhe, A., Gebremichael, Z. M., Adem, N. M., et al. (2021). Grazing exclosures increase soil organic carbon stock at a rate greater than "4 per 1000" per year across agricultural landscapes in Northern Ethiopia. *Sci. Total Environ.* 782, 146821. doi:10.1016/j.scitotenv.2021.146821

Obalum, S. E., Uteau-Puschmann, D., and Peth, S. (2019). Reduced tillage and compost effects on soil aggregate stability of a silt-loam Luvisol using different aggregate stability tests. *Soil Tillage. Res.* 189, 217–228. doi:10.1016/j.still.2019.02.002

Oztas, T., and Fayetorbay, F. (2003). Effect of freezing and thawing processes on soil aggregate stability. *Catena* 52, 1–8. doi:10.1016/S0341-8162(02)00177-7

Phefadu, K. C., and Munjonji, L. (2024). Assessing the impact of no-tillage duration on soil aggregate size distribution, stability and aggregate associated organic carbon. *Agronomy* 14, 2482. doi:10.3390/agronomy14112482

Pinay, G., Barbera, P., Carreras-Palou, A., Fromin, N., Sonié, L., Madeleine Couteaux, M., et al. (2007). Impact of atmospheric CO2 and plant life forms on soil microbial activities. *Soil Biol. biochem.* 39, 33–42. doi:10.1016/j.soilbio.2006.05.018

Pokharel, A. K., Jannoura, R., Heitkamp, F., Kleikamp, B., Wachendorf, C., Dyckmans, J., et al. (2013). Development of aggregates after application of maize residues in the presence of mycorrhizal and non-mycorrhizal pea plants. *Geoderma* 202–203, 38–44. doi:10.1016/j.geoderma.2013.03.005

Rabot, E., Wiesmeier, M., Schlüter, S., and Vogel, H.-J. (2018). Soil structure as an indicator of soil functions: a review. *Geoderma* 314, 122–137. doi:10.1016/j.geoderma.2017.11.009

Reinhart, K. O., Sanni Worogo, H. S., Rinella, M. J., and Vermeire, L. T. (2021). Livestock increase soil organic carbon in the northern great plains. *Rangel. Ecol. Manag.* 79, 22–27. doi:10.1016/j.rama.2021.07.006

Ren, S., Terrer, C., Li, J., Cao, Y., Yang, S., and Liu, D. (2024). Historical impacts of grazing on carbon stocks and climate mitigation opportunities. *Nat. Clim. Chang.* 14, 380–386. doi:10.1038/s41558-024-01957-9

Rojas-Briales, E. (2015). Sparing grasslands: FAO's active role. *Science* 347, 1211. doi:10.1126/science.347.6227.1211

Romero-Ruiz, A., Monaghan, R., Milne, A., Coleman, K., Cardenas, L., Segura, C., et al. (2023). Modelling changes in soil structure caused by livestock treading. *Geoderma* 431, 116331. doi:10.1016/j.geoderma.2023.116331

Schweizer, S. A., Bucka, F. B., Graf-Rosenfellner, M., and Kögel-Knabner, I. (2019). Soil microaggregate size composition and organic matter distribution as affected by clay content. *Geoderma* 355, 113901. doi:10.1016/j.geoderma.2019.113901

Shen, Y., Fang, Y., Chen, H., Ma, Z., Huang, C., Wu, X., et al. (2023). New insights into the relationships between livestock grazing behaviors and soil organic carbon stock in an alpine grassland. *Agr. Ecosyst. Environ.* 355, 108602. doi:10.1016/j.agee.2023.108602

Sidhu, B. S., Mehrabi, Z., Ramankutty, N., and Kandlikar, M. (2023). How can machine learning help in understanding the impact of climate change on crop yields? *Environ. Res. Lett.* 18, 024008. doi:10.1088/1748-9326/acb164

Six, J., and Paustian, K. (2014). Aggregate-associated soil organic matter as an ecosystem property and a measurement tool. *Soil Biol. biochem.* 68, A4–A9. doi:10.1016/j.soilbio.2013.06.014

Tian, L., Bai, Y., Wang, W., Qu, G., Deng, Z., Li, R., et al. (2021). Warm- and cold-season grazing affect plant diversity and soil carbon and nitrogen sequestration differently in Tibetan alpine swamp meadows. *Plant Soil* 458, 151–164. doi:10.1007/s11104-020-04573-6

Walshire, L. A., Zhang, H., Nick, Z. H., Breland, B. R., Runge, K. A., and Han, F. X. (2024). Modification of surface properties of clay minerals with exopolysaccharides from *rhizobium tropici*. *ACS Earth Space Chem.* 8, 137–147. doi:10.1021/acsearthspacechem.3c00296

Wang, J., Zhao, C., Zhao, L., Wen, J., and Li, Q. (2020a). Effects of grazing on the allocation of mass of soil aggregates and aggregate-associated organic carbon

in an alpine meadow. *PLoS ONE* 15, e0234477. doi:10.1371/journal.pone.0234477

Wang, J., Zhao, C., Zhao, L., Wen, J., and Li, Q. (2020b). Effects of grazing on the allocation of mass of soil aggregates and aggregate-associated organic carbon in an alpine meadow. *PLoS ONE* 15, e0234477. doi:10.1371/journal.pone.0234477

Wang, Z., Jiao, S., Han, G., Zhao, M., Ding, H., Zhang, X., et al. (2014). Effects of stocking rate on the variability of peak standing crop in a Desert Steppe of eurasia grassland. *Environ. Manag.* 53, 266–273. doi:10.1007/s00267-013-0186-6

Xi, Y., Shao, M., Li, T., Gan, M., Chen, M., and Li, Z. (2022). Soil macroaggregates determine soil organic carbon in the natural grasslands of the loess plateau. *Catena* 218, 106533. doi:10.1016/j.catena.2022.106533

Xiao, H., Liu, G., Liu, P., Zheng, F., Zhang, J., and Hu, F. (2017). Developing equations to explore relationships between aggregate stability and erodibility in ultisols of subtropical China. *Catena* 157, 279–285. doi:10.1016/j.catena.2017.05.032

Xue, B., Huang, L., Huang, Y., Yin, Z., Li, X., and Lu, J. (2019). Effects of organic carbon and iron oxides on soil aggregate stability under different tillage systems in a rice–rape cropping system. *Catena* 177, 1–12. doi:10.1016/j.catena.2019.01.035

Yang, J., Zhang, R., Cao, R., Dong, S., Baoyin, T., and Zhao, T. (2024). Seasonal grazing does not significantly alter the particle structure and pore characteristics of grassland soil. *Land* 13, 730. doi:10.3390/land13060730

Yang, X., Wang, B., Fakher, A., An, S., and Kuzyakov, Y. (2023). Contribution of roots to soil organic carbon: from growth to decomposition experiment. *Catena* 231, 107317. doi:10.1016/j.catena.2023.107317

Yao, Y., Ge, N., Yu, S., Wei, X., Wang, X., Jin, J., et al. (2019). Response of aggregate associated organic carbon, nitrogen and phosphorous to re-vegetation in agro-pastoral ecotone of northern China. *Geoderma* 341, 172–180. doi:10.1016/j.geoderma.2019.01.036

Ye, R., Yu, W., Yang, D., Yi, F., Zhang, P., Qiu, X., et al. (2023). Effects of precipitation and grazing on the diversity and productivity of desert steppe. *Land Degrad. Dev.* 34, 2622–2635. doi:10.1002/ldr.4635

Yu, Z., Zhang, J., Zhang, C., Xin, X., and Li, H. (2017). The coupling effects of soil organic matter and particle interaction forces on soil aggregate stability. *Soil Tillage. Res.* 174, 251–260. doi:10.1016/j.still.2017.08.004

Yudina, A., and Kuzyakov, Y. (2019). Saving the face of soil aggregates. *Glob. Change Biol.* 25, 3574–3577. doi:10.1111/gcb.14779

Yudina, A., and Kuzyakov, Y. (2023). Dual nature of soil structure: the unity of aggregates and pores. *Geoderma* 434, 116478. doi:10.1016/j.geoderma.2023.116478

Zhang, B., Beck, R., Pan, Q., Zhao, M., and Hao, X. (2019a). Soil physical and chemical properties in response to long-term cattle grazing on sloped rough fescue grassland in the foothills of the Rocky Mountains, Alberta. *Geoderma* 346, 75–83. doi:10.1016/j.geoderma.2019.03.029

Zhang, H., Zhang, L., Xu, Y., Wang, Z., and Lu, Y. (2019b). Characteristics of soil texture changes of soft rock and sand compound soil with different planting years. *IOP Conf. Ser. Earth Environ. Sci.* 300, 022122. doi:10.1088/1755-1315/300/2/022122

Zhang, M., Li, X., Wang, H., and Huang, Q. (2018). Comprehensive analysis of grazing intensity impacts soil organic carbon: a case study in typical steppe of inner Mongolia, China. *Appl. Soil Ecol.* 129, 1–12. doi:10.1016/j.apsoil.2018.03.008

Zhao, H.-L., He, Y.-H., Zhou, R.-L., Su, Y.-Z., Li, Y.-Q., and Drake, S. (2009). Effects of desertification on soil organic C and N content in sandy farmland and grassland of Inner Mongolia. *Catena* 77, 187–191. doi:10.1016/j.catena.2008.12.007

Zhu, G., Deng, L., and Shangguan, Z. (2018). Effects of soil aggregate stability on soil N following land use changes under erodible environment. *Agr. Ecosyst. Environ.* 262, 18–28. doi:10.1016/j.agee.2018.04.012

Zhu, G., Yuan, C., Gong, H., Peng, Y., Huang, C., Wu, C., et al. (2021). Effects of short-term grazing prohibition on soil physical and chemical properties of meadows in Southwest China. *Peerj* 9, e11598. doi:10.7717/peerj.11598

frontiers | Frontiers in Environmental Science

TYPE Original Research
PUBLISHED 18 February 2025
DOI 10.3389/fenvs.2025.1493668

OPEN ACCESS

EDITED BY
Mou Leong Tan,
Universiti Sains Malaysia, Malaysia

REVIEWED BY
Yahui Guo,
Central China Normal University, China
Ricky Anak Kemarau,
National University of Malaysia, Malaysia

*CORRESPONDENCE
Lili Li,
ngs_lily1123@163.com

RECEIVED 09 September 2024
ACCEPTED 27 January 2025
PUBLISHED 18 February 2025

CITATION
Wang D, Jia D, Zhang Y, Tao X, Han F, Ma Y, Guo Y, Li J and Li L (2025) Temporal lags and carbon-water coupling in the dry-hot valleys of southwest China over the past two decades. *Front. Environ. Sci.* 13:1493668. doi: 10.3389/fenvs.2025.1493668

Temporal lags and carbon-water coupling in the dry-hot valleys of southwest China over the past two decades

Dawei Wang[1,2,3], Duni Jia[1], Yao Zhang[1], Xin Tao[1], Feibing Han[1], Yanbin Ma[1], Yu Guo[1], Jinshan Li[4] and Lili Li[1,5]*

[1]College of Earth Science and Engineering, West Yunnan University of Applied Sciences, Dali, China, [2]College of Geography and Environmental Science, Northwest Normal University, Lanzhou, Gansu, China, [3]College of Geography and Environmental Science, Northwest Normal University, Research Center of Wetland Resources Protection and Industrial Development Engineering of Gansu Province, Lanzhou, China, [4]Grassland Workstation, Wuwei, China, [5]Northwest Institute of Eco-Environment and Resources, Chinese Academy of Sciences, Lanzhou, China

Water use efficiency (WUE), as an important parameter of ecosystem carbon-water cycle, is an important index to assess vulnerability to extreme drought events. However, little was known about the corresponding cumulative and lagged responses of WUE to drought in the dry and hot valleys of Southwest China. This region is covered by alpine-valley landscapes, fragmented topographic features, Foehn Effect, where drought response mechanisms are not yet fully understood. This study analyzed the spatial-temporal variation of WUE from 2000 to 2020 in Binchuan (BC) and Yuanmou (YM) regions and the time-lag and -accumulation effects of 12 monthly self-calibrating Palmer Drought Index (scPDSI) on the WUE. Given the variability of vegetation types, land use/cover change data was used to investigate the variability of WUE between the two areas. Subsequently, the Pearson Correlation coefficient (Pearson, R) analysis, considering the influence of drought on time-lag and -accumulation effects, was used to analyze the response mechanism of water use efficiency to scPDSI in BC and YM comparatively. The results show that (1) From 2001 to 2020, BC's average annual WUE was 2.59 gC m^{-2} mm^{-1}, and YM's was 2.84 gC·m^{-2}·mm^{-1}, with similar spatial distributions. (2) Over the past 2 decades, BC's WUE increased steadily at a rate of 0.012 gC m^{-2} mm^{-1} a^{-1}, while Yuanmou's WUE grew at 0.0082 gC m^{-2} mm^{-1} a^{-1}. (3) The lag response of WUE to drought is minimal in both regions, with BC's cultivated land showing greater sensitivity to drought than YM. (4) The cumulative effect of drought on WUE across different land uses in both BC and YM is generally small, with the lowest sensitivity in forest land to drought.

KEYWORDS

dry-hot valley, water use efficiency (wue), self-calibrating palmer drought index (scPDSI), time-lag effect, time-accumulation effect

1 Introduction

Drought, a complex and pervasive natural disaster (Ukkola et al., 2020; Xu et al., 2024), profoundly impacts vegetation and ecosystems, with severe events potentially altering niche thresholds and carbon-water balances (Zhang et al., 2022; Lili et al., 2023). It is defined as a condition of water scarcity where demand exceeds supply (Bradford et al., 2020; Zhao et al., 2020; Jiao et al., 2021). The scPDSI judged the water surplus and deficit by comparing local water demand with actual precipitation, and analyzing regional water supply variations (Zhao et al., 2023; Sun et al., 2020). China is one of the countries most severely affected by drought, with an average of 21.57×10^4 km^2 affected between 1950 and 2008 (Hao et al., 2015; Wei et al., 2020). Southwest China, influenced by South Asian monsoons and the Tibetan Plateau climate, experiences frequent severe droughts (Dong et al., 2014; Xu et al., 2024). Notable drought years include 2005, 2006, 2013, and 2023, along with prolonged spring droughts observed in 2010 and 2023 (Jiang et al., 2022). Global warming is expected to increase the frequency and intensity of droughts, heightening ecosystem vulnerability (Wang et al., 2013). Therefore, an in-depth understanding of the effects of drought on the carbon and water budgets of terrestrial ecosystems in southern China is essential for establishing a comprehensive natural hazard and ecological risk monitoring system.

WUE is an essential indicator for revealing the spatial and temporal variability of carbon and water cycles in terrestrial ecosystems, which is defined as the ratio of carbon sequestration to water consumption (Cristiano et al., 2020; Du et al., 2023; Guo et al., 2023).

Climatic, physiological, and vegetation factors significantly shape the water cycle and carbon assimilation, the spatial and temporal patterns of WUE likely aligning with these influences and climate responses (Jiang et al., 2022; Law et al., 2001; Yang et al., 2019). Water, essential for ecosystem function, drives plant growth and development, and its spatial variability causing distinct patterns in vegetation distribution and productivity (Li LL. et al., 2024). Global warming and drying, alongside increased CO_2 concentrations, affect temperature, photosynthesis, and transpiration, impacting carbon and water cycles and altering WUE (Anderegg et al., 2015; Wang et al., 2023). Mild water stress enhances plant WUE by inducing stomatal closure and lowering transpiration (Liu et al., 2017). However, extreme droughts pose significant threats to ecosystem health and stability, leading to a decrease in WUE (Law et al., 2001; Reichstein et al., 2002). In dry and hot valleys, evaporation rates are typically over three times that of precipitation, as a result, vegetation faces drought and heat stress even during the rainy season especially in southwest China (Wang et al., 2022). The analysis of the carbon-water coupling of the scPDSI and vegetation reveals plant adaptation strategies to drought, guides sustainable water resource management, and highlights the ecological impacts of drought in these regions.

In the context of climate and vegetation-driven constraints, time effects become an inescapable phenomenon, including time lags and accumulation (Ma et al., 2022). Climate change can exceed the adaptive capacity of vegetation, leading to delayed vegetation responses to such variations. For instance, drought can have a lingering effect on tree growth, reducing it and causing impacts that can persist for 1–4 years post-drought (Anderegg et al., 2015; Wen et al., 2018). Peng et al. (2019) identified strong cumulative and delayed effects of drought in the Northern Hemisphere on autumn leaf senescence, with more pronounced impacts observed at higher drought intensities. Li et al. (2021) highlighted distinct time-lag effects between NDVI and climate factors among plateau land types, illustrating a complex relationship with environmental conditions. Accurately assessing the consequence of climate change on vegetation is vital for formulating effective, sustainable restoration plans. Yet, the role of extreme climate events, along with the important dynamics of time lags and cumulative impacts on plant life, is often underestimated (Müller and Bahn, 2022; Yuan et al., 2024). Such oversights may skew our understanding of how climate change shapes vegetation patterns (Li L. et al., 2024; Ji et al., 2023). To fully understand how vegetation behaves and responds to climate, it is essential to consider the temporal effects of drought, including time lags and cumulative impacts ((Anderegg et al., 2015; Piao et al., 2020; Li et al., 2021), particularly in the dry-hot valley region of southwest China.

The dry-hot valleys along China's Jinsha River in the southwest, spanning over 2,000 km^2, are significantly impacted by soil erosion and environmental degradation, mainly in Yunnan, Sichuan, and Guizhou provinces (Qiao et al., 2022; Huang et al., 2017). BC and YM are located within the ecologically sensitive dry-hot valley of the Jinsha River, where they are faced with analogous natural and anthropogenic stressors.The water infrastructures of BC and YM are markedly different, while BC completed the "Yin-Bin" irrigation project in 1994, the system in YM remains under development (Zhao et al., 2023). However, the complex mechanisms underlying the carbon-water coupling dynamics of the valley's vegetation under different irrigation regimes and their responses to drought have not been thoroughly investigated. This is especially significant due to the theoretical insights for agricultural practices in the dry-hot valleys of the southwestern region, where it is essential to understand how vegetation reacts to drought as a result of climate change.

This study addresses this gap by utilizing MODIS products (at a spatial resolution of 500 m)and scPDSI (a spatial resolution of 0.5) to analyze nearly 2 decades of springtime carbon-water coupling fluctuations and their reactions to the spatiotemporal patterns of drought in BC and YM, Yunnan Province. The research aimed to investigate the following questions: (1) What are the temporal and spatial variations in WUE between BC and YM in the Southwest Dry-Hot Valley? (2) What is the lag effect of WUE on drought sensitivity in BC and YM, as indicated by the standardized precipitation index for the scPDSI? (3) How does the cumulative effect of WUE on drought sensitivity vary across different land uses in BC and YM? The results clarify how vegetation WUEreacts to drought in the context of climate change and the water utilization strategies employed in these dry-hot valleys. This study contributes to a better understanding of vulnerability to extreme drought events in the dry and hot valleys of southwest China and provides insights into the differential response mechanisms of WUE to drought between BC and YM, which are critical for global change biology and the development of strategies to mitigate the effects of drought on ecosystems in these regions.

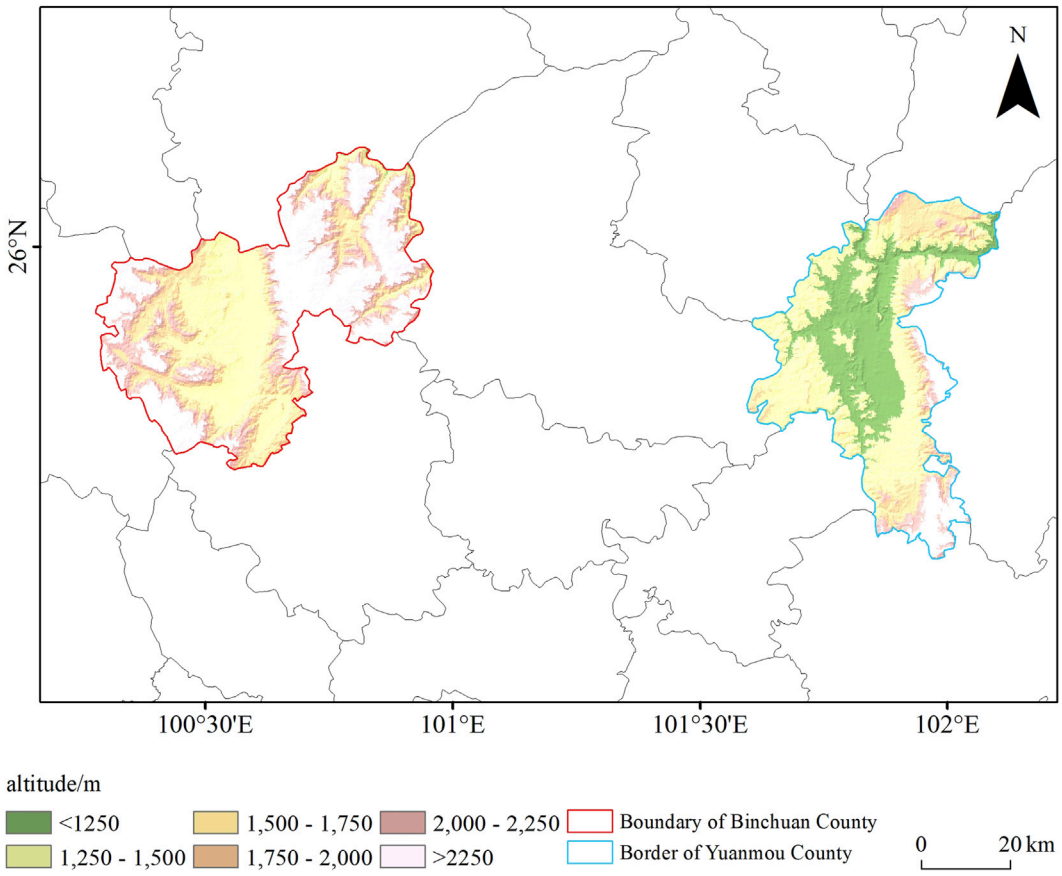

FIGURE 1
Elevation distribution of BC and YM.

2 Materials and methods

2.1 Study area

The study area for this research includes Binchuan County and Yuanmou County. Binchuan County is located in the Dali Bai Autonomous Prefecture, Yunnan Province (100°16′~100°59′E, 25°23′~26°12′N), on the edge of the Yunling mountain range, part of the southwestern Yunnan-Guizhou Plateau along the southern bank of the Jinsha River. The highest altitude point is at the summit of Mu Xiang Ping in the northwest (3,320 m), and the lowest point is where the Yupao River meets the Jinsha River (1,104 m). The mean annual temperature is 17.9°C, with an annual precipitation of 559.4 mm and the annual sunshine duration is 2,719.4 h.Yuanmou County is located in the northern part of the Chuxiong Yi Autonomous Prefecture, Yunnan Province (101°35′~102°06′E, 25°23'~26°06′N), in the northern part of the central Yunnan Plateau. The highest altitude point is at the mountain of Da Ying Pan in Jiangbian Township (2,835.9 m), and the lowest point is in the northeast of Heize Village, Jiangyi Township, where the Jinsha River exits (898 m) (Figure 1). The mean annual temperature is 22.6°C, with an annual precipitation of 637.5 mm and the annual sunshine duration is 2,183.8 h. Both regions share a valley terrain, characterized by low precipitation, abundant solar radiation, and external airflows obstructed by mountain ranges. Additionally, due to the relatively enclosed nature of the valleys, heat at the bottom is not easily dissipated, resulting in a "Foehn effect," ultimately forming a dry and hot valley climate (Yu et al., 2019). In recent years, thanks to the successful completion of the Erhai-to-Binchuan water diversion project, Binchuan County has seen significant improvements over Yuanmou County in areas such as vegetation growth and water quality deterioration.

2.2 Data acquisition and processing

2.2.1 Remote sensing data

The GPP and ET data utilized were procured from the MODIS series (MOD17A2, MOD16A2) (https://www.earthdata.nasa.gov/), products released by the (National Aeronautics and Space Administration (NASA), with a spatial resolution of 500 m and a temporal resolution of 8 days, spanning the period from 2001 to 2020.The GPP data were calculated based on the radiation use efficiency algorithm, with the specific calculation details outlined by Running et al. (2004). The ET data were calculated based on the Penman-Monteith equation, which considers three processes comprehensively: soil surface evaporation, evaporation of intercepted precipitation by the canopy, and plant transpiration. Further details may be found in (Mu et al. (2011). All of the

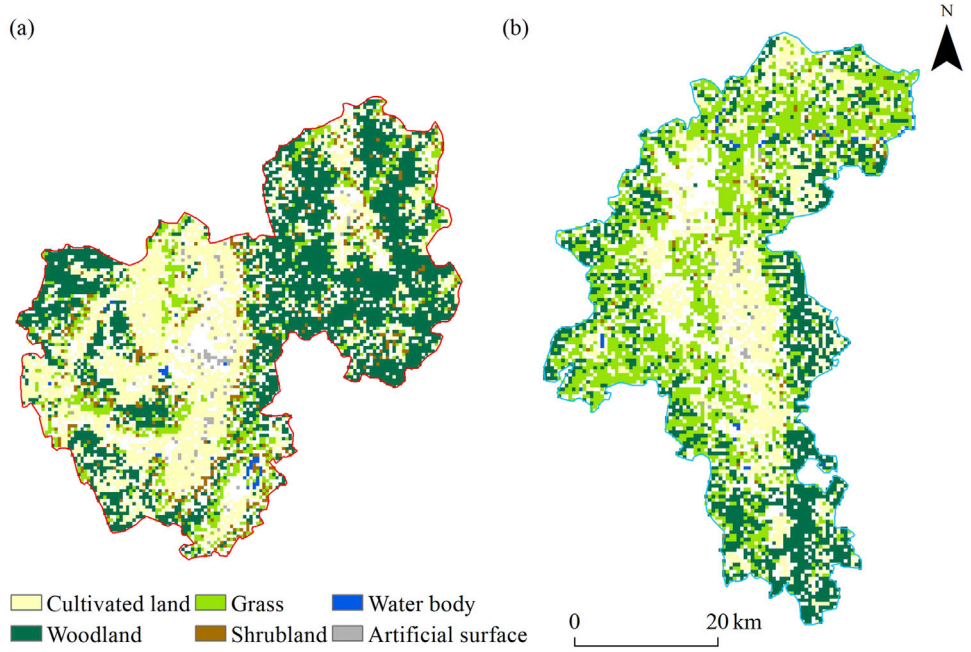

FIGURE 2
The land use types in BC differ from those in YM. **(A)** The land use types in BC; **(B)** The land use types in YM.

aforementioned products were processed using the MRT (Modis Reprojection Tool) software for batch splicing, clipping, and projection transformation of MODIS data. The reprojected data were then synthesized every month basis and clipped to the BC and YM. The MODIS GPP and ET product data have been validated in multiple studies using flux tower site data from various regions around the world, and their accuracy has been confirmed (Zhao et al., 2005; Jia et al., 2012; Chen et al., 2017; Wang et al., 2019).

2.2.2 scPDSI

The scPDSI is derived from the Global Gridded Drought Index dataset, which is provided by the Climatic Research Unit of the University of East Anglia in the Uited Kingdom (https://crudata.uea.ac.uk/). The data has a spatial resolution of 0.5 ° × 0.5 ° and a temporal resolution of monthly, spanning the years 2001–2020. For further details on the scPDSI algorithm (Table 1), please refer to the paper by Liu et al. (2017). To ensure consistency in spatial resolution, elevation information was employed as a covariate, and a variable difference method was used with the Aunsplin4.2 software to obtain monthly scPDSI data for BC and YM that aligned with the pixel size and projection of the MODIS data. It has been demonstrated in previous studies that data interpolated by the Aunsplin software is of high accuracy and reliability.

Aunsplin model algorithm (Formula 1): Aunsplin adopts the local thin disk smooth spline method, and its theoretical statistical model is expressed as follows (1): where z_i is the dependent variable located at point i in space; x_i is the independent variable of d-dimensional spline; f is the unknown smooth function to be estimated about x_i; y_i is the independent covariate of p-dimensional; b is the p-dimensional coefficient of y_i; e_i is the independent random error with expectation 0 and variance w_i; w_i is the known local relative variation coefficient as weight, is the error covariance, and is constant at all data points.

$$z_i = f(x_i) + b^T y_i + e_i \tag{1}$$

2.2.3 Vegetation type data

The vegetation types and the classification scheme were derived from the 2020 Global 30 m Land Cover Product with Fine Classification (CLCFCS30-2020) (Zhang et al., 2021). In ArcGIS, the product was spatially resampled to a 1 km resolution equal latitude-longitude projection data that matched the NDVI using the nearest neighbor method, and adjacent vegetation types were merged (Figure 2). Based on the vegetation classification scheme, the l in the study areas are categorized into six types: forest, cropland, grassland, water body, and artificial surface.

2.3 Calculation of WUE

WUE is assessed by calculating the ratio of GPP to ET within an ecosystem (Hu et al., 2009). The calculation formula remains unchanged as follows (Formula 2):

$$WUE = \frac{GPP}{ET} \tag{2}$$

where WUE is the WUE per unit time (g C m^{-2} mm^{-1}); GPP is the total primary productivity of vegetation ecosystem per unit time (gC m^{-2}); ET is the evapotranspiration of vegetation ecosystem per unit time (mm).

2.4 Methods

2.4.1 Trend analysis

In the entire study region, based on each pixel, used a univariate linear regression analysis to simulate the WUE from 2001 to 2020, obtaining the trend of change for the three, with the calculation formula as follows (Formula 3) (Wang et al., 2023):

$$\theta_{slope} = \frac{n \times \left(\sum_{i=1}^{n} i \times C_i\right) - \left(\sum_{i=1}^{n} i\right)\left(\sum_{i=1}^{n} C_i\right)}{n \times \sum_{i=1}^{n} i^2 - \left(\sum_{i=1}^{n} i\right)^2} \quad (3)$$

where n represents the number of years in the time period (n = 20), θ_{slope} is the slope of the trend, and C_i is the WUE for the i-th year. The significance of the annual WUE change is determined by θ_{slope}. A negative θ_{slope} indicates a decreasing trend in WUE, while a positive θ_{slope} indicates an increasing trend.

2.4.2 Lag effect of scPDSI on WUE

The Pearson correlation was selected due to its simplicity and effectiveness in measuring linear relationships, which is appropriate for the research context where we expect linear relationships to exist. The Pearson correlation coefficient (R) is employed to investigate the lagged effects of drought on grassland GPP (Lu et al., 2023). The coefficient ranges from -1-1, representing the transition from negative to positive correlations. To ensure comparability, the study utilizes monthly WUE and 1-month scPDSI data for BC and YM from 2001 to 2020. Monthly WUE is combined with scPDSI data from up to 12 previous months ($0 \le i \le 12$) to create a series. The R value is then calculated for each pixel at each lag, resulting in 12 correlation coefficients (Formula 4). For instance, a 3-month lag involves correlating monthly WUE data from January to July (2001–2020) with scPDSI data from April to October (2001–2020), and this process is repeated for up to a 12-month lag.

Finally, the maximum correlation coefficient R_{max_lag} is selected, and the corresponding lagging month is regarded as the lagging effect size and time scale of the pixel (Formula 5). When the R_{max_lag} lagging effect occurs between the monthly WUE and the 1-month scPDSI in April, the WUE lagging response time scale to scPDSI is recorded as 4 months, indicating that the drought conditions 4 months prior have a key impact on the changes in WUE.

$$R_i = corr\,(WUE, \mathrm{sc}PDSI)\ 0 \le i \le 12 \quad (4)$$

$$R_{\max\_lag} = \max\,(R_i) 0 \le i \le 12 \quad (5)$$

where WUE represents the monthly time series from 2001 to 2020 with an i-month lag, scPDSI is the 1-month scPDSI time series with an i-month lag, and R is the Pearson correlation coefficient with an i-month lag.

2.4.3 Accumulation effect of scPDSI on WUE

To quantify the accumulation impact of early drying on grassland WUE, the Pearson correlation coefficient between monthly WUE and accumulation scPDSI was used to obtain the scPDSI time scale corresponding to the maximum correlation (Lu et al., 2023). Unlike the lag effect using only scPDSI, it takes 0–12 months of scPDSI to calculate the accumulation effect. Therefore, the correlation was determined using the scPDSI dataset and WUE pixel values from 1–12 months between 2001 and 2020.

Firstly, correlate the WUE time series with the m-month scale scPDSI time series ($0 \le m \le 12$) and calculate R (Formula 6). Then, the accumulation months of scPDSI with the highest correlation with WUE, Rmax_comc, are considered as the time scale of accumulation effects (Formula 7), and Rmax_comc is determined as the accumulation effect quantity. For example, if the correlation between monthly WUE and 3-month scPDSI is the highest, then the time scale of accumulation effects is recorded as 3 months, indicating that the accumulated 3-month drought conditions before the current month have the greatest impact on WUE.

$$R_m = corr\,(WUE, m\mathrm{sc}PDSI)\ 0 \le i \le 12 \quad (6)$$

$$R_{\max\_acc} = \max\,(R_i)\ 0 \le i \le 12 \quad (7)$$

where m is the accumulation time scale of scPDSI, mscPDSI is the scPDSI time series with m accumulation months, and R_m is the Pearson correlation coefficient between WUE and mscPDSI.

3 Results

3.1 Temporal-spatial patterns of WUE

3.1.1 Spatial characteristics of WUE

The spatial distribution and trend of WUE in BC and YM from 2001 to 2020 are shown in Figure 3.Revealed that the average annual WUE values in BC ranged from 1.25 to 3.33 gC m^{-2} mm^{-1}, while in YM, they ranged from 1.75 to 3.71 gC m^{-2} mm^{-1}. The spatial distributions in both regions were similar, with WUE exhibiting significant spatial heterogeneity within each region. In BC, high WUE values were predominantly found at altitudes above 2,000 m, where WUE exceeded 2.5 gC m^{-2} mm^{-1}, accounting for approximately 28.59% of the county's total vegetated area. Because the vegetation type in the high altitude area of BC is mainly forest land, and the WUE of forest land is high, WUE in high altitude areas is higher than that in low altitude areas (Wang et al., 2023). In contrast, YM exhibited high WUE values primarily in areas below 2,000 m, with WUE exceeding 2.25 gC m^{-2} mm^{-1} and accounting for approximately 88.51% of the county's total vegetated area. This is due to the influence of human activities on the high altitude area of YM (Di et al., 2006), which results in lower WUE compared to flat terrain areas. From 2001 to 2020 the WUE in BC and YM showed an increasing trend, the increasing rate of WUE was 0.012 gC m^{-2} mm^{-1} a^{-1} and 0.008 gC m^{-2} mm^{-1} a^{-1}, respectively. YM showed no significant increase trend, accounting for 76.02% of the total vegetation area in YM, but a large area increased significantly in the southeast of YM.

Among the four land use types in BC and YM (Tables 2, 3), the average WUE value of forestland in BC is the highest, which is 2.68 gC m^{-2} mm^{-1}, and the average WUE value of grassland is the lowest, which is 2.57 gC m^{-2} mm^{-1}; YM is different from BC, and the average WUE value of cropland is the highest, which is 2.89 gC m^{-2} mm^{-1}, and the average WUE value of shrubland is the

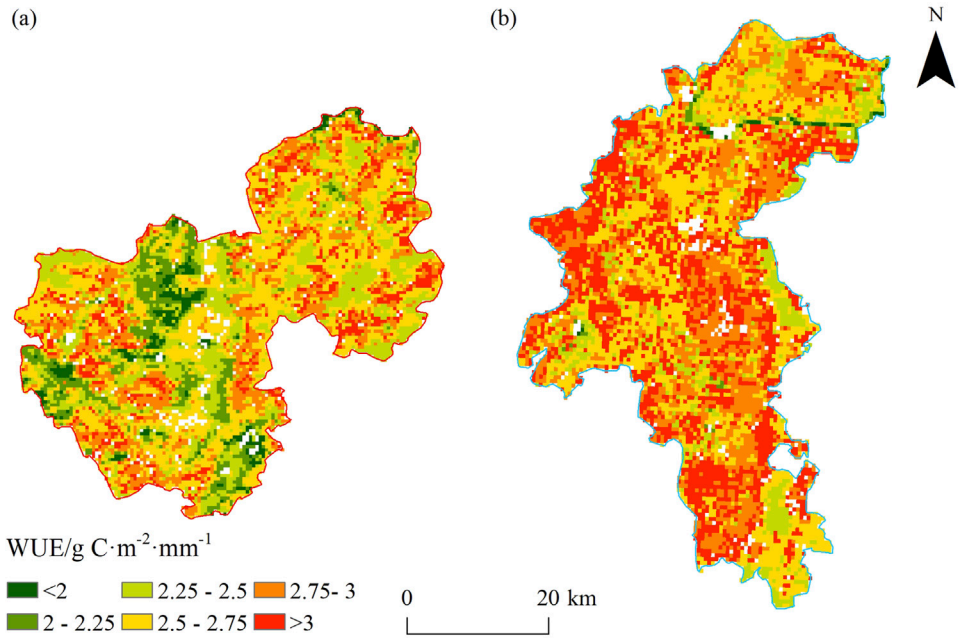

FIGURE 3
Mean WUE in BC and YM in the past 20 years. **(A)** Mean WUE in BC; **(B)** Mean WUE in YM.

TABLE 1 scPDSI Drought severity.

Drought severity	scPDSI
No drought	−0.99~0.99
Slight drought	−1.99~-1.00
Medium drough	−2.99~-2.00
Serious drought	−3.99~-3.00
Extreme drought	≤ −4.00

lowest, which is 2.75 gC m^{-2} mm^{-1}. In different land use types, the change rate of vegetation WUE in the two areas has obvious differences, but all show an increasing trend. As shown in Table 3, the highest average WUE growth rate in BC is grassland (0.0148 gC m^{-2} mm^{-1} a^{-1}), followed by shrubland (0.0144 gC m^{-2} mm^{-1} a^{-1}), and cropland (0.0116 gC m^{-2} mm^{-1} a^{-1}), the lowest growth rate of WUE was forestland, the average growth rate was 0.0099 gC m^{-2}·mm^{-1} a^{-1}. In YM, the land use type with the highest WUE average growth rate was forestland (0.0087 gC m^{-2} mm^{-1} a^{-1}), followed by grassland (0.0081 gC m^{-2} mm^{-1} a^{-1}), shrubland (0.0070 gC m^{-2} mm^{-1} a^{-1}), and cropland (0.0060 ggC m^{-2} mm^{-1} a^{-1}). Generally speaking, the growth rate of different land use types in BC is higher than that in YM.

3.1.2 Temporal variation characteristics of WUE

During 2001–2020, the interannual variation of WUE in BC and YM fluctuates obviously, but the overall trend is downward (Figure 4). The annual average WUE value of BC and YM is the largest in 2012, 2.81 gC m^{-2} mm^{-1} and 3.08 gC m^{-2} mm^{-1} respectively; the annual average WUE value of BC and YM is the smallest in 2016, 2.32 gC m^{-2} mm^{-1} and 2.58 gC·m^{-2} mm^{-1} respectively; The average WUE values of YM and BC during the past 20 years were 2.84 gC m^{-2} mm^{-1} and 2.59 gC m^{-2} mm^{-1}, respectively. This indicated that the two regions at the same latitude lost 1 mm of water through evapotranspiration at the same time, and the amount of CO_2 fixed by vegetation in YM was 0.25 g more than that in BC. In BC, the water stress of vegetation decreased at a rate of 0.012 gC m^{-2} mm^{-1}, and YM also decreased at a rate of 0.008 gC m^{-2} mm^{-1}, which was slightly lower than that of BC. This indicated that the water stress of vegetation in BC was obviously improved due to the existence of "introducing Erhu into BC," which changed the water use strategy of vegetation in BC.

The WUE of the two places fluctuates and decreases in general within a year, with the average WUE of YM being 2.83 gC m^{-2} mm^{-1} and BC being 2.58 gC m^{-2} mm^{-1} (Figure 5); during 2001–2020, the WUE of the two places increases from August to April of the next year, and the WUE values of the two places are generally higher due to the influence of water stress from January to April, among which the WUE of BC reaches the annual peak value of 3.15 gC·m^{-2} mm^{-1} in April; From August to December, affected by the decrease of precipitation, the vegetation water use strategy changed, among which WUE in YM reached the annual peak value of 4.02 gC m^{-2} mm^{-1} in October; From May to July, the precipitation in YM decreased, and July was the peak of precipitation in both places. Under the condition of sufficient water, vegetation growth was no longer restricted by soil water content, and soil ineffective evapotranspiration increased. Therefore, WUE in July was the lowest value of the whole year, among which, YM was 2.23 gC m^{-2} mm^{-1}, BC was 2.08 gC m^{-2} mm^{-1}. From the overall mean value of the two places, WUE in YM was generally higher than that in BC.

TABLE 2 WUE of different land use types in BC and YM in the past 20 years.

Region		Cropland	Forestland	Grassland	Shrubland
BC	Annual WUE/($gCm^{-2}mm^{-1}$)	2.47	2.68	2.57	2.59
YM		2.89	2.87	2.78	2.75

TABLE 3 Annual WUE growth rate of different land use types in Binchuan County and Yuanmou County in recent 20 years.

Region		Cropland	Forestland	Grassland	Shrubland
BC	Annual WUE/($gCm^{-2}mm^{-1}a^{-1}$)	0.0116	0.0099	0.0148	0.0144
YM		0.0060	0.0087	0.0081	0.0070

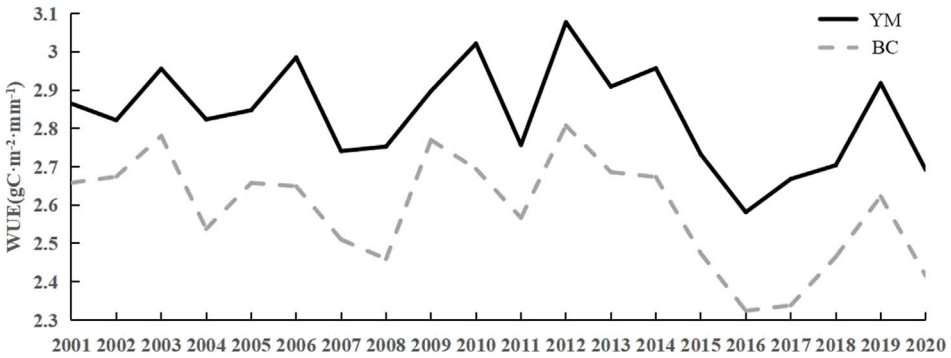

FIGURE 4
Interannual variations in WUE from 2001 to 2020 in BC and YM.

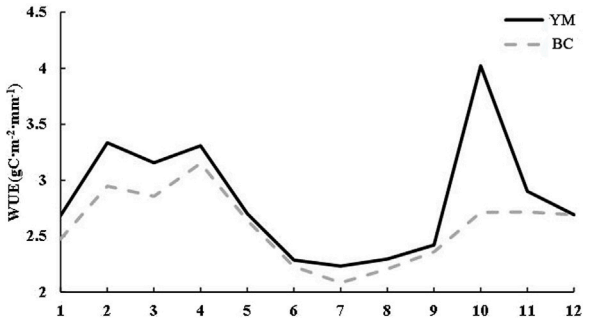

FIGURE 5
Intra-annual variations in WUE from 2001 to 2020 in BC and YM.

3.2 Lag effects of scPDSI on WUE

In BC and YM, the lag effect of scPDSI on WUE accounts for 13.41% and 13.29% of the positive correlation area, respectively, while the negative correlation area accounts for 86.59% and 86.71% respectively (Figure 6). The lag effect of scPDSI on WUE in BC is negative correlation, but there is a large positive correlation area in the northeast; YM is similar to BC, and also negative correlation, but there is a large positive correlation area in the south of Yangjie Town. By comparing the spatial distribution characteristics of the month with the maximum lag effect in the two regions (Figure 7), it can be found that about 81.58% of the vegetation in BC responds to drought with a time lag of 0–2 months, while about 64.74% of the vegetation in YM shows a time lag response in the same period. These results indicate that vegetation in BC is more sensitive to drought than that in YM.

Further analysis of the vegetation area showing lag effects in the two regions shows that there are significant differences in the lag time scale and lag effect intensity of different vegetation types on drought (Table 4). In BC, the main lag time of WUE affected by drought was 0 months, but in YM, the lag time of WUE affected by drought was 2–4 months. For forestland, the main lag time in BC is 0–2 months, while in YM it is 0 months, but there are also lag times of 6–7 months and 11–12 months. The lag effect intensity of drought on the four land use types in the two regions was mainly negative, but in the forestland of BC and YM, there was a large area of positive effect, of which the positive effect area accounted for 28.59% in BC and 24.09% in YM. Because both areas belong to dry-hot valley climates, vegetation is subjected to long-term water stress and has a strong memory effect on drought, so short-term drought has relatively little effect on vegetation WUE (Keersmaecker et al., 2015).

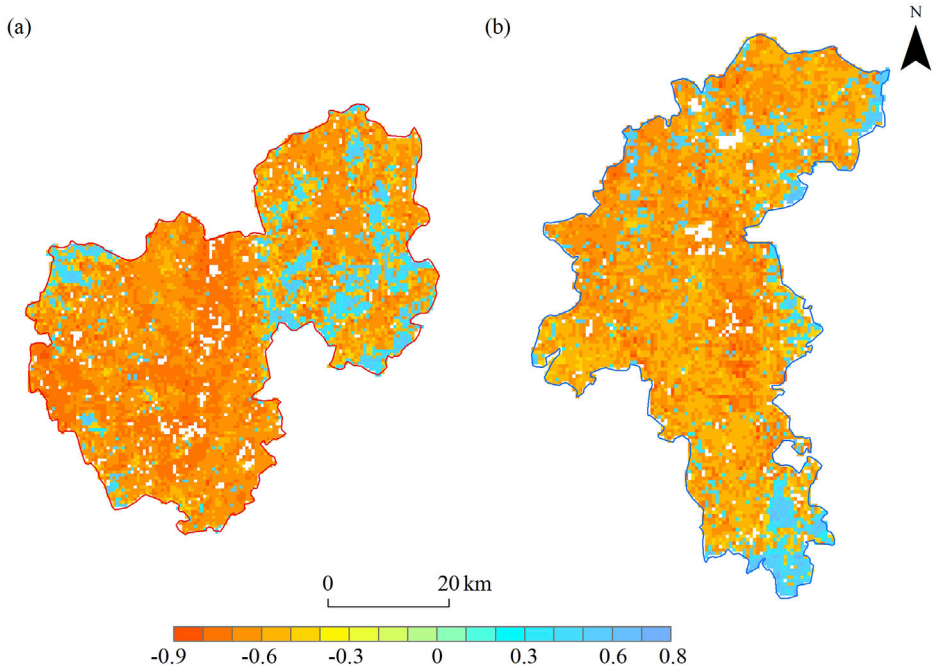

FIGURE 6
Maximum correlation coefficient of hysteresis effect between BC and YM. **(A)** Maximum correlation coefficient of hysteresis effect in BC; **(B)** Maximum correlation coefficient of hysteresis effect in YM.

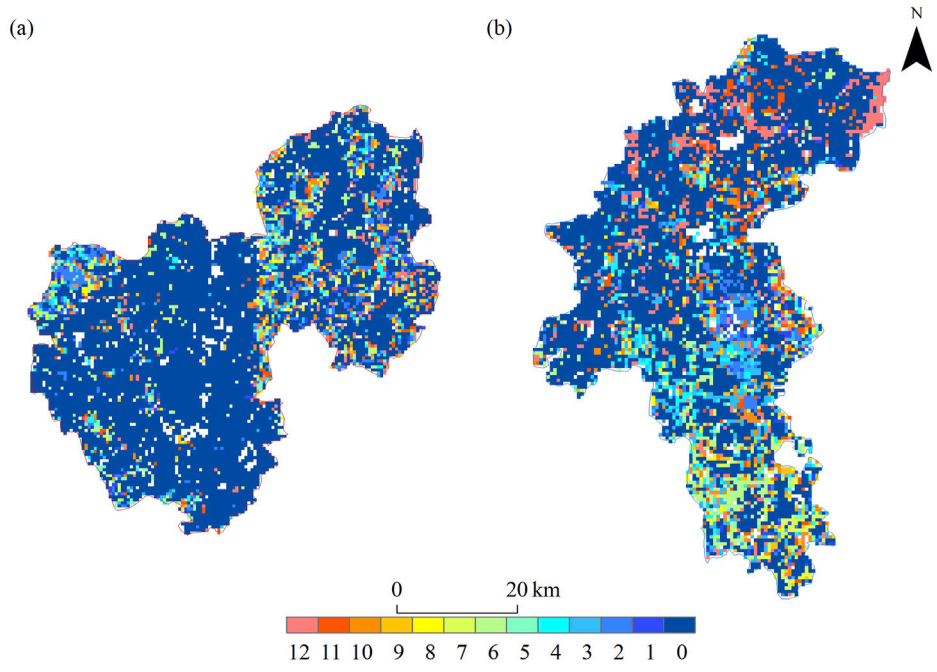

FIGURE 7
The maximum correlation coefficient of the lag effect in BC and YM corresponds to the number of lag months. **(A)** The maximum correlation coefficient of the lag effect in BC corresponds to the number of lag months; **(B)** The maximum correlation coefficient of the lag effect in YM corresponds to the number of lag months.

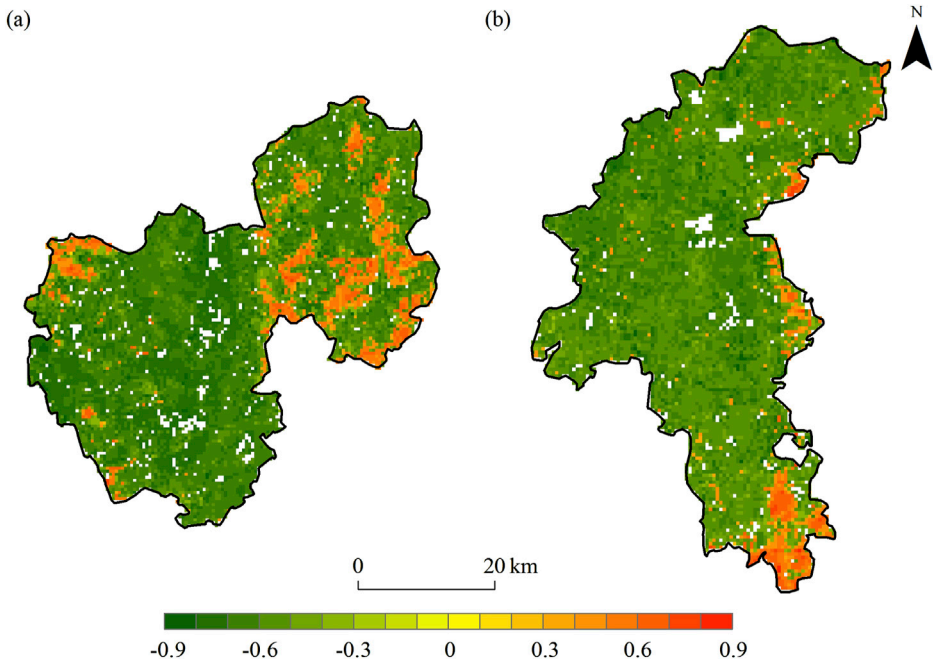

FIGURE 8
Maximum correlation coefficient of accumulation effects between BC and YM. **(A)** Maximum correlation coefficient of accumulation effects in BC; **(B)** Maximum correlation coefficient of accumulation effects in YM.

TABLE 4 Proportion of the area of lagging months for different land use types.

Region	Type	0	1	2	3	4	5	6
YM	Cropland	54.38%	1.74%	9.04%	9.39%	4.31%	1.18%	3.62%
	Forestland	54.72%	2.74%	2.40%	5.20%	3.97%	1.62%	6.04%
	Grassland	65.55%	0.50%	1.09%	4.03%	4.29%	1.30%	4.62%
	Shrubland	83.13%	0.00%	1.20%	1.20%	3.61%	—	1.20%
		7	8	9	10	11	12	
	Cropland	2.09%	0.49%	1.60%	3.69%	3.41%	5.08%	
	Forestland	4.64%	1.84%	3.07%	2.74%	4.02%	6.99%	
	Grassland	1.13%	0.84%	1.01%	2.35%	3.49%	9.79%	
	Shrubland	0.00%	—	1.20%	4.82%	0.00%	3.61%	
		0	1	2	3	4	5	6
BC	Cropland	91.39%	0.40%	0.89%	0.56%	0.40%	0.68%	2.66%
	Forestland	52.39%	4.75%	8.78%	3.55%	3.87%	4.81%	2.79%
	Grassland	88.82%	0.41%	1.23%	0.92%	1.13%	0.51%	2.26%
	Shrubland	87.37%	0.64%	2.14%	1.07%	0.64%	0.43%	1.93%
		7	8	9	10	11	12	
	Cropland	0.68%	0.12%	0.48%	0.24%	0.48%	1.01%	
	Forestland	3.52%	1.79%	2.52%	2.20%	3.49%	5.52%	
	Grassland	0.31%	0.51%	0.21%	0.21%	0.82%	2.67%	
	Shrubland	1.07%	0.64%	0.21%	0.86%	0.64%	2.36%	

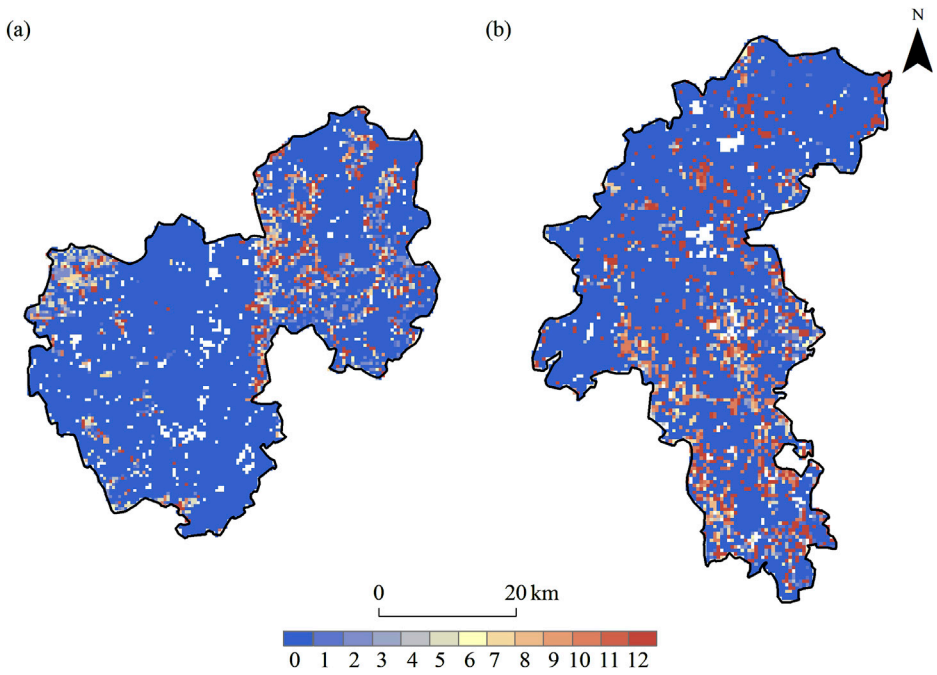

FIGURE 9
The maximum correlation coefficient of the accumulative effect between BC and YM corresponds to the number of lag months. **(A)** The maximum correlation coefficient of the accumulative effect in BC corresponds to the number of lag months; **(B)** The maximum correlation coefficient of the accumulative effect in YM corresponds to the number of lag months.

TABLE 5 The portion of the cumulative monthly area of different land use types.

Region	Type	0	1	2	3	4	5	6
YM	Cropland	73.16%	1.46%	1.18%	1.39%	2.16%	1.18%	1.04%
	Forestland	71.21%	3.07%	1.62%	0.73%	1.23%	1.06%	1.40%
	Grassland	83.28%	0.80%	0.50%	0.29%	0.92%	0.38%	0.55%
	Shrubland	91.57%	—	1.20%	—	—	—	—
		7	8	9	10	11	12	
	Cropland	1.60%	1.81%	0.83%	4.38%	1.04%	8.76%	
	Forestland	1.96%	0.89%	1.51%	3.19%	1.96%	10.17%	
	Grassland	1.05%	0.46%	0.63%	3.15%	1.64%	6.34%	
	Shrubland	—	—	—	2.41%	—	4.82%	
		0	1	2	3	4	5	6
BC	Cropland	96.66%	0.56%	0.40%	0.16%	0.28%	0.20%	0.24%
	Forestland	60.99%	5.66%	6.08%	2.17%	2.79%	2.73%	1.56%
	Grassland	94.15%	0.82%	0.41%	0.31%	0.62%	0.41%	0.21%
	Shrubland	92.29%	0.43%	1.71%	1.07%	0.21%	0.00%	0.43%
		7	8	9	10	11	12	
	Cropland	0.24%	0.08%	0.16%	0.08%	0.04%	0.89%	
	Forestland	3.05%	1.67%	1.79%	1.56%	0.97%	8.98%	
	Grassland	0.72%	0.41%	0.21%	0.21%	0.10%	1.44%	
	Shrubland	0.00%	0.00%	0.43%	0.43%	0.21%	2.78%	

3.3 Accumulation effects of drought on WUE

In BC and YM, the accumulative effect of scPDSI on WUE accounted for 12.38% and 8.03% of the positive correlation area, respectively, while the negative correlation area accounted for 87.62% and 91.97% respectively. On the whole, the high-value areas of R_{max_acc} in the BC are mainly concentrated in the northeast of the region, and the high-value areas of R_{max_acc} in YM are mainly concentrated in the southeast of the region; the areas with negative correlation distribution are the same in both places, and they are both concentrated in relatively gentle areas (Figure 8). The accumulative effect of scPDSI on WUE was negatively correlated in both regions because of the abundant water resources and the relatively small impact of drought on vegetation. Further analysis of the cumulative effect areas in the two regions (Figure 9) shows that the cumulative effect of 0-month scale is the most significant in both places, accounting for 81.93% in BC and 77.75% in YM; meanwhile, the cumulative effect of 12 months scale in both places also accounts for a large proportion. This indicates that vegetation in the two regions is sensitive to short-term drought, but due to the existence of water replenishment projects, the impact of drought on local vegetation growth needs a long time to accumulate.

In BC and YM, there were significant similarities in cumulative time scale and cumulative effect and lag effect of drought among different land use types in the cumulative effect area. The land use types of the two regions generally show cumulative effects of 0 months on different cumulative time scales, and among the four land use types, the cumulative area proportion of 0 months is generally slightly higher than the lag effect of 0 months (Table 5). In BC, the main cumulative time scale of the other three land use types was 0 months except for forestland, which was 0–2 months. In YM, the main cumulative time scale of cropland is 0 months, but there is also a certain distribution in 10–12 months; the main cumulative time scale of forestland is also 0 months, but there is a large area of cumulative effect in 12 months; the cumulative time scale distribution of the remaining two land use types is similar to cropland, mainly 0 months, and a small amount of distribution in 10–12 months. The cumulative effects of drought on the four land use types in the two areas were negative on the whole. However, there were large areas of positive effects in the forestland of BC and YM, among which the positive effect area accounted for 29.12% in BC and 20.57% in YM.

4 Discussion

4.1 Temporal-spatial characteristics of WUE in BC and YM

BC and YM, located in the dry-hot valley zone of the Jinsha River Basin, exhibit similarities in geomorphology, vegetation, and climate. While WUE (WUE) is increasing in both BC and YM, the rise is not significant. BC water projects have improved soil moisture, increasing ET and reducing stomatal conductance, along with warmer temperatures, which has enhanced vegetation's carbon sequestration and WUE (Li, 2018). In YM, stable soil moisture from natural watersheds and positive environmental feedback enhance vegetation WUE. Among the four land use types in BC, the highest WUE value is in high-altitude forests and the lowest WUE is in low-altitude grasslands. Forests possess high canopies, low resistance, strong vapor transport, and better interception than grasslands and farmlands (Yu et al., 2024), resulting in higher ET and WUE due to their complex structure, larger leaf area, and robust CO_2 fixation. In the YM region, cropland demonstrates the highest WUE, while shrubland shows the lowest. The central area, characterized by flat terrain and stable drainage basins, has good vegetation coverage and ample water sources, predominantly consisting of farmland and grassland. Human activities have expanded the cultivated area in the river valleys, leading to a complex crop structure and enhanced plant carbon fixation capacity. As a result, WUE in this area is higher than in other regions (Yu et al., 2019). The changes emphasize the importance of evaluating the impact of different land use types on WUE during drought mitigation and adaptive management. It is also crucial to apply effective vegetation management and strategies for distributing water resources.

Over the past 20 years,WUE of BC and YM have experienced a general decline, which can be attributed to warming and drying trends in the dry and hot valleys, coupled with inadequate water use regulation by vegetation due to climatic factors. In 2012, with rising temperatures and declining precipitation, WUE reached its maximum levels in BC and YM. However, the feedback mechanisms to drought differed. The "Yin-Bin" irrigation project at BC has significantly improved the water resource conditions, especially for agricultural irrigation, which plays a positive role in regulating the local climate and water cycle. In BC, suitable temperature promoted carbon fixation capacity, low precipitation made vegetation stomata small, and vegetation transpiration weakened, while water conservancy facilities reduced drought impact on the ecological environment, so WUE was still increasing and the value was the largest, including the period after 2012 (Zhang and Shan, 2002). The implementation of the irrigation project may have affected the transpiration and stomatal conductance of vegetation by increasing soil moisture, thereby affecting the WUE. In YM, drought stress aggravated vegetation water stress, water use formed memory and adaptation to drought, vegetation drought tolerance increased, resulting in increased CO_2 content fixed by unit water, and WUE was the largest. After 2012, under the combined effect of overall temperature decrease and precipitation increase, drought stress weakened, but due to the memory effect of vegetation on drought, WUE continued to decrease, so the WUE of both regions showed the lowest value in 2016.

The inter-annual variation of WUE highlights the adaptation of vegetation water consumption and productivity to the natural environment and human intervention process, while the pattern of intra-annual variation can more intuitively reflect the adaptation of different vegetation types to seasonal changes (Wang et al., 2023; Li et al., 2003). Yunnan is located at the low latitude plateau, affected by monsoon climate and topography, the unique characteristics of dry valley climate, resulting in droughts high frequency and long duration in BC and YM, mainly concentrated in winter and spring (December to May of the next year). From November to April of the following year, the low ET caused by low precipitation, and relatively

stable temperatures in BC and YM led to stable GPP. From May to July, influenced by the summer rainy season, precipitation increased significantly, stomatal conductance increased and transpiration enhanced, while the WUE decreased because of the weak carbon fixation capacity of vegetation at the development stage. From August to November, the influence of summer drought diminished as the warm and humid southwest airflow brought abundant moisture, alleviating drought conditions. Consequently, vegetation WUE in both regions exhibited an increasing trend from August through April of the following year.

4.2 Lagged effect of drought on WUE

After the drought event, the carbon-water coupling mechanism of the ecosystem remains affected by drought, leading to a "memory effect" in vegetation. The effect causes chaotic responses, resulting in multiple response states over an extended period, including lagged and cumulative effects on WUE that persist long after the drought. This memory effect may cause vegetation to exhibit varying adaptability and resilience to subsequent environmental changes, influencing its long-term water-carbon cycle and productivity (Ma et al., 2024; Sun et al., 2020). Pearson correlation analysis was employed to examine the relationship between scPDSI and WUE in BC and YM.

The lag effect of scPDSI on WUE in BC was 0 lag, and the largest cropland (91.39%), which is caused by the single planting structure of cash crops.The main cash crop in Binchuan is grapes, meaning that even small changes in water availability can lead to significant changes in productivity. This sensitivity is partly due to the fixed water consumption patterns and the high water demand during critical growth stages (Liu, et al., 2025). While, the longest lag (12 months) was forestland (5.52%), based on the strong water capacity, it is weaker to drought stress than cropland, grassland and shrubland, and forestland (Müller and Bahn, 2022; Yu et al., 2019).

YM, the land type with 0 hysteresis between scPDSI and WUE, was mainly shrubland (83.13%). The vegetation structure in this area is single, the vertical difference is significant, and the soil loss at high altitudes is serious. Thus, shrublands' WUE is highly sensitive to drought feedback (Cristiano et al., 2020; Jiang et al., 2022). While, longest lag (12 months) was (9.79%) farmland, which is due to the complex agricultural structure of Yuanmou County, in the process of environmental changes, the vegetation water utilization efficiency is remain stable (Du et al., 2023).

4.3 Accumulation effect of drought on WUE

The response mechanism of WUE to drought was significantly different among different land use types, and the effects of water stress on vegetation growth were persistent and cumulative. Cumulative effect can reflect the continuous influence of drought on vegetation growth from beginning to end, and comprehensively consider the interaction between WUE and drought of different land use types (Liu et al., 2017; Lu et al., 2023; Wen et al., 2019). In BC the most significant cumulative effects of scPDSI on WUE was cropland with 0-accumulation (91.39%),and the forestland with the longest feedback time for cumulative effects is forestland, which is consistent with the lag- effects of scPDSI and WUE in this area (Müller and Bahn, 2022; Yuan et al., 2024). The weakest accumulation effect of scPDSI on WUE in BC is in forest land (5.52%), which was least affected by human activities, regulates its own ecosystems, and is less sensitive to drought than other land use types (Xu et al., 2019). The cumulative effect of scPDSI on WUE in YM was 0 accumulation and the largest area is shrubland (91.57%); the cumulative effect of scPDSI on WUE with 12 accumulation was forestland (10.17%).The cumulative effect of forestland on drought was weaker than that of cropland, which indicated that the cumulative feedback mechanism of cropland ecosystem to drought was less stable than that of forestland ecosystem under the influence of long-term drought. All the above shows that forestland shows low cumulative effects under drought, while the construction of artificial forests has a positive impact on improving soil water conservation and soil erosion, thereby enhancing the WUE stability and drought resistance of regional vegetation (Zhao et al., 2023). These findings have important implications for understanding and coping with drought effects in the biology of global change (Yang, 2007).

5 Conclusion

In this study, the GPP and ET products were based on MODIS, to estimate spatiotemporal variation of WUE in BC and YM from 2001 to 2020. Combined with scPDSI, the lag and accumulation effects of WUE on drought in BC and YM were analyzed. The main conclusions are as follows:

(1) From 2001 to 2020, the average WUE in BC was 2.59 gC m^{-2} mm^{-1}, and the average WUE in YM was 2.84 gC m^{-2} mm^{-1}. The spatial distribution of the two regions is similar, and the WUE in the area shows significant spatial heterogeneity.
(2) In the past 20 years, the trend of WUE changes in BC and YM has shown a slow increase, with a growth rate of 0.012 gC m^{-2} mm^{-1} a^{-1} in BC and 0.008 gC m^{-2} mm^{-1} a^{-1} in YM. However, the overall WUE in YM is higher than that in BC.
(3) The lag effect of WUE on drought in different land use types in BC and YM is mainly manifested as 0 lag. Due to the influence of agricultural structure, the sensitivity of cropland WUE to drought in BC is stronger than that in YM.
(4) The accumulation effect of WUE on drought in different land use types in BC and YM is mainly manifested as zero accumulation. The vegetation structure of forest land is stable, and the sensitivity of forest land to drought in both areas is the weakest.

Data availability statement

The original contributions presented in the study are included in the article/Supplementary Material, further inquiries can be directed to the corresponding author.

Author contributions

DW: Conceptualization, Methodology, Writing–review and editing, Writing–original draft. DJ: Data curation, Formal Analysis, Writing–original draft, Writing–review and editing. YZ: Writing–review and editing, Investigation, Methodology, Writing–original draft. XT: Investigation, Project administration, Writing–original draft. FH: Data curation, Formal Analysis, Writing–original draft. YM: Software, Validation, Writing–original draft. YG: Software, Supervision, Writing–original draft. JL: Writing–original draft. LL: Conceptualization, Funding acquisition, Resources, Writing–review and editing.

Funding

The author(s) declare that financial support was received for the research, authorship, and/or publication of this article. This research was jointly supported by the Yunnan Provincial Basic Research (202301AT070084 and 202301AT070085), Western Yunnan University of Applied Sciences Talent Introduction Research Initiation Project ((2023RCKY0001 and 2022RCKY0003).

Conflict of interest

The authors declare that the research was conducted in the absence of any commercial or financial relationships that could be construed as a potential conflict of interest.

Publisher's note

All claims expressed in this article are solely those of the authors and do not necessarily represent those of their affiliated organizations, or those of the publisher, the editors and the reviewers. Any product that may be evaluated in this article, or claim that may be made by its manufacturer, is not guaranteed or endorsed by the publisher.

Supplementary material

The Supplementary Material for this article can be found online at: https://www.frontiersin.org/articles/10.3389/fenvs.2025.1493668/full#supplementary-material

References

Anderegg, W. R. L., chwalm, C., Biondi, F., Camarero, J. J., Koch, G., Litvak, M., et al. (2015). Pervasive drought legacies in forest ecosystems and their implications for carbon cycle models. *Science* 349 (624), 528–532. doi:10.1126/science.aab1833

Bradford, J. B., Schlaepfer, D. R., Lauenroth, W. K., and Palmquist, K. A. (2020). Robust ecological drought projections for drylands in the 21st century. *Robust Ecol. Drought Proj. Dryl. 21st Century. Glob. Change Biol.* 26 (7), 3906–3919. doi:10.1111/gcb.15075

Chen, X., Mo, X., Hu, S., and Liu, S. (2017). Contributions of climate change and human activities to ET and GPP trends over North China Plain from 2000 to 2014. *J. Geogr. Sci.* 27, 661–680. doi:10.1007/s11442-017-1399-z

Cristiano, P. M., Diaz Villa, M., De, D., Lacoretz, M., Madanes, N., and Goldstein, G. (2020). Carbon assimilation, water consumption and water use efficiency under different land use types in subtropical ecosystems: from native forests to pine plantations. *Agric. For. Meteorology* 291, 108094. doi:10.1016/j.agrformet.2020.108094

Di, B., Cui, P., Huang, S., and Yu, Y. (2006). Sediment yields and impact factors in xerothermic valley in Jinsha River in the last 50 years: a case study in Yuanmou County, Yunnan Province. *oil Water Conserv* (04), 20–24.

Dong, Y., Xiong, D., Su, Z., Li, J., Yang, D., Shi, L., et al. (2014). The distribution of and factors influencing the vegetation in a gully in the Dry-hot Valley of southwest China. *CATENA* 116, 60–67. doi:10.1016/j.catena.2013.12.009

Du, H., Fu, W., Song, T., Zeng, F., Wang, K., Chen, H., et al. (2023). Water-use efficiency in a humid karstic forest in southwestern China: interactive responses to the environmental drivers. *J. Hydrology* 617, 128973. doi:10.1016/j.jhydrol.2022.128973

Guo, X., Zhang, Y., Zha, T., Shang, G., Jin, C., Wang, Y., et al. (2023). Biophysical controls of dew formation in a typical cropland and its relationship to drought in the North China Plain. *J. Hydrology* 617, 128945. doi:10.1016/j.jhydrol.2022.128945

Hao, C., Zhang, J. H., and Yao, F. M. (2015). Combination of multi-sensor remote sensing data for drought monitoring over Southwest China. *Int. J. Appl. Earth Obs. Geoinf.* 35, 270–283. doi:10.1016/j.jag.2014.09.011

Hu, Z. M., Yu, G. R., Wang, Q. F., and Zhao, F. H. (2009). Ecosystem level water use efficiency: a review. *Acta Ecol. Sin.* 29 (3), 1498–1507.

Huang, L., He, B., Han, L., Liu, J., Wang, H., and Chen, Z. (2017). A global examination of the response of ecosystem water-use efficiency to drought based on MODIS data. *Sci. Total Environ.* 601-602, 1097–1107. doi:10.1016/j.scitotenv.2017.05.084

Ji, Y., Zeng, S., Tang, Q., Yan, L., Wu, S., Fan, Y., et al. (2023). Spatiotemporal variations and driving factors of China's ecosystem water use efficiency. *Ecol. Indic.* 148, 110077. doi:10.1016/j.ecolind.2023.110077

Jia, Z., Liu, S., Xu, Z., Chen, Y., and Zhu, M. (2012). Validation of remotely sensed evapotranspiration over the hai River Basin, China. *J. Geophys. Res. Atmos.* 117 (D13). doi:10.1029/2011jd017037

Jiang, J., Su, T., Liu, Y., Wu, G., and Yu, W. (2022). Southeast China extreme drought event in August 2019: context of coupling of midlatitude and tropical systems. *J. Clim.* 35 (22), 7299–7313. doi:10.1175/JCLI-D-22-0138.1

Jiao, W., Wang, L., Smith, W. K., Chang, Q., Wang, H., and D'Odorico, P. (2021). Observed increasing water constraint on vegetation growth over the last three decades. *Nat. Commun12* 3777, 3777. doi:10.1038/s41467-021-24016-9

Keersmaecker, W. D., Lhermitte, S., Tits, L., Honnay, O., Somers, B., and Coppin, P. (2015). A model quantifying global vegetation resistance and resilience to short-term climate anomalies and their relationship with vegetation cover[J]. *Glob. Ecol. Biogeogr.* 24 (5), 539–548. doi:10.1111/geb.12279

Law, B. E., Thornton, P. E., Irvine, J., Anthoni, P. M., and Van Tuyl, S. (2001). Carbon storage and fluxes in ponderosa pine forests at different developmental stages. *Glob. Change Biol.* 7 (7), 755–777. doi:10.1046/j.1354-1013.00439.x

Li, L., Yang, Y., Wang, D., Ma, X., Du, J., Lu, R., et al. (2024b). Spatiotemporal variation of water use efficiency in response to self-calibrating Palmer drought severity index in Yulong Snow Mountain and surrounding areas, China. *Chin. J. Ecol.* 43 (6), 1841.

Li, L. L., Yang, Y. M., Wang, D. W., et al. (2024a). Spatiotemporal variation of water use efficiency in response to self-calibrating Palmer drought severity index in Yulong Snow Mountain and surrounding areas, China. *Chin. J. Ecol.* 43 (6), 1841–1850.

Li, P., Wang, J. L., Liu, M. W., Xue, Z., and Bagherzadeh, A. (2021). Spatio-temporal variation characteristics of NDVI and its response to climate on the Loess Plateau from 1985 to 2015. *CATENA* 203, 105331. doi:10.1016/j.catena.2021.105331

Li, R. S., Xu, H. C., Yin, G. T., Yang, C., and Li, S. Z. (2003). Advances in the water use efficiency of plant. *For. Res.* 16 (003), 366–371.

Li, Y. (2018). *Impact assessment of trans water project in arid area on terrestrial vegetation in water diversion Area—Study case of the yinhajidang project*. Northwest University.

Lili, L. I., Jun, D. U., Yahui, L. I., Mingkun, C. H. E. N., Binwen, W. A. N., and Dawei, W. A. N. G. (2023). Changes of vegetation water use efficiency and their responding to scPDSI in frozen ground area of the Qilian Mountains from 2000 to 2020. *J. Glaciol. Geocryol.* 45 (2), 688–698.

Liu, H., Gao, X., Li, C., Cai, Y., Song, X., and Zhao, X. (2025). Intercropping increases plant water availability and water use efficiency: a synthesis. *Agric. Ecosyst. and Environ.* 379, 109360. doi:10.1016/j.agee.2024.109360

Liu, Y., Zhu, Y., Ren, L., Singh, V. P., Yang, X., and Yuan, F. (2017). A multiscalar Palmerdrought severity index. *Geophys. Res.Lett.* 44, 6850–6858. doi:10.1002/2017GL073871

Lu, J. T., Peng, J., Li, G. , Guan, J., Han, W., Liu, L., et al. (2023). Aesessment of time-lag and cumulative elfects of drought on gross prmar productivity of grassland in Central Asia from 1982 to 2018. *Acta Ecol. Sin.* 43, 9745–9757.

Ma, Y., Guan, Q., Sun, Y., Zhang, J., Yang, L., Yang, E., et al. (2022). Three-dimensional dynamic characteristics of vegetation and its response to climatic factors in the Qilian Mountains. *Catena* 208, 105694. doi:10.1016/j.catena.2021.105694

Ma, Y., He, Q., Zhang, Y., Shi, Y., Li, J., and Yuan, F. (2024). Influences of climate factors and human activities on vegetation leaf area index dynamics in the Songliao River Basin. *Acta Ecol. Sin.* 44, 12043–2056.

Mu, Q., Zhao, M., and Running, S. W. (2011). Improvements to a MODIS global terrestrial evapotranspiration algorithm. *Remote Sens. Environ.* 115 (8), 1781–1800. doi:10.1016/j.rse.2011.02.019

Müller, L. M., and Bahn, M. (2022). Drought legacies and ecosystem responses to subsequent drought. *Glob. Change Biol.* 28 (17), 5086–5103. doi:10.1111/gcb.16270

Peng, J., Wu, C., Zhang, X., Wang, X., and Gonsamo, A. (2019). Satellite detection of cumulative and lagged effects of drought on autumn leaf senescence over the Northern Hemisphere. *Glob. Change Biol.* 25, 2174–2188. doi:10.1111/gcb.14627

Piao, S., Wang, X., Park, T., Chen, C., Lian, X., He, Y., et al. (2020). Characteristics, drivers and feedbacks of global greening. *Nat. Rev. Earth Environ.* 1, 14–27. doi:10.1038/s43017-019-0001-x

Qiao, Y., Liu, J., and Gong, X. (2022). Phylogeography of Himalrandia lichiangensis from the dry-hot valleys in Southwest China. *Front. Plant Sci.* 13, 1002519. doi:10.3389/fpls.2022.1002519

Reichstein, M., Tenhunen, J., Roupsard, O., Ourcival, J., Rambal, S., Miglietta, F., et al. (2002). Severe drought effects on ecosystem CO_2 and H2O fluxes at three Mediterranean evergreen sites: revision of current hypotheses? Glob. *Chang. Biol.* 8 (10), 999–1017. doi:10.1046/j.1365-2486.2002.00530.x

Running, S. W., Nemani, R. R., Heinsch, F. A., Zhao, M., Reeves, M., and Hashimoto, H. (2004). A continuous satellite-derived measure of global terrestrial primary production. *Bioscience* 54 (6), 547–560. doi:10.1641/0006-3568(2004)054[0547:acsmog]2.0.co;2

Sun, X., Wang, M., Li, G., Wang, J., and Fan, Z. (2020). Divergent sensitivities of spaceborne solar-induced chlorophyll fluorescence to drought among different seasons and regions. *ISPRS Int. J. Geo-Inf.* 9, 542. doi:10.3390/ijgi9090542

Ukkola, A. M., De Kauwe, M. G., Roderick, M. L., Abramowitz, G., and Pitman, A. J. (2020). Robust future changes in meteorological drought in CMIP6 projections despite uncertainty in precipitation. *Geophys. Res. Lett.* 47, e2020GL087820. doi:10.1029/2020gl087820

Wang, D., Zhao, C., Fang, F., Lin, J., Li, L., and Yang, Y. (2023). Spatial-temporal dynamics of water use efficiency and responding to vapor pressure deficit in Shiyang River Basin, northwestern China. *Acta Ecol. Sin.* 43 (8), 3090–3102. doi:10.5846/stxb202111243322

Wang, X., Ma, M., Huang, G., Veroustraete, F., Zhang, Z., Song, Y., et al. (2019). Vegetation primary production estimation at maize and alpine meadow over the Heihe River Basin, China. *China Int. J. Appl. Earth Obs. geoinf.* 17, 94–101. doi:10.1016/j.jag.2011.09.009

Wang, Z., He, F., Fang, W., and Liao, Y. (2013). Assessment of physical vulnerability to agricultural drought in China. *Nat. Hazards* 67, 645–657. doi:10.1007/s11069-013-0594-1

Wang, Z., Liu, X., Zhou, W., Sinclair, F., Shi, L., Xu, J., et al. (2022). Land use intensification in a dry-hot valley reduced the constraints of water content on soil microbial diversity and multifunctionality but increased CO2 production. *Sci. Total Environ.* 852 (852), 158397. doi:10.1016/j.scitotenv.2022.158397

Wei, W., Pang, S., Wang, X., Zhou, L., Xie, B., Zhou, J., et al. (2020). Temperature vegetation precipitation dryness index (TVPDI)-based dryness-wetness monitoring in China. *Remote Sens. Environ.* 248 (2), 111957. doi:10.1016/j.rse.2020.111957

Wen, Y., Liu, X., Pei, F., Li, X., and Du, G. (2018). Non–uniform time–lag effects of terrestrial vegetation responses to asymmetric warming. *Agric. For. Meteorol.* 252, 130–143. doi:10.1016/j.agrformet.2018.01.016

Wen, Y., Liu, X., Xin, Q., Wu, J., Xu, X., Pei, F., et al. (2019). Cumulative effects of climatic factors on terrestrial vegetation growth. *J. Geophys.Res. Biogeosci.* 124, 789–806. doi:10.1029/2018JG004751

Xu, F., Qu, Y., Bento, V. A., Song, H., Qiu, J., Qi, J., et al. (2024). Understanding climate change impacts on drought in China over the 21st century: a multi-model assessment from CMIP6. *npj Clim. Atmos. Sci.* 7 (32), 32. doi:10.1038/s41612-024-00578-5

Xu, H. J., Wang, X. P., Zhao, C. Y., and Zhang, X. x. (2019). Responses of ecosystem water use efficiency to meteorological drought under different biomes and drought magnitudes in northern China. *Agric. For. Meteorology* 278, 107660. doi:10.1016/j.agrformet.2019.107660

Yang, H., Rood, S. B., and Flanagan, L. B. (2019). Controls on ecosystem water-use and water-use efficiency: insights from a comparison between grassland and riparian forest in the northern Great Plains. *Agric. For. Meteorology* 271, 22–32. doi:10.1016/j.agrformet.2019.02.034

Yang, Z. (2007). *Res. Veg. Landsc. Dyn. Veg. Restor. Yuanmou dry-hot Val. Chin. Acad. For.*

Yu, J. E., Si, H. M., Wu, X. T., Ma, X., Cao, J., Zhang, G. F., et al. (2019). Funcational traits of dodonaea viscosa leaf under eucalyputs platation in dry Hot Valley of Yuanmou county. *J. West China For. Sci.* 48 (1), 100–105.

Yu, X. X., Wu, Y. X., and Jia, G. D. (2024). Research progress of carbon-water processes and coupling mechanisms of forest vegetation at different scales. *J. Soil Water Conservation* 38 (1), 1–13.

Yuan, B., Guo, S., Zhang, X., Mu, H., Cao, S., Xia, Z., et al. (2024). Quantifying the drought sensitivity of vegetation types in northern China from 1982 to 2022. *Agric. For. Meteorology* 359, 110293. doi:10.1016/j.agrformet.2024.110293

Zhang, R. R., Qi, J. Y., Leng, S., and Wang, Q. (2022). Long-term vegetation phenology changes and responses to preseason temperature and precipitation in Northern China. *Remote Sens.* 14, 1396. doi:10.3390/rs14061396

Zhang, S. Q., and Shan, L. (2002). Research progress on water use efficiency of plant. *Agric. Res. Arid Areas* 20 (4), 1–5.

Zhang, X., Liu, L., Chen, X., Gao, Y., Xie, S., and Mi, J. (2021). GLC_FCS30: global land-cover product with fine classification system at 30 m using time-series Landsat imagery. *Earth Syst. Sci. Data* 13 (6), 2753–2776. doi:10.5194/essd-13-2753-2021

Zhao, J., Xu, T., Xiao, J., Liu, S., Mao, K., Song, L., et al. (2020). Responses of water use efficiency to drought in southwest China. *Remote Sens.* 12 (1), 199. doi:10.3390/rs12010199

Zhao, M., Heinsch, F. A., Nemani, R. R., and Running, S. W. (2005). Improvements of the MODIS terrestrial gross and net primary production global data set. *Remote Sens. Environ.* 95 (2), 164–176. doi:10.1016/j.rse.2004.12.011

Zhao, Z., He, L., Li, G., Ma, S., Cui, M., Liu, Y., et al. (2023). Partitioning beta diversity of dry and hot valley vegetation in the Nujiang River in Southwest China. *Front. Ecol. Evol.* 11, 1199874. doi:10.3389/fevo.2023.1199874

frontiers | Frontiers in Environmental Science

TYPE Original Research
PUBLISHED 19 March 2025
DOI 10.3389/fenvs.2025.1556083

OPEN ACCESS

EDITED BY
Xiaoping Wang,
Northwest A&F University, China

REVIEWED BY
Hongchao Dun,
Lanzhou University, China
Chunyuan Wang,
Chinese Research Academy of Environmental Sciences, China

*CORRESPONDENCE
Zhongju Meng,
mengzhongju@126.com

†These authors have contributed equally to this work

RECEIVED 06 January 2025
ACCEPTED 25 February 2025
PUBLISHED 19 March 2025

CITATION
An H, Zhao F, Li H, Meng Z, Ding H, Ding Y, Qin L and Xin J (2025) The typical sand-fixing plants in the Ulan Buh desert-oasis area significantly changed the distribution pattern of surface sediments.
Front. Environ. Sci. 13:1556083.
doi: 10.3389/fenvs.2025.1556083

The typical sand-fixing plants in the Ulan Buh desert-oasis area significantly changed the distribution pattern of surface sediments

Hua An[1,2,3†], Feiyan Zhao[1,2,3†], Haonian Li[1,2,3], Zhongju Meng[1,2,3*], Hailong Ding[1,2,3], Yanlong Ding[4], Lei Qin[5] and Jing Xin[6]

[1]College of Desert Control Science and Engineering, Inner Mongolia Agricultural University, Hohhot, China, [2]Key Laboratory of Aeolian Physics and Desertification Control Engineering from Inner Mongolia Autonomous Region, Inner Mongolia Agricultural University, Hohhot, China, [3]Key Laboratory of Desert Ecosystem Conservation and Restoration, State Forestry and Grassland Administration of China, Inner Mongolia Agricultural University, Hohhot, China, [4]College of Tourism, Inner Mongolia University of Finance and Economics, Hohhot, China, [5]Water Conservancy Development Center of Inner Mongolia Ancient Autonomous Region, Hohhot, China, [6]Ordos Forestry and Grassland Development Center, Ordos, China

Vegetation increases surface roughness, reduces wind speeds and decreases sand carrying capacity, thereby effectively intercepting wind-sand flows and promoting sand deposition. Exploring the distribution of sand-fixing plant sediment particles and the characteristics of plant morphology parameters in the desert-oasis transition zone can provide a certain theoretical foundation for regional ecological vegetation construction and desertification control. In this paper, the particle size of surface sediments (0–2 cm) under cover of five typical sandy vegetation in the desert-oasis transition zone at the northeastern edge of the Ulan Buh Desert was investigated, and the effects of plant morphometric parameters on the grain size distribution of sediments were analyzed. The results show: (1) Plant spatial configuration significantly influenced surface sediment characteristics, with Nitraria *tangutorum* having the largest crown width and number of branches with 283 cm and 385 branches compared to the other four species. In unit area, the degree of porosity from large to small is: *Psammochloa villosa* > *Agriophyllum squarrosum* > *Phragmites australis* > *Artemisia ordosica* > *Nitraria tangutorum*. On the whole, the interception effect of N.*tangutorum* shrub on transit airflow is more prominent. (2) The grain size distribution of the sandy material in the study area is unimodal with good particle sorting. Due to the interception of N. *tangutorum* and A. *ordosica* shrubs, the contents of medium sand and fine sand in the mechanical composition of sediments in the surface layer of vegetation-covered dunes decreased significantly, while the contents of clay, silt, and very fine sand increased significantly ($P < 0.05$); Compared to the bare dunes, the particle sorting becomes worse, and the particle size frequency curve shifts to a bimodal state with a positively skewed trend and a lower kurtosis value. Overall, the sediment grain composition in order of coarseness to fineness was: CK > P. *villosa* > A. *squarrosum* > P. *australis* > A. *ordosica* > N. *tangutorum*. (3) The mean grain size of sediments under vegetation coverage was positively correlated with sortability, kurtosis and skewness ($P < 0.01$). Mean particle size and sortability significantly correlated negatively with kurtosis and skewness ($P < 0.01$). (4) Mean grain size and sortability were

significantly positively correlated with plant crown width and branch number and significantly negatively correlated with porosity ($P < 0.05$). Skewness and kurtosis were significantly negatively correlated with plant crown width and branch number and significantly positively correlated with porosity ($P < 0.05$). (5)In this paper, the mean grain size of the sediment is used as an indicator of the above-mentioned plant windbreak and sand fixation. It is concluded that the lower leaves of N. *tangutorum* and A. *ordosica* are dense, the porosity is minor, and the particle composition of the sand material is fine, forming dense vegetation shrubs on the dunes, which is more powerful in windbreak and sand fixation. Screening plants with strong vitality and outstanding sand-fixing capacity is important for controlling quicksand, improving soil quality and preventing wind erosion.

KEYWORDS

sediment, grain size parameters, phytomorphological parameters, Ulan Buh desert, distribution pattern

1 Introduction

The desert-oasis transition zone is an ecologically sensitive and fragile area that serves as a bridge between the desert and oasis ecosystems and assumes the important functions of promoting the circulation of materials, energy flow, and the transmission and sharing of information (Li et al., 2016). The desert-oasis interface at the northeastern edge of the Ulan Buh Desert suffers from severe land degradation due to the natural environment and long-term human activities (Luo et al., 2022). Many natural or artificial sand-fixing plants grow within the desert-oasis transition zone. Most of these sand-fixing plants have simple community structure, less species composition, relatively low vegetation cover, drought resistance, wind erosion and sand burial resistance, etc., and have good wind and sand blocking functions (Gao et al., 2025). Vegetation in the transition zone can resist wind and sand erosion and has an important ecological function in protecting the stability of the oasis ecosystem by reducing the flow rate of wind and sand, preventing wind erosion, fixing sand dunes, and improving the physicochemical properties of the soil (Mayaud and Webb, 2017).

In arid wind-sand areas, the grain size distribution of wind-sand sediments is both an important factor affecting the process of surface wind erosion, transport, and accumulation and a result of the sorting of near-surface winds through surface erosion and deposition (Van Hateren et al., 2020). The loss of fine particles from the surface due to wind-sand activities causes coarsening of surface particles, resulting in loss of land nutrients and reduced productivity, while the ratio of particles of different sizes influences the stability of the particles, which also has an important impact on the intensity of wind erosion on the surface (Guan et al., 2024). The study of grain size distribution and sorting characteristics of wind-sand sediment deposits is of great significance for understanding the dynamics of near-surface sand transport, analyzing wind-sand depositional environments, and inverting changes in wind-sand environments (Wang et al., 2022). Soil particle size characteristics, as an important indicator of soil physical properties, characterize the proportion and distribution of mineral particles of different size classes in the soil. The change of its parameters is controlled by factors such as transport medium, transport mode, depositional environment and climate, which can explain the transportation of particles and then judge the evolution of the depositional environment, and is more and more widely used in the study of land desertification (Wu et al., 2021).

In recent years, the Ulan Buh Desert-Oasis transition zone has been subjected to anthropogenic interference, and internal sand-fixing plants have declined to varying degrees, affecting the stability of the fixed dunes and thus seriously threatening the oasis ecosystem (Hussein et al., 2021). With the degradation of sand-fixing plants, vegetation cover decreases, soil particles gradually become coarser, and ecological vegetation stability deteriorates (Moradi et al., 2024). Methods of combating desertification mainly include mechanical, chemical, and biological measures (plant measures)are the most direct (Amiraslani and Dragovich, 2011; Khalilimoghadam and Bodaghabadi, 2020), fundamental and practical measures in the prevention and control of wind and sand disasters (Wang et al., 2023). Soil particle composition, as the material basis for the growth and development of sand-fixing plants, is important in building a stable ecosystem. The distribution of surface vegetation strongly influences the variability in the grain size distribution of wind-sand sediments (Gonzales et al., 2018). The ability of plants to slow wind speeds and reduce sediment transport is closely related to the aerodynamic response to airflow triggered by their morphology (Miri et al., 2017). In addition to vegetation cover, the protective effect of shrub vegetation against surface wind erosion is impacted by factors such as vegetation shape and plant distribution pattern (Zheng et al., 2022). Numerous studies have shown that by increasing the surface roughness (Jiang et al., 2024), the above-ground part of the vegetation can, on the one hand, reduce the surface wind speed and weaken the sand-carrying force of the wind (Mayaud et al., 2016); on the other hand, it can intercept the wind-sand flow and promote the sedimentation of sand particles, thus playing a role in preventing the wind and blocking the sand (Kang et al., 2024). In arid sandy areas, due to climate and moisture conditions, it is difficult to achieve the ideal state of vegetation cover, height, and shape needed to resist wind and sand hazards in a short period. Consequently, it is of practical significance to analyze the influence of plant morphological parameters on sediment grain size distribution and select well-adapted sand plants for specific areas to maintain ecological stability of the transition zone and recovery of desert sandy soil.

Under field conditions, most of the research is carried out on the impacts of vegetation cover and structural characteristics on wind

erosion, and some scholars have found through field research that adjusting the shrub structure of the same configuration of windbreak forests can improve their effectiveness in windbreaks and sand fixation (Zhao et al., 2024). With the deepening of research in desertification control, the prevention of wind and sand fixation through plants and the protection of soil quality in sandy areas have become the focus of research (Guo et al., 2024). However, there are fewer studies on the effect of individual morphology of shrub plants on near-surface windbreaks and sand fixation, especially on the effect of morphological characteristics of sand-fixing vegetation on sediment grain-size distribution in the transition zone of Ulan Buh Desert-Oasis. In arid and sandy areas, the distribution of particle size has a significant effect on the intensity of wind erosion, material transport, and accumulation patterns on the surface and is the result of the natural screening of particles by near-surface winds through the complex process of erosion and deposition (Zhang et al., 2024). Taller plants and wider canopies promote the deposition of more sand particles, especially fine particulate matter, which is more readily immobilized by vegetation, thereby altering the sediment grain size distribution. The shading effect of vegetation branches and leaves reduces the scouring and transport of surface sand particles by wind-sand currents and promotes the deposition of sand particles near the vegetation, forming wind-shadowed dunes, which further enhances the sand-fixing capacity (Dupont et al., 2014). Therefore, the study of the effect of plant morphological indicators on sediment grain size distribution can quickly infer the dynamic changes of wind-sand transport near the ground, which is important for evaluating the wind and sand-fixing ability of different plant species (Cao et al., 2022).

In this study, we analyzed the grain size distribution of sediments and the characteristics of plant morphological parameters under cover of five desert plants in the Ulan Buh Desert-Oasis transition zone in the Inner Mongolia Autonomous Region, China, with the aim of: 1) Characterize the grain size distribution of surface sediments after types of plants have covered the surface; 2) To explore the relationship between sediment grain size parameters and plant morphological parameters; 3) To investigate the effect of plant morphological parameters on sediment grain size distribution. To analyze the role of different sand-fixing plants in the desert-oasis transition zone on the surface wind and sand activities, to provide a specific scientific basis for the screening of wind and sand-fixing plant species in the study area.

2 Materials and methods

2.1 Study area

The study area is 20 km southwest of Dengkou County, Inner Mongolia Autonomous Region, China (40.191°N, 106.839°E). The region is part of a temperate continental climate zone with strong northwesterly winds and frequent dust storms in the spring. The average annual temperature is stable at 7.5~8.1°C, the average annual precipitation is 142.7 mm, and the potential evaporation is 2258.8 mm. The mean annual wind speed is about 3.7 m/s, and the number of days with high winds is 10~32 days per year, especially during March ~ May in spring, and northwesterly and southwesterly winds dominate the wind direction. Mobile dunes of 6 ~ 15 m are widely distributed in the study area, with dune densities exceeding 0.8. The hard red clayey texture is widely distributed in the lowlands between the mounds and is covered by a sandy layer of varying thickness, ranging from 10 to 50 cm. Pioneer plants such as *Psammochloa villosa*, *Agriophyllum squarrosum*, *Artemisia ordosica*, *Phragmites australis*, *Nitraria tangutorum*, etc., are scattered on the dune slopes. In the distribution area of N.*tangutorum* shrub, the stability of sand dunes was significantly improved, and the height of these sandbags was primarily concentrated in the range of 0.5~5 m, and their surface was covered with finer-grained sandy material with a softer texture. The vegetation distribution in the study area is characterized as shown in (Table 1).

2.2 Sample collection

The selected sample site is a typical flat bare sandy land with homogeneous topography, where vegetation is the dominant factor influencing the wind speed and direction in the area. Sample plots were laid out to minimize the distance between plots while meeting the ecological minimum interval scale. Differences in the subsurface of the samples are mainly caused by differences in vegetation, the presence of which leads to changes in airflow and wind speed and direction, making vegetation the most significant control of the subsurface. Field measurements and sampling were conducted in late March 2024, which is usually the strongest wind in the study area in 1 year. Different sand-fixing plants (N. *tangutorum*, A. *ordosica*, P. *australis*, A. *squarrosum*, P. *villosa*) in the plot were selected as the research target, and the bare dunes were selected as the control (CK). Five 5 m × 5 m sample squares were set up for each plant species to be investigated, and four plants with good growth conditions and uniform morphology were selected as standard plants within each sample square, totaling 100 standard plants. Crown spread and plant height were measured, and the number of branches on the whole plant and the sparsity of the lateral projection of the plant were measured by photographic methods (Torita and Satou, 2007). A total of 20 plants of each species were measured, distributed over a 2 km^2 area. Figure 1 shows a rose diagram of sand fixing plants and wind direction in the study area (Figure 1). Photographic method: Lateral projection images of plants were taken under standard lighting conditions using a high-resolution digital camera. After denoising and contrast enhancement preprocessing, the separation of pore space from plant tissues was achieved by threshold segmentation. And the image processing software was used to calculate the pore area and the total projected area, and finally the porosity was calculated by the ratio of pore area to total projected area. To ensure the quality of the images and the accuracy of the porosity measurements, the photographs were taken under conditions where the sky was mostly covered with clouds but with a small amount of blue sky still visible, the light was soft and there was no noticeable harsh sunlight or dark shadows, there was no precipitation, there was no wind, and the cloud cover was stable. The porosity data we obtained is not in a particular direction, but is the average value in each direction calculated by selecting plants with relatively uniform growth and conformation, photographing them from multiple angles in eight directions, and combining them with advanced digital image processing algorithms.

Concentric circles were drawn around the base of a single plant as a core, with the inner circle radius being half the average crown width of the plant and the outer circle radius coinciding with the

TABLE 1 Characteristics of vegetation distribution in the study area.

Plant species	Habitat	Status of distribution	Density/(Plant·m^2)
P. villosa	Mobile sand dune	Independent distribution	0.12
P. *australis*	Mobile sand dune	Community distribution	0.41
A. squarrosum	Mobile sand dunes and semi-fixed sand dunes	Independent distribution	0.22
A. ordosica	Mobile sand dunes and semi-fixed sand dunes	Community distribution	0.23
N. tangutorum	Semi-fixed sand dunes and fixed sand dunes	Community distribution	2.54

Note: Five 5 m × 5 m quadrats were investigated for each plant.

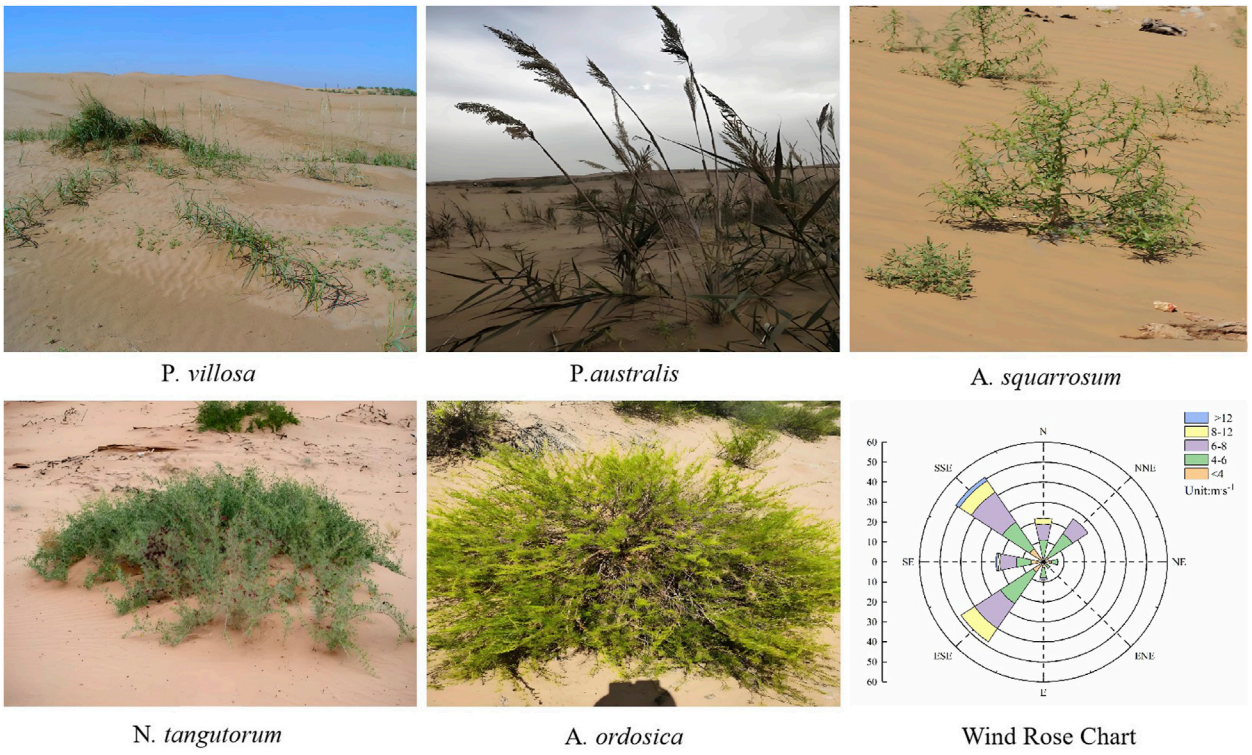

FIGURE 1
Photographs of sand-fixing plants in the study area and wind rose chart.

average crown width. Sediment samples with a surface depth of 2 cm were taken at four directional points, east, south, west, and north of the concentric circles. For the sampling of shrub sand piles, the center point of the shrub was used as the datum to ensure that the sampling area did not extend beyond the boundaries of the shrub, and sediment samples were collected at the appropriate depth in each direction as described above (Figure 2). All sediment samples beneath the same single plant were combined and thoroughly mixed to produce a mixed sediment sample of approximately 50 g. Twenty mixed samples were ultimately collected from each plant. Twenty bare dune samples were also collected as controls, for 120 mixed sediment samples. Winds in the study area are responsible for the transport of sandy material, surface erosion and accretion in multiple directions, but we are primarily concerned with wind-sand deposition processes dominated by the plant canopy itself. Concentric circle sampling covering multiple wind directions can eliminate the interference of a single wind direction on the sampling results, thus reflecting more comprehensively the integrated influence of plants on wind-sand deposition, revealing comprehensively the role of plants in regulating airflow and sediment, and providing a scientific basis for the study of spatial heterogeneity of wind-sand deposition.

2.3 Sediment sample determination

The collected samples were placed in a laboratory environment with smooth air circulation to dry naturally. After removing impurities, coarse particles larger than 2,000 μm were sieved through a 2-mm sieve. Then, ultrapure water and H_2O_2 solution

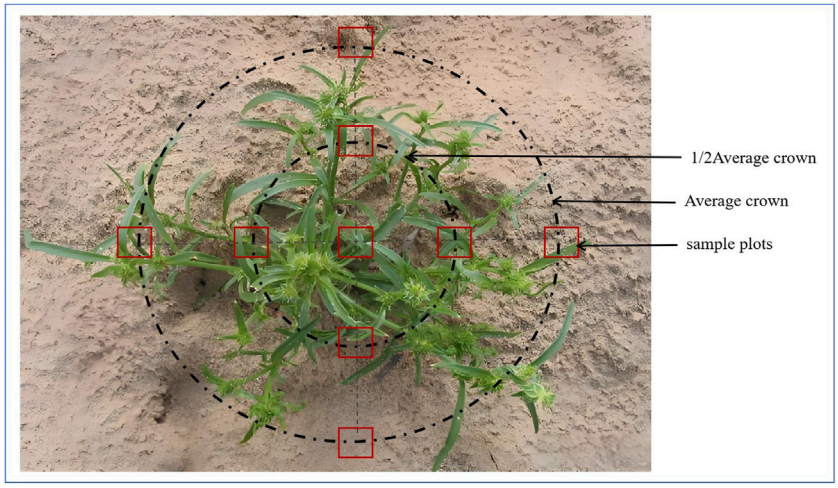

FIGURE 2
Schematic diagram of sample collection around the plant (using A.*squarrosum* as an example).

TABLE 2 Granularity parameter grading standard.

σ		SK		Kg	
≤0.35	Excellent sortability	−1.0~−0.3	Extreme negativity	≤0.67	Very wide
0.35~0.5	Very good sortability	−0.3~−0.1	Negative skewness	0.67~0.90	Wide
0.5~0.71	Better sortability	−0.1~0.1	Asymmetric	0.90~1.11	Medium
0.71~1.00	Medium sortability	0.1~0.3	Positive	1.11~1.56	Narrow
1.00~2.00	Poor sortability	0.3~1.0	Extremely positive	1.56~3.00	Very narrow
2.00~4.00	Very poor sortability			>3.00	Extremely narrow
>4.00	Extremely poor sortability				

were added and left for 24 h to remove organic matter. When no more bubbles are generated in the beaker, place an appropriate amount of the sample in the oven, heating it to dryness, which is used to volatilize all the residual H_2O_2 solution. The samples to be tested were placed in a stationary device, water and 10% HCL solution were added to dissolve the carbonates, and the supernatant was pipetted out after 24 h of stationary time. Test the pH of the sample with a pH meter by adding distilled water to the pH meter in the proper proportion until the pH is nearly neutral. The particle size composition of each sediment sample was determined independently three times using a Mastersizer 3000 high-precision laser particle sizer, and the arithmetic mean of the measurements was subsequently calculated to ensure the accuracy and reliability of the particle size data.

2.4 Particle size parameter model

Based on the Udden-Wenworth particle size classification system, the sediments were classified into six different grain sizes, namely, clay (<4 μm), silt (4–63 μm), very fine sand (63–125 μm), fine sand (125–250 μm), medium sand (250–500 μm), and coarse sand (500–1,000 μm). The Udden-Wentworth system delineates sand grains in great detail and accurately describes their grain size distribution, which helps to analyze the source of sand grains, the transport process and the depositional environment. In addition, the system is closely related to the wind transport capacity and depositional environment, which can better reveal the transport and deposition mechanism of sand grains in the Ulan Buh Desert under the action of wind. The Folk Grain Size Classification System focuses more on a combination of sand shape and sortability in the subdivision of the sand fraction, and is suitable for scenarios where sedimentary rock formation processes are being studied or where a comprehensive characterization of the sediment is required. The Krumbein phi (φ) system uses a logarithmic transformation, which is suitable for statistical analysis and can make the data more consistent with a normal distribution, facilitating hypothesis testing and modeling. Because particle size studies in the Ulan Buh Desert first require clarification of the size distribution of sand grains and their relationship to wind and sand activity, the use of the Udden-Wentworth system meets the need and avoids unnecessary complexity.

According to the Udden-Wenworth particle size classification system, combined with the Kum-dein conversion method, these particle diameters (D) are converted into Φ values according to Equation 1 by performing logarithmic conversion to facilitate more uniform analysis and comparison (Krumbein, 1934).

$$\Phi = -\log_2 D \tag{1}$$

The particle size parameters were calculated from Equations 2–5 using the Folk-Ward plotting method: mean particle size (Mz), sorting coefficient (σ), skewness (SK) and kurtosis (Kg) were calculated (Folk and Ward, 1957). Figures 4a–d were plotted and analyzed according to the grading criteria for particle size parameters (Table 2).

$$Mz = \frac{\Phi_{16} + \Phi_{50} + \Phi_{84}}{3} \tag{2}$$

$$\sigma = \frac{\Phi_{84} - \Phi_{16}}{4} + \frac{\Phi_{95} - \Phi_5}{6.6} \tag{3}$$

$$SK = \frac{\Phi_{16} + \Phi_{84} - 2\Phi_{50}}{2(\Phi_{84} - \Phi_{16})} + \frac{\Phi_5 + \Phi_{95} - 2\Phi_{50}}{2(\Phi_{95} - \Phi_5)} \tag{4}$$

$$Kg = \frac{\Phi_{95} - \Phi_5}{2.44(\Phi_{75} - \Phi_{25})} \tag{5}$$

where: Φ_5, Φ_{16}, Φ_{25}, Φ_{50}, Φ_{75}, Φ_{84}, Φ_{95} are the corresponding quartiles of the grain size distribution.

Mean particle size (Mz) characterizes the average distribution of soil particle size and is commonly used in studies of particle deposition patterns and in tracking particle movement processes. The sorting coefficient (σ) indicates the degree of discrete distribution of soil particles; the smaller its value indicates that the more concentrated the distribution of soil particles, the better the particle sorting. Skewness (SK) reflects the symmetry of the frequency curve of soil particle size, indicating the distribution characteristics of soil particles. Kurtosis (Kg) is a parameter of the concentration degree of soil grain size distribution on both sides of the average particle size, which represents the ratio of the tail expansion degree to the middle expansion degree of the frequency curve or the ratio between the two sides of the soil particle frequency curve and the sorting degree of the middle part. It can quantitatively measure the width and steepness of the peak shape of the soil particle frequency distribution curve. In general, the larger the Kg value, the stronger the peak sharpness, indicating that the grain size distribution of the sample is more concentrated.

2.5 Calculation of mean distance between cumulative frequencies of soil particle size

The average distance (d) between the cumulative frequency distribution of soil particle size can reflect the difference in soil quality between plots, which is mutually confirmed with the cumulative frequency curve of soil particle size and can provide evidence for the judgment of soil coarsening. Calculated from Equation 6:

$$d = \sqrt{\sum (P + \bar{P})^2 (K - 1)} \tag{6}$$

where: d is the average distance between the distributions of soil particle size accumulation frequency; P is the soil particle size accumulation frequency of a certain sample site; is the average of soil particle size accumulation frequency of six sample sites; K-1 is the degree of freedom, K = 6.

2.6 Calculation of the fractal dimension

The fractal dimension (D) is widely used in characterizing the structural properties of soils, and its value is related to the number of particles of different sizes in the soil, so it can not only quantitatively indicate the structural characteristics of the soil (Dong et al., 2022), but also reflect the indicators of soil water content, soil fertility, etc., which is widely used in the research of land degradation. In this paper, the volume fractal dimension is calculated by the volume content of different diameter particles of soil measured by the Mastersizer 3000 laser particle size analyzer. The calculation method is as follows (Equation 7):

$$\left(\frac{R_i}{R_{max}}\right)^{3-D} = \frac{V(r < R_i)}{V_T} \tag{7}$$

where D is the fractal dimension; r is the diameter of soil particles (mm); r_i is the diameter of a certain diameter soil particle (mm); V $(r < R_i)$ is the volume percentage of soil particles smaller than R_i diameter particles (%); V_T is the total volume percentage of particles in each diameter grade (%); R_{max} is the maximum particle diameter (mm).

2.7 Statistical analysis

Excel 2021 was used to preliminarily sort out and analyze the data, and the mean value and standard deviation were calculated. SPSS 22 was used for one-way analysis of variance, and the significance test of grain size parameters and morphological parameters of sediments under different vegetation coverage was carried out ($P < 0.05$). LSD method was used for multiple comparisons, and Origin 2021 was used to draw relevant graphs.

3 Results and analysis

3.1 Plant modality features

From Figure 3, it can be seen that the average plant height of N. *tangutorum*, P. *villosa*, A. *squarrosum*, P. *australis,* and A.*ordosica* is 116 cm, 143 cm, 52 cm, 72 cm, and 77 cm, respectively, (Figure 3a). Of these, N. *tangutorum* had the largest crown, averaging 283 cm which was significantly higher than the other four species; P. *australis* had the smallest crown, averaging 58 cm; The crowns of P. *villosa*, A. *squarrosum* and A. *ordosica* ranged from 100–130 cm (Figure 3b). The average number of branches of N. *tangutorum* was 385, while the number of branches of P.

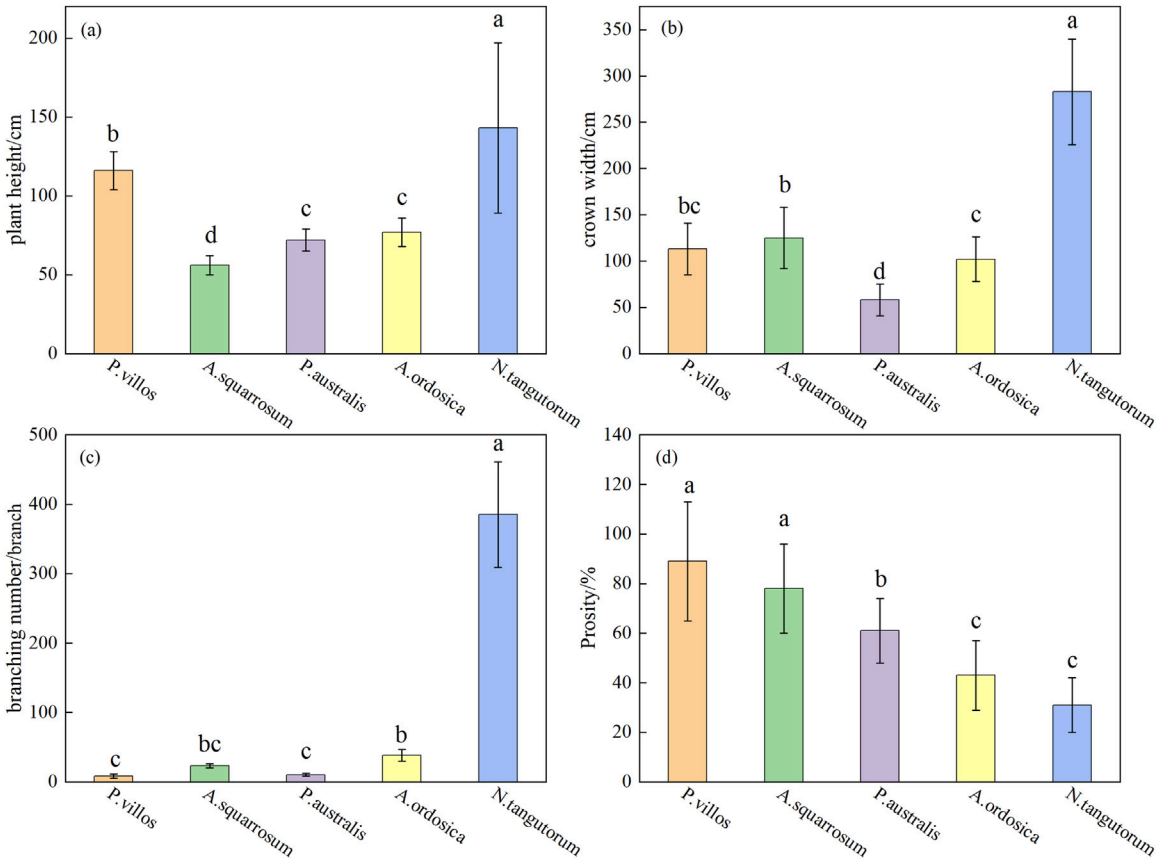

FIGURE 3
Morphological characteristics of plants.

TABLE 3 Mechanical composition of sediments covered by different plant species (%).

Sample area	Clay	Silt	Very fine sand	Fine sand	Medium sand	Coarse sand
P. villosa	0.10 ± 0.00c	1.25 ± 0.21d	15.74 ± 4.87c	52.03 ± 13.20ab	30.74 ± 5.15ab	0.14 ± 0.02a
A. squarrosum	0.10 ± 0.01c	1.53 ± 0.27d	18.13 ± 4.33bc	49.06 ± 9.37b	31.10 ± 6.44ab	0.08 ± 0.02b
P. australis	0.10 ± 0.00c	2.38 ± 0.63c	26.75 ± 5.17b	45.63 ± 6.42b	25.14 ± 3.99b	—
A. ordosica	0.81 ± 0.14b	11.04 ± 2.34b	37.71 ± 7.39a	37.06 ± 6.84c	13.38 ± 3.17c	—
N. tangutorum	2.46 ± 0.39a	36.28 ± 8.38a	23.58 ± 4.28b	27.21 ± 5.31d	10.34 ± 2.01c	0.13 ± 0.03a
CK	0.10 ± 0.01c	0.72 ± 0.14e	3.08 ± 0.55d	60.61 ± 15.85a	35.43 ± 6.08a	0.06 ± 0.01b

Note:The lowercase letters represented significant differences between different plants of the same grain size (LSD, $P < 0.05$), CK is the control (Bare sand dunes), same below.

villosa and P. *australis* was less, 8.35 and 10.35, respectively (Figure 3c). Significant differences were found among the five plants in terms of mean grain size, crown width, number of branches and porosity ($P < 0.05$).In the unit area, the order of porosity from large to small is: P. *villosa* > A. *squarrosum* > P. *australis* > A. *ordosica* > N. *tangutorum*. The porosity of P. *villosa* is the largest, indicating that the density of branches and leaves is the smallest, while the porosity of N. *tangutorum* is the smallest and the branches are the densest (Figure 3d).

3.2 Characteristics of sediment interception by plants

3.2.1 Characteristics of mechanical composition of sediment intercepted by plants

The mechanical composition of the sediment intercepted by the five plants is shown in Table 3. The fine sand and medium sand in the surface sediments of bare dunes are absolutely dominant, and their volume percentages are 60.61% and 35.43%, respectively. The

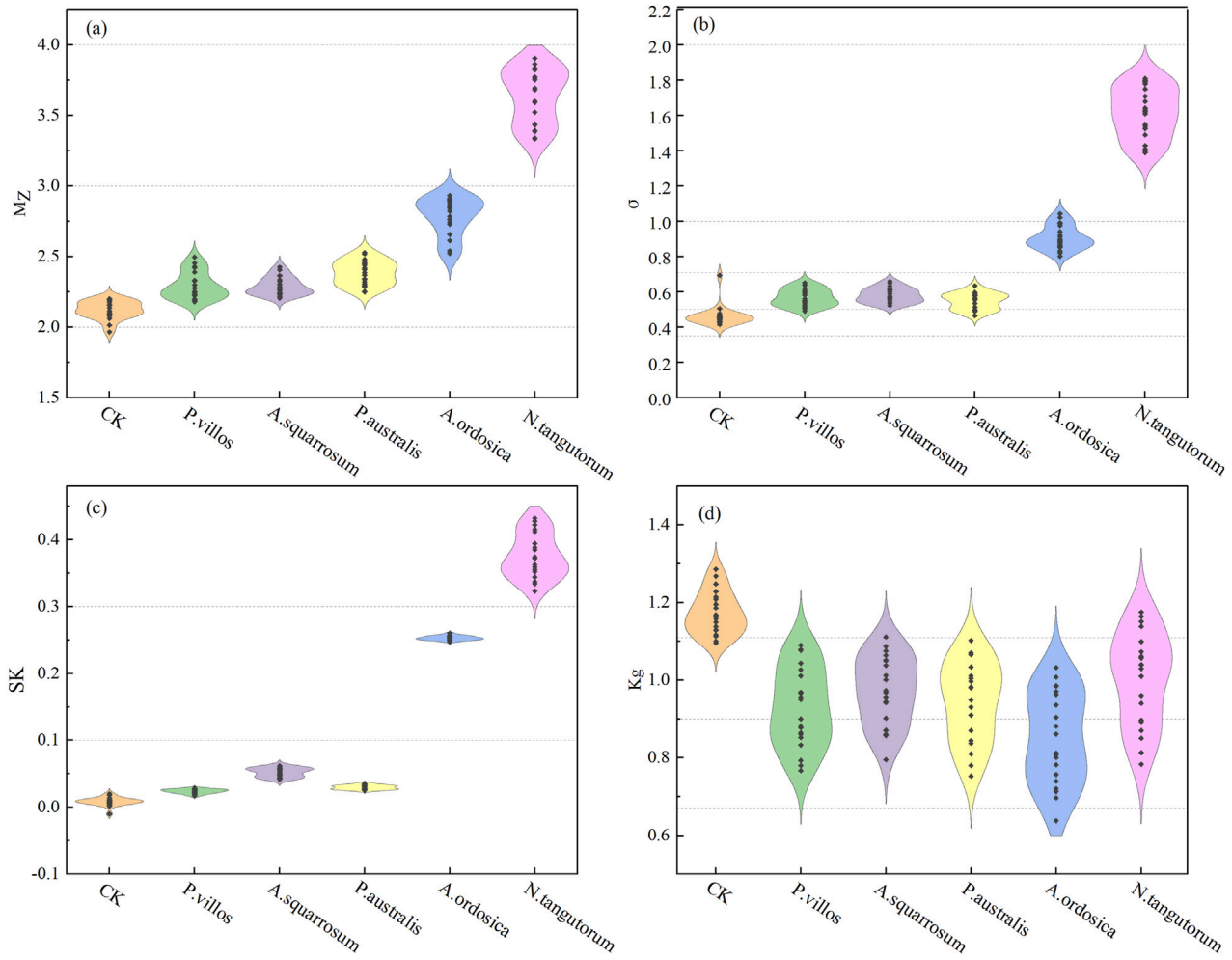

FIGURE 4
Grain size characteristics of sediments under different plant coverage.

trend of fine particle size of sediments after vegetation coverage is more obvious; the volume percentage of very fine sand, clay, and silt increases, and the volume percentage of fine sand and medium sand decreases. The variation trend of clay, silt, and very fine sand is basically the same, and the volume percentage is N. *tangutorum* > A. *ordosica* > P. *australis* > A. *squarrosum* > P. *villosa* > CK. The change trend of volume percentage content of fine sand and medium sand is basically the same, and its change trend under different plant coverage is opposite to that of fine particles such as silt and very fine sand. The change trend of volume percentage content of fine sand and medium sand is basically the same, and its change trend under different plant coverage is opposite to that of fine particles such as silt and very fine sand. The volume percentages of clay and silt in N. *tangutorum* sediment particles were the highest, at 2.46% and 36.28%, respectively. The contents of clay and silt were significantly higher than those of the other four vegetations ($P < 0.05$). The contents of fine sand and medium sand were significantly reduced ($P < 0.05$), and there was a small amount of coarse sand. Vegetation coverage significantly increased the content of fine particles in surface sediments ($P < 0.05$). The particle composition is mainly composed of fine sand, from coarse to fine: CK > P. *villosa* > A. *squarrosum* > P. *australis* > A. *ordosica* > N. *tangutorum*.

3.2.2 Grain size parameters of sediment intercepted by plants

The mean particle size of these five plantings showed: N. *tangutorum* > A. *ordosica* > P.*australis* > A. *squarrosum* > P. *villosa* > CK. According to the classification standard of the Folk-Ward graphic method, except that N.*tangutorum* is very fine sand, the rest are fine sand. The increase in the Φ value of the mean particle size of the sediment indicates a significant increase in the content of fine particles, indicating that the content of fine particles in the sediments of N.*tangutorum* and A.*ordosica* was significantly higher than that of the other three vegetations ($P < 0.05$). The mean particle size of sediments under different plant coverage was significantly different from that of CK ($P < 0.05$). N.*tangutorum* and A.*ordosica* have dense branches and leaves and relatively high plant morphology, which can form better surface coverage. The strong blocking effect on wind and sand allows the retention of fine particles in the sediment, so the Φ value of the average particle size is larger (Figure 4a).

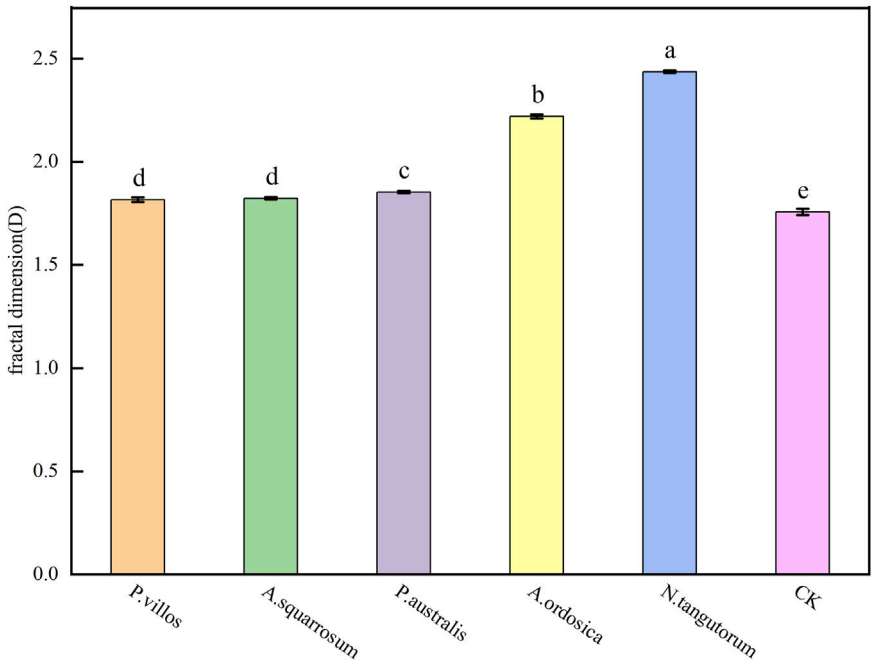

FIGURE 5
Fractal dimension of sediments covered by different plants.

According to Figure 4b, the sorting coefficient of sediments covered by vegetation is as follows: N. *tangutorum* > A. *ordosica* > A. *squarrosum* > P. *villosa* > P. *australis* > CK. The sorting levels are poor sorting, medium sorting, better sorting, better sorting, better sorting and very good sorting. With the emergence of vegetation, the sorting of particles became worse. Compared with A. *ordosica* and N. *tangutorum*, the sorting characteristics of surface sediment particles covered by P. *villosa*, P. *australis,* and A. *squarrosum* were better. The sorting coefficient of sediments under different plant coverage was significantly different from that of bare sand dunes ($P < 0.05$). By effectively reducing the wind speed, N.*tangutorum* and A.*ordosica* deposited larger particles near the vegetation, and the smaller particles were taken away by the wind, forming a deposition pattern with significant differences in particle size, and the sorting coefficient was large. However, P.*villosa*, A.*squarrosum* and P.*australis* have less influence on wind speed, uniform particle deposition and smaller sorting coefficient (Figure 4b).

The particle frequency distribution curves of bare sand dune, P. *villosa*, A. *squarrosum,* and P.*australis* are nearly symmetrical. A. *ordosica* and N. *tangutorum* have a skewness class of positive and very positive skewness, with an asymmetric pattern of surface sediment frequency curves, with the peak of the particle frequency curve biased toward the finer-grained side, where the tails are lower, and the main constituents are fine particles. A significant difference between the skewness of sediments under different plant covers ($P < 0.05$). The dense structure of A.ordosica and N.tangutorum significantly reduced the wind speed, forming a low-speed zone, resulting in coarse particle deposition, particle frequency distribution curve and positive or extremely positive bias. Bare sand dunes, *P. villosa*, *A. squarrosum* and *P. australis* had little effect on wind speed, and the particle deposition was uniform and the skewness was close to zero (Figure 4c).

The peak state of surface sediments covered by P.*villosa*, A.*squarrosum*, P.*australis* and N.*tangutorum* is medium, while the peak state of bare dunes is narrow, and A.*ordosica* is wide. It shows that the particle distribution of A.*ordosica* surface sediments is more dispersed than that of the other four vegetations. Significant differences between the kurtosis of each sediment ($p < 0.05$). Vegetation camping can change the direction and flow rate of the wind-sand flow as well as its internal structure, which promotes the settling of fine particles. The peak state values for sediments with vegetation cover were reduced compared to bare dunes, indicating a more dispersed and refined particle composition. The lack of vegetation cover on bare dunes and the direct action of wind on the surface of sand grains lead to strong jumping and creeping of sand grains under the action of wind. Due to the lack of vegetation, the wind speed is high, the fine particles are blown away, leaving the coarse particles, forming a sharp and narrow peak (Figure 4d).

The fractal dimensions of sediments with different vegetation cover in the study area are shown in Figure 5. Fractal dimension values for the five plant species and the control sediment were, in descending order: N. *tangutorum* > A. *ordosica* > P. *australis* > A. *squarrosum* > P. *villosa* > CK. Fractal dimension was negatively correlated with the content of coarse-grained components (gravel, coarse sand, etc.), which is consistent with the coarse and fine grain compositions of sediments with different vegetation covers in Table 3, where the differences between fractal dimensions of sediments under different vegetation covers were significant ($p < 0.05$). The fractal dimension is enhanced compared to the flowing dune due to the fact that after planting vegetation in the study area, when the wind speed reaches the sand initiating wind speed, the

10.3389/fenvs.2025.1556083

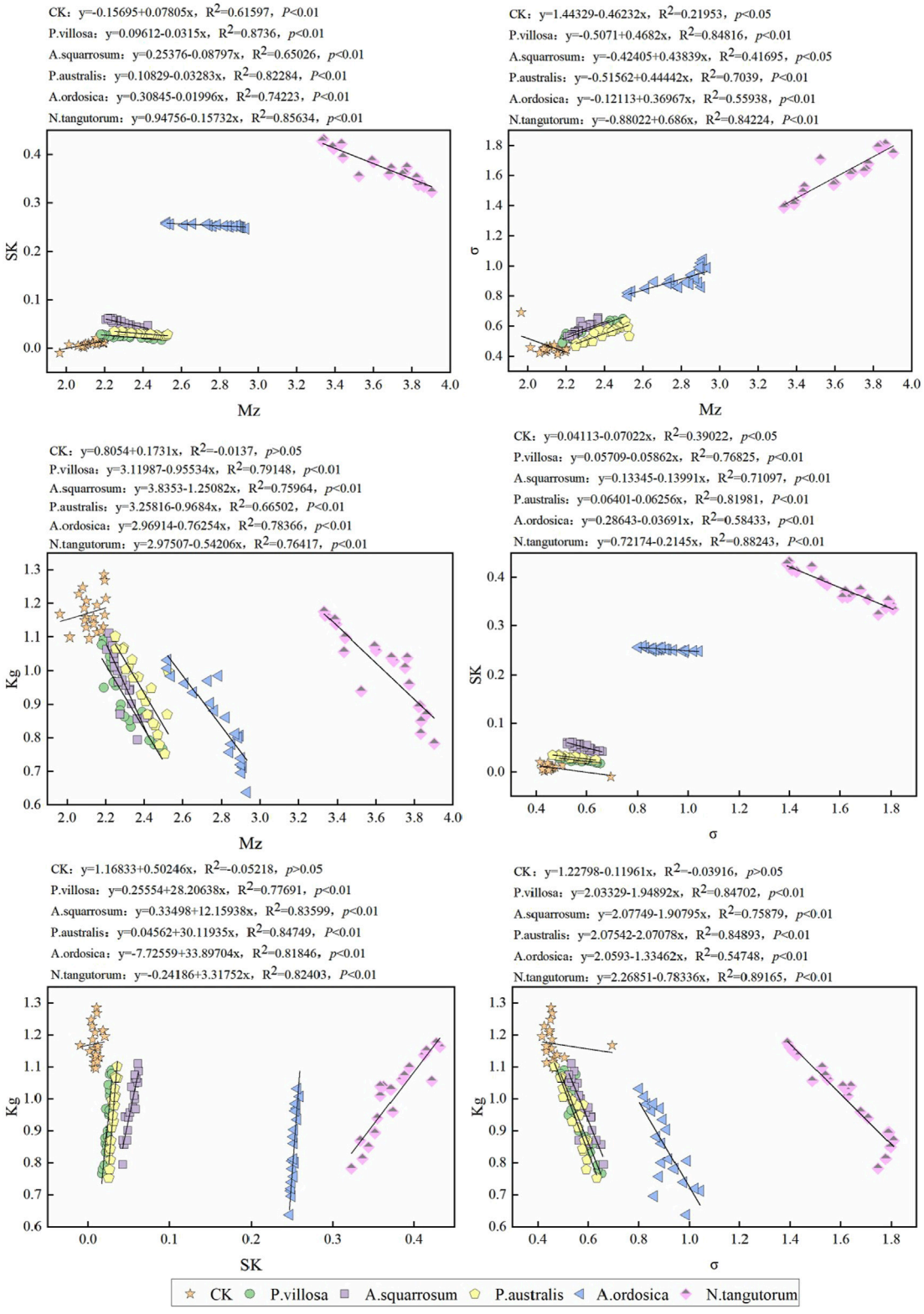

FIGURE 6
Scatter plot of sediment grain size parameters.

wind will carry the sandy material in the air, part of which will be intercepted by the plant canopy, thus accumulating underneath the plant canopy (Figure 5).

In order to visualize the distribution of the grain size parameters of the sample plots under cover of five different plants as well as the surface sediments of the bare sand dune (CK), each sampling point

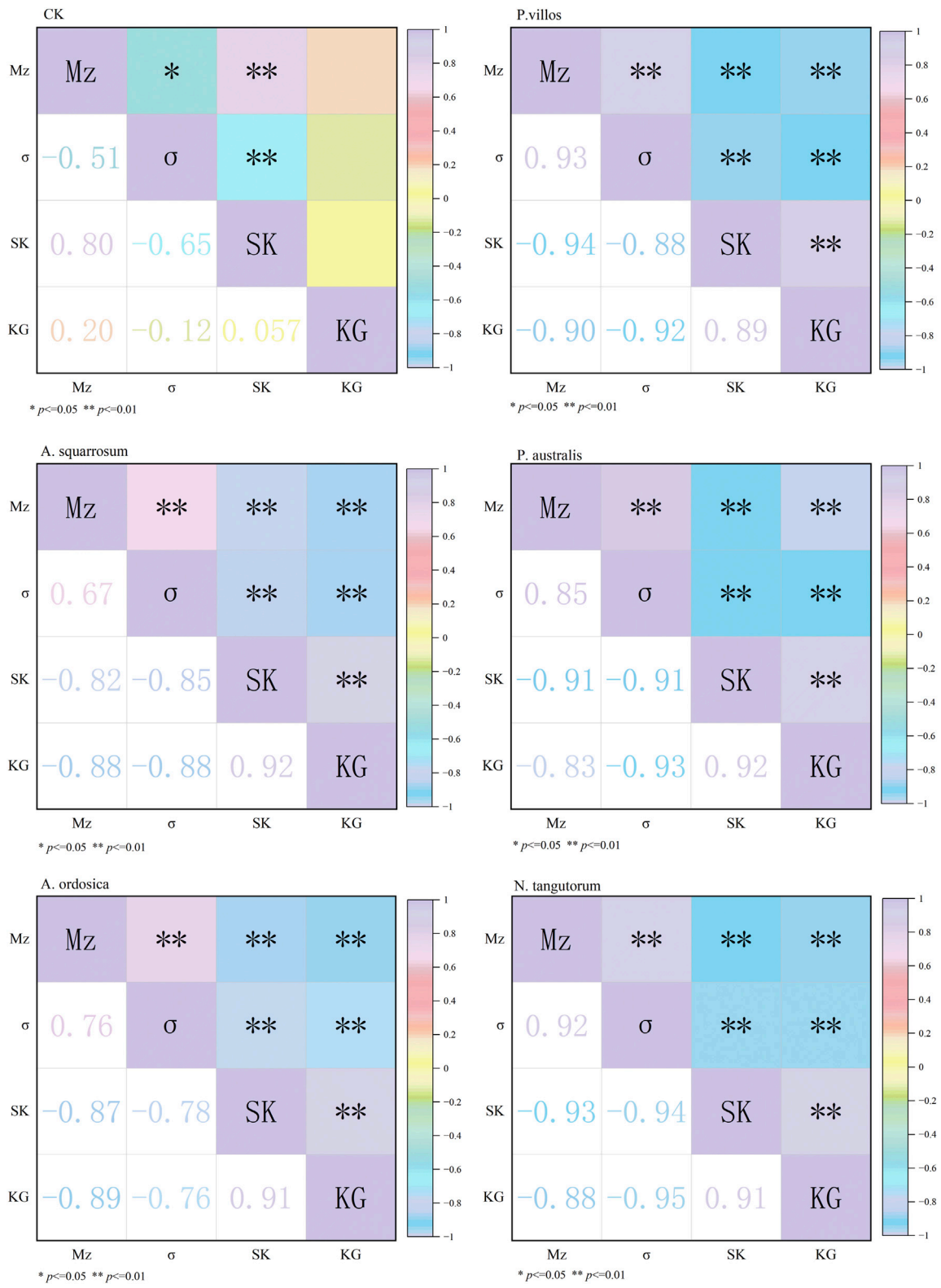

FIGURE 7
Correlation analysis of sediment grain size parameters.

of each plant was used as a data point to produce its scatterplot with its grain size parameters. As can be seen from Figure 6, A. *ordosica* and N. *tangutorum* have clear boundaries with the grain size parameters of CK, P. *australis*, A. *squarrosum*, and P. *villosa*. The scatter plots of each particle size parameter can distinguish them clearly, and the differences among the four sample sites of CK, P.

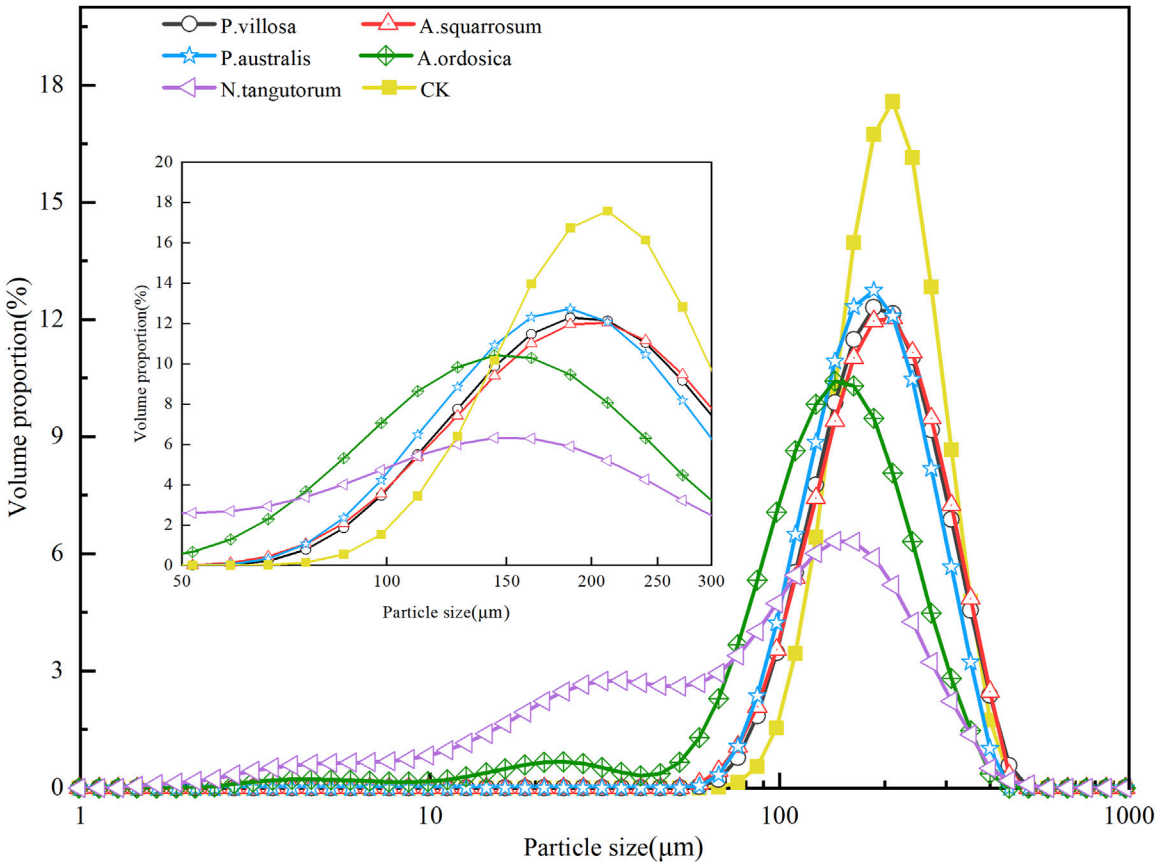

FIGURE 8
Sediment grain size frequency distribution curve.

villosa, A. *squarrosum*, and P. *australis* are not significant, and the scatter plots of particle size parameters show that the distribution of particle size parameters of the five species of plant-trapped sediment ranges from: N. *tangutorum* > A. *ordosica* > P. *villosa* > P. *australis* > A. *squarrosum* > CK. There was a highly significant correlation ($p < 0.01$) between the mean particle size, kurtosis, and sorting coefficient of N. *tangutorum*, P. *villosa*, and R^2 were all greater than 0.84, which was a good fit. There was a highly significant correlation ($p < 0.01$) between the mean particle size, sorting coefficient, and skewness of N. *tangutorum*, P. *australis*, and R^2 were all greater than 0.8, which was a good fit. There was a highly significant correlation between skewness and kurtosis for A. *squarrosum*, P. *australis*, A. *ordosica*, and N. *tangutorum*, ($p < 0.01$), and the R^2 was greater than 0.81, which was a good fit (Figure 6).

3.2.3 Correlation analysis of particle size parameters of plant-trapped sediments

Sorting coefficients of sediments from bare sand dunes showed a significant negative correlation with mean grain size and skewness ($P < 0.05$). The mean grain size of bare sand dune showed a highly significant positive correlation with skewness ($P < 0.01$). The bare sand duned kurtosis does not correlate well with Mean grain size, sorting factor, and skewness. In contrast, the mean grain size of sediments under vegetation cover showed a highly significant positive correlation with the sorting coefficient ($P < 0.01$), and the mean grain size and sorting coefficient showed highly significant negative correlation with kurtosis and skewness ($P < 0.01$), and kurtosis showed highly significant positive correlation with skewness ($P < 0.01$) (Figure 7).

3.2.4 Frequency distribution curves of sediment particles trapped by plants

Figure 8 shows the particle distribution curve of the sediments in the study area. The frequency distribution curve of CK surface sediments has a single-peak pattern, the peak grain size is located near 225 μm, the curve is higher and narrower, and the particle composition is aggregated. The distribution of P. *villosa*, A. *squarrosum*, and P. *australis* surface sediments was consistent with that of CK, all of which were unimodal, with a wider peak shape than that of CK, with smaller peak heights, diversification of particle composition, and a leftward shift of the overall peaks, i.e., the corresponding grain sizes of the peaks became finer, and the peak sizes centered on the 180–200 μm range. The sediment grain size curves of N. *tangutorum* and A. *ordosica* showed an asymmetric bimodal pattern.N. *tangutorum* has a distinct tail peak, A. *ordosica* has a lower tail peak, and the main peak grain size is concentrated near 150 μm, which is a fine sand fraction.The peak heights of the N. *tangutorum* and A. *ordosica* curves were reduced and widened, implying that N. *tangutorum* corresponded to higher levels of fine particulate matter. N. *tangutorum* sediment particles

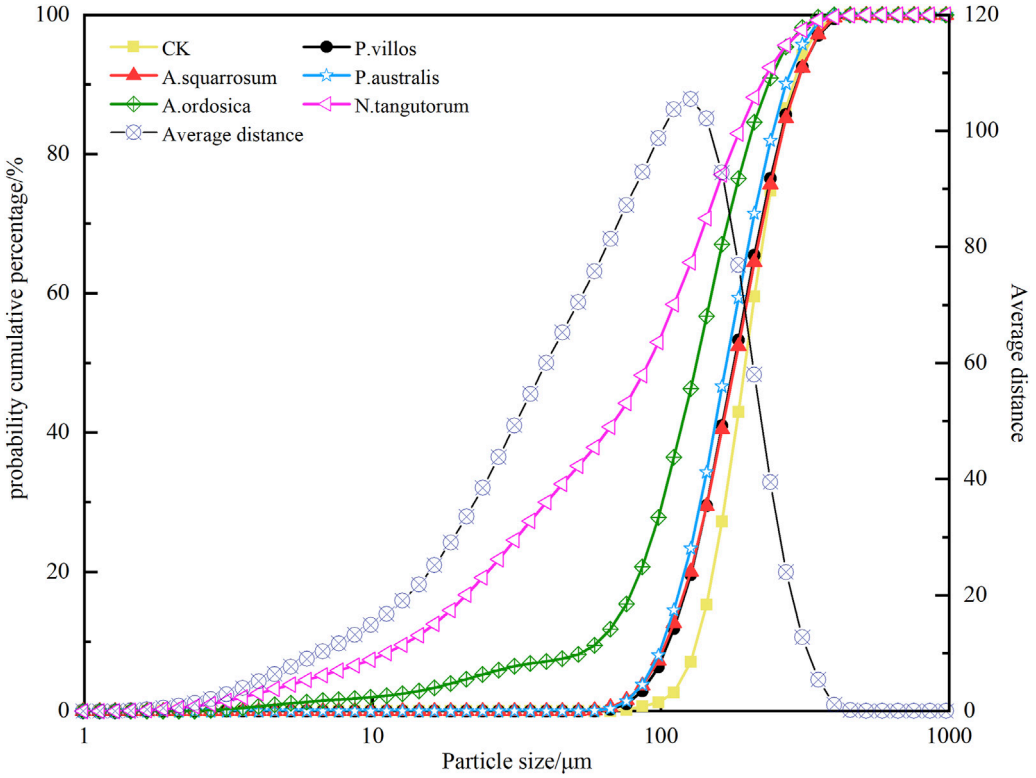

FIGURE 9
Sediment cumulative frequency distribution curve.

have the widest range of distribution and the shortest main peak, followed by A. *ordosica*. The particle distribution ranges from wide to narrow for N. *tangutorum* > A. *ordosica* > P. *australis* > A. *squarrosum* > P. *villosa* > CK. The main peaks are from high to low: CK > P. *australis* > P. *villosa* > A. *squarrosum* > A. *ordosica* > N.*tangutorum*. Due to the decrease of wind speed and particle capture, the particle sorting effect of dunes under vegetation coverage is weakened, and the peak deformation is wide and the peak height is reduced. N.tangutorum and A.ordosica further weakened the particle sorting due to their high vegetation density and complex stem and leaf structure, resulting in a wider particle distribution range, wider peak shape and lower peak height (Figure 8).

As can be seen from Figure 9, the cumulative frequency distribution curve can reflect the distribution of soil particles, and generally, the steeper the curve, the more uniform the distribution of particles. Analyzing the cumulative frequency distribution curves of the surface sediments of the five planted and bare dunes showed that the uniformity of distribution of the surface sediments under the five planted covers showed that N. *tangutorum* was the best and had a finer grain composition, followed by A. *ordosica*. The cumulative distribution curves of A. *squarrosum*, P. *villosa*, and P. *australis* subsurface sediments start off slowly and begin to steepen at about 76 μm, the bare sand dune steepens at about 100 μm and rises rapidly, and flattens out near 400 μm, suggesting that the particles tend to be concentrated in the 76–400 μm range; The sorting coefficients of the sediments under the cove of N. *tangutorum* and A. *ordosica* are larger in Figure 3, which shows that the particle sorting is poorer and finer compared to the other three covers.

Although the surface sediment particle frequency distribution curves (Figure 8) show different types in each sample, the appearance of wave crests and the shape of the curves show some consistency, and there is little difference in the sediment matrices. The mean distance between cumulative frequencies of sediment grain size reflects the grain differences between sample sites and qualitatively describes the range of wind-erosion-prone grains. The average distance between the cumulative frequencies of sediment grain sizes of the six sample sites in this study (Figure 9) was larger in the interval of grain sizes from 70 to 160 μm, and it can be assumed that the range of wind-eroded susceptible particles in the study area is from 70 to 160 μm. In general, it is believed that the wind erosion particle movement is dominated by leapfrog, and 100~150 μm size particles are the most likely to occur in the leapfrog range of particle sizes, and the range of wind erosion particles derived from this study is biased toward the finer particles (Figure 9).

3.3 Relationship between plant-trapped sediments and plant morphology

The results of Pearson's correlation analysis (Table 4) showed that the grain size parameters of sediments under different plant

TABLE 4 The correlation between grain-size parameters of surface sediments and plant morphology parameters.

Particle size parameters	Plant species	Plant height	Crown width	Branching number	Porosity
M_Z	*P. villosa*	0.71**	0.80**	0.84**	−0.76**
	A. squarrosum	0.75**	0.62*	0.72**	−0.67*
	P. australis	0.84**	0.85**	0.76**	−0.74**
	A. ordosica	0.67*	0.71**	0.57*	−0.76**
	N. tangutorum	0.85**	0.79**	0.77**	−0.90**
σ	*P. villosa*	0.80**	0.84**	0.78**	−0.81**
	A. squarrosum	0.77**	0.83**	0.74**	−0.80**
	P. australis	0.78**	0.77**	0.75**	−0.82**
	A. ordosica	0.64*	0.65*	0.72**	−0.78**
	N. tangutorum	0.82**	0.79**	0.75**	−0.86**
SK	*P. villosa*	−0.72**	−0.77**	−0.84**	0.74**
	A. squarrosum	−0.78**	−0.81**	−0.80**	0.79**
	P. australis	−0.84**	−0.83**	−0.74**	0.80**
	A. ordosica	−0.70*	−0.81**	−0.72*	0.75**
	N. tangutorum	−0.80**	−0.81**	−0.70**	0.84**
Kg	*P. villosa*	−0.83**	−0.88**	−0.87**	0.87**
	A. squarrosum	−0.87**	−0.81**	−0.84**	0.82**
	P. australis	−0.64*	−0.68**	−0.65**	0.74**
	A. ordosica	−0.71**	−0.78**	−0.60*	0.82**
	N. tangutorum	−0.83**	−0.72**	−0.77**	0.84**

Note: * indicates that there is a significant correlation at the significance level of 0.05 ($P < 0.05$). * * indicates that there is a significant correlation at the significance level of 0.01 (bilateral) ($P < 0.01$).

species: The mean particle size and sorting were positively correlated with plant height, crown width, and branch number ($P < 0.05$), and negatively correlated with porosity ($P < 0.05$). Skewness and kurtosis were significantly negatively correlated with plant height, crown width, and branch number ($P < 0.05$) and significantly positively correlated with porosity ($P < 0.01$). The correlation coefficients are all above 0.6, which has passed the test level of 0.05.

For different kinds of plants, the morphological parameters of each plant have different effects on the grain size distribution of surface sediments. In this paper, the mean particle size of sediments is used as an index to characterize the grain size distribution of sediments, and the influence of plant morphological parameters on the grain size distribution of surface sediments is analyzed. The mean particle size of P. *villosa* sediment particles had the best correlation with the number of branches, showing a very significant positive correlation ($P < 0.01$).The mean particle size of A. *squarrosum* had the best correlation with plant height, showing a very significant positive correlation ($P < 0.01$). The mean particle size of P. *australis* sediment particles had the best correlation with the crown width, showing a very significant positive correlation ($P < 0.01$), and the correlation coefficient was 0.85. For A. *ordosica* and N. *tangutorum*, the correlation between mean particle size and porosity was the best, showing a very significant negative correlation ($P < 0.01$), and the correlation coefficients were −0.76 and −0.90, respectively.

4 Discussion

4.1 The effect of plants on the distribution of underlying sand particles

The grain size distribution of wind-sand deposits is influenced by vegetation, sand sources, topography, and wind speed, and the presence of vegetation tends to increase surface roughness, alter the near-surface wind field, reduce wind speed, and deposit sand grains (Zhao et al., 2019). As the sand material gradually deposits near the plant, the wind-shadow dunes begin to form. Under the condition of a sufficient sand source, with the continuous development and succession of vegetation, the sand-blocking ability of the vegetation community will be significantly enhanced, and the sediment particles will settle in large quantities. The wind-shadow dunes gradually evolved into shrub dunes, and the dunes eventually tended to be fixed (Yang et al., 2019). Sediment frequency curves are critical for assessing sedimentation patterns. The change in the frequency curve reflects the change in the form of

sedimentation. Due to the addition of foreign or coarse or fine new components, resulting in poor sediment sorting, the frequency curve becomes asymmetric so that the skewness shows a negative bias or positive changes in bias (Pan et al., 2020a). The clay, silt, and very fine sand in the wind-sand flow are blocked by plants. The analysis of sediment particle size parameters under different plant species coverage (Figure 4) shows that the sediment sorting coefficient becomes larger, the sorting becomes worse after vegetation coverage, and the curve shape develops from near symmetry to positive deviation. The peak value of the frequency curve tends to decrease as a whole, and the composition of the sediment particles becomes finer. The peak type of the bare sand dune is unimodal, and the sand pile of N. *tangutorum* and A. *ordosica* shrub is bimodal. The sand grains under P. *villosa*, A. *squarrosum,* and P. *australis* are mainly fine sand and medium sand. The sand material of the A.*ordosica* plot is mainly composed of fine sand and very fine sand. The contents of clay and silt in the sediment particles of N. *tangutorum* were significantly higher than those of the other four vegetations ($P < 0.05$). The above differences in the spatial distribution of particles of different size classes in sediments are supposed to be caused by the different botanical characteristics of plants. This may be mainly due to the fact that A. *ordosica* and N. *tangutorum* communities have higher cover, and denser branches and are clumped together, which increases the surface roughness, and when the wind and sand flow passes through, the wind speed is weakened, and the material carried by the wind and sand flow settles down and increases the content of fine-grained material on the surface (Xiaohong et al., 2019). P. *villosa*, A. *squarrosum*, and P. *australis* plants have relatively obvious main trunks, relatively few and scattered basal branches, and the plants show a sparse structure with a weak sand fixation capacity.

4.2 Differences in particle size parameters and their correlation

The sorting coefficient σ indicates the degree of discrete distribution of soil particles, and an adequate sorting process can effectively improve the degree of sorting of wind-formed sand (Xi et al., 2024). The degree of vegetation cover significantly affects the sorting process of wind-formed sands. The influence of vegetation canopy on the wind-blown sand flow field will cause the sediment to be sorted, and the final deposition around the shrub will form a difference in grain size characteristics (Huang et al., 2024). The effect of vegetation on sorting action is mainly in the following areas: Vegetation cover can effectively reduce wind speed, thus weakening the erosive effect of wind on surface wind-formed sands, weakening the transport of wind-formed sands, intercepting coarse particles in motion, and increasing the content of fine-grained components, reducing the degree of wind-formed sand sorting (Fu et al., 2021). The results of this paper show that the sorting of particles deteriorates with the presence of vegetation. The sorting characteristics of surface sediment particles covered by A. *ordosica* and N. *tangutorum* were poorer compared to the other three plants. The fractal dimension values of A. *ordosica* and N. *tangutorum* were greater than those of the other three species. The value of soil fractal dimension is positively correlated with the content of fine particles such as clay and silt. The increase of fine particle content (clay and silt) will lead to the increase of fractal dimension, which is consistent with the higher content of clay and silt in N. *tangutorum* and A. *ordosica* in Table 3. In this paper, the sediment under vegetation coverage increases with the increase of the mean particle size of sand, the sorting coefficient becomes larger, and the sorting becomes worse. The skewness value decreases with the increase of the mean particle size Φ, indicating that the fine particles increase. The kurtosis value decreases with the increase of the mean particle size, indicating that the distribution range of sand particle size becomes dispersed. The sorting coefficient is negatively correlated with skewness and kurtosis, indicating that the smaller the sorting coefficient, the greater the skewness and kurtosis values; that is, the better the sorting of sand particles, the finer and more concentrated the grain size distribution.

4.3 Mechanisms by which sand plants influence the grain size composition of surface sediments

Vegetation modifies the near-surface flow field mainly by covering the surface, decomposing wind, and blocking sand transport, and different vegetation types lead to differences in sediment composition. Some scholars have studied the relationship between the windproof effect of shrubs and plant morphology through wind tunnel tests, and the results show that the windproof effect increases with the increase of shrub height and coverage, and the windproof efficiency is an exponential function of the relationship with the coverage (Pan et al., 2020b). Wind tunnel experiments have shown that the morphology and structure of the vegetation are preferred parameters to facilitate wind erosion control (Miri et al., 2017). Pan et al.conducted field observations on the wind-proof and sand-fixing effects of simulated shrubs with different configurations, and the results showed that plant morphology had a significant effect on sand-fixing ability (Pan et al., 2021). Studies have shown that the spatial differences in particle size composition and particle size parameters of sediments under shrubs are caused by the height, crown width, and coverage of shrubs themselves. The plant height and crown width were significantly positively correlated with the sand retention area, and the volume fraction of fine components in surface sediments was positively correlated with plant height, crown width, and branch number. With the increase in vegetation coverage, the sand-fixing and sand-blocking ability of vegetation increased, and the mean particle size of the soil decreased (Liu et al., 2020). The mean particle size of sediments in this study was significantly positively correlated with plant height, crown width, and branch number ($P < 0.05$), which was the same as the existing research results. Some scholars analyzed the distribution of soil particle size under different vegetation coverage, and all believed that the mean particle size of soil became thicker with the gradual decrease of vegetation coverage. In this paper, through the analysis of the particle size characteristics of surface sediments, it is concluded that the particle composition from coarse to fine is: CK > P.*villosa* > A.*squarrosum* > P.*australis* > A.*ordosica* > N.*tangutorum*. The Φ value of mean particle size was positively correlated with plant height, crown width, and branch number and negatively correlated with porosity. This shows that the plant species with high plant

community, dense branches and leaves, and high canopy density have fine sediment particles under their coverage and have strong sand fixation and sand blocking abilities; On the contrary, the plant species with sparse distribution and fewer branches and leaves, such as P.*villosa*, A.*squarrosum*, and P.*australis*, do not have strong sand-fixing ability. There are significant differences in sediment grain size parameters of different vegetation types. From the perspective of the influence of vegetation on the differential deposition of surface sediments, the height, crown type, and porosity of vegetation have great differences in the grain size characteristics of sediments, and the sand-blocking effect of compact vegetation is obvious. The vegetation with tall plants, wide crowns and dense branches and leaves can change the speed and direction of wind-blown sand flow in a larger spatial range, so that sand particles can be deposited in a wider area, and the screening effect on sand particle size is more obvious, resulting in more significant spatial differentiation of sand particles. With the increase of vegetation coverage, the grain size of sand around the dune is gradually refined, which weakens the transport capacity of wind-sand flow and promotes the deposition of fine particles due to the fixation of vegetation. The effect of short and sparse vegetation on wind-blown sand flow is relatively small, and the spatial differentiation of sand particles is relatively weak. The difference in morphological characteristics leads to the change of flow field around dunes, which affects the spatial differentiation of sand particle size characteristics.

4.4 Screening and synergistic effect of windbreak and sand-fixing plants

Our research is of great significance for guiding the screening and cultivation of windbreak and sand-fixing plants. In arid wind and sandy areas, many scholars have thoroughly explored the preferred strategies for wind and sand blocking forest trees. It was revealed that compact-structured shrubs such as N. *tangutorum* and A. *ordosica* exhibited more significant wind and sand blocking efficacy compared to sparsely structured herbs such as P. *australis*, P. *villosa*, and A. *squarrosum*. As the main sandy shrub in the study area, N. *tangutorum* has higher sand fixation and soil conservation ability than other vegetation. The shrub growth is concentrated and clustered, and the protection range is large, so it can be used as an excellent sand-fixing shrub in the study area (Li et al., 2024). A.*ordosica* also plays an indispensable role in windbreaks and sand fixation with its compact plant structure, complementing N. *tangutorum* and building a solid windbreak together. As for P. *australis*, P. *villosa*, and A. *squarrosum*, although their direct effect in preventing wind and blocking sand may be a little less effective, they form a sparse structure that contributes to the dispersion and slowing down of the wind, and at the same time, these plants can intercept and immobilize fine-grained materials to a certain extent, contributing to the improvement of soil properties. They each assume different roles, are interdependent and together constitute a multi-level protection system. It not only effectively intercepts the fine-grained material in wind-sand and reduces soil erosion but also provides the possibility of gradual improvement of soil properties through the cementing effect of the plant root system and the shading effect of the above-ground part. This diversified protection system is expected to have a strong, comprehensive effect on soil fertility enhancement, structural stabilization, and ecological restoration, laying a solid foundation for ecological management and sustainable development of the arid sandy wind area.

5 Conclusion

In this paper, the grain size distribution of surface sediments and morphological characteristics of plants under cover of five species of sand plants in the Ulan Buh Desert were determined. The effects of plant morphological parameters on sediment grain size distribution were analyzed to explore the inhibitory effect of vegetation cover on surface wind and sand activities and to compare the windproof and sand-fixing ability of sandy plants, which can provide a management basis for the screening of sand-fixing plants in desert areas.

(1) In the unit area, the porosity from large to small is: P. *villosa* > A. *squarrosum* > P. *australis* > A. *ordosica* > N. *tangutorum*, The porosity of P. *villosa* was the largest, indicating that its branch and leaf density was the smallest, while the porosity of N.*tangutorum* was the smallest and the branches were the densest.

(2) The distribution of surface sand material in P. *villosa*, A. *squarrosum*, and P. *australis* plots is the same as that of bare sand dunes, all of which are unimodal, while N. *tangutorum* and A. *ordosica* are bimodal. The particle distribution range from wide to narrow is: N. *tangutorum* > A. *ordosica* > P. *australis* > A. *squarrosum* > P. *villosa* > CK, After vegetation coverage, the content of fine sand and medium sand in surface sediments decreased, and the content of very fine sand, clay, and silt increased. Compared with bare sand dune, the sorting of sediment particles became worse, the curve tended to be positive, and the kurtosis value decreased. On the whole, the particle composition from coarse to fine is CK > P. *villosa* > A. *squarrosum* > P. *australis* > A. *ordosica* > N. *tangutorum*.

(3) Mean grain size of sediments under vegetation cover showed a highly significant positive correlation with sorting coefficient and kurtosis with skewness ($P < 0.01$). Mean particle size and sorting coefficient showed a highly significant negative correlation with peak state and skewness ($P < 0.01$). Mean particle size and sortability were significantly and positively correlated with plant height, crown width, and number of branches ($P < 0.05$) and significantly and negatively correlated with porosity ($P < 0.05$). Skewness and kurtosis were significantly and negatively correlated ($P < 0.05$) with plant height, crown width, and number of branches and highly significantly and positively correlated ($P < 0.01$) with porosity.

(4) As the main sandy shrub in the study area, N. *tangutorum* has strong sand fixation and soil conservation ability, which can effectively block the fine particles in the wind-sand flow and play a vital role in soil improvement and ecological protection.

Data availability statement

The original contributions presented in the study are included in the article/supplementary material, further inquiries can be directed to the corresponding author.

Author contributions

HA: Conceptualization, Investigation, Methodology, Visualization, Writing–original draft. FZ: Conceptualization, Methodology, Supervision, Writing–review and editing. HL: Investigation, Methodology, Writing–original draft. ZM: Conceptualization, Funding acquisition, Methodology, Writing–review and editing. HD: Methodology, Writing–review and editing. YD: Investigation, Methodology, Writing–original draft. LQ: Methodology, Writing–review and editing. JX: Conceptualization, Funding acquisition, Writing–original draft.

Funding

The author(s) declare that financial support was received for the research, authorship, and/or publication of this article. This study was supported by the Technology Integration and Demonstration of Integrated Management of Landscape, Forests, Fields, Lakes, Grasses and Sands (2024YFF1306305), Basic Research Funds for Universities-Innovation Team Building-Desert Ecosystem Protection and Restoration Innovation Team (BR22-13-03), Inner Mongolia Agricultural University establishes a research base for forging a strong sense of Chinese national community (ZLJD24033).

Conflict of interest

The authors declare that the research was conducted in the absence of any commercial or financial relationships that could be construed as a potential conflict of interest.

Generative AI statement

The author(s) declare that no Generative AI was used in the creation of this manuscript.

Publisher's note

All claims expressed in this article are solely those of the authors and do not necessarily represent those of their affiliated organizations, or those of the publisher, the editors and the reviewers. Any product that may be evaluated in this article, or claim that may be made by its manufacturer, is not guaranteed or endorsed by the publisher.

References

Amiraslani, F., and Dragovich, D. (2011). Combating desertification in Iran over the last 50 years: an overview of changing approaches. *J. Environ. Manag.* 92, 1–13. doi:10.1016/j.jenvman.2010.08.012

Cao, X., Jiao, J., Li, J., Qi, H., Bai, L., Wang, X., et al. (2022). Morphometric characteristics and sand intercepting capacity of dominant perennial plants in the Eastern Qaidam Basin: implication for aeolian erosion control. *CATENA* 210, 105939. doi:10.1016/j.catena.2021.105939

Dong, Z., Mao, D., Ye, M., Li, S., Ma, X., and Liu, S. (2022). Fractal features of soil grain-size distribution in a typical Tamarix cones in the Taklimakan Desert, China. *Sci. Rep.* 12, 16461. doi:10.1038/s41598-022-20755-x

Dupont, S., Bergametti, G., and Simoëns, S. (2014). Modeling aeolian erosion in presence of vegetation. *JGR Earth Surf.* 119, 168–187. doi:10.1002/2013JF002875

Folk, R. L., and Ward, W. C. (1957). Brazos River bar: a study in the significance of grain size parameters. *J. Sediment. Res.* 27 (1), 3–26. doi:10.1306/74D70646-2B21-11D7-8648000102C1865D

Fu, G., Xu, X., Qiu, X., Xu, G., Shang, W., Yang, X., et al. (2021). Wind tunnel study of the effect of planting Haloxylon ammodendron on aeolian sediment transport. *Biosyst. Eng.* 208, 234–245. doi:10.1016/j.biosystemseng.2021.05.018

Gao, F., Lv, K., Jiang, Q., Xiao, H., and Li, J. (2025). How did the regional water-heat distribution in oasis area vary with the different spatial patterns and structures of shelterbelt system—a case study in Ulan Buh desert oasis. *Agric. For. Meteorology* 362, 110345. doi:10.1016/j.agrformet.2024.110345

Gonzales, H. B., Ravi, S., Li, J., and Sankey, J. B. (2018). Ecohydrological implications of aeolian sediment trapping by sparse vegetation in drylands. *Ecohydrology* 11, e1986. doi:10.1002/eco.1986

Guo, X., Yang, G., Wu, J., Qiao, S., and Tao, L. (2024). Impacts of forest age on soil characteristics and fertility quality of *Populus simonii* shelter forest at the southern edge of the Horqin Sandy Land, China. *PeerJ* 12, e17512. doi:10.7717/peerj.17512

Guan, X., Wang, J., Liu, G., Xiao, M., Ding, Y., and Chen, J. (2024). Grain size characteristics of surface sediment in the Jilantai Salt Lake Protection System after long-term wind-sand activities. *Land Degrad Dev* 35, 321–333. doi:10.1002/ldr.4918

Huang, N., Song, Y., Li, X., Han, B., Xu, L., and Zhang, J. (2024). Spatial characteristics of aeolian sand transport affected by surface vegetation along the oshang railway. *Sustainability* 16 (10), 3940. doi:10.3390/su16103940

Hussein, E. A., Abd El-Ghani, M. M., Hamdy, R. S., and Shalabi, L. F. (2021). Do anthropogenic activities affect floristic diversity and vegetation structure more than natural soil properties in hyper-arid desert environments? *Diversity* 13, 157. doi:10.3390/d13040157

Jiang, N., Cheng, H., Liu, C., Fang, Z., and Zou, X. (2024). A wind tunnel study of the effects of vegetation structural characteristics on the airflow field. *CATENA* 242, 108064. doi:10.1016/j.catena.2024.108064

Kang, L., Zhang, M., Li, C., and Yang, Z. (2024). Effect of plant shapes on sand transport rate and aerodynamic particle entrainment rate from the perspective of plant drag. *CATENA* 237, 107818. doi:10.1016/j.catena.2024.107818

Khalilimoghadam, B., and Bodaghabadi, M. B. (2020). Factors influencing the relative recovery rate of dunes fixed under different sand-fixing measures in southwest Iran. *CATENA* 194, 104706. doi:10.1016/j.catena.2020.104706

Krumbein, W. C. (1934). Size frequency distributions of sediments. *SEPM JSR* 4. doi:10.1306/D4268EB9-2B26-11D7-8648000102C1865D

Li, X., Liu, H., Li, C., and Li, Y. (2024). A systematic review on the morphology structure, propagation characteristics, resistance physiology and exploitation and utilization of *Nitraria tangutorum* Bobrov. *PeerJ* 12, e17830. doi:10.7717/peerj.17830

Li, X., Yang, K., and Zhou, Y. (2016). Progress in the study of oasis-desert interactions. *Agric. For. Meteorology* 230–231, 1–7. doi:10.1016/j.agrformet.2016.08.022

Liu, X., Xie, Y., Zhou, D., Li, X., Ding, J., Wu, X., et al. (2020). Soil grain-size characteristics of *nitrariatangutorum* nebkhas with different degreesof vegetation coverage ina Desert-Oasis ecotone. *Pol. J. Environ. Stud.* 29, 3703–3714. doi:10.15244/pjoes/115866

Luo, F., Xiao, H., Gao, J., Ma, Y., Li, X., Li, J., et al. (2022). Microclimate and wind regime of three typical landscapes in the northeastern ulan Buh Desert. *Front. Environ. Sci.* 10, 939739. doi:10.3389/fenvs.2022.939739

Mayaud, J., and Webb, N. (2017). Vegetation in drylands: effects on wind flow and aeolian sediment transport. *Land* 6, 64. doi:10.3390/land6030064

Mayaud, J. R., Wiggs, G. F. S., and Bailey, R. M. (2016). Characterizing turbulent wind flow around dryland vegetation. *Earth Surf. Process. Landf.* 41, 1421–1436. doi:10.1002/esp.3934

Miri, A., Dragovich, D., and Dong, Z. (2017). Vegetation morphologic and aerodynamic characteristics reduce aeolian erosion. *Sci. Rep.* 7, 12831. doi:10.1038/s41598-017-13084-x

Moradi, E., Khosravi, H., Rahimabadi, P. D., Choubin, B., and Muchová, Z. (2024). Integrated approach to land degradation risk assessment in arid and semi-arid Ecosystems: applying SVM and eDPSIR/ANP methods. *Ecol. Indic.* 169, 112947. doi:10.1016/j.ecolind.2024.112947

Pan, X., Wang, Z., and Gao, Y. (2020a). Effects of compound sand barrier for habitat restoration on sediment grain-size distribution in ulan Buh Desert. *Sci. Rep.* 10, 2566. doi:10.1038/s41598-020-59538-7

Pan, X., Wang, Z., Gao, Y., and Dang, X. (2021). Effects of row spaces on windproof effectiveness of simulated shrubs with different form configurations. *Earth Space Sci.* 8, e2021EA001775. doi:10.1029/2021EA001775

Pan, X., Wang, Z., Gao, Y., Zhang, Z., Meng, Z., Dang, X., et al. (2020b). Windbreak and airflow performance of different synthetic shrub designs based on wind tunnel experiments. *PLoS ONE* 15, e0244213. doi:10.1371/journal.pone.0244213

Torita, H., and Satou, H. (2007). Relationship between shelterbelt structure and mean wind reduction. *Agric. For. Meteorology* 145, 186–194. doi:10.1016/j.agrformet.2007.04.018

Van Hateren, J. A., Van Buuren, U., Arens, S. M., Van Balen, R. T., and Prins, M. A. (2020). Identifying sediment transport mechanisms from grain size–shape distributions, applied to aeolian sediments. *Earth Surf. Dynam.* 8, 527–553. doi:10.5194/esurf-8-527-2020

Wang, M., Chen, P., Yi, P., and Ma, T. (2023). Effect of fines content on pore distribution of sand/clay composite soil. *Sustainability* 15, 9216. doi:10.3390/su15129216

Wang, S., Pan, C., Xie, D., Xu, M., Yan, Y., and Li, X. (2022). Grain size characteristics of surface sediment and its response to the dynamic sedimentary environment in Qiantang Estuary, China. *Int. J. Sediment Res.* 37, 457–468. doi:10.1016/j.ijsrc.2021.12.002

Wu, N., Ge, Y., and Abuduwaili, J. (2021). Grain size characteristics of sediments found in typical landscapes in the playa of ebinur lake, arid central asia. *Land* 10, 1132. doi:10.3390/land10111132

Xi, C., Zuo, H., Yan, M., and Yan, Y. (2024). Grain size characteristics of different types of surface sediments around Qixing Lake in Kubuqi Desert. *Front. Environ. Sci.* 12, 1409260. doi:10.3389/fenvs.2024.1409260

Xiaohong, D., Xia, P., Yong, G., Yang, L., Zhenyi, W., and Zhongju, M. (2019). Spatial heterogeneity of wind-eroded soil particles around Nitraria tangutorum nebkhas in the Ulan Buh Desert. *Écoscience* 26 (4), 347–358. doi:10.1080/11956860.2019.1646064

Yang, Y., Liu, L., Shi, P., Zhao, M., Dai, J., Lyu, Y., et al. (2019). Converging effects of shrubs on shadow dune formation and sand trapping. *JGR Earth Surf.* 124, 1835–1853. doi:10.1029/2018JF004695

Zhang, H., Liu, Y., Dang, X., Meng, Z., Li, S., and Gao, Y. (2024). Particle size characterization and sources of sediments in the Uzhumqin sand dunes. *J. Mt. Sci.* 21, 2631–2645. doi:10.1007/s11629-023-8577-5

Zhao, Y., Gao, X., Lei, J., Li, S., Cai, D., and Song, Q. (2019). Effects of wind velocity and nebkha geometry on shadow dune formation. *JGR Earth Surf.* 124, 2579–2601. doi:10.1029/2019JF005199

Zhao, Y., Huang, N., Sun, J., Zhan, K., Li, X., Han, B., et al. (2024). Numerical simulation of the plant shelterbelt configuration based on porous media model. *Atmosphere* 15, 602. doi:10.3390/atmos15050602

Zheng, Y., Yang, Q., Ren, H., Wang, D., Zhao, C., and Zhao, W. (2022). Spatial pattern variation of artificial sand-binding vegetation based on UAV imagery and its influencing factors in an oasis–desert transitional zone. *Ecol. Indic.* 141, 109068. doi:10.1016/j.ecolind.2022.109068

frontiers | Frontiers in Environmental Science

TYPE Original Research
PUBLISHED 22 April 2025
DOI 10.3389/fenvs.2025.1573022

OPEN ACCESS

EDITED BY
Zhiming Han,
Northwest A&F University, China

REVIEWED BY
Shengchao Li,
Guangdong University of Education, China
Maridee Weber,
Pacific Northwest National Laboratory (DOE), United States
Anıl Poyraz,
Budapest University of Technology and Economics, Hungary

*CORRESPONDENCE
Shuailong Wang,
3575714133@qq.com

RECEIVED 08 February 2025
ACCEPTED 02 April 2025
PUBLISHED 22 April 2025

CITATION
Wang S (2025) Carbon reduction effects of energy transition strategies: a discussion on multi-stakeholder carbon governance. *Front. Environ. Sci.* 13:1573022. doi: 10.3389/fenvs.2025.1573022

Carbon reduction effects of energy transition strategies: a discussion on multi-stakeholder carbon governance

Shuailong Wang*

School of Political Science and Public Administration, Henan Normal University, Xinxiang, China

Investigating the carbon reduction effects of the New Energy cities Demonstration Policy (NECDP) is crucial for promoting the energy transition strategy and meeting the "dual carbon" targets. This study, grounded in stakeholder theory, examines the mechanisms behind the NECDP's carbon reduction effects from the perspectives of both constraints and incentives. Using panel data from 266 cities at the prefecture level and above in China, A difference-in-differences model and mediation effect model are used to assess the impact and mechanisms of the NECDP on carbon emissions. The study's results indicate that: 1) The NECDP significantly reduced carbon emissions, and this conclusion holds up after robustness checks that control for other policies and variable replacements. From a dynamic perspective, the carbon reduction effect of the NECDP did not become significant until the third year, suggesting a certain time lag. 2) Mechanism tests show that the NECDP, as a weak constraint and weak incentive environmental policy. It generates both constraints and incentives for environmental stakeholders, such as governments, businesses, and the public. The government enhances environmental oversight and increases investment in technology, while the public becomes more environmentally conscious, engages in green and low-carbon consumption, and participates in environmental regulation. Businesses, in turn, innovate in green technologies and adopt clean, low-carbon production methods, which help drive industrial upgrades and reduce carbon emissions. 3) Heterogeneity analysis shows that the carbon reduction effects of the NECDP are stronger in regions with lower urbanization, fewer resource-based industries, greater digitization, and stronger government environmental focus.

KEYWORDS

new energy demonstration cities, stakeholder behavior, carbon emission reduction, incentives and constraints, energy conservation and carbon reduction

1 Introduction

China is a major energy consumer and carbon emitter. According to the "World Energy Statistics Yearbook 2021," China's energy consumption and carbon emissions accounted for about 26.5% and 30% of global totals, respectively. Meanwhile, China's energy consumption per unit GDP was 3.4 tons of standard coal per million USD, and its carbon emissions per unit GDP were 6.7 tons of CO_2 per million USD—1.5 and 1.8 times the global averages, respectively. As cities are the primary sources of energy consumption and carbon emissions (Allan et al., 2023), Advancing the low-carbon transition of urban energy systems is crucial

for achieving carbon peak and carbon neutrality goals ("dual carbon" goals). The "China's Energy Transition" white paper, released by the State Council Information Office in August 2024, emphasized the need to strengthen constraints on energy conservation and carbon reduction, foster green energy consumption patterns, and achieve energy-saving and carbon-reduction goals through collaboration among governments, businesses, and the public. Specifically, the government drives the low-carbon transition through regulatory constraints and policy incentives; businesses promote industrial transformation by adopting green technologies and clean energy; and the public contributes by increasing environmental awareness and engaging in green consumption. To support the development of the new energy industry and energy-saving, low-carbon technologies, and to improve urban energy efficiency, the National Energy Administration initiated the construction of NECDP in 2014. the National Energy Administration launched the NECDP. By promoting clean energy and developing green technological innovation, the policy aimed to reduce dependence on traditional fossil fuels, optimize the energy structure, and accelerate the transition to a green, low-carbon industry. These measures collectively support China's objectives of the "dual carbon" goals. In this context of urgent energy transition needs and the goal of achieving "dual carbon" targets, this study uses the NECDP as a case to explore how it can advance energy transition and carbon reduction through the collaborative efforts of government, businesses, and the public.

The structure of this paper is arranged as follows: Section 2 reviews the existing literature and highlights the marginal contributions of this study. Section 3 outlines the theoretical mechanisms and presents the research hypotheses. Section 4 summarizes the main models used in this study and organizes the relevant data. Section 5 presents the empirical results analysis, robustness tests, mechanism analysis, and heterogeneity analysis. Section 6 discusses the research findings. Section 7 covers the study's limitations and future directions, while Section 8 Summarizes conclusions and proposes policy suggestions.

2 Literature review

Achieving urban energy transformation and green, low-carbon development has become a major area of academic focus. The literature related to this research topic can be broadly categorized into two main groups. The first group centers on the factors influencing carbon emissions. Factors influencing carbon emissions can be broadly categorized into two types. The first includes factors that contribute to reducing carbon emissions, such as current environmental regulations (Chen et al., 2021; H; Wang et al., 2024) green technological innovation (Du et al., 2019) government intervention (Kou and Xu, 2022; Xiang et al., 2023) and industrial structure upgrading (Dong et al., 2020; Gu et al., 2022). The second includes factors that contribute to increasing carbon emissions, including industrial structure upgrading (Dong et al., 2020; Gu et al., 2022), urbanization (Dong et al., 2018), industrialization (Dong et al., 2019; Wang et al., 2019) foreign trade openness (Wang & Zhang, 2021; Z. H. Wang et al., 2021), population size (Hong et al., 2022; Kumar and Sen, 2025; Zhu and Peng, 2012) energy consumption (Shan et al., 2021; Wang et al., 2020) financial development (Acheampong et al., 2020; Huang and Guo, 2022) and economic development level (Sarkodie et al., 2020; Zhao et al., 2022) Among these, green technological innovation and industrial structure upgrading are widely recognized as two important mechanisms for reducing carbon emissions. (Wang et al., 2024). The second group of literature focuses on evaluating the effects of new energy demonstration city pilot policies. Some scholars have explored the green innovation effects of the NECDP, noting that it increases government funding support, promotes the concentration of human capital and other innovation factors, and enhances energy efficiency, thereby fostering green innovation (Chen et al., 2023; Feng et al., 2024; Song et al., 2024) Other studies have examined the environmental and economic effects of the NECDP. It has been shown to promote technological innovation and industrial upgrading (Yang et al., 2023), optimize resource allocation (Yang et al., 2021) strengthen environmental regulation (Ding et al., 2024) reduce energy consumption, and improve energy efficiency (Cheng et al., 2023; Liu et al., 2023), thus advancing high-quality economic development (Guo et al., 2023) characterized by pollution reduction, carbon reduction (Gao et al., 2024), and green growth (Yang et al., 2022).

In summary, existing literature primarily focuses on analyzing the factors influencing carbon emissions, as well as the environmental and economic effects of the NECDP. However, there is limited research that explores the mechanisms through which the NECDP affects carbon emissions from the perspective of multiple stakeholders, including government, businesses, and the public. Under the background of China's "dual carbon" goals and strategic constraints, this study leverages the exogenous variations in timing and selection of pilot cities induced by the NECDP. A multi-period Difference-in-Differences (DID) model is employed to effectively identify differences in carbon emissions between pilot and non-pilot cities, thus accurately evaluating the carbon reduction effects of NECDP. The potential contributions of this study are as follows: First, it provides a thorough analysis of the intrinsic mechanisms and pathways through which the NECDP influences carbon emissions. Given that the NECDP is an environmental policy with weak constraints and incentives, it exhibits typical environmental regulation features. By combining stakeholder theory, the study investigates the behavior choices of governments, businesses, and the public from both the constraint and incentive perspectives during the implementation of the NECDP. This approach helps uncover the mechanisms through which the NECDP impacts carbon emissions and establishes a logical framework linking the behavior of government, businesses, and the public with carbon reduction. Second, this study incorporates policy variables such as "low-carbon city pilot," "innovative city pilot," and "smart city pilot" into the empirical model, analyzing the net effects of carbon emissions after excluding the influence of various pilot policies. Additionally, it explores heterogeneity by considering factors such as government environmental awareness, urban clusters *versus* non-urban clusters, digitalization levels, and resource endowments.

3 Theoretical analysis

Carbon emissions inherently involve negative externalities, impacting broader society beyond the emission sources. Their complex and dynamic nature implies that emission mitigation

requires coordinated action from multiple stakeholders—including local governments, enterprises, and the public. The NECDP represents a comprehensive environmental governance policy involving these diverse stakeholders (Li et al., 2023), Thus, this study analyzes the carbon emission reduction mechanisms embedded within the NECDP, specifically by examining the behavioral motivations of local governments, enterprises, and the public. The detailed analyses are as follows.

3.1 The central government's incentives and constraints imposed on local governments

The NECDP) as an energy transition policy, is characterized by weak incentives and weak constraints. From the perspective of incentives, the central government does not explicitly provide additional financial support to pilot cities but instead reallocates existing fiscal resources. From the perspective of constraints, central government oversight is limited, with performance assessments conducted only at the conclusion of the 2015 planning period, lacking continuous monitoring of subsequent activities. Despite these limitations, local governments remain highly motivated to actively participate in NECDP implementation for two main reasons:

Firstly, active engagement in NECDP facilitates local governments in achieving performance evaluation targets and gaining promotion opportunities. China's environmental governance experience indicates that local governments' environmental efforts are significantly driven by central government performance evaluations, financial incentives, and political promotion opportunities (Chen et al., 2024; Miao and Gu, 2024). As early as the 11th Five-Year Plan (2006), China set explicit binding targets—reducing energy intensity by 20% and major pollutants emissions by 10%—signifying a shift from a GDP-centered assessment towards incorporating environmental performance indicators. Given China's increased emphasis on ecological civilization, environmental evaluation mechanisms strongly encourage pilot governments to fulfill environmental performance goals. NECDP specifically promotes the development of the new energy sector and green technology innovations, aligning closely with central performance assessments by driving local economic growth, environmental quality improvement, industrial upgrading, and employment (Lu and Wang, 2019).

Secondly, the central government's acknowledgment of local governments' political legitimacy facilitates resource allocation and priority policy support, enhancing local governmental authority and regulatory capabilities over enterprises and the public. To enhance political legitimacy and resolve central-local incentive incompatibility issues (Mei and Wang, 2017; Ye et al., 2024), pilot governments actively utilize policy instruments like environmental regulation and fiscal subsidies in implementing NECDP, thereby promoting energy efficiency and reducing carbon emissions. Accordingly, this leads to Hypothesis 1.

H1: Effective implementation of the NECDP significantly reduces urban carbon emissions, thus promoting cities' green and low-carbon transition.

3.2 Local governments' incentives and constraints imposed on enterprises

Enterprise production activities are the primary sources of energy consumption, greenhouse gas emissions, and pollutant emissions; therefore, they represent the main targets of governmental environmental regulation. From the perspective of constraints, NECDP, as a policy primarily focused on pollution prevention at the source, sets binding targets related to renewable energy adoption, energy consumption intensity, and environmental pollution. In response, pilot local governments distribute renewable energy utilization objectives to enterprises, mandating adjustments to meet specific renewable energy consumption ratios. Specifically, pilot governments employ regulatory tools that increase both the sunk and marginal costs for energy-intensive, high-carbon, and heavily polluting firms. These regulations effectively decrease the number of such enterprises, restrict low-end, energy-intensive production methods, and encourage these firms to either exit the market, merge, or transition towards renewable energy production and consumption. Under these regulatory pressures, enterprises are incentivized to eliminate outdated capacity, enhance efficiency, fulfill corporate social responsibility, and shift toward clean energy sectors. Consequently, they increase investment in renewable energy technology R&D, install renewable energy facilities, and enhance renewable energy consumption, ultimately promoting structural upgrading and significantly reducing fossil energy use and carbon emissions.

From the perspective of incentives, considering that green technology R&D requires substantial financial input, has long return cycles, and involves high uncertainties (Peng and Liu, 2012), enterprises often cannot fully internalize the environmental benefits generated. Thus, pilot governments and relevant provincial authorities provide enterprises with various financial incentives, including subsidies and preferential tax policies Enterprise production activities are the primary sources of energy consumption, greenhouse gas emissions, and pollutant emissions; therefore, they represent the main targets of governmental environmental regulation. From the perspective of constraints, NECDP, as a policy primarily focused on pollution prevention at the source, sets binding targets related to renewable energy adoption, energy consumption intensity, and environmental pollution. In response, pilot local governments distribute renewable energy utilization objectives to enterprises, mandating adjustments to meet specific renewable energy consumption ratios. Specifically, pilot governments employ regulatory tools that increase both the sunk and marginal costs for energy-intensive, high-carbon, and heavily polluting firms. These regulations effectively decrease the number of such enterprises, restrict low-end, energy-intensive production methods, and encourage these firms to either exit the market, merge, or transition towards renewable energy production and consumption. Under these regulatory pressures, enterprises are incentivized to eliminate outdated capacity, enhance efficiency, fulfill corporate social responsibility, and shift toward clean energy sectors. Consequently, they increase investment in renewable energy technology R&D, install renewable energy facilities, and enhance renewable energy consumption, ultimately promoting structural upgrading and significantly reducing fossil energy use and carbon emissions.

From the perspective of incentives, considering that green technology R&D requires substantial financial input, has long return cycles, and involves high uncertainties (Peng and Liu, 2018) enterprises often cannot fully internalize the environmental benefits generated. Thus, pilot governments and relevant provincial authorities provide enterprises with various financial incentives, including subsidies and preferential tax policies (Lu and Wang, 2019), Besides subsidizing renewable energy infrastructure and consumption, local governments also implement targeted tax deductions for enterprises' renewable energy technology R&D, addressing issues of market failure, technological spillover, and financial constraints associated with green innovation (Ma et al., 2021). Under the combined constraints and incentives provided by NECDP, enterprises proactively pursue green technological innovation and adopt cleaner, low-carbon production methods to achieve sustainable development and business continuity (Mai et al., 2024). Consequently, carbon emissions are substantially reduced. Thus, we propose the following hypothesis.

H2: Under NECDP constraints and incentives, enterprises actively engage in green technological innovation and cleaner, low-carbon production practices, thereby significantly reducing urban carbon emissions.

3.3 Public participation behaviors

As both supervisors and beneficiaries of the NECDP, public satisfaction with environmental quality has increasingly gained attention from the central government. The enhancement of public environmental awareness indirectly strengthens local governments' regulatory intensity, thereby influencing and constraining enterprise production behaviors (Wu et al., 2022). Firstly, by actively engaging with environmental news and leveraging social media platforms, the public effectively supervises local governments' environmental practices. This helps prevent local authorities from easing environmental regulations in pursuit of economic growth. Public pressure, coupled with central government inspections, ensures the rigorous enforcement of environmental policies. Secondly, public participation through reporting, petitions, and complaints effectively mitigates information asymmetry between local governments and enterprises, reducing the regulatory burden on local authorities (Chu et al., 2022), This increased transparency exposes high-energy-consuming and high-emission enterprises, prompting them to adopt low-carbon technologies and cleaner production processes to avoid penalties and enhance corporate reputation (Liu et al., 2024) ultimately reducing carbon emissions.

To cultivate green consumption behavior, pilot governments actively enhance public education initiatives focused on promoting green, low-carbon lifestyles, encouraging public transportation, walking, and cycling. On one hand, direct financial incentives such as subsidies for new energy vehicles and discounts for energy-efficient appliances are provided to lower the economic threshold for green consumption. For example, Shenzhen promotes new energy vehicle adoption by offering subsidies (up to 20,000 RMB per vehicle) and prioritized road access (e.g., bus lane privileges), which significantly boosted consumer demand for such vehicles. On the other hand, local governments adopt green procurement strategies to share R&D costs associated with low-carbon products, thereby reducing market prices and enhancing consumer willingness to purchase green products. This mechanism not only fosters green consumption but also incentivizes enterprises to adopt cleaner production methods, improving green production efficiency (Li and Zhao, 2024).

Overall, NECDP fosters public environmental awareness and cultivates green consumption behaviors through educational initiatives and financial incentives. This facilitates consumers' preference for eco-friendly products and green commuting, driving enterprises to innovate and upgrade towards greener production models. Such consumer-driven shifts promote industrial transformation towards low-carbon sustainability. Based on this analysis, the following hypothesis is proposed.

H3: NECDP significantly enhances public environmental awareness and facilitates the transition to green lifestyles, thereby promoting enterprise green technology innovation, driving industrial structure upgrading, and ultimately reducing carbon emissions the specific mechanism is illustrated in Figure 1.

4 Research design

4.1 Model construction

Given that the NECDP during the sample period is implemented in multiple batches, and referring to the research approach of Guo and Zhong, (2022), a multiple-period difference-in-differences (DID) model is constructed based on the temporal differences in policy implementation across cities. The baseline two-time-point fixed effects model is as follows:

$$\ln CO_{2it} = \alpha_0 + \alpha_1 NECP_{it} + \delta_i X_{it} + \mu_i + \lambda_t + \varepsilon_{it} \quad (1)$$

According to Equation 1, $\ln CO2_{it}$ is the dependent variable, representing the carbon emission level; $NECDP_{it}$ is the key independent variable, If city i implements NECDP in year t, then $NECDP_{it}$ will take a value of one for the current and subsequent years; otherwise, $NECDP_{it}$ will be 0. X_{it} represents the control variables, and μ_i and λ_t denote individual and time fixed effects, respectively. ε_{it} is the random error term.

The theoretical analysis suggests that local governments promote enterprise green technological innovation and industrial upgrading through environmental regulations and technological investments. Concurrently, the public contributes by enhancing environmental awareness and transitioning to greener lifestyles, which collectively support carbon emission reduction. To empirically validate Hypotheses 2, 3, and drawing upon the research framework of Wen and Ye, (2014), the following mechanism model is constructed:

$$\ln Y_{it} = \gamma_0 + \gamma_1 NECDP_{it} + \gamma_2 Med_{it} + \gamma_i X_{it} + \mu_i + \lambda_t + \varepsilon_{it} \quad (2)$$

$$Med_{it} = \beta_0 + \beta_1 NECDP_{it} + \beta_i X_{it} + \mu_i + \lambda_t + \varepsilon_{it} \quad (3)$$

$$\ln Y_{it} = \gamma_0 + \gamma_1 NECDP_{it} + \gamma_2 Med_{it} + \gamma_i X_{it} + \mu_i + \lambda_t + \varepsilon_{it} \quad (4)$$

In Equations 2-4, $\ln Y_{it}$ denotes industrial structure upgrading and green technological innovation, identified as two key pathways

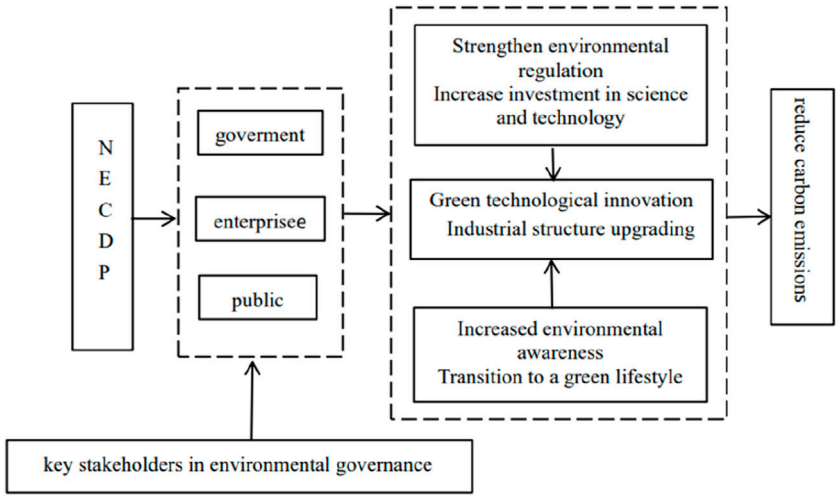

FIGURE 1
The carbon reduction mechanism of NECDP.

for promoting carbon emission reduction. The variable *Medit* represents the mediating mechanisms, including technological investment, environmental regulation, public environmental awareness, and the green transformation of public lifestyles. The coefficient β_1 measures the influence of NECDP on the mediating variables, while γ_1 captures the effect of NECDP on industrial upgrading or green technological innovation after accounting for the mediators. If both β_1 and γ_2 are statistically significant, and the significance or magnitude of γ_1 decreases, it indicates that the mediating variables exert a partial mediating effect in the relationship between NECDP and green technological innovation or industrial structure upgrading.

4.2 Variable definitions

4.2.1 Dependent variable

The dependent variable is urban carbon emissions ($lnCO_2$). Based on the method of continuous dynamic distribution proposed by Wu et al. (2016), the calculation results are obtained and logarithmic transformation is applied.

4.2.2 Independent variable

The NECDP variable (DID_{it}) is treated as a quasi-natural experiment in this study. If city i implements the NECDP in 2014, the group indicator variable is set to 1, otherwise it is set to 0. The time indicator variable for the years in which the city participates in the pilot program and the subsequent years is set to 1, while it is set to 0 for the years prior to the selection as a new energy demonstration city. The interaction term between the group indicator and the time indicator is used as the core independent variable to represent the impact of NECDP on carbon emissions.

4.2.3 Mediating mechanism variable

(1) Environmental regulation (*Eri*). environmental pollution control investment is selected as a variable representing government behavior, capturing the government's regulatory constraints on enterprises. It is important to note that due to the lack of data on environmental pollution control investment at the prefecture-level, we follow the method of Wang (2023), where the weight is determined by the ratio of the city's secondary industry output to the total secondary industry output of its province, and this ratio is then multiplied by the provincial-level environmental pollution control investment to estimate the city-level data.

(2) Technological investment intensity (*Kj*). Following the work of Dong et al. (2022), the ratio of government technological investment to GDP is used to measure governmental incentives provided to enterprises.

(3) Green technology innovation (*Pgpan*). Since patents effectively and intuitively reflect innovation ability (Lindman and Söderholm, 2016), the number of green patents per ten thousand people in each city is used to measure green technology innovation.

(4) Industrial structure upgrading (*Isu*). Following C. Wang et al. (2019), industrial upgrading is defined as the weighted product of the share of each industry and its corresponding labor productivity, with the formula as:

$$Isu = \sum_{j=1}^{3} \left(Y_{ij}/Y_i\right) \times \left(Y_{ij}/L_{ij}\right) \quad (5)$$

According to Equation 5, Y_{ij}/L_{ij} represents the labor productivity of industry j in region i. Since Y_{ij}/Y_i is dimensionless while Y_{ij}/L_{ij} has dimensions, a normalization method is applied to eliminate the dimensional differences.

(5) Public environmental concern (*Pub*). Referring to L. Wu et al. (2022), the Baidu haze search index is used to measure public environmental awareness. The reasons for using this index are twofold: first, Baidu, as the largest Chinese search engine, providing extensive coverage and high data availability,

providing comprehensive environmental search index data. Second, compared to keywords like "environmental pollution," the public has greater awareness of haze, so the level of concern about haze more accurately reflects public attention to environmental issues.

(6) Green transformation of public lifestyles (*Lz*). Building on the work of Peng et al. (2024), we construct a composite *Lz* index encompassing several key dimensions. Specifically, it incorporates green and low-carbon awareness (*per capita* park green space area), green travel (*per capita* number of public buses in operation at year-end), green environmental behavior (household *per capita* gas consumption), and digital life (*per capita* number of mobile phones, *per capita* telecommunications usage, and internet penetration rate). We then apply the entropy-weighted TOPSIS method to evaluate this composite index.

4.2.4 Control variables

To address the bias of endogeneity, a series of variables affecting carbon emissions are controlled for, as discussed in the literature review. These include: ①Economic development level (lnY), measured as the logarithm of *per capita* GDP, with GDP deflated to real values using 2005 as the base year. ②Population size (*lnPop*), represented by the logarithm of the total population. ③Financial development (*Fin*), measured as the ratio of total deposits and loans to regional GDP. ④Urbanization level (*Urb*), represented by the ratio of employment in the secondary and tertiary sectors to total employment. ⑤Openness level (*Open*), measured as the ratio of total import and export trade to GDP. ⑥Transport infrastructure (*Inf*), represented by *per capita* road area. To reduce heteroscedasticity issues, logarithmic transformation is applied to the control variables. ⑦Economic volatility (*Bd*),represented by the coefficient of variation in economic growth rates over a 5-year period. ⑧Government intervention (*Gov*),measured as the ratio of general budget fiscal expenditure to regional *GDP*.

4.3 Sample selection and data sources

The sample space selected in this study is panel data from 266 prefecture-level cities between 2005 and 2020, with 56 cities designated as the experimental group for the new energy demonstration program, and 210 cities not selected as the control group. Since the sample data includes cities at the prefecture level and above, certain cities that use industrial parks (e.g., Tianjin Eco-city, Dalian Sanlibao Industrial Park) or specific districts (e.g., Beijing's Changping District, Qingdao's Laoshan District) as pilot sites are excluded to ensure effective policy evaluation. The list of new energy demonstration cities is obtained from the "National Energy Administration website," patent data comes from the National Intellectual Property Administration, and the green patent classification codes are from the WIPO Green Patent List. Other data is sourced from the "China City Statistical Yearbook," the EPS database, and the WIND database.

Descriptive statistics for each variable are presented in Table 1. As shown, the minimum, mean, and maximum values of carbon emissions are 1.775, 6.082, and 9.432, respectively, highlighting significant regional differences in carbon emissions. There are also substantial variations among prefecture-level cities in terms of green technology innovation (*Pgpan*), industrial structure upgrading (*Isu*), environmental regulation (*Eri*), technological investment (*Kj*), energy consumption intensity (*Egyx*), environmental awareness (*Pub*), economic development ($\ln Y$), population size ($\ln Pop$), urbanization level (*Urb*), openness (*Open*), infrastructure (*Inf*), financial development (*Fin*), Green Transition of Lifestyle (*Lz*), and Economic volatility (*Bd*), Government intervention (*Gov*).

5 Empirical analysis

5.1 Parallel trend test

Before applying the multi-period DID model to evaluate the impact of NECDP on carbon emissions, it is necessary to perform a parallel trends test on the carbon emissions levels of the experimental and control groups. This study follows the event study approach proposed by Beck et al. (2010) to analyze the dynamic trends of the policy effects over time, and establishes a regression model that captures the policy shock effects at different time periods.

$$\ln CO2_{it} = \alpha_0 + \sum_{j=M}^{N} \delta_j Ploc_{i,t-j} + \delta_i X_{it} + \mu_i + \lambda_t + \varepsilon_{it} \quad (6)$$

According to Equation 6, *Ploc_(i,t-j)* is a dummy variable. If city *i* was selected as a new energy demonstration city at time *t-j*, this variable takes the value of 1; otherwise, it is 0 (M and N represent the number of periods before and after the policy, respectively). If the coefficients from δ_(-M) to δ_(-1) are not significant, it suggests that there were no significant differences in carbon emissions between the experimental and control groups prior to the policy implementation, thus supporting the parallel trends assumption. δ_(0) to δ_(N) represent the current period and lagged effects (m = 1, . . . , M) for city i after being selected as a new energy demonstration city. These terms are used to capture the dynamic effects of the policy. If these coefficients are significant, it indicates that NECDP has a significant impact on carbon emissions.

The parallel trend test results shown in Figure 2 indicate that in the 5 years before the policy implementation, the regression coefficients for the impact of NECDP on carbon emissions did not pass the significance test within the 95% confidence interval. This suggests that, prior to being selected as a new energy demonstration city, there was no significant difference in carbon emissions between selected and non-selected cities, which supports the parallel trend assumption. After the city was selected as a new energy demonstration city, the carbon reduction effect was not immediately observed, but became statistically significant in the third year. This indicates that the carbon reduction effect of the NECDP has a time lag. The delayed policy effects observed in this study can primarily be attributed to the following factors: 1) Institutional and Implementation Lag: Despite clear guidelines from central policies, their effectiveness at the local level may be limited by insufficient resource allocation, misinterpretations of

TABLE 1 Statistical description of variables.

Variable name	Min	Mean	Max	S.D	Sample size
Carbon Dioxide Emissions (*lnCO2*)	1.775	6.082	9.432	1.171	4,256
Policy Variable (*NECDP*)	0	0.092	1	0.289	4,256
Industrial Structure Upgrading (*Isu*)	0.115	1.391	9.246	0.991	4,256
Green Technology Innovation (*Pgpan*)	0.002	0.769	19.53	1.542	4,256
Environmental Regulation (*Eri*)	0.0840	22.82	1,049	37.04	4,256
Technology Investment (*Kj*)	0.002	0.216	6.310	0.245	4,256
Energy Consumption Intensity (*Egyx*)	0.004	0.088	4.189	0.138	4,256
Environmental Awareness (*Pub*)	0.000	24.783	439.344	41.978	4,256
Green Transition of Lifestyle (*Lz*)	1.010	1.140	1.744	0.083	4,256
Economic Development Level (*lnY*)	7.782	10.36	13.06	0.752	4,256
Population Size (*lnPop*)	2.846	5.861	8.140	0.693	4,256
Urbanization Level (*Urb*)	0.202	0.629	1	0.146	4,256
Openness (*Open*)	0	0.181	3.488	0.338	4,256
Infrastructure (*Inf*)	0.139	4.335	73.04	5.878	4,256
Financial Development (*Fin*)	0.556	2.305	19.57	1.292	4,256
Economic volatility (*Bd*)	−21.604	0.305	30.166	0.972	4,256
Government intervention (*Gov*)	0.011	0.187	3.760	0.157	4,256

policy details, and difficulties in inter-departmental coordination. These institutional challenges lead to a delay in policy impacts becoming evident. Moreover, variations among local governments in comprehending and executing policy goals further extend the time required for effective policy implementation. 2) Long Construction Cycles for New Energy Projects: New energy projects typically involve extended timelines, including initial planning, land approvals, securing funding, equipment procurement, construction, trial operation, and formal commissioning phases. Specifically, infrastructure projects such as power grid enhancements and renewable energy installations (photovoltaic and wind power projects) have an average construction period of 2–3 years, influenced by factors like policy approval processes, funding availability, and technical support. 3) Enterprise Technological Transformation Period: While policies encourage enterprises to adopt low-carbon technologies, the actual technological upgrading process—including research, development, experimentation, and production-line transformation—can take several years. Additionally, the diffusion and market acceptance of new green technologies typically involve a gradual learning curve. Consequently, the effects of policy implementation on enterprise behavior are often more apparent in the medium to long term.

5.2 Baseline regression analysis

Table 2 presents the results of the baseline regression. The robustness of the results is assessed by sequentially adding control variables. From columns (1) to (7), it is evident that the *NECDP* coefficient of the core explanatory variable is significantly positive at the 1% level, indicating that NECDP can significantly reduce carbon emissions and foster a green, low-carbon urban transformation. The reasons for this are: first, the development of new energy cities compels high-consumption, low-productivity industries to transition towards greener, low-carbon alternatives, promoting a resource-efficient and environmentally friendly industrial structure that helps achieve carbon reduction and pollution control targets. Second, by setting targets such as "new energy utilization," "energy consumption restrictions," "energy consumption per unit of GDP," and "industrial wastewater and exhaust treatment rates," new energy cities encourage a shift from an energy-intensive, high-emission growth model to a more sustainable, low-carbon economic model, which in turn reduces carbon emissions. Hypothesis H1 is supported.

5.3 Placebo test

To further verify that the reduction in urban carbon emissions is caused by NECDP and not by random influences from other unobservable factors, a placebo test was conducted, following existing studies (Zhang et al., 2021). First, 56 cities were randomly selected from the full sample to form the experimental group. A virtual variable representing the policy implementation time was then generated for each city. This resulted in the core explanatory variable $NECDP_{it}$, which includes both the experimental group and the policy implementation time. The random sampling process was repeated 500 times, and the baseline model was estimated repeatedly. As a result, 500 estimates of the $NECDP_{it}$ variable coefficients and their corresponding p-values were obtained. This randomization

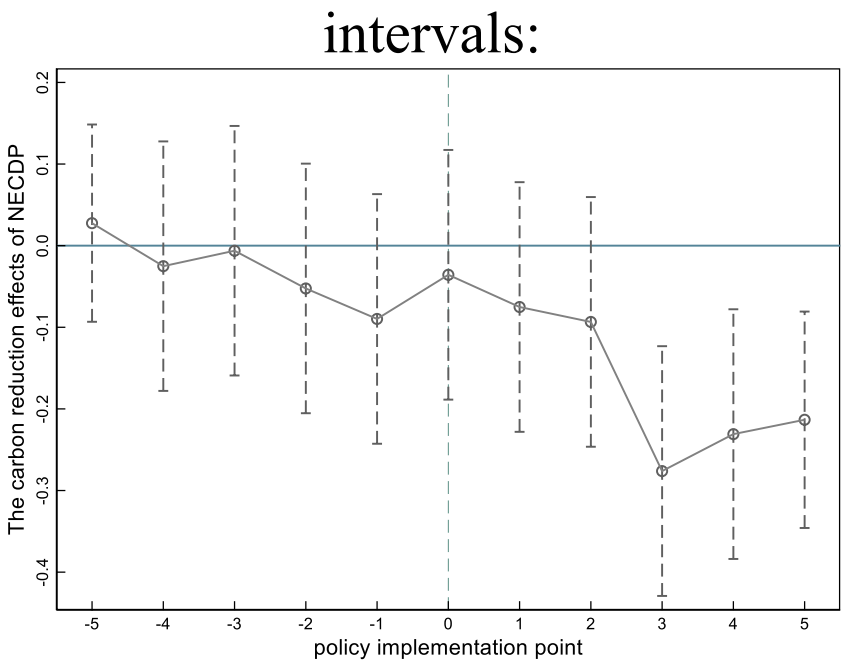

FIGURE 2
Parallel trend test results.

procedure helped eliminate the interference of other factors on the $NECDP_{it}$ variable within the NECDP framework. After this procedure, the regression coefficient for $NECDP_{it}$ was −0.049, with a p-value of 0.149, which did not pass the significance test. Figure 3 displays the kernel density distribution and the p-value scatter plot after randomization. It is evident that the actual estimated coefficient value is −0.155, significantly different from the coefficient values in the placebo test, and the p-values are concentrated around zero. This suggests that the policy effect of NECDP in reducing urban carbon emissions is real and not driven by random, unobservable factors.

5.4 Robustness analysis

5.4.1 Excluding other pilot policies

Previous studies have shown that pilot policies for low-carbon cities (LCT), smart cities (SC), and innovative cities (IC) can effectively reduce carbon emissions (Chiappinelli et al., 2024; Wang et al., 2015). Therefore, corresponding policy dummy variables are constructed and included in the empirical model to verify the net effect of NECDP on carbon emissions. If the coefficient of DID in the regression results is no longer significant, it would indicate that the negative impact of the new energy demonstration cities on carbon emissions is caused by other pilot policies in cities, and the baseline regression results would lack credibility. The regression model is specified as follows:

$$\ln CO2_{it} = \eta_0 + \eta_1 NECDP_{it} + \eta_j policj_{it} + \eta_i X_{it} + \mu_i + \lambda_t + \varepsilon_{it} \quad (7)$$

According to Equation 7, $policy_{1it}$ represents the impact of SC on carbon emissions, $policy_{2it}$ reflects the effect of LCT on carbon emissions, and $policy_{3it}$ represents the influence of IC on carbon emissions. The dummy variables are constructed as follows: (1) The first batch of SC was launched in 2012, with the latest batch in 2014. For the group dummy variable, cities that have both "smart city" and new energy demonstration city status are assigned a value of 1, while other cities are assigned a value of 0. For the time dummy variable, the years 2012–2020 are set to 1, and other years are set to 0. The interaction term between the group and time dummy variables is represented as $policy1_{it}$, which indicates the impact of the SC on carbon emissions. (2) The National Development and Reform Commission established the first batch of low-carbon pilot cities in 2010, with the most recent batch in 2017. Cities that simultaneously implement LCT and NECDP are coded as 1, while others are set to 0, forming the group dummy variable. The years 2010–2020 are set to 1, while other years are set to 0 for the time dummy variable. The interaction term between the group and time dummy variables, $policy_{2it}$, captures the impact of the "low-carbon city" policy on carbon emissions. (3) In 2008, China launched its first innovative city pilot program in Shenzhen, and by 2018, six batches of cities were included. For the group dummy variable, cities that have both the "new energy demonstration city" and "innovative city" titles are assigned a value of 1, while others are assigned a value of 0. The years 2008–2010 are set to 1, while other years are set to 0 for the time dummy variable. The interaction term between the group dummy variable and the time dummy variable, $policy_{3it}$, measures the impact of the "innovative city" policy on carbon emissions.

From the regression results in Table 3 (Columns 1–4), it is evident that NECDP did increase urban carbon emissions, but it is not the sole policy factor responsible for carbon emission reductions. Specifically, as shown in Columns (1) and (2), the *NECDP* coefficient is negative and significant at the 5% level, while the coefficients for

TABLE 2 Empirical results of baseline regression.

Variables	(1)	(2)	(3)	(4)	(5)	(6)	(7)	(8)	(9)
NECDP	−0.130***	−0.149***	−0.156***	−0.157***	−0.154***	−0.156***	−0.155***	−0.155***	−0.155***
	(0.029)	(0.028)	(0.028)	(0.028)	(0.028)	(0.028)	(0.028)	(0.028)	(0.028)
lnY		0.519***	0.521***	0.489***	0.472***	0.465***	0.480***	0.483***	0.485***
		(0.035)	(0.035)	(0.036)	(0.035)	(0.035)	(0.036)	(0.036)	(0.036)
lnPops			0.410***	0.372***	0.474***	0.426***	0.444***	0.447***	0.450***
			(0.102)	(0.102)	(0.102)	(0.104)	(0.104)	(0.104)	(0.104)
Urb				0.680***	0.520***	0.508***	0.473***	0.472***	0.474***
				(0.160)	(0.160)	(0.160)	(0.161)	(0.161)	(0.161)
Open					0.388***	0.380***	0.387***	0.386***	0.386***
					(0.048)	(0.048)	(0.048)	(0.048)	(0.048)
Inf						−0.007**	−0.006**	−0.006**	−0.006**
						(0.003)	(0.003)	(0.003)	(0.003)
Fin							0.021***	0.021***	0.021***
							(0.007)	(0.007)	(0.007)
Gov								0.038	0.038
								(0.047)	(0.047)
Bd									0.005
									(0.006)
_Cons	5.396***	0.528	−1.877***	−1.727**	−2.150***	−1.785**	−2.057***	−2.108***	−2.138***
	(0.023)	(0.328)	(0.681)	(0.680)	(0.677)	(0.696)	(0.702)	(0.705)	(0.706)
City FE	Yes	Yes	Yes	Yes	Yes	Yes	Yes	Yes	Yes
Year FE	Yes	Yes	Yes	Yes	Yes	Yes	Yes	Yes	Yes
R^2	0.651	0.669	0.671	0.672	0.677	0.678	0.678	0.678	0.679
N	4 256	4 256	4 256	4 256	4 256	4 256	4 256	4 256	4 256

Note: t-values in parentheses, *, **, and *** indicate significance at the 10%, 5%, and 1% levels. We controlled the city-fixed effect and year-fixed effect.

$policy_1$ and $policy_2$ are also negative and significant at the 1% level. Compared to Column (7) in Table 1, the absolute value of the *NECDP* coefficient has decreased, suggesting that both the LCT, which focuses on reducing carbon emissions and developing new clean energy, and the smart city policy, aimed at enhancing innovation capacity and digital transformation, also significantly reduce carbon emissions. In Column (4), after including the SC, LCT, and IC, the $NECDP_{it}$ coefficient decreases to −0.083, which remains significant at the 5% level. This indicates that, after controlling for other city pilot policies, the carbon reduction effect of NECDP remains significant.

5.4.2 PSM-DID regression

To mitigate the bias introduced by the non-random selection of NECDP, and to control for carbon emission differences arising from other unobservable factors, this study employs the propensity score matching difference-in-differences (PSM-DID) method for robustness checks of the regression results. Based on the approach outlined by Y. Chen et al. (2024), control variables are treated as covariates, and kernel matching is applied using the logit model to identify the regions most similar to the selected cities as the control group. This approach further verifies the effect of NECDP on urban carbon emissions. As shown in Column (5) of Table 4, the coefficient for the impact of NECDP on carbon emissions is significantly positive at the 1% level, confirming that the baseline regression results are robust and reliable.

5.4.3 Replace the dependent variable

Considering the strong link between economic development and carbon emissions, and following Lei et al. (2023) and Yang et al. (2022), this study adopts carbon emissions per unit of output as a measure of carbon intensity. Based on this approach, an empirical analysis is conducted. The results, presented in Columns (6) of Table 3, show that t The coefficient of *NECDP* is −0.083, which remains statistically significant at the 1% significance level, suggesting that NECDP can reduce carbon intensity, thereby driving low-carbon development in cities.

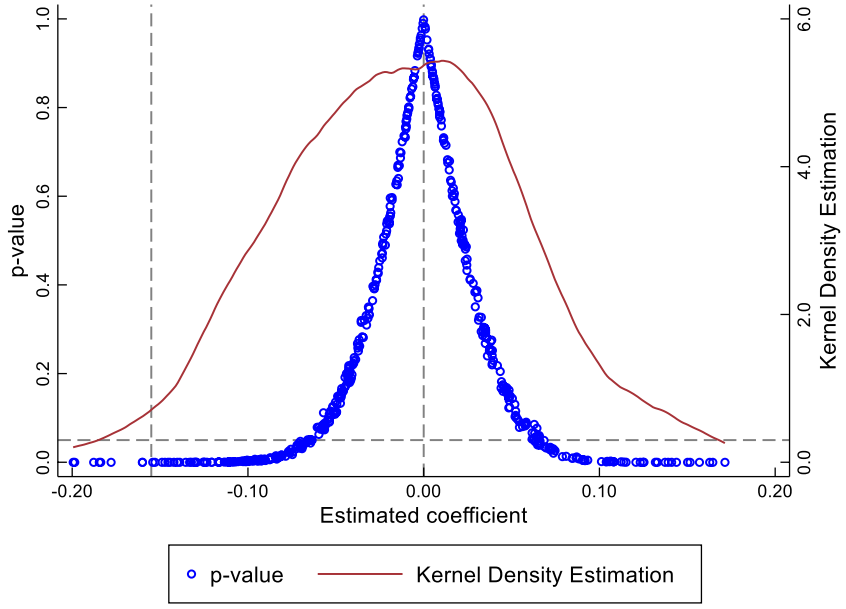

FIGURE 3
Placebo test.

TABLE 3 Robustness test of the Impact of NECDP on carbon emissions.

Variables	SC (1)	LCT (2)	IC (3)	Net effect (4)	PSM-DID (5)	Replace the dependent variable (6)	SDM (7)
NECDP	−0.116*** (0.033)	−0.118*** (0.030)	−0.145*** (0.030)	−0.083** (0.035)	−0.103*** (0.030)	−0.083*** (0.027)	−0.154*** (0.027)
W NECDP*							1.089** (0.447)
ρ							0.494*** (0.100)
$Policy_1$	−0.103** (0.047)			−0.107** (0.050)			
$Policy_2$		−0.161***		−0.162***			
		(0.048)		(0.049)			
$Policy_3$			−0.046 (0.051)	0.025 (0.055)			
Controls	Yes	Yes	Yes	Yes	Yes	Yes	
City FE	Yes	Yes	Yes	Yes	Yes	Yes	
Year FE	Yes	Yes	Yes	Yes	Yes	Yes	
R^2	0.908	0.909	0.908	0.909	0.898	0.711	0.524
LogL							−1,608.241
N	4 256	4 256	4 256	4 256	3 365	4 256	4 256

Note: same as Table 2.

5.4.4 Alternative estimation method

Cities are the primary sources of carbon emissions, which show significant spatial correlations. The NECDP may affect carbon emissions in neighboring regions. Therefore, a Spatial Durbin Model (SDM) is constructed to identify the spatial spillover effects of NECDP. The model formula is as follows:

TABLE 4 Testing the emission reduction mechanism through government behavior.

Variables	Government actions					
	Effect of technology expenditure			Effect of environmental regulation		
	Pgpan (1)	*Kj* (2)	*Pgpan* (3)	*Isu* (4)	*Eri* (5)	*Isu* (6)
NECDP	0.283***(0.061)	0.025**(0.012)	0.252*** (0.059)	0.090*** (0.026)	3.673*(1.971)	0.083***
Kj			1.216***(0.076)			
Eri						0.002***(0.000)
_Cons	−24.317*** (1.540)	−4.157***(0.314)	−19.248***(1.531)	−14.533***(0.646)	−351.967*** (49.842)	−13.573***(0.643)
mediating effect value	−0.031** (Z = −2.001)			0.007** (Z = 2.250)		
95% confidence interval	[0.0057, 0.076]			[0.0027, 0.2959]		
Controls	Yes	Yes	Yes	Yes	Yes	Yes
City FE	Yes	Yes	Yes	Yes	Yes	Yes
Year FE	Yes	Yes	Yes	Yes	Yes	Yes
R^2	0.529	0.304	0.558	0.701	0.153	0.707
N	4 256	4 256	4 256	4 256	4 256	4 256

Note: same as Table 2.

$$\ln CO_{2it} = \rho W \ln CO_{2it} + \alpha_1 NECDP_{it} + \alpha_2 WNECP_{it} + \delta_i X_{it} + \theta_i W X_{it} + \mu_i + \lambda_t + \varepsilon_{it} \quad (8)$$

According to Equation 8, W represents the geographic distance weight matrix, ρ is the spatial autoregressive coefficient, and α_2 and θ_i are vectors of spatial lag coefficients for explanatory and control variables, respectively. After conducting tests for spatial correlation, spatial effects, Wald, and LR tests (detailed results are omitted but available upon request), the SDM model with two-way fixed effects was selected for estimation. The results are shown in Column (7) of Table 3. Under the geographic distance weight matrix, the coefficient ρ passed the 1% significance level test, suggesting that urban carbon emissions are influenced by both local and neighboring regional factors. The coefficients of *NECDP* and *W* NECDP* are negative and positive at the 1% and 5% significance levels, respectively, indicating that NECDP reduced carbon emissions in pilot cities but increased them in adjacent non-pilot cities.

Three potential explanations are as follows: 1) Resource and Policy Siphon Effect: During policy implementation, pilot cities attracted substantial investments, technologies, and talents, causing a "siphon effect" that deprived neighboring non-pilot cities of resources. The resource shortage hindered these cities' green transformation, forcing them to rely more on traditional high-carbon industries, thereby increasing carbon emissions. 2) Policy Imitation Leading to Pollution Effect: Non-pilot cities may imitate the strategies of pilot cities. However, due to the lack of policy support, technological capacity, and management experience, such imitation is often superficial. Gaps in policy implementation and technology introduction may prevent effective industrial transformation, resulting in a "policy imitation pollution effect" where high-carbon industries continue to dominate. 3) Industrial Transfer Effect: Under demonstration policies, pilot cities are encouraged to develop green, low-carbon industries while restricting high-pollution enterprises. As a result, some high-carbon enterprises may relocate to neighboring non-pilot cities, contributing to a "pollution transfer effect" and raising emissions in these areas.

5.5 Mechanism test of the effect of NECDP on carbon emissions

The theoretical analysis suggests that local governments facilitate enterprise green technological innovation and industrial structure upgrading by implementing environmental regulatory constraints and providing technological investment incentives, ultimately contributing to carbon emission reduction. To test this transmission mechanism, technological output and environmental regulation are used as mediating variables. Table 4 shows the effects of NECDP on industrial structure upgrading and green technology innovation. From columns (2) and (5), the coefficients for NECDP's impact on technological spending and environmental regulation are significant at the 5% and 10% levels, respectively. This suggests that NECDP significantly encourages the government to strengthen environmental regulation and technological investment. From columns (3) and (6), the coefficients for the effects of technological spending and environmental regulation on green technology innovation and industrial structure upgrading are significantly positive at the 1% level. Additionally, the promoting effect of NECDP on green technology innovation and industrial structure upgrading is weaker compared to columns (1) and (4), implying that technological spending and environmental regulation

TABLE 5 Mechanism test of emission reduction under public behavior.

Variables	Public behavior					
	Effect of environmental awareness			Green transition of lifestyle (*Lz*)		
	Pgpan (1)	*Pub* (2)	*Pgpan* (3)	*Isu* (4)	*Lz* (5)	*Isu* (6)
NECDP	0.282***(0.061)	13.212***(1.823)	0.137** (0.018)	0.090*** (0.026)	0.003***(0.001)	0.084***(0.025)
Pub			0.011***(0.001)			
Lz						2.015***(0.270)
_Cons	−24.317*** (1.547)	−292.949***(46.095)	−21.331***(1.462)	−14.248***(0.644)		−16.227*** (0.694)
mediating effect value	0.145***(Z = 5.153)			0.006***(Z = 3.29)		
95% confidence interval	[0.0960, 0.2137]			[0.0028, 0.0105]		
Controls	Yes	Yes	Yes	Yes	Yes	Yes
City FE	Yes	Yes	Yes	Yes	Yes	Yes
Year FE	Yes	Yes	Yes	Yes	Yes	Yes
R^2	0.529	0.578	0.580	0.700		0.705
N	4 256	4 256	4 256	4 256	4 256	4 256

Note: same as Table 2.

are critical channels through which NECDP influences these outcomes.

Furthermore, The mediation effect test, conducted using the Bootstrap method with 1,000 random samples, reveals that the mediation effect values for both technological investment and environmental regulation channels fall outside the 95% confidence interval that includes zero. This indicates the significant presence of mediation effects. The results suggest that NECDP facilitates green technological innovation and industrial structure upgrading by enhancing technological investment and environmental regulation, thereby promoting carbon emission reduction. The conclusion is robust and reliable, confirming the validity of Hypothesis H2.

The theoretical analysis suggests that NECDP enhances public environmental awareness and facilitates the transition to greener lifestyles. This, in turn, promotes green technological innovation and industrial structure upgrading, ultimately contributing to carbon emission reduction. Considering public environmental awareness and lifestyle green transition as mediating variables, Table 5 presents the estimated results of NECDP's influence on green technological innovation and industrial structure upgrading through public behavior, thus supporting carbon reduction efforts. Columns (2) and (4) demonstrate that NECDP's influence on public environmental awareness and lifestyle green transition is significantly positive at the 1% level, indicating that NECDP effectively enhances public environmental engagement and promotes greener lifestyles. Columns (3) and (5) show that both public environmental awareness and lifestyle green transition have significant positive effects on green technological innovation and industrial structure upgrading, also at the 1% significance level. However, NECDP's direct promotion effect on green technological innovation and industrial structure upgrading slightly decreases compared to the effects observed in columns (1) and (4).

Furthermore, the mediation effect test, conducted using the Bootstrap method with 1,000 random samples, reveals that the mediation effect values for public environmental awareness and green lifestyle transition fall outside the 95% confidence interval that includes zero. This confirms the significant presence of mediation effects. The findings suggest that NECDP reduces carbon emissions by enhancing public environmental awareness and fostering low-carbon lifestyles. The conclusion is robust and reliable, confirming the validity of Hypothesis H3.

5.6 Heterogeneity analysis

5.6.1 Government environmental awareness

The government plays a central role in environmental governance. In cities where the government places higher priority on environmental issues, stricter environmental regulations are enforced, and investments in pollution control are increased. Given the differences in economic development, infrastructure, openness, and policy enforcement across regions in China, the impact of the NECDP on carbon emissions may vary regionally. The sample cities were categorized into high and low environmental concern groups for regression analysis. As shown in Columns (1) and (2) of Table 6, the regression coefficients for the effect of NECDP on carbon emissions in cities with high and low environmental concern are −0.188 and −0.096, respectively, both statistically significant at the 1% level. This suggests that the carbon reduction effect of NECDP is stronger in cities with higher levels of government environmental concern. The likely explanation is that

TABLE 6 Results of policy synergy effect test.

Variable	High Attention (1)	Low Attention (2)	High Digitalization (3)	Low Digitalization (4)	Urban Clusters (5)	Non-urban Clusters (6)	Resource-Based (7)	Non-resource-Based (8)
NECDP	−0.188*** (0.044)	−0.096*** (0.034)	−0.160***(0.033)	−0.091**(0.046)	−0.114***(0.037)	−0.213***(0.042)	−0.123**(0.049)	−0.157***(0.033)
_Cons	−4.414*** (1.125)	0.806 (0.912)	−2.945***(0.861)	−1.591 (1.134)	−0.863 (0.932)	−4.611***(1.158)	−7.348***(1.124)	2.303**(0.919)
Controls	Yes	Yes	Yes	Yes	Yes	Yes	Yes	Yes
City FE	Yes	Yes	Yes	Yes	Yes	Yes	Yes	Yes
Year FE	Yes	Yes	Yes	Yes	Yes	Yes	Yes	Yes
R^2	0.629	0.747	0.667	0.708	0.672	0.702	0.635	0.702
N	2 128	2 128	2 128	2 128	2 272	1 984	1 584	2 672

Note: same as Table 2.

when local governments are more focused on environmental issues, they implement stricter environmental regulations and offer more subsidies. This drives businesses to adopt cleaner, low-carbon production practices and encourages green technological innovation, facilitating the transition of industries toward greener, low-carbon alternatives and reducing reliance on fossil fuels, thereby cutting carbon emissions. Additionally, these governments guide the public towards low-carbon lifestyles by promoting the use of public transportation and shared bicycles and offering green consumption subsidies to encourage the purchase of environmentally friendly products.

5.6.2 Degree of digitalization

With the rise of the digital economy, the role of digital government development, enterprise digital transformation, and the upgrading of residents' digital consumption has become increasingly important in enabling cities to transition to green, low-carbon development. To investigate the varying impact of NECDP on carbon emissions across cities with different levels of digitalization, this study follows the methodology of Wang (2023), evaluating urban digitalization based on three dimensions: digital infrastructure, industrial digitalization, and digital industrialization. The cities in the sample are categorized into high and low digitalization groups, and the differences in the impact of NECDP on carbon emissions in these cities are assessed. As shown in Columns (3) and (4) of Table 6, the *NECDP* coefficients for high and low digitalization cities are −0.160 and −0.091, respectively, with statistical significance at the 1% and 5% levels. This suggests that the policy effect of NECDP is stronger in high-digitalization cities. The likely explanation is that in cities with higher levels of digitalization, the digital economy enables participation from the government, enterprises, and the public in the NECDP. This boosts government digital governance capabilities, increases public environmental engagement, and enhances the motivation for businesses to adopt green transformations, all of which help to establish a green, low-carbon lifestyle and production model. Therefore, the carbon reduction effect of NECDP is more pronounced in high-digitalization cities compared to low-digitalization ones.

5.6.3 Urban agglomerations and non-urban agglomerations

With the ongoing process of urbanization, city clusters and metropolitan areas have become the new drivers of economic growth in China. City clusters offer numerous advantages, such as industrial agglomeration, resource sharing, talent mobility, regional integration, and openness. These factors may lead to stronger carbon reduction effects of energy policies in cities within such clusters. To test this hypothesis, following the study of Zhang et al. (2023) the sample cities are divided into two categories: cities in city clusters, including the Beijing-Tianjin-Hebei, Central Yangtze River, Harbin-Changchun, Chengdu-Chongqing, Yangtze River Delta, Central Plains, Beibu Gulf, Guanzhong Plain, Hohhot-Baotou-Ordos-Yulin, Lanci, and Guangdong-Hong Kong-Macau Greater Bay Area city clusters, and cities outside these clusters. A grouped regression is then performed. As shown in Columns (5) and (6) of Table 6, the *NECDP* coefficients for cities within city clusters and non-city-cluster

cities are −0.114 and −0.213, respectively, both significant at the 1% level. This indicates that the carbon reduction effect of NECDP is significantly smaller in cities within city clusters than in non-city-cluster cities. The possible explanation is that, although cities in clusters benefit from industrial agglomeration, resource sharing, talent concentration, and policy coordination, which help to enhance inter-city collaborative innovation and industrial upgrading, these city clusters, as major economic hubs, are also the largest energy consumers and the regions with the most severe greenhouse gas emissions in China. Currently, the degree of economic agglomeration has not yet reached the point where energy-saving and carbon reduction effects occur. Therefore, the carbon reduction effect of NECDP is stronger in non-city-cluster cities.

5.6.4 Resource endowment

According to the "National Sustainable Development Plan for Resource-Based Cities (2013–2020)" issued by the State Council, the sample cities during the study period are classified into two categories: resource-based cities and non-resource-based cities. The impact of NECDP on carbon emissions is then assessed based on the cities' resource endowments. As shown in Columns (7) and (8) of Table 6, the *NECDP* coefficients for resource-based and non-resource-based cities are −0.123 and −0.157, respectively, both significant at the 1% level. This suggests that NECDP can reduce carbon emissions in both types of cities, with a stronger reduction effect in non-resource-based cities. The likely explanation is that NECDP effectively utilizes both command-and-control environmental regulations and market-driven competitive mechanisms, which stimulate green technological innovation in enterprises, forcing them to phase out outdated production capacities, enhance energy efficiency, and reduce carbon emissions. In resource-based cities, however, the long-standing path dependence and low-end lock-in development model result in a reduced carbon reduction effect of NECDP.

6 Discussion

This paper examines the carbon reduction effects of the NECDP in the context of energy transition strategies and urban low-carbon development. As the world's largest energy consumer and carbon emitter, China's efforts in energy conservation and emission reduction are crucial for achieving global carbon neutrality targets. Energy transition policies, as an environmental strategy centered on source prevention, create both incentives and constraints for local governments, businesses, and the public. Carbon emissions, with their negative externalities, broad impacts, dynamics, and complexity, cannot be addressed by government, market, or social mechanisms alone. Solving this issue involves the interests of the nation, government, businesses, and the public. Therefore, studying the energy-saving and carbon-reduction effects of this policy offers valuable insights for constructing a diversified environmental governance system.

This paper builds on existing research by explaining the carbon reduction mechanisms of NECDP from the perspectives of government, businesses, and the public. Empirical findings show that NECDP significantly reduces carbon emissions, although with a time lag effect, emphasizing the need for patience and continuity in policy formulation and implementation. The mechanism analysis reveals that NECDP promotes green technological innovation, clean low-carbon production, and industrial upgrading by influencing the actions of governments, businesses, and the public, thus supporting urban carbon reduction. Consequently, the central government should continue refining local environmental performance assessment systems and long-term supervision mechanisms. It should also expand subsidies for businesses' development of new energy technologies and related tax incentives, encouraging energy-saving and clean technologies as well as new energy product research and development. This will drive more resources into the new energy sector and help shift industrial structures from high-energy, low-efficiency models to green, low-carbon, and intensive forms. Additionally, local governments should guide the public toward green consumption and sustainable travel, promoting joint efforts from governments, businesses, and the public to drive urban energy consumption and low-carbon transformation.

Finally, the heterogeneity analysis highlights that the carbon reduction effect of NECDP is more significant in cities with high levels of government environmental attention, high digitalization, resource-based cities, and non-urban clusters. Thus, during policy implementation, greater emphasis should be placed on the flexibility and adaptability of the policy. Leveraging resource endowments and urbanization models, the coordinated development of digitalization and new urbanization should be accelerated. Digital economy tools can address the energy dependence and low-end lock-in effects in resource-based cities, promote free flow of factors and policy coordination across urban clusters, and accelerate the point at which economic agglomeration in urban clusters leads to energy-saving and emission-reduction effects.

7 Limitations and future research

This study provides an important assessment of the emission reduction effects of NECDP. However, several limitations remain, suggesting directions for future research improvement. 1) This study utilizes panel data from 266 cities in China spanning from 2005 to 2020. While this dataset is highly representative, both the policy environment and urban development dynamics may change over time. Future research could incorporate more recent data to capture the latest effects of policies on carbon reduction and to track the evolving trends of urban low-carbon transformations. Furthermore, in examining the mediating role of green technological innovation, future studies may benefit from using micro-level enterprise data for a more precise evaluation of its impact mechanisms. 2) In examining the carbon reduction mechanism related to public behavior, this study employs the public environmental awareness index to measure the public's level of environmental concern. Increased public environmental participation encourages more green consumption and sustainable travel. However, due to limitations in data availability, city-level data on public green consumption and travel could not be obtained, which broadens the scope of this mechanism analysis. 3) This study uses parallel trend tests, PSM-DID, and robustness checks—such as excluding other policies and substituting dependent variables—to evaluate the effect of NECDP on urban carbon emissions. While these methods provide solid evidence, future research could incorporate more formal statistical approaches, such as pre-trend testing, to further strengthen the robustness of the methodology. 4) This study primarily focuses on China's NECDP and does not fully

integrate an international perspective. For example, the EU's Clean Energy Framework emphasizes regulatory uniformity, cross-border coordination, and policy coherence, whereas NECDP is distinguished by stronger local autonomy, a gradual implementation approach, and region-specific pilot programs. Future research could undertake cross-national comparative analyses to assess how energy transition policies in different countries influence urban carbon emissions. Such comparative insights would be instrumental in informing the development of effective global low-carbon energy transition strategies.

8 Conclusion and policy implications

8.1 Conclusion

Using panel data from 266 prefecture-level cities between 2005 and 2020, this study examines the policy effects and mechanisms of NECDP on urban carbon emissions, treating it as an exogenous policy shock.

(1) The findings indicate that NECDP significantly reduces urban carbon emissions and promotes the green, low-carbon transformation of cities. This conclusion holds even after a series of robustness and placebo tests.
(2) The mechanism analysis shows that NECDP encourages governments to enhance environmental regulation and technological investment, raise public environmental awareness, and push businesses to innovate green technologies and adopt clean, low-carbon production practices. These efforts drive industrial restructuring, which in turn reduces urban carbon emissions.
(3) Heterogeneity analysis reveals that the carbon reduction effects of NECDP vary significantly based on government environmental attention, digitalization levels, resource endowment, and city size. Furthermore, while NECDP plays a significant role in reducing carbon emissions, it is not the sole factor; other policies, such as "low-carbon cities" and "smart cities," also facilitate the green and low-carbon transformation of urban areas.

8.2 Policy implications

Firstly, Continuously advance the development of New Energy Cities Demonstration Policy (NECDP). The NECDP effectively promotes collaborative participation from local governments, enterprises, and the public, facilitated by strengthened environmental regulation and subsidy incentives. It is crucial to further enhance environmental governance frameworks, provide clearer financial incentives, and broaden public engagement channels. By empowering the public with a stronger voice in environmental matters, stakeholders—government, enterprises, and the public—can better coordinate efforts toward sustainable, low-carbon production and consumption, ultimately facilitating successful urban low-carbon transition.

Secondly, it is essential to ensure balance in policy implementation. Flexible subsidy strategies should be designed to accommodate different enterprise types, reducing compliance costs for small and medium-sized enterprises to enhance policy fairness and effectiveness. Additionally, enterprise costs, employment impacts, and environmental performance should be monitored regularly. A phased, adjustable environmental regulatory mechanism should be adopted to maintain flexibility and minimize sudden disruptions to business operations. Moreover, the government should concurrently introduce retraining and employment transition programs for workers in traditional industries, alleviating employment pressures associated with the urban energy transition.

Thirdly, Leverage resource endowments and urbanization models to accelerate the coordinated development of digitalization and new urbanization. Specifically, accelerate the development of new infrastructure, enhance the role of the digital economy in driving industrial transformation, and address the energy dependence and low-end lock-in effects in resource-based cities. Facilitate the free movement of factors and policy coordination between cities in urban clusters, promoting the point at which economic agglomeration in urban clusters generates energy-saving and emission-reducing effects. This will help drive the development of greener, low-carbon cities and the digital transformation process during the construction of NECDP.

Data availability statement

The raw data supporting the conclusions of this article will be made available by the authors, without undue reservation.

Author contributions

SW: Conceptualization, Data curation, Methodology, Software, Validation, Writing – original draft, Writing – review and editing.

Funding

The author(s) declare that financial support was received for the research and/or publication of this article. This research was supported by the 2025 Henan Provincial Soft Science Research Program Project "Mechanisms and Implementation Pathways for Digital Economy-Driven High-Quality Development in the Zhengzhou Metropolitan Circle" (Project No. 252400411279).

Conflict of interest

The author declares that the research was conducted in the absence of any commercial or financial relationships that could be construed as a potential conflict of interest.

Generative AI statement

The author(s) declare that no Generative AI was used in the creation of this manuscript.

Publisher's note

References

Acheampong, A. O., Amponsah, M., and Boateng, E. (2020). Does financial development mitigate carbon emissions? Evidence from heterogeneous financial economies. *Energy Econ.* 88, 104768. doi:10.1016/j.eneco.2020.104768

Allan, G., Connolly, K., and Maurya, A. (2023). The city within the global: a framework for the simultaneous estimation of city emissions metrics. *J. Clean. Prod.* 429, 139323. doi:10.1016/j.jclepro.2023.139323

Beck, T., Levine, R., and Levkov, A. (2010). Big bad banks? The winners and losers from bank deregulation in the United States. *J. Financ.* 65 (5), 1637–1667. doi:10.1111/j.1540-6261.2010.01589.x

Chen, H., Guo, W., Feng, X., Wei, W., Liu, H., Feng, Y., et al. (2021). The impact of low-carbon city pilot policy on the total factor productivity of listed enterprises in China. *Resour. Conserv. Recycl.* 169, 105457. doi:10.1016/j.resconrec.2021.105457

Chen, J. H., and Long, X. W. (2024). Fiscal decentralization and local environmental governance when performance evaluation Matters. *Appl. Econ.*, 1–15. doi:10.1080/00036846.2024.2411464

Chen, M., Su, Y. T., Piao, Z. X., Zhu, J. H., and Yue, X. G. (2023). The green innovation effect of urban energy saving construction: a quasi-natural experiment from new energy demonstration city policy. *J. Clean. Prod.* 428, 139392. doi:10.1016/j.jclepro.2023.139392

Chen, Y., Chen, S., and Miao, J. (2024). Does smart city pilot improve urban green economic efficiency: accelerator or inhibitor. *Environ. Impact Assess. Rev.* 104, 107328. doi:10.1016/j.eiar.2023.107328

Cheng, Z. H., Yu, X. J., and Zhang, Y. (2023). Is the construction of new energy demonstration cities conducive to improvements in energy efficiency? *Energy* 263, 125517. doi:10.1016/j.energy.2022.125517

Chiappinelli, O., Dalò, A., and Giuffrida, L. M. (2024). "The greener, the better? Evidence from government contractors," in *UB economics–working papers, 2024*, E24/474.

Chu, Z., Bian, C., and Yang, J. (2022). How can public participation improve environmental governance in China? A policy simulation approach with multi-player evolutionary game. *Environ. Impact Assess. Rev.* 95, 106782. doi:10.1016/j.eiar.2022.106782

Ding, Y. Y., Bi, C. F., Qi, Y. X., and Han, D. R. (2024). Coordinated governance of energy transition policy and pollution and carbon reduction: a quasi-natural experiment based on new energy demonstration city policy. *Energy Strateg. Rev.* 53, 101395. doi:10.1016/j.esr.2024.101395

Dong, B., Xu, Y., and Fan, X. (2020). How to achieve a win-win situation between economic growth and carbon emission reduction: empirical evidence from the perspective of industrial structure upgrading. *Environ. Sci. Pollut. Res.* 27 (35), 43829–43844. doi:10.1007/s11356-020-09883-x

Dong, F., Wang, Y., Su, B., Hua, Y., and Zhang, Y. (2019). The process of peak CO_2 emissions in developed economies: a perspective of industrialization and urbanization. *Resour. Conserv. Recycl.* 141, 61–75. doi:10.1016/j.resconrec.2018.10.010

Dong, X., Wei, Y., and Xiao, X. (2022). How does fiscal decentralization affect green innovation? *China Popul. Resour. Environ.* 32 (8), 62–74.

Du, K., Li, P., and Yan, Z. (2019). Do green technology innovations contribute to carbon dioxide emission reduction? Empirical evidence from patent data. *Technol. Forecast. Soc. Chang.* 146, 297–303. doi:10.1016/j.techfore.2019.06.010

Feng, Y., Li, Y., Nie, C. F., and Chen, Z. (2024). Can an energy transition strategy induce urban green innovation? Evidence from a quasi-natural experiment in China. *Sustainability* 16 (8), 3263. doi:10.3390/su16083263

Gao, X. L., Zhang, G. X., Zhang, Z. H., Wei, Y. G., Liu, D. Y., and Chen, Y. D. (2024). How does new energy demonstration city pilot policy affect carbon dioxide emissions? Evidence from a quasi-natural experiment in China. *Environ. Res.* 244, 117912. doi:10.1016/j.envres.2023.117912

Gu, R., Li, C., Li, D., Yang, Y., and Gu, S. (2022). The impact of rationalization and upgrading of industrial structure on carbon emissions in the beijing-tianjin-hebei urban agglomeration. *Int. J. Environ. Res. Public Health* 19, 7997. doi:10.3390/ijerph19137997

Guo, B. N., Feng, Y., Wang, X., and Lin, J. (2023). New energy demonstration city construction and high-quality economic development. *Singap. Econ. Rev.*, 1–22. doi:10.1142/S0217590823470069

Guo, Q., and Zhong, J. (2022). The effect of urban innovation performance of smart city construction policies: evaluate by using a multiple period difference-in-differences model. *Technol. Forecast. Soc. Chang.* 184, 122003. doi:10.1016/j.techfore.2022.122003

Hong, S., Hui, E. C. M., and Lin, Y. (2022). Relationships between carbon emissions and urban population size and density, based on geo-urban scaling analysis: a multi-carbon source empirical study. *Urban Clim.* 46, 101337. doi:10.1016/j.uclim.2022.101337

Huang, J., and Guo, L. (2022). Research on the impact of financial development in different regions on the decoupling of carbon emissions from economic growth. *Energy Environ.* 34 (6), 2007–2030. doi:10.1177/0958305X221107341

Kou, J., and Xu, X. (2022). Does internet infrastructure improve or reduce carbon emission performance? --A dual perspective based on local government intervention and market segmentation. *J. Clean. Prod.* 379, 134789. doi:10.1016/j.jclepro.2022.134789

Kumar, S., and Sen, R. (2025). Are larger or denser cities more emission efficient? Exploring the nexus between urban household carbon emission, population size and density. *Appl. Energy.* 377, 124500. doi:10.1016/j.apenergy.2024.124500

Lei, L., Liu, J., and Zhou, X. (2023). Addressing carbon inequity: examining factors driving the path to just transition. *Environ. Impact Assess. Rev.* 103, 107280. doi:10.1016/j.eiar.2023.107280

Li, X., and Zhao, C. K. (2024). Did innovative city constructions reduce carbon emissions? A quasi-natural experiment in China. *Environ. Dev. Sustain.* 26 (3), 6315–6340. doi:10.1007/s10668-023-02964-0

Li, Y., Cheng, H., and Ni, C. (2023). Energy transition policy and urban green innovation vitality: a quasi-natural experiment based on the new energy demonstration city policy. *China Popul. Resour. Environ.* 33 (1), 137–149.

Lindman, Å., and Söderholm, P. (2016). Wind energy and green economy in Europe: measuring policy-induced innovation using patent data. *Appl. Energy.* 179, 1351–1359. doi:10.1016/j.apenergy.2015.10.128

Liu, X. Q., Wang, C. A., Wu, H. T., Yang, C. Y., and Albitar, K. (2023). The impact of the new energy demonstration city construction on energy consumption intensity: exploring the sustainable potential of China's firms. *Energy* 283, 128716. doi:10.1016/j.energy.2023.128716

Liu, Y., Chen, Y., Xie, T., and Xia, Y. (2024). A three-player game model for promoting enterprise green technology innovation from the perspective of media coverage. *Front. Public Health* 11, 1253247. doi:10.3389/fpubh.2023.1253247

Lu, J., and Wang, E. (2019). Impact of new energy demonstration city construction on regional environmental pollution control. *Resour. Sci.* 41 (11), 2107–2118. doi:10.18402/resci.2019.11.13

Ma, J. T., Hu, Q. G., Shen, W. T., and Wei, X. Y. (2021). Does the low-carbon city pilot policy promote green technology innovation? Based on green patent data of Chinese a-share listed companies. *Int. J. Environ. Res. PUBLIC HEALTH* 18 (7), 3695. doi:10.3390/ijerph18073695

Mai, Y., Yu, K., and Zhang, X. (2024). Enhancing corporate carbon performance through green innovation and digital transformation: evidence from China. *Int. Rev. Econ. Financ.* 96, 103630. doi:10.1016/j.iref.2024.103630

Mei, C. Q., and Wang, X. N. (2017). Political incentives and local policy innovations in China. *J. Chin. Polit. Sci.* 22 (4), 519–547. doi:10.1007/s11366-017-9513-8

Miao, L., and Gu, H. (2024). From quantity to quality: do the political incentives matter for green transformation in China? *J. Chin. Polit. Sci.* 29 (4), 613–648. doi:10.1007/s11366-023-09869-9

Peng, H., Ling, K., and Zhang, Y. (2024). The carbon emission reduction effect of digital infrastructure development: evidence from the broadband China policy. *J. Clean. Prod.* 434, 140060. doi:10.1016/j.jclepro.2023.140060

Peng, H., and Liu, Y. (2018). How government subsidies promote the growth of entrepreneurial companies in clean energy industry: an empirical study in China. *J. Clean. Prod.* 188, 508–520. doi:10.1016/j.jclepro.2018.03.126

Sarkodie, S. A., Owusu, P. A., and Leirvik, T. (2020). Global effect of urban sprawl, industrialization, trade and economic development on carbon dioxide emissions. *Environ. Res. Lett.* 15 (3), 034049. doi:10.1088/1748-9326/ab7640

Shan, S., Genc, S. Y., Kamran, H. W., and Dinca, G. (2021). Role of green technology innovation and renewable energy in carbon neutrality: a sustainable investigation from Turkey. *J. Environ. Manage.* 294, 113004. doi:10.1016/j.jenvman.2021.113004

Song, Y., Pang, X. Q., Zhang, Z. Y., and Sahut, J. M. (2024). Can the new energy demonstration city policy promote corporate green innovation capability? *Energy Econ.* 136, 107714. doi:10.1016/j.eneco.2024.107714

Wang, C., Zhang, X., Vilela, A. L. M., Liu, C., and Stanley, H. E. (2019). Industrial structure upgrading and the impact of the capital market from 1998 to 2015: a spatial econometric analysis in Chinese regions. *Phys. A Stat. Mech. its Appl.* 513, 189–201. doi:10.1016/j.physa.2018.08.168

Wang, H., and Guo, J. (2024). Research on the impact mechanism of multiple environmental regulations on carbon emissions under the perspective of carbon peaking pressure: a case study of China's coastal regions. *Ocean. Coast. Manage* 249, 106985. doi:10.1016/j.ocecoaman.2023.106985

Wang, Q., and Su, M. (2019). The effects of urbanization and industrialization on decoupling economic growth from carbon emission - a case study of China. *Sust. Cities Soc.* 51, 101758. doi:10.1016/j.scs.2019.101758

Wang, Q., and Yi, H. T. (2021). New energy demonstration program and China's urban green economic growth: do regional characteristics make a difference? *Energy Policy* 151, 112161. doi:10.1016/j.enpol.2021.112161

Wang, Q., and Zhang, F. (2021). The effects of trade openness on decoupling carbon emissions from economic growth – evidence from 182 countries. *J. Clean. Prod.* 279, 123838. doi:10.1016/j.jclepro.2020.123838

Wang, S. (2023). Digital economy development for urban carbon emissions:accelerator' or speed bump. *China Popul. Resour. Environ* 33 (6), 11–22. doi:10.12062/cpre.20230124

Wang, X. C., Klemes, J. J., Wang, Y. T., Dong, X. B., Wei, H. J., Xu, Z. H., et al. (2020). Water-Energy-Carbon Emissions nexus analysis of China: an environmental input-output model-based approach. *Appl. Energy.* 261, 114431. doi:10.1016/j.apenergy.2019.114431

Wang, X. R., Long, R. Y., Sun, Q. Q., Chen, H., Jiang, S. Y., Wang, Y. J., et al. (2024). Spatial spillover effects and driving mechanisms of carbon emission reduction in new energy demonstration cities. *Appl. Energy.* 357, 122457. doi:10.1016/j.apenergy.2023.122457

Wang, Y. F., Song, Q. J., He, J. J., and Qi, Y. (2015). Developing low-carbon cities through pilots. *Clim. Policy.* 15, S81–S103. doi:10.1080/14693062.2015.1050347

Wang, Z. H., Zhao, Z. J., and Wang, C. X. (2021). Random forest analysis of factors affecting urban carbon emissions in cities within the Yangtze River Economic Belt. *PLoS One* 16 (6), e0252337. doi:10.1371/journal.pone.0252337

Wen, Z., and Ye, B. (2014). Analyses of mediating effects: the development of methods and models. *Adv. Psychol. Sci.* 22 (5), 731–745. doi:10.3724/sp.j.1042.2014.00731

Wu, J., Wu, Y., Guo, X., and Cheong, T. S. (2016). Convergence of carbon dioxide emissions in Chinese cities: a continuous dynamic distribution approach. *Energy Policy* 91, 207–219. doi:10.1016/j.enpol.2015.12.028

Wu, L., Yang, M., and Sun, K. (2022). Impact of public environmental attention on environmental governance of enterprises and local governments. *China Popul. Resour. Environ.* 32 (2), 1–14.

Wu, S. P. (2022). Smart cities and urban household carbon emissions: a perspective on smart city development policy in China. *J. Clean. Prod.* 373, 133877. doi:10.1016/j.jclepro.2022.133877

Xiang, Y., Cui, H., and Bi, Y. (2023). The impact and channel effects of banking competition and government intervention on carbon emissions: evidence from China. *Energy Policy* 175, 113476. doi:10.1016/j.enpol.2023.113476

Xu, Q., Dong, Y. X., and Yang, R. (2018). Urbanization impact on carbon emissions in the Pearl River Delta region: kuznets curve relationships. *J. Clean. Prod.* 180, 514–523. doi:10.1016/j.jclepro.2018.01.194

Yang, M., Liu, Y., Tian, J., Cheng, F., and Song, P. (2022). Dynamic evolution and regional disparity in carbon emission intensity in China sustainability, 14. (Reprinted.

Yang, M. W., Yang, W. J., Wang, Z., and Liu, J. (2023). Does the pilot construction of new-energy cities promote particulate matter 2.5 (PM2.5) reduction? Evidence from China. *Front. Environ. Sci.* 11. doi:10.3389/fenvs.2023.1094935

Yang, X. D., Wang, W. L., Wu, H. T., Wang, J. L., Ran, Q. Y., and Ren, S. Y. (2022). The impact of the new energy demonstration city policy on the green total factor productivity of resource-based cities: empirical evidence from a quasi-natural experiment in China. *J. Environ. Plan. Manag.* 66 (2), 293–326. doi:10.1080/09640568.2021.1988529

Yang, X. D., Zhang, J. N., Ren, S. Y., and Ran, Q. Y. (2021). Can the new energy demonstration city policy reduce environmental pollution? Evidence from a quasi-natural experiment in China. *J. Clean. Prod.* 287, 125015. doi:10.1016/j.jclepro.2020.125015

Ye, Z. P., Gao, H. Y., and Wu, W. X. (2024). Local government capacity and response strategies to central policy piloting goals: a case study of China's new-type urbanization plan. *Hum. Soc. Sci. Commun.* 11 (1), 1648. doi:10.1057/s41599-024-04170-3

Zhang, S., Ding, J., Zheng, H., and Wang, H. (2023). Does spatial functional division in urban agglomerations reduce negative externalities in large cities? Evidence from urban agglomerations in China. *Heliyon* 9 (10), e20419. doi:10.1016/j.heliyon.2023.e20419

Zhang, Z., Zhang, J., and Feng, Y. (2021). Assessment of the carbon emission reduction effect of the air pollution prevention and control action plan in China *international Journal of environmental Research and public health*. *Int. J. Environ. Res. Public Health* 18, 13307. (Reprinted. doi:10.3390/ijerph182413307

Zhao, X. C., Jiang, M., and Zhang, W. (2022). Decoupling between economic development and carbon emissions and its driving factors: evidence from China. *Int. J. Environ. Res. PUBLIC HEALTH* 19 (5), 2893. doi:10.3390/ijerph19052893

Zhu, Q., and Peng, X. Z. (2012). The impacts of population change on carbon emissions in China during 1978-2008. *Environ. Impact Assess. Rev.* 36, 1–8. doi:10.1016/j.eiar.2012.03.003

frontiers | Frontiers in Environmental Science

TYPE Original Research
PUBLISHED 30 April 2025
DOI 10.3389/fenvs.2025.1581983

OPEN ACCESS

EDITED BY
Jing Zhao,
Xi'an University of Technology, China

REVIEWED BY
Sukun Cheng,
University of Reading, United Kingdom
Kai Feng,
North China University of Water Resources and Electric Power, China
Biyao Zhai,
Nanjing Hydraulic Research Institute, China

*CORRESPONDENCE
Chao Li,
nmndlc@imau.edu.cn
Shuixia Zhao,
zhaosx@iwhr.com

RECEIVED 23 February 2025
ACCEPTED 07 April 2025
PUBLISHED 30 April 2025

CITATION
Cui S, Zhao S, Li C, Wu Y, Kolerski T and Zhang M (2025) Modelling and evaluation of net ecosystem productivity and its driving factors in Inner Mongolia.
Front. Environ. Sci. 13:1581983.
doi: 10.3389/fenvs.2025.1581983

Modelling and evaluation of net ecosystem productivity and its driving factors in Inner Mongolia

Shengjie Cui[1,2], Shuixia Zhao[2,3]*, Chao Li[1]*, Yingjie Wu[2,3], Tomasz Kolerski[4] and Mengmeng Zhang[5]

[1]College of Water Conservancy and Civil Engineering, Inner Mongolia Agricultural University, Hohhot, Inner Mongolia, China, [2]Yinshanbeilu Grassland Ecohydrology National Observation and Research Station, China Institute of Water Resources and Hydropower Research, Beijing, China, [3]Institute of Pastoral Hydraulic Research, Ministry of Water Resources, Hohhot, Inner Mongolia, China, [4]Faculty of Civil and Environmental Engineering, Gdańsk University of Technology, Gdańsk, Poland, [5]College of Geographical Science, Inner Mongolia Normal University, Hohhot, China

Net ecosystem productivity (NEP) is a critical indicator for characterizing the carbon cycle dynamics within terrestrial ecosystems. This study employs six different combinations of methods for calculating Net Primary Productivity (NPP) and heterotrophic soil respiration (R_h) to estimate monthly NEP values in Inner Mongolia from 2001 to 2021. The carbon flux observation data obtained through the eddy covariance method are used to validate and evaluate these combinations, and the best NEP estimation model combination is selected, and the spatiotemporal distribution patterns of NEP along with its primary driving factors are analyzed. Results show that: 1) The NEP estimates derived from MODIS NPP combined with the Global Soil Respiration Model (GSMSR) and Bond-Lamberty's R_s-R_h relationship model exhibit a strong correlation with validated data; 2) The NEP in Inner Mongolia shows a significant increasing trend, with an annual average value of 168.73 gC·m^{-2}·a^{-1}, or 177.57 gC·m^{-2}·a^{-1} when excluding barren. Forests, croplands, and grasslands are identified as the primary carbon sinks during the growing season, with average NEP values of 84.81, 46.41, and 32.95 gC·m^{-2}·mth^{-1}, respectively; 3) Precipitation is the dominant meteorological factor driving the spatiotemporal variations of NEP across the region, contributing 72.29% to NEP during the growing season. Additionally, over 80% of areas influenced by human activities exhibit a positive impact on NEP; 4) The interannual and growing season increases in NEP are primarily attributed to climate change and anthropogenic activities, which account for 57% and 66.3% of NEP variations, respectively. These effects are particularly pronounced in the eastern forested regions and central grasslands of Inner Mongolia. The findings of this study provide valuable insights for regional carbon sink management and ecological environment protection.

KEYWORDS

net ecosystem productivity, CASA model, MODIS NPP, driving factors, Inner Mongolia

1 Introduction

The acceleration of global industrialization has precipitated a substantial increase in greenhouse gas emissions, particularly CO_2 (Raihan et al., 2022). According to the synthesis report of the Sixth Assessment Report (AR6) by the United Nations Intergovernmental Panel on Climate Change (IPCC) in 2023, atmospheric CO_2 concentrations have surged to

their highest levels in nearly two million years, accompanied by a global temperature rise of 1.1°C above pre-industrial levels (IPCC, 2023). These changes have triggered unprecedented climatic shifts worldwide, with extreme weather events such as intense heatwaves, heavy precipitation, and prolonged droughts becoming increasingly frequent, thereby disrupting the carbon balance within ecosystems (Kelong et al., 2011). To mitigate the adverse effects of carbon cycle imbalances on ecological systems and human livelihoods, the international community has emphasized the importance of enhancing carbon sinks, making their development across various ecosystems a critical strategy for achieving national "dual carbon" goals (Yu et al., 2022). Consequently, investigating the spatiotemporal dynamics of ecosystem carbon cycles and their driving factors is essential for advancing ecological civilization and ensuring the sustainability and security of human society. Inner Mongolia, situated within an arid and semi-arid region, represents the most extensive and diverse ecological functional area in northern China. The alterations in its ecosystem carbon storage have a considerable impact on the global ecosystem carbon cycle (Cao et al., 2023; Jiang et al., 2019; Meng et al., 2020). Therefore, investigating the spatiotemporal distribution patterns of terrestrial Net Ecosystem Productivity (NEP) and its drivers in Inner Mongolia is of significant scientific importance, enabling a scientifically informed explanation of the regional ecosystem carbon cycle and facilitating the rational use of forest and grassland resources.

Gross Primary Productivity (GPP), Net Primary Productivity (NPP), and NEP are key indicators of ecosystem carbon cycling, reflecting the response of different ecosystems to climate change and the productive capacity of plant communities under natural environmental conditions (Zhou et al., 2020; Hou et al., 2023; Zheng et al., 2023; Huang et al., 2023a; Li et al., 2022; Liu et al., 2022; Ding et al., 2025). NEP, representing NPP minus the products of photosynthesis consumed by heterotrophic soil respiration (R_h) and soil total respiration (R_s), more accurately reflects the relationship between photosynthesis, respiration, and energy balance within ecosystems compared to GPP and NPP. NPP is highly effective for quantitatively evaluating an ecosystem's carbon sequestration potential in relation to climate change, serving as a crucial indicator for measuring carbon sinks, sources, and the global carbon balance of ecosystems (Mendes et al., 2020; Song et al., 2020; Zou et al., 2022; Chen et al., 2024). NEP can be measured directly using carbon flux or eddy correlation techniques or estimated based on physiological or ecological models. Although direct measurements are the most straightforward method with minimal errors, they are generally infeasible for large-scale studies due to site layout and accuracy requirements (Lees et al., 2018; Berg et al., 2022; Zhi et al., 2024). Estimation of NEP based on Carnegie-Ames-Stanford Approach (CASA) and Carbon Exchange in Vegetation–Soil–Atmosphere System (CEVSA) models, integrated with remote sensing and other geographic information systems, has become the primary method for the quantitative assessment of NEP. However, these model-based estimates are subject to subsurface influences at varying spatial and temporal scales, often leading to significant uncertainty (Liang et al., 2023; Qiu et al., 2022; Zuo et al., 2023; Ouyang et al., 2021; Xu et al., 2024; Zhang et al., 2025).

The carbon cycle in terrestrial ecosystems is influenced by a complex array of environmental factors, making the exploration of its drivers and dominant factors a prominent focus in global carbon change research. Correlation analysis, random forest modelling, regression analysis, and other machine learning techniques are the primary research methods. For instance, Lu et al. (2023) found that NEP in Xinjiang is more sensitive to rainfall, while Wang et al. (2022a) observed that climatic factors had the largest contribution to NEP changes in the mountainous arid regions of northwestern China, with anthropogenic activities contributing negatively. Zhang et al. (2024) identified elevation as the dominant factor influencing NEP changes in Heilongjiang Province, and Cao et al. (2022) found precipitation to be the main climatic factor influencing the spatial distribution of NEP in the Yellow River Basin. Variations in NEP patterns, driving factors, and spatial distribution within the same region are markedly influenced by regional subsurface conditions and vegetation types (Huang et al., 2023b; Wang et al., 2022b; Bejagam and Sharma, 2022). Current research methodologies are limited by their dependence on singular carbon sink estimation models and exhibit insufficient comparative analysis of carbon sink estimation outcomes from alternative models.

Forest and grassland ecosystems, indispensable components of terrestrial ecosystems, play a crucial role in the global carbon cycle (Ahlström et al., 2015; Bai and Cotrufo, 2022). Data from the third national land survey indicate that the forested area in Inner Mongolia is 24.37×10^4 km^2 (23%), encompassing the temperate coniferous forest belt, the mid-temperate deciduous broadleaf forest belt, and the warm-temperate deciduous broadleaf forest belt. The grassland area extends to 54.37×10^4 km^2, representing the most extensive terrestrial ecosystem in Inner Mongolia, with meadow steppes, typical steppes, desert steppes, and grassland desertification areas accounting for 5.57%, 37.10%, 10.75%, and 11.55%, respectively. The total cropland area is 11.50×10^4 km^2. These ecosystems are essential terrestrial ecological resources for achieving the dual carbon targets (Balasubramanian et al., 2020; Liu et al., 2019). As a vital livestock and grassland production base in China and a northern ecological security barrier, Inner Mongolia is significantly affected by pronounced spatiotemporal climate variations and frequent interannual extreme climate events, resulting in an unclear understanding of the regional NEP and its driving factors.

This paper estimates monthly NEP in the study area from 2001 to 2021 using six NPP and R_h model combinations. The best fit model combination is selected from the vorticity-related data of desert grassland and typical grassland to analyze the spatial and temporal distribution pattern of NEP. Furthermore, the principal driving factors and contribution rates of carbon sources and sinks in Inner Mongolia are assessed based on influencing factors, including climate change and human activities.

2 Materials and methods

2.1 Research area

The Inner Mongolia Autonomous Region is located in northern China, spanning from 37°24′-53°23′N to 97°12′-126°04′E. Encompassing the northeastern, northern, and northwestern parts of the country, it stretches approximately 2,400 km from east to west and 1,700 km from north to south. The region's diverse

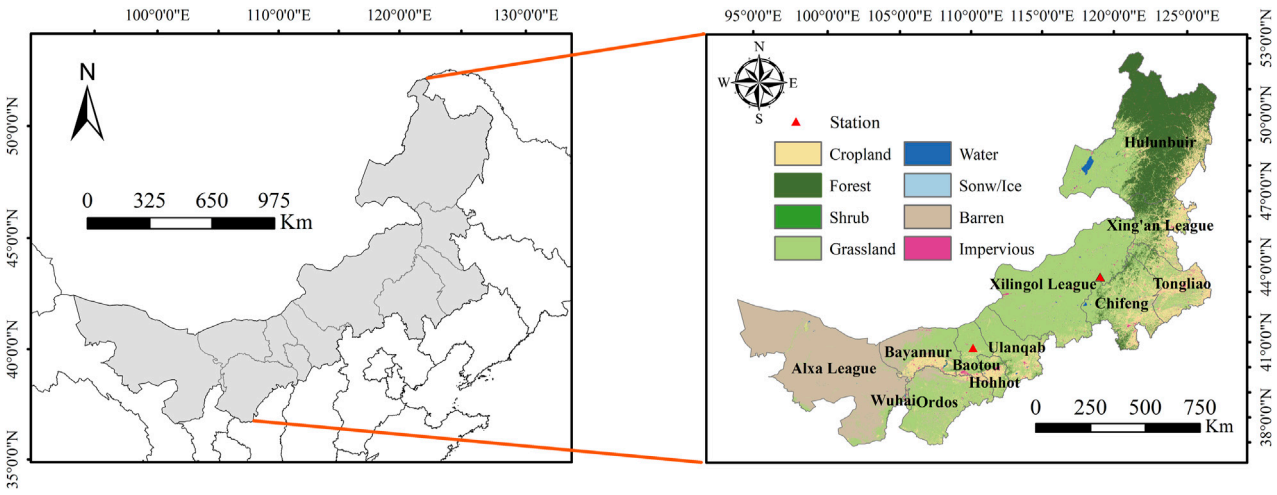

FIGURE 1
Overview of the study area.

TABLE 1 Data sources and units.

Data	Unit	Time span	Spatial resolution	Data sources
GPP	$gC{\cdot}m^{-2}$	8 days	500 m × 500 m	https://earthdata.nasa.gov/
NPP	$gC{\cdot}m^{-2}$	Year	500 m × 500 m	https://earthdata.nasa.gov/
TEM	0.1p	Month	1 km × 1 km	http://data.tpdc.ac.cn
PRE	0.1 mm	Month	1 km × 1 km	http://data.tpdc.ac.cn
NDVI	—	Month	500 m × 500 m	https://earthdata.nasa.gov/
SOL	$W\ m^{-2}$	Month	500 m × 500 m	https://cds.climate.copernicus.eu
Land use	—	Year	30 m × 30 m	https://zenodo.org/
PET	0.1 mm	Month	1 km × 1 km	http://data.tpdc.ac.cn
Soil carbon density	$kg/\ m^2$	-	1 km × 1 km	https://doi.org/10.4060/cc3823en

landscape includes forested and grassy areas in the east, expansive grasslands in the central region, and predominantly barren terrain in the west, as depicted in Figure 1.

With an average altitude exceeding 1,000 m, the region's topography is characterized by higher elevations in the southwest compared to the northeast. Inner Mongolia experiences a medium-temperate continental monsoon climate, marked by distinct seasonal variations. The climate transitions from humid and semi-humid conditions in the east to semi-arid and arid conditions in the west. Annual average temperatures range from 0°C to 8°C, while precipitation varies significantly across the region, from 50 mm to 450 mm annually. The annual total solar radiation here ranges from 5,400 to 5,900 $MJ{\cdot}m^{-2}$, with an average of about 5600 $MJ{\cdot}m^{-2}$. The spatial distribution of this resource shows a gradual increase from the northeast to the southwest.

Due to the diverse underlying surfaces across different zones, there are notable variations in annual potential evapotranspiration. For instance, areas near the Greater Khingan Mountains have potential evapotranspiration values below 1,200 mm, whereas most other regions exceed this threshold. It is important to note that Inner Mongolia's ecological environment is relatively fragile, with frequent occurrences of extreme droughts.

2.2 Data sourcing and preprocessing

The meteorological and remote sensing datasets utilized in this study, covering a comprehensive time span from 2001 to 2021, are systematically presented in Table 1. These datasets encompass a wide range of variables, including but not limited to precipitation (PRE), temperature (TEM), solar radiation (SOL), potential evapotranspiration (PET), and vegetation indices (NDVI), which are critical for analyzing the climatic and environmental dynamics over the two-decade period. The integration of these multi-source data provides a robust foundation for the subsequent analysis and modeling efforts in this research.

The carbon flux data associated with vortex measurements, obtained from the desert grassland site (Damao Station) (Song et al., 2022) and the typical grassland site (Xiwuqi Banner

Station) (Tan et al., 2023), were meticulously selected for model validation.

The meteorological and remote sensing raster datasets underwent standardized preprocessing in terms of spatial extent and resolution using ArcGIS. This preprocessing included raster projection transformation, resampling, and clipping procedures to ensure consistency across the datasets.

2.3 Research methods

2.3.1 NPP estimation model

The estimation of NPP in this study utilized MODIS annual NPP and 8-day GPP products, in conjunction with the CASA models. The monthly NPP formula derived from MODIS products is presented as Equations 1, 2:

$$NPP_8 = \left(GPP_8 / GPP_y\right) \times NPP_y \quad (1)$$

$$NPP_m = \sum NPP_{8i} \quad (2)$$

Where NPP_8 is 8-day NPP data in gC·m^{-2}; GPP_8 is the 8-day GPP data in gC·m^{-2}; GPP_y is the annual total GPP data in gC·m^{-2}; NPP_y is the annual total NPP in gC·m^{-2}; NPP_m is the monthly total NPP in gC·m^{-2}; NPP_{8i} indicates the NPP_8 data in the month i in gC·m^{-2}.

The present study employs the CASA model to compute monthly NPP (Piao et al., 2001), reducing the estimation time scale to 1 month and refining the input parameters of the model for enhanced accuracy. Finally, NPP data is estimated to have a temporal resolution of 1 month and a spatial resolution of 1 km. The NPP estimation in this model is based on the assimilated photosynthetic active radiation (APAR) by plants and their effective utilization of light energy (ε). The estimation formula is shown in Equation 3:

$$NPP(x,t) = APAR(x,t) \times \varepsilon(x,t) \quad (3)$$

Where, $\varepsilon(x,t)$ is the actual light energy utilization rate in gC·MJ^{-1}; $APAR(x,t)$ is the photosynthetically active radiation absorbed, calculated by the Equation 4 pixel x at t time in gC·m^{-2} in $\varepsilon(x,t)$ is calculated by the Equation 8:

$$\varepsilon(x,t) = T_{\varepsilon 1}(x,t) \times T_{\varepsilon 2}(x,t) \times W_{\varepsilon}(x,t) \times \varepsilon_{max} \quad (4)$$

Where, $T_{\varepsilon 1}(x,t)$ and $T_{\varepsilon 2}(x,t)$ are the stress coefficients of the maximum and minimum TEM on the actual light energy utilization $\varepsilon(x,t)$, $W_{\varepsilon}(x,t)$ is the, calculated separately using Equations 5, 6 water stress coefficient, and ε_{max} is the maximum light energy utilization under ideal conditions calculated using Equation 7.

$$T_{\varepsilon 1}(x,t) = 0.8 + 0.02 \times T_{opt}(x) - 0.0005 \times T_{opt}(x)^2 \quad (5)$$

$T_{opt}(x)$ is the optimal TEM for vegetation growth.

$$T_{\varepsilon 2}(x,t) = \frac{1.184}{1 + e^{0.2 \times T_{opt}(x) - 10 - t(x,t)}} \times \frac{1}{1 + e^{0.3 \times \left(T(x,t) - 10 - T_{opt}(x)\right)}} \quad (6)$$

When the average TEM of a month is 10°C higher or 13°C lower than the optimum TEM $T_{opt}(x)$, the $T_{\varepsilon 2}(x,t)$ of the month is equal to half of the average TEM of the month $T_{opt}(x)$.

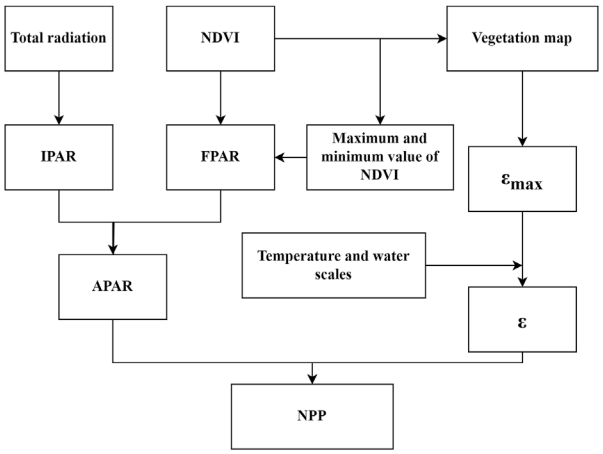

FIGURE 2
Flowchart for estimating NPP with CASA model.

$$W_{\varepsilon}(x,t) = 0.5 + 0.5 \times \frac{EET(x,t)}{PET(x,t)} \quad (7)$$

Where EET represents the actual evapotranspiration of the region.

$$APAR(x,t) = SOL(x,t) \times FPAR(x,t) \times 0.5 \quad (8)$$

Where $SOL(x,t)$ represents the SOL at the pixel x at time t in MJ·m^{-2}; $FPAR(x,t)$ is the photosynthetic active radiation absorption ratio of vegetation canopy; and, $FPAR(x,t) = \frac{NDVI(x,t) - NDVI_{min}}{NDVI_{max} - NDVI_{min}}$. The overall process of the CASA model to estimate NPP is shown in Figure 2.

2.3.2 R_h estimation model

The R_h of Inner Mongolia was estimated in this study using three well-established and validated models: the Pei. model (Pei et al., 2009), the GSMSR model (Yu et al., 2010) coupled with Bond-Lamberty, and the R_s-R_h relationship model developed by Shi (2015).

The calculation formula of the soil microbial heterotrophic respiration model established by Pei is as Equation 9:

$$R_h(x,t) = 0.22 \times \left(exp(0.0912T(x,t)) + ln(0.3145R(x,t) + 1)\right) \times 30 \times 46.5\% \quad (9)$$

Where, $T(x,t)$ is the average TEM of the pixel x at time t in °C; $R(x,t)$ is the average PRE of the pixel x at time t in mm.

The GSMSR model is primarily utilized for the computation of R_s, followed by the utilization of the R_s-R_h relationship model to calculate R_h. The calculation formula for the GSMSR model is as Equation 10:

$$R_s = (R_{DS=0} + M \times D_s) \times e^{ln\alpha e^{\beta t}/10} \times \frac{P + P_0}{P + K} \quad (10)$$

Where R_s is soil total respiration in gC·m^{-2}; D_s is the soil carbon density at a depth of 20 cm in kg/ m^2; $R_{DS=0}$ = 0.588; M = 0.118; α = 1.83; β = −0.0006; P_0 = 2.97; K = 5.66; P is the regional average monthly PRE in cm.

The R_h was calculated using the R_s-R_h relationship model constructed by Bond-Lamberty et al. (2004) and Shi (2015), respectively. The equation developed by Bond-Lamberty et al. is as Equation 11:

$$\ln R_h = 1.22 + 0.73\, ln\, R_s \tag{11}$$

The R_s-R_h relationship constructed by Shi is as Equation 12:

$$R_h = -0.0009R_s^2 + 0.6011R_s + 4.8874 \tag{12}$$

2.3.3 NEP estimation model

Without considering the influence of other natural and human factors, NEP is equal to the difference between vegetation NPP and R_h (Tang et al., 2016), and the calculation formula is as Equation 13.

$$NEP(x,t) = NPP(x,t) - R_h(x,t) \tag{13}$$

Where, $NEP(x,t)$ is the net ecosystem productivity of vegetation of the pixel x at time gC·m^{-2}. When NEP >0, vegetation acts as a carbon sink, otherwise, as a carbon source.

2.3.4 Correlation and significance analysis

The key climate factors influencing regional NEP changes were identified as PRE, TEM, SOL, and PET. Their spatial correlation with NEP at both annual and growing season scales was analyzed at the pixel level. The correlation coefficient (r) was calculated using the Equation 14.

$$r = \frac{\sum_{i=1}^{n}(x_i - \bar{x})(y_i - \bar{y})}{\sqrt{\sum_{i=1}^{n}(x_i - \bar{x})^2 \sum_{i=1}^{n}(y_i - \bar{y})^2}} \tag{14}$$

Where x_i and y_i are the time series of NEP and climatic elements, $\bar{x}$ and $\bar{y}$ are the annual average values of NEP and climatic factors. The value range of the correlation coefficient is between −1~1, r > 0 indicates a positive correlation between the two groups of variables, and r < 0 indicates a negative correlation. The greater the magnitude of |r|, the stronger the correlation between the two sets of variables.

T-test is used to determine whether the correlation between NEP and climate factors is significant. The calculation formula of the T-value is as Equation 15:

$$t = \frac{r\sqrt{n-2}}{\sqrt{1-r^2}} \tag{15}$$

If the absolute value of t is greater than $t_{0.05}$ it means that the correlation between the two groups of variables passes the 0.05 level significance test; otherwise, it means that the correlation is not significant.

2.3.5 NEP trend analysis

The trend of the NEP long-time series was analyzed using the Theil-Sen (Sen) median analysis combined with the Mann-Kendall (M-K) test method. Sen median analysis is a robust nonparametric trend statistical method (Cai and Yu, 2009), and its calculation formula is as Equation 16:

$$S_{NEP} = Median\left(\frac{NEP_j - NEP_i}{j - i}\right) \tag{16}$$

Where NEP_j and NEP_i represent the NEP index of the year j and the year i respectively, and S_{NEP} is the changing trend of NEP. A S_{NEP} >0 indicates an increasing NEP is while S_{NEP} = 0 and S_{NEP} <0 indicate a constant and decreasing NEP, respectively. Larger absolute value of S_{NEP}, indicate a stronger change in the trend.

Sen median analysis lacks a statistical significance test for trend analysis, thus the M-K test was employed for evaluation. The M-K test is a non-parametric statistical test that can be utilized to determine the presence of a significant trend in a time series. The formula for the M-K test is as Equations 17–19:

$$S = \sum_{i=1}^{n-1}\sum_{j=i+1}^{n} sgn\left(NEP_j - NEP_i\right) \tag{17}$$

$$sgn\left(NEP_j - NEP_i\right) = \begin{cases} 1 & NEP_j > NEP_i \\ 0 & NEP_j = NEP_i \\ -1 & NEP_j < NEP_i \end{cases} \quad \forall\, i < j \tag{18}$$

$$Var(S) = \frac{n(n-1)(2n+5)}{18} \tag{19}$$

Where n ≥ 10 indicates a normal distribution for the statistic S, with S representing the test statistic, n denoting the length of the time series, sgn indicating the symbolic function, and Var(S) representing variance. For this study's time series length of 21 (2001–2021), after standardizing the test statistics, the calculation by Equation 20.

$$Z = \begin{cases} \dfrac{S}{\sqrt{Var(S)}} & S > 0 \\ 0 & S = 0 \\ \dfrac{S+1}{\sqrt{Var(S)}} & S < 0 \end{cases} \tag{20}$$

The threshold of the test statistic Z is set under various significance levels to determine the statistical significance of the trend. Specifically, when |Z| exceeds 1.96, it indicates that the trends pass the significance test at the confidence level of 95%.

2.3.6 NEP driver analysis

The method of partial derivative correlation was employed to quantitatively assess the respective contributions of climate factors and human activity factors to NEP (Liu and Sun, 2016). The calculation formula is provided as Equation 21.

$$\begin{aligned} \frac{dNEP}{dt} &\approx \frac{\delta NEP}{\delta PRE} \times \frac{dPRE}{dt} + \frac{\delta NEP}{\delta TEM} \times \frac{dTEM}{dt} + \frac{\delta NEP}{\delta SOL} \times \frac{dSOL}{dt} \\ &\quad + \frac{\delta NEP}{\delta PET} \times \frac{dPET}{dt} + H_{con} \\ &= PRE_{con} + TEM_{con} + SOL_{con} + PET_{con} + H_{con} = C_{con} + H_{con} \end{aligned} \tag{21}$$

Where $PRE_{con}, TEM_{con}, SOL_{con}, PET_{con}$ are the contributions of PRE, TEM, SOL, and PET to NEP, respectively. C_{con} represents the contribution of climate factors to NEP variation as $C_{con} = PRE_{con} + TEM_{con} + SOL_{con} + PET_{con}$; H_{con} represents the contribution of other factors (human activities, natural disasters, etc.) to the change of NEP, and it is generally believed that human activities play a major role (Qu et al., 2020); $\frac{dNEP}{dt}, \frac{dPRE}{dt}, \frac{dTEM}{dt}, \frac{dSOL}{dt}, \frac{dPET}{dt}$ are the variation trends of NEP, PRE, TEM, SOL, and PET with time t, respectively, calculated by the multiple linear regression model as Equation 22.

TABLE 2 Method for identifying primary factors influencing NEP changes in Inner Mongolia and the calculation principle for contribution rates.

Effecting factor		Identification (yr^{-1})		Contribution rate (%)	
		C_{con}	H_{con}	Climate change	Human activities
$\frac{dNEP}{dt}>0$	Combined contribution	>0	>0	$\frac{C_{con}}{C_{con}+H_{con}}$	$\frac{H_{con}}{C_{con}+H_{con}}$
	Climate change	>0	<0	100	0
	Human activities	<0	>0	0	100
$\frac{dNEP}{dt}<0$	Combined contribution	<0	<0	$\frac{C_{con}}{C_{con}+H_{con}}$	$\frac{H_{con}}{C_{con}+H_{con}}$
	Climate change	<0	>0	100	0
	Human activities	>0	<0	0	100

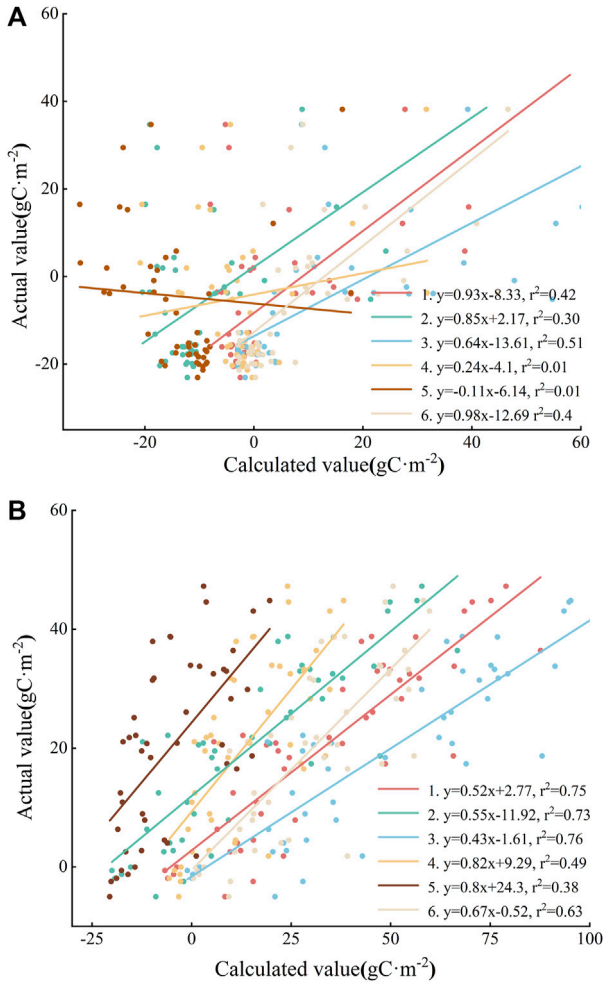

FIGURE 3
Comparison of calculated and measured NEP values across various grassland types **(A)**. Desert grassland, **(B)**. Typical grassland 1. Formula (1) + (9); 2. Formula (1) + (10) + (12); 3. Formula (1) + (10) + (11); 4. Formula (3) + (9); 5. Formula (3) + (10) + (12); 6. Formula (3) + (10) + (11)

$$\frac{dx}{dt}=\frac{\sum_{i=1}^{n}(i\times x_i)-\frac{1}{n}\left(\sum_{i=1}^{n}i\right)\left(\sum_{i=1}^{n}x_i\right)}{\sum_{i=1}^{n}i^2-\frac{1}{n}\left(\sum_{i=1}^{n}i\right)^2} \quad (22)$$

Here, $\frac{\delta NEP}{\delta PRE}$, $\frac{\delta NEP}{\delta TEM}$, $\frac{\delta NEP}{\delta SOL}$, $\frac{\delta NEP}{\delta PET}$ are partial derivatives of each climate factor to NEP, taking into account that each factor has a linear effect on NEP. By eliminating the influence of other variables, each partial derivative is equal to the corresponding correlation coefficient (Wu et al., 2020). The positive and negative contributions represent the positive and negative effects of impact factors on NEP respectively.

The specific discrimination method and contribution rate calculation are shown in Table 2:

3 Results

3.1 Model validation

In this study, the NPP values were estimated using two approaches: one based on MODIS NPP data and the other based on the CASA model. These NPP estimates were then coupled with the R_s-R_h soil respiration model to calculate the net ecosystem productivity NEP values for the study area across different time periods. To validate the accuracy of the models and select the most suitable one, measured eddy covariance data from both desert steppe and typical steppe ecosystems were employed, as depicted in Figure 3. The NEP values derived from coupling the MODIS NPP product with the GSMSR and the R_s-R_h relationship model proposed by Bond-Lamberty and Shi demonstrated a strong correlation with the observed values in both ecosystem types. These results confirmed the reliability of the selected model, which was subsequently used to analyze the spatial and temporal distributions of NEP and to investigate the key driving factors influencing these patterns.

3.2 NEP spatiotemporal distribution in Inner Mongolia

3.2.1 Interannual spatiotemporal distribution of NEP in Inner Mongolia

Figure 4 illustrates the interannual and spatial distribution of NEP in Inner Mongolia from 2001 to 2021. Over the past 21 years, the overall NEP has shown an increasing trend. The mean annual NEP ranged between 114.96 and 201.05 $gC{\cdot}m^{-2}{\cdot}a^{-1}$, with an annual average of 168.73 $gC{\cdot}m^{-2}{\cdot}a^{-1}$. The minimum value was observed in

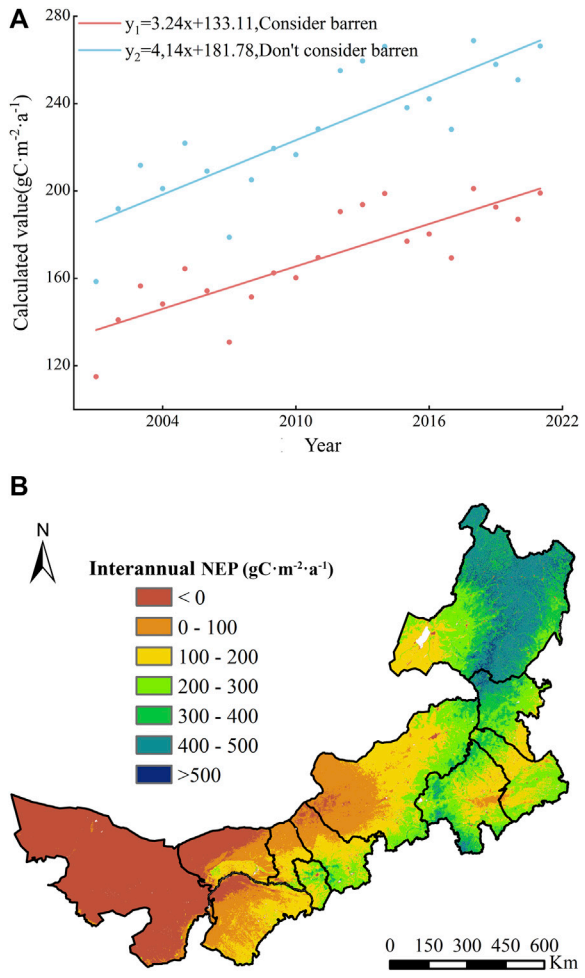

FIGURE 4
Spatial and temporal variation trend of interannual NEP in Inner Mongolia **(A)** Temporal scale; **(B)** Spatial scale.

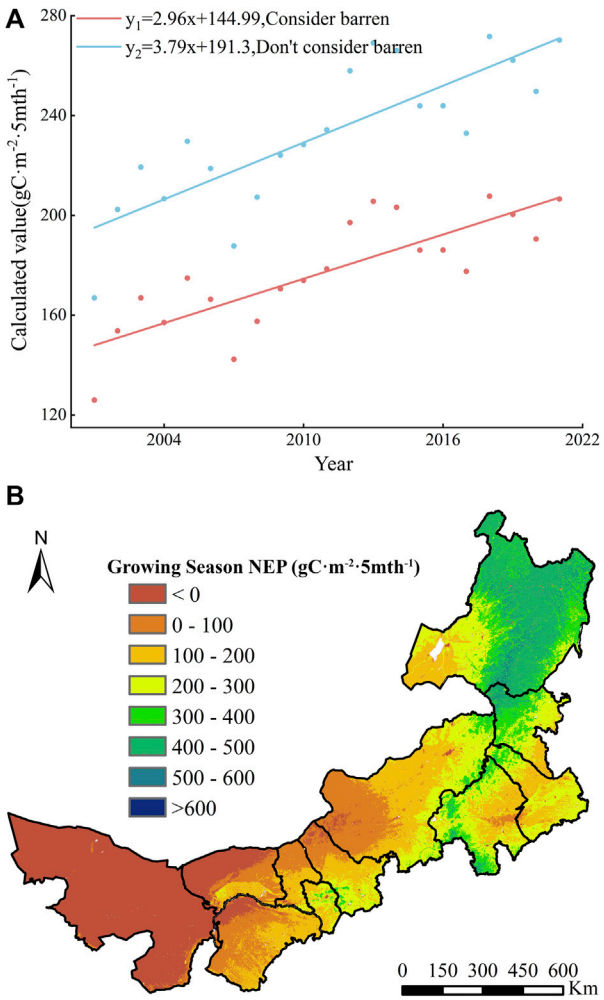

FIGURE 5
Spatial and temporal variation of NEP in Inner Mongolia during the growing season **(A)** Temporal scale; **(B)** Spatial scale.

2001, while the maximum occurred in 2018, indicating distinct interannual variability with an annual trend of 0.91. Spatially, NEP in Inner Mongolia exhibits a pattern of higher values in the northeast and lower values in the southwest, reflecting clear regional differences. Furthermore, different ecosystem types exhibit varying levels of NEP, with forests > cropland > grassland having corresponding annual averages of 419.14 gC·m^{-2}·a^{-1}, 228.19 gC·m^{-2}·a^{-1}, and 158.48 gC·m^{-2}·a^{-1}.

3.2.2 Spatial and temporal distribution of NEP during the growing season in Inner Mongolia

The vegetation growth season in Inner Mongolia was defined as May to September. The spatial and temporal NEP distribution during this period was analyzed, as illustrated in Figures 5, 6.

The long-term average NEP values throughout the growing season range from 125.96 to 207.69 gC·m^{-2}·5 mth^{-1}, peaking in July at 53.04 gC·m^{-2}·mth^{-1}, marking a significant carbon sink phase. Spatial analysis indicates that NEP patterns during the growing season remain consistent across years, with distinct regional characteristics. Specifically, different ecosystem types show a

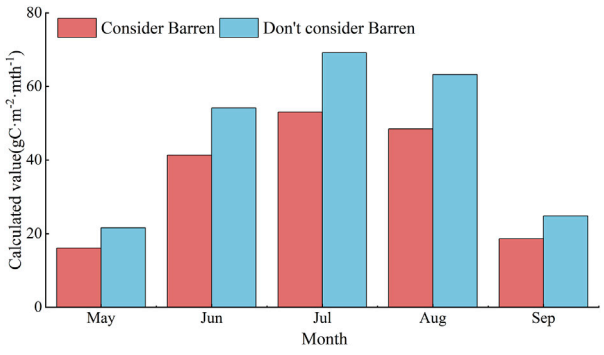

FIGURE 6
Monthly average NEP during the growing season.

hierarchy of NEP as in the following order: forest > cropland > grassland, with corresponding monthly averages of 84.81, 46.41, and 32.95 gC·m^{-2}·mth^{-1}.

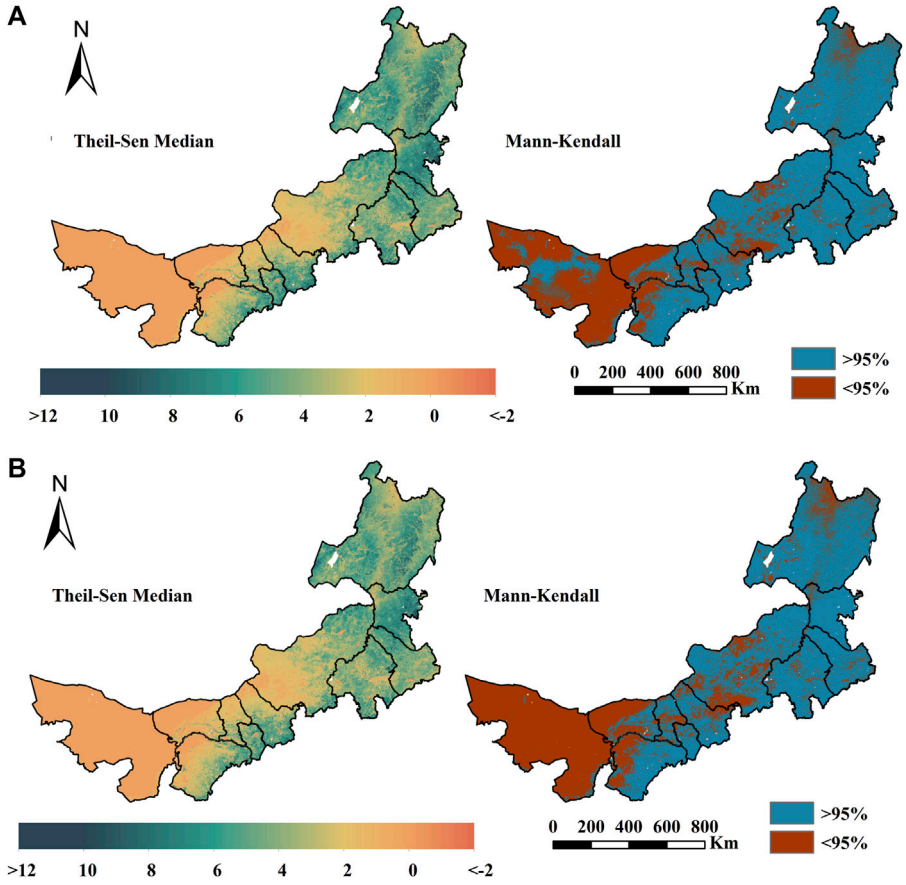

FIGURE 7
The trend of NEP variations and its significance test in Inner Mongolia **(A)** interannual, **(B)**. Growing season.

3.2.3 Interannual and growing season variation of NEP in Inner Mongolia

To further quantify the temporal variation trend of NEP in Inner Mongolia from 2001 to 2021, both the M-K test and the Sen median estimator were employed. These methods were used to investigate the interannual and seasonal growth patterns at a regional level as illustrated in Figure 7. NEP exhibits pronounced spatial differences, with a general trend of "higher in the northeast and lower in the southwest." Moreover, forests demonstrate the highest upward trend followed by grassland and cropland. Due to the unfavorable vegetation site conditions in barren areas, NEP tends to be predominantly negative. Consequently, the results for the entire region are significantly influenced by the NEP in western barren areas, both during the growing season and throughout the year. Moreover, an overall weak or downward trend was observed. Significance tests reveal that, except for the western barren area which did not meet a significance level of 0.05, all other regions exhibited significant changes in trend. Therefore, our subsequent analysis will primarily focus on NEP variations within vegetated areas while omitting a detailed examination of the western barren.

3.3 Analysis of NEP drivers in Inner Mongolia

3.3.1 Correlation analysis

The spatial and average correlation coefficients between NEP and meteorological driving factors (PRE, TEM, SOL, and PET) in Inner Mongolia are illustrated in Figures 8, 9.

NEP exhibits a positive correlation with various meteorological factors, except for certain areas in barren and desert grasslands. Particularly, in the eastern part of the forest and grassland areas, NEP demonstrates the most significant positive response to meteorological factors. Conversely, cultivated land displays a weak positive correlation with these factors. Notably, the disparity between PET and TEM manifests itself as the most pronounced difference. There was a weak to moderate negative correlation between NEP and meteorological factors in the barren grasslands located at the Yinshanbeilu in central and western China. Specifically, during the growing season, there was a significant decrease in the correlation between SOL and PET with NEP. Additionally, the positive interannual effect observed in certain regions during this period was hindered due to the influences of regional underlying surface conditions. The impact of PRE on NEP differs across different land types, with grassland and cultivated land

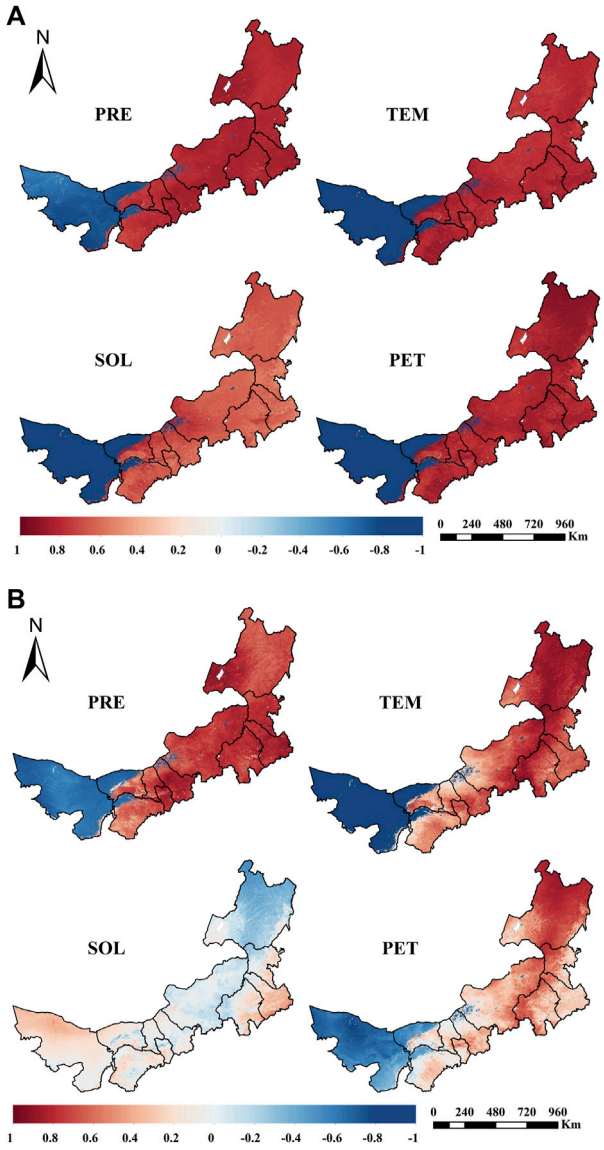

FIGURE 8
Spatial correlation between NEP and various meteorological factors **(A)**. Interannual, **(B)**. Growing season.

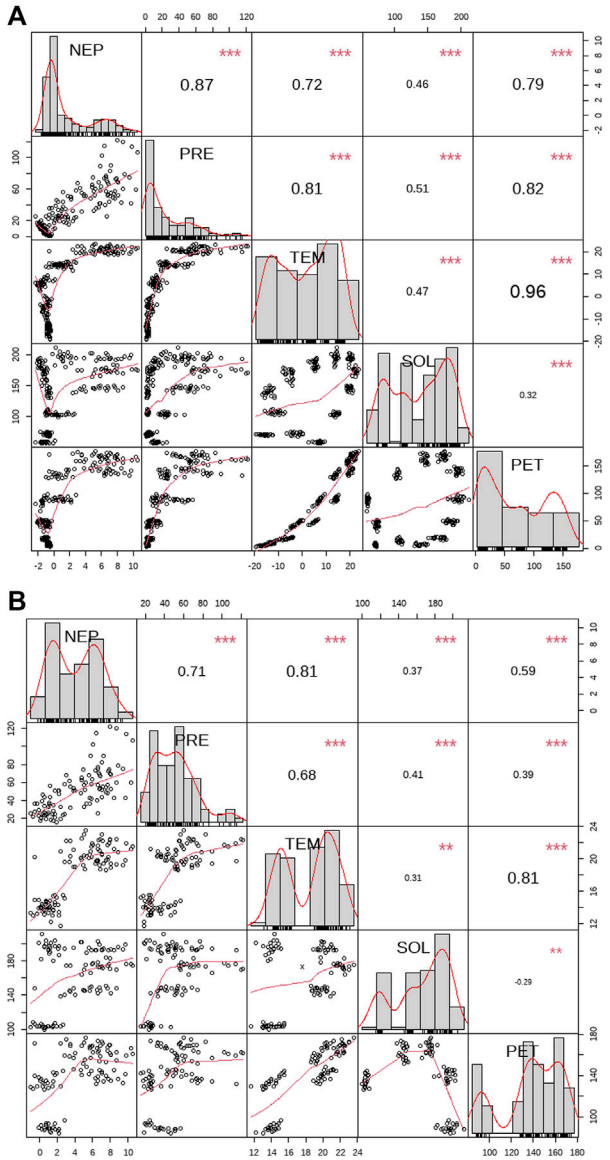

FIGURE 9
The correlation coefficient between NEP and various meteorological factors **(A)**. Interannual, **(B)**. Growing season (The red * represents the significance level of the correlation between variables. ** indicate a significance level of $p < 0.01$; and *** indicate a significance level of $p < 0.001$.).

being more affected compared to forest areas. Conversely, TEM and PET exhibit an opposite trend. Based on the correlation coefficients, PRE shows the strongest correlation (0.868), followed by PET and TEM (0.785 and 0.721, respectively), while SOL demonstrates the weakest correlation (0.456). During the growing season, TEM exhibits the highest correlation (0.811), followed by PRE (0.709), PET (0.588), and SOL (0.371).

3.3.2 Contribution analysis

① Contribution rate of climate factors to NEP change. To further investigate the contributions of climate factors and human activities to changes in NEP in Inner Mongolia, we employed the partial derivative correlation analysis. The contribution rates of meteorological factors to NEP during the interannual and growing seasons are illustrated in Figure 10. It is evident that on the interannual scale, PRE has the greatest contribution to forest and meadow areas in the eastern region, while the impact of NEP on TEM-coupled PRE is more significant in the western region. The contribution rate of PET to NEP remains unstable due to its comprehensive dependence on vegetation conditions, TEM, and SOL. In certain cultivated land and desert grassland areas, there is a transition from positive to negative contribution to NEP. Throughout the growing season, the impact of PRE on forests and grasslands in eastern China was paramount, while the influence of PET significantly diminished in comparison to interannual variations. The contribution of SOL to the NEP changes in the eastern

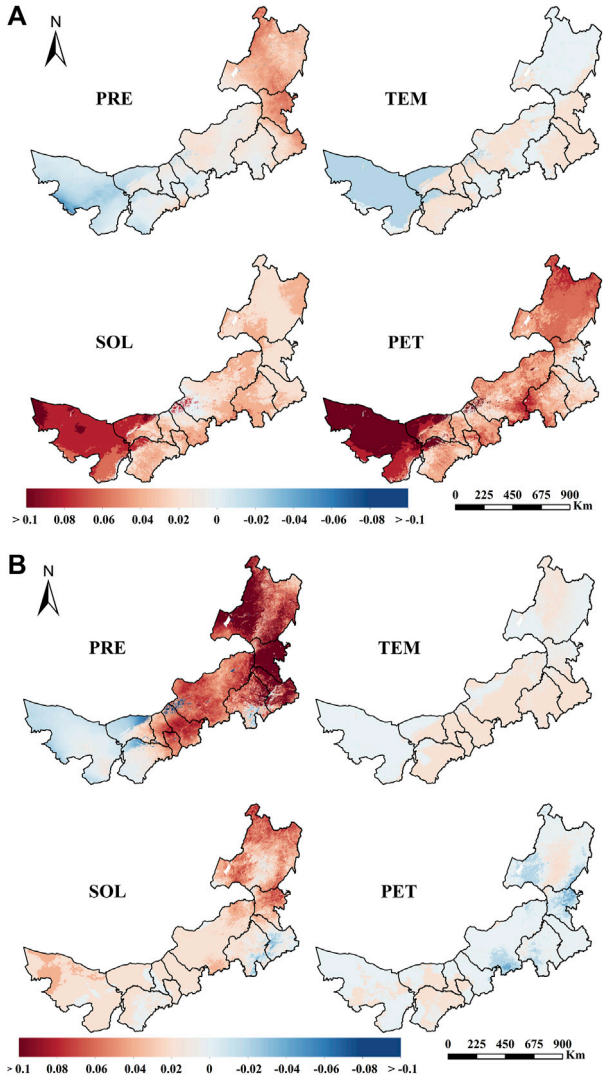

FIGURE 10
Contribution of meteorological factors to NEP **(A)**. Interannual, **(B)**. Growing season.

forest and grassland areas was more significant. However, the contribution of the TEM is low, and the changing trend of spatial distribution is not significant.

② Contribution of climate factors and human activities to NEP. Table 3 shows the contribution of climate factors and human activity to NEP changes in Inner Mongolia (Positive and negative denote positive and negative contribution effects, respectively). The primary drivers of interannual NEP variation in the study area, excluding the western barren, are predominantly climate-related, with human activities contributing 24% to this change. There are some differences between the driving factors of the growing season and the interannual ones. The influence of climate factors and human activities on NEP in the study area is 45.36% and 54.64%, respectively. PRE is the main factor affecting NEP during the growth season in Inner Mongolia, and the contribution rate of TEM and SOL to the region as a whole has a certain inhibitory effect.

Considering the potential impact of NEP instability on research outcomes in the western barren region, this study provides a supplementary analysis of climate factors and human activities on NEP in non-vegetated barren areas. As presented in Table 3 it is evident that human activities have significantly contributed to changes in NEP, while rainfall has shown a significant influence among climate factors.

Figure 11 illustrates the contribution of various influencing factors to NEP in Inner Mongolia, with positive and negative areas distinguished. Human activities and climate factors make up over 60% of the positive contribution to NEP in Inner Mongolia, while the negative impact of climate change on NEP surpasses that of the human activities. The most significant negative contributions come from SOL and TEM, whereas more than 80% of PRE can promote regional NEP changes.

③ Analysis of driving factors of NEP change in Inner Mongolia. The primary driving factors behind the NEP spatial change trend in Inner Mongolia were examined, as illustrated in Figure 12, by integrating the classification criteria of contribution rate of different driving factors presented in Table 2. It can be seen that climate change and human activities have impacted over 60% of Inner Mongolia, primarily concentrated in the eastern and southern regions. Furthermore, a decrease of approximately 20% in NEP was attributed to climate factors, mainly occurring in the western

TABLE 3 2001–2021 Contribution magnitude and rate of each factor in Inner Mongolia.

			PRE	TEM	SOL	PET	Climatic factor	Human activity
Considered barren	Contribution degree	Interannual	0.013	−0.007	−0.029	0.046	0.095	0.030
		Growing season	0.047	−0.0005	−0.014	0.007	0.069	0.082
	Contribution rate	Interannual	13.68%	−7.36%	−30.53%	48.42%	76.00%	24.00%
		Growing season	68.11%	−0.73%	−20.29%	10.14%	45.36%	54.64%
Excluding barren	Contribution degree	Interannual	0.02	−0.002	−0.018	0.036	0.076	0.034
		Growing season	0.06	0.0002	−0.015	0.008	0.083	0.099
	Contribution rate	Interannual	26.32%	−2.63%	−23.68%	47.37%	69.09%	30.91%
		Growing season	72.29%	0.24%	−18.07%	9.64%	45.60%	54.40%

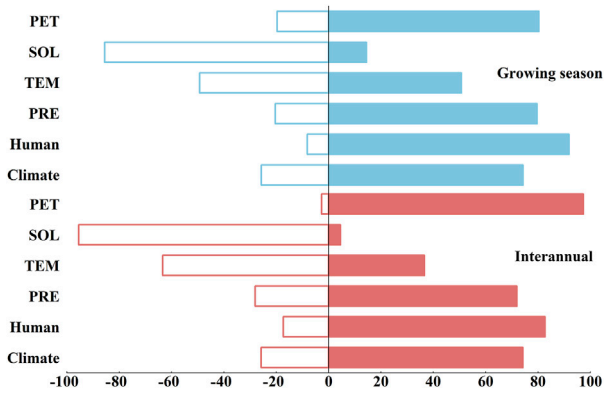

FIGURE 11
The ratio of positive to negative contribution areas of each influencing factor to NEP.

barren area. The increase of NEP in the Yinshanbeilu and west of Ordos is predominantly influenced by climate factors, while human activities dominate the rise of NEP in southwest Alashan and south Ordos.

4 Discussion

4.1 Uncertainty analysis of NEP estimation

In this paper, based on different estimation models of NPP and soil heterotrophic respiration, the NEP values of vegetation net primary productivity in the study area from 2001 to 2021 was derived under the six combination models, and it was found that the NEP values obtained from the results of different models had large deviations. This is because changes in NEP are jointly influenced by NPP and soil heterotrophic respiration and by a combination of controlling variables such as vegetation cover, SOL, PRE, TEM, PET, subsurface characteristics, soil organic carbon density, *etc.* Existing studies of NEP are mainly based on soil monitoring, remote sensing inversion, and model simulation, and these data sources have limitations in terms of accuracy and generality. The NEP values obtained from ground monitoring are insufficient to encompass the entire study area; the NEP derived from remote sensing inversion is influenced by cloud cover and atmospheric conditions, while the NPP estimation model is constrained by variations in spatial and regional scales across different models, the resolution of remote sensing data, pre-processing techniques, and the impact of parameter weighting, among other factors. Consequently, discrepancies persist in the regional boundaries and parameter rates of various land covers, including forests, grasslands, and croplands, as well as at the global scale. The estimation of R_h is crucial for delineating the ratio of soil heterotrophic respiration to vegetation root autotrophic respiration within soil respiration. However, significant discrepancies exist in the R_s-R_h relationship curves derived from various methodologies. The curve modeling presents one of the most challenging scientific problems to address. In this study, based on the validated vegetation NEP of desert grassland and typical grassland, we selected the most accurate estimation model to reflect the NEP in the study area. But for future application, it remains essential to enhance the precision of NEP calculations derived from physiological and ecological processes.

4.2 Spatiotemporal variation trends of NEP

In terms of time trends, the NEP of Inner Mongolia shows an overall upward trend from 2001 to 2021, which is consistent with

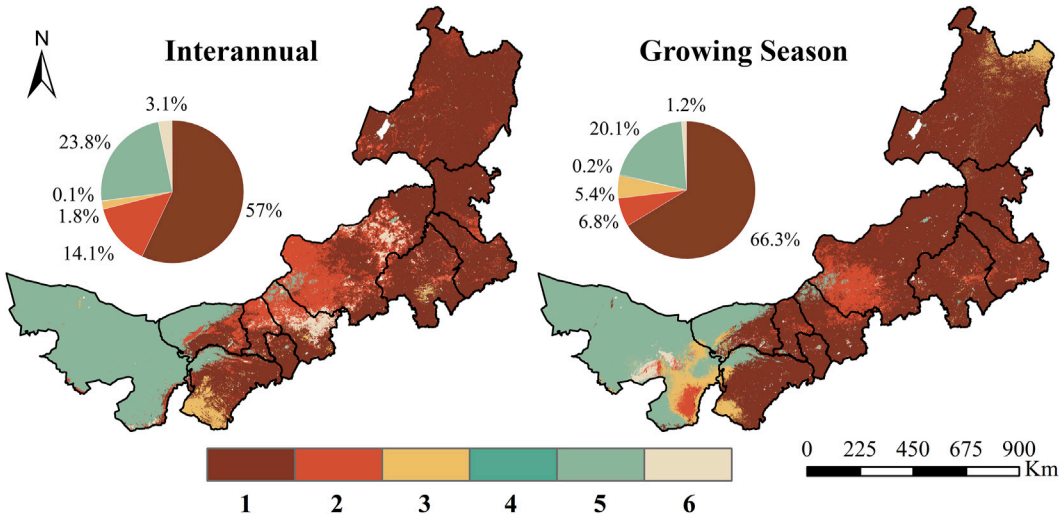

FIGURE 12
The dominant factors of annual and growing season NEP in Inner Mongolia from 2001 to 2021 (1. NEP increases due to climate and human factors; 2. NEP increases due to climate factors; 3. NEP increases due to human activities; 4. NEP decreases due to climate and human factors; 5. NEP decrease due to climate; 6. NEP decrease due to human factors).

TABLE 4 Land transfer matrix table (unit:$10^4 km^2$).

2000 / 2020	Cropland	Forest	Grassland	Shrub	Wetland	Water	Impervious	Barren	Sum
Cropland	16.35	0.08	3.67	0.05	0.10	0.06	0.13	0.51	20.95
Forest	0.09	17.31	2.21	0.04	0.01	0.02	0.00	0.00	19.69
Grassland	1.93	2.03	62.44	0.36	0.33	0.10	0.06	4.58	71.84
Shrub	0.02	0.02	0.80	0.24	0.01	0.00	0.00	0.03	1.12
Wetland	0.02	0.00	0.21	0.01	0.45	0.09	0.00	0.02	0.80
Water	0.05	0.01	0.10	0.00	0.06	0.58	0.00	0.03	0.84
Impervious	0.51	0.01	0.56	0.01	0.01	0.01	0.79	0.06	1.95
Barren	0.02	0.00	1.36	0.03	0.07	0.04	0.01	34.34	35.87
Sum	18.98	19.48	71.35	0.74	1.05	0.90	1.00	39.56	——

the findings of Zhai et al. (2024) and Liang et al. (2023). This is partly due to a series of ecological restoration and management projects implemented in Inner Mongolia since 1978, such as the "Three North" Protective Forest Project, the Beijing-Tianjin Wind and Sand Source Management Project, the Grassland Ecological Protection and Restoration Project, the Soil and Water Conservation and Desertification Management Project, *etc.*, which have resulted in significant vegetation restoration in Inner Mongolia (Kang et al., 2021). On the one hand, the increase in vegetation cover has increased vegetation photosynthesis and carbon sequestration capacity of regional ecosystems. On the other hand, It has mitigated soil erosion to some degree, enhanced soil organic carbon levels, and diminished carbon emissions from soil disturbances, increasing NEP (Sha et al., 2022; Qiu et al., 2021; Tian et al., 2022). Conversely, NEP in western Inner Mongolia exhibited no significant alterations or a declining trend, as this region predominantly comprises desert grasslands and barrens, characterized by minimal vegetation cover and reduced carbon sequestration capacity, while elevated soil temperatures augmented microbial respiration. This results in the release of more soil carbon into the atmosphere in the form of carbon dioxide, coupled with a fragile regional ecological environment and a more pronounced response to extreme climatic events such as drought, all of which can lead to a decline in NEP (Guan et al., 2021).

Annual carbon sequestration by vegetation occurs in the growing season. Because soil microorganisms are active in the growing season due to higher TEM and high PRE, the carbon sequestration capacity is significantly higher than in the non-growing season (Yun et al., 2022). The variation in NEP throughout the growing season is the primary factor affecting the annual regional change in NEP. The significant decrease in NEP values in the study area in 2007, 2010, and 2016 was due to extreme drought events in these years, where low PRE and high TEM resulted in the closure or partial closure of plant stomata, limiting carbon dioxide uptake and reducing the rate of photosynthesis (Kapoor et al., 2020; Hu et al., 2023). Furthermore, higher TEM can expedite soil organic matter decomposition and augment soil respiration, leading to a decreased NEP.

The present study also unveiled substantial spatial heterogeneity in the vegetation's carbon sequestration capacity within Inner Mongolia, exhibiting a distinct east-west distribution pattern that corresponds to the regional underlying vegetation types. These findings are consistent with previous investigations conducted by Zhai et al. (2024) and Hao et al. (2023). Furthermore, the investigated areas displayed notable disparities in both vegetation types and carbon sequestration capacity, which were influenced by various meteorological factors such as mean TEM, PRE, and elevation. The overall ranking of these characteristics was as follows: forest > grassland > cropland > impervious > barren; within the grassland ecosystem, meadow steppe surpassed typical steppe and barren steppe.

4.3 Analysis of driving factors influencing carbon sink/source

Climate change is one of the key factors affecting the productivity level of vegetation. Some scholars believe that TEM and PRE are the most dominant factors affecting the change of vegetation carbon cycle (Wei et al., 2014). Some scholars conclude that SOL and PET also have an important effect on vegetation carbon sequestration capacity, while TEM has a relatively small effect on vegetation carbon sequestration capacity (Li et al., 2020). Therefore, in this study, four key factors (PRE, TEM, SOL, and PET) affecting the changes in NEP were screened for the analysis of climate-driven factors. Different climate factors have different effects on the vegetative carbon sequestration capacity. PRE supplies the requisite water for vegetative growth, and enhances plant productivity and biomass, thereby augmenting the carbon sequestration potential of vegetation. In Inner Mongolia, is mostly arid or semi-arid, and water is the main factor limiting vegetation growth (WEI et al., 2014; Zhang et al., 2019). TEM can change the activity of plant enzymes, which in turn affects the vegetative photosynthesis rate and its carbon sequestration capacity. Generally, elevated TEM enhance plant photosynthesis; however, the relationship between photosynthesis rate and TEM is not linear.

If TEM surpass the optimal range for plant growth, they may inhibit photosynthesis, leading to a reduction in Net Ecosystem Production (Moore et al., 2021). SOL can affect the photosynthesis active radiation received by the plant. PET has an impact on plant photosynthesis by affecting vegetation transpiration and soil moisture (Post et al., 1992). According to the analyses in this study, PRE is the main meteorological factor affecting NEP changes in Inner Mongolia.

Positive anthropogenic contributions can significantly increase the carbon sequestration capacity of vegetation, while negative anthropogenic activities have a decreasing effect. This study shows that more than 90% of the anthropogenic contributions in Inner Mongolia are positive, as can be seen from the land transfer matrix from 2000 to 2020 (Table 4).

The area of cropland, forest, grassland, and shrubland increased by 10.36%, 1.08%, 0.69%, and 52. 2% while the bare land area decreased by 9.33%. This indicates the importance of the Inner Mongolia Sand Control Project which has improved the regional ecosystem environment. These measures have played an important role in the increase of vegetation NEP, reflecting the positive role of human activities. A major negative role of human activities is manifested in the degradation of grassland due to overgrazing and intense grazing which have led to the degradation of the aboveground biomass. Land degradation has resulted in the reduction of grassland productive capacity. Some scholars found that the changes in grassland ecosystems in Inner Mongolia from 1999 to 2015 were mainly due to human activities by as much as 78.8% (Wang et al., 2021). This suggests that although China has implemented ecological protection and construction projects such as "returning pasture to grass" and "natural grassland protection" in grassland areas, many areas are still in a state of overgrazing.

5 Conclusion

This study utilized monthly multi-source remote sensing data, meteorological data, and ground-measured carbon flux data from 2001 to 2021 in Inner Mongolia. The CASA model, MODIS NPP data, and the R_h soil respiration model were employed and evaluated to estimate NEP. Furthermore, the spatiotemporal distribution of NEP and its driving factors in Inner Mongolia were analyzed. The main findings are as follows:

1) The NEP model, which integrates MODIS NPP products with the GSMSR model and the R_s-R_h relationship model developed by Bond-Lamberty, demonstrated the best performance. The fitting coefficients for typical grassland and desert grassland were 0.76 and 0.51, respectively.
2) The annual average NEP in Inner Mongolia from 2001 to 2021 was 168.73 $gC{\cdot}m^{-2}{\cdot}a^{-1}$. The multi-year average NEP during the growing season was 177.57 $gC{\cdot}m^{-2}{\cdot}5\ mth^{-1}$. The seasonal variation in NEP was distinct, with the region acting as a carbon sink from May to September and as a carbon source during the remaining months. There was a seasonal transition between carbon sink and source behavior. The peak NEP value occurred in July, reaching 53.04 $gC{\cdot}m^{-2}{\cdot}mth^{-1}$. Due to ecological restoration and management efforts, NEP showed a fluctuating upward trend, with vegetation conditions improving year by year.
3) The large east-west extent of Inner Mongolia and the diverse climatic conditions led to significant spatial heterogeneity in NEP. Vegetation ecosystems showed higher density in the northeastern regions compared to the sparser southwestern areas. The arid western region, experiencing warming and drying trends, exhibited a tendency toward carbon source behavior, substantially influencing both annual and growing season NEP patterns.
4) All Climatic conditions collectively influence the magnitude and variation of NEP. Based on correlation coefficients, PRE emerged as the primary meteorological driver of interannual NEP variations in Inner Mongolia. TEM and PRE during the growing season jointly influenced NEP. In terms of contribution rates, PRE remained the dominant meteorological factor affecting NEP changes in the study area.
5) When considering barren and non-barren areas, the contribution rates of climate change and human activities to NEP variations were relatively similar. Over 55% of areas with increasing NEP were influenced by both climate change and anthropogenic activities, predominantly located in the eastern and south-central regions of Inner Mongolia. In contrast, climate factors were the primary drivers of the approximately 20% decline in NEP, mainly observed in the arid western regions of Inner Mongolia.

Data availability statement

The original contributions presented in the study are included in the article/Supplementary Material, further inquiries can be directed to the corresponding authors.

Author contributions

SC: Writing – original draft. SZ: Conceptualization, Funding acquisition, Writing – review and editing. CL: Formal Analysis, Supervision, Writing – review and editing. YW: Data curation, Validation, Writing – review and editing. TK: Supervision, Writing – review and editing. MZ: Resources, Software, Writing – review and editing.

Funding

The author(s) declare that financial support was received for the research and/or publication of this article. We acknowledge the financial support from the IWHR Research & Development Support Program (No. MKKH2024JK020, No. MK0145B022021), First-Class Discipline Research Special Project (YLXKZX-NSD-027), the Inner Mongolia Autonomous Region Science and Technology Support Program (No. 2023JBGS0007, No. 2024MS04002, No. 2023YFSH0002, No. 2023MS05023), the Basic Scientific Research Business Fee of Directly-affiliated Universities in Inner Mongolia Autonomous Region (No. BR231516), the IWHR Internationally-oriented Talents Program, and the Inner Mongolia Autonomous Region's Start-up Support Program Project for Returned Overseas Students' Innovation and Entrepreneurship.

Acknowledgments

We would like to thank Editage (www.editage.cn) for English language editing, thank Professor Shusen Wang from the Remote Sensing Center of Canada for review & editing, and validation.

Conflict of interest

The authors declare that the research was conducted in the absence of any commercial or financial relationships that could be construed as a potential conflict of interest.

Generative AI statement

The author(s) declare that no Generative AI was used in the creation of this manuscript.

Publisher's note

All claims expressed in this article are solely those of the authors and do not necessarily represent those of their affiliated organizations, or those of the publisher, the editors and the reviewers. Any product that may be evaluated in this article, or claim that may be made by its manufacturer, is not guaranteed or endorsed by the publisher.

References

Ahlström, A., Raupach, M. R., Schurgers, G., Smith, B., Arneth, A., Jung, M., et al. (2015). The dominant role of semi-arid ecosystems in the trend and variability of the land CO_2 sink. *Science* 348 (6237), 895–899. doi:10.1126/science.aaa1668

Bai, Y., and Cotrufo, M. F. (2022). Grassland soil carbon sequestration: Current understanding, challenges, and solutions. *Science* 377 (6606), 603–608. doi:10.1126/science.abo2380

Balasubramanian, D., Zhou, W. J., Ji, H. L., Grace, J., Bai, X. L., Song, Q. H., et al. (2020). Environmental and management controls of soil carbon storage in grasslands of southwestern China. *J. Environ. Manag.* 254, 109810. doi:10.1016/j.jenvman.2019.109810

Bejagam, V., and Sharma, A. (2022). Impact of climatic changes and anthropogenic activities on ecosystem net primary productivity in India during 2001–2019. *Ecol. Inf.* 70, 101732. doi:10.1016/j.ecoinf.2022.101732

Berg, P., Huettel, M., Glud, R. N., Reimers, C. E., and Attard, K. M. (2022). Aquatic eddy covariance: the method and its contributions to defining oxygen and carbon fluxes in marine environments. *Annu. Rev. Mar. Sci.* 14 (1), 431–455. doi:10.1146/annurev-marine-042121-012329

Bond-Lamberty, B., Wang, C., and Gower, S. T. (2004). A global relationship between the heterotrophic and autotrophic components of soil respiration. *Glob. Change Biol.* 10 (10), 1756–1766. doi:10.1111/j.1365-2486.2004.00816.x

Cai, B., and Yu, R. (2009). Advance and evaluation in the long time series vegetation trends research based on remote sensing. *J. Remote Sens.* 13 (6), 1170–1186. doi:10.11834/jrs.20090614

Cao, S., He, Y., Zhang, L., Sun, Q., Zhang, Y., Li, H., et al. (2023). Spatiotemporal dynamics of vegetation net ecosystem productivity and its response to drought in Northwest China. *GIScience and Remote Sens.* 60 (1), 2194597. doi:10.1080/15481603.2023.2194597

Cao, Y., Sun, Y., Jiang, Y., and Wan, J. (2022). Analysis on temporal-spatial variations and driving factors of net ecosystem productivity in the Yellow River Basin. *Ecol. Environ.* 31 (11), 2101. doi:10.16258/j.cnki.1674-5906.2022.11.001

Chen, Z., Zhu, Z., Zhang, X., Jiao, Y., Cheng, Y., Wang, S., et al. (2024). Study on spatio-temporal evolution of ecosystem services, spatio-temporal pattern of tradeoff/synergy relationship and its driving factors in Shendong mining area. *Front. Environ. Sci.* 12, 1445833. doi:10.3389/fenvs.2024.1445833

Ding, S., Sun, Q., Guo, Y., and Wei, X. (2025). The spatiotemporal evolution and prediction of vegetation NPP in the Huangshui river basin of Qilian Mountains. *Front. Environ. Sci.* 12, 1459669. doi:10.3389/fenvs.2024.1459669

Guan, C., Zhang, P., Zhao, C., and Li, X. (2021). Effects of warming and rainfall pulses on soil respiration in a biological soil crust-dominated desert ecosystem. *Geoderma* 381, 114683. doi:10.1016/j.geoderma.2020.114683

Hao, L., Zhai, Y., Qi, W., and Lan, Q. (2023). Spatial-temporal dynamics of vegetation carbon sources/sinks in Inner Mongolia from 2001 to 2020 and its response to climate change. *Ecol. Environ.* 32 (5), 825. doi:10.16258/j.cnki.1674-5906.2023.05.001

Hou, Q., Yang, H., Wu, J., and Yu, X. (2023). Carbon budget response to climate change varies with grassland type in Qilian Mountains, China. *Glob. Ecol. Conservation* 47, e02670. doi:10.1016/j.gecco.2023.e02670

Hu, L., Wang, Z., Huang, M., Sun, H., and Wang, Q. (2023). A remote sensing based method for assessing the impact of O3 on the net primary productivity of terrestrial ecosystems in China. *Front. Environ. Sci.* 11, 1112874. doi:10.3389/fenvs.2023.1112874

Huang, C., Sun, C., Nguyen, M., Wu, Q., He, C., Yang, H., et al. (2023a). Spatio-temporal dynamics of terrestrial Net ecosystem productivity in the ASEAN from 2001 to 2020 based on remote sensing and improved CASA model. *Ecol. Indic.* 154, 110920. doi:10.1016/j.ecolind.2023.110920

Huang, Y., Wang, F., Zhang, L., Zhao, J., Zheng, H., Zhang, F., et al. (2023b). Changes and net ecosystem productivity of terrestrial ecosystems and their influencing factors in China from 2000 to 2019. *Front. Plant Sci.* 14, 1120064. doi:10.3389/fpls.2023.1120064

IPCC (2023). "Climate change 2023: synthesis report. Contribution of Working groups I, II, and III to the Sixth assessment report of the Intergovernmental Panel on climate change Core Writing Team,". Editors Lee, H., and Romero, J. (Geneva, Switzerland: IPCC), 35–115.

Jiang, Y., Zhang, Q., Niu, J., and Wu, J. (2019). Pastoral population growth and land use policy has significantly impacted livestock structure in Inner Mongolia—a case study in the Xilinhot region. *Sustainability* 11 (24), 7208. doi:10.3390/su11247208

Kang, Y., Guo, E., Wang, Y., Bao, Y., Bao, Y., and Mandula, N. (2021). Monitoring vegetation change and its potential drivers in Inner Mongolia from 2000 to 2019. *Remote Sens.* 13 (17), 3357. doi:10.3390/rs13173357

Kapoor, D., Bhardwaj, S., Landi, M., Sharma, A., Ramakrishnan, M., and Sharma, A. (2020). The impact of drought in plant metabolism: How to exploit tolerance mechanisms to increase crop production. *Appl. Sci.* 10 (16), 5692. doi:10.3390/app10165692

Kelong, C., Yanli, H., Sheng-kui, C., Jin, M. S., Guangchao, C., and Hui, L. (2011). The study of vegetation carbon storage in Qinghai lake valley based on remote sensing and CASA model. *Procedia Environ. Sci.* 10, 1568–1574. doi:10.1016/j.proenv.2011.09.249

Lees, K. J., Quaife, T., Artz, R. R. E., Khomik, M., and Clark, J. M. (2018). Potential for using remote sensing to estimate carbon fluxes across northern peatlands–A review. *Sci. Total Environ.* 615, 857–874. doi:10.1016/j.scitotenv.2017.09.103

Li, L., Zha, Y., Zhang, J., Li, Y., and Lyu, H. (2020). Effect of terrestrial vegetation growth on climate change in China. *J. Environ. Manag.* 262, 110321. doi:10.1016/j.jenvman.2020.110321

Li, X., Lin, G., Jiang, D., Fu, J., and Wang, Y. (2022). Spatiotemporal evolution characteristics and the climatic response of carbon sources and sinks in the Chinese grassland ecosystem from 2010 to 2020. *Sustainability* 14 (14), 8461. doi:10.3390/su14148461

Liang, L., Wang, Q., Qiu, S., Geng, D., and Wang, S. (2023). NEP estimation of terrestrial ecosystems in China using an improved CASA model and soil respiration model. *IEEE J. Sel. Top. Appl. Earth Observations Remote Sens.* 16, 10203–10215. doi:10.1109/jstars.2023.3325774

Liu, L., Sayer, E. J., Deng, M., Li, P., Liu, W., Wang, X., et al. (2022). The grassland carbon cycle: mechanisms, responses to global changes, and potential contribution to carbon neutrality. *Fundam. Res.* 3 (2), 209–218. doi:10.1016/j.fmre.2022.09.028

Liu, M., Dries, L., Huang, J., Min, S., and Tang, J. (2019). The impacts of the eco-environmental policy on grassland degradation and livestock production in Inner Mongolia, China: an empirical analysis based on the simultaneous equation model. *Land Use Policy* 88, 104167. doi:10.1016/j.landusepol.2019.104167

Liu, W., and Sun, F. (2016). Assessing estimates of evaporative demand in climate models using observed pan evaporation over China. *J. Geophys. Res. Atmos.* 121 (14), 8329–8349. doi:10.1002/2016jd025166

Lu, X., Chen, Y., Sun, Y., Xu, Y., Xin, Y., and Mo, Y. (2023). Spatial and temporal variations of net ecosystem productivity in Xinjiang Autonomous Region, China-based on remote sensing. *Front. Plant Sci.* 14, 1146388. doi:10.3389/fpls.2023.1146388

Mendes, K. R., Campos, S., da Silva, L. L., Mutti, P. R., Ferreira, R. R., Medeiros, S. S., et al. (2020). Seasonal variation in net ecosystem CO_2 exchange of a Brazilian seasonally dry tropical forest. *Sci. Rep.* 10 (1), 9454. doi:10.1038/s41598-020-66415-w

Meng, Z., Dang, X., Gao, Y., Meng, Z., Dang, X., and Gao, Y. (2020). Land degradation action plan in Inner Mongolia. *Public-private Partnersh. desertification control Inn. Mong.*, 171–194. doi:10.1007/978-981-13-7499-9_6

Moore, C. E., Meacham-Hensold, K., Lemonnier, P., Slattery, R. A., Benjamin, C., Bernacchi, C. J., et al. (2021). The effect of increasing temperature on crop photosynthesis: from enzymes to ecosystems. *J. Exp. Bot.* 72 (8), 2822–2844. doi:10.1093/jxb/erab090

Ouyang, X., Wang, J., Chen, X., Zhao, X., Ye, H., Watson, A. E., et al. (2021). Applying a projection pursuit model for evaluation of ecological quality in Jiangxi Province, China. *Ecol. Indic.* 133, 108414. doi:10.1016/j.ecolind.2021.108414

Pei, Z. Y., Ouyang, H., Zhou, C. P., and Xu, X. L. (2009). Carbon balance in an alpine steppe in the Qinghai-Tibet Plateau. *J. Integra. Plant. Biol.* 51 (5), 521–526. doi:10.1111/j.1744-7909.2009.00813.x

Piao, S. L., Fang, J. Y., and Guo, Q. H. (2001). Application of CASA model to the estimation of Chinese terrestrial net primary productivity. *Chin. J. Plant Ecol.* 25 (5), 603. Available online at: https://www.plant-ecology.com/EN/Y2001/V25/I5/603

Post, W. M., Pastor, J., King, A. W., and Emanuel, W. R. (1992). Aspects of the interaction between vegetation and soil under global change. *Water, Air, Soil Pollut.* 64, 345–363. doi:10.1007/bf00477110

Qiu, L., Zhu, H., Liu, J., Yao, Y., Wang, X., Rong, G., et al. (2021). Soil erosion significantly reduces organic carbon and nitrogen mineralization in a simulated experiment. *Agric. Ecosyst. and Environ.* 307, 107232. doi:10.1016/j.agee.2020.107232

Qiu, S., Liang, L., Geng, D., Wang, Q., Mu, J., and Shi, Y. (2022). Remote sensing estimation of European NEP based on improved CASA model and soil respiration model. *10th Int. Conf. Agro-Geoinformatics (Agro-Geoinformatics), IEEE* 2022, 1–6. doi:10.1109/agro-geoinformatics55649.2022.9858994

Qu, S., Wang, L., Lin, A., Yu, D., Yuan, M., and Li, C. (2020). Distinguishing the impacts of climate change and anthropogenic factors on vegetation dynamics in the Yangtze River Basin, China. *Ecol. Indic.* 108, 105724. doi:10.1016/j.ecolind.2019.105724

Raihan, A., Muhtasim, D. A., Farhana, S., Pavel, M. I., Faruk, O., Rahman, M., et al. (2022). Nexus between carbon emissions, economic growth, renewable energy use, urbanization, industrialization, technological innovation, and forest area towards achieving environmental sustainability in Bangladesh. *Energy Clim. Change* 3, 100080. doi:10.1016/j.egycc.2022.100080

Sha, Z., Bai, Y., Li, R., Lan, H., Zhang, X., Li, J., et al. (2022). The global carbon sink potential of terrestrial vegetation can be increased substantially by optimal land management. *Commun. Earth and Environ.* 3 (1), 8. doi:10.1038/s43247-021-00333-1

Shi, Z. (2015). "Spatial-temporal simulation of vegetation carbon sink and its Influential factors based on CASA and GSMSR model," in *Shaanxi Province* (Yangling: Northwest A&F University).

Song, C., Wang, G., Hu, Z., Zhang, T., Huang, K., Chen, X., et al. (2020). Net ecosystem carbon budget of a grassland ecosystem in central Qinghai-Tibet Plateau: integrating terrestrial and aquatic carbon fluxes at catchment scale. *Agric. For. Meteorology* 290, 108021. doi:10.1016/j.agrformet.2020.108021

Song, J., Zhou, L., and Zhou, G. (2023). A dataset of carbon and water fluxes of the temperate desert steppe in Damao Banner, Inner Mongolia (2015–2018). *Science Data Bank*. doi:10.57760/sciencedb.o00119.00043

Tan, X., Zhang, B., and Chen, S. (2023). A dataset of observational key parameters in carbon and water fluxes in a semi-arid steppe, Inner Mongolia (2012–2020): based on a long-term manipulative experiment of precipitation pattern. *Sci. Data Bank*. 2023-02-10. doi:10.11922/11-6035.csd.2023.0052.zh

Tang, X., Fan, S., Qi, L., Guan, F., Du, M., and Zhang, H. (2016). Soil respiration and net ecosystem production in relation to intensive management in Moso bamboo forests. *Catena* 137, 219–228. doi:10.1016/j.catena.2015.09.008

Tian, H., Ji, X., and Zhang, F. (2022). Spatiotemporal variations of vegetation net primary productivity and its response to meteorological factors across the Yellow River Basin during the period 1981–2020. *Front. Environ. Sci.* 10, 949564. doi:10.3389/fenvs.2022.949564

Wang, C., Zhao, W., and Zhang, Y. (2022a). The change in net ecosystem productivity and its driving Mechanism in a mountain ecosystem of arid regions, northwest China. *Remote Sens.* 14, 4046. doi:10.3390/rs14164046

Wang, J., Yang, Y., Zuo, C., Gu, F., and He, H. (2021). Impacts of human activities and climate change on gross primary productivity of the terrestrial ecosystems in China. *Acta Ecol. Sin.* 41 (18), 7085–7099. doi:10.5846/stxb202104130956

Wang, M., Zhao, J., Wang, S., and Chen, B. (2022b). Regional contributions and climate attributions to interannual variation of global net ecosystems production by an ECOSYSTEM processed model driven by remote sensing data over the past 35 years. *Remote Sens.* 14 (13), 3208. doi:10.3390/rs14133208

Wei, Z. F., Ren, Z. Y., and Zhang, C. (2014). Changes of vegetation cover and its correlation with precipitation and temperature in Northwest China. *Bull. Soil Water Conservation* 34 (3), 283–289. doi:10.13961/j.cnki.stbctb.2014.03.056

Wu, L., Wang, S., Bai, X., Tian, Y., Luo, G., Wang, J., et al. (2020). Climate change weakens the positive effect of human activities on karst vegetation productivity restoration in southern China. *Ecol. Indic.* 115, 106392. doi:10.1016/j.ecolind.2020.106392

Xu, M., Guo, B., and Zhang, R. (2024). Variations of terrestrial net ecosystem productivity in China driven by climate change and human activity from 2010 to 2020. *Forests* 15, 1484. doi:10.3390/f15091484

Yu, G., Zheng, Z., Wang, Q., Fu, Y., Zhuang, J., Sun, X., et al. (2010). Spatiotemporal pattern of soil respiration of terrestrial ecosystems in China: the development of a geostatistical model and its simulation. *Environ. Sci. and Technol.* 44 (16), 6074–6080. doi:10.1021/es100979s

Yu, G., Zhu, J., Li, X., and He, N. (2022). Technological approaches to enhance ecosystem carbon sink in China: Nature-based solutions. *Bull. Chin. Acad. Sci.* 37 (4), 490–501. doi:10.16418/j.issn.1000-3045.20220121002

Yun, H., Tang, J., D'Imperio, L., Wang, X., Qu, Y., Liu, L., et al. (2022). Warming and increased respiration have transformed an alpine steppe ecosystem on the Tibetan Plateau from a carbon dioxide sink into a source. *J. Geophys. Res. Biogeosciences* 127 (1), e2021JG006406. doi:10.1029/2021jg006406

Zhai, Y., Wang, X., Hao, L., Qi, W., Wang, Y., Geng, J., et al. (2024). Multi-time scale analysis of net ecosystem productivity pattern in Inner Mongolia from 2001 to 2020. *Ecol. Environ. Sci.* 33 (2), 167–179. doi:10.16258/j.cnki.1674-5906.2024.02.001

Zhang, H., He, Z., Zhang, L., Cong, R., and Wei, W. (2024). Spatial–temporal changes and driving factor analysis of net ecosystem productivity in Heilongjiang Province from 2010 to 2020. *Land* 13, 1316. doi:10.3390/land13081316

Zhang, H., Lv, X., Ni, Y., Zhang, Q., Wang, J., and Ma, L. (2025). Time-lag effects of NEP and NPP to meteorological factors in the source regions of the Yangtze and Yellow Rivers. *Front. Plant Sci.* 15, 1502384. doi:10.3389/fpls.2024.1502384

Zhang, S., Chen, H., Fu, Y., Niu, H., Yang, Y., and Zhang, B. (2019). Fractional vegetation cover estimation of different vegetation types in the Qaidam Basin. *Sustainability* 11 (3), 864. doi:10.3390/su11030864

Zheng, J., Zhang, Y., Wang, X., Zhu, J., Zhao, G., Zheng, Z., et al. (2023). Estimation of net ecosystem productivity on the Tibetan plateau grassland from 1982 to 2018 based on random forest model. *Remote Sens.* 15 (9), 2375. doi:10.3390/rs15092375

Zhi, L., Chai, Y., Sun, C., Li, R., and Hu, T. (2024). Spatiotemporal evolution and driving factors of vegetation net ecosystem productivity in Henan Province over the past 20 years. *Front. Environ. Sci.* 12, 1400425. doi:10.3389/fenvs.2024.1400425

Zhou, W., Li, J., Yue, T., Zhou, W., Li, J., and Yue, T. (2020). Research progress of the grassland carbon cycle and grassland degradation in China. *Remote Sens. Monit. Eval. Degraded Grassl. China Account. Grassl. Carbon Source Carbon Sink*, 1–16. doi:10.1007/978-981-32-9382-3_1

Zou, C., Li, H., Chen, D., Fan, J., Liu, Z., Xu, X., et al. (2022). Spatial-temporal changes of carbon source/sink in terrestrial vegetation ecosystem and response to meteorological factors in Yangtze River Delta Region (China). *Sustainability* 14 (16), 10051. doi:10.3390/su141610051

Zuo, C., Wang, J., Zhang, X., Ye, H., Wang, S., Watson, A. E., et al. (2023). Drought will constrain ongoing increase in net ecosystem productivity under future climate warming over alpine grasslands on the Qinghai-Tibetan Plateau, China. *Ecol. Indic.* 154, 110823. doi:10.1016/j.ecolind.2023.110823

Frontiers in
Environmental Science

Explores the anthropogenic impact on our natural world

An innovative journal that advances knowledge of the natural world and its intersections with human society. It supports the formulation of policies that lead to a more inhabitable and sustainable world.

Discover the latest Research Topics

See more →

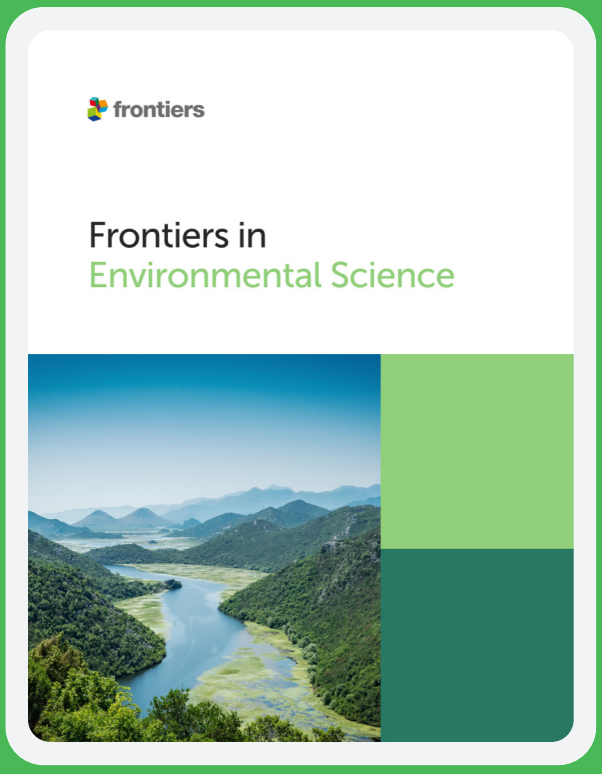

Frontiers

Avenue du Tribunal-Fédéral 34
1005 Lausanne, Switzerland
frontiersin.org

Contact us

+41 (0)21 510 17 00
frontiersin.org/about/contact